Toward Synthetic Flavoenzymes

Brian Fitzpatrick

Submitted in the fulfilment of the requirements for the Degree of Doctor of Philosophy.

October 2010

Department of Chemistry

Abstract:

The objective of this research was to develop and investigate a number of flavoenzyme model systems which were designed to mimic the microenvironment created by the natural apoenzyme's active site and which would ultimately lead to controlling the redox properties of the flavin cofactor. In natural flavoenzymes the same cofactor is known to catalyze a wide range of reactions according to the interactions involved in stabilizing the three main flavin redox states; the neutral flavin oxide Fl_{ox}, the flavin radical anion $Fl_{rad}^{\bullet -}$ and the fully reduced neutral flavin $Fl_{red}H_2$. Previous work reported within the group had focused on simple but effective small molecule solution model systems to isolate and probe these properties. This next generation of model systems employed a combination of general synthetic and polymerization techniques to firstly create synthetic flavoenzymes which were water soluble and therefore able to exist in solution phase under physiological conditions and secondly to utilize recently developed controlled molecular motion techniques as a novel method of interacting and modulating the cofactors behaviour. This thesis was therefore incorporated under two broad heading, "Polymeric flavoenzyme model systems" and "Controlled molecular motion", both of which share a common flavin theme.

Chapter 1 provides a brief introductory background to flavins, living radical polymerization (LRP) and included several examples of interlocked molecular systems which can be induced to exhibit controllable motion. Subsequently the two main themes described above were further subdivided into three to give six individual project chapters. In Chapter 2, the objective was to explore the effect of donor-atom$-\pi$ interaction and $\pi-\pi$ interaction employed by the natural apoenzyme to modulate the flavin's electrochemical and photochemical properties. In Chapter 3, the objective was to mimic the hydrophobic environment found in the active site of a natural enzyme thus facilitating conditions suitable for modulation the flavin's redox properties through hydrogen bonding. A water soluble linear PEG polymer was synthesised in order to explore the feasibility of hydrogen bonding interactions between a flavin and DAP units while cocooned within the polymer chain while under physiological conditions. In Chapter 4, we explored the novel method of modulating of the flavin's environment though a photochemical controlled molecular shuttling of a flavin-based fumaramide [2]rotaxane while similarily encapsulated within a PEG polymer chain. Irradiation of the fumaramide group with UV light @ 254nm is understood to induce it to photoisomerise to the weaker bonding malemide group resulting in a translocation of the benzylic amide macrocycle onto the flavin The effects of hydrogen bonding between flavin and macrocycle, while protected within the hydrophobic environment created by the poly(PEG) model enzyme system, would be examined electrochemically and photochemically. Finally Chapters 5 to 7 further investigate the physical characteristics of a small molecule flavin-based [2]pseudorotaxane, [2]rotaxane and [2]catenane respectively.

Analysis of the results that follow combines several chemistry disciplines such as photochemistry to study the sensitivity of the flavin's absorbance and fluorescence emission spectra in order to determine variations in the polarity of the microenvironment; ^{1}H NMR spectroscopy to provide evidence of hydrogen bonding interactions; dynamic light scattering (DLS) and size exclusion chromatography (SEC) to establish the polymer physical characteristics. The analysis also focuses predominately on the electrochemistry aspect using two common techniques; cyclic voltammetry (CV) and square wave voltammetry (SWV), to elucidate and understand the redox mechanisms involved. On occasions we have adopted a technique developed specifically for studying the electrochemistry of natural enzymes, known as protein film voltammetry (PFV), primarily to overcome some of the voltammogram distortions which resulted from slower diffusing and random orientation of these large polymer particles onto the electrode surface before electron transfer could occur. It is hoped that future readers will find some of the ideas and conclusions found within this work to have potential value.

Acknowledgements:

I would like to express my gratitude to Dr Graeme Cooke, my supervisor, for his encouragement, guidance, support and advice. His constructive comments and intuitive views have helped me to progress during this research.

My thanks go to the many research students and staff who I have met at the University of Glasgow. In particular, Dr Stuart Caldwell for the numerous feedback and suggestions during his post doc period with the group, Catherine Maclean for her support and enthusiasm within the lab and also for her "wacky" sense of humour, Jim McIver for the informative help and advise regarding various lab equipment, and Dr Jim Tweedie for the occasional "emergency" mass spectrogram.

I would also like to thank Alison, my girlfriend, for being patient and putting up with my grumpiness over that last few years.

Table of Contents:

Abbreviations:

3-21G	A Split-Valance Basis set (Molecular Mechanics)
6-31G	A Split-Valance Basis set (Molecular Mechanics)
6-31G*	A modified 6-311G Basis set (Molecular Mechanics)
ATRP	Atom Transfer Radical Polymerization.
B3LYP	A Hybrid Density Functional model (Mol Mech)
br	Broad.
bpy (or bipy)	2,2'-Bipyridine.
$CHCl_3$	Chloroform.
COSY	Correlation Spectroscopy.
CV	Cyclic Voltammetry.
d	Doublet
dd	Doublet of a doublet
DAP	Diamidopyridine
DCM	Dichloromethane.
DFT	Density Functional Theory (Molecular Mechanics)
DLS	Dynamic Light Scattering.
DMF	Dimethylformamide.
DMAP	4-(Dimethylamido) pyridine.
DMSO	Dimethysulfoxide.
$E_{1/2}$	Half wave potential.
E^{θ}	Formal potential
EDCI	1-Ethyl 3-(3-dimethylaminopropyl) carbodiimide.
EI	Electron ionization.
EtOH	Ethanol.
FAB	Fast atom bombardment.
FAD	Flavin adenine dineucleotide.
FMN	Flavin mononucleotide
GPC	Gel Permeation Chromatography.
H (or h)	Hour
HF	Hartree-Fock (Molecular Mechanics)
HOMO	Highest occupied molecular orbital.
HCl	Hydrochloric acid.
HOBt	1-Hydroxybenzotriazole hydrate.
Log	Logarithm to the base 10.
LUMO	Lowest unoccupied molecular orbital.
MeOH	Methanol.
MeCN	Acetonitrile.
mL	mille-litre
mV	mille-volt

MM.....Molecular Mechanics
$NaBH_4$ .....Sodium borohydride.
$NaHCO_3$ .....Sodium bicarbonate.
NaOH.....Sodium Hydroxide.
NEt_3 .....Triethylamine.
nm.....nanometer
NMR.....Nuclear magnetic resonance
NOESY.....Nuclear Overhauser Effect Spectroscopy.
Pd(C) .....Palladium(on carbon).
PEG .....Polyethylene glycol.
pent.....Pentet
PMDETA.....N,N,N',N',N''-Pentamethyldiethylenetriamine.
ppm.....Parts per million.
q.....Quartet
quin.....Quintet
r.t. .....Room temperature
SCF.....Self Consistent Field (Molecular Mechanics)
sept.....Septet
SWV .....Square Wave Voltammetry.
TBDMS (or TBS).....t-Butyl dimethyl silane.
TBSCl.....t-Butyl dimethyl silane chloride.
THF .....Tetrahydrofuran.
UV/Vis.....Ultraviolet/Visible light
UHF .....Unrestricted Hartree-Fock (Molecular Mechanics)
Vs^{-1} .....Volts per second
2^{nd} generation Grubbs' catalyst .....Benzylidene[1,3-bis(2,4,6-tirmethylphenyl)-2-imidazolidinylidine]dichloro(tricyclohexylphosphine)ruthenium.

Declaration:

I hereby declare that the substance of this thesis has not been submitted, nor is currently submitted in candidature for any other degree. Portions of the work described herein have been published elsewhere and are listed below.

I also declare that the work presented in this thesis is the result of my own investigations and where the work of other investigators has been used, this has been fully acknowledged within the text.

Brian Fitzpatrick.

Dr Graeme Cooke.

CHAPTER 1

INTRODUCTION.

1.1 Flavoenzymes in nature.

Flavoenzymes can be found in many living creatures from simple bacteria to humans. Their responsibilities range from electron transfer in cell membrane to regulation of neurotransmitters.[1-3] The flavoenzyme consists of two components, the apoenzyme and a redox active cofactor. The latter can be either FAD (flavin adenine dinucleotide) or FMN (flavin mononucleotide), both of which are synthesised in the body from riboflavin, also commonly known as vitamin B2. The three structures are shown below in Figure 1.1.

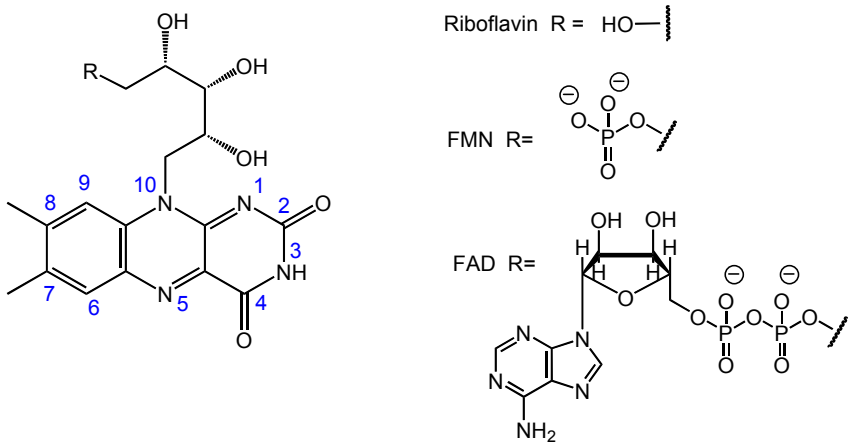

Figure 1.1 Basic 7,8-dimethyl isoalloxazine ring system, with R=OH for Riboflavin, R= -phosphate for FMN and R= phosphate-adenosine for FAD.

The enzymes use a molecular recognition system that not only orientate and noncovalently "lock" the flavin cofactor into place but also modulates its reactivity. Figure 1.2 shows some typical interactions that can occur within the *lipoamide dehydrogenase* from the small microbial *Desulfovibrio Vulgaris* flavodoxin which contains a molecule of noncovalently bound FMN.

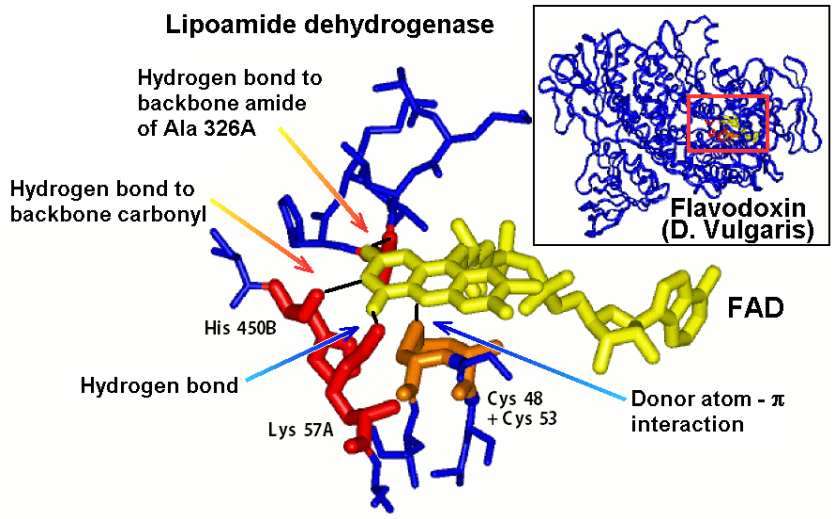

Figure 1.2 The interactions within the microenvironment of the enzyme consist mainly of hydrogen-bonding and donor atom - π stacking.

This cofactor is able to catalyse a wide variety of different reactions by employing a combination of interactions, such as hydrogen-bonding and π-stacking, to control and stabilize specific oxidation and reduction states. Since each individual effect would be impossible to isolate and examine amongst the many complicated interactions that exist within the biological enzyme system, we first need to create simplified synthetic model systems to isolate and quantify how specific interactions influence these redox states. The tools we use to probe these physical properties are mainly electrochemistry and spectroscopy (UV/visible/NMR). The structural layout of this thesis starts by looking at previous model studies that offered some insight into the controllability of the flavin's redox properties, before ultimately discussing the methods and reasons behind the synthesis and design of alternative model systems.

1.2 Modulation of the flavin's redox properties.

1.2.1 Solution phase models:

The simplest model we can use to probe the flavin's redox properties is an aprotic solution of low dielectric constant (e.g. methylene chloride, chloroform).[4] This environment mimics the hydrophobic interior of the enzyme. Flavoenzymes can control the redox pathways to allow catalysis to occur such that the flavin oxide Fl_{ox} can be reduced either directly in a two-electron process to $Fl_{red}H^-$ or sequentially via two one-electron processes involving radicals $Fl_{rad}{}^{-\bullet}$ and $Fl_{rad}H^{\bullet}$ as shown in Figure 1.3.

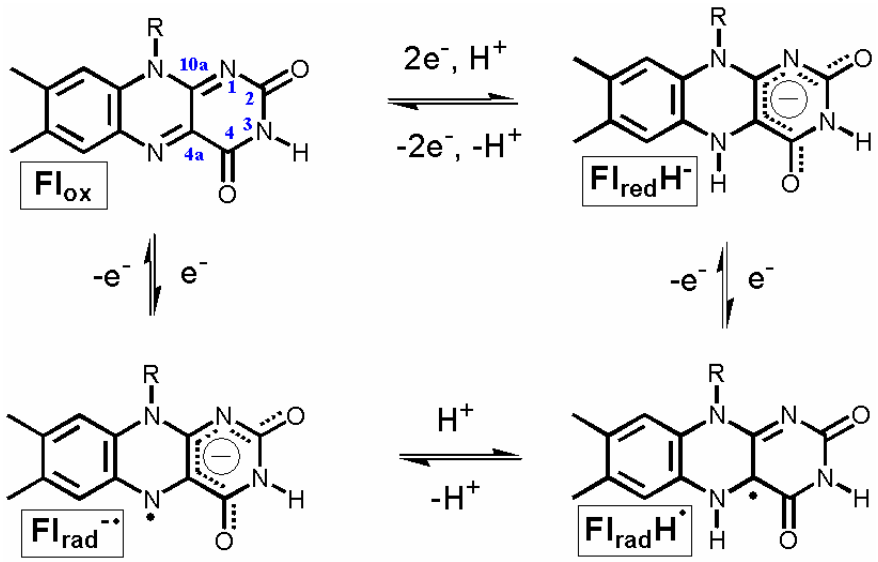

Figure 1.3 Common redox and protonation states of the flavin cofactor. (lumiflavin, R=CH_3; FMN, R=$CH_2((CHOH)_4$-phosphate); FAD, R= $CH_2((CHOH)_4$-phosphate-adenosine).

In cyclic voltammetry the potential will start at an initial potential $E_{initial}$ and increase to maximum $E_{\max}$ after rising linearly at some pre-chosen sweep rate (ν). The sweep direction is then inverted and the potential will decrease linearly until reaching some pre-chosen minimum $E_{\min}$, as shown in Figure 1.4 during a typical sweep cycle where $E_{\min} = E_{initial} = E_{final}$.

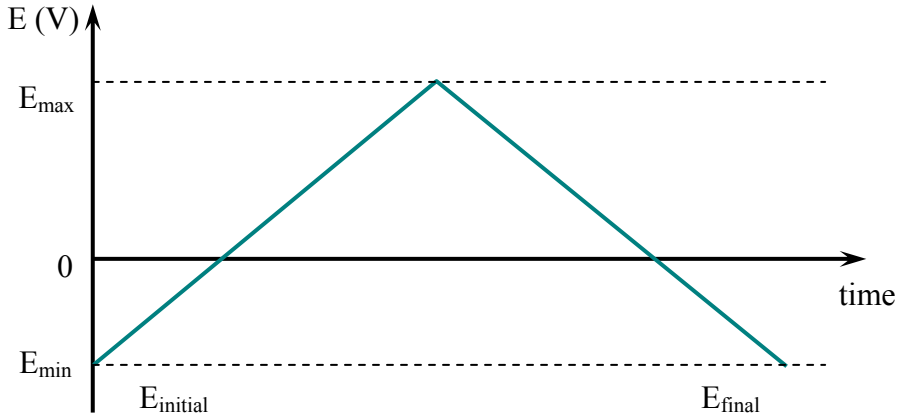

Figure 1.4 Variation of applied potential with time in cyclic voltammetry, showing initial potential $E_{initial}$, final potential E_{final}, maximum $E_{\max}$ and minimum $E_{\min}$. The sweep rate $\nu = dE/dt$.

If we examine these pathways in the aprotic media of our simple model using cyclic voltammetry (CV), we observe that during the linear increasingly negative sweep the neutral Fl_{ox} becomes reduced to the relatively stable anion $Fl_{rad}^{-\bullet}$ at the electrode as shown in Figure 1.5.

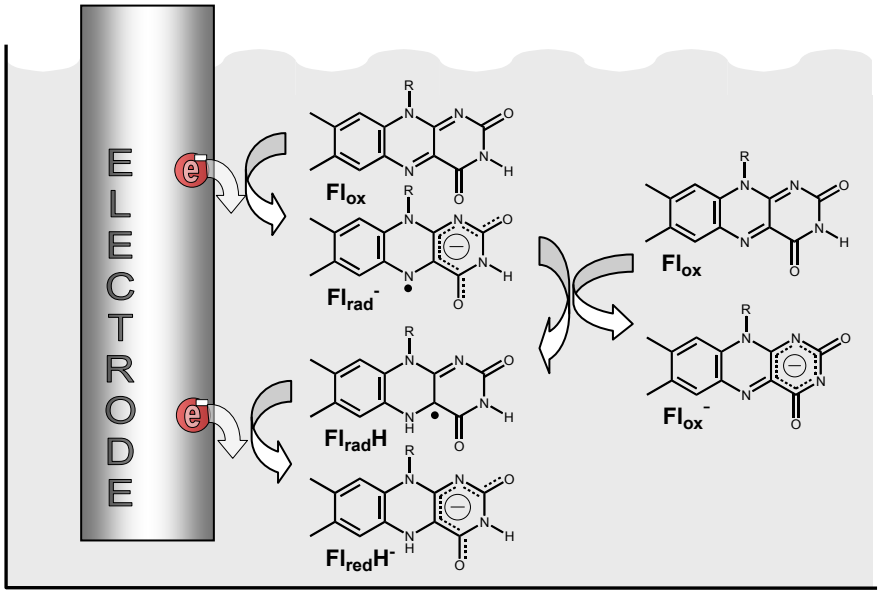

Figure 1.5 Schematic representation of the electrode-chemical-electrode (ECE) pathways for two-electron reduction of flavins in aprotic media (e.g. methylene chloride, chloroform). Revised from [5].

Addition of a 2nd electron would normally occur at a "more" negative reduction potential than Fl_{ox} as it is obviously more difficult to add another electron to an already negatively charges species. However protonation of the $Fl_{rad}^{-\bullet}$ creates the neutral radical species $Fl_{rad}H^{\bullet}$ which is now easier to reduce than the starting species. It has been shown [4] that in an aprotic solvent this proton can only come from the remaining Fl_{ox} in bulk solution as shown in Figure 1.5. The 2nd electron transfer will occur immediately after protonation and because the $Fl_{rad}H^{\bullet}$ has a "less" negative reduction potential than Fl_{ox}, the overall process gives rise to only one visible reduction wave in the cyclic voltammogram shown below in Figure 1.6 as peak I (the red/upper curve).

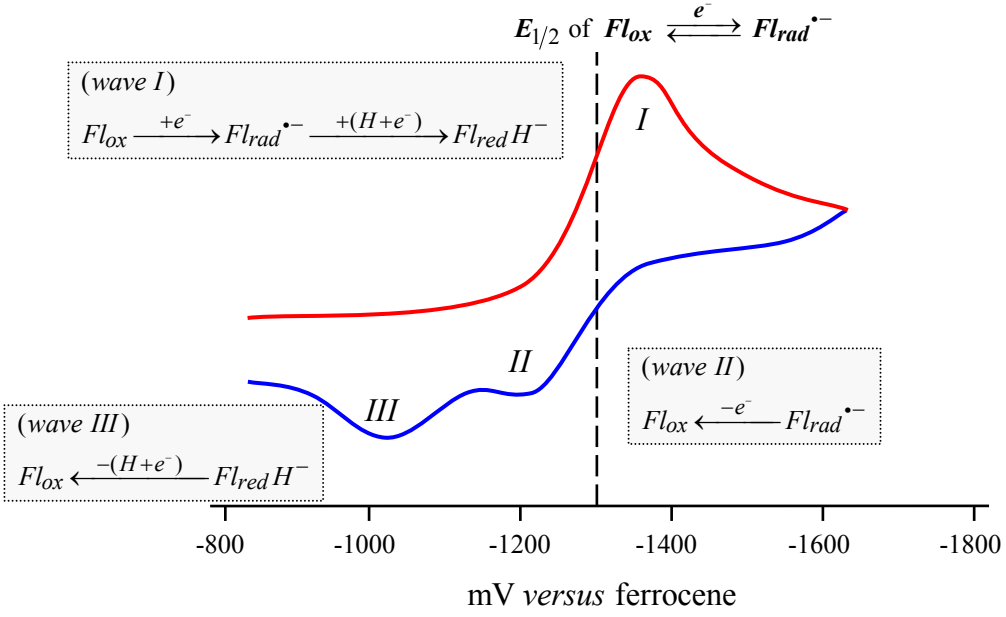

Figure 1.6 Cyclic Voltammogram of flavin **1** (Figure 1.9) consisting of the reduction wave I caused by the ECE process and two oxidation waves II and III caused by reoxidation of $Fl_{red}^{-\bullet}$ and $Fl_{red}H^{-}$, respectively. Revised from [4].

During the reoxidation phase, induced by the decreasing CV sweep, we observe two oxidation waves, one due to the oxidation of $Fl_{ox} \leftarrow Fl_{rad}^{-\bullet}$ and one at the less negative potential for $Fl_{ox} \leftarrow Fl_{red}H^{-}$ as shown by the blue/lower curve in Figure 1.6. The free energy ΔG for the reversible couple $Fl_{ox} \leftarrow Fl_{rad}^{-\bullet}$, can be directly calculated using the Equation 1.1 and the half wave potential $E_{1/2}$ between the reduction wave (I) and the first oxidation wave (II).

$$\Delta G = -nFE_{1/2} \qquad \text{(Eqn 1.1)}$$

1.2.2 Flavin charge density:

Computational calculations of the charge density of the neutral Fl_{ox} and anionic $Fl_{rad}^{-\bullet}$ forms of a trifluoromethyl flavin have been carried out using B3LYP-DFT methods.[6] This showed that the one electron reduction of the flavin increased the negative potential of the carbonyls O(2) and O(4) from –62 kJ/mol (Fl_{ox}) to –500 kJ/mol ($Fl_{rad}^{-\bullet}$) thus making them stronger hydrogen-bond acceptors. This is indicated in the electrostatic potential map shown in Figure 1.7(b) of $Fl_{rad}^{-\bullet}$ by the increased red colour at the carbonyls marked O(2) and O(4).

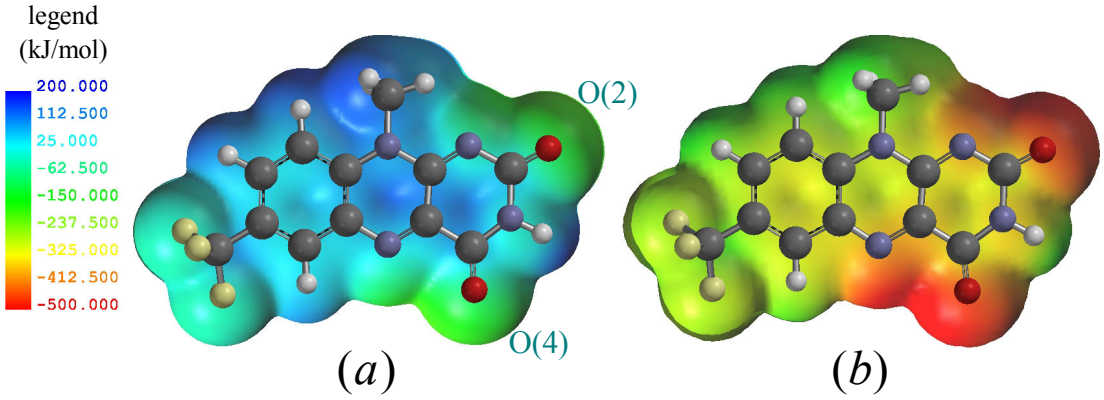

Figure 1.7 Electrostatic potential maps derived from 6-31G* B3LYPDFT//3-21G UHF calculations for a trifluoromethyl flavin in **(a)** the oxidized (Fl_{ox}) and **(b)** the radical anion ($Fl_{rad}^{-\bullet}$) forms. Revised from reference [6] where a comparative electrostatic potential maps have been calculated for lumiflavin.

However, not all electrostatic changes created favourable flavin-enzyme binding. The electron deficient aromatic framework of neutral Fl_{ox} has a positive electrostatic potential of +100 kJ/mol in contrast to the negative electronegative potential of –200 kJ/mol, thereby changing favourable attraction due to electron-rich π-stacking interactions within the apoenzyme into an unfavourable repulsion. Again this is indicated in Figure 1.7 by the central region changing from blue (a) to orange (b).

1.2.3 Modulation of redox properties through hydrogen-bonding:

The enzyme-flavin hydrogen-bonding interactions are typically similar to those found in the active site of the *lipoamide dehydrogenase* depicted below in Figure 1.8. [7]

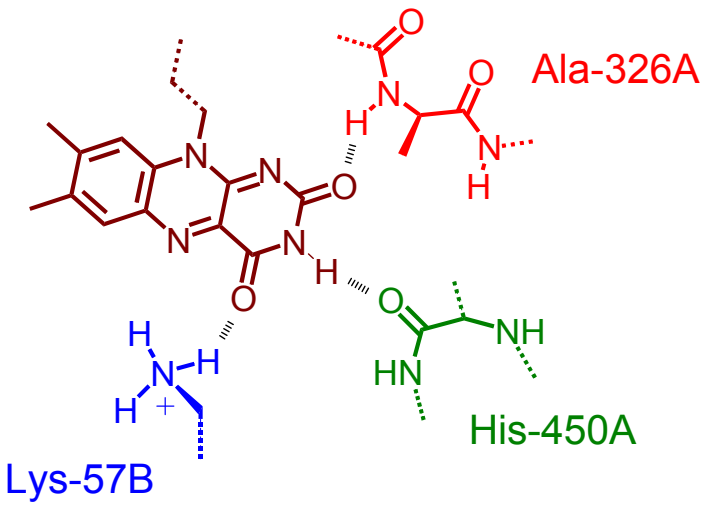

Figure 1.8 Schematic representation of the acitve site of *lipoamide dehydrogenase*.

It can be seen that the characteristic acceptor-donor-acceptor (ADA) motif of the carbonyl oxygens O(2) and O(4) and the imide proton N(3)H find a complementary binding arrangement within the enzyme framework. Synthetic analogues such as receptor **2** (Figure 1.9(a)) that are capable of replicating this complementary binding motif have been used to probe the role of these hydrogen-bonding interactions. These experiments were repeated using the control N(3) methyl flavin, shown as receptor **3** (Figure 1.9(b)), which is sterically unable to bind using this motif to receptor **2**.

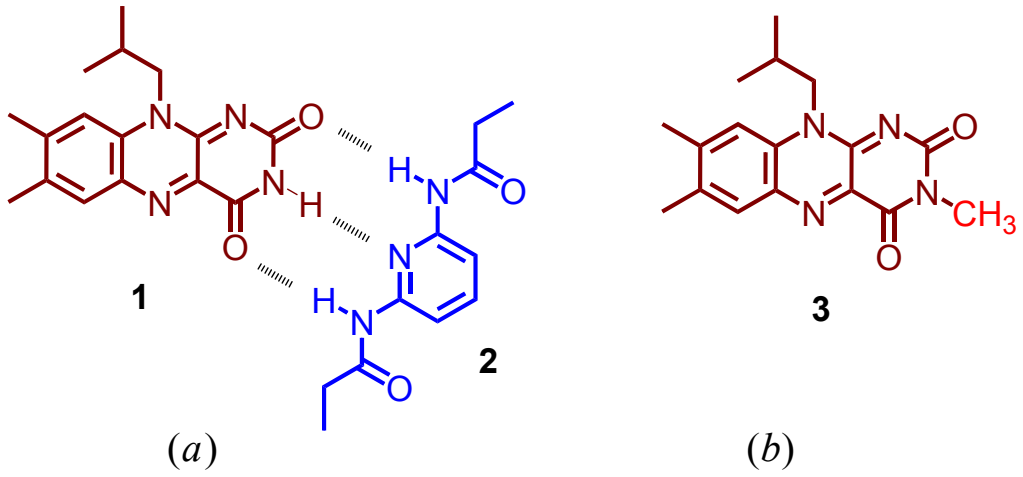

Figure 1.9 **(a).** Flavin **1** – receptor **2** complex, **(b).** the control, N(3) methyl flavin **3**.

The first step was the determination of a binding constant $K_a(ox) = 537\text{M}^{-1}$ for the receptor•Fl_{ox} complexation by plotting the ^{1}HNMR shifts of the flavin's N(3)H in $CDCl_3$ versus equivalents of the receptor added with a non-linear least-square fit of the resulting NMR titration curve to a 1:1 isotherm.. Later observation of an intramolecular NOESY cross-peak correlation between the flavin N(3)H and amide protons of the diaminopyridine (DAP) receptor supported the proposed binding geometry. [8, 9]

The next step was to determine what effect this hydrogen-bonding imposed on the redox properties of the flavin. This was carried out using cyclic voltammetry in CH_2Cl_2 and the result of adding the receptor had a two fold effects on the flavin stability.[8] It showed not only increased stabilization as indicated by a +155 mV (3.6 kcal/mol) shift in the half wave potential E½, but also during the reoxidation it showed both an increased presence of the 1st wave (II) and a reduced presence of the 2nd wave (III) compared to the free unbound flavin (Figure 1.10). An explanation of the latter is due to the receptor moiety of the flavin-receptor complex sterically suppressing the initial reduction pathway $Fl_{rad}{}^{-\bullet} \rightarrow Fl_{rad}H^{\bullet} \rightarrow Fl_{red}H^{-}$ which was previously shown to occur in bulk media (see Figure 1.5). In other word, not only was the flavin anion $Fl_{rad}{}^{-\bullet}$ easier to form but there was more of it. This change in reduction did not occur upon addition of the receptor to the control N(3) methyl flavin **3** (Figure 1.9), which is physically unable to hydrogen bond complex using this same geometry.

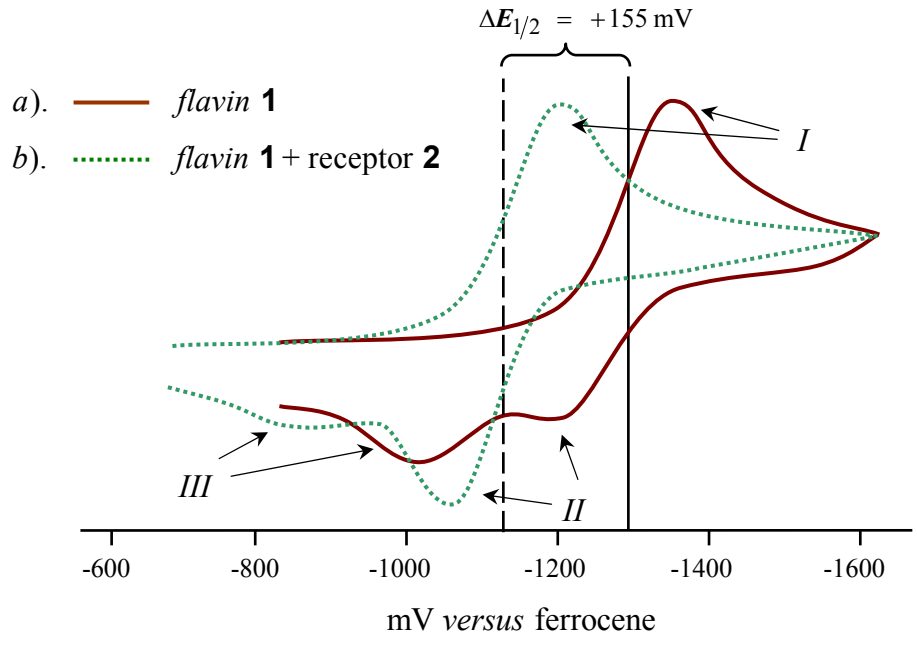

Figure 1.10 Cyclic voltammograms for (a) flavin **1** and (b) the flavin **1**-receptor **2** complex showing the single reduction wave (I) and the two oxidation waves corresponding to reoxidation of $Fl_{rad}{}^{-\bullet}$ (II) and $Fl_{red}H^{-}$ (III). Revised from [4].

1.2.4 Calculation of free energy ΔG

It was discovered during these electrochemical studies that near maximal shift (155 mV) started to occur at receptor concentrations at which only 22% of the neutral flavin Fl_{ox} would be bound.[4] This means that after reduction of $Fl_{ox} \rightarrow Fl_{rad}^{-\bullet}$ the binding had substantially increased (i.e from 22% to almost 100%). This agreed with the computational studies that predicted increased charge density on the carbonyl oxygens O(2) and O(4), hence making them stronger hydrogen acceptors.

The Rotello group were able to quantify this enhanced receptor recognition using the thermodynamic cycle (Figure 1.11) and Equation 1.2 to calculate $K_a(red)$ from the experimentally derived $K_a(ox) = 537\ \text{M}^{-1}$ and both half wave potentials, $E^1\!/_2(unbound) = -1297$ mV and $E^1\!/_2(bound) = -1142$ mV.

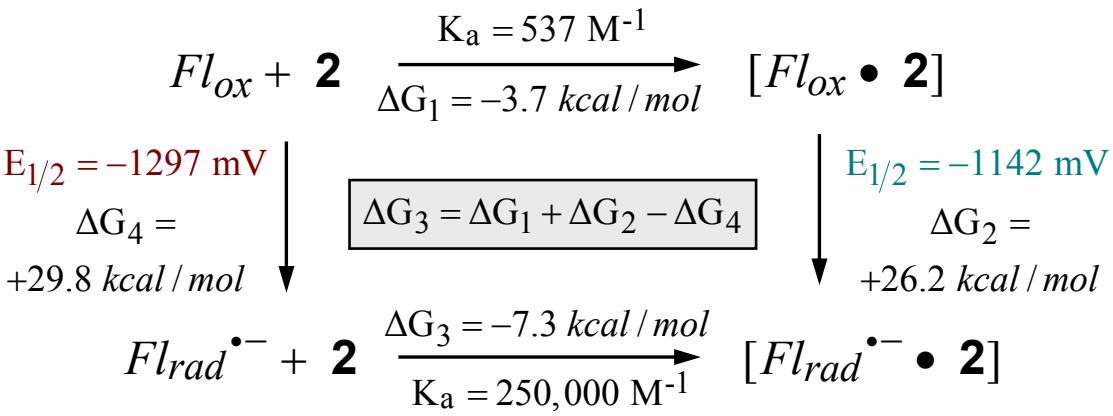

Figure 1.11 Thermodynamic cycle quantifying radical anion-receptor recognition.

Equation 1.2 determined that binding of the receptor to the flavin increased almost 500 fold upon reduction of $Fl_{ox} \rightarrow Fl_{rad}^{-\bullet}$.[4] ΔG_1 has been calculated from the Gibbs equation $\Delta G = -RT \ln K_a$ ($1\ cal = 4.184$ J). ΔG_2 and ΔG_4 have been calculated from Equation 1.1. (i.e., $\Delta G = -nFE_{1/2}$). ΔG_3 is equal to the vector sum of the free energy acquired or expended via other pathways i.e. ($\Delta G_1 + \Delta G_2 - \Delta G_4$) as shown in Figure 1.11.

$$\text{E}_{1/2}(bound) - \text{E}_{1/2}(unbound) = \frac{2.303RT}{nF} \log\left(\frac{K_a(red)}{K_a(ox)}\right) \qquad (Eqn\ 1.2)$$

rearranging..

$$K_a(red) = K_a(ox) \times 10^{\left(\frac{n\Delta \text{E}_{1/2}}{58\ \text{mV}}\right)} \quad \text{at 293 K}$$

therefore..

$$K_a(red) = 537 \times 10^{\frac{+155\ \text{mV}}{58\ \text{mV}}} \simeq 250{,}000\ \text{M}^{-1}$$

1.2.5 Unfavourable π -stacking following the $Fl_{ox} \rightarrow Fl_{rad}^{-\bullet}$ reduction.

The position of the flavin cofactor in many flavoenzymes is typical of that shown in Figure 1.12. as being flanked on both side by an aromatic dyad such as tryptophan/tyrosine or tryptophan/methionine. [10] Mutation studies have demonstrated the importance of Try98 in its involvement in both redox modulation as well as stabilization of the neutral flavin. [11, 12]

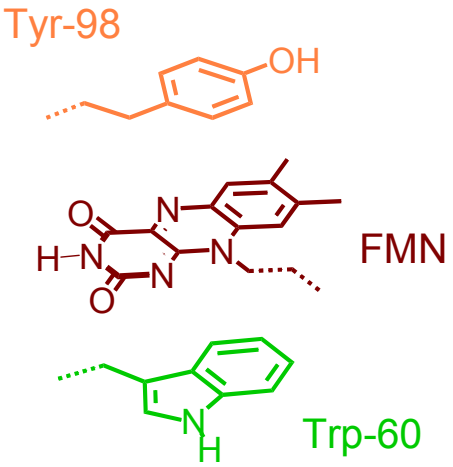

Figure 1.12 Aromatic residues flanking the flavin cofactor in the FMN binding site of a *Desulfovibrio Vulgaris* flavodoxin. Revised from [10].

The effect of this π -stacking of the flavins redox behaviour has been explored using a series of xanthene based receptors (**6a-c**) as shown in Figure 1.13. [13]

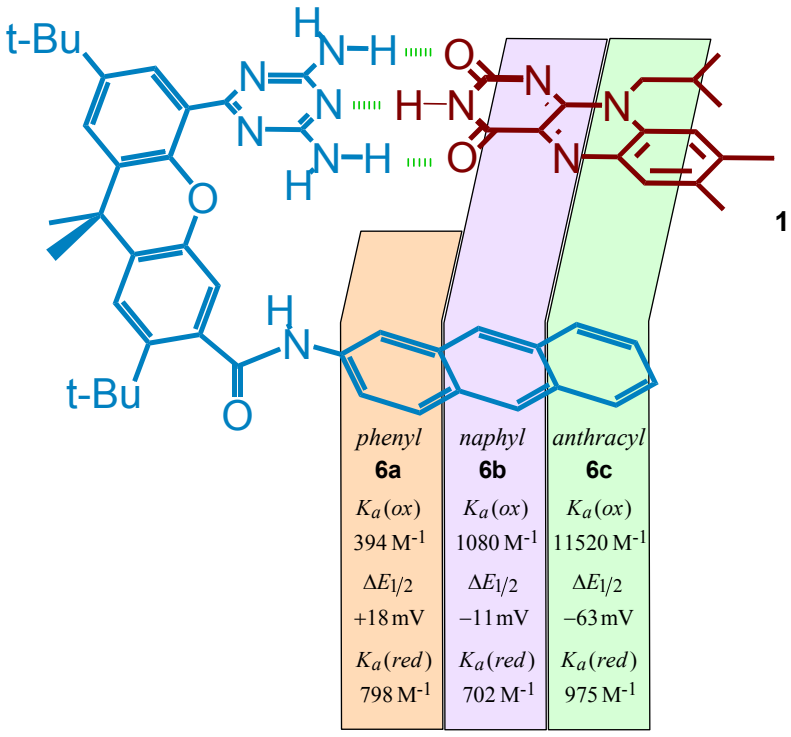

Figure 1.13 Molecular modeling structure of the flavin **1**•receptor **6** complex and thermodynamic constants for host-guest binding. Revised from [13].

These receptors provided a rigid scaffold that permitted the arrangement of each recognition element to be orientated in the correct geometry. The triazine group at the top provides the complementary hydrogen-bonding motif while simultaneously positioning the aromatic face of the flavin above the receptor's lower aromatic substituents. The π-stacking interaction was confirmed using UV/visible spectroscopy. As predicted a progressive decrease in fluorescence emission was produced by increasing π-overlap. It was found that this developed into almost complete quenching with the anthracenyl receptor **6c**. Using the control N(3) methyl flavin, no quenching was observed again due to the flavin's inability to form complementary hydrogen-bonding. NMR titration experiments carried out on these three receptors shown in Figure 1.13, with neutral flavin Fl_{ox}, revealed that the association constant K_a, increased by up to 44 fold as the result of favourable π-stacking interactions, an equivalent ΔG change of –22 kcal/mol.

However only the phenyl receptor produced a less negative (favourable) shift in the cyclic voltammogram, following reduction $Fl_{ox} \rightarrow Fl_{rad}^{-\bullet}$, but even then this was only an 18mV shift. This was accompanied by an enhancement of the reversible reoxidation wave (peak II in Figure 1.10). Both the shift and peak enhancement ultimately result in increased stabilization of the ($Fl_{rad}^{-\bullet}$ • receptor **6**) complex.

Although increased π-stacking interactions help to stabilize the neutral Fl_{ox} with the other two receptors, they have an adverse effect on the formation and stability of the reduced radical anion $Fl_{rad}^{-\bullet}$. First, the π-stacking produces a more negative shift in the CV half wave potential $E_{1/2}$ by as much as –81 mV resulting in a ΔG change of up to 1.5 kcal/mol which ultimately makes flavin **1** harder to reduce. Secondly, as predicted by previous computational studies, the electron-rich aromatic system of the $Fl_{rad}^{-\bullet}$ results in mutual repulsion between the receptors aromatic substituents. Therefore although there is an increase in the complementary hydrogen bonding between $Fl_{rad}^{-\bullet}$ and receptor **6**, this increase is offset by the unfavourable π-stacking repulsion. Overall this manifests as much lower association constant K_a, with in the case of receptor **6c** has dropped from 11,520 M^{-1} for Fl_{ox} to only 975 M^{-1} for $Fl_{rad}^{-\bullet}$.

1.2.6 The effect of donor atom interaction.

The proximity of electron-rich donor atoms such as oxygen and sulphur can be found close to the aromatic face of the flavin cofactor with some variants of flavoenzyme such as the cysteine disulphide found in *Pseudomonas fluorescens* lipoamide dehydrogenase as shown below in Figure 1.14. [7]

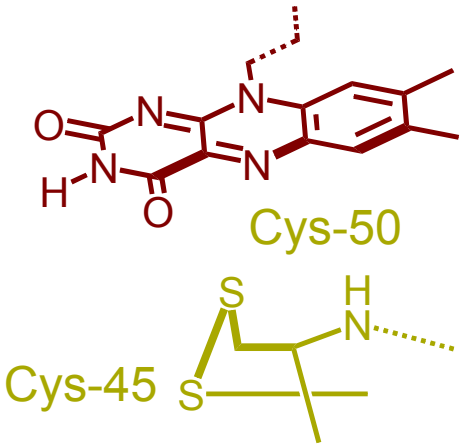

Figure 1.14 Flavin binding site of *Pseudomonas fluorescens* lipoamide dehydrogenase. [7]

The effect of "donor atom $-\pi$ interaction" was probed using the same xanthene scaffold structure as adopted previously. This structure was used to position a series of five differing functional groups in close proximity to the lower aromatic face of flavin **1**, as shown in Figure 1.15. [4]

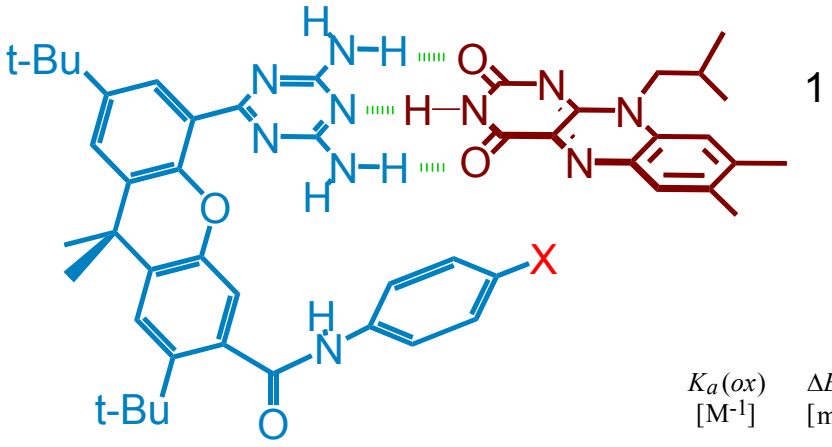

		$K_a(ox)$ [M^{-1}]	$\Delta E_{1/2}$ [mV]	$K_a(red)$ [M^{-1}]
7a	X = F	2,910	9	4,100
7b	X = Br	3,500	-3	3,100
7c	X = OCH_3	2,210	8	3.000
7d	X = SCH_3	4,830	11	3,100
7e	X = CH_2CH_3	960	23	2,400

Figure 1.15 Flavin **1**-receptor **7** complex and thermodynamic constants for host-guest binding. Revised from [4].

Although donor atom series was limited and included an ethyl group as a control, these experiments determined, generally, that the efficiency of the donor atom $-\pi$ interaction with neutral flavin Fl_{ox} was directly correlated to both the size and the polarizability of the donor atom. Using the table shown in Figure 1.15, we can roughly compare $K_a(ox)$ within this donor atom series. Bromine is the largest atom but its $K_a(ox)$ value falls second to the sulphur atom which has a higher polarizability. As predicted by computational studies, the reduction of $Fl_{ox} \rightarrow Fl_{rad}{}^{-\bullet}$ resulted in unfavourable π-interactions, but the overall effect this reduction has on the association constant K_a depends on the balance between these unfavourable interactions and the increased complementary hydrogen bonding. The table in Figure 1.15 depicts the thiomethoxy receptor **7d** as the most adversely affected with K_a falling from 4830 M^{-1} (Fl_{ox}) to 3100 M^{-1} ($Fl_{rad}{}^{-\bullet}$).

1.3 Atom Transfer Radical Polymerization (ATRP).

1.3.1 Mechanism of ATRP.

ATRP (atom transfer radical polymerisation) was the technique employed during the synthesis of all polymeric flavoenzyme model systems described within this thesis. It is a simple and extremely efficient technique that has proven itself over the last two decades in the production of controlled or living polymers with a wide variety of architecture and functionality. [14] As with all types of polymerization there are three main stages, initiation, propagation and termination. The initiator can take the form of a radical, a cation or an anion. These act as electron transferring agents, which after contact with a specific monomer transform it into a new radical species. This is the start of propagation stage and the polymer will grow as it comes into contact with other monomers up to a point where the final stage termination occurs. This happens when the terminal end of the polymer is neutralized either by another radical or the electron is transferred to a solvent molecule or some reactive impurity. The key step to this controllability is the abstraction of a (pseudo)halogen by a transition metal catalyst, from the initiator (or dormant polymer chain) to create a radical. Only in this active state can the polymer propagate or self-terminate with other growing polymer radicals and by alternating between this state and the more predominate dormant state (i.e. halogen capped) is it able to avoid classical termination and exhibit its so-called "living" propagation character, Figure 1.16.

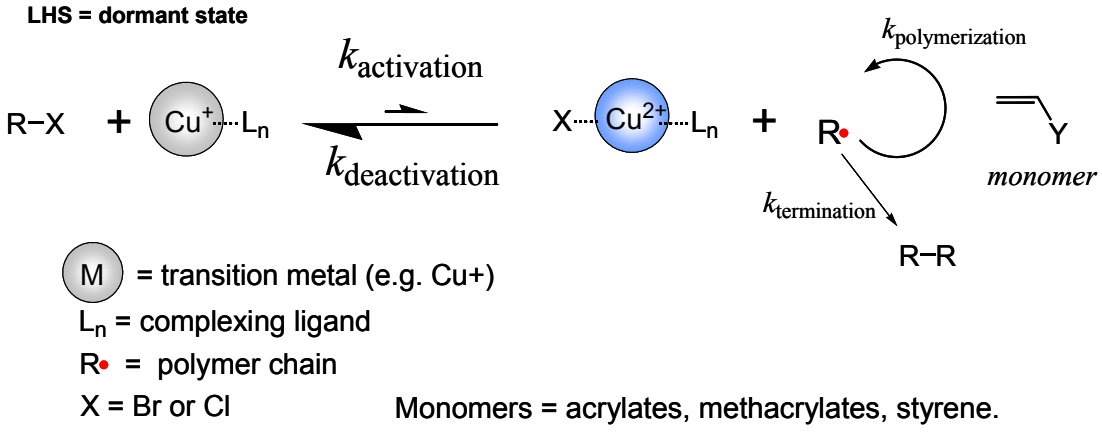

Figure 1.16 Initiation and propagation stages of ATRP.

Because of this "living" character, the molecular ratio of monomer to initiator sets the theoretical average polymer molecular weight.

$$\text{theoretical MWt} = \text{MWt of monomer} \times \frac{\text{N}^{\text{o}}\text{ moles monomer}}{\text{N}^{\text{o}}\text{ moles initiator}}$$

The degree of polymerization (DP) can also easily be predicted as ….

$$D.P \propto \frac{[Monomer]}{[Initiator]} \qquad \text{(Eqn 1.3)}$$

Polymerization can be a random uncontrolled process where polymer strands can have a wide distribution of chain lengths and molecular weight, not to mention the numerous possibility of branching. This distribution in molecular weight is generally described by the polydispersity index (PDI) which is defined as the ratio of $M_W : M_n$ (where M_W and M_n are statistical variations defined as the weight and number average molecular weights: see Equation 1.7). Living polymerization offers some scope of control of the propagation (and termination) with the result that distribution of molecular weights will be narrow (comparison shown in Figure 1.17) and the PDI will generally fall between $1.0 < M_W/M_n < 1.5$.

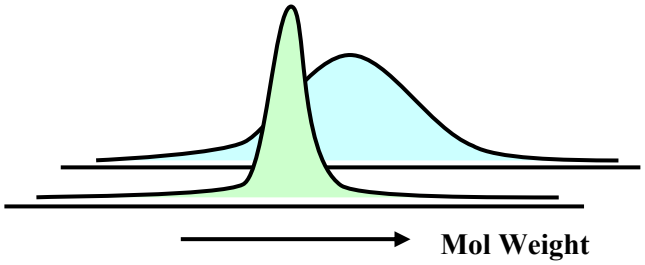

Figure 1.17 Distribution of molecular weight represented by the polydispersity index (PDI). A broad distribution will have a high PDI and a narrow distribution will have a low PDI.

In our reported experiments the ratio monomer to initiator was typically set at 100:1. The transition metal used was copper in the form Cu(I)Cl, which is insoluble in most solvents including water. The solubility was improved in the polymerisation media by forming a copper complex with commonly used bipyridyl ligand (i.e. 2,2-bipyridine). The main role of the Cu(I) complex is the generation of radicals via atom transfer. However in a series of experiments reported by the Matyjaszawski group, [15] they discovered that Cu(I) actually played no part in the deactivation of the radical. This exclusive role was carried out by any Cu(II) complex that was created during the reaction. They also reported that the addition of $Cu(II)X_2$ to catalyst Cu(I)X in a ratio of 1:9 (or 0.1:0.9 equivalents per initiator) played a vital role in both lowering the polymerisation rate and more importantly the polydispersity index of the final polymer (note: X=halide, Cu, Br, etc.).

The Haddleton group [16] provided further insight into the transfer mechanism that occurs during ATRP and described how the methacrylate monomer exchange with the pyridinyl ligand of the Cu complex may be driven by a chelation effect involving functional groups of the monomer. The example shown in Figure 1.18, show how this might occur between the ester and amine groups of DMAEM (dimethylamino ethyl methacrylate). Interestingly within the ATRP experiments performed within this thesis, polymerization of DMAEM monomer required the shortest reaction time and lowest temperatures. Furthermore, following a number of attempts involving the synthesis of anionic water soluble polymers (further details of which will not be reported in this thesis), it was in due course realized that the inability of specific methacrylate monomers to chelate could also explain the huge difference in polymer yield, {e.g. under identical conditions poly(MMA) yield was $< 1\%$ whereas poly(NMGly) yield was $> 80\%$ }.

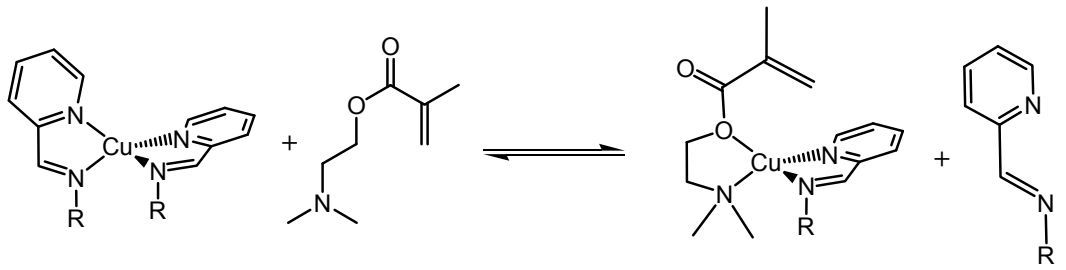

Figure 1.18 Proposed equilibrium involving the chelation effect of the DMAEMA/N-propyl 2-pyridylmethanimine/copper(I).complex

Matyjaszewski [17] later suggested a plausible situation involving (pseudo)halide abstraction, in which the tetrahedral copper complex is transformed into a trigonal bipyramidal cationic Cu(I) structure as shown in Figure 1.19. Presumably monomer-ligand exchange described by Haddleton can occur just as equally before or after this event. In the latter case the radical will be in the proximity of the next monomer both immediately after activation and/or just before deactivation. In either case the copper ion appears to act as a template during polymerisation.

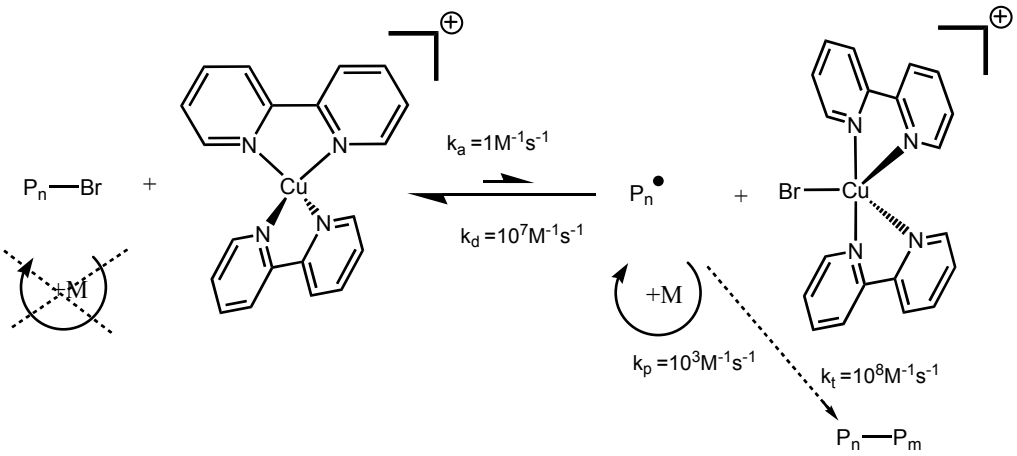

Figure 1.19 Showing the alkyl halide and the transition metal species Mt^n reversibly form alkyl radicals and $X - Mt^{n+1}$ species.

1.3.2 Definition of "living" radical polymerization (LRP).

One of the ultimate aims of adopting the ATRP method was the synthesis of polymeric model system with uniformity in their molecular weights. Achieving this would depend on maintaining the radical polymerizations "living" characteristic. A "living" radical polymerization is generally accepted as displaying the following features, [18] all of which will be used to verify the degree of "living" character exhibited during the experimental work within this thesis.

a). First order kinetic behaviour.

b). Pre-determined degree of polymerisation (DP).

c). Narrow molecular weight distribution.

d). Long lived polymer chains.

1.3.3 First order kinetic behaviour:

This implies the rate of polymerisation (or rate of monomer consumption) R_p with respect to the monomer concentration $[M]$ will be a linear function of time. We base this rationale is on the absence of termination (i.e. the propagating species $[P^*]$ remains constant) as shown in the proportionality equation below.

$$Rp = \frac{-d[M]}{dt} \propto [M]\times[P^*]$$

By rearranging and inserting a propagation constant k_p we obtain …

$$\frac{-d[M]}{[M]} = k_p[P^*]dt$$

and then by integrating to provide Equation 1.4 …

$$\int_{M_0}^{M} \frac{-d[M]}{[M]} = k_p[P^*]\int_0^t dt$$

$$= \ln\frac{[M_0]}{[M]} = k_p[P^*]\,t \qquad \text{(Eqn 1.4)}$$

The key attribute of Equation 1.4 is that plot of $\ln([M_0]/[M])$ versus t will be linear for LRP as shown in Figure 1.20. Any variation from linearity will be an indication that the in concentration of $[P^*]$ is no longer constant and that polymerization reaction is losing its "living" characteristic. An upward curve would indicate an increase in $[P^*]$ which could possibly be the result of slow initiation. A downward curve would indicate a decrease in $[P^*]$ and could possibly be due to either termination increasing the persistent radical concentration,

the catalytic system becoming poisoned or some redox processes affecting the radical. The disadvantage of this plot is that it gives no indication of processes that can modify the propagating species such as chain transfer process. This problem is remedied by the next feature.

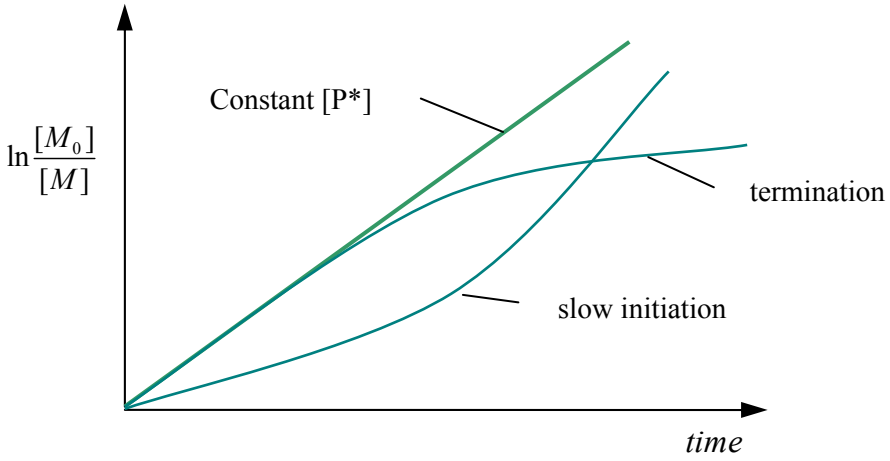

Figure 1.20 Plot showing the dependence of the natural $\log M_0/M$ *vs time*. The slope is equal to the rate of polymerization k_P times the propagating species concentration $[P^*]$. If $[P^*]$ remains constant the slope should be linear.

1.3.4 Pre-determined degree of polymerisation (DP):

The degree of polymerization (DP) is defined as …

$$DP = \frac{\text{monomer conversion}}{\text{initiator conc}^n} = \frac{[M]_0 - [M]_t}{[I]_0} = \frac{\Delta[M]}{[I]_0} \qquad \left(= \frac{[M]_0}{[I]_0} \quad as \quad [M]_t \to 0 \right)$$

where $[M]_0$ is the monomer concentration at the start (time $t = 0$), $[M]_t$ is the monomer concentration after reaction time t, and $[I]_0$ is the initiator concentration at the start.

also....

$$DP = \frac{polymer\ MWt}{monomer\ MWt} = \frac{M_n}{M_m} \qquad therefore \qquad \frac{M_n}{M_m} = \frac{\Delta[M]}{[I_0]}$$

rearranging....

$$M_n = \left(\frac{M_m}{[\mathrm{I}]_0} \right) \bullet \Delta[M] \qquad \text{(Eqn 1.5)}$$

Therefore a plot of M_n versus monomer conversion $\Delta[M]$ similar to that shown in Figure 1.21 will produce a straight line so long as the following conditions apply.

1). All chains start to grow simultaneously (fast initiation)

2). No chain transfer
No termination
No coupling
} i.e. **the number of chains stays constant**

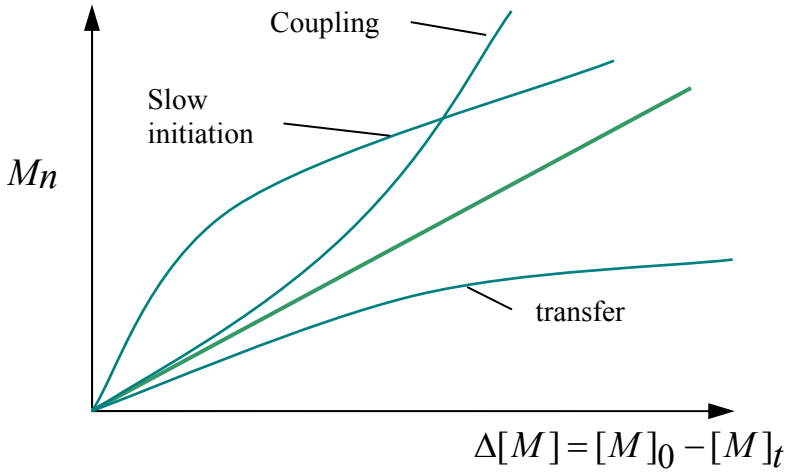

Figure 1.21 Plot showing the dependence of M_n *vs* ΔM. The slope is equal to M_m/I_0 and provides a measure of the changing degree of polymerization (DP).

Coupling between high molecular weight polymers results in a rapid rise increase in the molecular weight M_n. This is presented in Figure 1.21 by an upward curve and can be due to polymer-polymer termination but cross-coupling mechanisms are more likely. Slow initiation is an effect cause when not all initiators become actively engaged with the catalytic system simultaneously. Those initiated polymers receive an unequal share of the monomers at the start and therefore grow at a higher than predicted DP. However the overall monomer consumption is slow as there are less propagating species. As the other initiators become available and there is an increase in monomer consumption (i.e, overall polymer growth increases). This becomes represented on the plots as a downward curve in Figure 1.21 and as an upward curve of the $\ln([M_0]/[M])$ *vs time* plot previously shown in Figure 1.20.

1.3.5 Narrow molecular weight distribution:

Although not strictly a pre-condition reserved for "living" polymerization, we can verify the narrow molecular weight distribution by calculating the polydispersity index (PDI). This is shown in Equation 1.6 as equal to…

$$PDI = \frac{M_w}{M_n} \tag{1.6}$$

where M_w and M_n are statistical averages of the molecular weight distribution calculated according to the Equations 1.7.

$$M_n = \frac{\Sigma N_i M_i}{\Sigma N_i} \qquad \text{and} \qquad M_w = \frac{\Sigma N_i M_i^2}{\Sigma N_i M_i} \tag{1.7}$$

The PDI can be influence by a number of polymerization properties such as of rate of initiation, exchange and depropagation all of which can lead to unavoidably higher than expected values.

1.3.6 Long lived polymer chains:

This is an ability of all polymer to retaining there active centre after full consumption of the all monomers. There must be negligible chain transfer and termination. Ultimately the test for this in our set experiments will be to successfully carry out a two step ATRP process and synthesise diblock copolymers.

1.4 Controlled Molecular Motion.

The concept of a machine operating at the molecular level was derived through the numerous examples of biological systems found in Nature, such as proton pumps and ion gates. The energy required to control these molecular machines can be electrochemical, chemical, photochemical or thermal. [19-22] The common component that these machines employ is the making and breaking of non-covalent reversible bonds. Catenanes and rotaxanes are non-covalently bonded, multi-component molecules that have potential applications in switching devices or molecular machines. Fraser Stoddart and co-workers [23, 24], who initiated most of the initial pioneering work with these basic molecular machines, based their original strategies on charge transfer (CT) and $C-H\cdots O$ hydrogen bonding interactions to design molecular models that could adopt one of two metastable positions along a straight length molecular axle. By using bulky "stopper" groups or a combination of interlocked rings these molecules are designed so that their sub-molecular components have restricted degrees of freedom. The non-covalent bonds between intermolecular components allow mutual rearrangement while still conferring stability to the system. This stability is determined by the strength of individual intermolecular interaction which has the potential to be modulated upon application of some external stimulus. Controlled molecular movement can be both linear and rotational. A linear translation is the most commonly implemented motions of the molecular machine concept and is commonly referred to as "shuttling".

An important criteria for the many variations on the rotaxane architecture is the ability to easily induce and detection of translation motion. The attraction of the flavin rotaxane is that it is bulky enough to act as one of the two stoppers required along the axle but also its appealingly tuneable electrochemical properties, three point hydrogen bonding motif and its easily detectable spectroscopic properties. Both catenane and rotaxane utilize a non-covalently attached benzylic amide ring shown in Figure 1.23(c) as the second or [2] component. This was self-assembled around either the succinamide or the fumaramide stations of the flavin macrocycle and axle respectively, by means of the template mechanism first described by Leigh. [25]

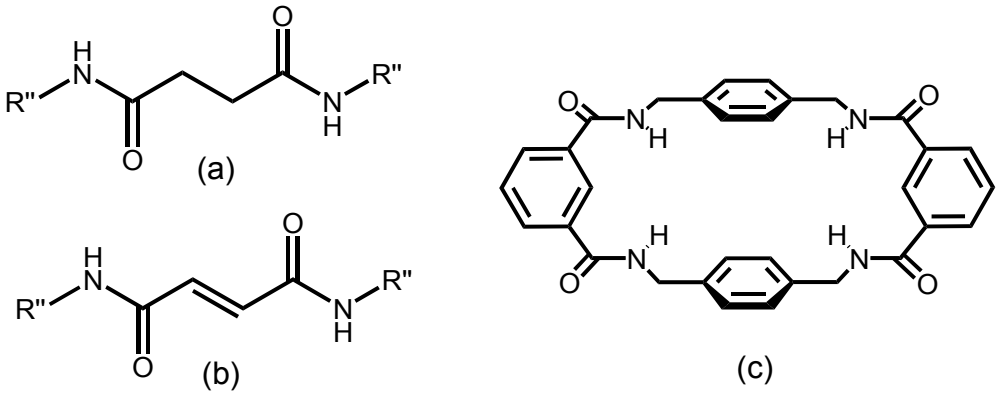

Figure 1.23 (a). The succinamide station, (b). The fumaramide station, and (c). the benzylic amide macrocycle.

The flavin catenane, rotaxane and pseudo-rotaxane to be described within this thesis incorporate two stations. In the case of the larger macrocycle of the [2]catenane these stations comprised the dicarbonyl of a electroactive flavin unit and a succinamide group shown in Figure 1.23(a). The axle of the [2]rotaxane, and [2]pseudorotaxane, also incorporate the electroactive flavin unit but the second station became a fumaramide group shown in Figure 1.23(b). The benzylic amide ring for the pseudorotaxane was synthesised separately using a method similar to that described by Leigh and which involved an easily dissembled temporary axis template. Investigation into the history of the benzylic amide macrocycle provides a better understanding of the conditions required in optimizing yield.

1.4.1 The benzylic amide (BA) macrocycle: Leigh's CO_2 trap.

The Leigh group, while under British Gas funding to develop chemical sensors for small gas molecules [25, 26] used molecular modelling software to identify the benzylic amide macrocycle as a potential molecular receptor for CO_2 as shown in Figure 1.24.

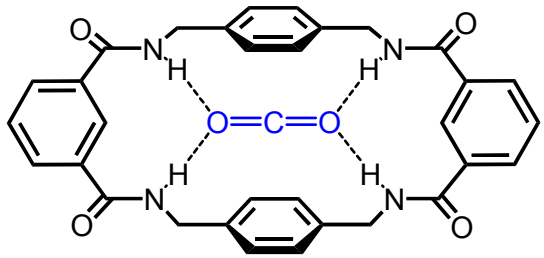

Figure 1.24 The benzylic amide macrocycle with CO_2.

Synthesis of the molecule was attempted by a direct [2 + 2] condensation of equimolar quantities of isophthaloyl dichloride and p-xylylenediamine in a solution of NEt_3 and $CHCl_3$. The ^1H, ^{13}C NMR's and low resolution (EI) mass spectrum were as anticipated for the single compound that formed but the macrocycle was unable to complex with CO_2. It wasn't until an X-ray crystal structure was obtained that they realized they had actually synthesised a [2]catenane shown in Figure 1.25.

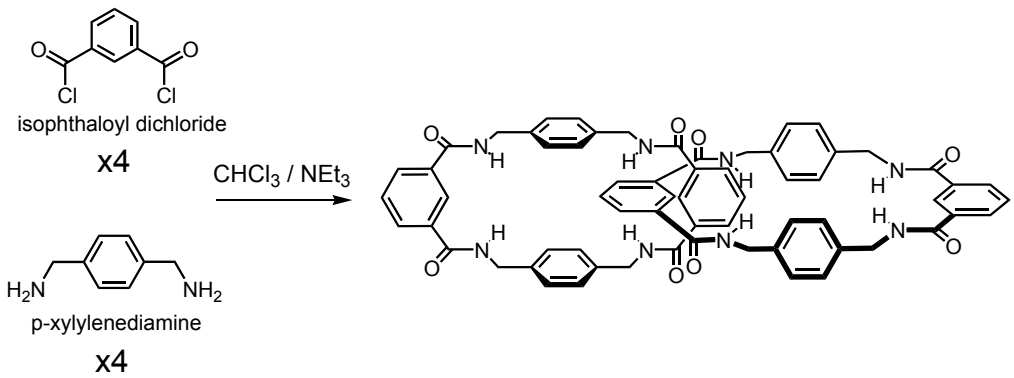

Figure 1.25 One step, eight molecule condensation synthesis of the benzylic amide [2]catenane.

Introducing larger molecules into the reaction that contained multiple hydrogen binding stations such as the fumaramide or succinamide groups allowed the synthesis of numerous variations of [2], [3] and even up to [4] component benzylic amide catenanes and rotaxanes. Like any good pioneer, Leigh provided a list of "do's and don'ts" to avoid failure, most notably, the explicit use of a dry, low dielectric solvent (i.e. $CHCl_3$) stabilized with amylenes (not ethanol). Leigh reported in the same initial paper that if the solvent either wasn't dried or contained trace ethanol, then by-products would form from partial hydrolysis of the starting acid chloride and that these would be difficult to remove. Amylenes are added to chlorinated solvents as stabilizers to prevent phosgene gas formation. Ethanol is a common alternative to amylenes(used ~100ppm) and for the reasons mentioned above must be avoided.

Since benzylic amide [2]catenane formation is competitive with any succinamide or fumaramide component present, maximum yield of the principal rotaxane/catenane would occur when the corresponding axle or ring was in excess and this would happen when it was both completely dissolved and at the beginning of the reaction. The building blocks of the benzylic amide (BA) ring (*isophthaloyl dichloride* and *p-xylylenediamine*) would need to be added gradually to minimise the concentration build up of BA ring precursor (Figure 1.26a) and the likelihood of BA**:**BA ring closure. This could be achieved by adding these two compounds simultaneously at a dropwise rate using a motor driven syringe pump.

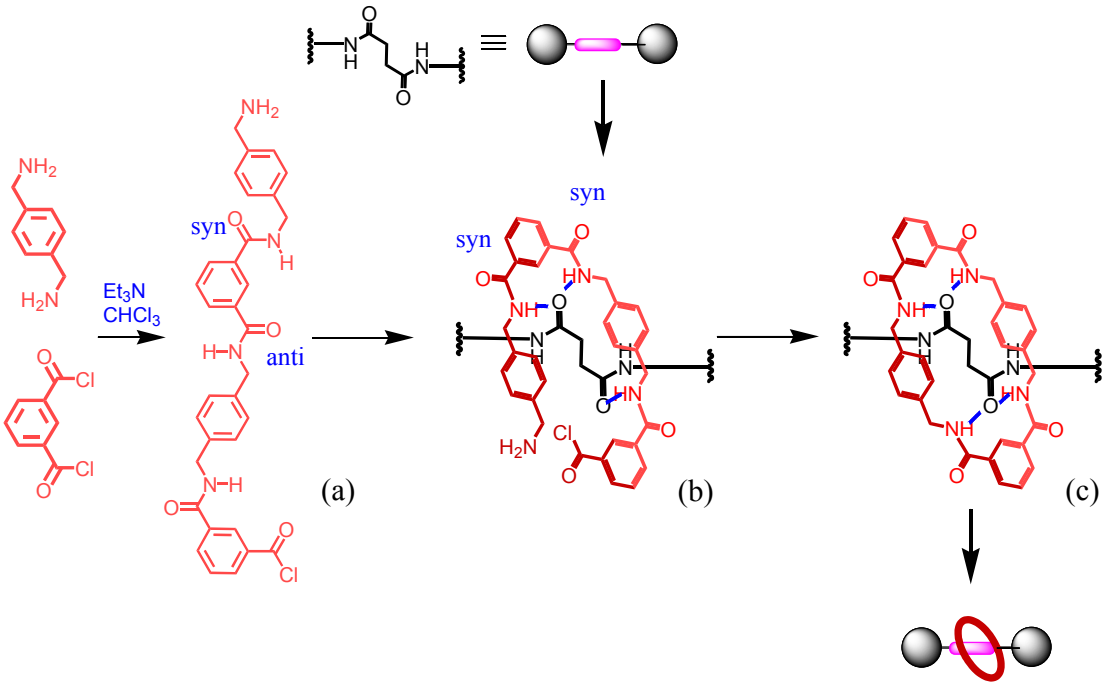

Figure 1.26 Mechanism of interlocked ring closure between benzylic amide intermediate precursor and the succinamide axle. Figure **(a)** shows the rings linear precursor with *syn-anti* conformation **(b)** shows the precursor with *syn-syn* conformation and **(c)** shows final benzylic amide ring closure.

1.4.2 The dramatic influence of preorganized binding sites.

The intermediate precursor to the formation of the benzylic ring previously shown in Figure 1.26a, will preferentially adopt a linear conformation with the 1,3 diamide unit favourably arranged in a *syn-anti* orientation. [26] This effectively hold the two reactive ends spatially far apart, resulting in a long lived structure that is more likely to dimerize than undergo intramolecular ring closure. Under rotaxanes-forming reaction conditions, the precursor and axle form multiple hydrogen bonds that promote the *syn-syn* conformational changes that bring the amide and acid chloride into close proximity. The additional interactions between the binding sites second carbonyl and the precursor ensure efficient rotaxanes formation as they hold one or both ends in the appropriate position allowing for rapid ring closure and the desired interlocked product, Figure 1.26b.

However the succinamide axle possesses several degrees of freedom. This flexibility means that it can adopt the hydrogen bonding stabilized seven membered ring shown in Figure 1.27. This conformation leads to less favourable hydrogen bonding interactions between the axle and precursor mentioned above but it also would suggest that a more rigid fumaramide axle would allow a more efficient rotaxanes synthesis. This was indeed shown by Leigh to be the case during the reported synthesis of a fumaramide rotaxanes with a remarkable 97% yield. [27]

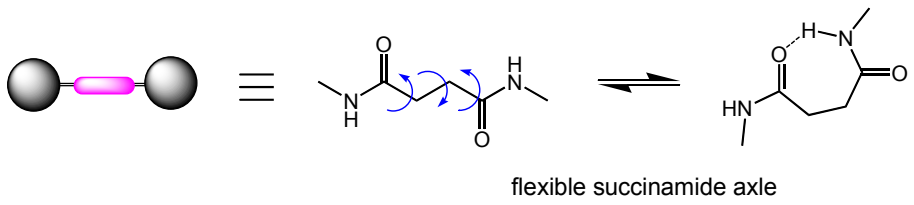

Figure 1.27 Mechanism of interlocked ring closure between benzylic amide intermediate precursor and the succinamide axle.

This pre-organization of the fumaryl axle allowed Leigh's group to demonstrate the significance of the amide groups, which act as excellent hydrogen bond acceptors, (hydrogen-bond basicity, β_2^H, typically ~0.66). [28, 29] Amongst common functional groups, this level of hydrogen-bond basicity is only is only exceeded by groups with pronounced mesomeric or ionic character (N^+-O^-, S^+-O^-, P^+-O^-, etc.). [30] This pre-organization effect was so effective at enhancing the template effect for the benzylic amide ring formation that it allowed even weaker hydrogen bond acceptors to generate the interlocked rotaxane architecture. Although the di-ester (Figure 1.28) produced a very modest yield of 3%, the fact that this reaction occured at all in an entropically unfavourable five component assembly process in the presence of significantly stronger hydrogen-bond acceptors such as amide, amines and halides (eg. NEt_3^+ and HCl^-) was unexpected. Rotaxane formation was also possible in the experimental work carried out in this thesis using a solvent mixture of 10% DMF in chloroform. Yields as high as 50% were achieved using this very polar mixture but a procedure which was necessary due to the insolubility of the relevant axis in non-polar solvent.

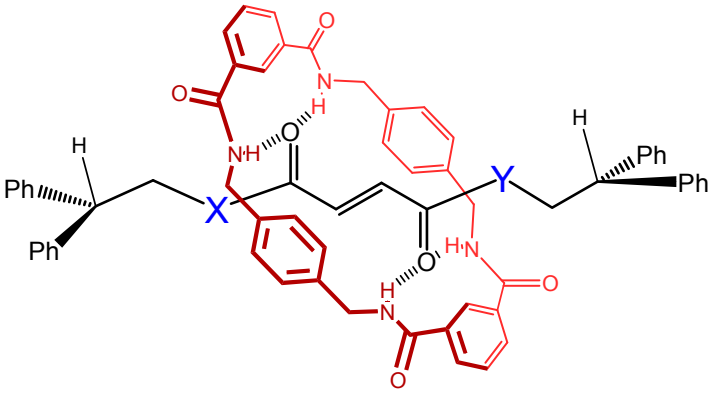

Figure 1.28 Rotaxane formation through the preorganized, rigid fumaryl-based hydrogen bond template.

1.4.3 Translational control through reversible covalent chemistry.

The Diels-Alder (DA) reaction is a well-documented procedure which involves the simultaneous formation of two new C-C bonds across an alkene. The cyclic addition of a diene and a dienophile equilibrates in favour of the new cyclo-adduct, but under the appropriate conditions it can also undergo a reversible reaction with a conservation of stereochemistry. These procedures were performed by Leigh and co-workers [31] who successfully used them to demonstrate reversible chemical translocation of the BA macrocycle.

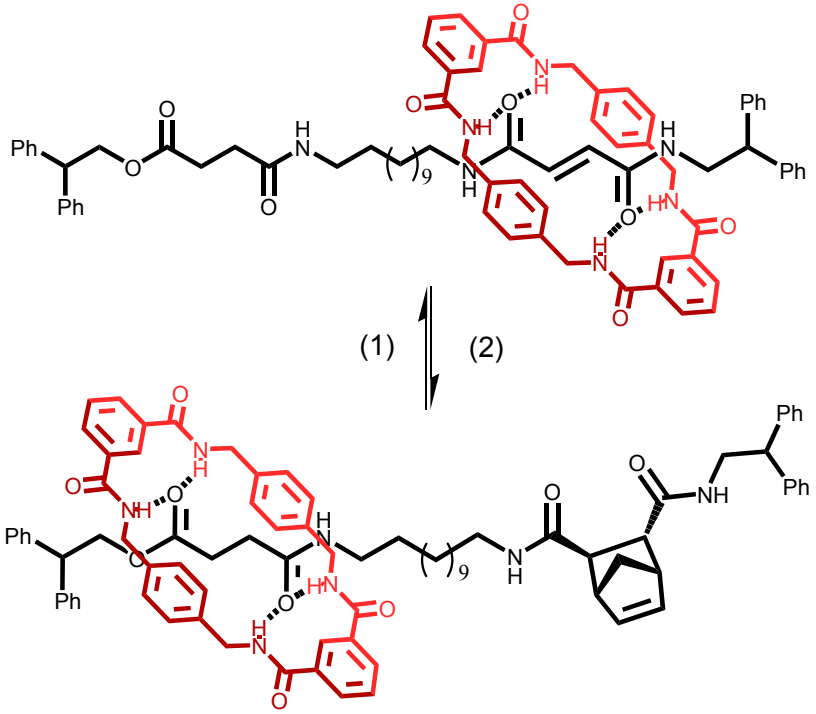

Figure 1.29 The Benzylic amide ring discriminates between a more favourable binding position of the fumaramide compared to the weaker binding succinamide ester station. However after sterically blocking the fumaramide station with the DA reaction the benzylic amides ring translocates to the succinamide ester station.

The double bond of the fumaramide axle offers up the possibility of utilizing the DA reaction to trigger a shift in position of the benzylic amide ring of the rotaxanes. Addition of a diene to the fumaramide station would change both it hydrogen bonding geometry as well as increasing its steric bulk. The combined effect would thus alter the binding preference of the benzylic amide ring towards the previously less favoured station of a [2]rotaxane. If a diene such as cyclopentadiene is used then the retro-Diels-Alder (r-DA) can easily be accomplished the cyclopentadienes evaporation under high temperature and low pressure. Together the DA and r-DA provide an interesting method of inducing reversible but well defined positional changes of the benzylic amide ring along the fumaramide rotaxane axle ad depicted in Figure 1.29.

1.4.4 Photo-switchable molecular shuttle.

Photo-isomerization of the fumaramide to its maleamide isomer can be used to switch 'off' the strong complementary binding match with the benzylic amide ring by adopting the geometrically less favourable conformation shown in Figure 1.30. The fumaramide alkene can be made to flip from trans to cis when exposed to UV light of 245 nm for 30 mins in CH_2Cl_2 to give yields varying from 40-55% or UV light of 350 nm with benzophenone for 5 mins in CH_2Cl_2 to give yields from 60-65%. The maleamide can then be converted back to the thermodynamically more stable fumaramide isomer by heating at 120°C for 1-7 days in $C_2H_2Cl_4$ to give 85-95% yields. [32]

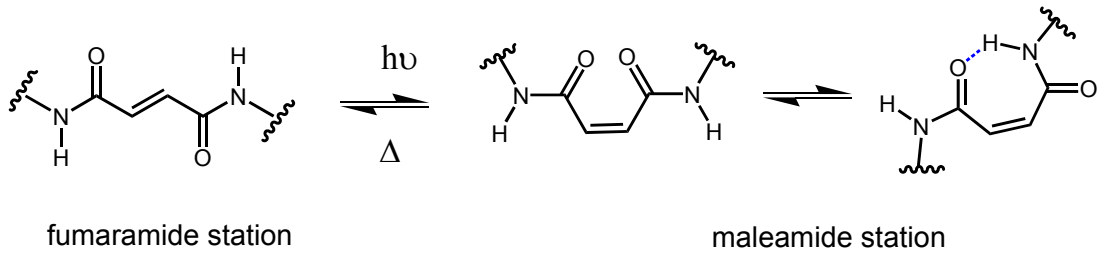

Figure 1.30 The photochemical E → Z conversion of the fumaramide alkene and the reverse process of thermal Z → E conversion. The malamide station is able to undergo self-binding (seven memebered ring system) that weakens further any interaction between the interlocked benzylic amide ring.

Irradiation of the trans-fumaramide to the cis-maleamide results in the maximum possible hydrogen binding sites with the benzylic amide ring changing from four to two. By incorporating more than one binding site on the rotaxane axle as the dicarbonyl of the flavin shown below in Figure 1.31 it was possible to generate photoinduced, thermally reversible translation of the rotaxane components. [31] By switching "off" the strongest binding station the benzylic amide ring was shown to "shuttle" across the axle to the unoccupied second station. This method of translocation relied solely upon modifying the intrinsically weak, non-covalent binding modes between the two interlocked components. No other reagents are introduced to alter the positional discrimination of the system.

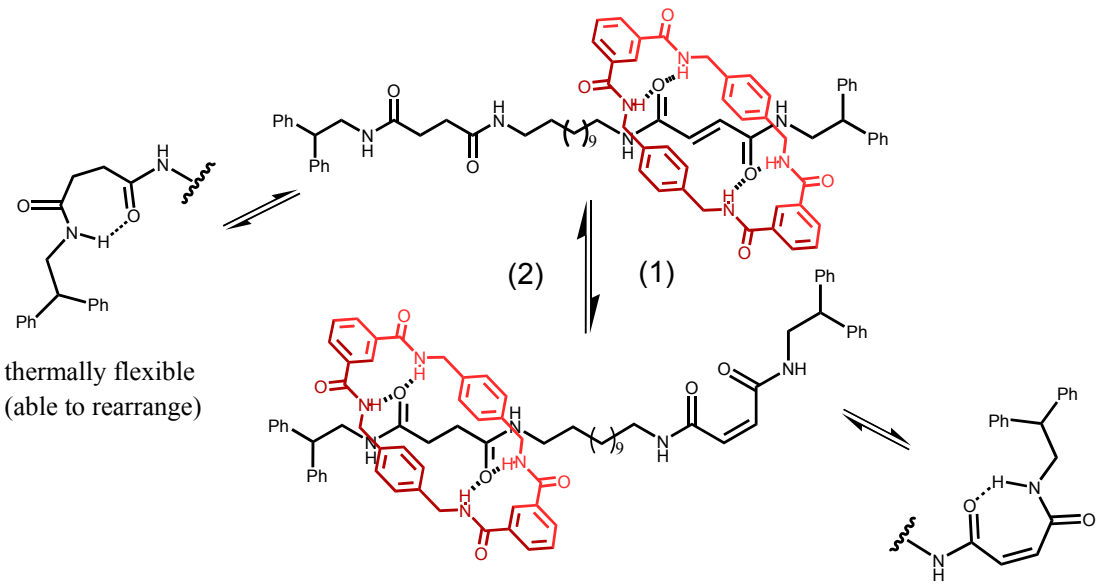

Figure 1.31 The Benzylic amide ring has been shown to reside over the fumaramide station compared to the succinamide station with occupancy ratio greater than 95% (experimental limits). This was believed to be primarily due to the fumaramides inability to undergo self-binding in comparison to the flexible succinamide station. **(1).** This role is reversed when the fumaramide is converted to its cis-isomer by irradiation with UV light 254nm, CH_2Cl_2. 30 min. **(2).** The process can be reverted by heating or a reversible Michael addition reaction (catalytic ethylenediamine, 60°C, 4h, 75-85%). Revised from [32].

CHAPTER 2

COPOLYMER FLAVOENZYME MODEL SYSTEMS.

2.1 Synthesis.

2.1.1 Copolymer synthesis strategy.

The flavin copolymer synthesis followed the two step Atom Transfer Radical Polymerisation (ATRP) procedure shown in Figure 2.1. The mechanism of ATRP is described in Chapter 1 (Section 1.3) and specific synthesis details can be found in the Experimental section, Chapter 8. The first step would be to produce a hydrophobic monoblock polymer tethered to a single flavin unit. This monoblock polymer would be synthesise from one of the seven different monomer types depicted in Figure 2.2, each one selected according to the unique electron donating/withdrawing ability provided by their respective pendant functional group. The basic concept behind linking the flavin directly to a hydrophobic polymer unit was that it would be readily positioned to become encapsulated within a solvatophobic constrained polymer units. This was achieved by converting a N(10)-hydroxyhexyl flavin into an alkyl halide to afford compound **C-1**, a common procedure used to create a variety of ATRP initiators and which has previously been reported within the Cooke group. [33]

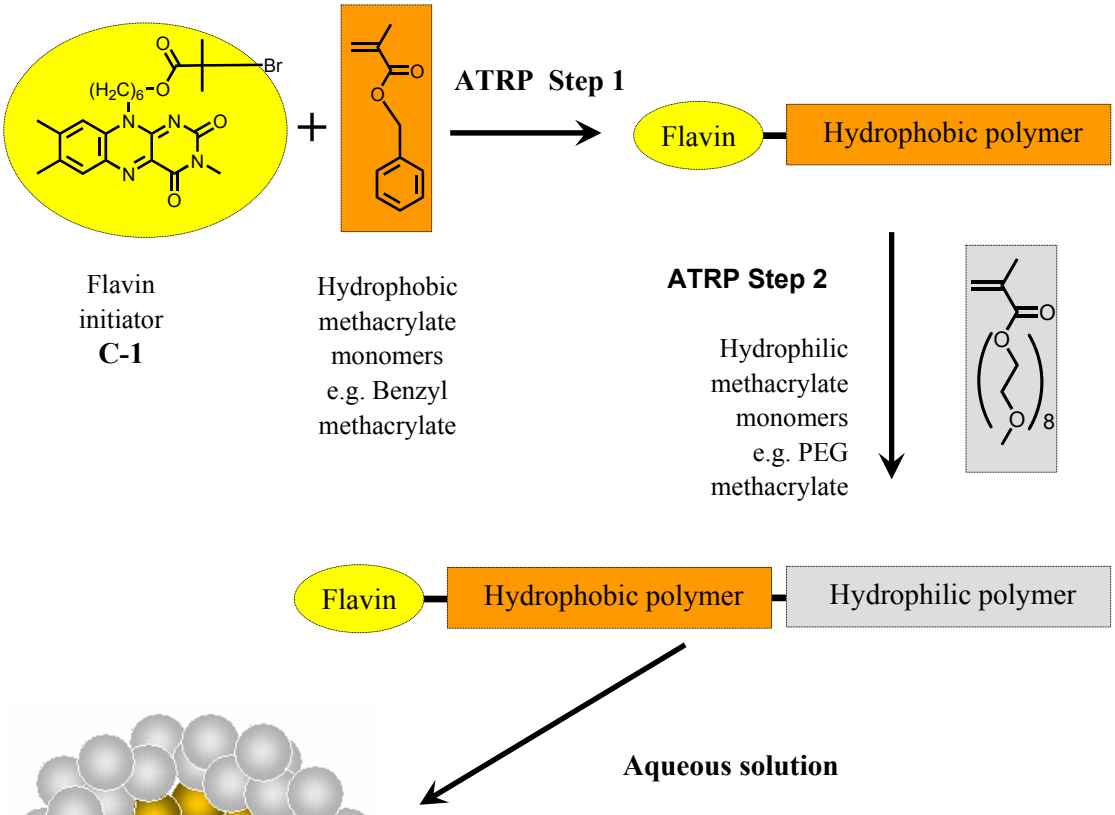

Figure 2.1 ATRP copolymer synthesis using a flavin initiator with hydrophobic monomers (**Step 1**) to create a monoblock hydrophobic polymer. This was subsequently used in **Step 2** as a macroinitiator during synthesis of the water soluble copolymer. In aqueous media the hydrophobic forces would encapsulate the flavin unit within the interior created by the hydrophobic block.

The monoblock polymer produced from this first step became the macroinitiator for the second ATRP reaction (**Step 2**, Figure 2.1) and it was therefore crucial that the percentage of "dead" polymers (due to uncontrolled termination) was kept to minimum. We achieved this through the controlled "living" radical polymerization capacity of ATRP combined with early controlled termination (i.e. keeping yield < 85%). The second step afforded the hydrophilic block of the copolymer and was synthesised during these experiments using the non-ionic poly-ethylene glycol (PEG) methacrylate monomers. The hydrophobic block of the copolymer had been incorporated to impart water solubility to the entire unit. Dynamic Light Scattering (DLS) experiments used to measure the particle size of these polymers in solution provided confirmation that they were constrained by the solvatophobic effect, (see Section 2.2.3).

2.1.2 Building blocks for the hydrophobic monoblock polymers:

Seven hydrophobic monoblock polymers were synthesised using the hydrophilic methacrylate monomers shown in Figure 2.2. These were selected from a range of commercially available methacrylates based on the potential electron withdrawing and electron donating properties of their respective pendant groups. Only one of these monomers was not commercially available, 1-naphthalenemethyl methacrylate **C-8**. Its obvious rich aromatic properties were considered important for these investigations and it was therefore specifically synthesised. Synthesis is provided in the Experimental section, Chapter 8.

Note: Polymers synthesised from 2-(dimethylamino) ethyl methacrylate (DMAEM) are generally water soluble due the amphiphilic nature of the monomer. However in aqueous solution, it would seem more realistic that the hydrophobic flavin unit would prefer to remain buried within the organic environment created by the DMAEM polymer unit.

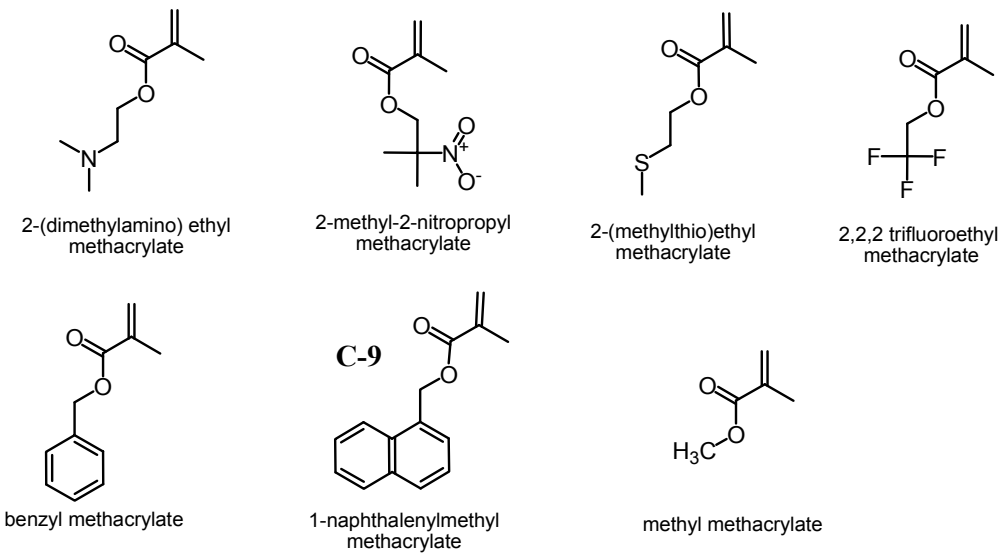

Figure 2.2 The seven methyl methacrylate monomers used to synthesise the hydrophobic monoblock polymers. 1-naphthalenemethyl methacrylate **C-9** was not commercially available and was therefore specifically synthesised.

Throughout this chapter we have adopted an abbreviated terminology when referring to each specific mono and diblock polymer. For example, to avoid continuously rewriting the long version of the flavin-polymers name (i.e. flavin poly(benzyl methacrylate)) or a traditional mnemonic compression of the polymer name (i.e. poly(BMA)) we have adopted the following "short name" version shown in Table 2.1, deeming it more instantly intuitive in recognizing the specific polymers pendant group.

Monomer	Corresponding polymer's "short name"
benzyl methacrylate	**Benzyl**
2,2,2 trifluoroethyl methacrylate	**CF3**
2-(dimethylamino) ethyl methacrylate	**DMAEM**
methyl methacrylate	**Methyl**
1-naphthalenylmethyl methacrylate	**Naphth**
2-methyl-2-nitropropyl methacrylate	**Nitro**
2-(methylthio)ethyl methacrylate	**Thio**

Table 2.1 Polymer "short names" that correspond to each of the monomers types shown in Figure 2.2.

2.1.3 Synthesis of flavin ATRP initiator:

Full synthesis details can be found in the Experimental section, Chapter 8. The following scheme shown in Figure 2.3 is a short summary of the synthesis of the flavin ATRP initiator **C-7**.

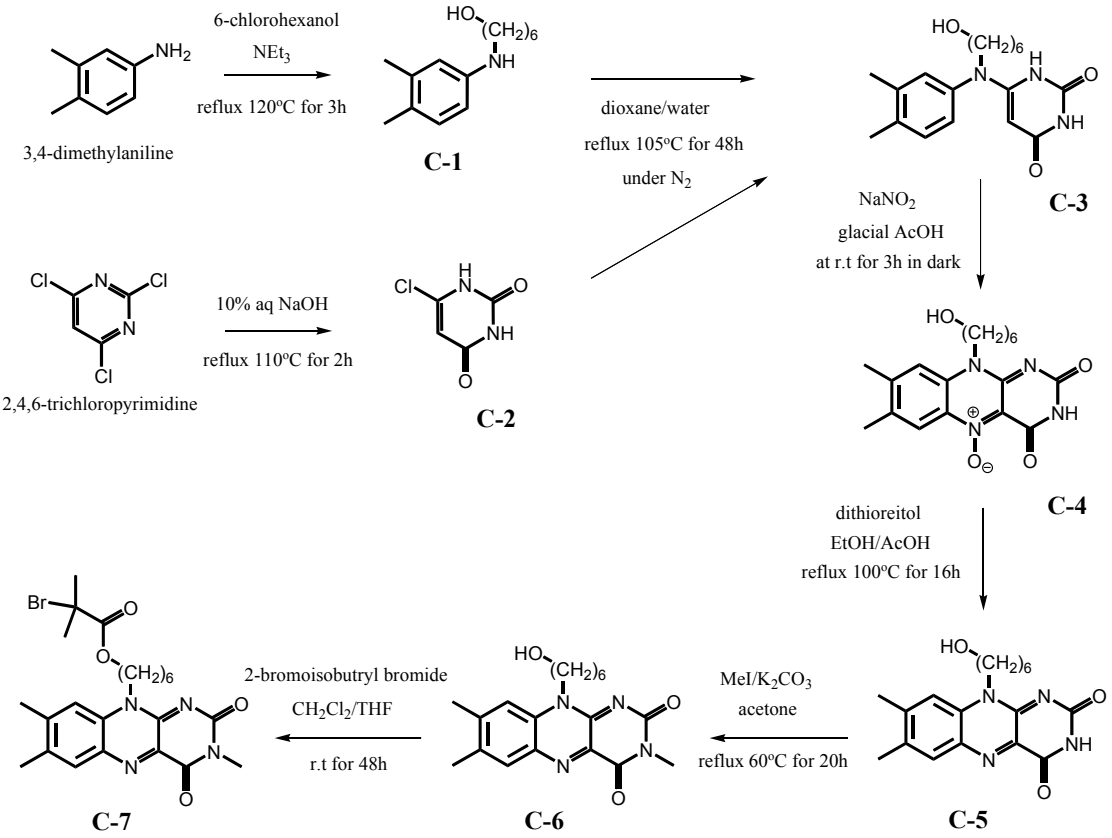

Figure 2.3 Synthetic scheme for the flavin ATRP initiator **C-7**. Compound **C-1** commercially available 3,4-dimethylaniline, heating under reflux under non-solvent conditions with 6-chlorohexanol and triethyl amine. Compound **C-2** was provided from commercially available 2,4,6-trichloropyrimidine after heating under reflux in 10% aq NaOH. Compounds **C-1** and **C-2** were heated under reflux in dioxane/water for 2 days to afford uracil **C-3**. Sodium nitrite was added to **C-3** in glacial acetic acid while kept under dark conditions and stirred for 3h at r.t before assign water. The N-oxide product **C-4** was reduced using dithioreitol and heating under reflux at 100C for 16h in ethanol/acetic acid to afford the hydroxylhexyl flavin **C-5**. The N(3) amide of the flavin was methylated using iodomethane in acetone to afford **C-6**. Finally the alkyl halide ATRP initiator **C-7** was provide at r.t following acylation of the flavin hydroxyl group with 2-bromobutryl bromide.

2.1.4 Synthesis of mono and diblock polymers:

There are many procedural similarities carried out during the synthesis of both mono and diblock polymers. It would therefore seem less confusing and better for quick comparison to describe the general ATRP procedure utilized. The scheme for the synthesis of the hydrophobic monoblock copolymer is depicted in Figure 2.4(a). This monoblock polymer would later be employed as a macroinitiator shown in Figure 2.4(b), during the synthesis of the PEG block copolymer.

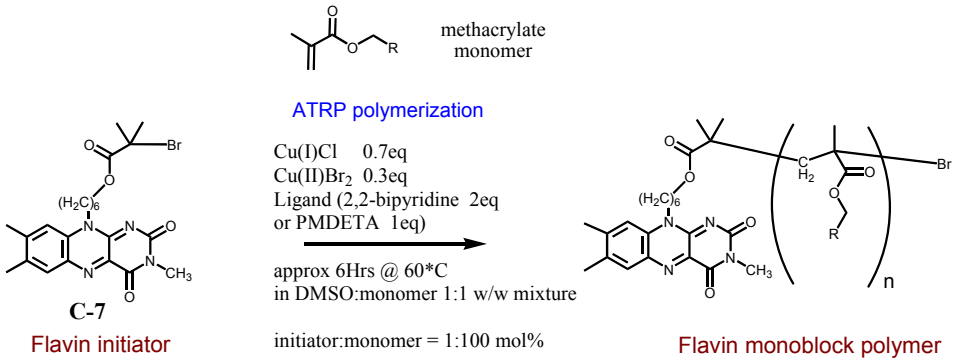

Figure 2.4(a) General synthetic scheme of a flavin monoblock polymer where the methacrylate monomer would be one selected from Figure 2.2.

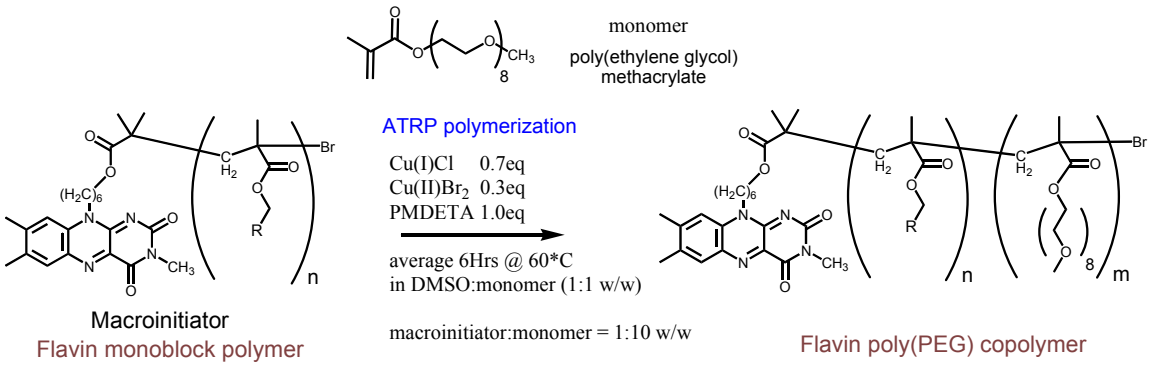

Figure 2.4(b) General synthetic scheme of a flavin diblock copolymer where poly(ethylene glycol) methacrylate (PEG) was used in each case as the hydrophilic methacrylate monomer.

Typical published procedures describing many ATRP reactions generally seem to entail adding the initiator last, usually by injection under an in inert atmosphere using a gas tight syringe. It is only at this point that the catalytic system and the initiator come together and the reaction would therefore be deemed officially started. Although this methodology was followed, it was achieved in a slightly modified manner. The flavin initiator **C-7** and the monoblock polymer used as a macroinitiator in Figures 2.## and 2.## are both solid materials and can take several minutes to full dissolve at room temperature even in DMSO. It therefore seemed essential to have the flavin initiator (or macroinitiator) already fully dissolved at the critical start of the reaction (as opposed to published ATRP reactions were the alkyl halide initiator would be a small molecule in liquid form). Therefore to overcome this problem, the flavin initiator (or macroinitiator) and monomer were therefore combined in DMSO (solvent) in one flask and the catalytic system (Cu(I), Cu(II) and ligand) were added to a second flask

and dissolved also in DMSO. Both mixtures were purged of oxygen by the "freeze-pump-thawing" technique (3 cycles) and then just prior to immersing the reaction flask in an oil-bath at the reaction temperature the Cu(I)/Cu(II)/ligand mixture was injected by means of a gas tight syringe into the centre of the stirring reaction under a fast flowing nitrogen purge. One particular advantage of having the catalytic system in a separate flask was that when small quantities were required (e.g 2.5mg Cu(I)Cl) these quantities could then be scaled up 10 times (easier and more accurate to weigh-out), diluted with 10 times the volume of solvent and the appropriate fraction withdrawn when required using a syringe.

DMSO was chosen as the reaction solvent because of it excellent solubility properties and was added in equal weight to that of the methacrylate monomer utilized during each specific ATRP reaction. The methacrylate monomers were all in liquid form at room temperature and therefore weighed into a two neck round bottom flask using a pipette at a pre-calculated weight of 100 molar equivalents that of the flavin initiator. The reaction was diluted with an equal weight of DMSO such that the monomer to solvent ration was 1:1 (w/w). However, as 1mL of DMSO would be added along with the catalytic system, the flask containing the monomer was dilute with an equal mass of DMSO minus 1 mL. The solid flavin initiator (1 equivalent) was dissolved in this mixture with stirring.

A second two neck round bottom flask was used for the catalytic system. For the monoblock polymers this would require Cu(I)Cl, Cu(II)Br_2 and 2,2-bipyridine in ratios $0.7:0.3:2$ molar equivalence. For the diblock copolymers this would require Cu(I)Cl, Cu(II)Br_2 and pentamethydiethyltetraamine (PMDETA) in ratios $0.7:0.3:1$ molar equivalence. The quantities were scale up (5 times for the monoblock polymers and 10 times for the diblock copolymer), then diluted appropriately so that withdrawal of 1mL of DMSO would contain the required quantities.

Both flasks underwent three cycles of "freeze-pump-thaw" to evacuate all trace of the free radical oxygen gas using nitrogen gas (O_2 free) as the protective atmosphere. After the final thaws the flash containing the initiator and monomer was placed ready for immersion into and oil-bath at the reaction temperature (generally 60°C). A gas tight syringe was used to withdraw 1mL of the catalytic system (under N_2 purge) from the second flask which was then transferred immediately into the stirring solution in the first flask, also under nitrogen purge. This flash was then sealed under nitrogen and immersed into the oil-bath for the duration of the reaction. The ATRP was terminated typically after 6 hours by slowly pouring the reaction mixture into a 500mL conical flask of vigorously stirring methanol (approx 300mL) which precipitated the polymer. The Methyl and CF3 polymers were precipitated by pouring into volume of methanol:H_2O (200mL:100mL) and the DMAEM polymer was precipitated into diethyl ether:hexane (150mL:150mL). The polymers were allowed to settle at the base of the flask then isolated by decanting and filtering. The polymer was then dissolved in $CHCl_3$ (approx 40mL) and passed through as short column of alumina oxide to remove the copper catalyst. The filtrate was then either filtered through a $0.2\mu m$ syringe filter or centrifuged for 1 hour to remove trapped alumina (the latter method was adopted for larger MWt copolymers which were unable to pass through a micrometer syringe filter). The polymers were then re-precipitated in the same manner as before and after allowing to settling for up to 1h were isolated by decanting and filtering.

2.1.5 Monitoring procedure during ATRP synthesis:

Samples were withdrawn during the ATRP reaction, the number and the interval between each sample depended on the speed of the reaction but was generally repeated at 30 minutes, 1 hour and then hourly until the reaction was terminated. These samples were diluted with THF and run through a Gel Permeation Chromatograph (GPC) in order to determine the reaction progress. Details of the GPC procedure are described later in this section. A typical GPC analysis of such a sample is shown in Figure 2.5 for the flavin-Benzyl polymer after 1Hr and 6h reaction time. The small peak (labelled 1) represents the polymer which elutes first from the column. The higher the molecular weight of the polymer the quicker it passes through the column. As would be expected, as the polymer grow its corresponding peak move further left along the time axis. The position of the peak on this time axis allows an estimation of the molecular weigh via reference to the diagonal calibration curve and the corresponding scale on the right hand axis (labelled MW).

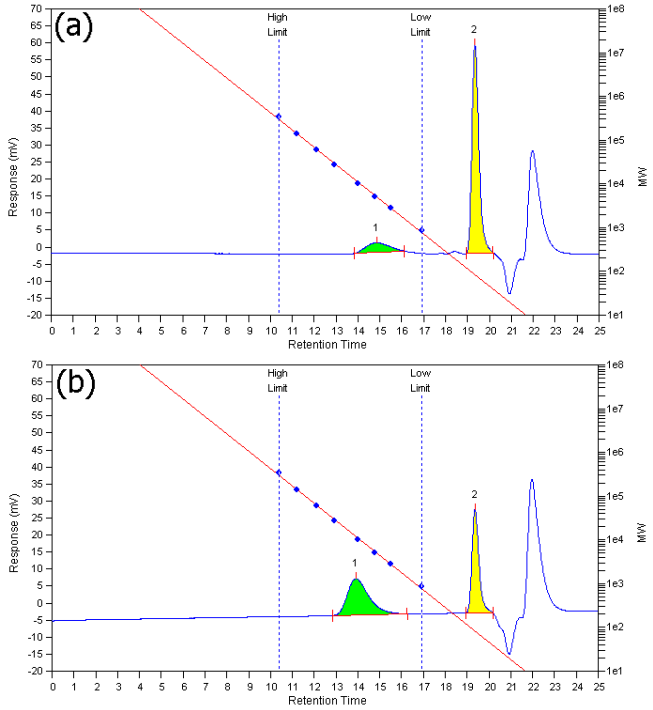

Figure 2.5 GPC profiles for the Flavin-Benzyl polymer at (a). 1Hr and (b). 6Hrs reaction time. Peak 1 represents the polymer and Peak 2 represents the monomer. The third peak represents the reaction solvent (i.e. DMSO) present during extraction of the sample.

The areas under peak 1 (A_{peak1}) and peak 2 (A_{peak2}) correspond to the concentrations of polymer and monomer respectively at that particular time. These areas were calculated using the peak analysis functions of the Cirrus software provide by Varian Inc. The GPC data gathered at appropriate intervals throughout each ATRP reaction was used to plot two sets of graphs and allowed the progress of the reaction kinetics and degree of polymerization to be determined. First order kinetics was demonstrated by plotting a set of graphs for $\log(Mo/M)$ vs *time* where $\log(Mo/M)$ is calculated using Equation 2.1.

$$\log\left(\frac{M_o}{M}\right) = \log\left(\frac{A_{peak1}+A_{peak2}}{A_{peak1}}\right) \qquad \text{Eqn (2.1)}$$

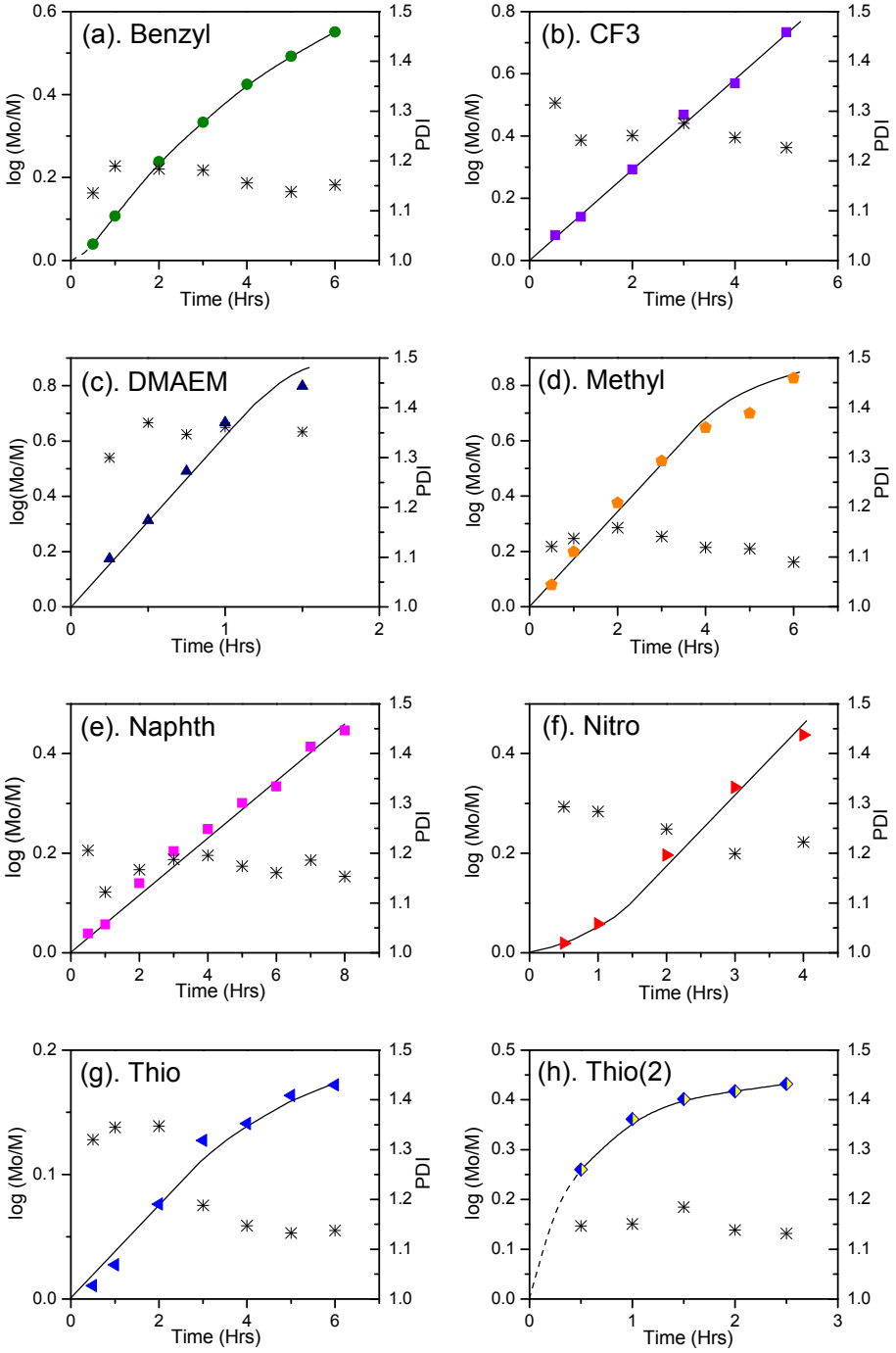

Figure 2.6 Plots showing $\log(M_o/M)$ versus time during the ATRP synthesis of Flavin monoblock polymers. In each case the right-hand vertical represents the polydispersity index (PDI) and the corresponding data points are represented by the asterisk ($*$) symbol.

Plots are shown in Figure 2.6 (a-f) for the first six methacrylate monomer used in the range shown in Figure 2.2. They generally show overall good 1st order kinetics although with some minor downward curvature towards the end of the reaction. This behaviour is discussed in Chapter 1 (section 1.3), where it has been describes as an indication that "living" polymer radical concentration $[P^*]$ was decreasing. It was suggested this could be due possibly either to termination or catalytic system poisoning.

Examination of Figure 2.6(g) shows that the flavin-Thio polymer yield was very poor ($\log(M_0/M) = 0.18$ corresponding to a 32% conversion). The kinetic plot in Figure 2.7 also shows this in a comparison of the all polymers synthesised where the Thio polymer demonstrating the shallowest growth. The polymer reaction probably would have continued to produce a higher yield had it been allowed to continue for a longer period (i.e. 24h), but because Figure 2.6(g) also showed signs of downward curvature and therefore possible termination, it was decided that modifying the reaction conditions with more active catalyst would be the better option. Figure 2.6(h), corresponds to an ATRP reaction labelled Thio(2) where 2,2-bypyridine has been replaced with the more active tridentate ligand pentamethydiethyltetraamine (PMDETA). The overall catalytic system used was therefore Cu(I):Cu(II):PMDETA at ratios of 0.7:0.3:1eq and the reaction carried out at the lower temperature of 40°C

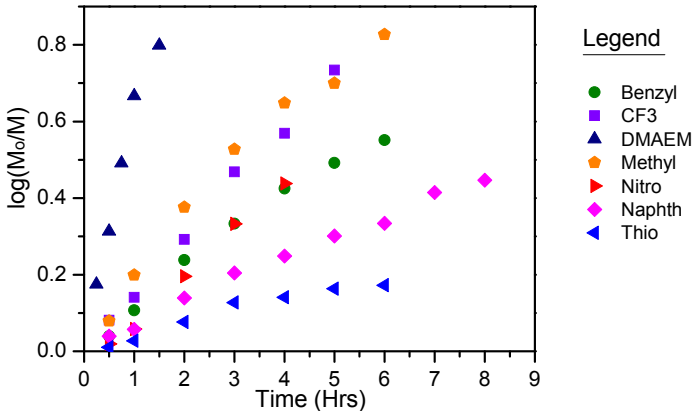

Figure 2.7 Kinetic plot $\log(M_0/M)$ versus time showing the variation in ATRP reactions rates for all methacrylate monomer types. The DMAEM polymer was the fasted synthesised despite being carried out at the lowest temp (25°C). The Thio polymer was the slowest synthesised when the ATRP reaction took place under the same general reaction conditions as the main group of polymers. Slope = $k_p[P^*]$ or $k_p[I]$ (see ATRP section).

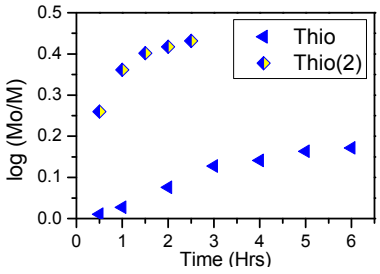

Figure 2.8 Plot $\log(M_0/M)$ versus time comparing the rates of ATRP for the two Thio polymer reactions. ATRP of Thio(2) involved subsutuition of bypiridine for 1eq of the more active tridentate ligand PMDETA.

The Thio(2) ATRP reaction proceeded much faster (requiring less than half the time) and produced over a 60% conversion. A kinetic plot comparing the polymerization rates for these two polymers is shown in Figure 2.8. Both rate curves show downward curvature however the Thio(2) polymer was ultimately used in subsequent reactions and characterization, primarily because of the higher yield.

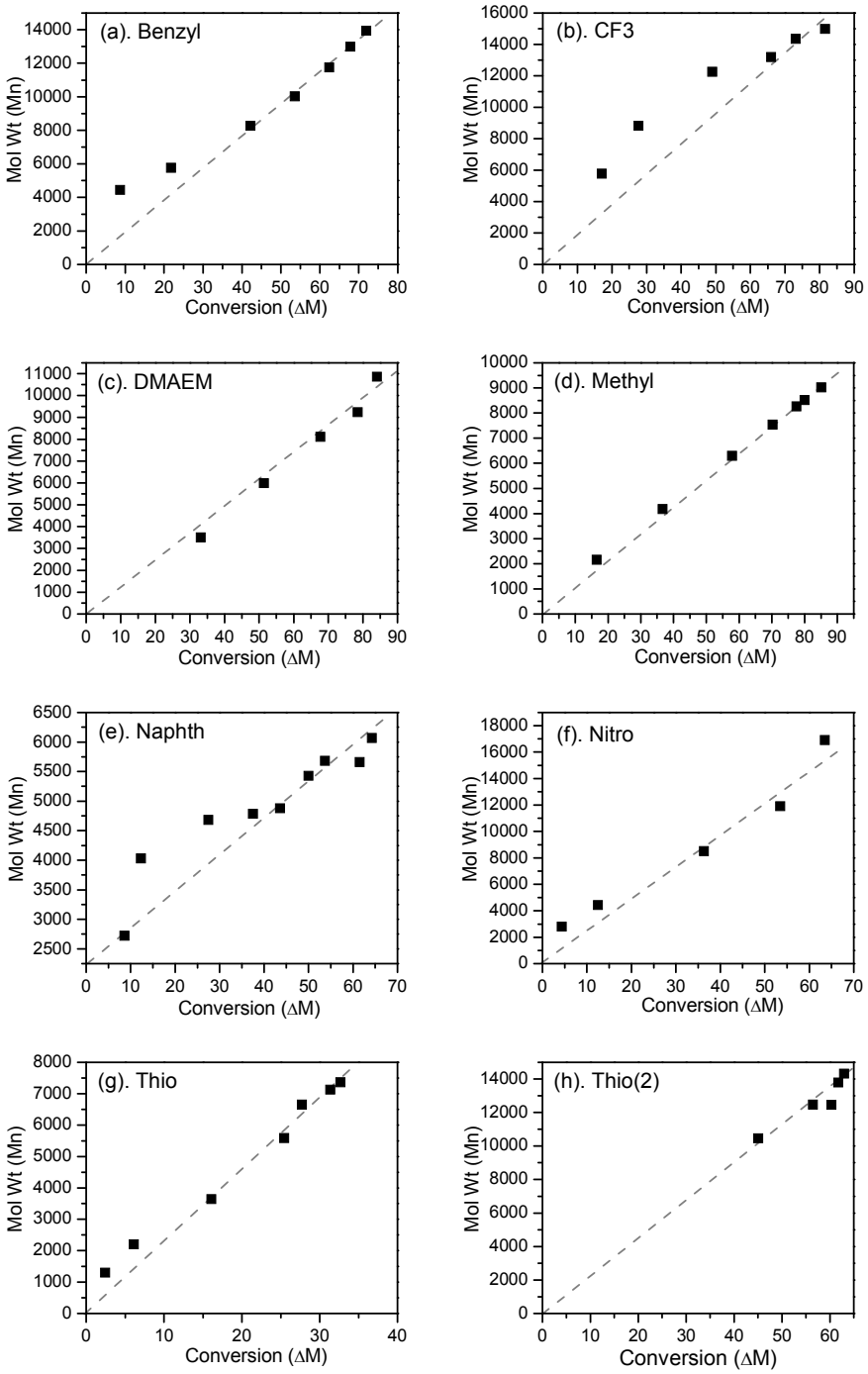

Figure 2.9 Plots of polymer molecular weight (M_n) versus monomer conversion (ΔM) showing the degree of polymerization (DP) for each monomer type during ATRP.

2.2 Polymer characterization.

2.2.1 Verification of the predicted Degree of Polymerization:

The second classifying feature of "living" polymerization is the pre-determinable degree of polymerization (DP). Verification of the DP was demonstrated plotting the set of graphs for each ATRP reaction as shown on the next page in Figure 2.9 (a-h). The molecular weight was determined through GPC analysis. For the majority of the graphs the molecular weight M_n shows a good linear relationship versus conversion ΔM (i.e. a straight line passing through the origin). Benzyl, Naphth, Nitro and CF3 polymers showed slightly higher values of M_n during low conversion however they did start to demonstrate a more linear relationship at higher conversions. These discrepancies could be due to slow initiation as described in the ATRP section. If only a percentage of the polymer radical $[P^*] < [I_o]$, the initiator concentration, then some of the polymers will start to grow rapidly in the excess of monomers. Eventually when the slow initiators begin to polymerize the monomer concentration is partly depleted and the degree of polymerization (DI) (i.e. the slope of M_n *vs* ΔM) decreases. As more $[P^*]$ become available the overall reaction rate increases. This should therefore be displayed in the plots shown in Figure 2.9 as upward curvature of the $\log(M_O/M)$ *vs* time slope. However this was only observed for the Benzyl and Nitro polymers. Another possible explanation therefore is that because the GPC was calibrated using methyl methacrylate (MMA) polymer standards, the GPC molecular weight can only truly be accurate if the polymer being analysed is also an MMA polymer.

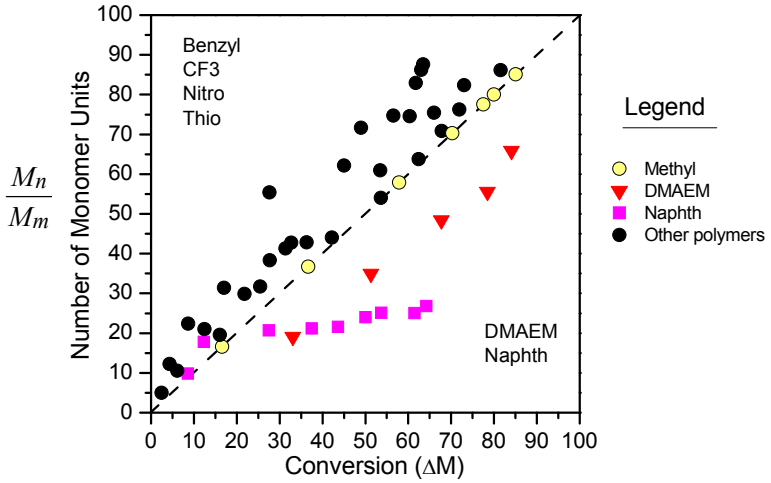

Figure 2.10 Plots of the calculated number of monomer units versus monomer conversion (ΔM) showing the degree of polymerization (DP) for each monomer type during ATRP. The diagonal (dashed) line represents an ideal one to one conversion and coincides almost exactly with the data points corresponding to the Methyl polymer (yellow circles). The plot indicates various discrepancies in GPC MWt results depending on the polymer pendant group

According to Equation 1.5, (Chapter 1: Section 1.3) the slope of the plot for M_n *vs* $\Delta[M]$ is equal to $M_m/[I_O]$ where M_m = the monomer MWt and $[I_o]$ = initiator concentration. In order to characterize the GPC molecular weight results, plots were normalized by basing the y-axis on the number on monomer units for all the polymers M_n/M_m as shown in Figure 2.10. The slope of M_n/M_m *vs* $\Delta[M]$ should in theory be independent of polymer type and equal to $1/[I_O]$ according to Equation 2.2.

$$\frac{M_n}{M_m} = \left(\frac{1}{[I_O]}\right) \times \Delta M \qquad \text{Eqn (2.2)}$$

The diagonal dashed line bisecting the plot from bottom-left to top-right and coincides almost exactly with the GPC data corresponding to the flavin-Methyl polymer. This is a good indication of the accuracy of the GPC in determining molecular weights of methyl methacrylate (MMA) polymers using a calibration curve produced using methyl methacrylate polymer standards. The region above the dashed line represents those polymers that the GPC overestimated their molecular weights. Discrepancies here can be as much as 37%. The region below the dashed line shows the polymers hat the GPC has underestimate their molecular weights. Discrepancies here can be as much over 60%. These various discrepancies are thought to be the result of residual Liquid Absorption Chromatography (LAC) where in the former case the polymers are encouraged to remaining longer in the mobile phase, the polymer elutes faster which results in a higher than genuine molecular weight. In the lower region the opposite occurs and the polymer remain longer in the stationary phase thereby eluting later than normal and suggesting a lower than genuine molecular weight. This region includes the DMAEM and Naphth polymers. The Napth polymer is particularly retarded and the GPC results suggesting a final molecular weight of only $M_n = 6068\ (g/mol)$. The theoretical MWt based on an experimental yield of 57% was $57 \times 226.1 + 504.1 = 13{,}392\ (g/mol)$. The theoretical molecular weight based on monomer conversion of 64.3% was $14{,}538\ (g/mol)$. The DMAEM polymer could be persuaded to elute faster by altering the mobile phase to 1% triethyl-amine in THF. This changed the GPC evaluation of molecular weight from $M_n = 10863\ (g/mol)$ to $30309\ (g/mol)$ and the polydispersity index (PDI) to decrease from 1.352 to 1.242 . However, there was little effect when this procedure was applied to the Naphth polymer.

Previous ATRP reactions involving the synthesis of the Nitro polymer showed the characteristic signs of coupling (an upward curvature of the M_n *vs* ΔM plot) and hence a rapid rise in M_n towards the end of the reaction. Under standard reaction described earlier, the reaction mixture became very viscous and within 2 hours eventually set as a gel. This was also visibly observed on the GPC profile in Figure 2.11 which shows what is commonly known as a high molecular weight shoulder. Similar reports have bee published elsewhere and recommendations were that the polymerization reaction need to be performed at low temperature. The ATRP reaction for the synthesis of the polymer referred to here as Nitro, was carried out at 40°C and the reaction was terminated after just for hours before the high molecular weight shoulder had begun to appear on the GPC profile. Examination of the M_n *vs* ΔM plot in Figure 2.9(f) Nitro, does however still show moderate signs of upward curvature.

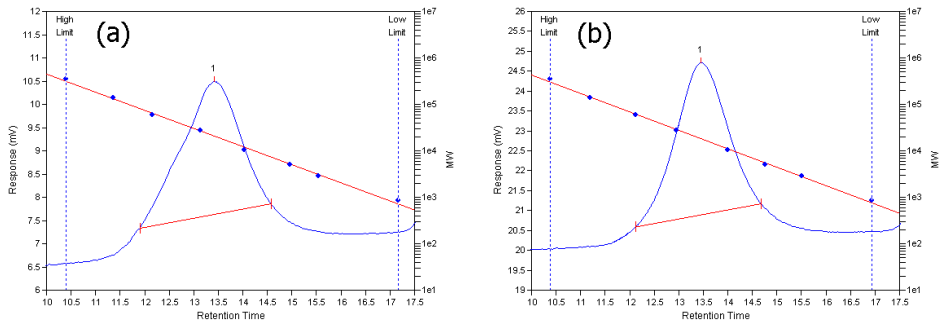

Figure 2.11 GPC profiles of the flavin-Nitro polymer under two reaction conditions. In plot **(a)** the reaction temperature was 60°C for 6h. A high molecular weight shoulder is clearly visible to the left hand side of the main peak. In plot **(b)** the reaction temperature was 40°C and the reaction was terminated after only 4h in order to minimise cross coupling reactions. The peak is also clearly more symmetrical.

2.2.2 *Summary of MWts for mono and diblock polymers*

The monoblock polymer molecular weight values M_n depicted in Table 2.2, range from just over $6{,}000$ to $17{,}000\ g/mol$. The GPC results are generally slightly higher that the molecular weights predicted from monomer conversion using the method previously described in Section 2.1.4. These molecular weight values depend of course primarily on the product of the monomer molecular weight M_m times the number of units. Therefore we would expect give the same number of monomer units, the Methyl polymer ($M_m = 100.1\ g/mol$) would be smaller than for example the Benzyl polymer ($M_m = 176.2\ g/mol$). However the GPC value of M_n for the Naphth polymer is approximately 40% that of the predicted MWt. Both these discrepancies have been interpreted in the previous sub-section as due to residual Liquid Absorption Chromatography (LAC) effect where the polymers are encouraged to remaining longer in the mobile phase. Almost all polydispersity index (PDI) values are less than 1.25, which is a good indicator of controlled polymerization. The only exception was the DMAEM polymer where the $PDI = 1.35$. However, if the GPC eluent was replaced with a mixture of THF(+1% NEt_3) and calibrated, the following results are obtained: $Mn = 30309\ g/mol$ and $PDI = 1.24$. This variation emphasises the difficulty in obtaining accurate molecular weights using the GPC which has been calibrated using non-similar polymer type standards.

monoblock polymer	GPC Results			MWt predicted from monomer conversion
	M_n	M_w	PDI	
Benzyl	13944	16059	1.15	12670
CF3	14984	18385	1.23	13710
DMAEM	10863	14686	1.35	13221
Methyl	9023	9831	1.09	8610
Naphth	6068	6997	1.15	14527
Nitro	16906	20663	1.22	11887
Thio(2)	14324	16213	1.13	10095

Table 2.2 Summary of molecular weights (g/mol) obtained by GPC analysis for the flavin monoblock polymers.

The diblock PEG copolymer molecular weight values M_n are depicted in Figure 2.2 and range from just less than $30{,}000$ to approximately $65{,}000\ g/mol$. The GPC results are generally significantly lower that the molecular weights predicted using the monomer conversion method. The polydispersity index (PDI) values now much greater than 1.25 which would suggest lack of controlled polymerization. The GPC profiles for these copolymers (not shown) were generally quite broad and as the ATRP reaction proceeded, these profiles generally developed a small trough. We were initially uncertain how/why this was happening despite numerous precautions and repeated experimentation. One explanation is that this is a characteristic of running a block copolymer through a GPC column and is the result of the two polymer blocks interacting with one another thus producing "folded" and hence effectively "shorter" polymers which elute from the GPC column much later. Interestingly, we repeated these results for just two of the PEG copolymers at a much higher temperature (i.e. 50°C) and have subsequently observed improved results indicating both higher molecular weights and lower polydispersity index (PDI) values as well as the absence of the small trough.

Nitro-PEG: $Mn = 128853\ g/mol$, $M_W = 158472\ g/mol$, $PDI = 1.23$.

CF3-PEG: $Mn = 102904\ g/mol$, $M_W = 115905\ g/mol$, $PDI = 1.26$.

The PDI values are moderately high yet low enough to infer controlled radical polymerization. It is assumed that the temperature increase simply provided a way of disrupting this interaction and ultimately provided M_n values more in line with those predicted in Table 2.3. Unfortunately however, high temperature GPC results for the remaining polymers are at this time pending a repair of the GPC apparatus.

diblock copolymer	GPC Results			MWt predicted from monomer conversion
	M_n	M_w	PDI	
Benzyl-PEG	64372	99785	1.55	105144 (64%)
CF3-PEG	38264	50029	1.50	93359 (55%)
DMAEM-PEG	44593	65099	1.46	97788 (61%)
Methyl-PEG	34370	45719	1.33	91673 (58%)
Naphth-PEG	27940	38555	1.38	84443 (55%)
Nitro-PEG	52299	77585	1.48	105256 (62%)
Thio(2)-PEG	28727	38359	1.34	89849 (53%)

Table 2.3 Summary of molecular weights (g/mol) obtained by GPC analysis for the flavin diblock PEG copolymers

2.2.3 Particle sizing by Dynamic Light Scattering (DLS):

Figure 2.12 shows Dynamic Light Scattering (DLS) results for the seven flavoenzyme polymer systems (see Chapter 8 for Experimental procedures). These results would seem to suggest that solvent molecules interact with the polymers in solution forcing them into small soluble particle of diameters between approximately 3 and 9 nm. Table 2.4 provides a comparison between the molecular weights obtained by GPC and the particle diameter for all polymers. The Naphth monoblock polymer forms the smallest particle size (3.75nm diameter). The molecular weight obtained by GPC also shows this to have the lowest value (6068 g/mol). However both these low values disagree with the predicted molecular weight based on an 65% conversion (see Figure 2.8) and a 60% yield which would equate at the very least a molecular weight over 14000 g/mol. These observations may suggest that the construct of the polymer has a determining effect on particle size, a behaviour that may also be solvent dependant. However due to time constraints this was not investigated further.

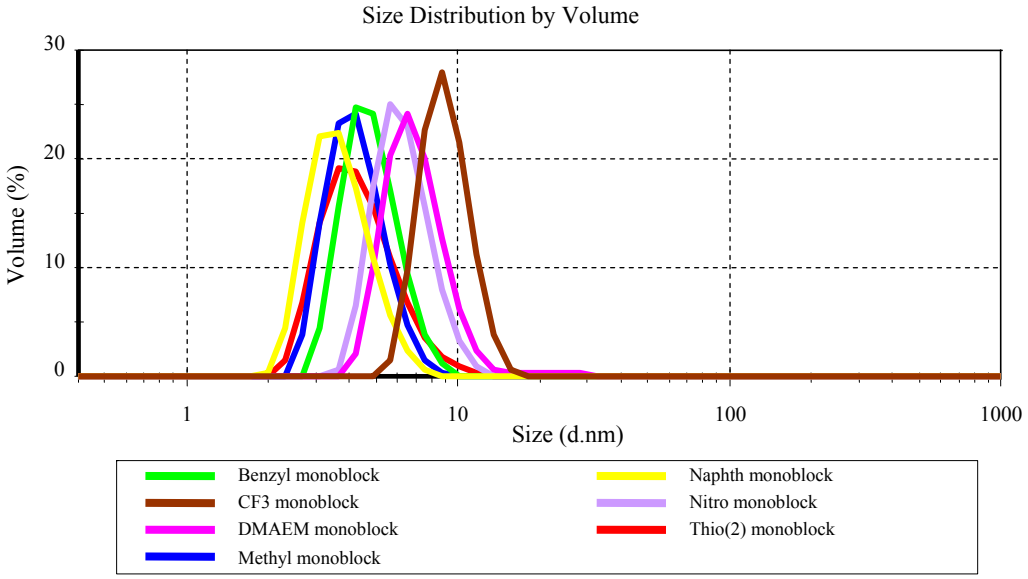

Figure 2.12 Dynamic Light Scattering (DLS) results confirm the polymers become constrained by the solvatophobic effect into forming small particles with diameters ranging between 3 and 9 nm in $CHCl_3$.

monoblock polymer	DLS Results Z-average diameter (nm)	GPC Results M_n (g/mol)
Benzyl	4.855	13944
CF3	9.039	14984
DMAEM	7.032	10863
Methyl	4.275	9023
Naphth	3.754	6068
Nitro	6.325	16906
Thio(2)	5.127	14324

Table 2.4 Comparison of polymer particle size obtained using Dynamic Light Scattering (DLS) in $CHCl_3$ with results for the polymer molecular weight M_n obtained by Gel Permeation Chromatography (GPC).

Figure 2.13 shows the DLS results for the flavoenzyme PEG copolymer systems in $CHCl_3$. The polymers form particles of diameters between approximately 10 and 25 nm as indicated by the Z-average values shown in Table 2.5. We observe reasonable correlation between the molecular weights obtained by GPC and the particle diameter for these copolymers. This would seem reasonable since the bulk of the copolymer structures have similar block PEG component, however it is interesting that the two aromatic base copolymers are at opposite ends of the size scale. Furthermore, it is two larger copolymers, Benzyl-PEG and Nitro-PEG, appear to be forming micelles at approximately 200 to 300 nm.

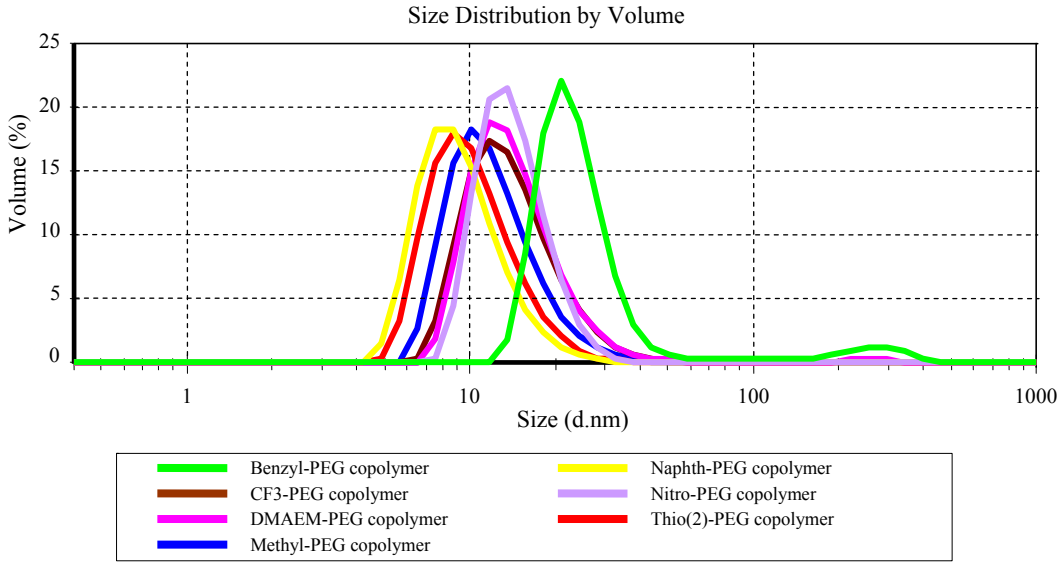

Figure 2.13 Dynamic Light Scattering (DLS) results for the PEG copolymers demonstrating particles sizes with diameters ranging between 9 and 24 nm in $CHCl_3$.

diblock copolymer	DLS Results Z-average diameter (nm)	GPC Results M_n (g/mol)
Benzyl-PEG	24.34	64372
CF3-PEG	14.85	38264
DMAEM-PEG	15.16	44593
Methyl-PEG	12.52	34370
Naphth-PEG	9.58	27940
Nitro-PEG	14.46	52299
Thio(2)-PEG	10.57	28727

Table 2.5 Comparison particle size obtained for the PEG copolymers using DLS with results for polymer molecular weight M_n obtained by GPC.

2.3 Electrochemistry:

The objective of the following electrochemical experiments was to determine if there was any significant influence on the redox properties of the flavin while encapsulated within the hydrophobic environment created by the different polymer composite. Initial experiments were carried out using dichloromethane (DCM) as the solvent medium. Results were ambiguous with cyclic voltammograms showing either two, three or even no oxidation waves. The formal potential for each of the flavin-polymer systems were determined at best as being reasonably similar. There was a question mark over whether the electroactive species was under the influence of solvent molecules (DCM) trapped within the polymer unit. The solvent molecules could thereby neutralize any influence due to encapsulation within the different hydrophobic polymer side-chain units.

The next approach (after researching further the techniques involved in Protein Film Voltammetry (PFV)) was to repeat the electrochemistry experiments but with the polymers immobilised onto the surface of a glassy carbon electrode. Carrying out the surface electrochemistry in aqueous media had the double advantage of inducing the required hydrophobic effect and forcing encapsulation of the flavin unit within the polymer side-chain. It also provides an environment in which the polymers would remain insoluble and strongly attached to the electrode surface. Electrochemical analysis procedures can be found in Chapter 8: Experimental section.

2.3.1 Cyclic Voltammetry:

Figure 2.14 shows cyclic voltammograms (CV's) recorded for the flavin-DMAEM polymer over a range of scan rates between 0.1 and 100Vs^{-1}. These CV's are representative for all the other flavin-polymers which differ only in peak heights and positions (summarised later). The CV's show both "raw" and FT smoothed, background subtracted data. The background subtracted data was utilized to determine peak separation ΔE_p, positions $E_{p,c}$ *and* $E_{p,a}$, peak heights $I_{p,c}$ *and* $I_{p,a}$ and half-peak width $E_{p/2}$. It can be seen from Figure 2.14 that even at the lowest scan rate the anodic and cathodic peak are not symmetrically positioned about the potential axis and are therefore clearly not demonstrating electrochemical reversibility. The peak shift ranges from 26mV at 0.1Vs^{-1} increasing to 97mV at 100Vs^{-1}. As the scan rate increases the peaks broaden and increase in height by a factor of 125 from 4×10^{-7} to 5×10^{-5}. The cathodic half-peak widths ranged from 112mV at 0.1Vs^{-1} to 152mV at 100Vs^{-1}. Given a value of $\alpha = 0.5$, this suggests quasireversible electrochemical kinetics at the low scan rate (i.e. $E_{p/2} > 90.6\text{mV}$) and becoming totally irreversible at the higher scan rates (for an excellent review on surface immobilized cyclic voltammetry, see reference [34, 35]). The anodic half-peak widths are unreliably immeasurable as a result of distortion produced by not including a wide enough potential bandwidth during the experiment. However, at high scan rates they appear to be identical in shape.

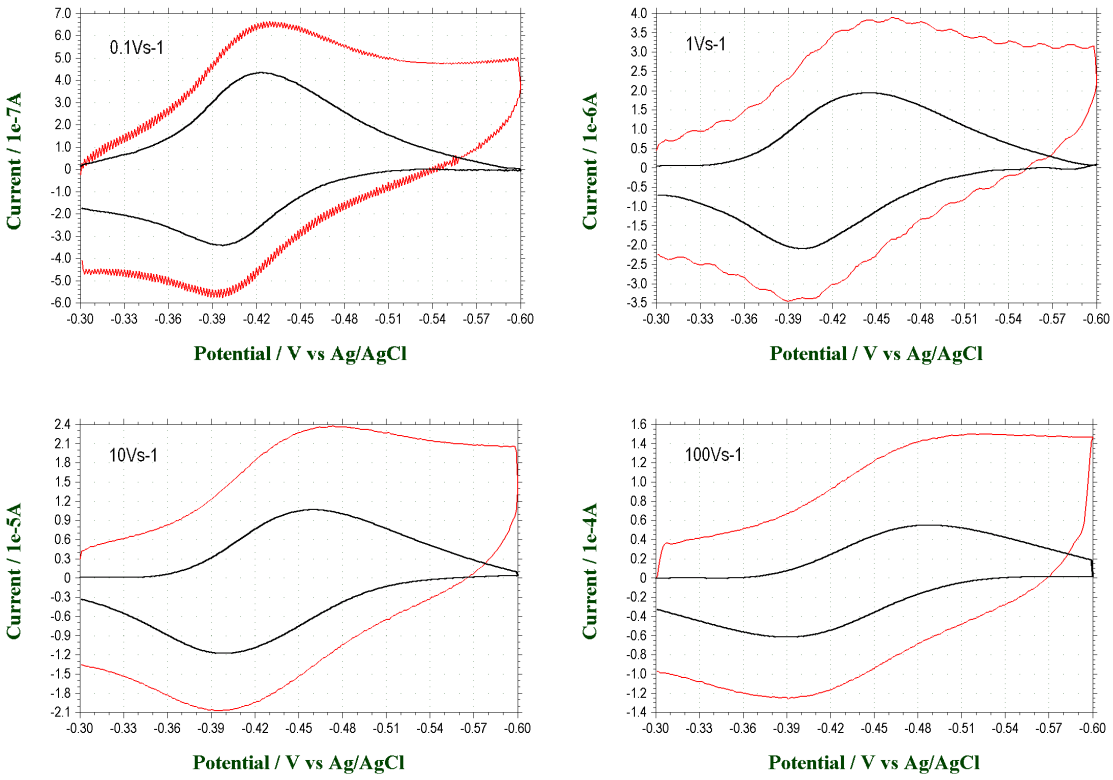

Figure 2.14 Cyclic voltammograms of the flavin DMAEM polymer absorbed onto a glassy carbon electrode (pH 7.0, 0.5M NaCl) at different scan rates. Both the raw data (outside) and the FT smoothed background subtracted data (inside) are shown.

Figure 2.15 shows three comparative CV's for the blue copper protein Azurin. This was included primarily to indicate the similarity between the long range electron transfer (>15 Å), that takes place within both natural enzymes and our polymer enzyme model system.

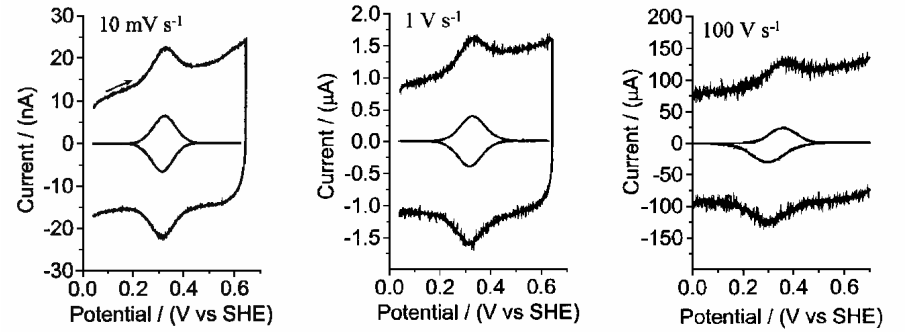

Figure 2.15 Comparison CV's for the blue copper protein Azurin, immobilized onto a pyrolytic graphite edge (PGE) electrode. [36]

The ratio of $E_{p,c} - E^{\theta}$ to $E_{p,a} - E^{\theta}$ provides some indication of the value of the transfer coefficient α. Peak positions versus scan rate are shifted equally either side of E^{θ} when $\alpha = 0.5$ whereas if the cathodic peaks shift more with respect to the anodic peaks then $\alpha > 0.5$, which appears to be the case here. Figure 2.16. This shows a plot for the cationic and anodic peak shifts for the flavin-DMAEM polymer versus $\log(\nu)$. The formal potential $E^{\theta} = 0.412\text{V}$ was selected as the midpoint between the most positive cathodic peak and the most negative anodic peak. Although this should ideally be the intercept of two lines, one passing through the cathodic peaks the other passing through the anodic peak positions. This method was chosen as in most cases it was difficult to draw anything other than a parabola curve through the erratically shifting anodic peak positions (see Figures 2.17 and 2.18).

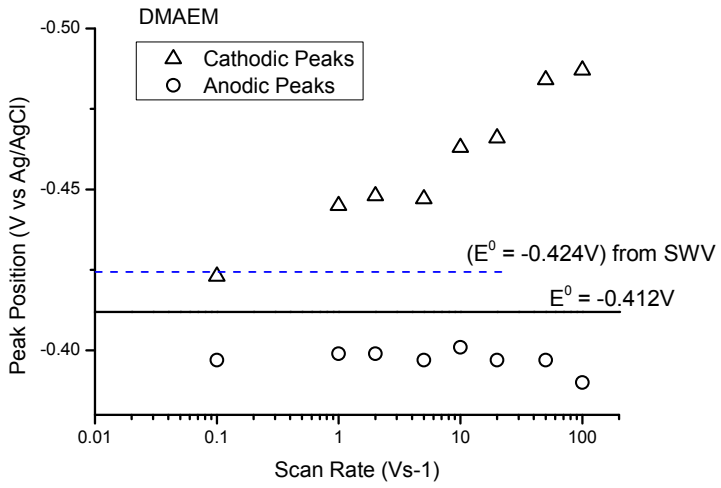

Figure 2.16 Plot for the flavin-DMAEM polymer shows larger cathodic peak shifts versus increasing scan rate υ, compared to the corresponding anodic peak shifts.

The electron transfer rate k_o is usually determined by differences in cathodic and anodic peak separation as the CV scan rate is increased. This method was first demonstrated in 1965 by Nicholson [37, 38] and later to be followed by two modified versions from Kochi [39] and Gileadi [40] in 1981. However all three of these methods involved the diffusion parameter of the electroactive species in solution. It was Laviron who in 1979 demonstrated a method for obtaining the electron transfer rate from peak separation for diffusionless (surface immobilized) electrochemical systems.[41] The method used falls under two criteria depending on the value $n\Delta Ep$ (the product of the number of electrons times the total peak separation). For $n\Delta Ep < 200\text{mV}$ a graphical technique must be used while for $n\Delta Ep > 200\text{mV}$, a simple equation, known as Laviron's equation, can be used. This is shown in Equation 2.4.

$$\log k_o = \alpha \log(1-\alpha) + (1-\alpha)\log\alpha - \log\left(\frac{RT}{nF\nu}\right) - \frac{\alpha(1-\alpha)nF\Delta E_p}{2.3RT} \qquad \text{Eqn (2.4)}$$

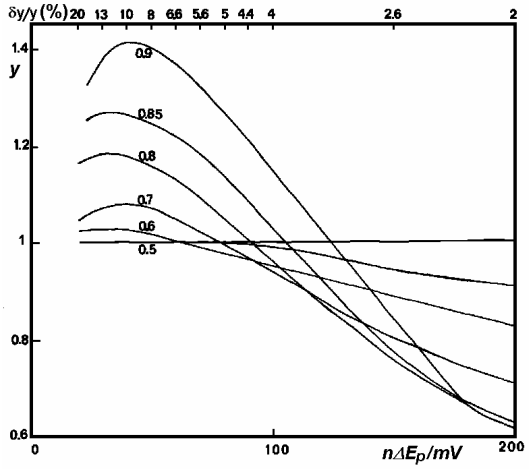

Figure 2.17 Plot used by Laviron to estimate the transfer coefficient from variations of the ratio $y = \left|(Ep,c - E^{\theta})\right| \Big/ \left|(Ep,a - E^{\theta})\right|$ with $n\Delta Ep$. The value of α is indicated on each curve. [41]

All of the peak separation values encountered in these experiments fall under the criterion $n\Delta Ep < 200\text{mV}$, and therefore as suggested by Laviron we will be following the graphical method for determining the electron transfer rate. First the transfer coefficient α is obtained from Figure 2.17. This shows how the ratio of the cationic to anodic peak shifts relative to the formal potential ($(Ep,c - E^{\theta})/(Ep,a - E^{\theta})$) varies with the product of the number of electrons times the total peak shift ($n\Delta Ep$) which has been calculated for values of α between 0.5 and 0.9. However Figure 2.18 shows that the cationic peak shift more significantly than the anionic peaks in the range of scan rates examined ($0.1 - 100\text{Vs}^{-1}$) and this suggests that the value of $\alpha > 0.5$. Apart from the two peaks at $\upsilon = 0.1$ in Figure 2.18, the ratio $y > 3$ (the vertical scale of the graph in Figure 2.17) is too small to allow precise estimation of α. However despite this, I have used an estimated value of $\alpha = 0.9$ in the subsequent calculations.

The second and final step is to determine a value of $(m)^{-1}$ from Figure 2.18 using one of the values for $n\Delta Ep$ against one of the corresponding slopes representing a range of α's Equation 2.5 describes the term $(m)^{-1}$ as …

Eqn (2.5)

$$\frac{1}{m} = \frac{nF}{RT}\frac{\nu}{k_o}$$

… where ν is the scan rate, k_O is the heterogeneous electron transfer rate constant (n, F, R and T have their usual meanings).

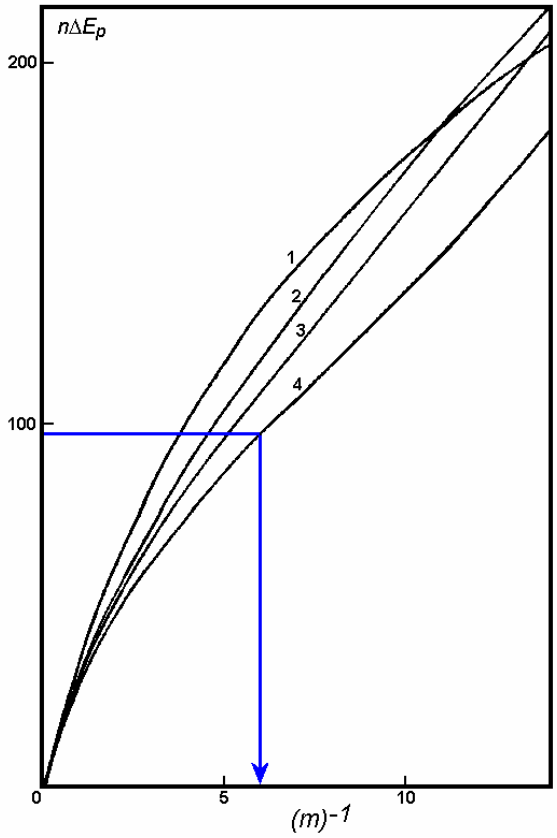

Figure 2.18 Variation of $n\Delta Ep$ with $1/m$. **(1)** $\alpha = 0.5$ **(2)** $\alpha = 0.8$ **(3)** $\alpha = 0.85$ **(4)** $\alpha = 0.9$. Partially revised from [41].

Using data from the flavin-DMAEM polymer which was used to plot Figure 2.16, a scan rate of $\upsilon = 100 Vs^{-1}$ confers a value of $n\Delta Ep = 97 mV$ ($n = 1$). This corresponds to a value of $(m)^{-1} = 6$ (blue arrow in Figure 2.18) for $\alpha = 0.9$. Rearranging Equation 2.5 to calculate the electron transfer rate constant we obtain the value $k_O = 667\ s^{-1}$ (@ T=290K).

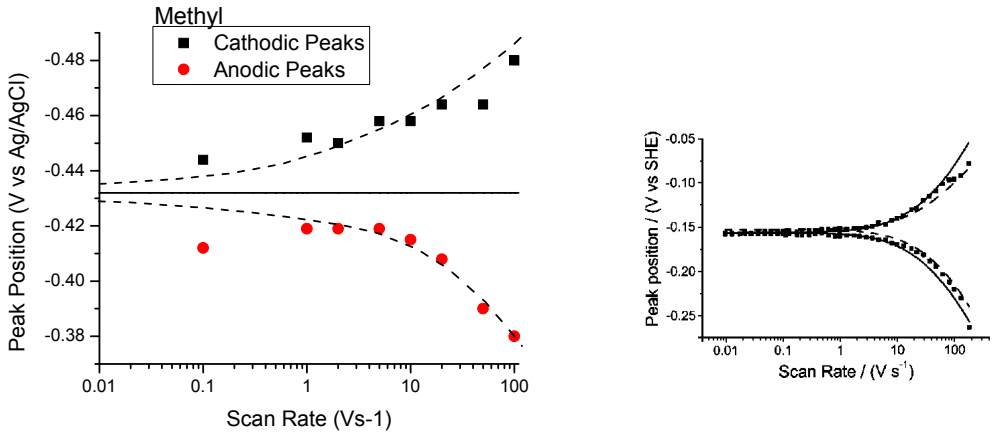

Figure 2.19 Plot for the flavin-Methyl polymer showing larger cathodic peak shifts versus increasing scan rate υ, compared to the corresponding anodic peak shifts. The inset shows a similar plot for Flavocytochrome c_3 with $k_O = 970 s^{-1}$. [42] Solid lines represent simulations.

The general trend for all the flavin-polymers is that the anodic peak positions gradually shift slightly more negative with increasing scan rate. As the scan rate increases further the anodic peaks slowly begin shifting position in the direction opposite to the cathodic peak position. An example of this has already been shown in Figure 2.16 for the flavin-DMAEM polymer. Within the range of scan rates examined, only the cyclic voltammograms of the flavin-Methyl polymer system (Figure 2.19) showed more symmetry in peak shifting behaviour in comparison to the other polymer systems in Figures 2.14 and 2.18. Although the anodic peak positions start to shift slowly at first at low scan rates (Figure 2.19), above $10\,Vs^{-1}$ these peak separations rapidly increase. It therefore seems reasonable to assume that this behaviour might also be observed for the other flavin-polymer systems if higher scan rates ($>1000\,Vs^{-1}$) had been achievable. The inset in Figure 2.19 shows a comparable plot for *Flavocytochrome* c_3 [42], an enzyme with a similar electron transfer rate $k_O = 970\,s^{-1}$.

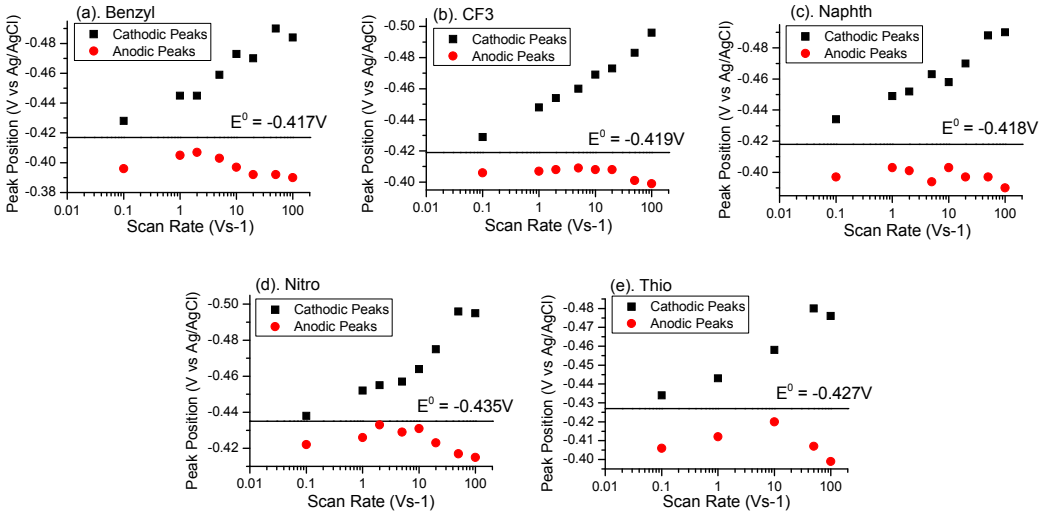

Figure 2.20 Peak potential versus Scan rate plots for flavin-polymers **(a).** Benzyl, **(b).** CF3 **(c).** Naphth **(d).** Nitro and **(e).** Thio. Each system showing larger cathodic peak shifts as scan rate υ increases in comparison with the corresponding anodic peak shifts.

2.3.2 Cyclic Voltammetry summary:

Table 2.6 summarizes the CV result so far.

Polymer	CV Results			
	E^{θ} (V vs Ag/AgCl)	$n\Delta E_p$ (mV) at ν = 100Vs^{-1}	$(m)^{-1}$ from Figure 2.18	k_o (s^{-1})
Benzyl	-0.417	94	6.0	667
CF3	-0.419	97	6.0	667
DMAEM	-0.412	97	6.0	667
Methyl	-0.432	100	6.0	667
Naphth	-0.418	100	6.0	667
Nitro	-0.435	80	4.5	890
Thio(2)	-0.427	77	4.5	890

Table 2.6 Summary of Flavin polymer CV results, showing formals potential E^{θ}, and the heterogeneous electron transfer rate k_o, calculated using the Laviron method described above.

Interestingly both the flavin-Nitro and flavin-Thio polymers show slightly increased electron transfer rate constants of $k_o = 890\ s^{-1}$ (approx) calculated from the smaller peak shifting observed at the scan rate $\nu = 100\text{Vs}^{-1}$, calculated using a value of $(m)^{-1} = 4.5$ for both systems. This is equivalent to a 33% increase in the electron transfer rate compared to the other 5 polymer systems. Marcus theory links changes in the electron transfer rate to either the reorganization energy λ, the Gibbs free energy ΔG^o or the electronic coupling factor H_{ab}.

2.3.3 Square Wave Voltammetry:

Figure 2.21 shows Square Wave voltammograms (SWV's) recorded for the flavin-DMAEM polymer over a range of SW amplitudes E_{SW} between 25 and 200mV. These CV's are again representative for all the other flavin-polymers which differ only in peak heights and positions (summarised later). As expected the separation between the forward and reverse peaks increases with E_{SW} and at higher values of E_{SW} the difference peak becomes broader before eventually separating into two peak. As discussed in Appendix A (SWV section), the optimum value of SW amplitude is when $nE_{SW} = 50\text{mV}$ where in this case the number of electrons $n = 1$. This optimum is the balance between a peak height and a narrow peak width.

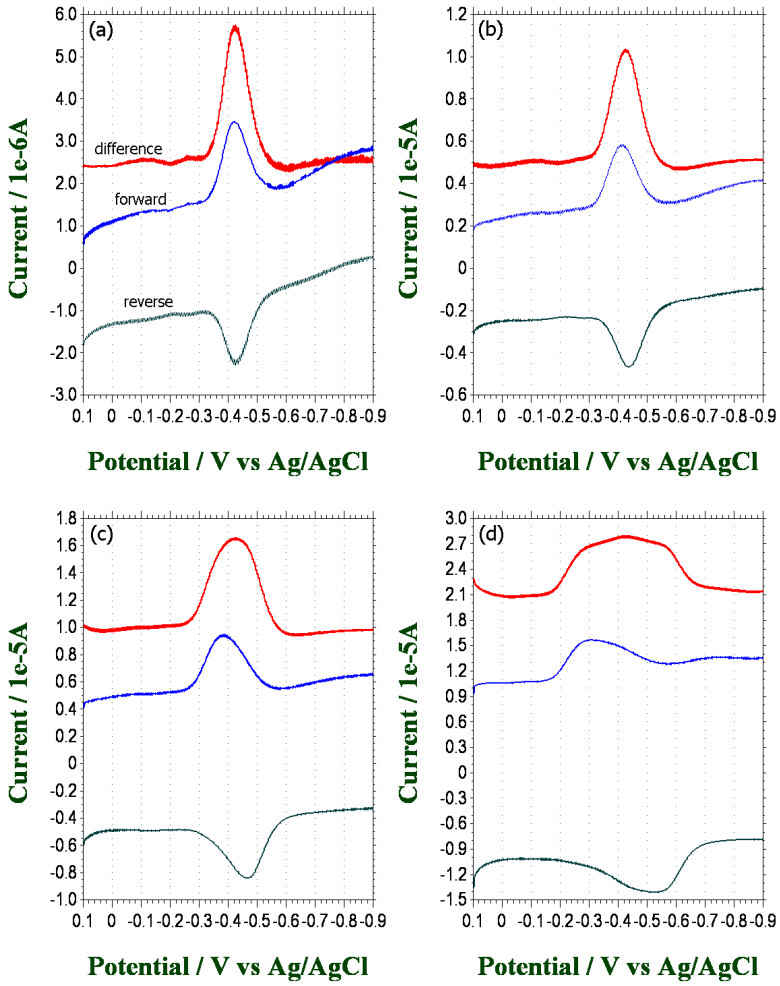

Figure 2.21 Square Wave Voltammograms recorded for the flavin-DMAEM polymer at a pulse amplitudes E_{SW} equal to (a). 0.025V (b). 0.050V (c). 0.100V and (d). 0.200V. $E_{step} = -2\text{mV}$ and SW frequency equal to 100Hz. The difference peak is shown (top), the forward peak (middle) and the reverse peak (bottom).

Figure 2.22 shows a plot of SWV peak positions for the flavin-DMAEM polymer versus SW pulse frequency. The inset is a similar plot for of Flavocytochrome c_3 and will be for later comparison.

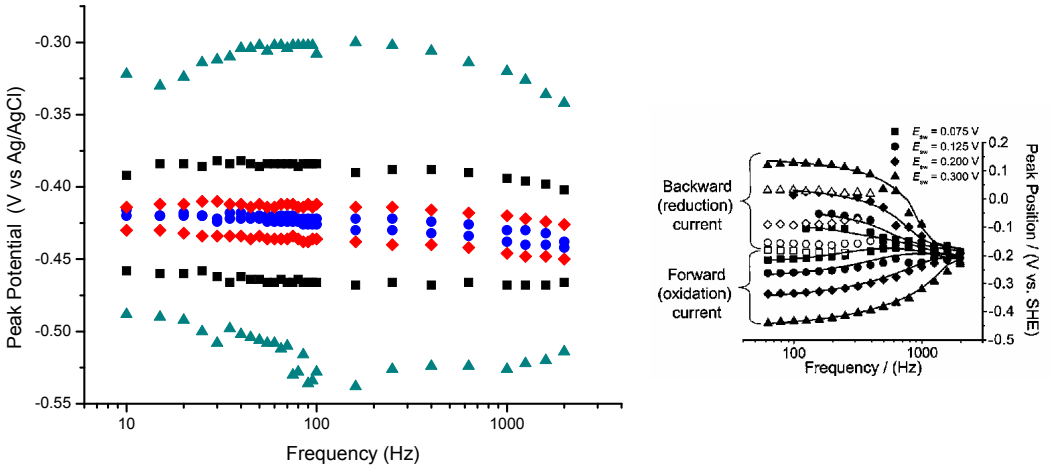

Figure 2.22 Observed peak positions for the forward and backward currents of SWV's for Flavin-DMAEM polymer at four different magnitudes of E_{SW}. (●)= 0.025V (◆)= 0.050V (■)= 0.100V (▲)= 0.200V. The inset show a similar plot for Flavocytochrome c_3 [42] with $k_O = 970s^{-1}$ and at four different values of E_{SW} as indicated. Solid lines represent simulations.

As described in Appendix A: SWV, peak splitting is a consequence of the increased electron transfer rate with overpotential and as expected this peak separation starts to converge as the SW frequency increases. This is because the sum $k_{red} + k_{ox} \longrightarrow$ limit given by Equation 2.6 [see Equation C.4. Appendix C: Marcus Theory] and that limit is dependant on the value $k_{\max}$ and the reorganizational energy λ. This limit is ultimately achieved at large overpotentials induced by large amplitude high frequency SW pulses.

However if we compare the plot for flavin-DMAEM polymer shown in Figure 2.22 with that of the inset for the Flavocytochrome c_3, it is clearly seen that even at a larger SW amplitude of 300mV the peaks of the natural enzyme appear to merged almost into one single peak at a SW frequency of 2000Hz. This convergence is an indication that the limit of Equation 2.6 has already been reached at a SW frequency of about 2000Hz, whereas the peak positions of the polymer enzyme are still converging. This suggests that the reorganizational energy λ of our flavin polymer synthetic enzyme is much greater that that found for the natural enzyme [see Marcus Theory]. This can be justified by the knowledge that natural enzymes have evolved to selectively "grip" the electroactive species by a just a few amino-acid residues located on the inside walls of the enzymes active site. Furthermore this configuration alters very little once the electron transfer has taken place. As a result the reorganizational energy is small and generally $0.1 < \lambda < 0.7\text{eV}$. On the other hand, our polymer enzyme presumably tightly "smothers" the electroactive species by encapsulating it with the hydrophobic structure of the polymer and we would therefore expect the reorganizational energy λ to be much larger. Although it may appear that fast electron transfer at high overpotentials is a desirable quality, it not. For reasons examined earlier in the Marcus Theory section regarding the "inverted" regime, the electroactive species is more stable and longer lived after electron transfer when the reorganizational energy is small and high overpotentials are never achieved in biological systems in any case.

$$k_{red/ox} = k_{\max}\sqrt{\frac{RT}{4\pi\lambda}}\int_{-\infty}^{\infty}\frac{\exp\{-\{(\lambda \pm F(E-E^{\theta})/RT - x\}^2\, RT/4\lambda\}}{\exp(x)+1}\,dx \qquad \textbf{(2.6)}$$

Interestingly, there also appears to be some constriction in the peak splitting at around 15 Hz shown in Figure 2.22. This is more noticeable at the high overpotential generated by the larger SW amplitude $E_{SW} = 200\text{mV}$. A somewhat similar constriction was observed by Armstrong and co-workers [42] for Fumarate reductase enzyme (FrdAB) and suggests that this may be due to some alternative electron transfer mechanism. In the case of FrdAB this involved a hopping mechanism with heme groups enhancing the electronic coupling.

2.3.4 *Determination of formal potentials* E^{θ} *:*

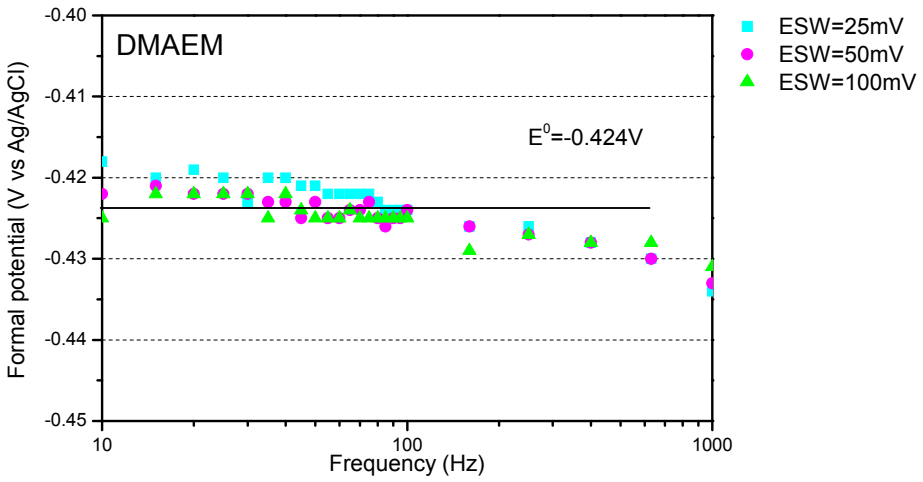

Figure 2.23 Plot of formal potential E^0 versus SW pulse frequency for the Flavin-DMAEM polymer. The formal potential E^0 appears to remain reasonable steady between $10-100\text{Hz}$ for $E_{SW} = 25,\ 50$ and 100mV, therefore the value of E^0 shown is the average value taken between SW frequencies $10-100\text{Hz}$ for $E_{SW} = 50\text{mV}$.

Figure 2.23 shows a plot of the formal potentials E^0 for the flavin-DMAEM polymer. Each data point corresponds to the midpoint between the forward peak $E_{p,f}$ and the reverse peak $E_{p,r}$ of the SW scan (i.e. $(E_{p,f} + E_{p,r})/2$). The formal potential E^0 seems to remain reasonable steady between SW frequencies $10 \rightarrow 100$ Hz for SW amplitudes $E_{SW} = 25,\ 50$ and 100 mV, therefore the value of E^0 shown has been calculated as the average value taken between SW frequencies 10 and 100 Hz at the optimum SW amplitude $E_{SW} = 50$ mV. Similar plot for the other six flavin–polymers systems are shown in Figure 2.24 and for clarity only calculated values of E^0 at $E_{SW} = 50$ mV have been shown. The average values of E^0 (represented on each plot by a horizontal line) have again been calculated from the formal potentials taken between SW frequencies 10 and 100 Hz.

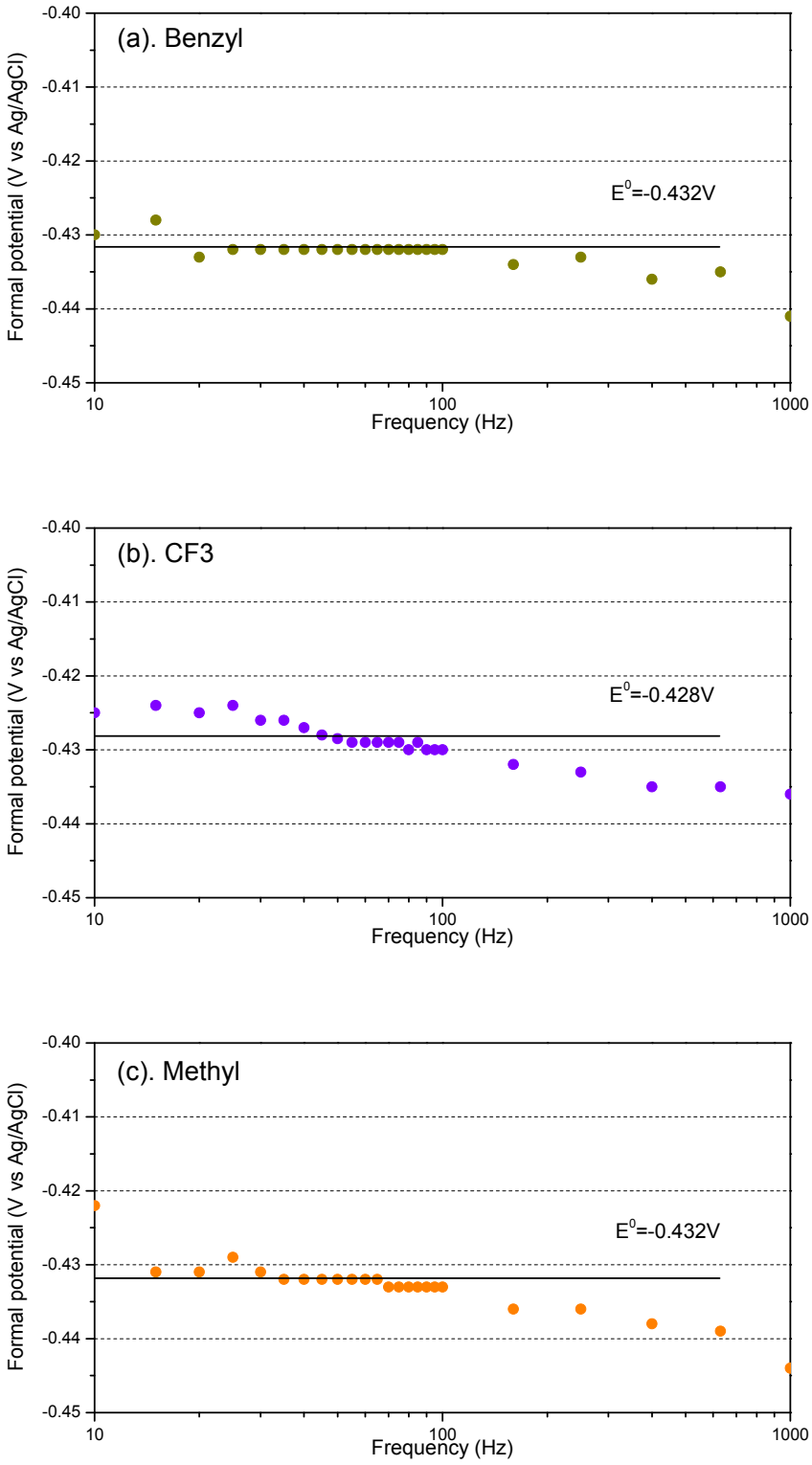

Figure 2.24 (a-c) Plots of the formal potentials E^{θ} (at $E_{SW} = 50$ mV) versus SW pulse frequency for flavin-polymers **(a).** Benzyl, **(b).** CF3, **(c).** Methyl.
The value of E^{θ} shown is the average value taken between SW frequencies 10 and 100 Hz.

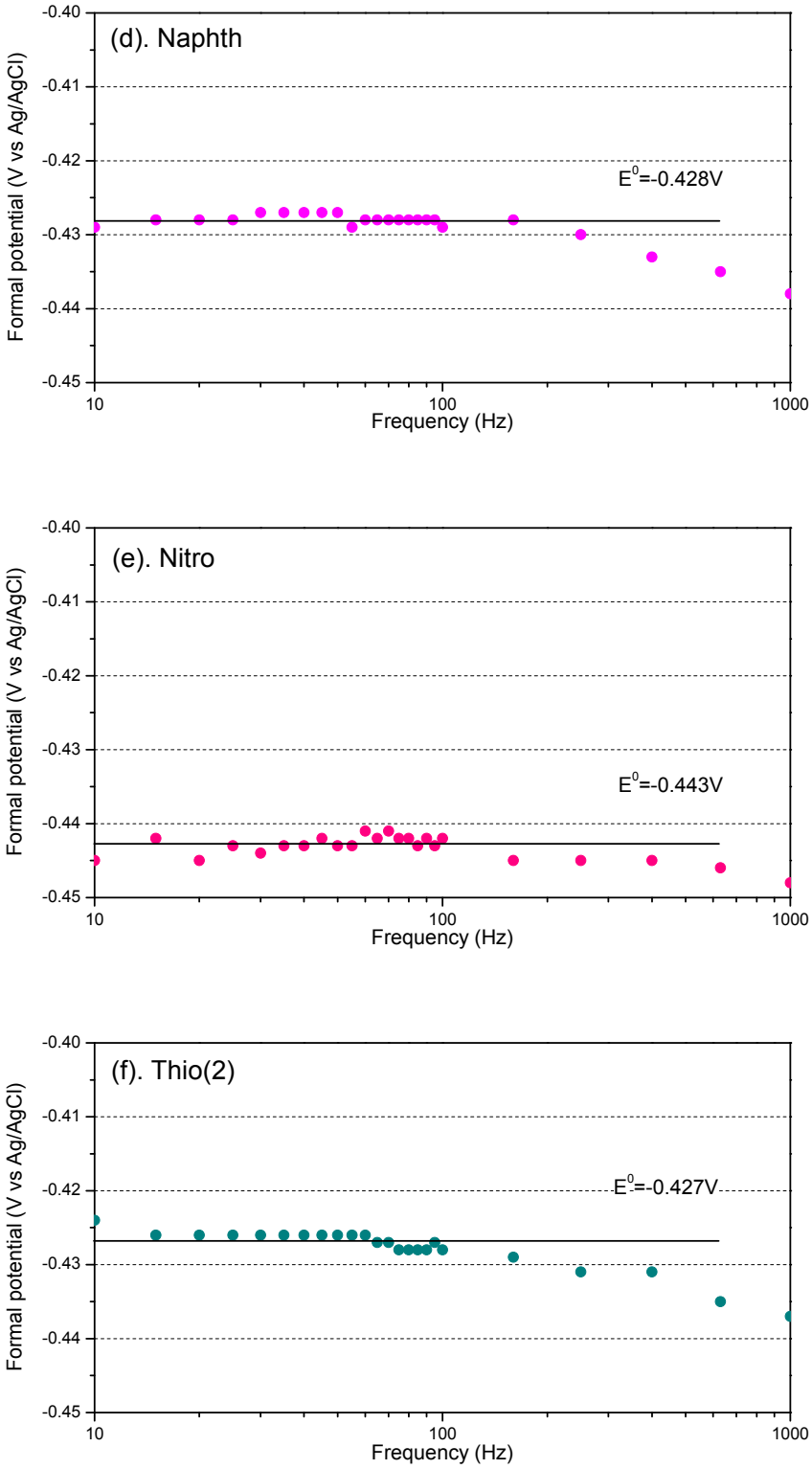

Figure 2.24 (d-f) Plots of the formal potentials E^{θ} (at $E_{SW} = 50$ mV) versus SW pulse frequency for flavin-polymers **(d).** Naphth, **(e).** Nitro and **(f).** Thio(2).
The value of E^{θ} shown is the average value taken between SW frequencies 10 and 100 Hz .

The formal potentials obtained from Figures 2.21 and 2.22 a summarised in Table 2.7 which includes for comparison the cyclic voltammetry (CV) results from Table 2.6.

monoblock polymer	Formal Potential E^0 (V vs Ag/AgCl)	
	SWV Results	CV Results
Benzyl	-0.432	-0.417
CF3	-0.428	-0.419
DMAEM	-0.424	-0.412
Methyl	-0.432	-0.432
Naphth	-0.428	-0.418
Nitro	-0.443	-0.435
Thio(2)	-0.427	-0.427

Table 2.7 Comparison of results for the Flavin-polymers formal potentials E^0 as measured by SWV and CV techniques. The SWV values were obtained by averaging over SW frequencies between 10 and 100 Hz using parameters $E_{SW} = 50\text{mV}$ and $E_{step} = -2\text{mV}$.

For improved clarity the results shown in Table 2.7 have been plotted in the bar chart shown in Figure 2.25. This clearly shows the differences between the SWV results and the CV results. The SWV results appear approximately $8-15\text{mV}$ more negative than the CV results for all but the Methyl and Thio(2) polymer systems were they are identical.

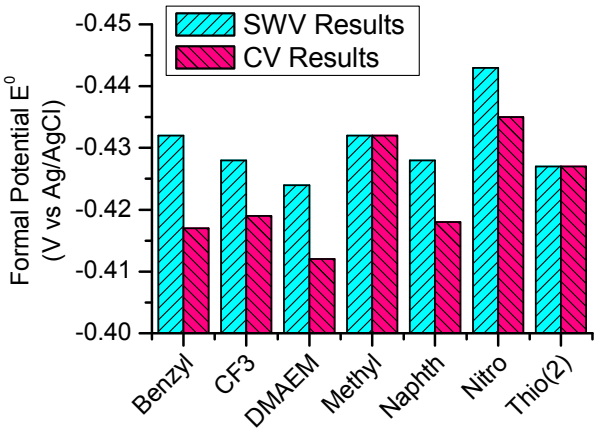

Figure 2.25 Bar chart comparison of the formal potential E^0 results measured by square wave voltammetry (SWV) and cyclic voltammetry (CV) taken from Table 2.7.

Although these results make it difficult to arrange the polymer systems in order of their formal redox potentials, we can reasonably state that the flavin-DMAEM polymer system has the most positive E^0 whereas the flavin-Nitro polymer system has the most negative E^0 separated a difference of approx 20mV, but apart from that the overall results are somewhat ambiguous.

2.3.5 Surface coverage:

The internal software supplied by CH Instruments was used to integrate the area under the CV response peak (background subtracted). This was then used to calculate the surface coverage Γ of the flavin-DMAEM polymer on the electrode this using Equation 2.7 (see reference [35]).

$$peak\ area = nFA\Gamma \qquad \text{Eqn (2.7)}$$

Peak area under the CV response at a scan rate of $0.1\ Vs^{-1}$ is shown in Figure 2.26 as $5.6\times10^{-7}C$. Other parts of Equation 2.7 are $A=\pi(0.31)^2=0.3cm^2$, $F=96485\ C$ and $n=1$. This equates to a surface coverage $\Gamma=19.3\times10^{-12}\ mol.cm^{-2}$. Typical surface coverage's have been quoted as high as $50\times10^{-12}\ mol.cm^{-2}$ using PGE electrodes. [35]

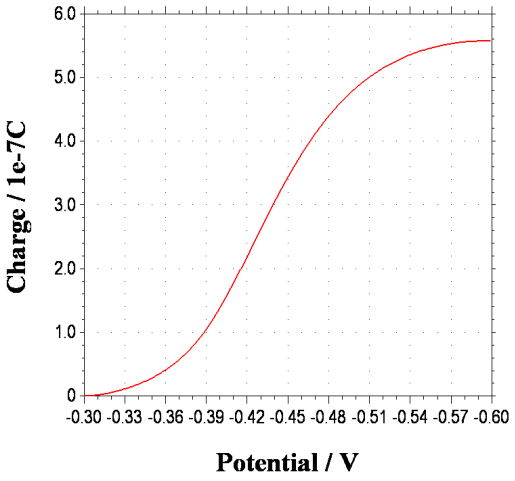

Figure 2.26 Calculation of the area under the CV reduction peak ($\nu=0.1Vs^{-1}$), using the CH Instrument internal software's integration function.

Figure 2.27 shows the peak current response versus SW frequency for all flavin-polymer systems with the DMAEM polymer showing the strongest response. As the peak response is determined by the surface concentration Γ of polymer it suggests that the DMAEM polymer "sticks" better to the glassy carbon electrode, most probably because of the strong affinity that the carbon electrode has for polar groups (carbonyls, amines etc.[34, 35]). At the other extreme, the aromatic polymers (Benzyl and Naphth) show the weakest response and it would therefore suggest that these polymers interact unfavourably with the electrode surface. Surprisingly, despite being a water-soluble, the DMAEM polymer remained attached to the electrode surface for the duration of the voltammetry experiments (approx 1hour) with little loss in signal strength.

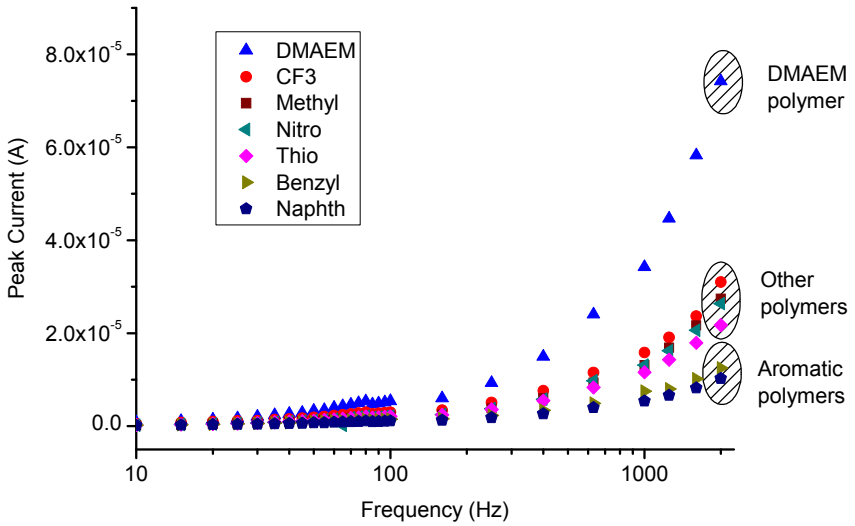

Figure 2.27 Observed peak currents plotted versus frequency. Show clearly the stronger response observed for DMAEM polymer and the weaker response observer for the two aromatic polymers. All other polymers fall midway.

2.4 Cationic copolymer systems.

We also briefly explored the synthesis of DMAEM copolymers and converting these by a simple single step reaction with methyl iodide into cationic copolymers of TMAEM as shown in Figure 2.28. Several unsuccessful attempts explored the synthesis of cationic copolymer during a single step ATRP reaction from the monoblock macroinitiator and trimethylaminoethyl methacrylate (TMAEM) iodine salt. Both of these could be individually dissolved using the "universal" solvent DMSO. However the combination of the two together appeared to adversely affect overall reaction solubility. A single attempt at adding the TMAEM monomer gradually to the ATRP reaction also proved unsuccessful. However ATRP synthesis in near bulk DMAEM monomer as solvent (i.e. DMSO (1.0 mL) used only to dissolve the catalyst) provided each of the respective copolymers in good yields. The subsequent TMAEM copolymer was then quickly and easily produced in a quantitative yield following the addition of approximately 2 equivalents of methyl iodide at room temperature as shown in Figure 2.28.

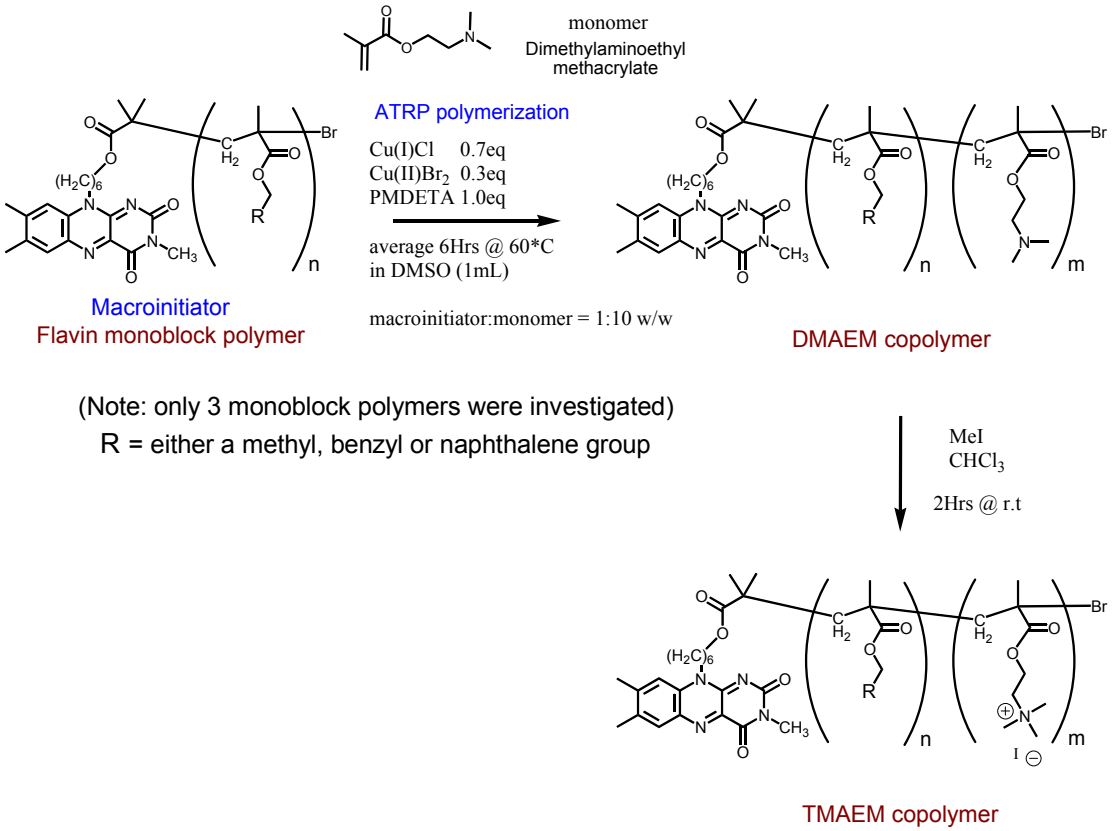

Figure 2.28 Two step synthesis of a cationic diblock copolymer. **Step 1**: ATRP polymerization using monoblock macroinitiator to synthesise a DMAEM copolymer. **Step 2**: Rapid conversion of the DMAEM to a TMAEM iodide polymer using methyl iodine in chloroform at r.t. It is interesting that this reaction did not appear to be exothermic as was the case observed during a similar conversion of methacrylate "monomers" DMAEM to TMAEM.

The reaction scheme shown in Figure 2.28 has so far only been performed using three monoblock macroinitiators, namely $flavin-poly(\mathbf{methyl})$, $flavin-poly(\mathbf{benzyl})$ and $flavin-poly(\mathbf{naphth})$. The proton NMRs of these DMAEM copolymers are shown in Figure 2.29(a to c) stacked above the proton NMR of their respective monoblock polymer macroinitiators for functional group comparison. Integration of the area under specific peaks (as highlighted by the red asterisk ✻) was used to determine the ratio $m:n$ of DMAEM monomer units (m) to hydrophobic monomer units (n). The value of n for each monoblock polymer was in turn calculated from the GPC determined number average molecular weight M_n. Ultimately this not only provided us with a reasonably accurate means of determining the total number of units, the relative ratio (by weight and by number) but also provided an alternative method of measuring the molecular weight of the copolymer. GPC analysis of the DMAEM copolymer was possible and was indeed performed at periodic intervals during the ATRP reaction but the results obtained were ambiguous and therefore unconvincing based on the monomer consumption (i.e. derived from the ratio of polymer to monomer GPC peak area, e.g. Figure 2.5.). The characteristic GPC profile in each example indicated an increasingly high molecular weight distribution as the copolymer became larger. This would perhaps suggest that the ATRP reaction was uncontrolled but as the author was unable to obtain comparative GPC profiles that have been published for similar size large block copolymers. He is therefore unconvinced that this is the case and instead believes that this wide variation in elution time from the GPC is a characteristic behaviour of some complex interactions between copolymer + copolymer and/or the stationary phase within the column. It may however be possible to repeat the GPC results at high temperature

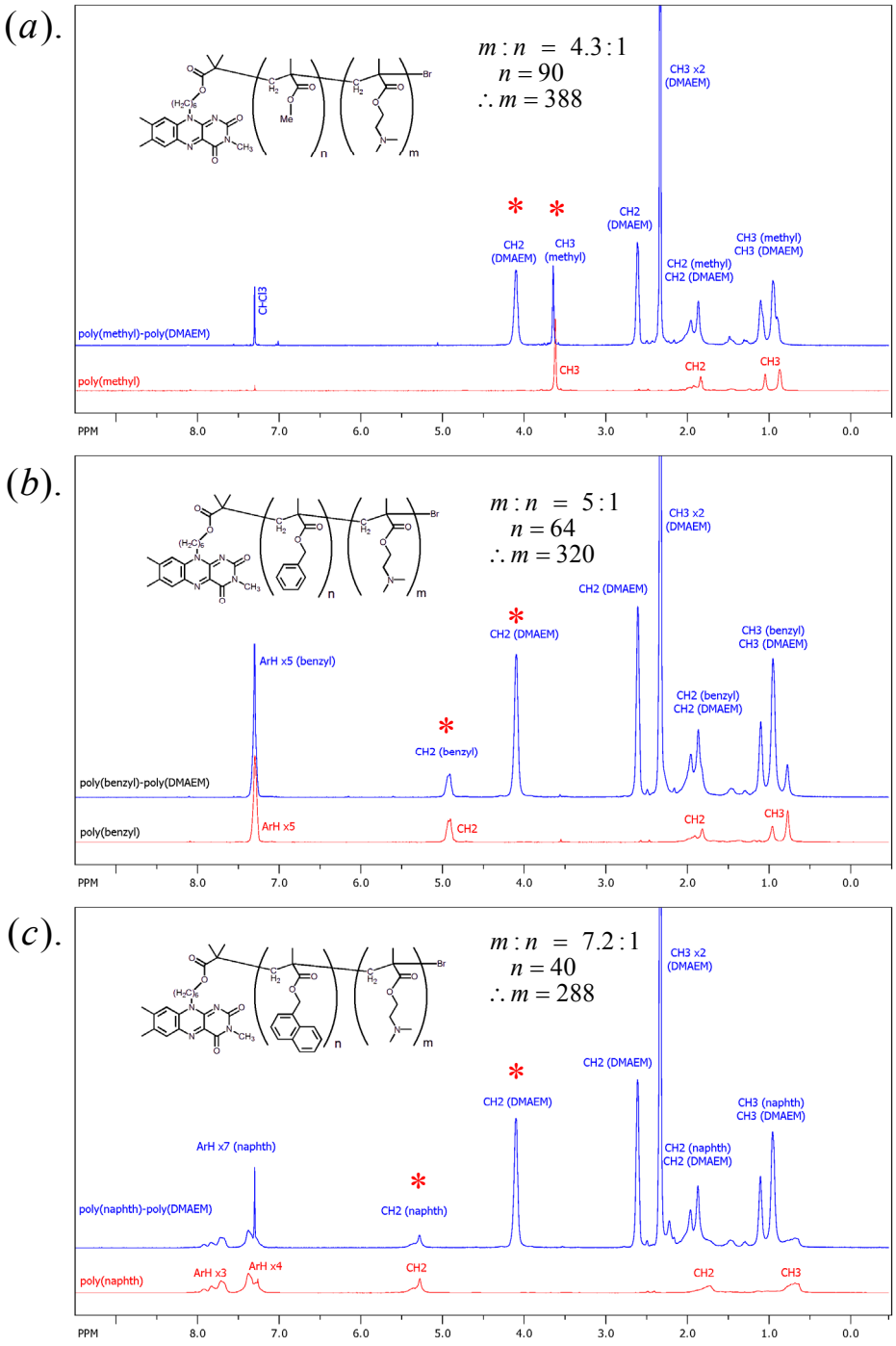

Figure 2.29 Proton NMR spectra for the three DMAEM copolymers (*blue line*) stacked above the proton NMR spectra for the monoblock macroinitiator (*red line*). (a) *poly*(**methyl**)-*b*(**DMAEM**) (b) *poly*(**benzyl**)-*b*(**DMAEM**) (c) *poly*(**naphth**)-*b*(**DMAEM**). Integration of the area under specific peaks (highlighted by the red asterisk ✻) was used to determine the ratio $m:n$ of DMAEM monomer units (m) to hydrophobic monomer units (n). This was later used to estimate the copolymer molecular weights (see Table 2.8).

Values obtained for *m*, *n* and the estimated molecular weight of each of the three DMAEM and TMAEM copolymers are shown below in Table 2.8. These values allowed us to estimate the % weight component of cationic TMAEM to be between 91 and 87% for our three example copolymers. The copolymers were all water soluble forming instantaneous gels at concentrations as low as 1% w/w (e.g. 10mg per 1mL of water) with the aromatic based block copolymers achieving gel formation at 0.5% w/w. The photograph shown below in Figure 2.30 demonstrates this solid gel behaviour by an upturned vial of a 1% w/w concentration of the *flavin – poly*(**benzyl**)-*poly*(**TMAEM**) block copolymer. Interestingly we have discovered that after preforming ultrasonication for only a few minutes, the gel matrix becomes irreversibly disrupted transforming it to a very viscous non-gel solution. At present however we have no further information to report, though future work is planned to explore the physical, electrochemical and photochemical characteristics of these gel forming copolymers

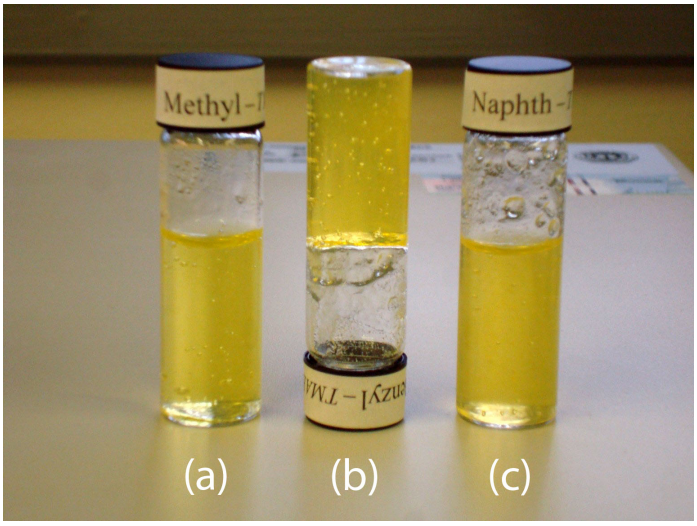

Figure 2.30 Three vials of 1% w/w aqueous flavin cationic copolymer sol-gels. (a) *poly*(**methyl**)-*b*(**TMAEM**) (b) *poly*(**benzyl**)-*b*(**TMAEM**) (c) *poly*(**naphth**)-*b*(**TMAEM**).

copolymer	*no of units per block*		*MWt per unit*		*MWt of each block* (*g*/*mol*)		
	1st block	2nd block	1st block	2nd block	1st block	2nd block	TOTAL
p(*methyl*)-*b*(**DMAEM**)	90	388	100.1	157.2	9009	60994	**70003**
p(*benzyl*)-*b*(**DMAEM**)	64	320	176.2	157.2	11277	50304	**61581**
p(*naphth*)-*b*(**DMAEM**)	40	288	226.1	157.2	9044	45274	**54318**
p(*methyl*)-*b*(**TMAEM**)	90	388	100.1	229.1	9009	88891	**97900**
p(*benzyl*)-*b*(**TMAEM**)	64	320	176.2	229.1	11277	73312	**84589**
p(*benzyl*)-*b*(**TMAEM**)	40	288	226.1	229.1	9044	65981	**75025**

Table 2.8 Summary of copolymer composition based on the proton NMR spectra shown in Figure 2.27 and the GPC results of the associated monoblock macroinitiator. The MWt of each block was calculated from the (*no of units per block*) × (*MWt per unit*).

2.5 Conclusions:

2.5.1 Overview of the flavin polymer's E^{θ} values:

Difficult to accurately determine the formal potential E^0 from CV results due to the irregularly shifting pattern of the anodic peaks at different scan rates. Both the CV and SWV results place the flavin-DMAEM polymer as having the most positive E^0 and the flavin-Nitro polymer as having the most negative E^0. As expected this positioning is appropriately based on the nature of the polymer pendant groups being the most electron withdrawing (DMAEM) and electron donating (Nitro). Molecular modelling in Figure 2.31 shows these pendant groups to have contrasting regions of electron density. It is therefore believed that these groups are able to electrochemically influence the flavin cofactor though either a polarization effect or through acting as a surrogate electron Donor/Acceptor. Although the SWV results shown in Figure place the other polymer systems within 5mV of each other. It is therefore likely that any localized influence from these pendant groups will have been mostly neutralized by the redistribution of electron density within the polymer structure.

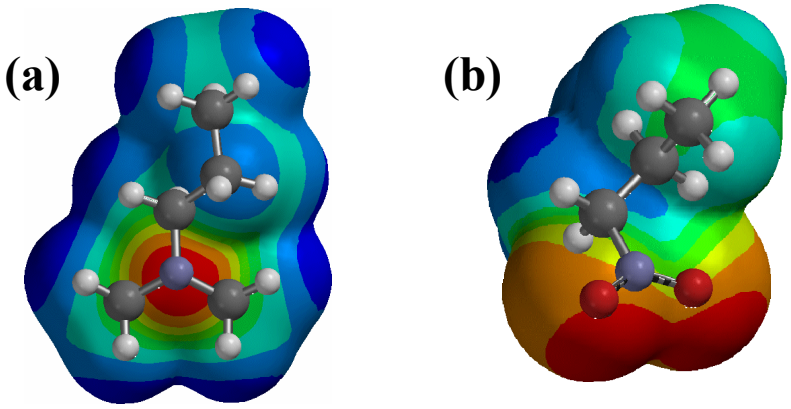

Figure 2.31 Electrostatic potential maps for **(a)** N,N-dimethylpropylamine and **(b)** 1-nitropropane (representing the DMAEM and Nitro polymer pendant groups respectively) which were derived using a Spartan quantum mechanical program with Basis Set = 6-31G* method = RB3LYP HF-DFT SCF calculation.

2.5.2 Comments regarding the synthetic enzyme design strategy:

Enzymes appear to have evolved active site structures that minimize the reorganizational energy λ. Although fast electron transfer rates at high overpotential may appear to be a desirable quality, it isn't. It is more beneficial for the enzyme to be able to easily alter the redox state of the electroactive species and to maintain it for a prolonged period. The smaller the value of λ the easier it is for the electroactive species within the active site of the enzyme to enter the Marcus "Inverted" regime. As discussed earlier, while in this regime, the back transfer of an electron by any subsequently formed charge separated species becomes slower and overall the lifetime of the excited state molecule increases. The longer lifetime becomes the desirable quality of the excited species because the longer it can survive in an excited state the greater the likelihood it will react with some other species.

A suitable synthetic design strategy that might mimic the active site of an enzyme could therefore involve some rigid structure with predefine co-ordination geometry that would "grip" the electroactive species in such a way that it remains unaltered regardless of oxidation state and therefore require negligible reorganizational energy λ.

2.5.3 Comments regarding future experimental procedure:

At the time it was intuitively considered that it may have been better to have used a larger polishing grain which would generate a rougher surface and hence more contact points for the polymers to adhere to. Although, this idea was not pursued it was later discovered to be method adopted by other researchers [35] to attach enzymes to pyrolytic graphite "edge" (PGE) electrodes. Various polar functional groups such as -C=O and –OH, are attached to carbon materials due to the graphite-like sp2 hybridized planar bonding structure. The Armstrong group [35] suggests that the roughness created the coarser polishing allowed irregularly shaped macromolecules to make multiple polar contacts with the electrode. Absorption and stabilization were understood to be optimized at low temperatures (e.g. 0°C), by suitable choice of electrolyte conditions ionic strength and adding stabilizers or co-adsorbents such as aminocyclitols to create ternary salt bridges. By examination of the peak currents plotted versus frequency in Figure 2.27 we can see that binding of the very polar DMAEM polymer to the electrode surface appears much stronger than the others and is represented by the much larger peak current response at any given frequency. A weaker response is observed for the less polar aromatic polymers, these pendant groups somehow hindering any favourable interaction between the polymers methacrylate backbone and the electrode surface. All other polymers in this series seem to fall roughly midway between these two boundaries. Although the voltammetry responses from these polymers absorbed under similar conditions onto smooth 0.05 μm alumina polished GC electrodes were adequate and fairly similar in response to those published by Armstrong for PFV. [35, 36, 42] It is highly likely the responses could have been stronger if the electrode had been roughly polished using 0.1 μm alumina.

CHAPTER 3

FLAVIN-DIAMIDOPYRIDINE POLY(PEG) SYSTEM.

3.1 Background introduction.

Chapter section 1.2 discussed in detail how flavin redox properties could be modulated through hydrogen bonding interaction and how these changes were experimentally determined through a combination of ^{1}H NMR titration experiments and electrochemistry. To briefly recap, the binding constant K_a of the diamidopyridine (DAP) to the flavin in its oxidized form was first determined by ^{1}H NMR ($CDCl_3$) to be 537 M^{-1}. The reduction of the flavin to its radical anion, strengthen the binding further by increasing the negative charge on the carbonyl oxygens. This resulted in a shift of +155 mV in the cyclic voltammetry half wave potential $E_{1/2}$ (in CH_2Cl_2) which corresponded to an almost 500 fold increased in the binding constant to $K_a(red) = 250,000$ M^{-1}, as depicted in Figure 3.1.

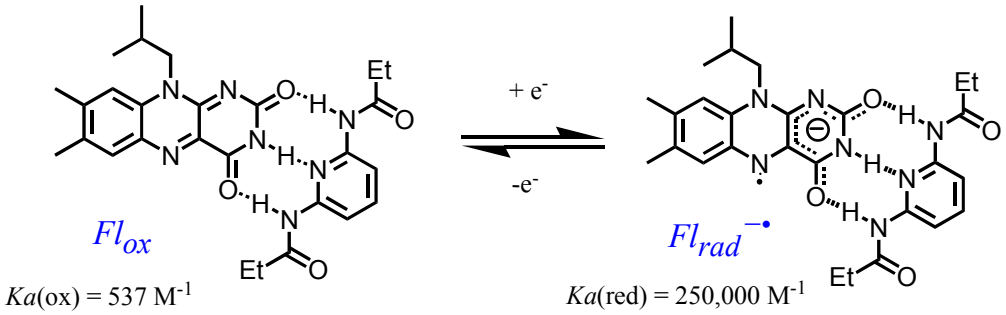

Figure 3.1 An approximate 500 fold increase was observed in the association constant K_a between the flavin and diamidopyridine (DAP). [4]

Rotello's experiments [4] were carried out in a non-polar solvent (i.e. DCM/$CHCl_3$) which fashioned as a simple system for mimicking the non-polar environment of the flavoenzyme active site. The main objective of these following set of experiments was therefore to replicate the active site created within the apoenzyme by encapsulating the flavin with the polymer structure while dissolved in both polar and non-polar solvents (e.g. dichloromethane and water). Results would be verified by a combination of electrochemistry, UV/Vis and fluorescence spectroscopy. Particle size in solution would be determined by Dynamic Light Scattering (DLS) and would provide confirmation whether the polymer chains were indeed condensed into individual units or forming micelle structures.

3.2 Experimental design strategy.

3.2.1 The flavin-diamidopyridine (flavin-DAP) polymer.

The basic strategy involved molecular linking the flavin and DAP units via a flexible alkyl chain which would provide sufficient degree of freedom to permit the two complementary hydrogen-bonding units to interact. By functionalizing the molecule as an alkyl halide it could be used as an initiator for ATRP polymerization. Polyethylene glycol (PEG) methyl methacrylate would be used as a monomer as it provides a polymer with excellent solubility properties in both aqueous and organic solvents. This would allow us to make comparative analysis in both polar and non-polar solvents.

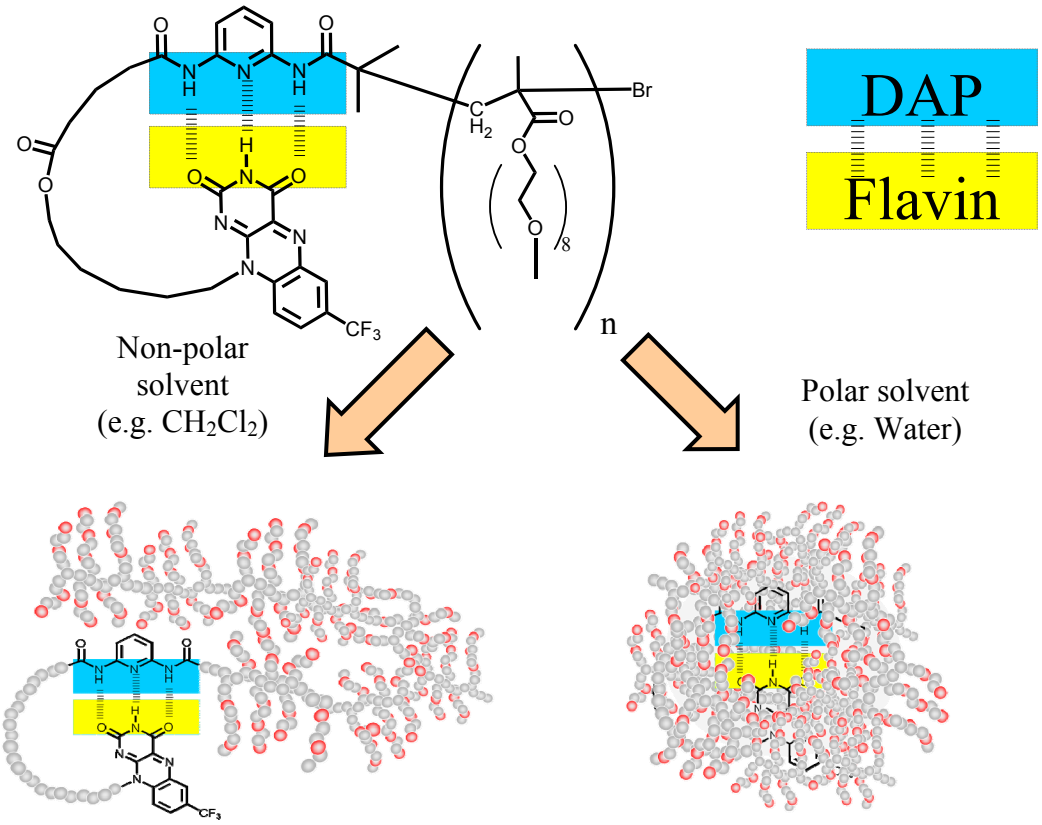

Figure 3.2 Expected behaviour of the flavin-DAP polyethylene glycol (PEG) polymer in both polar and non-polar solvents.

Figure 3.2 pictorially represents how we might envisage the flavin-DAP polymer to behave in different solvents. The flavin-DAP unit (symbolized by the yellow and blue rectangles respectively) is soluble in dichloromethane but insoluble in water. The solvatophobic forces are conceptually considered to be stronger in water than DCM due to the prevalent hydrogen bonding. Figure 3.2 therefore depicts the flavin-DAP unit as not fully encapsulated by the polymer is just as likely to be exposed to the non-polar solvent molecules as to the polyethlene glycol molecules. However because the flavin-DAP unit is insoluble in water it is reasonable to assume that it will favour the environment farthest from the water molecules and therefore bury itself within the polymer structure. This concept will be tested later during the determination of particle size by Dynamic Light Scattering (DLS) with a more

compact structure expected in water. Variations in the electrochemical and photochemical characteristics of the flavin would provide insight into it immediate environment. To act as a control for the experiment we also synthesised an N(3) methyl protected flavin-DAP polymer where the methyl group would physically prevent direct hydrogen bonding with the DAP unit. As a comparison for both these systems we synthesised their corresponding flavin polymer counterpart without the DAP unit. All four proposed structures are shown in Figure 3.3.

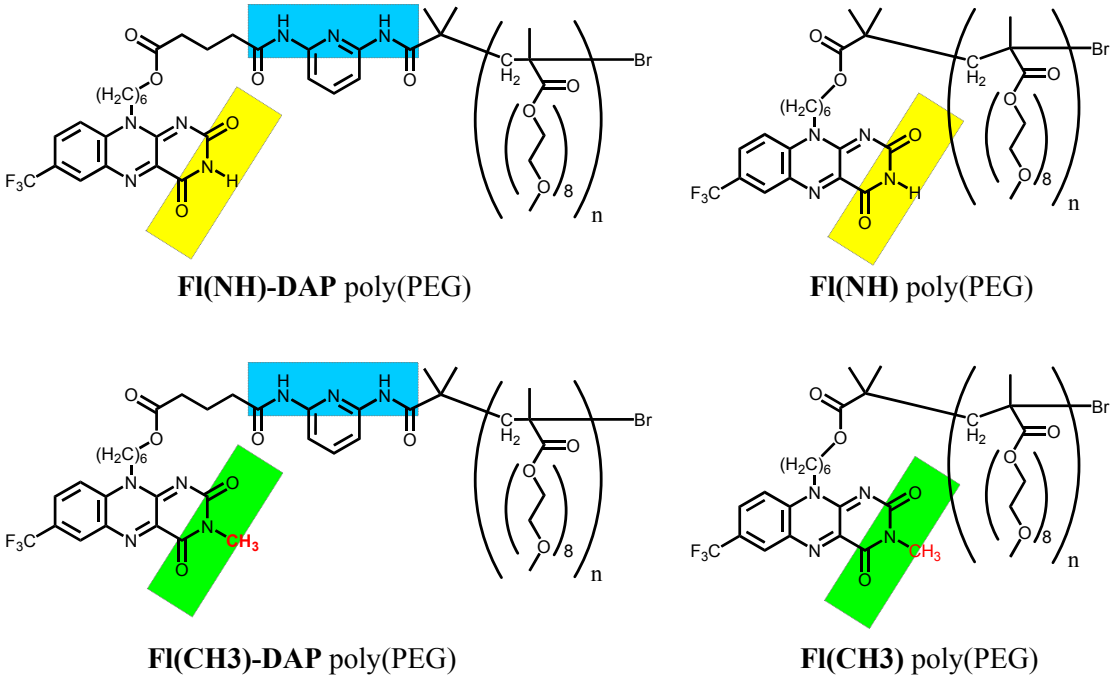

Fl(NH)-DAP poly(PEG)

Fl(NH) poly(PEG)

Fl(CH3)-DAP poly(PEG)

Fl(CH3) poly(PEG)

Figure 3.3 Proposed structures for the four the Flavin-DAP and Flavin-(non-DAP) polymers. The N(3) methyl protected Flavins are represented by the green rectangles and N(3)H Flavins are represented by the yellow rectangles The labelling underneath will be used as a shorthand notation to identify a specific structure in the following text.

3.2.2 Overview:

Results have not been as expected and seem to suggest that the reduced flavin is stabilized more within the polymer structure for the N(3)-methyl protected systems, in particular the flavin(CH3)-DAP and not, as was predicted, the flavin(NH)-DAP polymer system. The experimental evidence suggests that the DAP unit may be forced to adopt a normally unfavourable stacking conformation directly above the flavin's tricyclic aromatic surface as illustrated by Figure 3.4. This molecular model of a Fl(CH3)-DAP unit was created using Spartan quantum mechanical software by manoeuvring the flavin and DAP units into the approximate positions shown and processed using "minimized energy" algorithm. The model shows that the flavin O(2) and O(4) lone pairs have line up to bind with the corresponding DAP hydrogen atoms and demonstrates that a two point hydrogen-bonding motif is possible although in free solution it might not be easily attained.

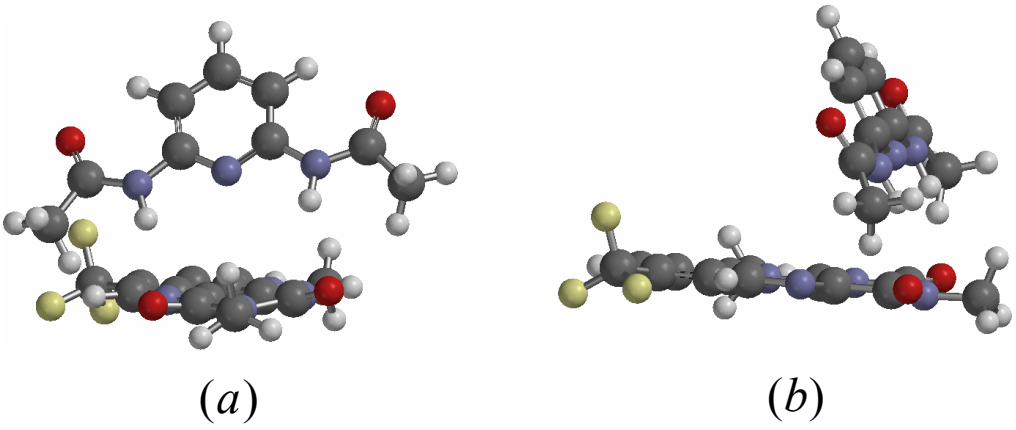

Figure 3.4 A 3D molecular model of a flavin(NCH3)-DAP showing one possible hydrogen-bonding conformation with the DAP unit aligned at an oblique angle above the aromatic surface of the flavin. This model was derived using a Spartan quantum mechanical program with Basis Set = 6-31G* Method = RB3LYP HF-DFT SCF calculation of N(3)-methyl protected flavin and showsg **(a)** front view **(b) s**ide view depicting hydrogen bonding with the diethylamidopyridine molecule aligned directly above.

While in this conformation the DAP unit may be able to form a hydrogen bonding motif with the flavin's O(2) and O(4) carbonyls which would promote a redox modulating ability through stabilization of the reduced flavin. The $\pi - \pi$ stacking interaction has been shown to diminishes the stability of the 2nd electron transfer which would lead to the fully reduced flavin anion $Fl_{red}H^-$. This has been described by Rotello as due to the build up of electrostatic repulsion generated by the electron rich aromatic centre of the flavin radical as was shown in Chapter 1, Figure 1.7(b). The balance between hydrogen-bonding and $\pi - \pi$ stacking would result in a more electrochemical reversible redox system. The following results should support this conclusion.

3.3 Synthesis.

3.3.1 Flavin-DAP polymer synthesis:

The following is a brief outline of the procedures and conditions involved during the synthesis full details of which are provided in Chapter 8: Experimental. The synthesis described in Figure 3.6 starts at route (a) with compounds C-14 and C-15. It describes the synthesis of the non-DAP flavin polymer systems, Fl(NH)poly(PEG) and Fl(CH3)-poly(PEG). The first step in route (a) is an esterfication to form either C-16 or C-17 using 2-bromoisobutryl bromide in THF to provide either the Fl(NH) or the Fl(CH3) alkyl halide initiator. These were taken forward to the next step, using the general ATRP polymerisation procedure described in the next sub-section, to afford the two flavin-poly(PEG) polymers Fl(NH)-poly(PEG) and Fl(CH3)-poly(PEG).

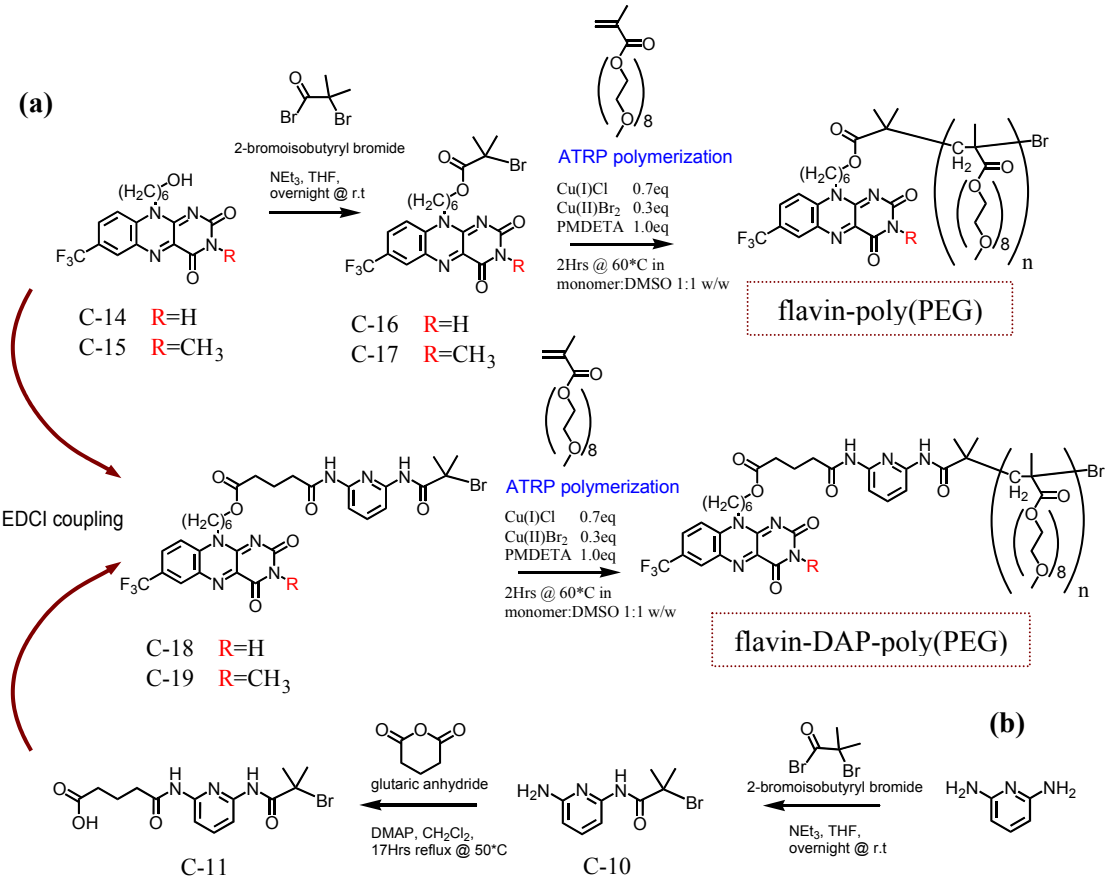

Figure 3.5 Synthesis of (a). flavin-poly(PEG) and (b). flavin-DAP-poly(PEG) where R = H *or* CH_3.

Route (b) starts by reacting 2,6-diamidopyridine with 2-bromoisobutryl bromide in THF to afford compound C-10. This was then heated under reflux with glutaric anhydride and a catalytic amount of DMAP to afford compound C-11. EDCI coupling with either flavin compound C-12 or C-13 at room temperature in DCM would finally afford either the Fl(NH)-DAP or Fl(CH3)-DAP alkyl halide initiators which have been labelled in Figure 3.6 as compounds C-18 and C-19 respectively. These were used during the general ATRP polymerisation procedure described in the next sub-section, to afford the two flavin-DAP polymers Fl(NH)-DAP poly(PEG) and Fl(CH3)-DAP poly(PEG).

3.3.2 General ATRP polymerization procedure for routes (a) and (b).

The same ATRP procedure was used for all four flavin initiators. Polyethylene glycol (PEG) methyl methacrylate (150 equivalents) was weighed into a two neck flask. This would become the reaction flask. To this was added an equal weight of DMSO (solvent) and the flavin initiator (1 equivalent). The catalytic system, Cu(I)Cl, Cu(II)Br and PMDETA in ratios 7:3:10 equivalents were added to the second flask and dissolved in DMSO (10mL). Both mixtures were purges of oxygen by the "freeze-pump-thaw" technique (3 cycles). Just prior to immersing the reaction flash into a temperature controlled oil-bath set to a constant 60°C, 1mL of the catalytic mixture was injected by means of a gas tight syringe into the centre of the stirring reaction maintained under a fast flow of nitrogen gas. The reaction was stirred at 60°C for 2h while sealed under nitrogen and then terminated by pouring into a vigouously stirring flash of diethyl ether (300mL). The polymer precipitated as a green-yellow residue which was allowed to settle for 30min before carefully decanting the ether. The remaining green-yellow residue was dissolved in $CHCl_3$ (50mL) then passed through a short flash column of Al2O3 to remove traces of copper. The filtrate was condensed to a smaller volume (25mL) under vacuum then filtered through a syringe filter ($0.45\ \mu m$ PTFE) and precipitated again by pouring into a second stirring flask of diethyl ether (300mL). The remaining yellow residue was collected by decanting and dried under high vacuum for 48h.

3.4 Polymer characterization.

General analytical procedures for GPC and DLS analysis can be found in Chapter 8: Experimental section.

3.4.1 Gel permeation chromatography (GPC) analysis:

The GPC profiles and peak positions (Mp) for the four flavin polyethylene glycol (PEG) polymers systems are shown in Figure 3.7. The molecular weights M_n M_w and polydispersity index (PDI) are summarized in Table 3.1. The results show good living characteristics with $\text{PDI} \leq 1.25$.

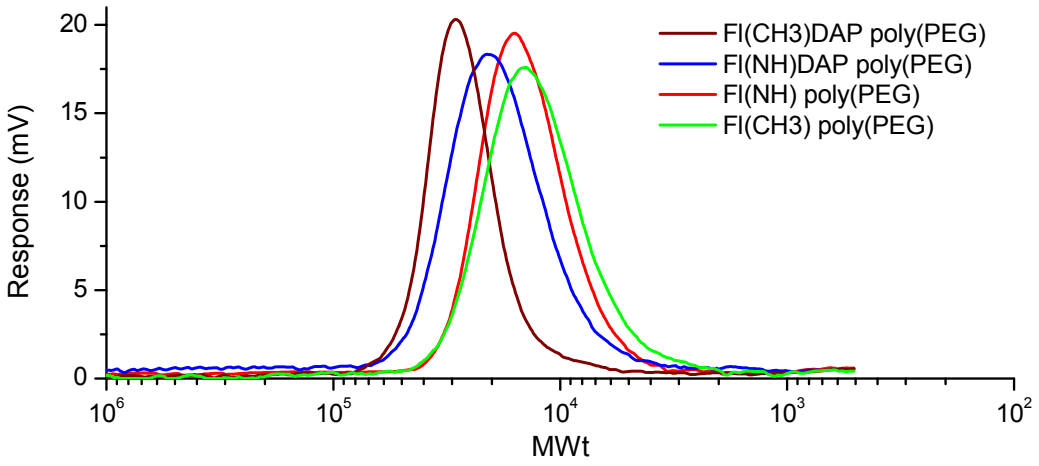

Figure 3.6 GPC profiles and peak positions for the four flavin (PEG) polymers.

Sample Name	Mn	Mw	Mp	PDI
Fl(NH) poly(PEG)	13136	15556	15745	1.18
Fl(NH)DAP poly(PEG)	17325	21017	21018	1.21
Fl(CH3)DAP poly(PEG)	24722	28365	28921	1.15
Fl(CH3) poly(PEG)	11540	14406	14156	1.25

Table 3.1 Summary of the molecular weight and polydispersity values obtained by GPC.

3.4.2 Particle sizing by dynamic light scattering (DLS):

Figure 3.8 shows the particle size distribution by volume for the flavin-DAP polymers in water. No micelle formation was evident from these plots and the polymers appeared to form individual units with diameters between 5 and 12nm. These polymer units clearly show an equivalent order of size to the molecular weight values obtained from Gel Permeation Chromatography (GPC), as shown in Table 3.2 with larger particles corresponding to a higher molecular weight polymer and vice versa.

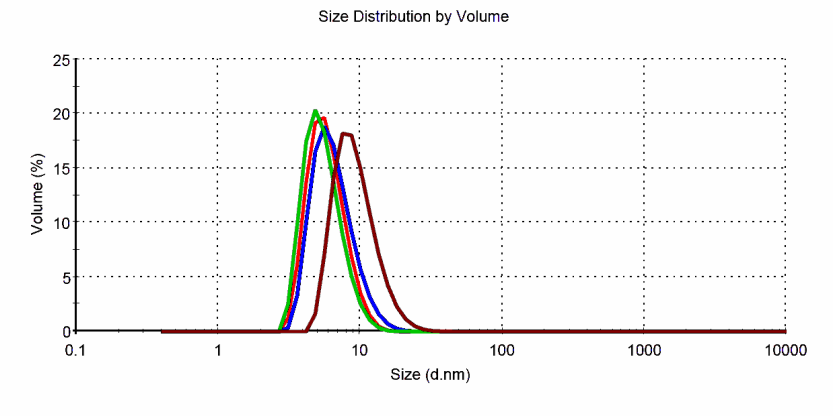

Figure 3.7 Particle size distribution by Volume for the Flavin-DAP polymers in Water. *Diameters* = (red) $Fl(NH)-PEG = 5.992\text{nm}$, (blue) $Fl(NH)DAP-PEG = 6.654\text{nm}$, (green) $Fl(CH3)-PEG = 5.616\text{nm}$, (brown) $Fl(CH3)DAP-PEG = 9.556\text{nm}$.

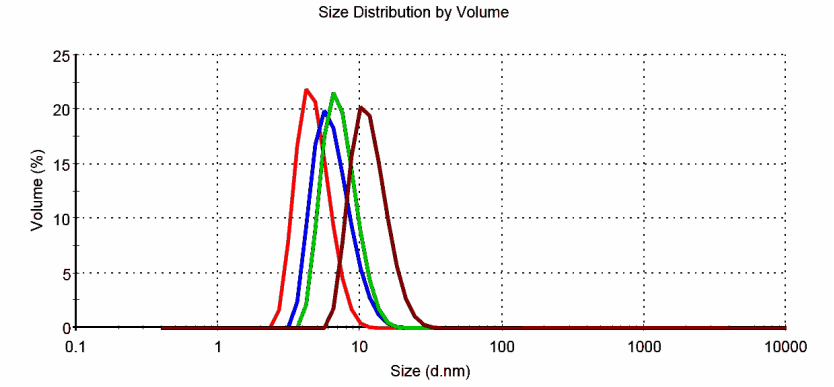

Figure 3.8 Particle size distribution by Volume for the Flavin-DAP polymers in THF. *Diameters* = (red) $Fl(NH)-PEG = 4.816\text{nm}$, (blue) $Fl(NH)DAP-PEG = 6.596\text{nm}$, (green) $Fl(CH3)-PEG = 7.392\text{nm}$, (brown) $Fl(CH3)DAP-PEG = 11.976\text{nm}$.

It is interesting to compare the DLS particle size values obtained from water, Figure 3.8, with the corresponding values obtained in THF shown in Figure 3.9. The polymer particles are more widely dispersed in size with the N(3) methyl protected polymer system larger by some 25 to 30%. Smaller more compact polymer particles in aqueous solution would suggest that strong hydrophobic forces are at work compressing the polymer structure

into more compact units thereby creating the conditions that would most likely push the encapsulated flavin and DAP units into an unfavourable stacking conformation.

Polymer	DLS Results Particle diameter (nm)		GPC Results Mn (g/mol)
	Water	THF	
Fl(NH) poly(PEG)	5.992	4.816	13136
Fl(NH)DAP poly(PEG)	6.654	6.596	17325
Fl(CH3) poly(PEG)	5.616	7.392	11540
Fl(CH3)DAP poly(PEG)	9.556	11.960	24722

Table 3.2 Comparison particle size obtained using Dynamic Light Scattering (DLS) with results for polymer molecular weight M_n obtained by Gel Permeation Chromatography (GPC).

3.5 Electrochemistry.

3.5.1 Cyclic voltammetry of flavin initiators in DCM.

Figure 3.9 shows the cyclic voltammograms (CV's) for the flavin initiators separated into two diagrams for clarity. Figure 3.9(a) compares the CV's for the two unprotected N(3) initiators, flavin(NH) and flavin(NH)-DAP. Figure 3.9(b) compares the CV's for the two methyl protected N(3) initiators, flavin(NCH3) and flavin(NCH3)-DAP. In both cases, the two non-DAP initiator are *red* and the two DAP initiators are *blue* .

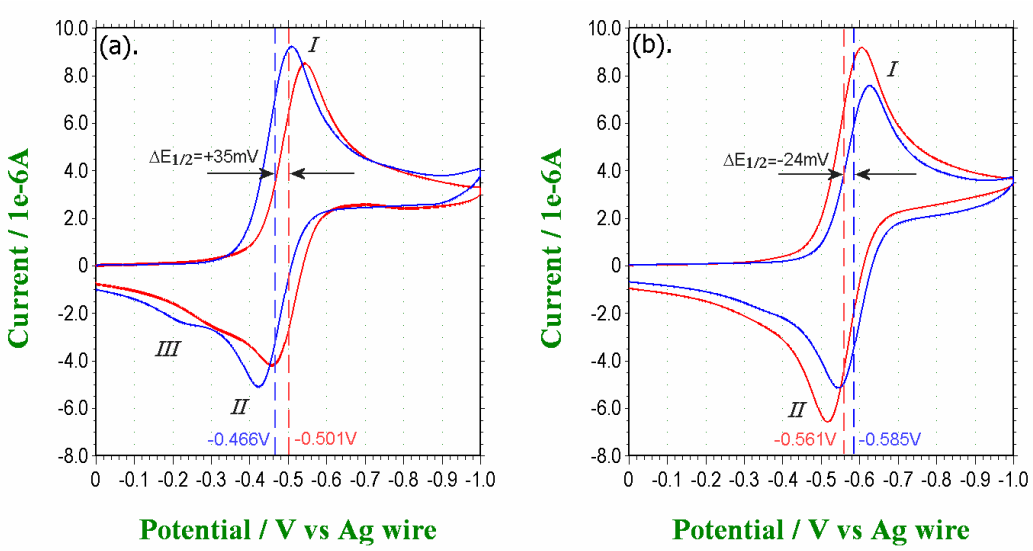

Figure 3.9 Cyclic voltammograms (CV's) of flavin initiators (0.5mM) in DCM with $0.1\text{M}\ TBA\cdot PF_6$ as the supporting electrolyte and at a scan rate $\nu = 0.1\text{Vs}^{-1}$.
Figure **(a)** shows CV's for Flavin(NH) in *red* ($E_{1/2} = -0.501\text{V}$) and Flavin(NH)-DAP in *blue* ($E_{1/2} = -0.466\text{V}$). Figure **(b)** shows CV's for Flavin(NCH_3) in *red* ($E_{1/2} = -0.561\text{V}$) and Flavin(NCH_3)-DAP in *blue* ($E_{1/2} = -0.585\text{V}$).

The cyclic voltammograms (CV's) in Figure 3.9(a) illustrate the characteristic binding interactions between the flavin(NH) and DAP unit previously described in Chapter section 1.2. The reductive peak (wave *I*) for the flavin(NH)-DAP (*blue*) initiator appears slightly larger in amplitude than that for flavin(NH) (*red*) and also occurs at a more positive redox potential. The first re-oxidation peak (wave *II*) of the Fl(NH)-DAP initiator occurs at a more positive potential and is larger in amplitude relative to the non-DAP flavin(NH).

Both re-oxidation peaks (waves *II* (at -0.45V) and *III* (at -0.32V)) in the CV for flavin(NH) (*red*) are practically merged together. The same two re-oxidation waves for flavin(NH) (*blue*) appear better defined (-0.42V and -0.22V). These characteristics are suggestive of the ease at which the flavin(NH)-DAP can now become reduced from $Fl_{ox} \rightarrow Fl_{rad}^{-\bullet}$. The flavin radical $Fl_{rad}^{-\bullet}$ is stabilized through complementary hydrogen-bonding with the DAP unit. The decrease and positive shift of wave *III* both signify the decline of the subsequent chemical-electrochemical (CE) steps $Fl_{rad}^{-\bullet} \xrightarrow{+H} Fl_{rad}H^{\bullet} \xrightarrow{+e^-} Fl_{red}H^{-}$.

Figure 3.9(b) compares the CV's for the two N(3) methyl protected flavin initiators. The profile mainly describes a single electron transfer process (i.e. one reductive wave and one oxidation wave with a quasireversible peak separation of approx $80-90\text{mV}$). There is however a slight hint of a second oxidation wave which may suggest the presence of some unknown proton source that could promote the CE reaction just described in the previous paragraph.

Comparison of the CV's Figures 3.10(a) and (b) clearly shows that the there is a positive shift in the half wave potential $\Delta E_{1/2} = +35\text{mV}$ from adding a DAP unit to the flavin(NH) system and a negative shift of $\Delta E_{1/2} = -24\text{mV}$ from adding the DAP to the methyl protected flavin(CH3) system. We could conclude that there is overall a negative redox effect of molecularly adding both methyl group and DAP unit to the flavin and that therefore at best the hydrogen-bonding influence of the DAP unit to the flavin(NH) system might at best be calculated as the difference between the $\Delta E_{1/2}$, i.e., $\Delta E_{1/2} = +35-(-26) = +59\text{mV}$.

However this is still along way off from the half wave potential difference of $\Delta E_{1/2} = +155\text{mV}$ reported by Rotello.[4] One possible reason could involve the electronegative bromide atom competitively interacting and disrupting the hydrogen-bond between the flavin's O(4) carbonyl and the corresponding DAP amine as depicted in Figure 3.10. According to the Pauli's "Table of Electronegativity", bromine and oxygen have fairly similar electronegativity ratings (3.0 and 3.5 respectively).[43] In addition the two bulky methyl groups and the bromide atom would also generate steric hindrance that would limit the proximity of the DAP amine much more in comparison with ethyl groups of diethyl amidopyridine used by Rotello.

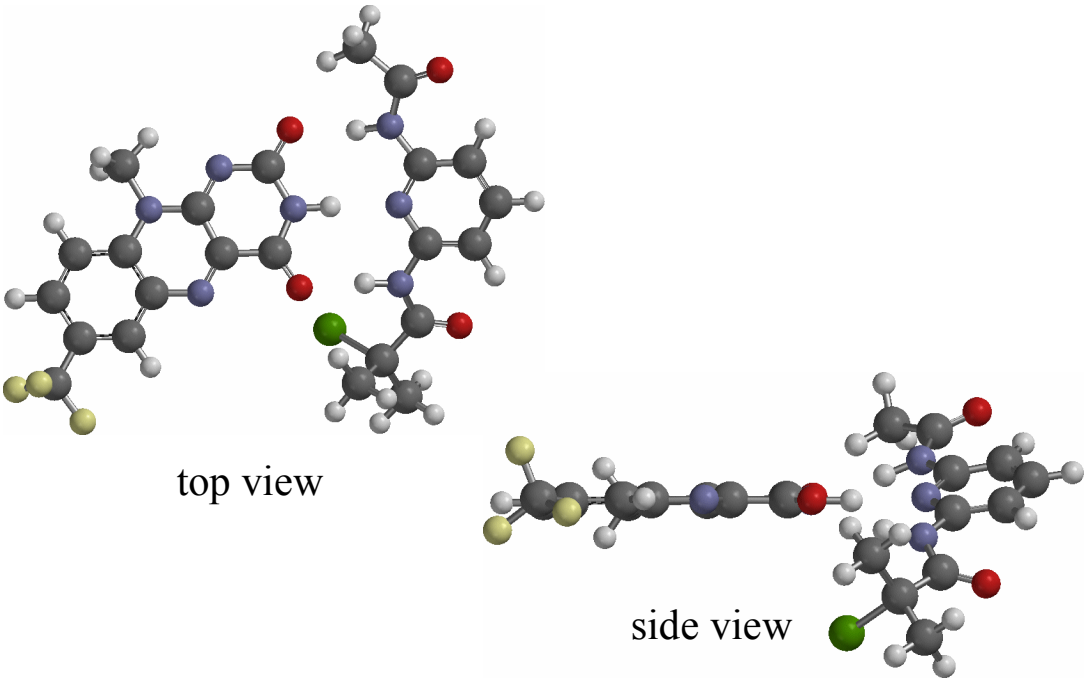

Figure 3.10 A 3D model of the flavin(NH)-DAP initiator created using Spartan quantum mechanical software and processed possible position of the bromide atom (*green*). The bulky bromide atom appears to disrupt and weaken the hydrogen bonding interaction between the flavin carbonyl thus forcing the DAP unit to fall out of planar alignment with the flavin (compare this with the flavin N(3)H - DAP pair shown in Figure 3.34, Section 3.7.)

3.5.2 Cyclic voltammetry of flavin PEG polymers in DCM.

The cyclic voltammograms for the flavin-PEG polymers are shown in Figure 3.12. Again the differences are best described by separately showing the plots for the Fl(NH) and Fl(CH3) polymer systems. There are four main observational points regarding these CV's worth discussing.

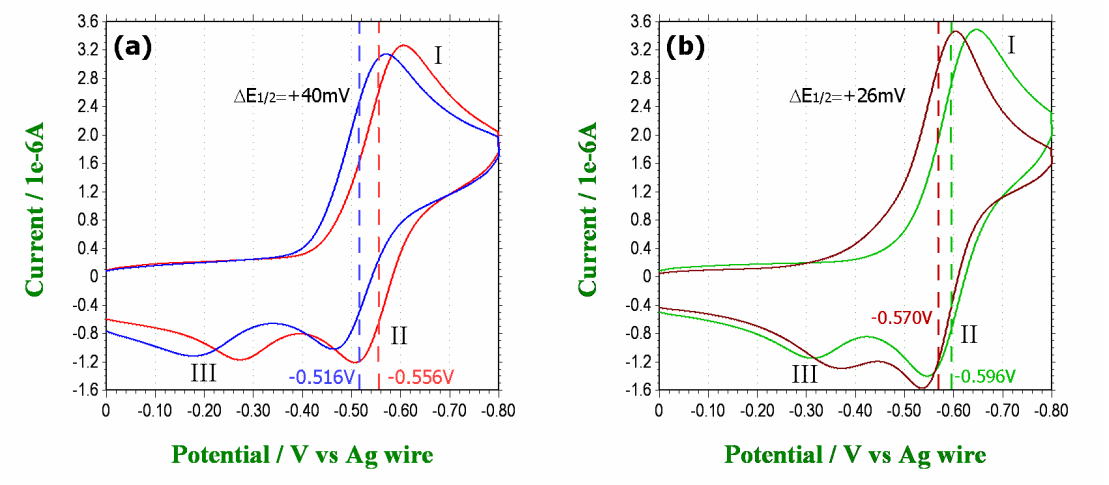

Figure 3.12 Cyclic voltammograms (CV's) of flavin PEG polymer (0.5mM) in DCM with 0.1M $TBA \cdot PF_6$ as the supporting electrolyte and a scan rate of 0.1Vs^{-1}. Figure (a) shows CV's for flavin(NH)-poly(PEG) in *red* and flavin(NH)-DAP-poly(PEG) in *blue*. Figure (b) shows CV's for flavin(NCH_3)-poly(PEG) in *green* and flavin(NCH_3)-DAP-poly(PEG) in *brown*.

Observation 1.

The most unexpected feature is the pronounced presence of a 2nd oxidation peak (wave *III*) in all four polymer systems. This would suggest the presence of a proton sources which must have a pKa value of less than 10. [4] It has been described earlier that if an aprotic solvent is used, another flavin can act as the sole proton source. However since the flavins in these experiments are either encapsulated within the polymer structure or at the very least sterically shielded by the polymer structure it makes a second flavin an unlikely source. Residual DMSO from the ATRP reaction was considered but there is no ^{1}H NMR evidence which explain its presence and besides DMSO's $pKa = 35$. Water was also considered but it has a of $pKa = 15.7$ and therefore also ruled out. Lastly we've also considered the PEG polymer which was intended to encapsulate the electroactive flavin. Although an exact pKa value for PEG could not be found, ethyl acetate can be consider a close approximate to the polymer structure and it has a $pKa = 25$.

We have no satisfactory explanation for this and at the moment and can only comment that it is also observed for other polymeric flavoenzyme model systems which we synthesised. The second oxidation wave appears only during solution phase cyclic voltammetry and not during surface immobilized CV (Section 3.5.7) where the polymer was applied to the electrode as a thin film. We therefore considered that this might be a diffusion related problem which occurs as a result of the sluggish diffusion of large molecules (i.e. diffusion of a reduced flavin polymer away from the electrode and it return during the reverse scan. A simple test which would distinguish this would be that as the scan rate increased we

would expect the second oxidation peak (wave *III*) to move towards the first oxidation peak (wave *II*). Figure 3.13 shows the CV's for the Fl(NH)-DAP polymer at three different scan rates. This shows the second oxidation peak, wave *III* increasing its separation from wave *II* moving more positive potential and therefore ruling out diffusion.

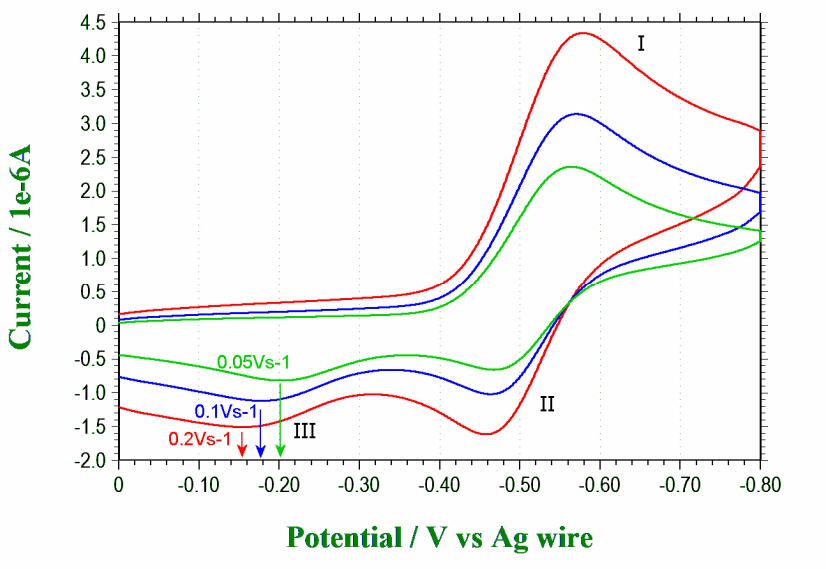

Figure 3.13 Cyclic voltammograms (CV's) showing Flavin(NH)-DAP polymer in DCM at three different scan rates of $0.1Vs^{-1}$. $0.2Vs^{-1}$ (*red*), $0.1Vs^{-1}$ (*blue*) and $0.05Vs^{-1}$ (*green*). As scan rate increased the 2nd oxidation wave shifts to a more positive potential.

Observation 2.

The second unexpected result was that both flavin-DAP polymers appear to be reduced at a more positive redox potential relative to non-DAP flavin polymers. We had expected only to observe a positive change in $\Delta E_{1/2}$ for the Fl(NH)-DAP polymer due to the stabilization influence provide by the flavin-DAP hydrogen bonding and not flavin(CH3)-DAP polymer system with the N(3) methyl group is sterically hindering any interaction. Again with values of $\Delta E_{1/2} = +40$ and $+26\text{mV}$, the stabilization energies $\Delta G = -nF\Delta E_{1/2}$ were not as impressive as those reported by Rotello but are greater that those observed for the corresponding flavin initiators. Also because the stabilization energy for the Fl(NH)-DAP system is 50% greater than that observed for the Fl(CH3)-DAP system, it begins to suggest that this might be achieve if the DAP unit were to piggy-back itself onto the aromatic surface of the N(3) methyl protected flavin and hydrogen-bonding with the two carbonyl as previously shown in Figure 3.4. These two carbonyls are key to stabilization of the flavin reduction $Fl_{ox} \longrightarrow Fl_{rad}{}^{-\bullet}$. They have been shown to become stronger hydrogen bond acceptors due to the increase electron density in the flavin's pyrimidine ring. The hydrogen bond that would have existed between the DAP and the flavin N(3)H would consequently become weaken by the electron rich flavin radical and therefore superfluous as a hydrogen donor.

This situation seems more likely to occur if the flavin and DAP unit where to become pushed into close proximity during encapsulation by the polymeric structure. If the hydrogen bonding was non-linear, the interactions would be weaker and therefore the resulting shift in $\Delta E_{1/2}$ would be less pronounced which might be the case for the flavin(CH3) DAP system.

Observation 3.

As expected, separation between the oxidation waves *II* and *III* in the CV for the flavin(NH)-DAP polymer has increase (Figure 3.12(a)). This was explained by Rotello [4] as due to the increased stability of the flavin radical which retards the ECE reaction…

$$Fl_{red}H^{-} \xrightarrow{-e^{-}} Fl_{rad}H^{\bullet} \xrightarrow{-H^{+}} Fl_{rad}{}^{-\bullet} \xrightarrow{-e^{-}} Fl_{ox}$$

However in Figure 3.12(b) the separation has decreased between the oxidation waves *II* and *III* in the CV for Fl(CH3)DAP polymer. This could be explained by the close proximity of the aromatic DAP pyridine ring stacked directly above the aromatic flavin which would unfavourably interact with electron rich $Fl_{rad}{}^{-\bullet}$ and $Fl_{red}H^{-}$ making them easier to re-oxidize.

Observation 4.

The difference between cathodic and anodic peaks ΔE_p was generally found to be around 100 mV for Fl(NH), Fl(CH3) and Fl(NH)DAP poly(PEG) systems but only 68 mV for the Fl(CH3)DAP polymer as shown in Table 3.3. This is also much lower than that observed for any of the flavin initiator examined at the beginning of this section. This value is within 10 mV of the predicted 59 mV (at 298 K) which describes a totally reversible Nernstian system. This therefore tells us the Fl(CH3)-DAP system is displaying some interesting electrochemically reversible behaviour in DCM.

Polymer	CV Results in DCM at $\upsilon = 0.1$ Vs^{-1}		
	$E_{1/2}$ (V vs Ag wire)	ΔE_p (mV)	E_{pa}(wave III) 2nd oxidation peak (V)
Flavin(NH) poly(PEG)	-0.556	99	-0.271
Flavin(NH)-DAP poly(PEG)	-0.516	107	-0.178
Flavin(CH3) poly(PEG)	-0.596	100	-0.310
Flavin(CH3)-DAP poly(PEG)	-0.570	68	-0.357

Table 3.3 Summary of the Flavin polymer CV results in DCM at $\nu = 0.1$ Vs^{-1}.

3.5.3 Cyclic voltammetry of flavin polymers in water.

Figure 3.14 shows the cyclic voltammograms for the four flavin polymer systems in water. The CV for the Fl(CH3)-DAP appears the most well defined and electrochemically reversible with a $\Delta Ep = 88\text{mV}$ as shown in Table 3.4. The anodic and cathodic peaks of the three other flavin polymer systems progressively increase in separation with the anodic becoming more poorly defined. The flavin(NH) polymer does not display any distinguishing peaks (either cathodic or anodic) but instead the current plateaus at the end of each voltage sweep which suggests that the electron transfer is tending toward irreversible. As a result the peak separation is immeasurable at a scan rate $\nu = 0.1\text{Vs}^{-1}$ yet registering almost 200mV at a slower scan rate of $\nu = 0.01\text{Vs}^{-1}$ as shown in Table 3.4. In general, all we can determine from these voltammogram profiles that the half wave potentials $E_{1/2}$ in water come within a few milliVolts of each other with the two N(3) methyl protected flavin polymers with the flavin(CH3)-DAP system marginally more positive. The main distinguishing difference appears to be the electrochemical reversibility of the systems.

There is no visible presence of the 2nd oxidation wave which was inexplicably observed for the polymers in DCM. Either it is absence or the $E_{1/2}$ for the 1st electron transfer coincides with that of the 2nd electron transfer. In order to help determine this we now need to examine the square wave voltammograms of the flavin polymer systems.

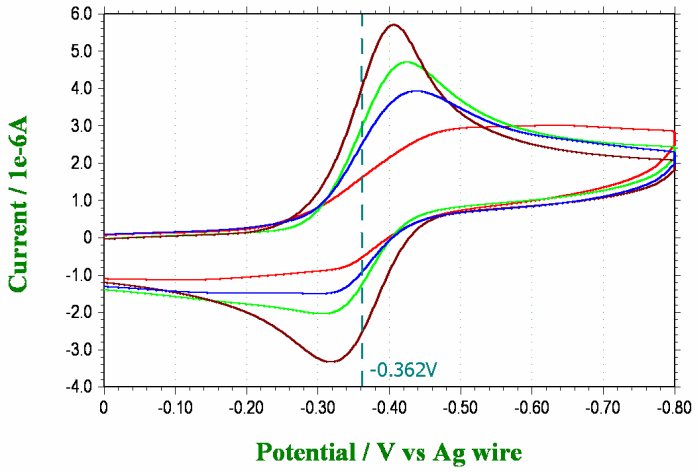

Figure 3.14 Cyclic voltammograms (CV's) of Flavin PEG polymer (0.5mM) in water with 0.1M *NaCl* as the supporting electrolyte and a scan rate of 0.1Vs^{-1}. *(red) = Fl(NH) – PEG*, *(blue) = Fl(NH)DAP – PEG*, *(green) = Fl(CH3) – PEG* and *(brown) = Fl(CH3)DAP – PEG*.

Polymer	CV Results in Water		
	$E_{1/2}$ (V vs Ag wire)	ΔE_p (mV) at $\upsilon = 0.1\text{Vs}^{-1}$	ΔE_p (mV) at $\upsilon = 0.01\text{Vs}^{-1}$
Flavin(NH) poly(PEG)	immeasurable	immeasurable	192
Flavin(NH)-DAP poly(PEG)	-0. 383	130	124
Flavin(CH3) poly(PEG)	-0. 365	118	99
Flavin(CH3)-DAP poly(PEG)	-0. 362	88	71

Table 3.4 Cyclic voltammograms (CV's) of Flavin PEG polymer in water at scan rates of 0.1Vs^{-1} and 0.01Vs^{-1}.

3.5.4 Square wave voltammetry (SWV) of flavin polymers.

The SWV for the flavin polymers are shown in Figures 3.15(a) and (b). The voltammograms represent the net response (i.e. $I_{for} - I_{rev}$). For further details on the SWV technique, refer to Appendix A. The SW parameters used are as described in Figure 3.15's description. In DCM (Figure 3.15(b)) the order of the peak positions correlate reasonably well with the half wave potential $E_{1/2}$ obtained earlier by CV as summarized in Table 3.4.

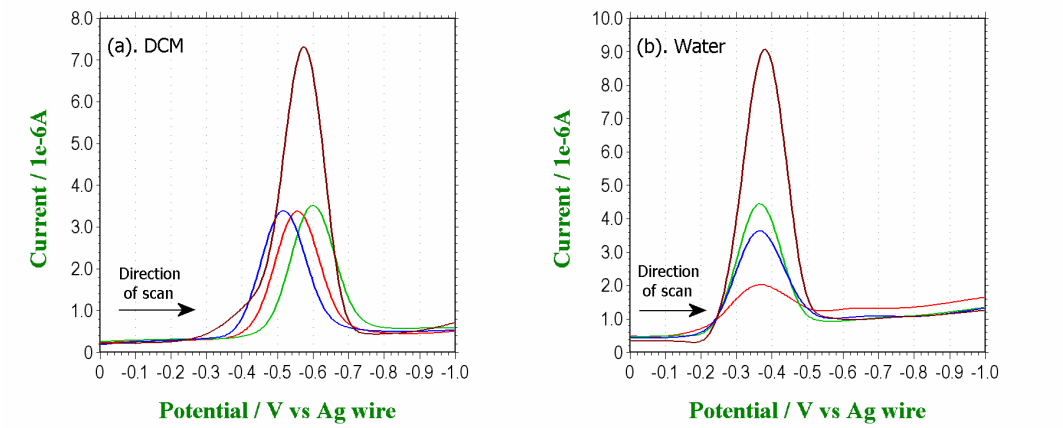

Figure 3.15 SW voltammograms for flavin polymers (0.5mM) in (a). DCM using 0.1M $TBA \cdot PF_6$ as the supporting electrolyte and (b). Water using 0.5M $NaCl$ as the supporting electrolyte. Colour code: $(\text{red}) = Fl(NH) - PEG$, $(\text{blue}) = Fl(NH)DAP - PEG$, $(\text{green}) = Fl(CH3) - PEG$ and $(\text{brown}) = Fl(CH3)DAP - PEG$. Square Wave parameters were: $E_{step} = 0.004\text{V}$, $E_{SW} = 0.025\text{V}$, $E_{accum} = 2\,\text{sec}$ and $\text{SW}_{freq} = 15\text{Hz}$.

The SW peak for Fl(CH3)-DAP polymer is more than twice the height of the three other flavin polymer systems both in DCM and in water. This can be attributed to the comparably faster electron transfer kinetics which occurs during the short duration of the SW pulse. We observed this before in the CV profile of the same polymer system in Figure 3.12 in DCM (and Figure 3.14 in water). The (reduction) waves are narrow, well defined and the peak separations ΔEp are smaller.

Polymer	CV Results in DCM	SWV Results in DCM
	$E_{1/2}$ (V vs Ag wire)	$Ep(difference)$ (V vs Ag wire)
Flavin(NH) poly(PEG)	-0.56	-0.55
Flavin(NH)-DAP poly(PEG)	-0.52	-0.52
Flavin(CH3) poly(PEG)	-0.60	-0.60
Flavin(CH3)-DAP poly(PEG)	-0.57	-0.57

Table 3.5 Comparison of Cyclic and SW voltammograms results for the Flavin polymers in DCM

The SWV in water (Figure 3.15(b)) show a variation in peak height corresponding to the systems varying electron transfer rates. This order of electron transfer kinetics is agreement with the values of CV peak separation ΔEp previously shown in Table 3.4, (i.e. large peak separation corresponding to slow electron transfer).

All peak positions are within a few mVolts of -0.36 V with Fl(CH3)-DAP polymer again showing the strongest response. As we will see shortly, because this overall net response is derived from the difference between the forward and backward current responses (i.e. $I_{diff} = I_{for} - I_{rev}$) the exact peak positions of I_{diff} cannot reliably be used to determine the formal potentials E^{θ} of each system.

3.5.5 Summary of SWV results in DCM.

A closer analysis of the other currents that make up the overall response of the SWV provides some useful insight into the mechanism of electron transfer. Figure 3.16 shows the complete SWV's for **(a)** the Fl(NH)-DAP polymer and **(b)** Fl(CH3)-DAP polymer systems in DCM where the voltammogram for the Fl(NH)-DAP polymer is a representative of the other missing polymer systems as they were all fairly similar in magnitude. It is worth noting because of the difference in y-axis scale between (a) and (b) reverse current response I_{rev} (*green*) is approx the same in both DAP polymers but the forward current response I_{for} (*blue*).for the Fl(CH3)-DAP polymer is twice that of the Fl(NH)-DAP polymer.

Initial thoughts were that the featureless backward response of I_{rev} was the result of both systems unable to re-oxidize the $Fl_{rad}^{-\bullet}$ during the short period of the SW pulse. However the I_{rev} response is mostly positive which suggest that a reductive electron transfer is still taking place during the reverse pulse, (see Appendix A: SWV). This would only make sense if there was a second electron transfer of accumulated $Fl_{rad}^{-\bullet}$ product from the first electron transfer and which is occurring at a slightly more positive potential as described in Chapter section 1.2. This would also explain with the second oxidation peak (wave *III*) previously observed in the CV in DCM as was shown in Figure 3.12.

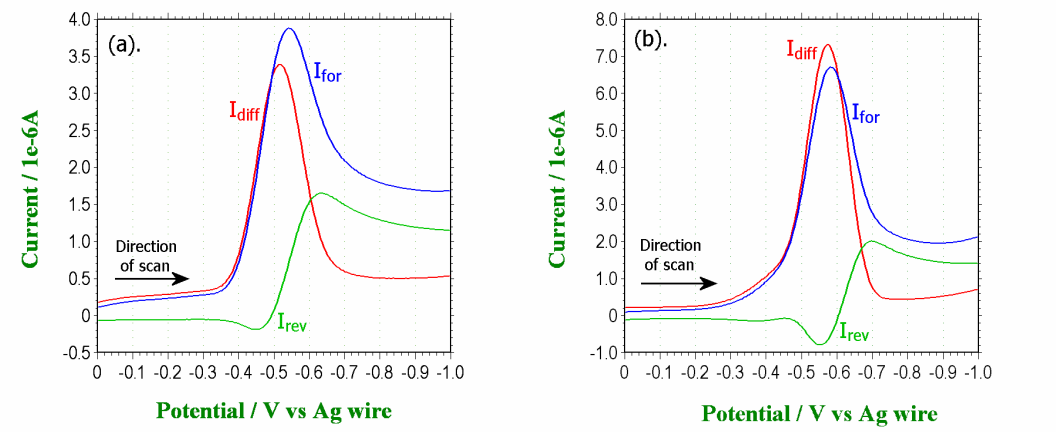

Figure 3.16 SW voltammograms for **(a).** Flavin(NH)-DAP and **(b).** Flavin(CH3)-DAP PEG polymers in DCM showing the difference (I_{Diff}), forward (I_{for}) and reverse(backward) (I_{rev}) current responses. The featureless backward response is due to the presence of a second electron transfer process occurring as a slightly more positive potential.

A reversal of the SW scan direction from −1 to 0 V (with an accumulation period, $E_{accum} = 2$ sec at −1 V) demonstrates the presence of this second redox peak. This is shown in Figure 3.17 for **(a).** Fl(NH)DAP and **(b).** Fl(CH3)-DAP polymers systems in DCM.

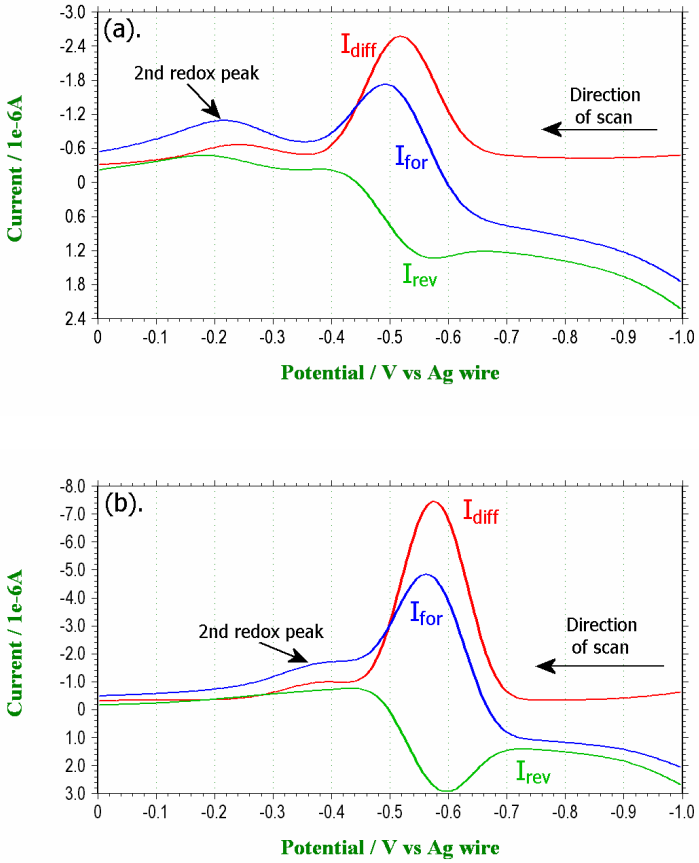

Figure 3.17 SW voltammograms scan in reversed direction from -1 to 0V for **(a)**. Flavin(NH)-DAP and **(b)**. Flavin(CH3)-DAP PEG polymers in DCM showing the difference (I_{Diff}), forward (I_{for}) and reverse(backward) (I_{rev}) current responses. The reverse scan indicates the presence of a hidden redox wave. SW parameters are as shown in Figure 3.15.

3.5.6 Summary of SWV results in water.

Figure 3.18 shows the complete SW voltammograms for the **(a)**. Fl(NH)-DAP and **(b)**. Fl(CH3)-DAP polymer in water where the direction of scan was 0 to $-1\,\mathrm{V}$. The observations made with the Fl(NH)-DAP polymer were also observed for the other two missing polymer systems. In Figure 3.18 (a) and (b) there is clearly a fairly featureless reverse current response I_{rev} ($green$) however they both display a weak minimum at around -0.3 to $-0.35\mathrm{V}$. These minimums are greater that than those observed for the same polymers in DCM (Figure 3.16) with the minimum found to be greater for Fl(CH3)DAP in both cases. The reverse response I_{rev} then starts to becoming positive at around -0.4 to $-0.43\mathrm{V}$ both rising to approx $2\times10^{-6}\,\mathrm{A}$. This again is supportive of a second electron transfer process but it suggests that the formal potentials for these two electron transfer processes $E^{\theta 1}$ and $E^{\theta 2}$ must be much closer together in water than in DCM, otherwise we would not have observed the deepening of the minimum.

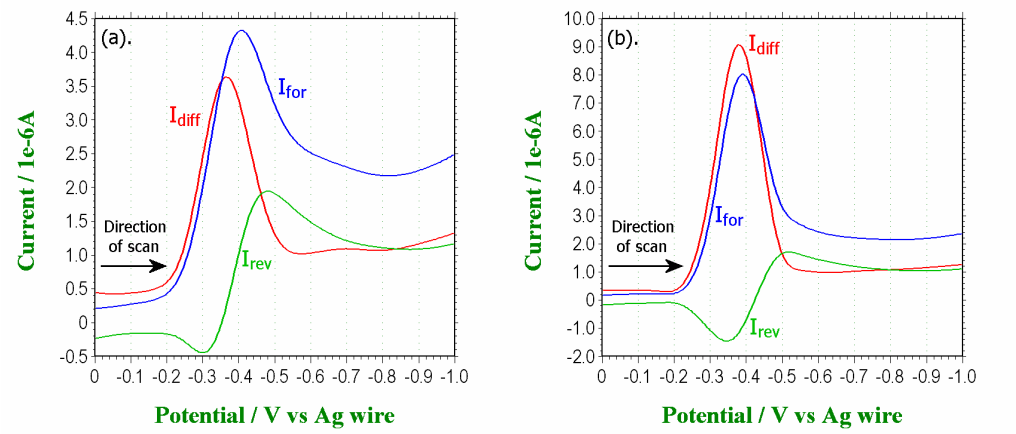

Figure 3.18 SW voltammograms for **(a).** Flavin(NH)-DAP and **(b).** Flavin(CH3)-DAP PEG polymers in Water showing the difference (I_{Diff}), forward (I_{for}) and reverse(backward) (I_{rev}) current responses. The featureless backward response is now indicating a small minimum. Results suggest that the 2nd redox wave is indistinguishably close to the 1st redox wave. SW parameters are as shown in Figure 3.15.

Figure 3.19 shows the SWV in the reverse direction of scan (-1 to $0\,\mathrm{V}$) for the two flavin-DAP polymers. These were recorded in an attempt to extract further information regarding the redox mechanism, as according to Appendix A.6.1. However, there was no visible occurrence of a second redox process, but this again might only be observed if there was a reasonable separation between $E^{\theta 1}$ and $E^{\theta 2}$. Consequently, because overall, we observe so much distortion in the reverse SW response I_{rev}, we cannot rely on the peak position of the overall SW response I_{diff}, as an accurate means of determining the redox potential. The four flavin-polymers in water (Figure 3.15(b)) demonstrate an overlapped peak position of $E_{p(diff)} = -0.38\mathrm{mV}$, but for the reasons just describe this doesn't tell us very much. We could perhaps try and make some comparative analysis base on the position of the forward current response peak, $E_{p(forward)}$, but as the formal potential E^{θ} is defined as the midway point between $E_{p(forward)}$ and $E_{p(reverse)}$ we would also need to know the peak separation to determine E^{θ}.

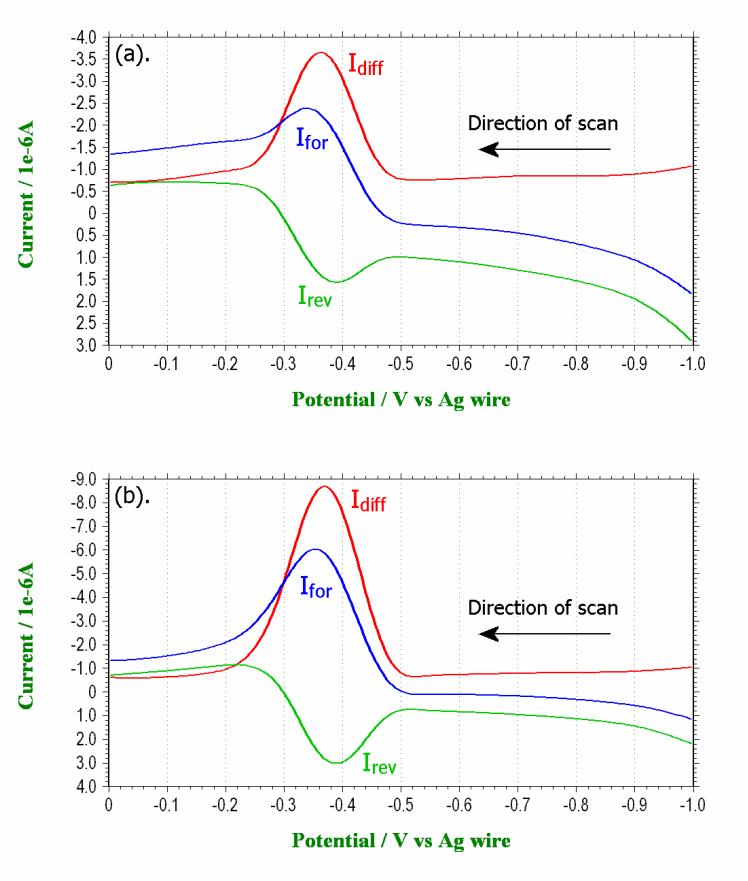

Figure 3.19 SW voltammograms scan in reversed direction from -1 to 0 V for: **(a)**. Fl(NH)-DAP and **(b)**. Fl(CH3)-DAP PEG polymers in DCM showing the difference (I_{Diff}), forward (I_{for}) and reverse(backward) (I_{rev}) current responses. The reverse scan indicates the presence of a hidden redox wave. SW parameters are as shown in Figure 3.15.

A summary of the SW peak positions for the flavin polymers in water based on I_{for} is given in Table 3.6. Note that since the SW amplitude E_{SW} was equal to 25mV the true values of formal potential E^{θ} will never differ more than +25mV from the peak potential $E_{p(forward)}$. For comparison therefore the SWV results for the flavin polymers in DCM are also shown. The difference between $E_{p(forward)}$ and $E_{p(forward)}$ in DCM is −12mV for Fl(CH3)-DAP poly(PEG) and approx −24mV for the other three polymers.

Polymer	SWV Results in Water	SWV Results in DCM	
	$Ep(forward)$ (V vs Ag wire)	$Ep(difference)$ (V vs Ag wire)	$Ep(forward)$ (V vs Ag wire)
Flavin(NH) poly(PEG)	-0.480	-0.552	-0.576
Flavin(NH)-DAP poly(PEG)	-0.408	-0.516	-0.540
Flavin(CH3) poly(PEG)	-0.392	-0.600	-0.620
Flavin(CH3)-DAP poly(PEG)	-0.388	-0.572	-0.584

Table 3.6 Summary of SW voltammograms results for the flavin polymers in water based soley on the Forward Current response peaks in the scan direction 0 to -1V. The true formal potential E^{θ} for the 1st redox process would theoretically be expected to be within a few mVolts ($< 25mV$). SW parameters are as shown in Figure 3.15.

If we apply these same differences to the polymers in water in order to estimate E^{θ} (or $E_{p(difference)}$) and then compare with the flavin (NH) polymer system we find that the greatest stabilization benefits are observed for the Fl(CH3)DAP polymer system where the formal potential shift is approx 80mV. In water therefore, this polymer system seems to provide an environment for the flavin where it is the easier to reduce (lower redox potential) and is more electrochemically reversible.

3.5.7 Surface immobilized SW voltammograms.

It is perhaps worth quickly comparing the SWV for the flavin polymers which were recorded following surface immobilization onto a glassy carbon working electrode against an aqueous medium. The procedure involved placing a small drop of the flavin PEG polymer onto a sheet of clean filter paper and rotating the electrode surface with small but firm circular movements. The excess was removed to reveal a very thin polymer film. Although these PEG polymers are water soluble, it was discovered that the voltammetry response remained considerably strong (i.e. the polymer remains attached to the electrode surface) even after 1H in the $0.5\,\mathrm{M}$ NaCl aqueous solution of the electrochemical cell.

The SW voltammograms overall response (I_{Diff}) for the four flavin PEG polymers are shown in Figure 3.20 with the direction of scan from 0 to -1 V. If we compare these responses with those in Figures 3.15(a) and (b) we see again that the strongest voltammogram response is afforded by the Fl(CH3)-DAP polymer system and the weakest response as observed in Figure 3.15(b) is afforded by the Fl(NH) polymer. It is always reassuring to obtain the similar results obtained by different methods. However it will also be observed that the position of the overall response peaks have shifted anodically by approximatey +0.1 V relative to the response peaks obtained in Figure 3.15. At the present time we attribute this to the different reference electrodes employed for each experiment. Here we have used a $Ag\,/\,AgCl$ reference electrode, whereas in all previous examples we used a $Ag\ wire$. This will need to be re-examined. It is also interesting to compare the scales on the y-axis of each voltammogram as the observed response here is approximately 6 to 7 times that obtained previously in solution phase as shown in Figure 3.15(b).

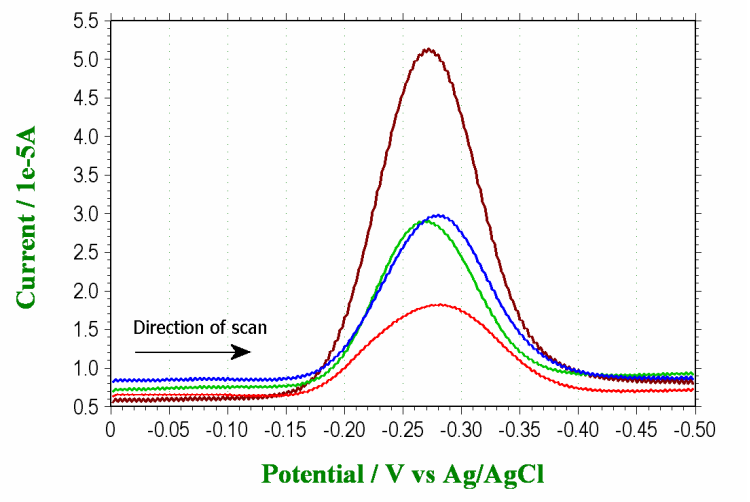

Figure 3.20 SW voltammograms overall response (I_{Diff}) for the flavin PEG polymers in water using $0.5\,\mathrm{M}$ NaCl as the supporting electrolyte with pH adjusted to 7.0 ± 0.02 by phosphate buffer. Polymer applies as a paste directly to glassy carbon electrode and then removed using clean filter paper to provide a thin film over electrode surface. Colour code: $(\text{red}) = Fl(NH) - PEG$, $(\text{blue}) = Fl(NH)DAP - PEG$, $(\text{green}) = Fl(CH3) - PEG$ and $(\text{brown}) = Fl(CH3)DAP - PEG$. Other SW parameters were: $E_{step} = 0.002\mathrm{V}$, $E_{SW} = 0.050\mathrm{V}$ and $\mathrm{SW}_{freq} = 100\mathrm{Hz}$.

3.6 Photochemistry.

General experimental procedures for UV/Visible and Fluorescence photochemical analysis can be found in Chapter 8: Experimental Section.

3.6.1 UV/Vis absorbance spectrum:

The spectra below shows the flavin polymers in DCM (Figure 3.21) and then in distilled water (Figure 3.22). Flavins generally exhibit four absorbance peaks at around 220, 265, 375 and 445 nm in aqueous solution. [44] All absorption maxima posses high-molar absorptivities ($>10^4$ $M^{-1}cm^{-1}$) which is indicative of $\pi \rightarrow \pi *$ transitions. The exact position of the absorption maxima and the values of molar absorptivities depend on the environment of the flavin chromophore. [44] Data recorded at wavelengths lower than 250 nm is not shown here as it was either distorted by charge transfer noise or exceeded the detection limit of the spectrometer and was therefore of no value. The spectra therefore show three of the possible four described above.

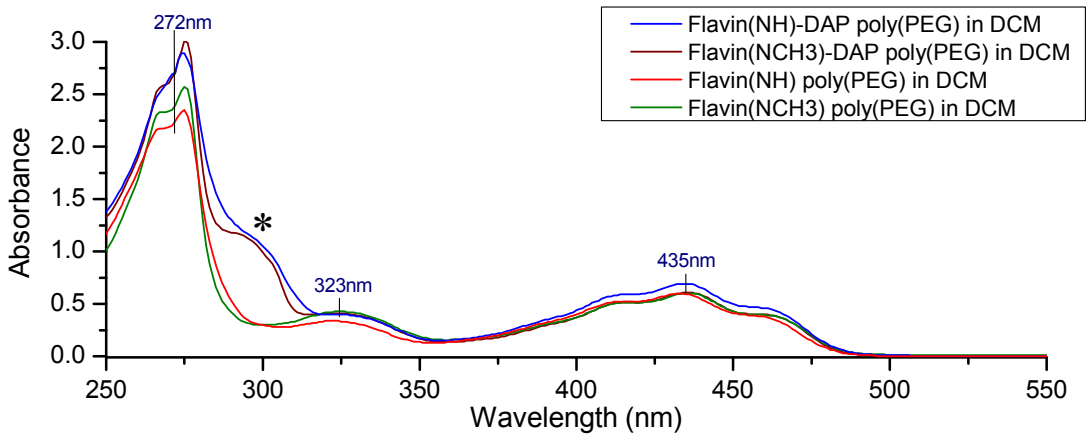

Figure 3.21 UV/Vis absorbance spectra of the flavin-polymers in DCM at 20°C, (1×10^{-4} M).

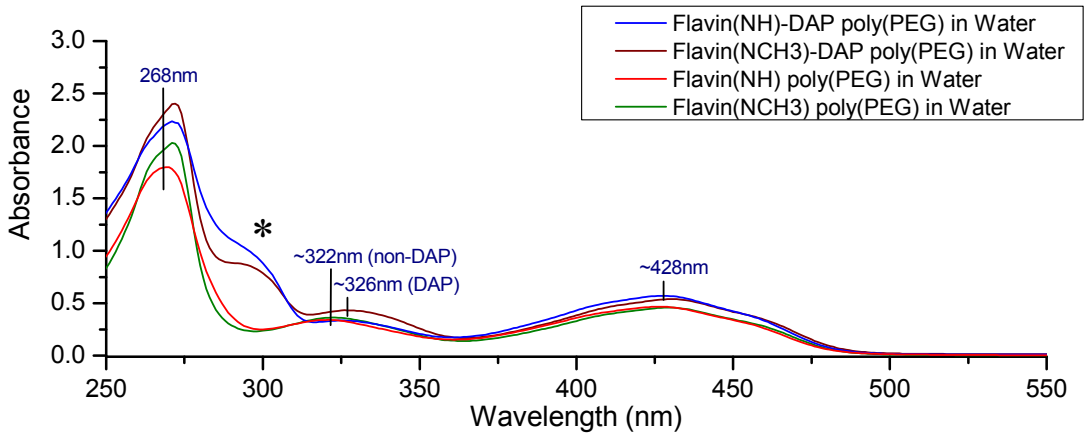

Figure 3.22 UV/Vis absorbance spectra of the flavin-polymers in distilled water at 20°C, (1×10^{-4} M).

In DCM the three absorbance maxima occur at 272, 324 and 435 nm. The absorbance at $\lambda_{max} = 435$ nm averaged as $A = 0.55 \pm 0.05$ for all flavin polymers. In non-polar solvents such as DCM, this maxima is known to display two well defined shoulders either side of a central peak. This detail is thought to be defined by vibrational energy levels of the $S_0(v=0) \xrightarrow{h\nu} S_1(v=1,2,3)$ energy transition. The corresponding peaks for the flavin polymers in water are found to be 268, 327 and 428nm. The absorbance at $\lambda_{max} = 428$nm averaged as $A = 0.51 \pm 0.05$ suggesting a slightly smaller extinction coefficient (ε) for the PEG polymer system in water ($\varepsilon = 5100 M^{-1}cm^{-1}$) compared to DCM ($\varepsilon = 5500 M^{-1}cm^{-1}$). (Note: for free FMN $\varepsilon = 12,500 M^{-1}cm^{-1}$) The maxima at 428nm has blue shifted relative to the corresponding maxima in DCM and the two shoulder are barely identifiable. This loss of definition is usually observed in polar environment where the reorganizational energy is greater. Overall the spectra suggest that the flavins are in slightly different environments despite indications from DLS that these polymers systems are capable of forming particle size structures. This perhaps suggest that the flavin (and DAP) are not encapsulated within the polymer structure while dissolved in DCM.

Polymer	Absorbance Maxima position (nm)			
	Band I		Band II	
	DCM	Water	DCM	Water
Fl(NH) poly(PEG)	433	427	322	321
Fl(NH)-DAP poly(PEG)	435	428	323	325
Fl(CH3) poly(PEG)	435	429	324	323
Fl(CH3)-DAP poly(PEG)	435	430	323	327

Table 3.7 Absorption maxima positions for the flavin-polymers in DCM and water.

The absorbance spectra for the two flavin-DAP polymers in DCM and water (Figures 3.21 and 3.22 respectively) show a region of high molar absorption at 300 nm. This region is unique to the polymers containing DAP and will be discussed further in Section 3.6.3 which examines the excitation spectra of these systems.

3.6.2 Fluorescence spectroscopy.

As described in Chapter section 1.2, the ability to stabilize the flavin radical is linked to the enzymatic function within the flavoprotein. The characteristic intense yellow-green fluorescence of the flavin generally occurs at around $\lambda_{F\max} = 520\text{nm}$ (free FMN in water). The exact position and intensity is particularly influenced by both the environment and the different oxidation states of the fluorophore. Exposure to polar environment will cause the wavelength of $\lambda_{F\max}$ to increase (red shift) while non-polar environments will cause the wavelength to decrease (blue shift).

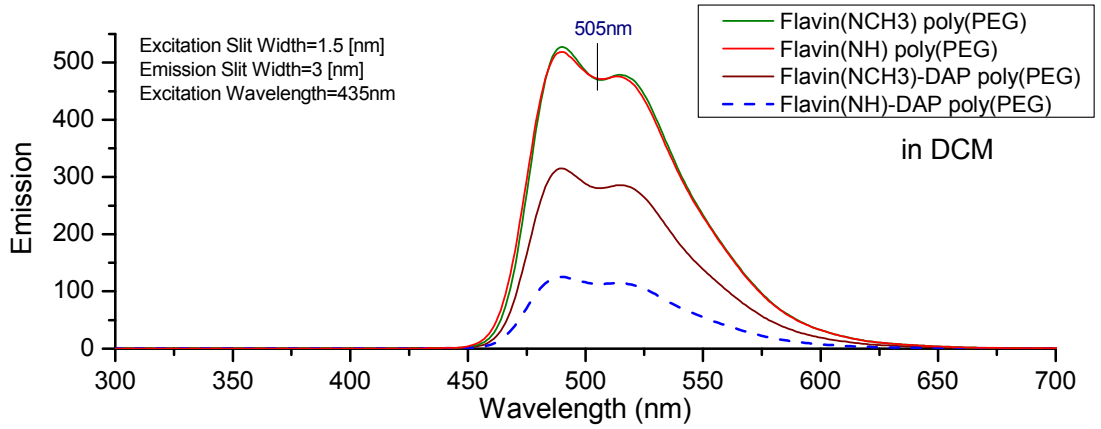

Figure 3.23 Fluorescence spectrum recorded in DCM with $A = 0.1 \pm 0.005$ at $\lambda_{\max} = 435\text{nm}$. Flavin(NH)_DAP poly(PEG) is emphasised by the blue (- - - -) peak..

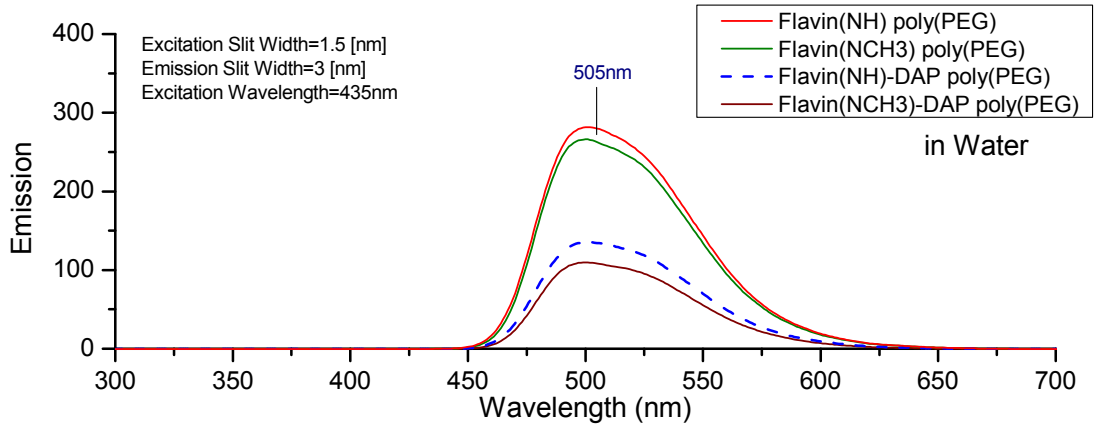

Figure 3.24 Fluorescence spectrum recorded in water with $A = 0.1 \pm 0.005$ at $\lambda_{\max} = 430\text{nm}$. Flavin(NH)_DAP poly(PEG) is emphasised by the blue (- - - -) peak.

The fluorescent spectra in Figure 3.23 for the flavin polymers in DCM shows a maximum at $\lambda_{F\max} = 505\text{nm}$. The centre of the maxima is taken to be the trough midway between the two small peak. The characteristic double hump is due to the transition form the fluorescent excited state $S_1^F(v=0) \xrightarrow{-h\nu_1} S_0^F(v=1)$ and $S_1^F(v=0) \xrightarrow{-h\nu_2} S_0^F(v=0)$, the two vibrational states of the fluorescent electronic ground state. The spectra shown in Figure 3.24 for the flavin polymers in water shows no shift in the $\lambda_{F\max}$ peak position relative to DCM but there is loss of peak definition for the same reason as described in the last section.

Strong fluorescence intensity is expressed in DCM for both non-DAP systems, Fl(NH and Fl(CH3). As might be expected the Fl(NH)-DAP polymer demonstrates the weakest fluorescent, due to the energy transfer quenching which occurs through hydrogen-bonding interactions between the flavin and DAP units. Fl(CH3)-DAP is also exhibiting a moderate degree of fluorescent quenching in relation to the other polymer systems which might suggest some interaction between the flavin and DAP unit was still possible.

We had expected to observe a similar order of fluorescence quenching in water (Figure 3.24). Within this media all four polymer systems exhibited generally much lower level of fluorescence, however both flavin-DAP polymers experience substantial fluorescence quenching with the Fl(CH3)-DAP the weaker of entire group. This experiment was repeated two more times to reconfirm this unexpected order. We can only conclude that the energy transfer interaction (hydrogen-bonding and/or $\pi - \pi$ stacking) between the N(3) methyl protected flavin and the DAP unit must be greater than that which exist between the unprotected flavin and DAP in this environment.

3.6.3 Excitation spectrum:

The excitation spectrums for the two flavin-DAP polymers are shown below in Figures 3.26 and 3.27 along with an overlay of their corresponding absorbance spectrum. The excitation spectrums are produced by monitoring the fluorescence emission at the fluorescence maximum $\lambda_{F\,\max} = 520\text{nm}$. It therefore has an obvious similarity in appearance with the absorbance spectrum since every photon that is absorbed increases the population of the excited species Fl^{*}_{ox} which would ultimately result in the $S_1 \xrightarrow{\hbar\nu} S_0$ fluorescence photon emission.

As mentioned earlier in Section 3.6.1, the absorbance peak at around 300nm is unique for the flavin-DAP polymer systems (see Figures 3.26 and 3.27). We can therefore assume that if this peak does correspond just to photon absorption by the DAP unit then it would be unlikely that we would observe any corresponding peak in the excitation spectrums, since this by design only records the (flavin) fluorescence emission at $\lambda_{F\,\max} = 520\text{nm}$. Consequently, because these peaks are present in both spectrums it would suggest that absorbed energy from the excited DAP* unit has been transfer to the flavin. This would become a more likely if the flavin and DAP unit are in close enough proximity for electron exchange.

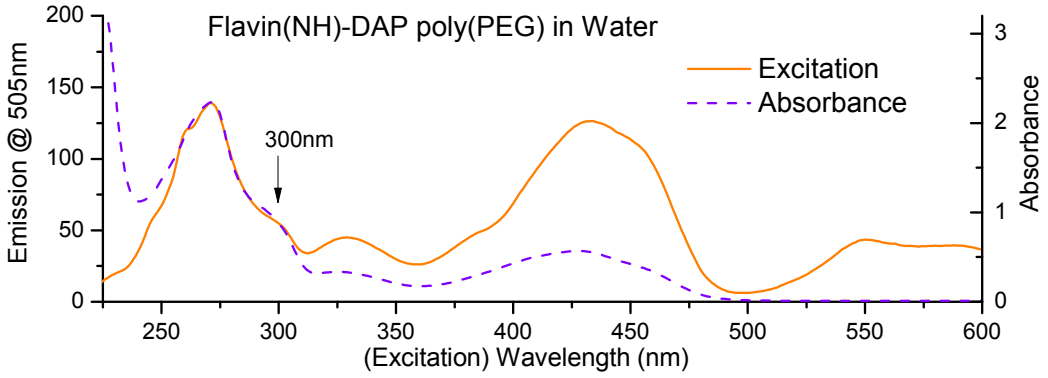

Figure 3.26 Comparison of the flavin(NH)-DAP polymer's Excitation spectrum recorded at the fluorescence maximum $\lambda_{F\,\max} = 505\text{nm}$ versus the absorbance spectrum.

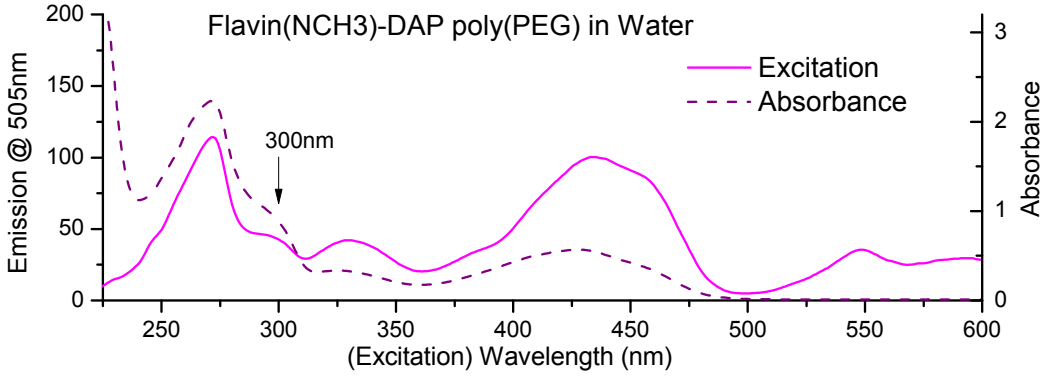

Figure 3.27 Comparison of the flavin(NCH3)-DAP polymer's Excitation spectrum recorded at the fluorescence maximum $\lambda_{\max} = 505\text{nm}$ versus the absorbance spectrum.

However is the absorbance peak at 300nm really produced by the DAP structure? One simplest way to prove this was to obtain an absorbance spectrum of a pre-component of flavin-DAP initiator synthesis. This is shown in Figure 3.28 along with its absorbance spectrum (solid red line). We clearly see that there are two absorption maxima each showing high extinction coefficients, one at 220nm ($\varepsilon = 3\times10^4$ $M^{-1}cm^{-1}$) but more importantly one at 294nm ($\varepsilon = 1.5\times10^4$ $M^{-1}cm^{-1}$). This provided unambiguous confirmation of energy transfer quenching is occurring between the flavin and DAP unit.

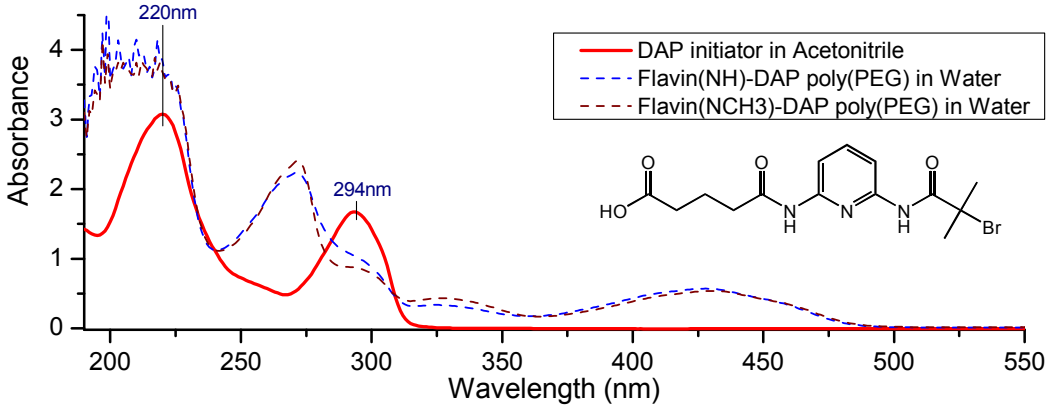

Figure 3.28 Absorbance spectrum of the DAP compound (structure shown inset) at 0.1mM in acetonitrile overlapped with the absorbance spectra of the two Flavin-DAP polymer's (0.1mM). The DAP unit shows two absorbance maxima at $\lambda = 220$ and 294nm which have ultimately contributed to the Flavin-DAP polymer spectra.

It worth noting that this emission/absorbance peak at 300nm is also observed in DCM both the flavin-DAP polymers where in particular, moderate fluorescent quenching is observed for the flavin(NCH3)-DAP polymer system (Figure 3.23).

3.7 Conclusions:

3.7.1 Binding interaction within the flavin encapsulated polymer.

To summarise, the redox and photochemical properties of the flavin and its binding interaction with the DAP unit have not behaved in a manner we predicted they would. We attempted create a non-polar micro environment similar to the active site of an enzyme, by utilizing the solvatophobic forces to induce the polymeric encapsulation of the electroactive flavin and DAP unit. The DAP unit has previously been shown to have favourable redox modulating ability which it achieves thought complementary hydrogen bonding interactions with the flavins pyrimidine ring. For these interactions to take place however the flavin and DAP must exist in a non-polar environment in order to minimise unwanted binding interactions. This "non-polar" environment would be provided by the polyethylene glycol (PEG) structure of the encapsulating polymer. Although perhaps not strictly non-polar it would still provide an environment in relative terms less polar than water and would also have the advantage of dual solubility in both aqueous and organic solvent.

Gel Permeation Chromatography (GPC) results showed that the flavin polymers synthesised were of low polydispersity and high molecular weight. Dynamic Light Scattering (DLS) experiments show that the polymers when in solution do indeed form particle size structure of between 5 and 12 nm in diameter in both organic solvent and water. The UV/Vis absorbance spectra in DCM suggest that the flavin(-DAP) unit may not be entirely encapsulated within the polymer structure as it differs slightly in appearance to the corresponding spectra in water. This observation is supported by the fluorescence spectra which although shows no movement of the fluorescent maxima there was significant loss of peak definition for spectra recorded in water. Encouraged however, by the observation that not all definition has been lost in both UV/Vis absorbance and fluorescence spectra (as it is for FMN in water) we can be reasonably assured that the flavin is most likely encapsulated with the PEG structure and therefore protected from the aqueous environment. Any small changes in peak position of the absorbance spectra are most likely induced by the flavin in contact with the more non-polar DCM solvent molecules.

The considerable fluorescent quenching between the flavin and DAP of the Fl(NH)-DAP polymer system in DCM is believed to be cause by the hydrogen-bonding interaction. The moderated fluorescent quenching of the Fl(CH3)-DAP polymer system in DCM is believed must be related to some interaction, either weak non-linear hydrogen-bonding or $\pi - \pi$ stacking. The presence of the peak at 300nm on the excitation spectra for flavin-DAP polymers and which corresponds to the absorbance of the DAP unit, proves unambiguously that energy can be transferred from DAP to flavin and we would presume that the same mechanisms may be involved in fluorescent quenching. These interactions come into force with the Fl(CH3)-DAP polymer system in water. Here we suggest that the polymeric structure is restricting the degree of freedom available to the tethered flavin and DAP unit such that they become forced to adopt a conformation that would otherwise be unfavourable attainable in free solution as shown in Figure 3.29 for Fl(CH3)-DAP and Fl(NH)DAP polymers.

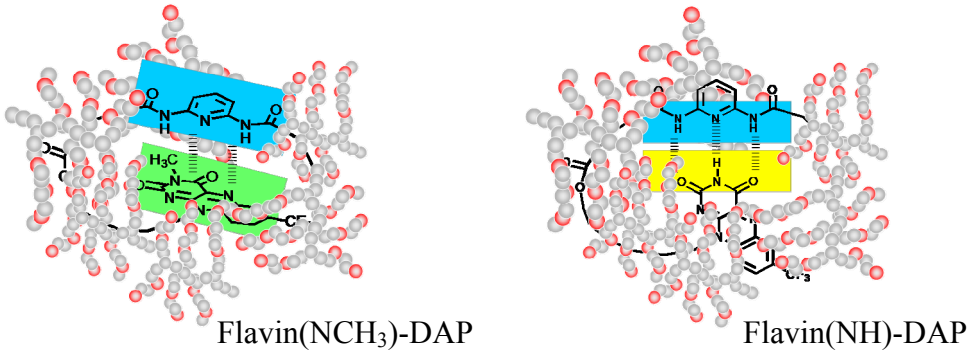

Figure 3.29 Suggested scenario involving the interactions between the Flavin and DAP unit while encapsulated within the polymer structure.

The voltammetry experiments in DCM demonstrated that greatest stabilization effect on the redox properties of the flavin polymers, as demonstrated by a anodic shift in half-wave potential, was achieved, as expected, through the hydrogen-bonding interaction between the DAP and the unprotected flavin(NH). However we also observed some positive influence from the partial interactions between the DAP and the methyl protected flavin(CH3). Perhaps by restricting the movement of the encapsulated flavin and the DAP units, the more they can interact with one another. This would seem to agree with the electrochemistry results recorded in water, where the water insoluble flavin and DAP units are forced to become encapsulated within the polymer structure (i.e. smaller particle size as measured by DLS). The end result we find is that the Fl(CH3)-DAP polymer system demonstrates the better redox stabilizing effect and also exhibits electrochemical reversibility much higher than that achieved by the flavin initiator in DCM.

3.7.2 Charge transfer static quenching.

There are other reported examples of fluorescent quenching in natural systems. One flavin related example was reported by Spencer and Weber [45] and also reviewed by Lakowicz[46, p278] who both provide an explanation why flavin adenine dinucleotide (FAD) has a fluorescence quantum yield $\Phi_F = 0.03$ whereas flavin mononucleotide (FMN) is $\Phi_F = 0.27$, almost 10 times larger. Simply, FAD is linked to an aromatic heterogeneous adenine molecule which is capable of forming a charge transfer complex with the (photo) excited flavin as shown in Figure 3.30. This is similar to the manner which we have suggested occurs with our flavin-DAP system. However, with fewer complementary pairs available in the FAD charge-transfer complex there will be the minimal possibility of producing hydrogen bonding interactions which are believed key to the redox stabilization process. Nevertheless, the difference in fluorescence quantum yield is substantial. Compare to that observed with our flavin-DAP system the best was a 5 fold difference demonstrated between Fl(NH) and Fl(NH)-DAP in DCM. It would be interesting to explore the redox modulating properties of such an arrangement.

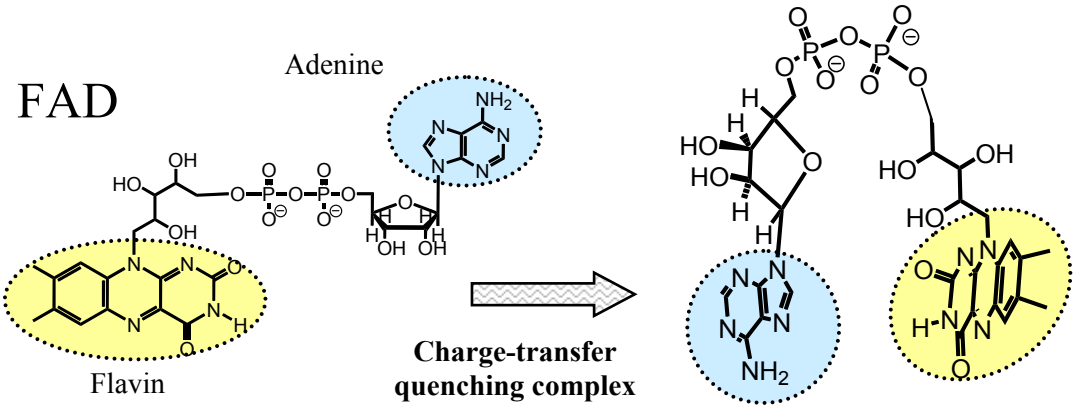

Figure 3.30 Suggested charge transfer mechanism by which fluorescent quenching is known to occur with flavin adenine dinucleotide (FAD). This is thought to involve $\pi - \pi$ stacking interaction between the adenine and flavin moiety.

3.7.3 Spartan 3D molecular modelling of flavin-DAP systems.

In an attempt to demonstrate that a simple stacking conformation of the aromatic flavin and DAP was achievable, we went back to the flavin and diethylamidopyridine model original devised by Rotello.[4] Using Spartan quantum mechanical software to construct the models of an N(3)H (Figure 3.34) and N(3)methyl flavin (Figure 3.35) with diethylamidopyridine (DAP). The structures were then aligned close to each other so as to promote hydrogen bonding between the flavin carbonyls and the DAP amines. The DFT calculation were evoked and the calculated distances between the flavin-DAP complementary pairs measured. These were found to be $N-O(2)=1.929\,Å$, $N-HN=2.032\,Å$ and $N-O(4)=1.962\,Å$. The flavin N(3) hydrogen was then replace with a methyl group and the process repeated as shown in Figure 3.34. The distances between the carbonyl and DAP amines changed respectively by 15 and 17% to $N-O(2)=2.220\,Å$ and $N-O(4)=2.306\,Å$. Interestingly, the calculated energy for the N(3)-methyl protected flavin was -49910.56 eV versus the N(3)H flavin which was calculated as -48841.18 eV, which is over 1000 eV lower.

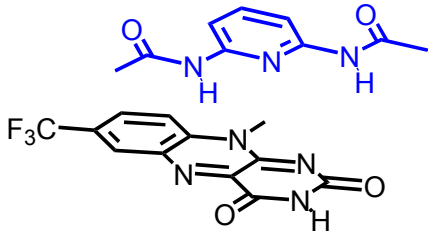

Figure 3.33 A 2D skeletol model of N(3)H flavin and a diethylamidopyridine molecule stacked directly above in close proximity for hydrogen bonding.

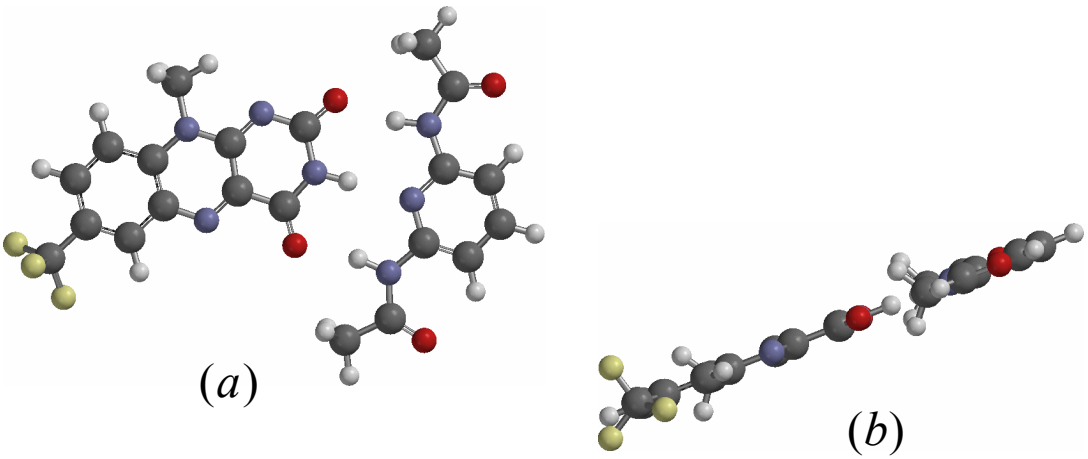

Figure 3.34 A 3D molecular model derived using a Spartan quantum mechanical program with Basis set = 6-31G* Method = RB3LYP HF-DFT SCF calculation of N(3)-H flavin showing **(a)** top view and **(b)** side view depicting hydrogen bonding with the diethylamidopyridine molecule positioned and planar alignment.

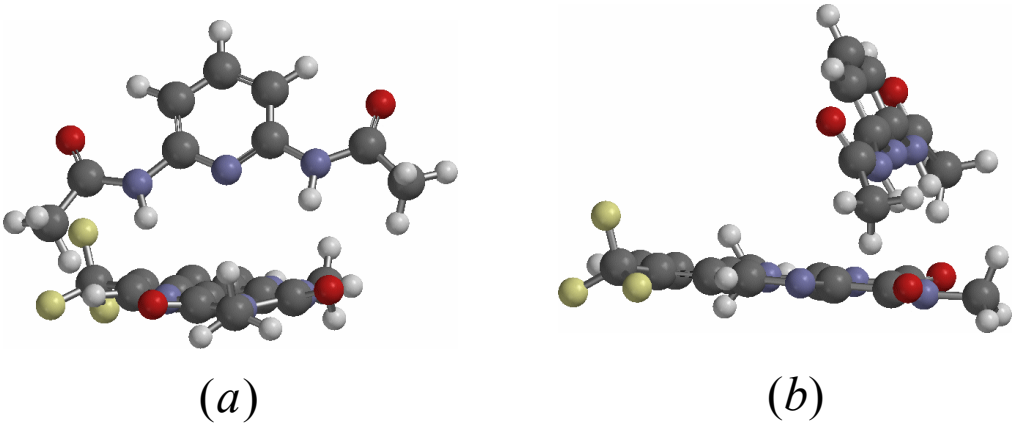

Figure 3.35 A 3D molecular model derived using a Spartan quantum mechanical program with Basis set = 6-31G* Method = RB3LYP HF-DFT SCF calculation of N(3)-CH3 protected flavin showing **(a)** front view **(b) s**ide view depicting hydrogen bonding with the diethylamidopyridine molecule positioned directly above.

Both Seddon [47] and Atkins [48] mention experimental evidence from structural studies to support both linear and non-linear hydrogen-bonding arrangements. Typical hydrogen-bond distances are quoted in Atkins and appear to be between $1.7-2.7\,\text{Å}$. Non-covalent bond distances which are greater than $2.8\,\text{Å}$ will come under the heading of Van der Waal forces.

Due to time constrains it has not been possible to perform similar calculations between the DAP unit and the reduced flavin radical anion $Fl_{rad}^{-\bullet}$.

CHAPTER 4

FLAVIN-FUMARAMIDE [2]ROTAXANE POLY(PEG) SYSTEM.

4.1 Introduction.

In order to help discuss the various co-conformational states of the [2]rotaxane system we have adopted a short-hand notation in the subsequent text where the square brackets [ ] represent the location of the benzylic amide (BA) ring on the *flavin – fumaramide* axle. For example, $Fl_{ox}-[fumaramide]$ the BA ring is located over the *fumaramide* station and not the oxidized flavin station, Fl_{ox}. Occasionally *flavin – fumaramide* axle poly(PEG) will be abbreviated as **axle** and *flavin – fumaramide* [2]rotaxane poly(PEG) will be abbreviated **rotaxane**.

4.1.1 Experimental design strategy.

The objective of these experiments was to create a hydrophobic environment for the flavin based [2]rotaxane which would allow hydrogen-bond formation between the benzylic amide (BA) macrocycle and the complementary binding stations located on the axle. The imide of the flavin and the di-amide of the fumaramide would form the two complementary binding stations for this axle. The fumaramide station has been shown to be a near-perfect binding partner for the BA macrocycle and was effectively used as a template during the 5 component synthesis of the rotaxane as shown in step (i) of Figure 4.7. The flavin imide on the other hand, is a weaker hydrogen binding acceptor for the macrocycle. Previous attempts to use naphthalimide, a similar imide compound, as a template to synthesise a rotaxane were unsuccessful [49, 50].

The rotaxane structures shown in Figure 4.1 depict the translocation of the BA macrocycle from the fumaramide station to the flavin following an electron transfer. The electron can occur by either electrochemical (delivered directly from the electrode during voltammetry experiments) or photochemically (after the photoexcitation to the excited flavin $Fl*$ and subsequent radical anion $Fl^{-\bullet}$ in the presence of an electron donor).

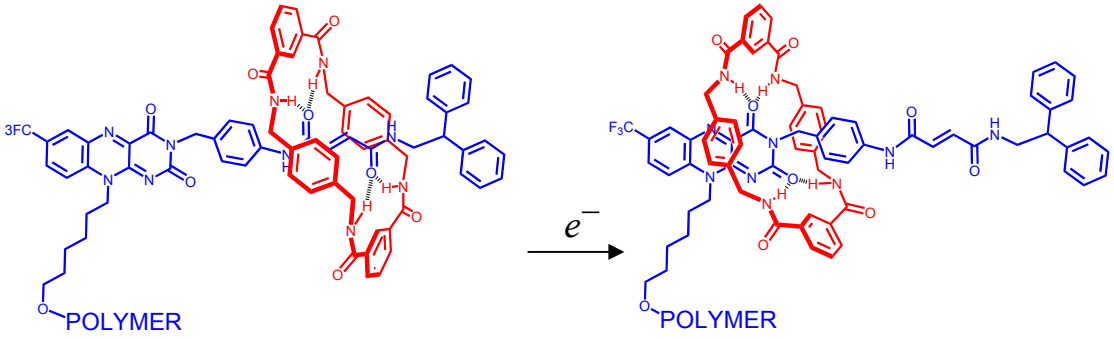

Figure 4.1 Possible shuttling motion induced by the electrochemical reduction of a neutral $flavin-[fumaramide]$ rotaxane to a $[flavin(radical)^{-\bullet}]-fumaramide$ rotaxane.

An alternative method of inducing translocation of the BA macrocycle onto the flavin station is by the photoisomerization of the fumaramide (*trans*) isomer into the maleamide (*cis*) isomer as shown in Figure 4.2. Through irradiation at 254 nm we can therefore effectively "switch-off" the stronger hydrogen-bonding station and the rotaxane would ultimately adopt an alternative minimum energy co-conformation which would involve the macrocycle to shuttle across and hydrogen-bond with the weaker neutral flavin station. This process of fumaramide-maleamide isomerization is reversible and can be achieved photochemically through irradiation at a higher wavelength (approx 300 nm) where the photochemical absorbance difference between the cis and the trans isomer is significantly greater. In both translocation techniques the effect of this translocation would be detected through the photochemical and electrochemical changes induced through interactions between the BA macrocycle and the flavin.

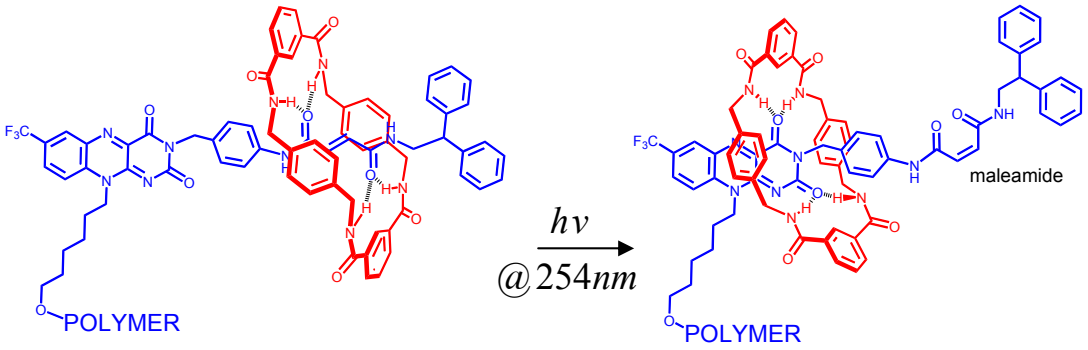

Figure 4.2 Shuttling motion induced by the photochemical isomerization of a neutral [*flavin*] – *fumaramide* rotaxane to a neutral [*flavin*] – *maleamide* rotaxane.

The dumbbell symbol representation shown below in Figure 4.3 of the **axle** and **rotaxane** will be used to simplify many of the pictorial descriptions that follow. The flavin acts as both stopper and station. The flavin in its neutral state is coloured yellow and the fumaramide coloured green. The bulky diphenyl group functions as the second stopper.

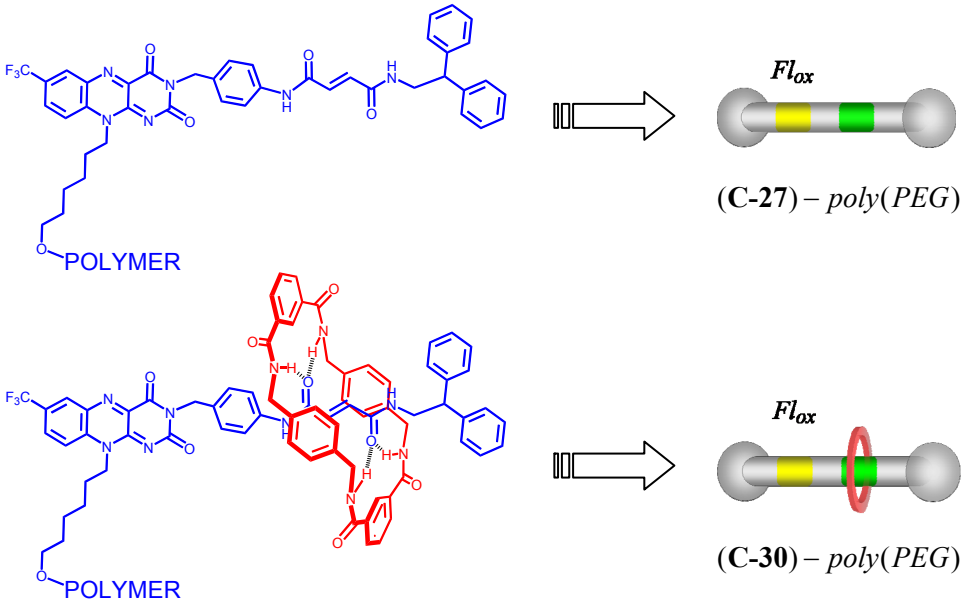

Figure 4.3 Dumbbell representation of the **axle** and **rotaxane** polymer showing the neutral flavin (*yellow*) and fumaramide (*green*) stations and the BA macrocycle ring (*red*).

4.1.2 Overview.

The results to be described here appear to suggest that the BA macrocycle may not be predominately located as expected over the fumaramide station. Instead it would seem that the macrocycle can probably also be located midway between the two stations where it interacts partially with the flavin as shown in Figure 4.4. ^{1}H NMR spectrum of the rotaxane initiator **C-30** showed more than one amide peak for the fumaramide section of the axle. At the time this was thought to be due to an unavoidable isomerization from natural light and we were therefore unable to purify.

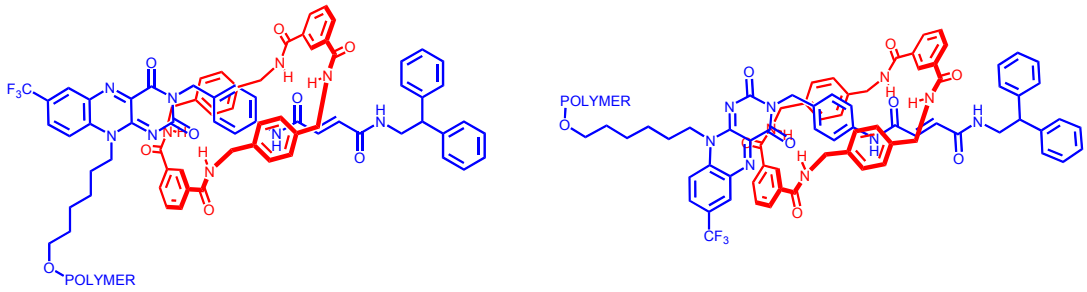

Figure 4.4 Two possible rotaxane co-conformation where the benzylic amide macrocycle occupies a position midway between the flavin and fumaramide binding stations. This would explain the significant differences in the redox properties between the neutral flavin in the **rotaxane** in comparison with the **axle**.

Further experimental evidence which supports this is provided by both photochemical and electrochemical analysis. Comparison of the absorbance maxima for the **axle** and **rotaxane**, in particular Bands *I* and *II*, suggest that there is some interaction between the BA macrocycle and the neutral flavin. Electrochemically induced shuttling motion is still achievable upon reduction of the flavin to a stronger hydrogen bond acceptor radical anion $Fl_{rad}^{-\bullet}$, the movement however appears to be sluggish, particularly in aqueous media.

Results also show that the cathodic peak from Cyclic Voltammetry experiments appear to shift positive (anodically) with repeated sweeps while the anodic peak remains fixed. This would suggest that once the macrocycle has been electrochemically or photochemically induced to shuttle across to the flavin station it will most likely on its return translocation remain in the first metastable co-conformation encountered, thereby raising the population of mid-way position. A proposed thermodynamic energy profile for the possible co-conformations of the neutral flavin **rotaxane** is shown in Figure 4.5.

Photoisomerization of the fumaramide component of the **rotaxane** (and **axle**) is also achievable but again this appears to be slow. With both these cases the sluggishness could be attributed to an environment of restricted movement created by the encapsulation of the **rotaxane** (and **axle**) within the polymer structure, particularly in aqueous media where particle sizing by dynamic light scattering (DLS) shows the polymer structure compressed into a slightly smaller diameter.

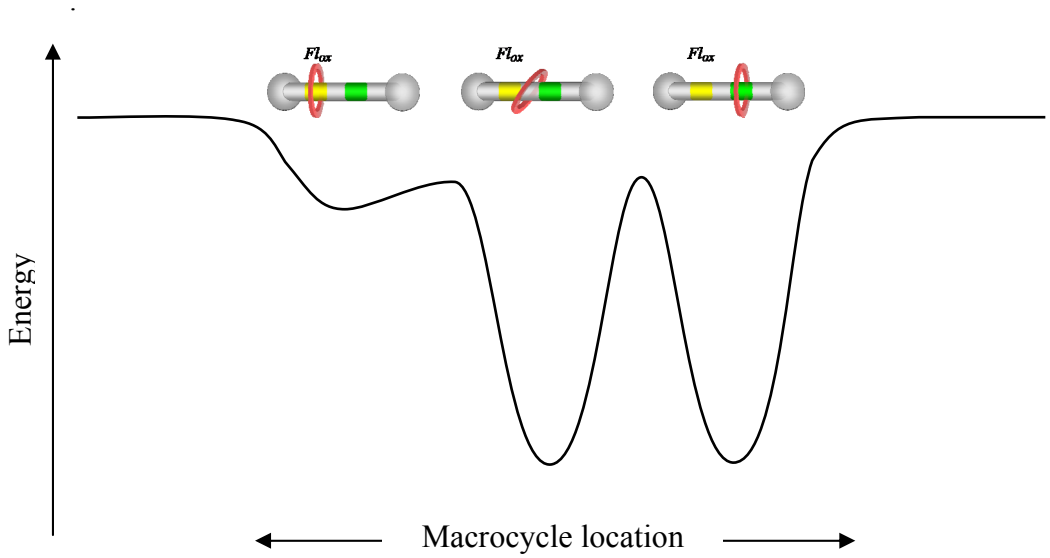

Figure 4.5 Possible Thermodynamic Energy profiles for the three rotaxane co-conformation where the benzylic amide macrocycle is able to occupy a metastable position midway between the neutral flavin (*yellow*) and fumaramide (*green*) binding stations.

A second intriguing observation attained from these results was the dramatic increase in fluorescence emission obtained upon fumaramide isomerization of both **axle** and **rotaxane**. This suggest the initially existed a strong quenching mechanism which becomes diminished following the isomerization of the fumaramide to the maleamide. A tentative explanation for this increase in fluorescence is therefore proposed which is based on a recent paper (2009) by Marco Garavelli and David Leigh [51] who examined the unique photochemical induced relaxation pathways for the fumaramide thread. In brief, they used computation techniques to determine the minimum energy pathways (MEP) of the multiple photoexcited states of a fumaramide. Interesting they predicted that the fumaramide does provide an energy level at which it could fluoresce at 246nm but also show that the relaxation channels that would make this possible are bypassed by other competitive MEP's. These same MEP's could become an energy sink for the excited state flavin and that isomerization to the maleamide would rearrange these MEP's. Unfortunately the paper seemed primarily to focus on the MEP's for the fumaramide isomer and the twisting mechanism through which it can rotate at the C=C bond while in an excited state and isomerise to the maleamide. They do not explore the reverse process. Simply showing that the maleamide isomer was fluorescent would help support this proposal.

4.2 Synthesis.

Full synthesis details are provided in the Chapter 8: Experimental. The following is a brief outline of the procedures and conditions involved during the synthesis. It has been separated into two parts. The first part describes the synthesis of the flavin-fumaramide axle and rotaxane ATRP initiators **C-27** and **C-30** respectively. The second part will describe the procedures involved to synthesis and purify the final polymer product.

4.2.1 ATRP initiator synthesis.

The synthesis scheme for the axle and rotaxane initiators is shown in Figure 4.6. The first half of the axle synthesis starts with **(a).** 7-(trifluoromethyl)-10-(6-hydroxyhexyl)isoalloxazine (**C-14**) was refluxed in acetone with 1.5 equivalents of p-nitro benzyl chloride for 4 days to provide **C-22**. **(b)** The hydroxy group was protected by dissolving the flavin in the minimum amount of DMF, adding tert-butyl dimethyl silyl chloride (TBSCl) (1.5eq) and a catalytic amount of DMAP (0.1eq). The mixture was stirred at r.t for 20min before adding triethyl amine (2eq) dropwise by pipette. **(c)** The nitro group of **C-23** was reduced by palladium (on carbon) using ammonium formate as the hydrogen source to afford **C-24**. The reaction worked best in methanol with the flask sealed with an expansion balloon. Adding a few drops of glacial acetic acid seems to improve yields. **(d)** The second half of the axle started from the commercially available 2,2-diphenyl amine (1eq) and fumaric acid monoethyl ester (1eq) with catalytic DMAP (0.1eq) and EDCI.HCl (1.2eq) stirred in DCM at r.t for 2h to afford **C-20**. **(e)** The ethyl group was removed by hydrolysis by adding aqueous NaOH to an ethanol solution to afford **C-21**. **(f)** The subsequent carboxylic acid was coupled to **C-24** using EDCI.HCl, HOBt and catalytic DMAP in DCM at r.t for 18h to provide **C-25**.

(g) To produce the axle initiator **C-27**, the TBS protecting group was first removed by adding aqueous (7.5M) HCl to a solution of **C-25** in THF at r.t. The mixture was stirred for 1h and precipitated by adding water. **(h)** The sparingly soluble hydrolysed **C-26** was first dissolved in the minimum amount of DMF then diluted with THF (25:1 ratio) and triethylamine (9eq). 2-Bromobutryl bromide (3eq) was added dropwise to the stirring mixture at r.t then left overnight. The product **C-27** was precipitated by adding diethyl ether and filtering.

(i) Producing the rotaxane initiator **C-30** started by using the TBS protected axle **C-25** as a template for the benzylic amide macrocycle assembly. The TBS protecting group was left attached as it improved the compounds solubility in non-polar solvents. Isophthaloyl dichloride and p-xylxyenediamine were added simultaneously dropwise by a motor driven syringe pump over 4h to the TBS axle dissolved in dry DCM with triethylamine. **(j)** The TBS protecting group was then removed by first dissolving rotaxane **C-28** in the minimum amount of DMF and diluting with THF (10:1 ratio) and triethyl amine (9eq). Aqueous (7.5M) HCl was added to the stirring solution at r.t. which was then left for 1h. Rotaxane **C-29** was precipitated by adding water. **(h)** Rotaxane **C-29** was dissolved in the minimum amount of DMF then diluted with THF (15:1 ratio) and triethylamine (9eq). 2-Bromobutryl bromide (3eq) was added dropwise to the stirring mixture at r.t then left overnight. The product **C-30** was precipitated by adding diethyl ether and filtering.

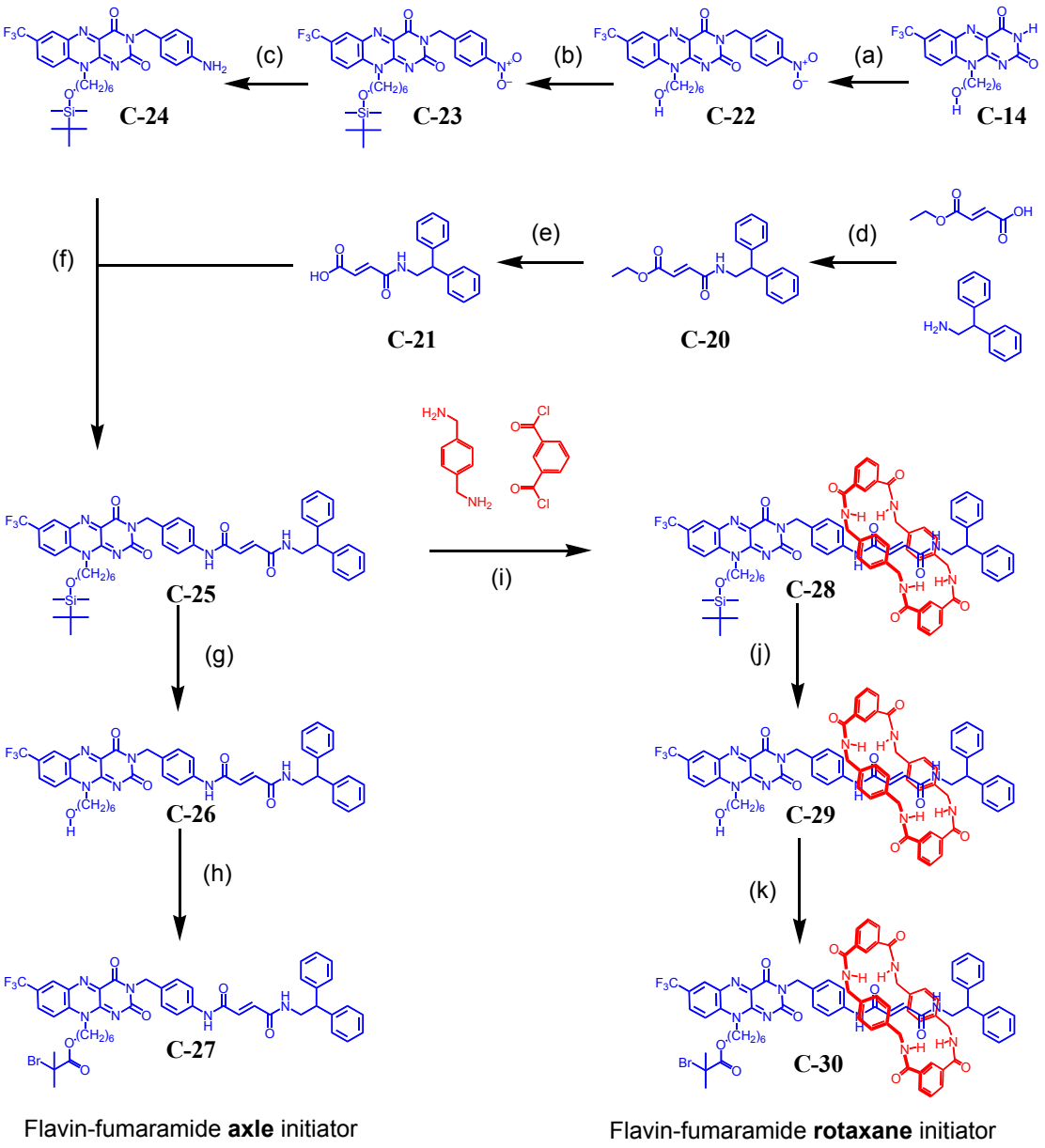

Figure 4.6 Synthesis of the axle and rotaxane ATRP initiators. **(a).** 4-Nitrobenzyl chloride and potassium carbonate in acetone under reflux for 4 days. **(b).** TBDMSCl and DMAP(catalytic) in DMF at r.t then slowly adding triethyl amine. **(c).** 5% Pd(C) and ammonium formate in MeOH. **(d).** EDCI.HCl and DMAP in DCM at 0°C. Reaction left to warm to r.t and stirred for 24h. **(e).** Aqueous NaOH added to stirring solution of (d) in EtOH. **(f).** EDCI.HCl, HOBt and DMAP(catalytic) stirred in DCM at r.t for 18h. **(g).** Aqueous HCl added to (f) in THF at r.t. **(h).** 2-bromoisobutryl bromide added dropwise to a stirring solution of (g) and triethyl amine in THF/DMF (25:1) . **(i).** Isophthalyl dichloride and p-xylylenediamine added dropwise over 4h to a stirred solution of (f) in dry DCM and triethylamine at r.t. **(j).** Aqueous HCl added dropwise to a stirred solution of (i) and triethyl amine in THF/DMF (10:1). **(k).** 2-bromoisobutryl bromide added dropwise to a stirring solution of (j) and triethyl amine in THF/DMF (15:1).

4.2.2 ATRP polymer synthesis.

The ATRP synthesis of the flavin-fumaramide **axle** and **rotaxane** are shown below in Figure 4.7. The conditions for the synthesis were identical and therefore the following will be a general procedure for the ATRP polymerization.

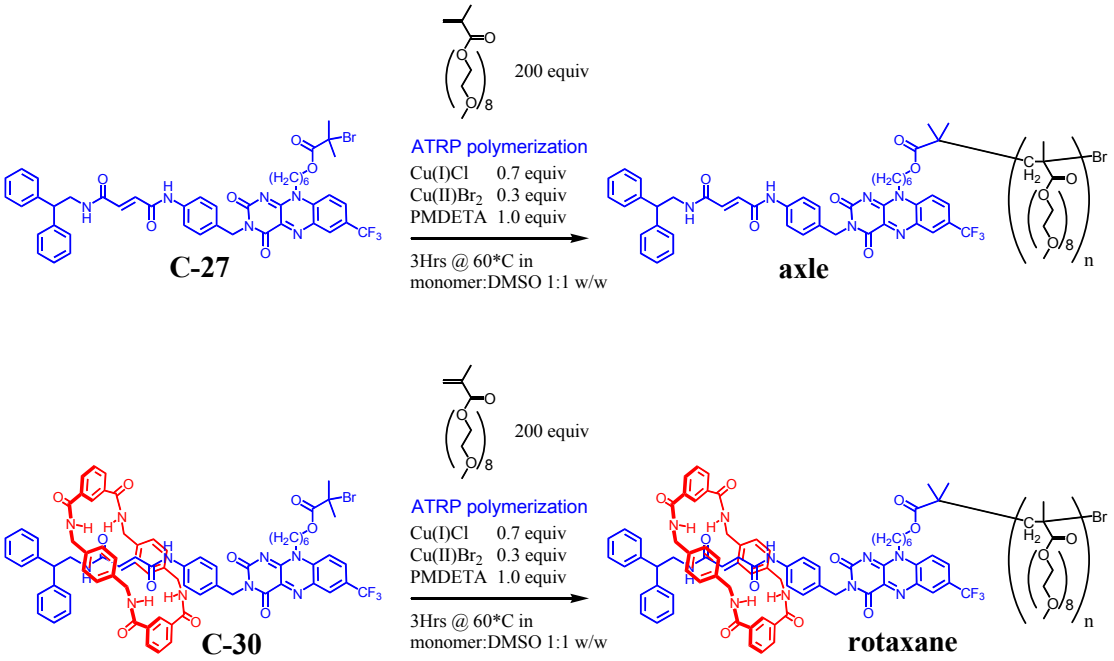

Figure 4.7 ATRP synthesis of the axle and rotaxane PEG polymers.

The initiator (**C-27** or **C-30**) (0.1mmol) was dissolved in DMSO (8.5mL) and PEG monomer (9.5g) in a two neck flask. DMSO was used as a solvent because of it excellent solubility properties. The catalyst system Cu(I)Cl(7eq), Cu(II)Br_2(3eq) and ligand pentamethyldiethyltriamine (PMDETA)(10eq) were added to a second two neck flask and dissolved in DMSO (10mL). Oxygen was removed by subjecting both mixtures to three cycles of "Freeze-Pump-Thaw". Using a gas tight syringe 1mL of the catalyst mixture (i.e. 0.7, 0.3 and 1equiv of the above) was transferred to the stirring solution in the first flask while both were under a fast nitrogen gas flow. The first flask was then sealed under nitrogen gas and placed in a thermostatically controlled oil bath at 60°C and stirred for 3h. The reaction was terminated by pouring the reaction mixture into a vigorously stirring conical flask of diethyl ether (400mL) to afford a yellow-green residue. After allowing to settle for approx 30min the residue was separated by decanting and then dissolved in chloroform (40mL). The copper was removed by passing this solution though a short column of alumina. The filtrate was then centrifuged for approx 1h to remove cloudiness, reduced in volume to approx 30mL and then precipitated into diethyl ether as described above to afford a clear yellow residue. This was collected by decanting and dried under high vacuum for 24h.

4.3 Polymer characteristics.

The polymer molecular weights were characterised by Gel Permeation Chromatography (GPC) and Dynamic Light Scattering (DLS). Analytical procedures are found in Chapter 8: Experimental section.

4.3.1 Gel permeation chromatography (GPC) analysis.

The GPC profiles and peak positions (M_p) for the Flavin-fumaramide polyethylene glycol (PEG) polymers systems are shown in Figure 4.8. The molecular weights M_n M_w and polydispersity index (PDI) are summarized in Table 4.1. The results show excellent living characteristics with PDI $\simeq$ 1.1.

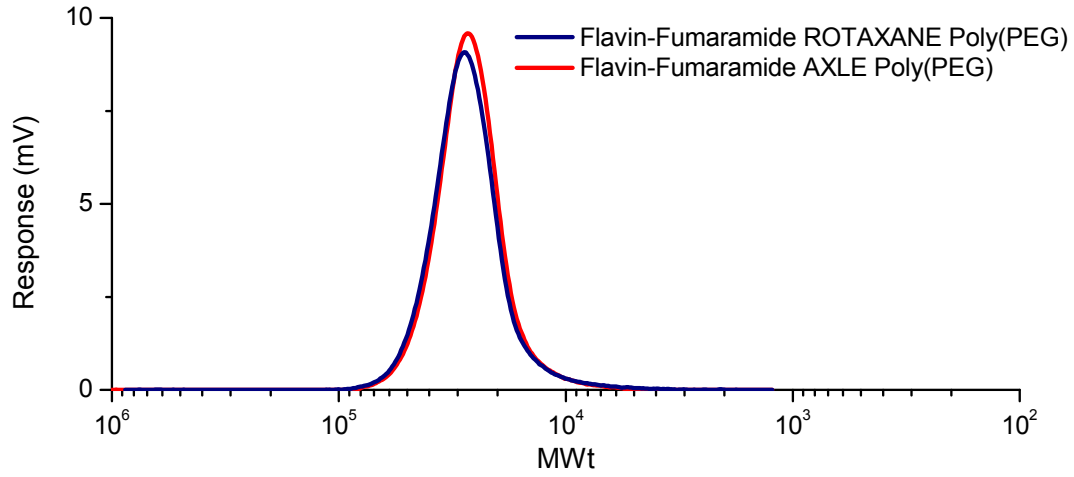

Figure 4.8 GPC profiles and peak positions for the flavin-fumaramide axle and rotaxane (PEG) polymers.

Polymer	Molecular Weights (g/mol)			PDI
	Mn	Mw	Mp	
axle poly(PEG)	25350	28173	27134	1.1114
rotaxane poly(PEG)	26649	29309	27973	1.0998

Table 4.1 Summary of the GPC obtained molecular weights and polydispersity values for the flavin-fumaramide axle and rotaxane (PEG) polymers.

4.3.2 Particle sizing by dynamic light scattering (DLS).

Figures 4.9 and 4.10 show the particle size distribution by volume for the flavin-fumaramide **axle** and **rotaxane** polymers in water and chloroform respectively. No micelle formation was evident from these plots and the polymers appeared to form individual units with diameters between 10.5 and 12.8 nm. These polymer units clearly show an equivalent order of size to the molecular weight values obtained from gel permeation chromatography (GPC), as shown in Table 4.2 with larger particles corresponding to a higher molecular weight polymer and vice versa. Oddly a comparison of the GPC molecular weight result for the **rotaxane** and **axle** show that the **rotaxane** is approx 5% larger. A comparison of the particles size shows again the **rotaxane** is larger but that the diameters differ by approx 18% in both water and chloroform. This in turn would correspond to a volume difference of 68%. No explanation at present can be given for this except for the margins of experimental error.

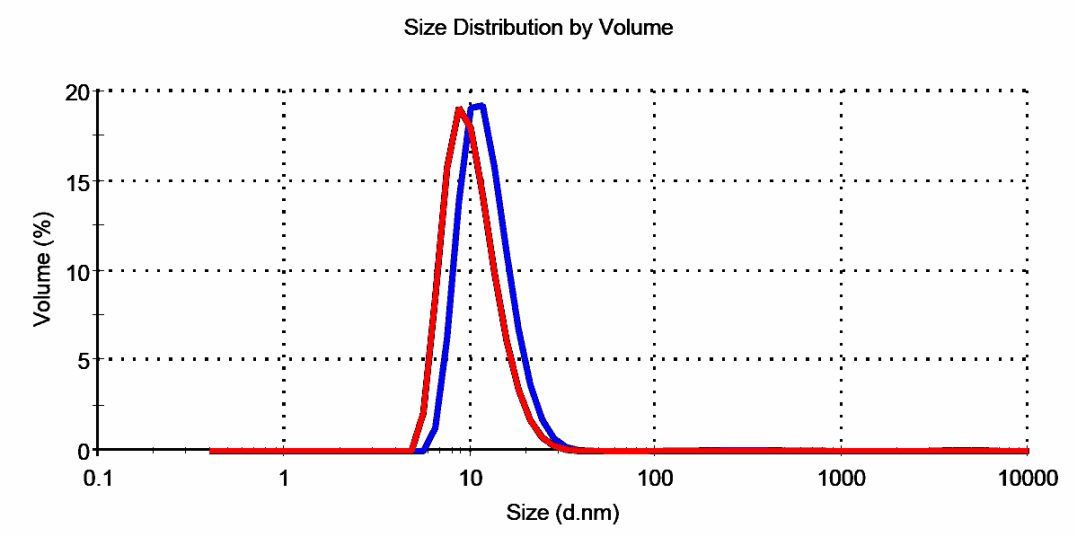

Figure 4.9 Particle size distribution by Volume for the flavin-fumaramide **axle** and **rotaxane** polymers in water.
Diameters recorded were **axle** (*red*) = 10.59nm , **rotaxane** (*blue*) = 12.57nm .

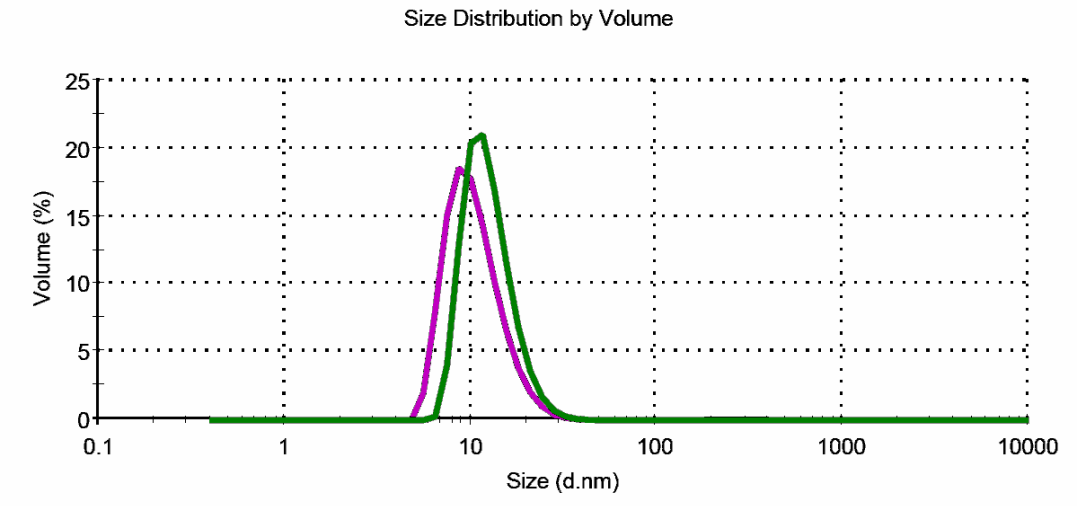

Figure 4.10 Particle size distribution by Volume for the flavin-fumaramide **axle** and **rotaxane** polymers in chloroform.
Diameters recorded were **axle** (*purple*) = 10.83nm , **rotaxane** (*green*) = 12.76nm .

The polymer particles are fairly similar size in both solvent types, with the an approx 2% smaller particle size achieved in water. Smaller more compact polymer particles in aqueous solution would suggest that strong hydrophobic forces are at work compressing the polymer structure into more compact units thereby creating the conditions that would most likely retard any translocation or isomerization process.

Polymer	DLS Results Particle diameter (nm)		GPC Results Mn (g/mol)
	Water	CHCl3	
axle poly(PEG)	10.59	10.83	25350
rotaxane poly(PEG)	12.57	12.76	26649

Table 4.2 Comparison particle size obtained using Dynamic Light Scattering (DLS) with results for polymer molecular weight M_n obtained by Gel Permeation Chromatography (GPC).

4.4 Electrochemistry.

4.4.1 Cyclic voltammetry in DCM.

Figure 4.11 compares the CV's for the flavin-fumaramide **rotaxane** and **axle** polymers. The voltammograms were recorded at a slow scan rate ($\nu = 0.01 Vs^{-1}$). At faster scan rates the responses obtained were flat and featureless as might be expected as a result of the sluggish diffusion of the polymer particles. Consequently the current response was very weak ($I_p \propto \nu^{1/2}$) but the profiles were more defined. It was therefore necessary to increase the **axle** polymer concentration to 2.0 mM in order to obtain the reasonable response shown below as the red voltammogram. The concentration of the **rotaxane** polymer was increased further to 4.0 mM to take account for an even flatter, featureless current response. The difference in peak magnitude would seem to support the SW analysis to be discussed later which depicts the **rotaxane** voltammogram as primarily composed of a one electron transfer reduction whereas the **axle** voltammogram involves a two electron and proton transfer process.

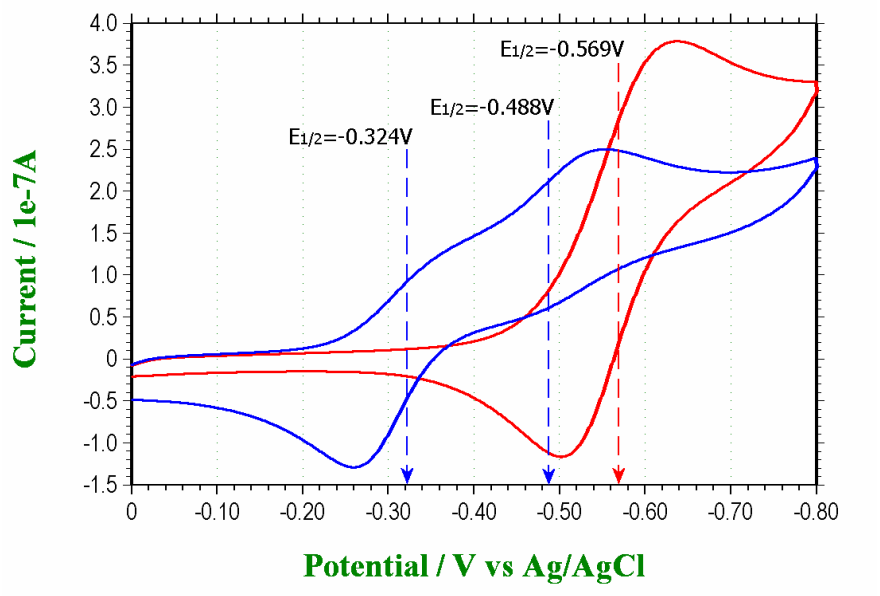

Figure 4.11 Cyclic voltammograms for flavin-fumaramide **rotaxane** polymer (*blue*) 4.0mM and flavin-fumaramide **axle** polymer (*red*) 2.0mM in dry CH_2Cl_2. Scan rate $\nu = 0.01 Vs^{-1}$ with 0.5M TBA·PF_6 as the supporting electrolyte using a glassy carbon working electrode.

Peak separation ΔE_p from the **axle** polymer (*red*) voltammogram was measured as 130mV. This was used to approximate the position of the two half wave potentials shown in Figure 4.11 for the **rotaxane** polymer (*blue*) by subtracting or adding 65mV to the positions of the voltammograms well defined anodic and cathodic peaks respectively. This allowed us to calculate a difference in half wave potential $\Delta E_{1/2} = 164$ mV. Using Equation 4.1 this corresponds to a 660 fold increase in the binding association constant $K_{a(red)}$ of the flavin radical anion to the benzylic amide ring.

$$K_a(red) = K_a(ox) \times 10^{\frac{nF}{RT}\left(\mathrm{E}_{1/2}(bound) - \mathrm{E}_{1/2}(unbound)\right)} \qquad \text{Eqn (4.1)}$$

It is perhaps worth comparing this with similar results reported by Leigh as shown in Figure 4.12 which shows the CV's for the succimamide – naphthalimide rotaxane (**1**) and axle (**2**). Here they reported a difference in half wave potential $\Delta E_{1/2} = 510\,\mathrm{mV}$ which corresponded to a staggering 6×10^8 fold increase in the binding association constant $K_a(red)$ of the reduced naphthalimide radical anion.

However, you will noticed that there is approx only 10mV difference between the cathodic peaks for rotaxane (**1**) and axle (**2**) in the CV of Figure 4.12 (quoted as $Epc(1) = -1.40\mathrm{V}$ and $Epc(2) = -1.41\mathrm{V}$). The difference observed between the cathodic peaks for our **rotaxane** and **axle** polymer systems (Figure 4.11) is a much larger 84mV ($\Delta Epc = -0.553 - (-0.637)\mathrm{V}$). This clearly suggests some difference in the environment of the flavin in the **axle** and the **rotaxane**. We could try and explained by suggesting that the BA ring while resident over the fumaramide station effectively shields the flavin's pyrimidine ring from the polymeric structure. Alternatively, it is more likely that the **rotaxane** is able to adopt a co-conformation where the BA ring resides between the flavin and fumaramide stations partially hydrogen binding with both as shown again in Figure 4.13.

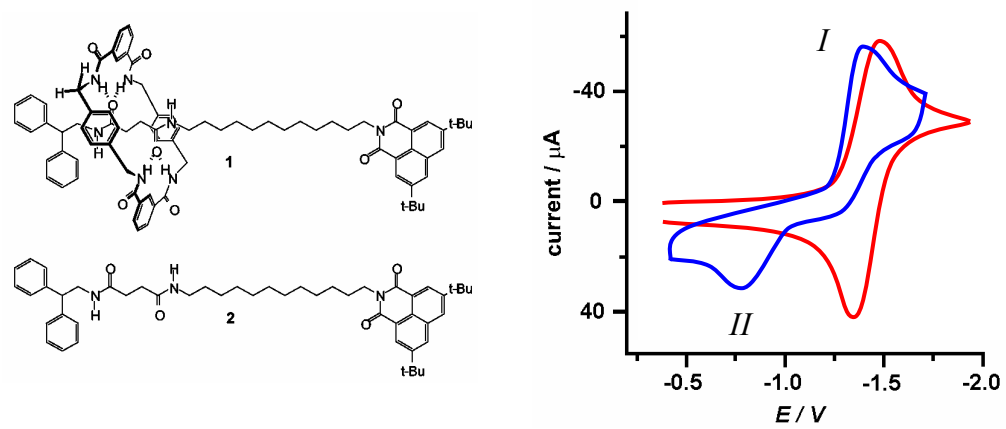

Figure 4.12 Comparison CV's for rotaxane **1** (*blue*) and axle **2** (*red*) in anhydrous THF. Image revised from reference [49]. Scan rate $\nu = 2\mathrm{Vs}^{-1}$ with 1.0mM substrate concentration and 0.05M $\mathrm{TBA{\cdot}PF_6}$ as the supporting electrolyte using a platinum working electrode.

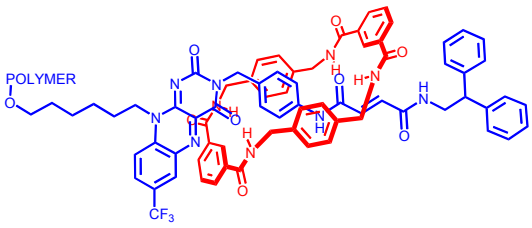

Figure 4.13 One of two possible rotaxane co-conformation where the benzylic amide macrocycle occupies a position midway between the flavin and fumaramide binding stations. This would explain the significant differences in the redox properties between the neutral flavin in the **rotaxane** in comparison with the **axle**.

Figure 4.14 shows the CV's for several successive scans of the **rotaxane** polymer in DCM. The initial CV (green) was very flat with its cathodic peak shown here labelled (A) at a more negative. With each successive scan the cathodic peak shifts approx 20mV more positive while the oxidation (anodic) peak increases in magnitude. The region between these cathodic and anodic peaks begins to deepen as a 2nd reductive peak starts to emerge at around -0.32V. Overall this seems to suggest an increased presence of an irreversible product which is stable enough to remain present over the period between scans. When we examined the SW voltammograms for the **rotaxane** polymer in DCM (discussed later) we detected an electrochemically reversible peak at approx $E^{\theta} = -0.29\text{V}$ which would seem to be in good agreement with the half wave potential $E_{1/2}$ of this product.

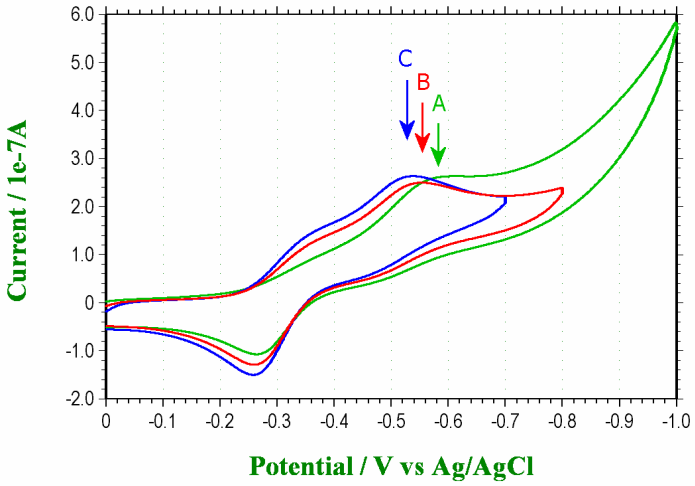

Figure 4.14 Successively recorded CV's for the **rotaxane**. Cathodic current peak shown here as positive.

We propose that during the initial CV sweep the neutral flavin Fl_{ox} is first reduced to the radical anion $Fl_{rad}^{-\bullet}$. The $Fl_{rad}^{-\bullet} - [fumaramide]$ **rotaxane** will be encourage to adopt a lower energy co-conformation through translocation of the BA macrocycle onto the new stronger hydrogen acceptor $Fl_{rad}^{-\bullet}$ station to form $[Fl_{rad}^{-\bullet}] - fumaramide$. This sequence is described in Figure 4.15(a).

During the reverse oxidative CV sweep , the BA macrocycle stabilizes the $Fl_{rad}^{-\bullet}$ radical anion making it more difficult to oxidized. This stabilization results in the large cathodic to anodic peak separation that typically describes an electrochemical irreversible system. Following the oxidation of the $[Fl_{rad}^{-\bullet}]-fumaramide$ to the $[Fl_{ox}]-fumaramide$ the BA macrocycle will again be encourage to adopt a lower energy co-conformation through translocation. However before it can attain stability as $Fl_{ox}-[fumaramide]$ it encounters the metastable co-conformation where the macrocycle is partially hydrogen-bonding with both flavin and fumaramide as depicted by the sequence in Figure 15(b).

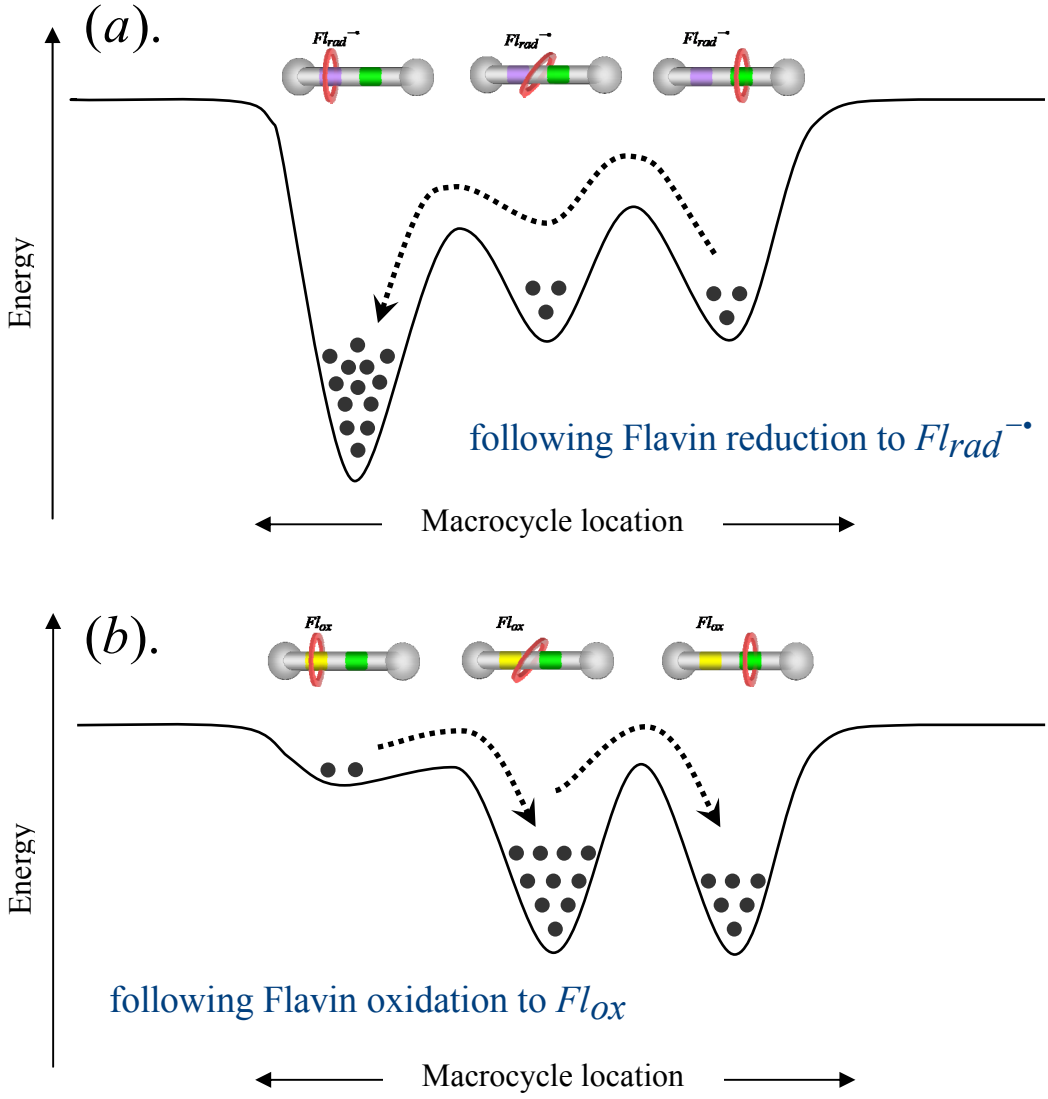

Figure 4.15 Possible translocation sequence for the BA macrocycle (*red*) along the thermodynamic energy profiles following (a). flavin reduction to $Fl_{rad}^{-\bullet}$ (*violet*) and (b). re-oxidation to Fl_{ox} (*yellow*) where the benzylic amide macrocycle remains stable in a metastable position midway between the flavin and fumaramide (*green*) stations. The small filled circles (●) represents the weighted population of each co-conformation.

We can reasonably assume that a rotaxane co-conformation where the flavin is not bound to the BA macrocycle will display a half wave potential $E_{1/2}$ for the 1st electron transfer approximately equal to the $E_{1/2}$ for the flavin **axle** (i.e. $E_{1/2} = -0.569\text{V}$ as in Figure 4.16). This can be understood if the BA macrocycle is unable to interact with the flavin and therefore does nit influence is basic redox properties at this point. This provides us with an estimated value of $E_{1/2}$ depicted in the electrochemical scheme of Figure 4.17 for the 1st electron transfer to the **rotaxanes** unbound flavin. If we assume also for a moment that a co-conformation exist for a **rotaxane** where the BA macrocycle is located midway between the flavin and the fumaramide stations as shown also in Figure 4.17 and that this is mainly responsible for the redox peak (*wave I*) as it becomes reduced at an $E_{1/2} = -0.488\text{V}$. As the electrode potential becomes more negative then the unbound flavin **rotaxane** co-conformation will ultimately become reduced.

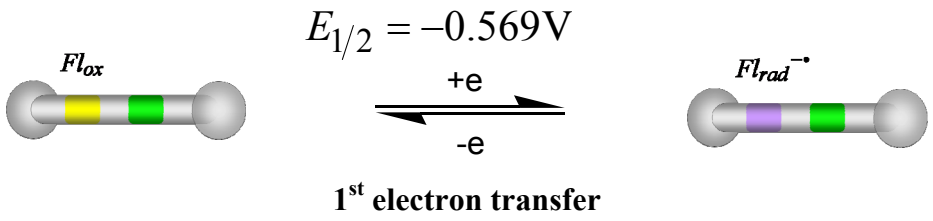

Figure 4.16 Electrochemical scheme for 1st electron transfer of the **axle** in DCM.

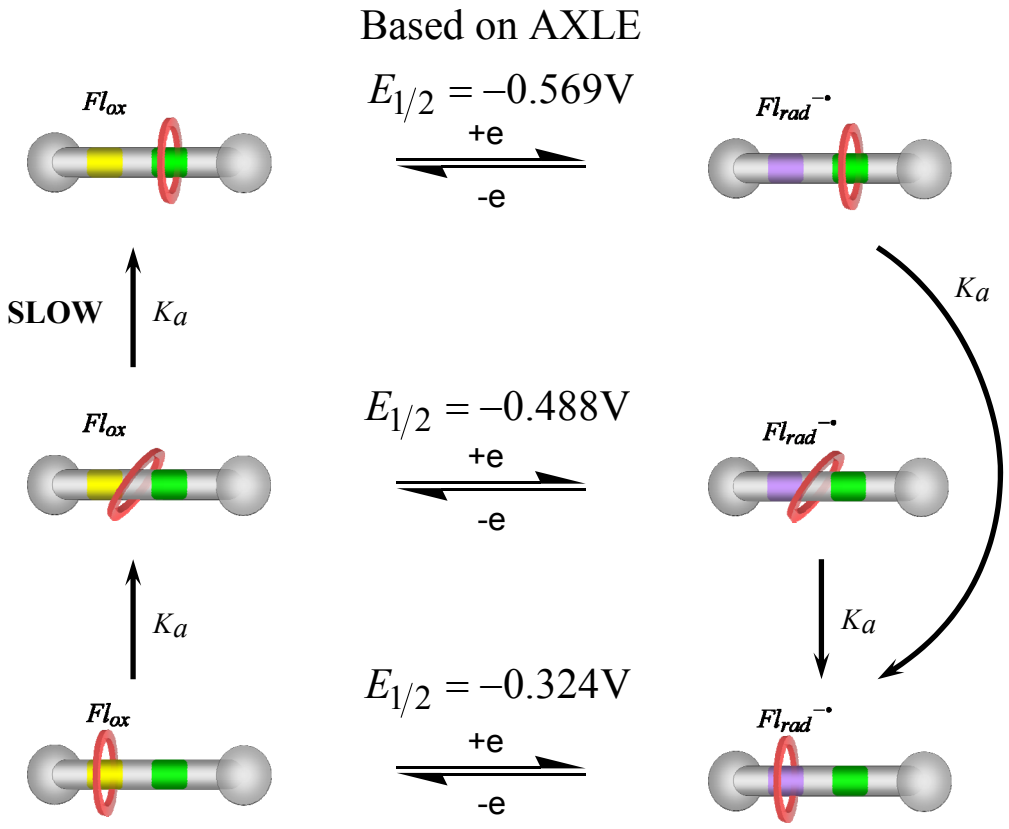

Figure 4.17 Electrochemical scheme for 1st electron transfer of the **rotaxane** in DCM.

Both events are followed by a co-conformational change as the BA macrocycle "shuttles" across the axle thread to hydrogen bond with the reduced flavin radical anion. The end results is an electrochemically stabilised flavin **rotaxane** co-conformation which will only become re-oxidized at an $E_{1/2} = -0.324$ V as shown in Figure 4.17.

4.4.2 Square wave voltammogram in DCM.

The square wave voltammograms (SWV) which follows shows us that the redox process is not limited to a single electron transfer. Unexpectedly, the flavin is somehow able to abstract a hydrogen cation from somewhere in the bulk medium and in so doing will undergo a 2nd electron transfer reduction to produce the anion $Fl_{red}H^-$. At present the source of this proton is unknown however we will show that this is more likely to occur with the **axle** than the **rotaxane**. We observed similar indications of this during cyclic voltammetry where the **axle** voltammogram appeared much pronounced than that for the **rotaxane** (Figure 4.11).

4.4.2.1 The flavin-fumaramide axle polymer.

The overall SWV response I_{diff} shows single peak -0.6V (vs Ag/AgCl) with a trailing shoulder at more negative potential. However closer examination of the forward and backward SW responses, I_{for} and I_{rev} respectively, provides us with an explanation of the possible redox mechanism

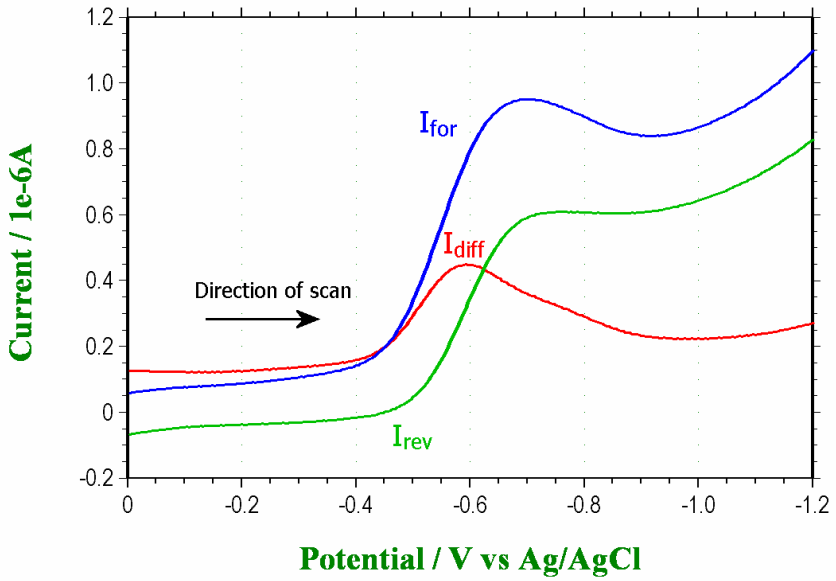

Figure 4.18 SWV's for **axle** in DCM using parameters $SW_{freq} = 15$Hz, $E_{SW} = 0.050$V and $E_{step} = 0.004$V. Net response I_{diff} shown in red, the forward and reverse responses, I_{for} and I_{rev} respectively, are shown in blue and green.

The forward response I_{for} reaches a maximum at -0.7V and corresponds mainly to the reduction of $Fl_{ox} - fumaramide$ to $Fl_{rad}{}^{-\bullet} - fumaramide$. However, during the reverse(backward) SW pulse we observe the I_{rev} response becoming more positive and

eventually producing a maximum (rather than a re-oxidation minimum) at -0.73V. This response is typical of other flavin-polymer substrates examined in this thesis and is believed to be produced by the proton and second electron transfer (H^+, e) which produces the axle anion $Fl_{red}H^- - Fumaramide$ as shown in Figure 4.1. The I_{rev} response is approx 75% the magnitude of the forward response I_{for}. A combination of this positive magnitude and lagging position produces the trailing shoulder in the overall response I_{diff}.

As a consequence of this distorted SW voltammogram we cannot rely on the peak positions to determine the formal potential E^θ of the redox system. However we can complete the electrochemical scheme shown in Figure 4.16 by the addition of the proton and 2nd electron pathway (H^+, e) as shown in Figure 4.19. All we can be certain of regarding the half wave potential $E_{1/2}{}^{(2)}$ of the 2nd electron transfer is that it will be more positive than the half wave potential $E_{1/2}{}^{(1)}$ for the 1st electron transfer.

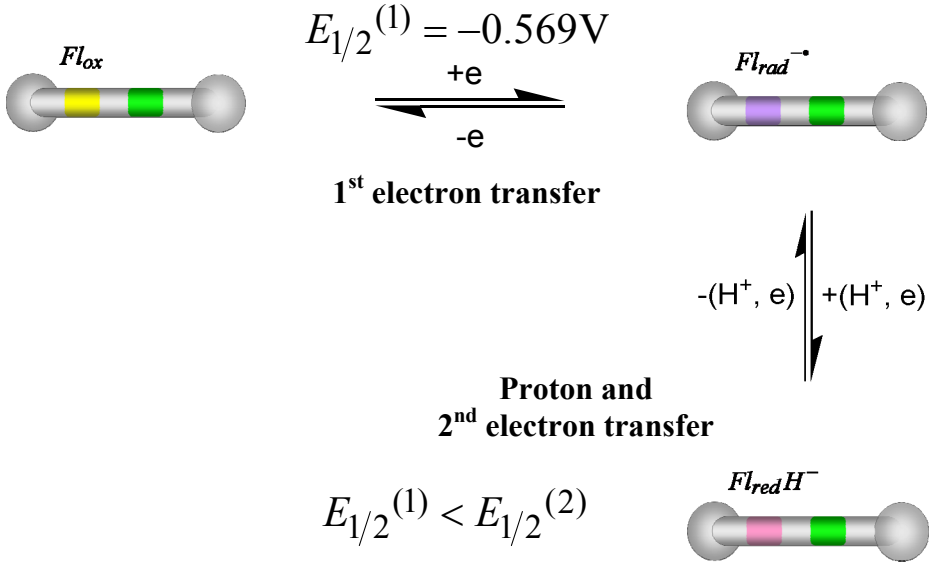

Figure 4.19 Electrochemical scheme a two electron and one proton transfer for the flavin-fumaramide **axle**.

4.4.2.2 The flavin-fumaramide rotaxane polymer.

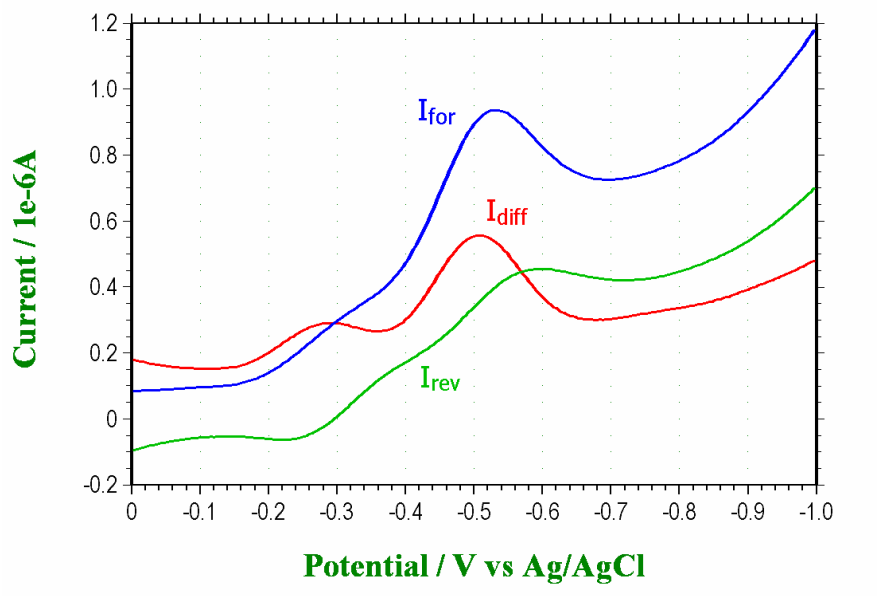

Figure 4.20 SWV's for the **rotaxane** in DCM using parameters $SW_{freq} = 15\text{Hz}$, $E_{SW} = 0.050\text{V}$ and $E_{step} = 0.004\text{V}$. Net response I_{diff} shown in red, the forward and reverse responses, I_{for} and I_{rev} respectively, are shown in blue and green.

The SWV for the **rotaxane** is shown in Figure 4.20. Overall response I_{diff} peaks are found at -0.292 and -0.508V (vs Ag/AgCl). The smaller forward response I_{for} at -0.3V could be attributed to the **rotaxane** co-conformation where the BA macrocycle is still lingering over the neutral Fl_{ox}, despite the imide being a known weak hydrogen-bonding station [49, 50]. This could be a consequence of the sluggish movement of the BA macrocycle in returning to the non-flavin side of the axle which could be due to some restriction brought on if the **rotaxane** was tightly encapsulated within the polymeric structure. These SW voltammograms were recorded immediately after the cyclic voltammagrams and the corresponding product appeared to increase in concentration following successive sweeps (see Figure 4.14).

The larger more negative I_{diff} peak response can be attributed to the combined reduction/oxidation of co-conformations $Fl_{ox}-[fumaramide]$ and $Fl_{ox}[-]Fumaramide$, where in the latter the BA macrocycle is partially binding with both the flavin and fumaramide stations. The forward response (I_{for}) peak at -0.528V is more negative than the half wave potential ($E^{\theta} = -0.488\text{V}$) obtained during cyclic voltammetry (see Figure 4.11). The lagging reverse response (I_{rev}) should be presenting a minimum had this been a single electron transfer process. However it shows a positive current response with a maximum at -0.588V. We also observed this in the previous section with the SWV for the **axle**. There we attributed it to a 2nd electron (plus proton) transfer to the flavin. However it can also be attributed here to the single electron transfer to two flavin **rotaxane** co-conformation which have redox potentials that are different but are very close (i.e. approx 84mV).

Therefore to summarise what we think is taking place, as the SW voltammogram potential becomes more negative, its first redox encounter is $[Fl_{ox}]-fumaramide$ where the BA macrocycle is impeded from moving from the oxidized flavin. Here we observe a small by electrochemically reversible response with a positive I_{for} peak and a negative I_{rev} peak. As the scan potential becomes increasing negative its second redox encounter is that for the co-conformer $Fl_{ox}[-]fumaramide$ where the BA macrocycle is located midway and partially hydrogen-bonding with both flavin and fumaramide stations. The absence of a negative I_{rev} current response suggests that the process is electrochemically irreversible. The product formed during the forward SW pulse can be attributed to either a proton and 2nd electron transfer (i.e. H^+, e) or the translocation of the BA macrocycle to the reduced flavin thereby creating a more stable $Fl_{rad}^{-\bullet}$ product. We lean towards the latter explanation for the following reasons.

Partial hydrogen-bonding of the BA macrocycle to the neutral Fl_{ox} may provide some steric protection to the flavins ability to receive a proton, particularly if it is the flavins O(4) carbonyl participating in these interactions with the macrocycle, (see Figure 4.13) where the isophthaloyl component of the macrocycle appears very close to the flavin's N(5) nitrogen and C(4a) carbon. This is where a proton would ordinarily be accepted. We will later examine photochemical evidence that suggests that the flavins O(4) carbonyl is participating in these interactions. We would also imagine that if translocation was achievable with the short period of the SW pulse, then the BA macrocycle would provide both steric protection and stability to the $Fl_{rad}^{-\bullet}$. In reality, either of theses cases could be employed to explain the irreversible characteristic of the SW response. The increasingly positive reverse current response I_{rev} can also be explained by either the ECE () reaction or as we are suggesting, the redox process from the alternate stable co-conformation $Fl_{ox}-[Fumaramide]$ which should occur at a slightly more negative potential based on the **axle** half wave potential $E_{1/2}=-0.569\text{V}$.

This clearly needs to be investigate further but a preliminary indications suggest after comparing the area measured under the CV response (i.e. total charge) in Figure 4.11 of the **axle** at $0.2\,\text{mM}$, is slightly larger than the area under the **rotaxane** CV response at $0.4\,\text{mM}$, twice the concentration of the **axle**. This would seem to imply that the **axle** was undergoing a two electron transfer process whereas the **rotaxane** was undergoing a single electron transfer, which supports the above proposal.

We therefore suggest that the somewhat electrochemical scheme shown in Figure 4.21 for the **rotaxane**, where the single electron redox process and subsequent translocation is emphasised within the green box. We have included in the scheme the proton and 2nd electron transfer (H^+, e) mechanism primarily to emphasise that it is competing with the macrocycle translocation and also that steric shielding to a proton donation would be provide by the positioning of the BA macrocycle as emphasised by the processes included in the grey box. These redox processes may still occur but are not observed during the timescale of the voltammograms.

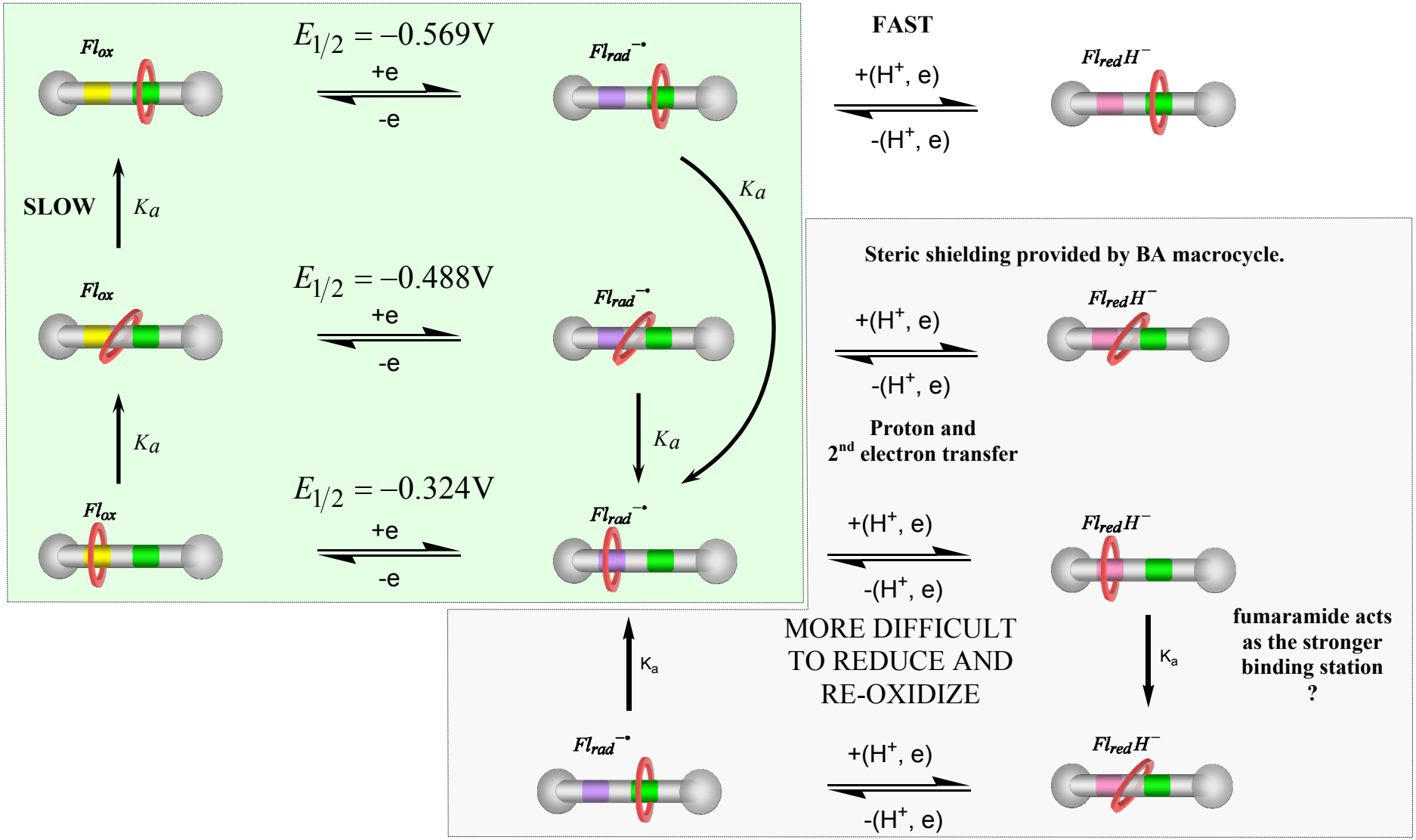

Figure 4.21 Electrochemical scheme. Proton and 2nd electron transfer should in theory be more difficult because of the stabilization effect of the benzylic amide ring on the flavin radical $Fl_{rad}^{-\bullet}$.

4.4.3 Surface immobilized voltammetry in water.

The cyclic voltammograms of the **axle** and **rotaxane** which were initially performed in aqueous solution were weak and poorly defined. An alternative procedure employed to exploring the redox properties of these two polymers in water involved a surface immobilized technique commonly known as protein film voltammetry (PFV) [35] where the polymer was directly applied as a thin film to the surface of glassy carbon working electrode as described in Section 4.4.1.

4.4.3.1 Cyclic Voltammetry.

The CV for the surface immobilized **axle** and **rotaxane** are shown in Figure 4.22 as the red and blue voltammograms respectively. The voltammograms have been preserved in their unfiltered form and the background has not been subtracted. Interestingly we note that both cathodic (reductive) peaks appear almost identical in peak position and magnitude. The anodic (oxidation) peak for the **rotaxane** however appears broader and larger in magnitude than the corresponding **axle** anodic peak. The reason for this become clear when we increase the scan rate to 0.1Vs^{-1} and then to 0.01Vs^{-1} as shown in Figures 4.23(a and b). Here we observe the emergence of second oxidation peak (wave *III*) which appears to shift more positive as the scan rate increases and which we would attribute to the $[Flrad^{-\bullet}]-fumaramide$ co-conformer. At a fast sweep rate the two oxidation peaks are merged into one broad wave. This initially would seem to be opposite to the finding of Leigh who performed the CV (Figure 4.12) at fast scan rates (1Vs^{-1}) in order better observe the voltammogram of a stabilized rotaxane co-conformation product for which the BA macrocycle component carried a fast recovery stroke (10^4s^{-1}). [49, 50]

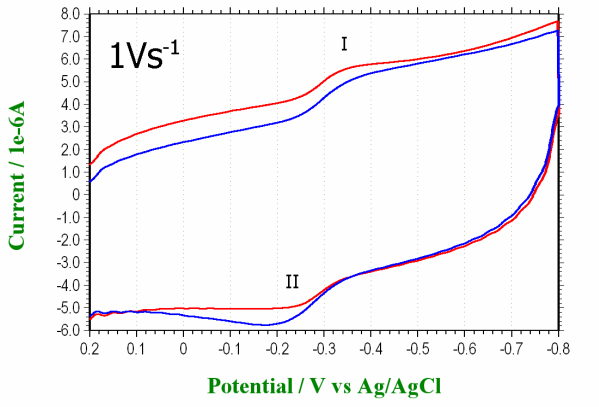

Figure 4.22 Cyclic voltammogram of the immobilized **axle** (*red*) and **rotaxane** (*blue*) polymer at scan rate of (a). $\nu = 1\text{Vs}^{-1}$ (b). $\nu = 0.1\text{Vs}^{-1}$ (c). $\nu = 0.01\text{Vs}^{-1}$.

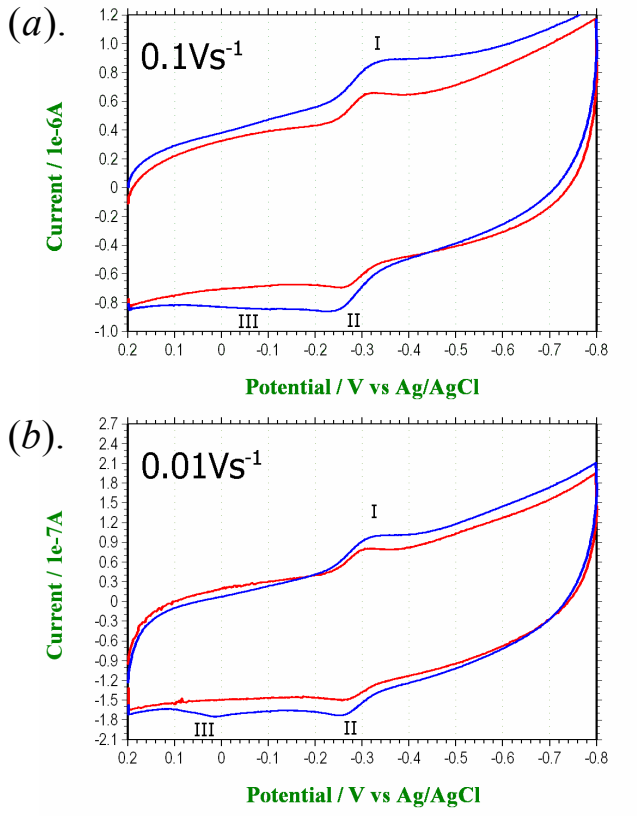

Figure 4.23 Cyclic voltammogram of the immobilized **axle** (*red*) and **rotaxane** (*blue*) polymer at scan rate of (a). $\nu = 0.1\text{Vs}^{-1}$ (b). $\nu = 0.01\text{Vs}^{-1}$.

However if the BA macrocycle for our **rotaxane** is restricted by the polymer structure, as suggested earlier, then BA macrocycle translocation could only be sufficiently achieved by a prolonged exposure to a potential more negative than peak I. This is achieved during the slow sweep rate of $\nu = 0.01\text{Vs}^{-1}$ which would take 200sec to complete the full scan shown above. Therefore in order to determine that the second oxidation wave (*III*) was not just product of slow scan rate but was indeed a product of the duration at which the electrode was exposed to a high negative potential a series of CV were performed where the oxidation sweep was held at -1V for a period ranging from $50-150$ sec before commencing the sweep at a relatively fast scan rate of $\nu = 0.1\text{Vs}^{-1}$. This would provide an increasing longer period for the accumulation of $[Fl_{rad}^{-\bullet}]-$ *fumaramide* product

The results from this are shown in Figure 4.24 which depicts the magnitude of the second oxidation wave (*III*) increasing as the accumulation period increased. Unfortunately only the oxidation sweep was carried out as it would have been interesting to see if the corresponding reduction peak of this co-conformer was formed. However we can report that only one cathodic peak is observed following a substantial period between sweeps.

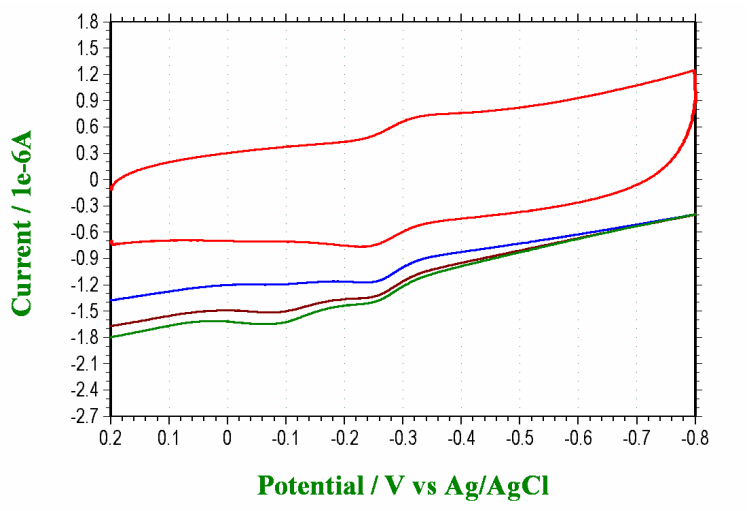

Figure 4.24 Cyclic voltammogram of the immobilized **rotaxane** polymer at scan rate $\nu = 0.1\ \mathrm{Vs}^{-1}$. During the subsequent sweeps the electrode was held at $-1\mathrm{V}$ for $50\,\mathrm{sec}$ (*blue*), $100\,\mathrm{sec}$ (*brown*) and $150\,\mathrm{sec}$ (*green*) before beginning the second (oxidative) segment.

4.4.3.2 Square wave voltammetry.

The surface immobilized SW voltammograms for the **rotaxane** in water are shown in Figures 4.25 and 4.26. The overall SWV response I_{diff} (*red line*) in Figure 4.24 shows a small peak at approx -0.08V which we again attribute to the small presence of a $[Flox]-fumaramide \rightleftharpoons [Flrad^{-\bullet}]-fumaramide$ redox couple. The response is reversible, as depicted respectively by the presence of small maxima and minimum for the I_{for} and I_{rev} responses shown in the small inset. The larger I_{diff} SWV response at -0.296V we attribute to an overlap of the $Flox[-]fumaramide \rightleftharpoons Flrad^{-\bullet}[-]fumaramide$ and $Flox-[fumaramide] \rightleftharpoons Flrad^{-\bullet}-[fumaramide]$ redox process. It also demonstrates a reversible SW response as shown in the small inset by the presence of small maxima and minimum for the I_{for} and I_{rev} respectively. The formal potentials of these two redox couples must be very close otherwise we would observe a positive reverse response I_{rev} similar to that presented in Figure 4.20.

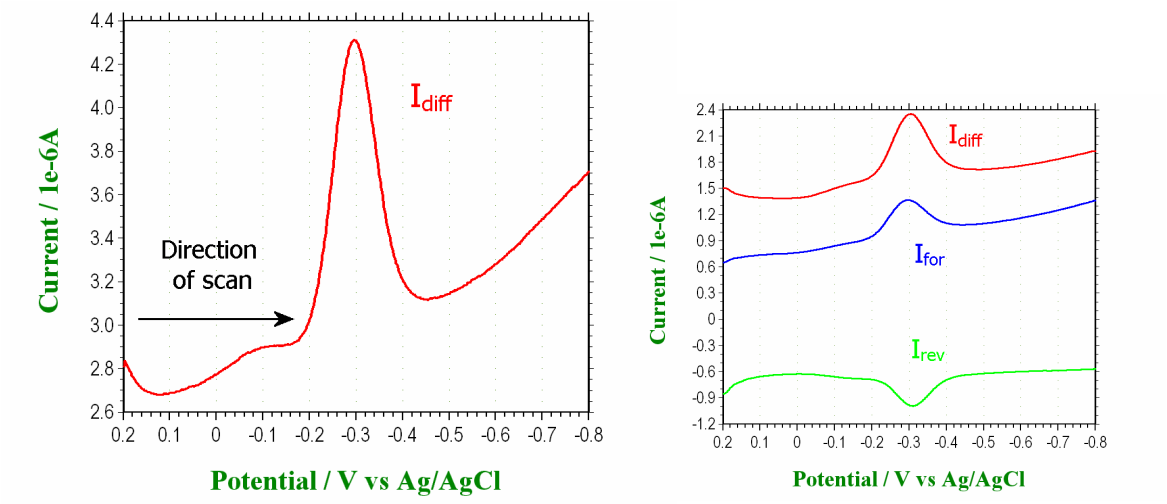

Figure 4.25 SW voltammogram of the immobilized **rotaxane** polymer 0.2 to -0.8V, $SW_{freq} = 100$ Hz, $E_{SW} = 0.025$ V.

A change in the direction of the scan (as indicated by the black arrow) can sometimes provide additional information regarding the presence of irreversibly formed redox species. Figure 4.26 shows the **rotaxane** SW voltammogram scanned in the direction shown form -0.8 to 0.2V after a 10sec accumulation period to promote the formation of the reduced co-conformation $[Flrad^{-\bullet}]-fumaramide$. Here we observe an increase in the response for the redox couple $[Flrad^{-\bullet}]-fumaramide \rightleftharpoons [Flox]-fumaramide$ at -0.05V. Again both the forward and reverse responses shown in the inset depict the redox process for each separate co-conformation as an electrochemically reversible process.

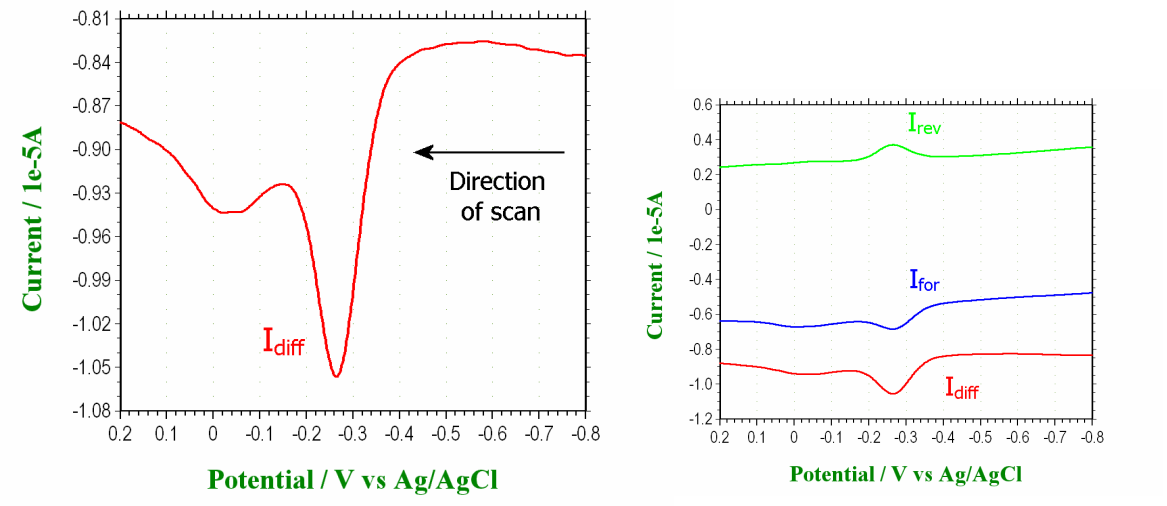

Figure 4.26 SW voltammogram of the immobilized **rotaxane** polymer -0.8 to 0.2V , using parameters SW_{freq} = 100 Hz , E_{SW} = 0.025 V and E_{accum} = 10sec @ -1 V .

We can compare these SWV with those obtained for the **axle** polymer which is shown in Figure 4.27 and 4.28. The overall response I_{diff} shows a single redox peak at –0.292V and the forward and reverse responses shown in the inset confirm that the process is electrochemically reversible.

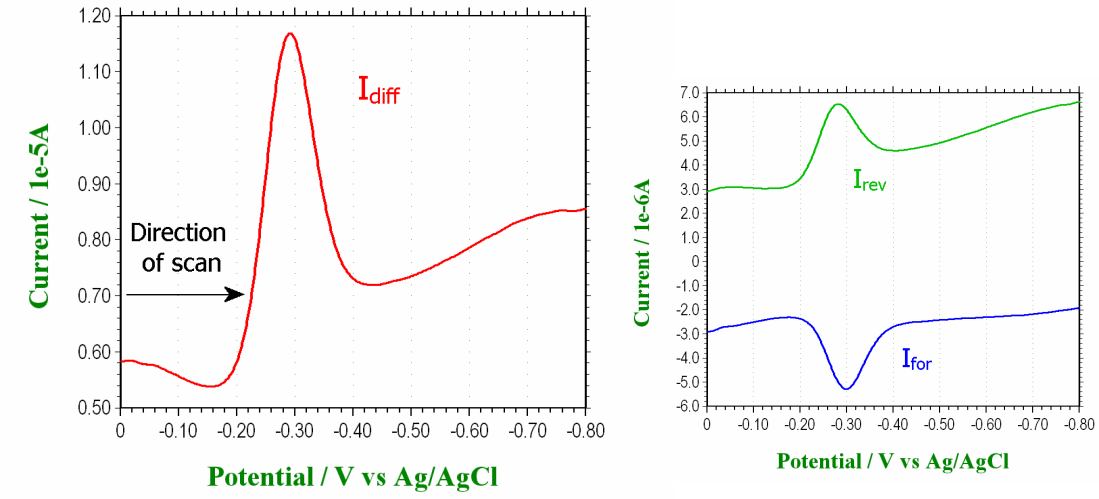

Figure 4.27 SW voltammogram of the immobilized **axle** polymer 0 to -0.8V , SW_{freq} = 100 Hz , E_{SW} = 0.025 V .

Changing the direction of the SW scan only produces a single peak at −0.272V as shown in Figure 4.28.

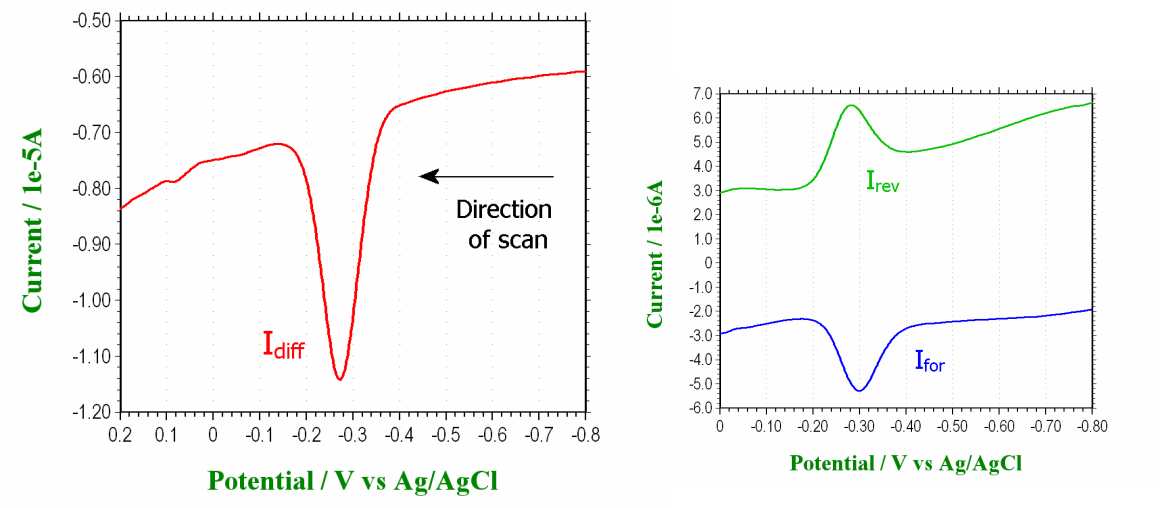

Figure 4.28 SW voltammogram of the immobilized **axle** polymer from −0.8V to 0.2V, using parameters SW_{freq} = 100 Hz, E_{SW} = 0.025 V and E_{accum} = 10sec @ -1 V.

4.5 Photochemistry.

4.5.1 Jablonski diagram of flavin transition states.

The analysis of these spectra is base on the photophysical and photochemical properties of flavins reported by Heelis[52] and the effects of hydrogen-bonding on the first two absorption band (*Band I* and *II*) by Nishimoto [53-56]. *Band I* corresponds to the $S_0 \rightarrow S_1$ transition (Figure 4.29) and *Band II* corresponds to the $S_0 \rightarrow S_2$ transition. Some useful information regarding the fluorescence spectra has been provided by both Yagi[57] and Heelis[52].

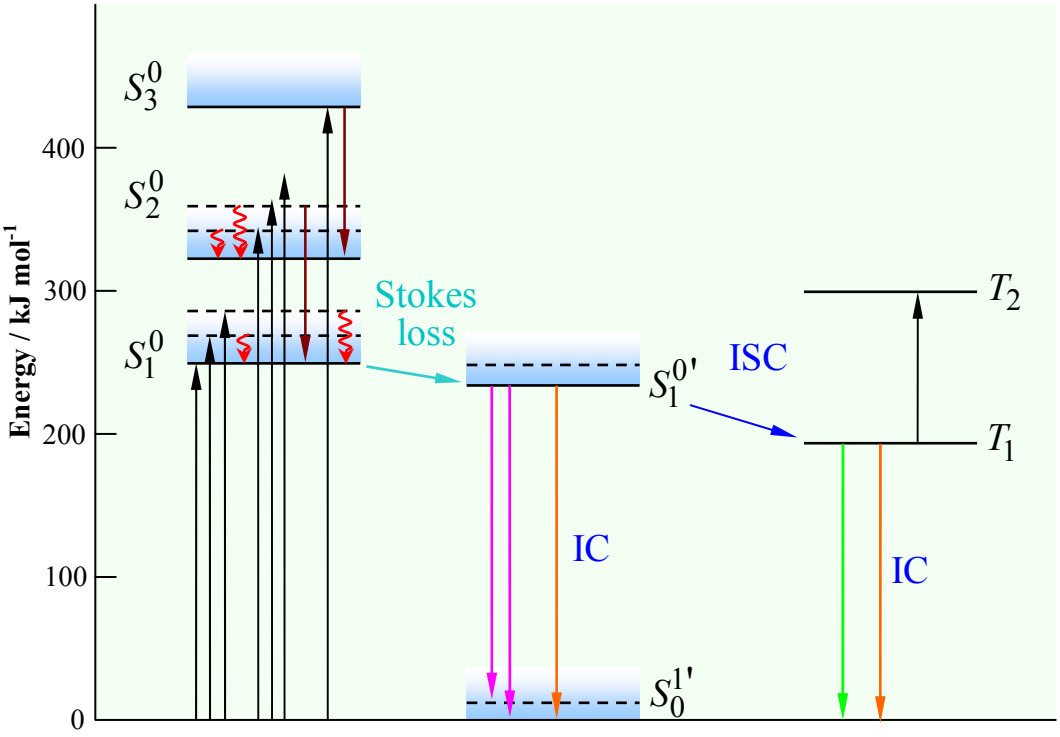

Figure 4.29 Jablonski-type diagram for flavins showing the energy levels above ground state (black horizontal lines) and vibrational (dashed horizontal). Vertical black arrows are absorptions; brown arrows are non-radiative deactivation; red curly arrows are thermal equilibration of vibrational levels; pink arrows are fluorescence emissions; green arrows are phosphorescence; orange arrows are non-radiative internal conversion (IC); the blue arrow is intersystem crossing (ISC) and the cyan arrow is Stokes loss due to solvent relaxation. S is the singlet state, T is the triplet state, subscript denotes electronic energy level and superscript denotes vibrational energy level.

Revised from reference [52].

4.5.2 Absorbance spectra.

The absorbance spectra for the **axle** and **rotaxane** polymer systems are shown in Figure 4.30 for both polar (e.g. water) and non-polar (e.g.$CHCl_3$) solvents accompanied by a summary of the peak positions for *Bands I* and *II* in Table 4.3. Overall, there is very little difference between the **rotaxane** and **axle** *Band I* peak position in water (both 432nm) and in $CHCl_3$ (both 438nm). Heelis[52] reports that there should be virtually no change expected in this peak on moving from water to less polar solvents and therefore this red shift observed (6nm) on changing water to $CHCl_3$ is at present unexplained. Also, apart from a slight increase in molar absorptivity in water, there is no significant difference between the position of *Band II* for the **axle** in water and $CHCl_3$ where both maxima are at 317nm. The same can be said for the **rotaxane** in water and $CHCl_3$ where both maxima are at 322nm. In other word the solvent media has no effect here. The observed increase in peak magnitude and 5nm red-shift between **axle** and **rotaxane** can therefore only be logically be explained through some interaction between the flavin and the macrocycle of the **rotaxane**. The *Band II* peak position is particularly sensitive to specific hydrogen bonding at the N(5), O(4), O(2), N(3) and N(1) heterogeneous atoms of the flavin. These have been arranged in order of red shift that they imposed on the *Band II* maxima, with N(5) causing the largest red shift and N(1) having a negligible effect on it. However hydrogen-bonding to the N(5) would also induce a red shift of the *Band I* maxima. Hydrogen bonding to either O(2) and/or N(3) do not seem to induces a large enough red shift, reportedly achieving only 2 and 1nm red shift respectively. [53-56] This only leaves hydrogen-bonding with O(4) which provides both a moderate red shift in *Band II* and negligible shift in *Band I*. This neatly supports the proposal that the macrocycle is partially binding with the neutral flavin. Hydrogen-bonding with O(4) rather than O(2) would also make more sense on account of the steric hinderance produced by the flavins N(10) hydroxyhexyl sidechain.

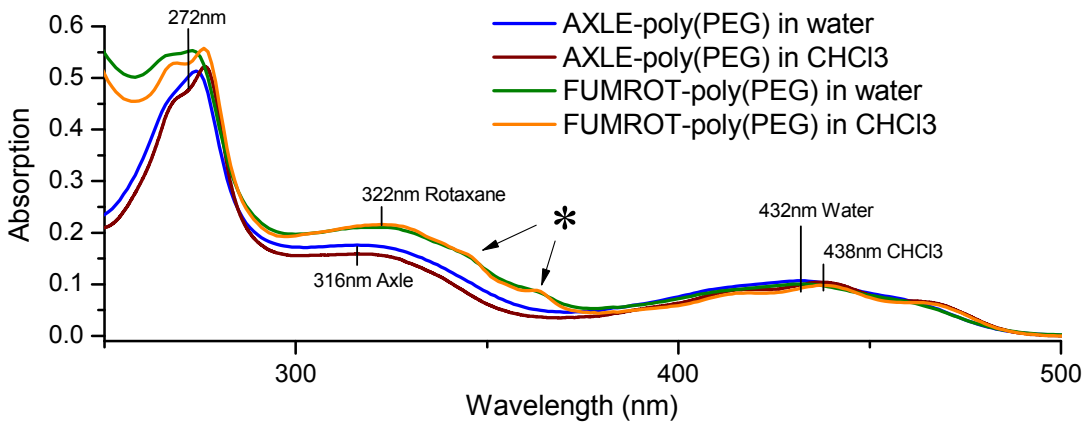

Figure 4.30 Absorbance spectra for **axle** and **rotaxane** in water and chloroform. The arrows highlighted by the asterisk occur only within the rotaxane spectra (both water and $CHCl_3$). They appear to be vibrational level peak definition similar to that observed in *Band I* which is a feature generally only visible in non-polar solvents.

Polymer	Absorbance Maxima position (nm)			
	Band I		Band II	
	$CHCl_3$	Water	$CHCl_3$	Water
axle polymer	438	432	317	316
rotaxane polymer	438	432	322	320

Table 4.3 Absorbance maxima positions for *Bands I* and *II* in water and chloroform for **axle** and **rotaxane** polymer systems.

Two small peak can be observed on the spectra for the **rotaxane** at 345 and 364nm (emphasised by the arrows) in both water and $CHCl_3$. There appears to be no shift in position with this change in solvent but better definition is observed in $CHCl_3$. At present we do not have a satisfactory explanation for their origin, however they appear to resemble the two shoulder peaks observed in *Band* 1. These are produced by the S_1 vibrational energy levels and are usually only visible in non-polar solvent or from the rigidity imposed on the flavin within a proteins active site. Although, to my knowledge, the S_2 vibrational energy levels are never observed because *Band* 2 is in fact a mixture of two different transitions ($\pi \rightarrow \pi^*$ and $n \rightarrow \pi^*$) [52], it may be possible that this some increased vibrational resolution is provide by the rigidity of benzylic amide ring. The corresponding vibrational peaks on the opposite side of *Band* 2 would be buried under the overlap with *Band* 3.

4.5.3 Fumaramide photoisomerization.

The flavin **axle** and **rotaxane** polymers were irradiated under a UV lamp at 254 nm in $CHCl_3$. The resulting absorbance spectra are shown in Figures 4.31 for the **axle** and Figure 4.32 for the **rotaxane**. The corresponding fluorescence emissions are shown in Figures 4.34 and 4.35 respectively and will be discussed shortly. Both the absorbance spectra have been expanded to include the shorter wavelengths from 230 nm upwards. This part of the spectrum includes a fourth peak at 240 nm which is produced through absorbance of the fumaramide component of both **axle** and **rotaxane**. A reference spectrum of a non-flavin fumaramide test compound (**C-53**) is shown in Figure 4.33 for comparison and was used to determine the absorbance maxima for the fumaramide component of the **rotaxane** system to be approximately in the region of 250 – 270 nm.

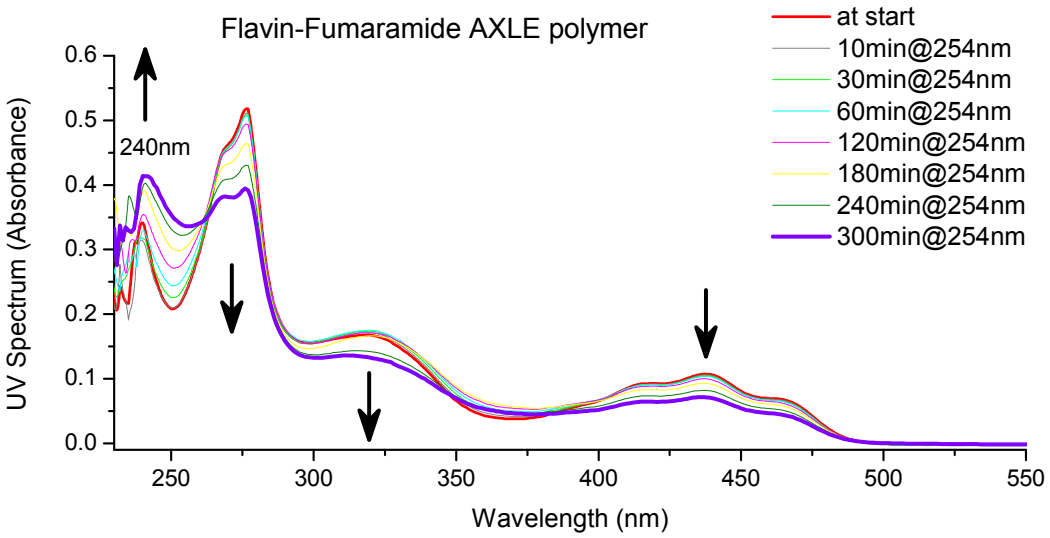

Figure 4.31 Absorbance spectra for **axle** in chloroform after a period of exposure to UV lamp @ 254nm.

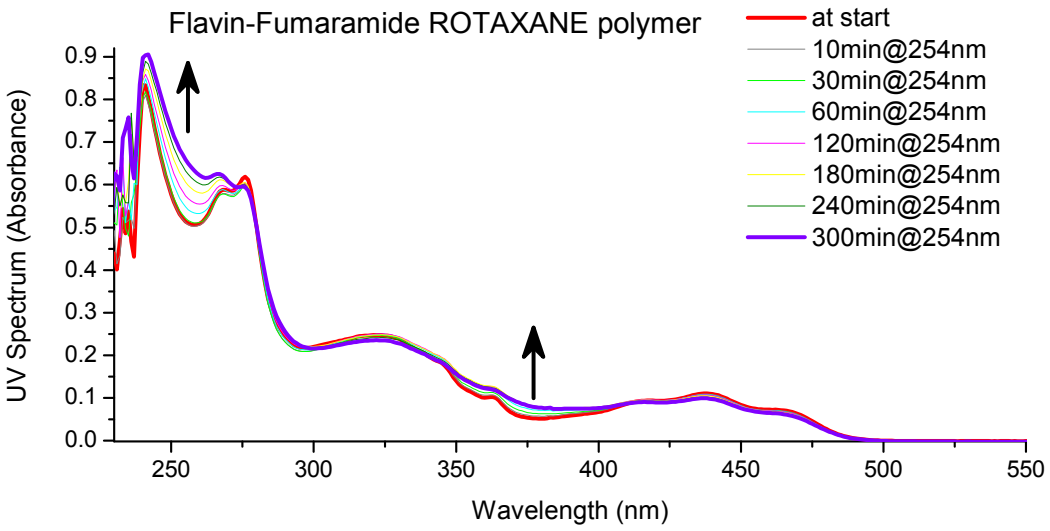

Figure 4.32 Absorbance spectra for **rotaxane** in chloroform after a period of exposure to UV lamp @ 254nm.

The **axle** demonstrates an overall decrease in magnitude of the three flavin absorbance bands at 272, 316 and 432 nm accompanied by a blue-shift in *Band I* (1 nm) and *Band II* (6 nm). This decrease in peak height could probably be explained by photobleaching of the flavin which resulted from the long exposure to the UV radiation. But this probably wouldn't explain the blue-shift. The only part of the spectrum that increases is peak region for the fumaramide component of the **axle** also red-shifts slightly by approx 2 nm. The largest change observed appears to be in the trough region which starts with a minimum at 251 nm which reduces in depth and red-shifts to 256 nm after 6h exposure to UV irradiation.

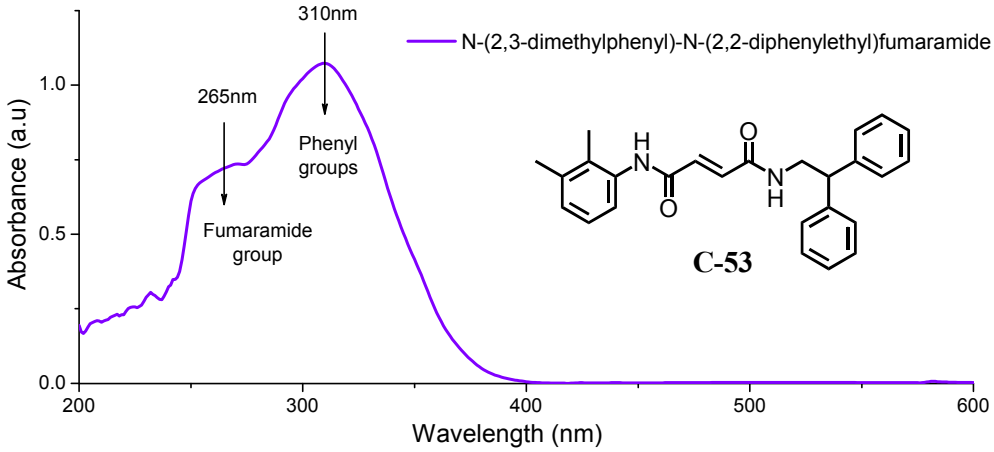

Figure 4.33 Absorbance spectra for N-(2,3-dimethyl)-N-(2,2-diphenylethyl)fumaramide (**C-53**) at 1×10^{-4} M in solvent mixture DCM/DMF(99:1). This spectra from this test compound was used to determine the absorbance maxima for the fumaramide component of the **rotaxane** system and was found to be in the region of 250 - 270nm.

In comparison the **rotaxane** appears relatively less affected by the exposure to UV irradiation. Apart from a slight decrease in magnitude and a 1 nm blue-shift in both *Bands I* and *II*, the flavin absorbance bands seem relatively unaffected. The fumaramide absorbance peak at 241nm increases in magnitude by approx the same amount observed in the **axle** but red-shifts very slightly (>1nm). Again the largest level increase appears to be in the trough region which starts with a minimum at 258 nm which shifts to 262 nm after 6h of UV irradiation. One final observation is the small but noticeable increase in the region between *Bands I & II*. This could be associated with the two unexplained peaks at 345 and 364nm.

4.5.4 Fluorescence spectra.

The fluorescence emission for the **axle** and **rotaxane** in $CHCl_3$ are shown in Figures 4.34 and 4.35 respectively. The spectra were produced from the same cuvette sample taken immediately after the recording of the absorbance spectra shown in the insets. The excitation frequency was taken as $\lambda_{max} = 438$ nm and despite using a sample with an absorbance of approx $A = 0.1$, an order of magnitude more concentrated that normal, it is clearly obvious that at the start the fluorescence emission is heavily quenched. However there is a linear correlation between the fluorescence emission increase and the exposure time of irradiation at 254 nm as shown in Figure 4.36.

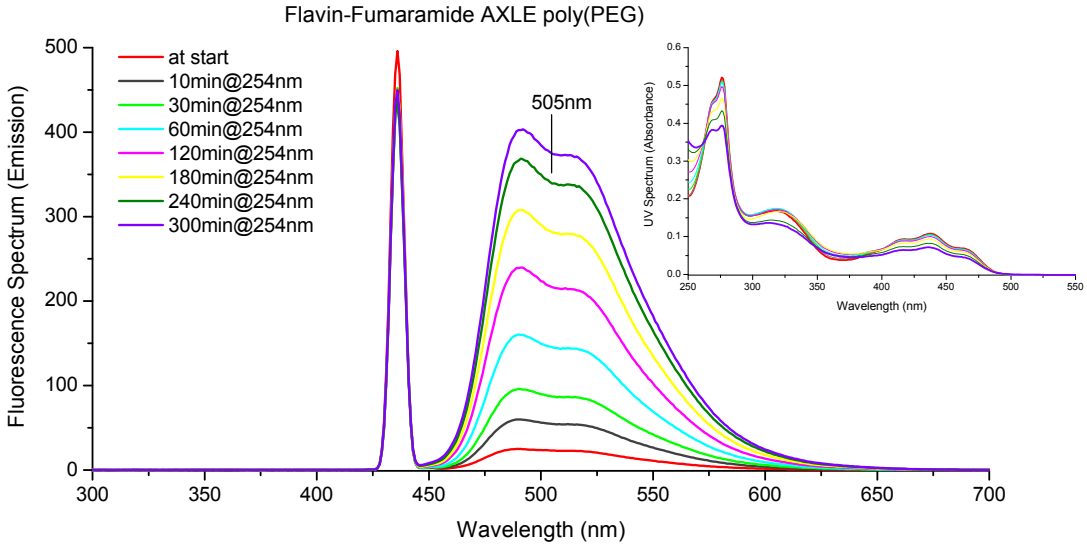

Figure 4.34 Fluorescence emission spectra for the **axle** in chloroform. The corresponding absorbance spectra is shown in the inset.

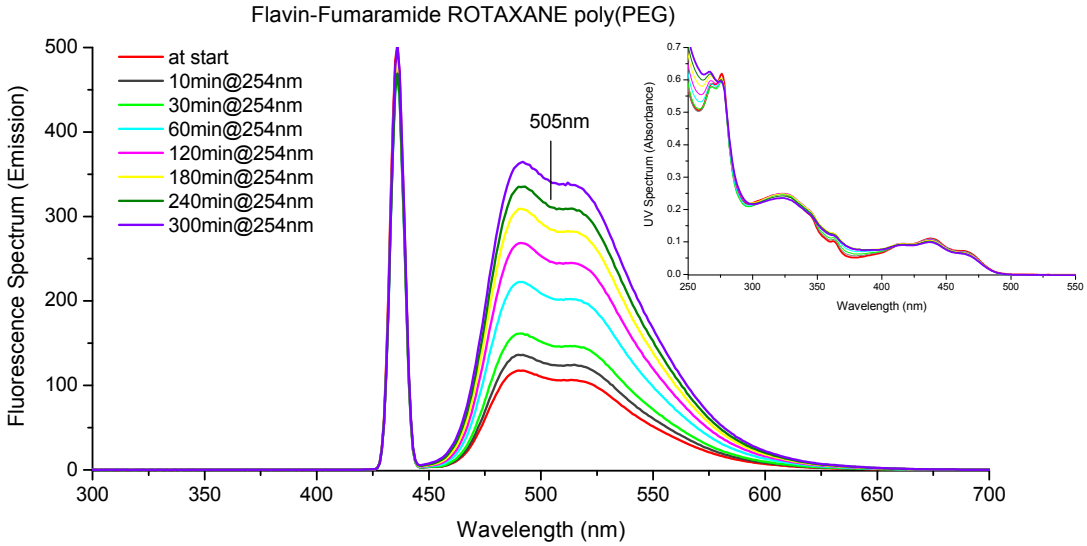

Figure 4.35 Fluorescence emission spectra for the **rotaxane** in chloroform. The corresponding absorbance spectra is shown in the inset.

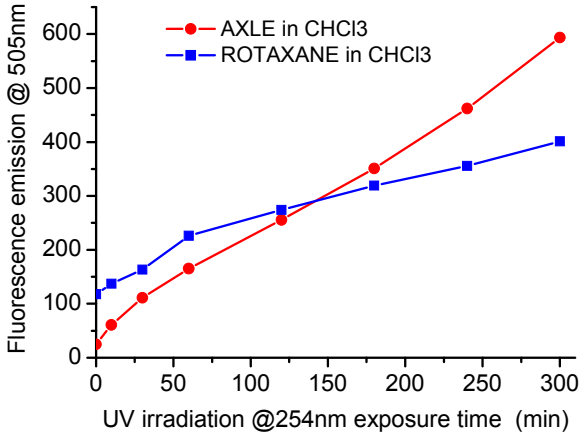

Figure 4.36 Plot showing a linear correlation between UV irradiation exposure time and emission peak height in chloroform. The fluorescent emission has been factored to allow for the decreases in the absorbance maxima at $\lambda_{max} = 438\text{nm}$.

Fluorescent emission increases were also observed for the **axle** and **rotaxane** polymer systems in water. These emission peak increases are summarized in the linear plot shown in Figure 4.37. In comparison with **axle** and **rotaxane** in chloroform (Figure 4.36) the rate of increase in fluorescence emission is not as pronounced but it does seem to be steadily increasing even after 6h. The slower rate of change may be attributed to the difficulty encountered by the fumaramide in rotating about the C=C bond while encapsulated within the polymer structure. This polymer structure has been predicted as being more tightly bound in an aqueous medium. It could also therefore be argued that shallower slope for the **rotaxane** in Figure 4.36 could be attributed to the stabilization effect of the BA macrocycle hydrogen-bonding to the fumaramide station.

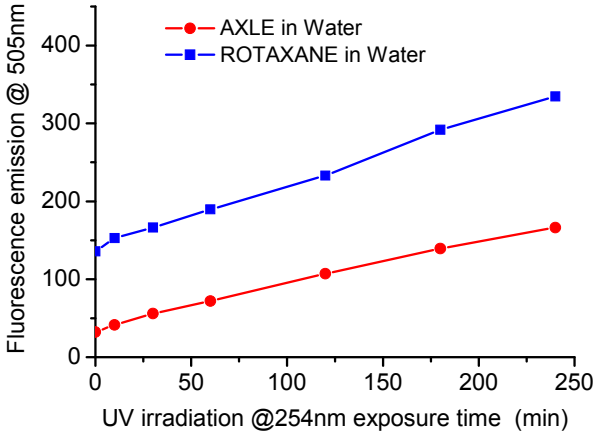

Figure 4.37 Plot showing a linear correlation between UV irradiation exposure time and emission peak height in water. The fluorescent emission has been factored to allow for the decreases in the absorbance maxima at $\lambda_{max} = 432\text{nm}$.

The neutral flavin is typically highly fluorescent therefore for strong fluorescence quenching to occur there must also be quenching mechanism. It is now known that the quenching mechanism in flavoproteins is due to photoinduced electron transfer (PET) [58, 59]. Electron transfer occur over very short distances and the type of PET described by Yang and Xie[58] involved one of three tyrosine amino acid residues Tyr^{35}, Tyr^{72} and Tyr^{116} located at distances of 4.5, 9.6 and 7.0 Å. Fluorescent quenching was later attributed primarily to the closest tyrosine Tyr^{35}. Another example of PET describes the fluorescent quenching of the tricyclic fluorophore, Neutral Red (NR), using three different types of aromatic amines which act as electron donors as shown in Figure 4.38. [46, 60] Quenching increases according to the number of electron donating groups on the amine, which, through stabilization of the amine cation, increases its ability to donate an electron to the photoexcited Neutral Red fluorophore.

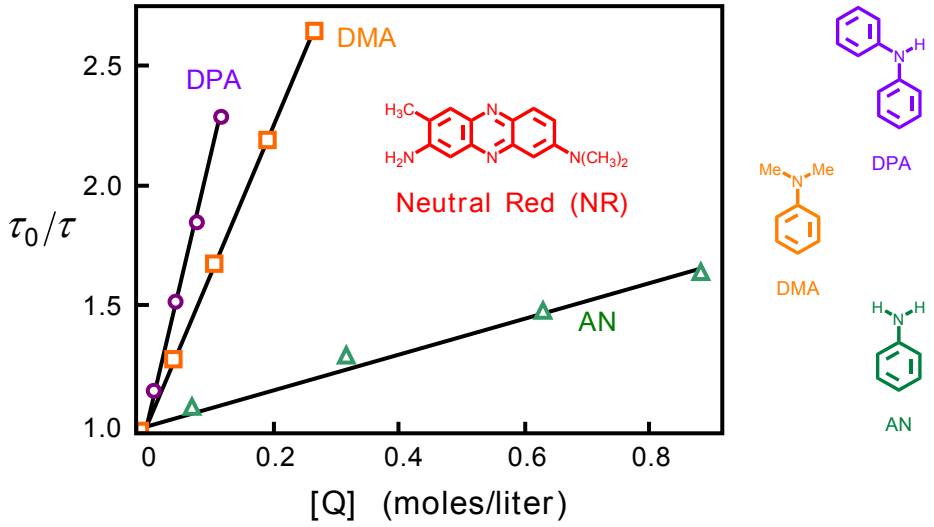

Figure 4.38 A Stern-Volmer plot showing the PET fluorescent quenching of Neutral Red by aromatic amines. Revised from [46, 60].

The distance between electron acceptor (A) and donor (D) can be controlled by covalently attaching the electron donor to the fluorophore electron acceptor. An example of this was readily observed following the reduction (in this work) of an N(3)-nitrobenzyl flavin to the N(3)-aminobenzyl flavin shown below in Figure 4.39. The nitrobenzyl flavin is highly fluorescent yellow colour in solution yet upon reduction to the aminobenzyl colour becomes dull brown and non-fluorescent. Here the amine electron donor is separated from the flavin acceptor by one methyl and one phenyl group which would effectively act as a type of electron conduit.

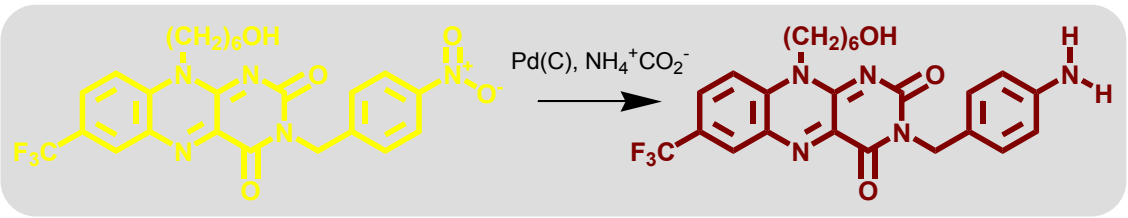

Figure 4.39 Fluorescent quenching observed following reduction of a nitrobenzyl flavin to the aminobenzyl flavin.

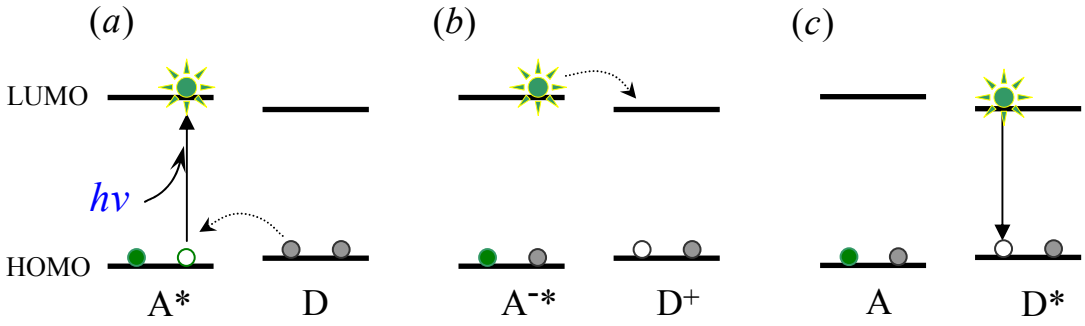

Figure 4.40 Fluorescent quenching mechanism by Photoinduced electron transfer (PET). **(a).** An electron from acceptor A is photoexcited to a higher energy state A* leaving in its wake a new LOMO, as represented by the empty circle ○, thereby promoting an the electron transfer from donor D. **(b).** The excited electron in excited anion A^{-}* now has to find a new Minimum energy pathway (MEP) to ground state. It starts by moving into donor D's LUMO to create initially the excited state D*. **(c).** It ends by finding an MEP to ground state within the relaxation channels available to donor D.

Since photoinduced electron transfer is shown to be possible, it follows that the electron in the excited state can no longer lose this energy by photon emission in order to returning to the acceptor ground state (GS). It will need to find a non-radiative route to the LUMO of the electron deprived donor D^{+} where ultimately it will either fluoresce or undergo some internal conversion. This sequence is depicted above in Figure 4.40.

Garavelli and Leigh [51] explored the possible MEP's for the multiple photoexcited states of a fumaramide thread using CASPT2/CASSCF computational techniques. One of the discoveries they made was that the fumaramide does provide an energy level at which it could fluoresce at 246nm but described how relaxation channels that would make this possible are bypassed by other competitive MEP's. Following the sequence describe above for the excited state flavin we begin to realize how the fumaramide thread may be quenching the flavin fluorescence. If the maleamide isomer exhibits the ability to fluoresce, then it would explain how and why the flavin fluorescence is increased after isomerization.

4.6 Conclusions.

4.6.1 Evidence for a second stable rotaxane co-conformation.

The red shift observed in *Band* 2 of the absorbance spectrum suggests that hydrogen-bonding interaction between the flavin O(4) carbonyl and the benzylic amide macrocycle. Comparing the peak area under the **axle** and **rotaxane** cyclic voltammetry sweep (which corresponds to the total Coulombic charge passed during the scan) suggests that the **axle** is undergoing a 2 electron transfer process and the **rotaxane** is restricted to one. The positive shift observed in the cathodic peak (reductive wave I) of the cyclic voltammetry experiments supports the proposal that a second stable rotaxane co-conformation exists where the BA macrocycle can partially hydrogen-bond with both flavin and fumaramide stations. The gradual positive shift if this cathodic peak following sequential reoxidation sweeps suggests an increased occupancy of this co-conformation. This evidence is supported by square wave voltammetry where the positive reverse response can be explained by the presence of two independently different co-conformations with redox potentials that were significantly different but close enough to appear merged in the overall response.

Surface immobilized voltammetry in water suggests that BA macrocycle translocation following reduction is possible yet sluggish. A single redox response was observes at fast CV sweep rates and the second only appearing after prolonged accumulation period at -1 Volt. Dynamic Light Scattering revealed that the polymer particle size was much smaller in water compared to organic solvent. Hydrodynamic compression of the polymer particles would therefore provide an explanation for this increased restriction in macrocycle movement. Similarity in redox potential of the two major **rotaxane** co-conformers and the **axle** could be explained if water molecules were able to permeate through the polymer structure and hydrogen-bond to the flavin carbonyls. This would also explain the approx +0.3V shift observed in the formal potential E^{θ} when compared to voltammograms recorded in DCM. Loss of definition in both the absorbance and fluorescence spectra would support this.

An attempt was made at exploring the **rotaxane** photoisomerization by exposing the contents of the electrochemical cell to a low intensity UV light at 254 nm for a prolonged period. No significant difference in the CV response was observed. This was either because photoisomerization was ineffective or most probably because the newly formed isomer was also able to adopt the co-conformation shown in Figure 4.41 where the BA macrocycle is located midway between the flavin and the maleamide group.

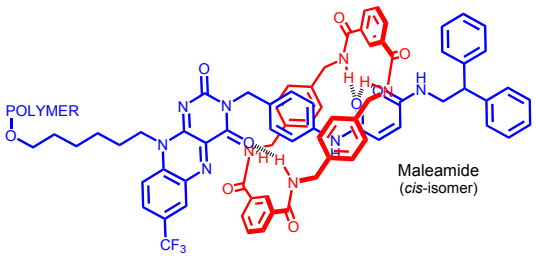

Figure 4.41 Rotaxane co-conformation showing how the BA macrocycle is still able to partially hydrogen-bond with the flavin O(4) carbonyl and the maleamide isomer.

4.6.2 *Fluorescence quenching mechanism.*

Fluorescence emission of both **axle** and **rotaxane** were shown to be highly quenched. Photoisomerization through exposure to low intensity UV light at 254nm revealed a dramatic increase in the emission which suggested that deactivation of the flavin excited state may be occurring through a fumaramide connected Minimum Energy pathway (MEP). Isomerization effectively switches off this deactivation pathway through a mechanism that still needs to be explored. Following *fumaramide* → *maleamide* photoisomerization however, it was noted that the emission maxima at 505 nm does not red-shift, as might be expected for an energy loss electron transfer to the fumaramide group. This would suggest that the fluorescence increase might be achieved by reducing the ability of the donor amine nearest the flavin to donate an electron. This would allow the flavin's electron to return to the newly formed LUMO created during photoexcitation (see Figure 4.40). Delocalization of the amine's lone pair would place a positive net charge onto the nitrogen atom, ultimately converting it into a poor electron donor. Figure 4.42 below suggests how this charge might become delocalized over 7 atoms (Figure 41b) of the maleamide group as opposed to just 3 atoms for the fumaramide (Figure 4.42a).

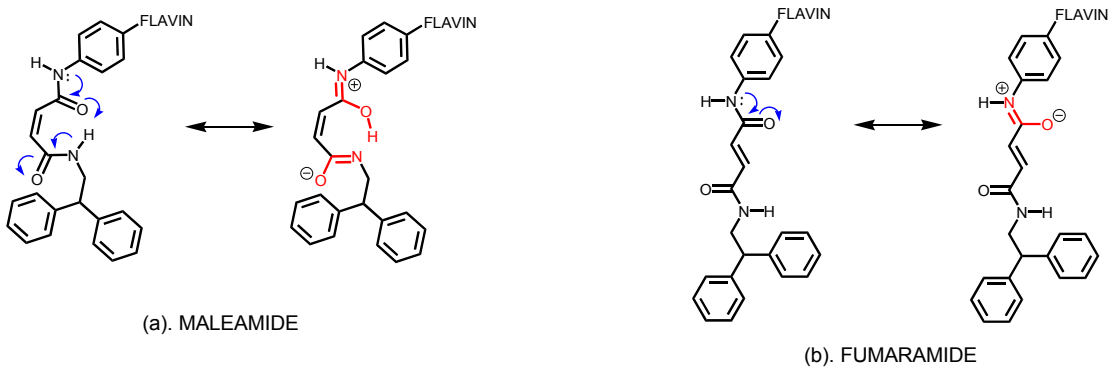

Figure 4.42 Possible amine lone pair delocalization pathways for the **(a)** maleamide and **(b)** fumaramide axle.

CHAPTER 5

FLAVIN-FUMARAMIDE [2]PSEUDOROTAXANE.

5.1 Introduction.

5.1.1 Experimental design strategy.

The synthesis strategy was to produce a flavin-fumaramide axle and benzylic amide macrocycle both of which were independently soluble in a non-polar solvent such as dichloromethane or chloroform. This solvent environment would support strong Hydrogen bonding interactions which would promote a stable [2]pseudorotaxane upon threading of the flavin axle through the macrocycle as shown in Figure 5.1. Confirmation that a stable two component pseudorotaxane has indeed formed would be demonstrated though electrochemical and spectroscopic differences observed in the absence and presence of the macrocycle.

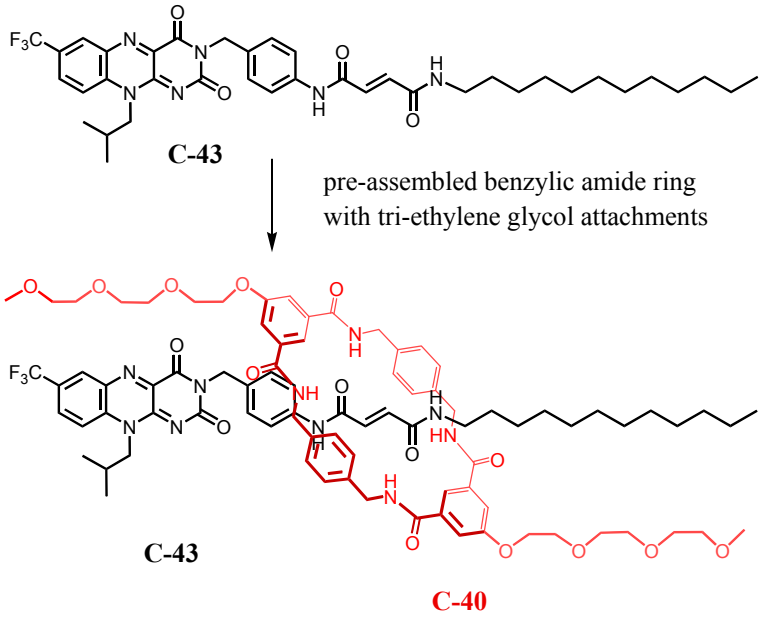

Figure 5.1 Flavin-fumaramide [2]pseudorotaxane **C-43** formation upon addition of a tri-ethylene glycol benzylic amide (BA) macrocycle **C-40**. The pseudorotaxane ideally requires that both axle and macrocycle components are soluble in non-polar aprotic solvents.

5.1.2 Overview.

In this chapter we demonstrate through voltammetry experiments that pseudorotaxane formation occurs in achievable and detectable in a solvent mixture of dichloromethane (DCM) and dimethyl formamide (DMF) at ratios up 70:30 thereby re-confirming the near perfect hydrogen-bonding partnership between the axle fumaramide component and the benzylic amide (BA) macrocycle. We examine the electron transfer mechanism of the electroactive flavin component of the axle in order to determine if it undergoes either a one electron or two electron and one proton redox process.

We explore a possibility that the fumaramide component of the axle demonstrates fluorescence emission at 548 nm while rigidly constrained by hydrogen bonding interactions with the benzylic amide macrocycle. This fluorescence emission was predicted by a recent publication by Garavelli and Leigh [51] but which is described as "*unobserved*" due to the alternative more favourable relaxaton process that involve the fumaramide C=C bond undergoing a twisting motion. Photochemical data would seem to suggest that these relaxation pathways become modified when the fumaramide hydrogen bonds with the BA macrocycle following (pseudo)rotaxane formation thus permitting the fluorescence pathway to be adopted. If this is the case then photoexcitation of the fumaramide does not take place as would be expected at the absorbance $\lambda_{max} = 265\text{nm}$, but rather could involve a double photon excitation at approx twice this wavelength (i.e. $\lambda = 515\text{nm}$) similar to the process shown in Figure 5.2.

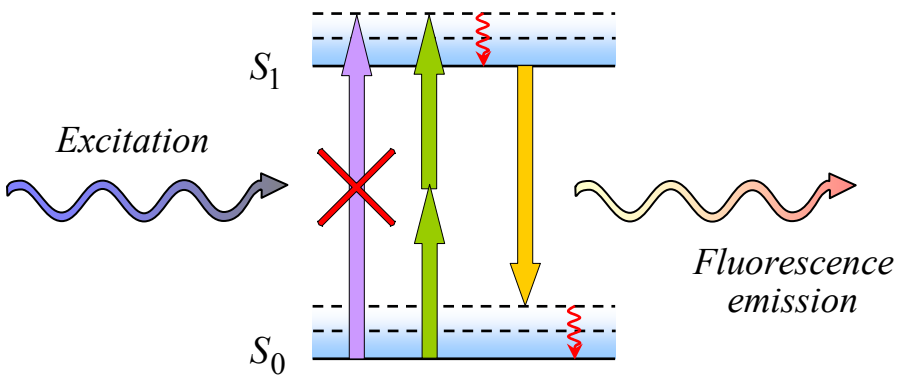

Figure 5.2 Jablonski diagram depicting a double photon absorbance by the fumaramide component of the (pseudo)rotaxane would explain the significant fluorescence emission observed at approx 548 nm.

5.2 Synthesis

The synthesis is divided into two separated parts each one dealing with the individual components of the pseudorotaxane. The first part of the synthesis section begins with a brief description of the flavin-fumaramide axle while the second section discusses the synthesis of the tri-ethylene glycol macrocycle.

5.2.1 Synthesis of flavin-fumaramide axle.

The axle synthesis starts, as shown in Figure 5.3, from the commercially available 1-chloro-2-nitro-4(trifluoromethyl)benzene and isobutyl amine which are reacted in an S_NAr reaction in THF with tri-ethylamine to form 4-(trifluoromethyl)-N-isobutyl-2-nitroaniline. The nitro group from this was reduced to an amine using catalytic Pd(C) with ammonium formate in MeOH under an inert atmosphere. The amine was then reacted with alloxan monohydrate in glacial acetic acid with boric oxide to form the 3-trifluoromethyl flavin.

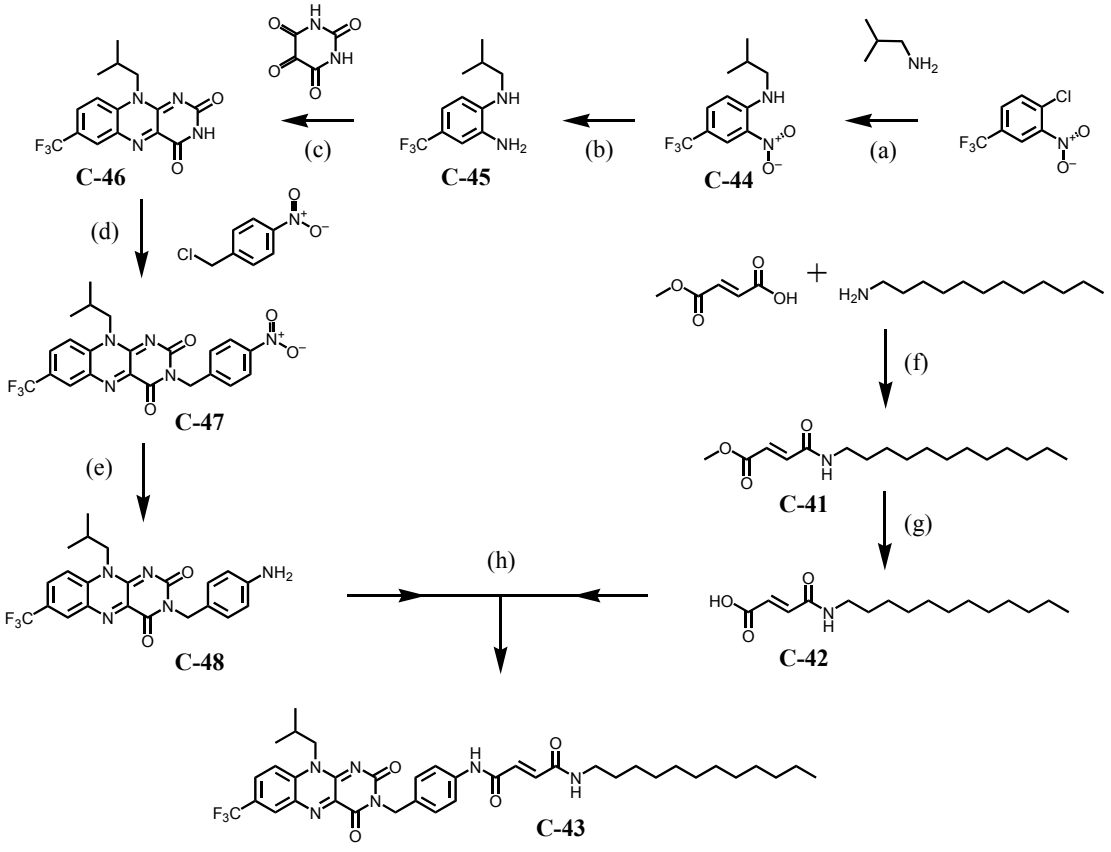

Figure 5.3 Synthesis of the flavin-fumaramide axle. **(a)** 1-Chloro-2-nitro-4(trifluoromethyl)benzene, isobutyl amine and tri-ethylamine were refluxed in THF for 20h. **(b)** 10% palladium (on carbon) and ammonium formate in MeOH for 1h at r.t. **(c)** Alloxan monohydrate, boron oxide stirred in glacial acetic acid at r.t for 2h. **(d)** 4-nitrobenzyl chloride and potassium carbonate in DMF/acetone (1:4) stirred at r.t for 2 days. **(e)** 5% Palladium (on carbon) and ammonium formate were stirred as a suspension in THF/MeOH (1:3) for 30min at r.t. **(f)** Mono-methyl fumarate, dodecylamine, DMAP and EDCI.HCl were stirred in chloroform at r.t for 2h. **(g)** 10% Aqueous HCl added to a stirring solution of (f) in THF at r.t. **(h)** EDCI.HCl added to a stirring suspension of (e) and (g) in chloroform at 0°C, then allowed to warm to r.t overnight.

Nitrobenzyl chloride was reacted with the flavin in an S_N2 reaction with potassium carbonate as a weak base. The flavin was only partially soluble in acetone, a solvent in which similar reactions were found to work well, therefore it was first dissolved in DMF and diluted 4:1 with acetone. The nitro group was then reduced to the amine using the same Pd(C) method discussed before to form a 3-aminobenzyl-7-trifluoromethyl flavin **C-48**. This would become the flavin station side of the axle.

The fumaramide station side of the axle would start by the EDCI coupling of commercially available mono-methyl fumarate and dodecylamine in chloroform with a catalytic amount of DMAP. The methyl ester was cleaved in THF following addition of 10% aqueous HCl to form (E)-3-dodecylcarbamoyl acrylic acid. Axle **C-43** was finally formed following the EDCI coupling the acrylic acid with the 3-aminobenzyl-7-trifluoromethyl flavin described above.

5.2.2 Synthesis of the benzylic amide macrocycle.

Synthesis of a benzylic amide (BA) macrocycle required the use of a template axle. We therefore employed a modified version of the method first introduced by Leigh [25, 26] which was designed to circumvent the formation of an eight molecule condensation of a BA [2]catenane as opposed to the desired single BA macrocycle. The reaction scheme is shown in Figure 5.4 and involved the synthesis of a tri-ethylene glycol (TEG) isophthalamide dichloride **C-38** from commercially available compounds (*red scheme* steps **(a)** to **(e) in** Figure 5.4). This was followed by the synthesis of a temporary isophthalamide axle **C-33** (*blue scheme* steps **(f)** to **(h)** in Figure 5.4). Full details of these reactions can be obtained in Chapter 8: Experimental.

Step (i). During the template assembly of the temporary [2]rotaxane **C-39** both TEG isophthalamide dichloride and commercially available p-xylylenediamine were simultaneously added dropwise to a stirring solution of the isophthalamide axle in dry chloroform. **Step (j).** Finally disassembly of the rotaxane was achieved by cleavage of the isophthalamide axles ester groups using sodium methoxide in MeOH to provide the tri-ethylene glycol BA macrocycle **C-40**.

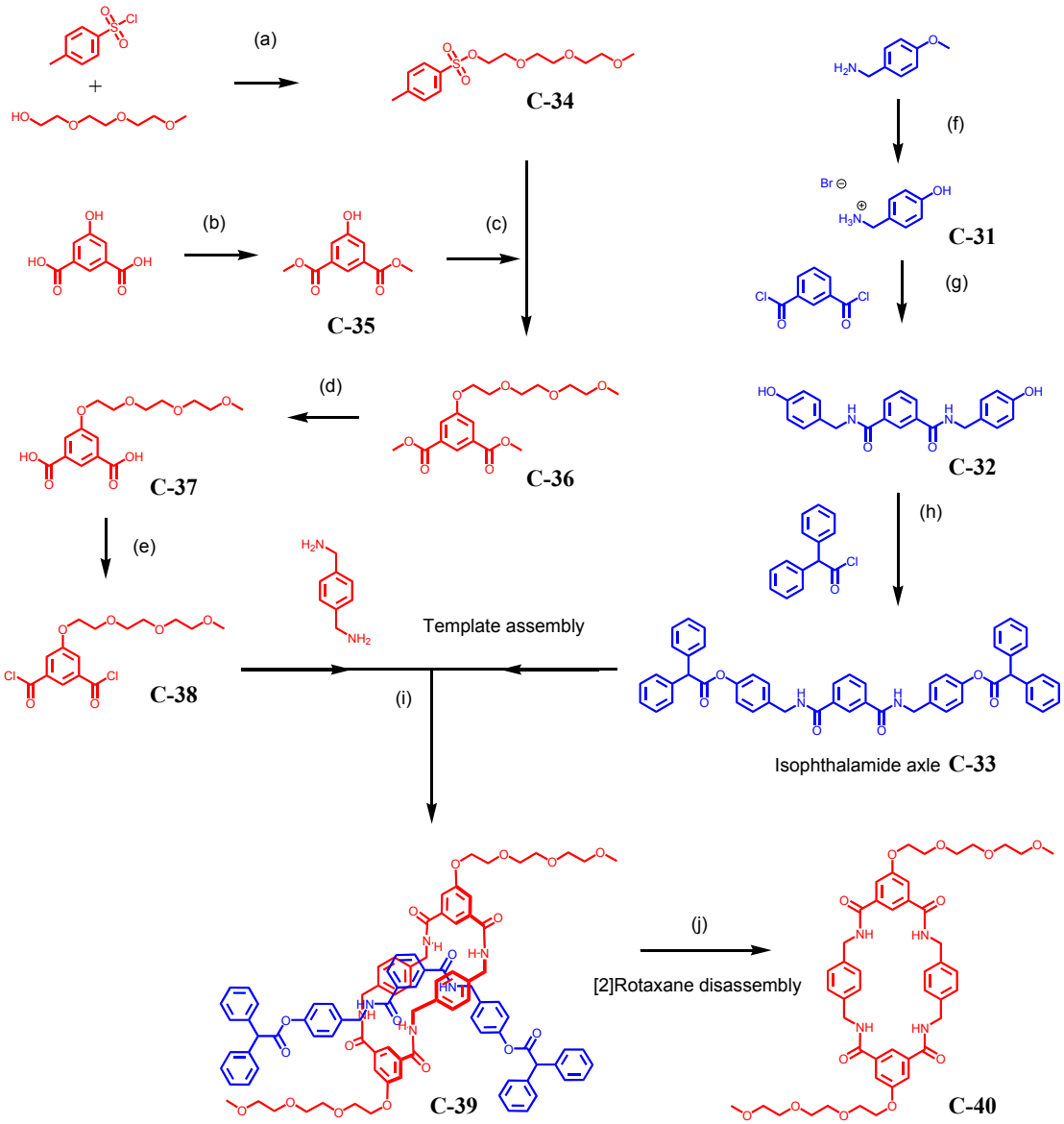

Figure 5.4 Synthesis of the tri-ethylene glycol BA macrocycle. **(a)** p-Toluenesulfonyl chloride and triethylene glycol monoethyl ether stirred in pyridine at 0°C for 4h. **(b)** 5-Hydroxyisophthalic acid and conc H_2SO_4 (catalytic) was refluxed in MeOH for 17h. **(c)** Products from (a) and (b) were refluxed MeCN for 15h. **(d)** Aqueous NaOH added to solution of reactant in ethanol then refluxed for 14h. **(e)** Oxalyl chloride added to solution of reactant in dry THF with catalytic DMF then stirred under nitrogen for 3h at r.t. **(f)** 4-Methoxybenzylamine slowly added to a stirring solution of 48% HBr the refluxed at 130°C for 18h. **(g)** Product from (f) and tri-ethylamine was refluxed in dry THF for 30min then cooled to r.t. Isophthaloyl dichloride pre-dissolved in dry THF was added to this stirring reaction and then left for 2 days. **(h)** Diphenyl chloride pre-dissolved in DCM was slowly added dropwise to a stirring suspension of (g) and tri-ethylamine in DCM then left for 4h.
(i) Template assembly: p-Xylenediamine and the product from (e) were pre-dissolved separately in dry $CHCl_3$ and simultaneously added dropwise to the product from (h) and tri-ethylamine dissolved in dry $CHCl_3$.
(j) Rotaxane disassembly: Sodium methoxide pre-dissolved in MeOH was added to a stirring solution of the rotaxane template in THF at r.t then left stirring for a further 4h.

5.3 NMR spectroscopy.

Figure 5.5 show a partial ^{1}H NMR's for the macrocycle **C-40** the flavin-fumaramide axle **C-43** and the pseudorotaxane (**C-43** plus 1 equivalent of **C-40**). The latter two spectra were recorded in a deuterated solvent mixture $CHCl_3$/DMF-d7 at a ratio 95:5 due to the poor solubility properties of **C-43** in non-polar solvents. The proton peaks are labelled according to the letter scheme shown in Figure 5.6 and have been assigned with the aid of COSY NMR recorded in deuterated solvent DMSO-d6. Unfortunately we were unable to

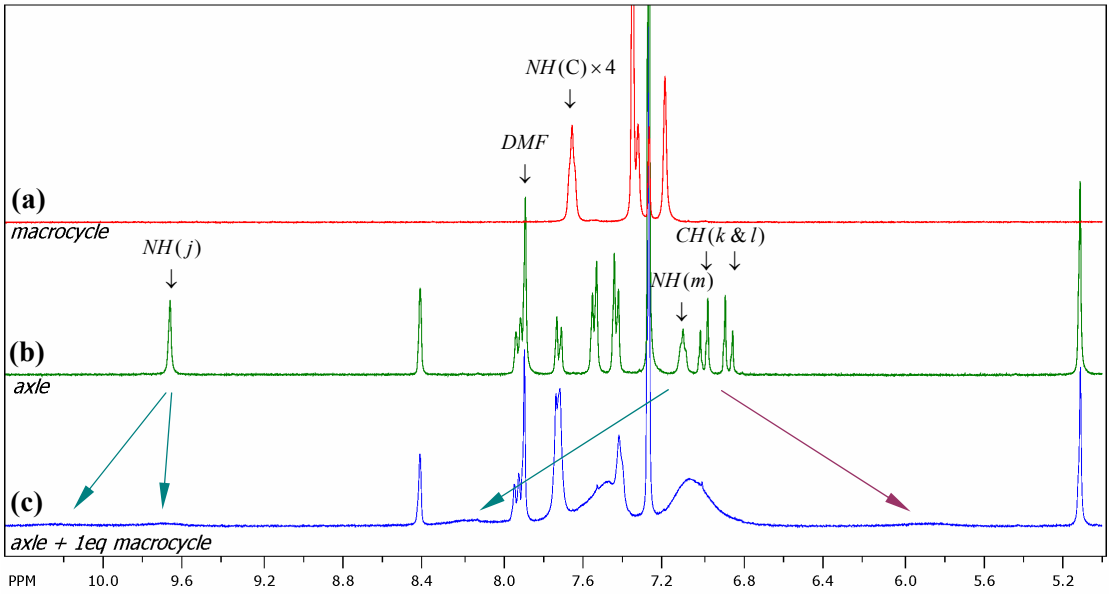

Figure 5.5 Stacked partial ^1HNMR spectra recorded in $CDCl_3$ / $DMF-d7$ (ratio 95:5) for: (a) the macrocycle **C-31**, (b) the axle **C-41** and (c) pseudorotaxane indicating a suggested concomitant amide NH downfield shift and alkene CH upfield shift. This difference would be induced by the hydrogen-bonding interactions between the macrocycle and fumaramide component of the axle.

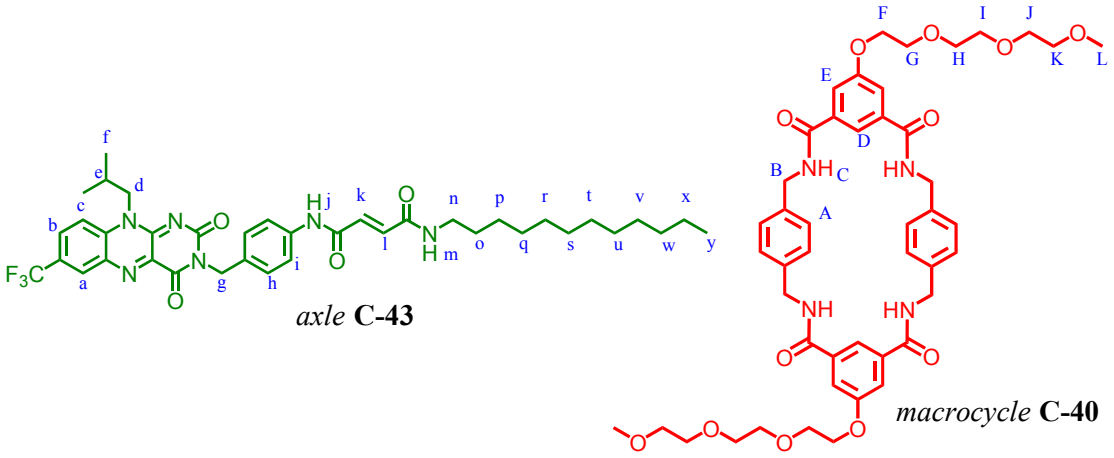

Figure 5.6 Proton peak identification scheme for Figure 5.5 uses small case letters from $a \rightarrow y$ for the axle **C-43** and capital case letters from $A \rightarrow L$ for macrocycle **C-40**.

carry out this same procedure using the above solvent mixture described above since axle **C-43** would precipitate after approximately 10-15 min at room temperature, which is too short a period to record a COSY NMR. Nevertheless, despite high concentration of polar solvent the effect of hydrogen bonding interaction is still evident, with a clearly visible change in both **C-43** amide $NH(j)$ and alkene protons k & l. However, until we can overcome this solubility problem, it is only possible to make an educated guess on the pseudorotaxane proton peak assignment. We will show in Chapter 6: (Flavin-fumaramide [2]rotaxane), Figure 6.3, that the corresponding amide protons for [2]rotaxane **C-52** has shifted downfield to approximately $\delta = 10.2$ ppm and $\delta = 8.4$ ppm. The corresponding two alkene protons have shifted upfield to approximately $\delta = 5.9$ ppm. This would seem therefore to be in good agreement with broad peaks (or bulge) found located at $\delta = 10.2$ ppm, $\delta = 8.2$ ppm and $\delta = 5.9$ ppm in Figure 5.5 as indicated by the large arrows. Interestingly the amide proton peak for $NH(j)$ would seem to exist at two locations $\delta = 10.2$ and 9.7 ppm which may perhaps be explained, along with the broad peak formation, by the transient state produced by having an open end to this molecular interlocked system.

5.4 Electrochemistry.

The dodecyl alkyl chain component of the flavin-fumaramide axle had been introduced to improve the solubility in non-polar solvents. Previous attempts at synthesising other similar open ended axles involved using either a shorter tri-ethylene glycol or a hexyl end chain. These ultimately proved to be too short and the resulting flavin axles were found to be sparingly soluble in non-polar solvents such as chloroform and DCM. As a result it was impossible to verify hydrogen bonding interactions were taking place between the axle and macrocycle using commonly applied techniques such as proton NMR or electrochemistry. The dodecyl alkyl chain was thus employed as a compromise to circumvent an inevitable precondition, too long and the axle might be unable to thread through the macrocycle, too short and the axle would be insoluble. Unfortunately, this longer alkyl chain was still unable to provide sufficient solubility in many organic solvents including even THF and MeCN. To overcome this solubility predicament the axle was first dissolved in DMF (0.6mL) and then diluted with 10 equivalents (by volume) of a non-polar solvent such as DCM. This method allowed the axle to remain soluble sufficiently long enough for voltammetry experiments to be carried out.

The tri-ethylene glycol benzylic amide macrocycle also had solubility issues although not a severe as the axle. The macrocycle readily dissolved after adding a measured amount in solid form directly into the electrochemical cell containing 10% DMF. The effects of adding one and then two equivalents of macrocycle were observed. The final part of the voltammetry experiments explored the effect of increasing the polar solvent volume concentration from 10 to 20% by further addition of DMF (0.6mL) to the cell which also slightly improved the solubility of the mixture. Details of experimental procedures are found in Chapter 8.

5.4.1 Cyclic voltammetry for the axle in DCM / DMF (9:1).

Figure 5.7 shows the CV for flavin-fumaramide axle **C-43** in a DCM/DMF(9:1) solvent mixture. The voltammogram appear to show a single reduction and oxidation wave during the cathodic and anodic sweeps respectively. At a sweep rate $\upsilon = 0.1\text{Vs}^{-1}$, the system displayed reasonably good electrochemical reversibility with peak separation $\Delta E_p = 73\text{mV}$, cathodic and anodic currents $I_C \approx I_a$ and a half wave potential $E_{1/2} = -0.549\text{V}$. The voltammograms appears typical of the expect single electron transfer described by the scheme in Figure 5.8 where in the absence of a proton source a second electron transfer is unachievable. However confirming whether this is the case requires an examination of the SW voltammograms for axle **C-43**.

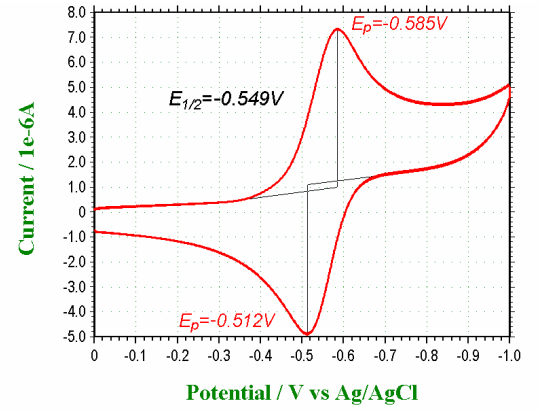

Figure 5.7 Cyclic voltammogram (CV) for the flavin-fumaramide axle **C-43** at sweep rate $\upsilon = 0.1\text{Vs}^{-1}$ in a DCM/DMF (9:1) solvent mixture.

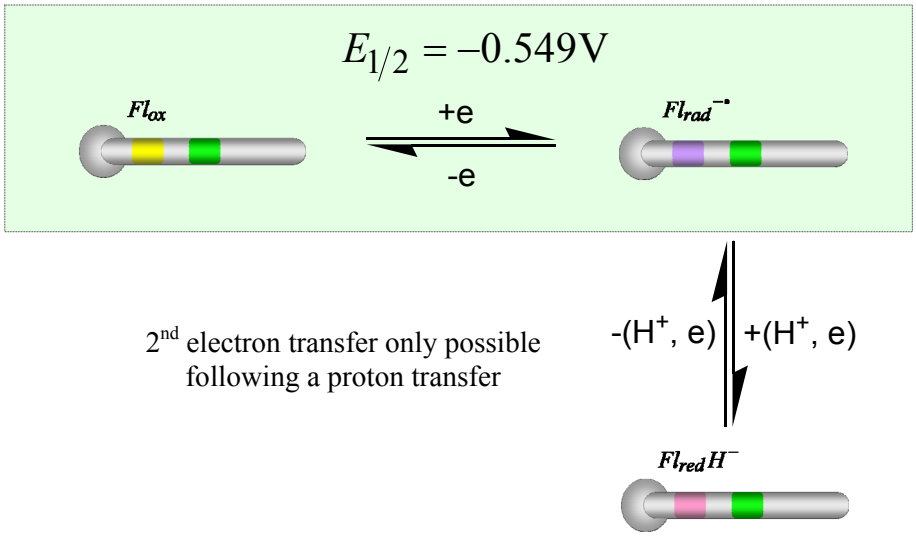

Figure 5.8 Proposed electrochemical scheme for the flavin-fumaramide axle. The ability of the flavin to accept a second electron is only possible once the flavin radical has adopted a more positive charge from a chemical reaction such as a proton (H^+) transfer.

5.4.2 Square Wave Voltammetry for the axle in DCM / DMF (9:1).

Figure 5.9 below shows the SW voltammograms for the flavin-fumaramide axle with the direction of scan is from 0 to −1V in a DCM/DMF(9:1) solvent mixture. For increased clarity, the overall net response (I_{Diff}) is shown Figure 5.9(a) and is depicted by the single peak. The plot shown in Figure 5.9(b) provides a closer analysis of the components that make up the net response $I_{Diff} = I_{for} - I_{rev}$. Here we observe a significantly larger maximum (I_{for}) accompanied by a smaller minimum (I_{rev}). The position of the I_{rev} minimum should also be more negative than the I_{for} maximum for reasons discussed in Appendix A: SWV. Figure 5.9(b) therefore suggests that within the extremely short SW pulse period, the redox process is displaying electrochemically irreversible characteristics. We can rationally explain this if some subsequent chemical reaction such as a proton transfer followed the first electron transfer, thereby altering the stability of the system and re-oxidation electrochemically irreversible. This process is perhaps better understood through close examination of the SW pulse "snapshots" shown in overleaf in Figure 5.10. It may also be helpful before beginning to remind the reader that the response produced (either forward or reverse) is the result of current flowing to restore the equilibrium at the electrode potential. This is why we observe either a maximum or minimum at around the relevant formal potentials of any involved redox couples.

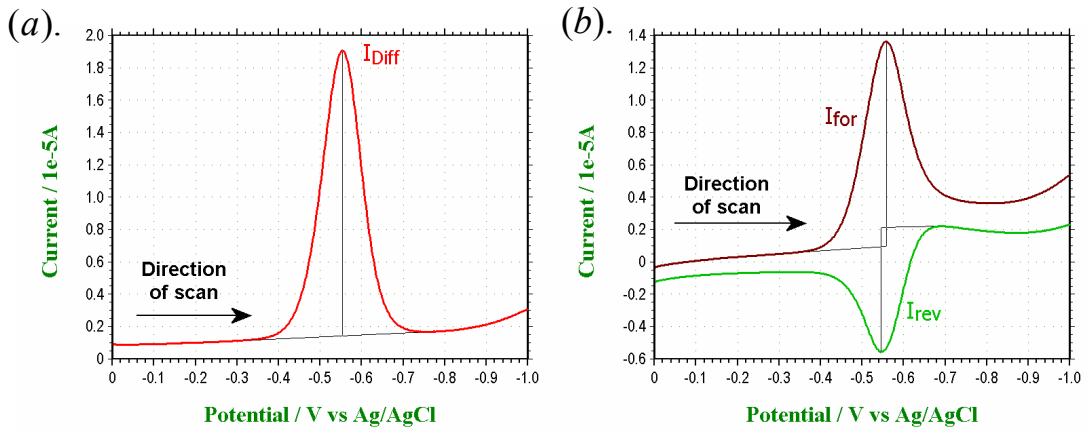

Figure 5.9 Square Wave voltammogram (SWV) for the flavin-fumaramide axle **C-43** with direction of scan from 0 to −1V (a) the overall response (I_{Diff}) and (b) the forward (I_{for}) and reverse (I_{rev}) responses. Other SW parameters $E_{SW} = 0.025\text{V}$, $E_{step} = 0.002\text{V}$ and $SW_{freq} = 25\text{Hz}$.

The scheme in Figure 5.10 shows the SW pulse at the period during the scan when the step potential is centred on E_1^{θ} (the formal potential of the 1st electron transfer). During the forward pulse, the electrode becomes more negative than E_1^{θ} , thereby promoting electron transfer in the reduction reaction $Fl_{ox} \xrightarrow{e^-} Fl_{rad}^{\bullet -}$ (Note that I have used the "greater than" symbol ">" to signify "more negative"). Since E_1^{θ} is more negative than E_2^{θ} (the forward potential of the 2nd electron transfer) it follows that the reaction $Fl_{rad}^{\bullet -} \xrightarrow{(H^+ + e^-)} Fl_{red}H^-$ is also able to occur subject to proton availability. As a consequence a current will begin to flow in an attempt to re-establish the electrochemical equilibrium.

During the reverse SW pulse when the potential is more positive than the formal potential E_1^θ but more negative than E_2^θ then only the single electron re-oxidation $Fl_{ox} \xleftarrow{-e^-} Fl_{rad}^{\bullet -}$ will be able to occur. If we assume for a moment that a fraction of the 1st electron transfer product ($Fl_{rad}^{\bullet -}$) which was generated during the forward SW pulse has now been chemically altered by a slower proton transfer then only a the remaining fraction will be available for re-oxidation and we would observe a much weaker reverse current (I_{rev}) response in comparison to the 2 electron forward current (I_{for}) response. The difference in magnitude would depend on proton availability and transfer rate, but we would expect this to be a rate determining step. Overall therefore we would expect this to be the case given the comparative magnitude of the forward and reverse responses. Furthermore the position of E_1^θ and E_2^θ must be very close given that small magnitude of the SW pulse amplitude $E_{SW} = 25\text{mV}$ there was no evidence of peak separation.

It will be also noticed from Figure 5.9 (b) that the magnitude of I_{rev} becomes slightly positive much further along the direction of scan. This can be explained by the reduction of any remaining $Fl_{rad}^{\bullet -}$ species to $Fl_{red}H^-$ (axle) as the potential of the reverse SW pulse eventually becomes more negative than E_2^θ. Finally as the SW pulse centres on a much higher negative potential than that shown in Figure 5.10 then both the variation in potential produced during the forward and reverse pulses have very little effect on the electrochemical equilibrium. Consequently, the current flow from both responses varies very little.

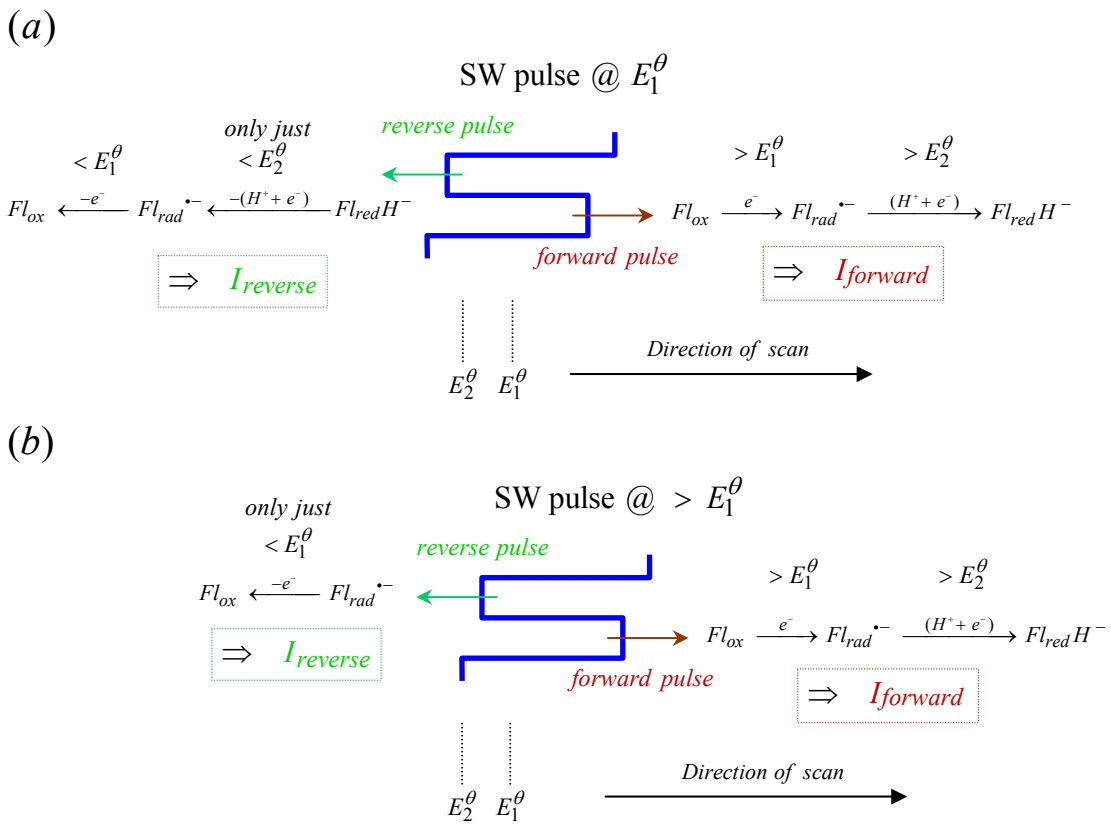

Figure 5.10 A snapshot of the SW pulse as it centres on the formal potential E_1^θ of the first electron transfer. The formal potential of the second electron transfer is depicted as E_2^θ and occurs more positive potential that E_1^θ. Note that here I am depicting more negative by the symbol (>) and more positive (less negative) by the symbol (<).

Occasionally a reversal of SW scan direction can provide further information regarding the electrochemical mechanism and as we shall see when we examine the SW response for the pseudorotaxane it will allow us to detect the presence of a second redox species. The reasoning behind this method (in this case) is that by maintaining the electrode at a high negative potential allows the accumulation of reduced species at the surface. However, with regards to the axle, only a single peak is observed when the direction of scan is from -1 to 0V as shown by the overall response (I_{Diff}) in Figure 5.11(a). We can nevertheless still extract some information regarding the mechanisms using the forward (I_{for}) and reverse (I_{rev}) components of the SW response as shown in Figure 5.11(b). To do this it will help to examine the "snapshot" of the SW pulse shown in the scheme of Figure 5.12. This method is worth discussing here for comparison purposed later.

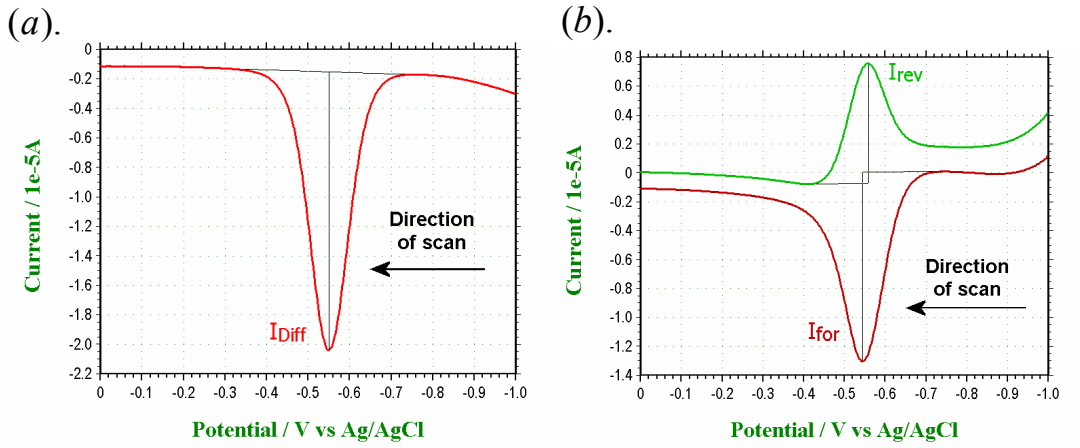

Figure 5.11 Square Wave voltammogram (SWV) for the flavin-fumaramide axle **C-43** with direction of scan from -1 to 0V (a) the overall response (I_{Diff}) and (b) the forward (I_{for}) and reverse (I_{rev}) responses. Other SW parameters $E_{\text{SW}} = 0.025\text{V}$, $E_{\text{step}} = 0.002\text{V}$, $SW_{freq} = 25\text{Hz}$ and accumulation period $E_{accum} = 10\,\text{sec}$.

The scheme shown in Figure 5.12(a) is a snapshot the SW pulse as it centres on the formal potential E_1^{θ}. As stated earlier, during the period prior to this snapshot there would have been an accumulation of reduced species $Fl_{red}H^-$ at the electrode surface from the reaction $Flox \xrightarrow{e^-} Fl_{rad}^{\bullet -} \xrightarrow{(H^+ + e^-)} Fl_{red}H^-$. The electrode would have attained a steady state equilibrium which would alter very little during the forward and reverse SW pulses both of which remained at potentials more negative than E_1^{θ}. We only begin to observe a significant increase in reverse current response ($Irev$) when the forward SW pulse becomes less negative than E_1^{θ} as depicted in Figure 5.12(a) and as a result the above reduction reaction momentarily comes to a halt. It is this brief pause and re-starting during a subsequent reverse SW pulse that generates the Faradaic process which respond to rapidly return the electrode to equilibrium. It is therefore at approximately this potential that we observe a maximum in the reverse current response ($Irev$).

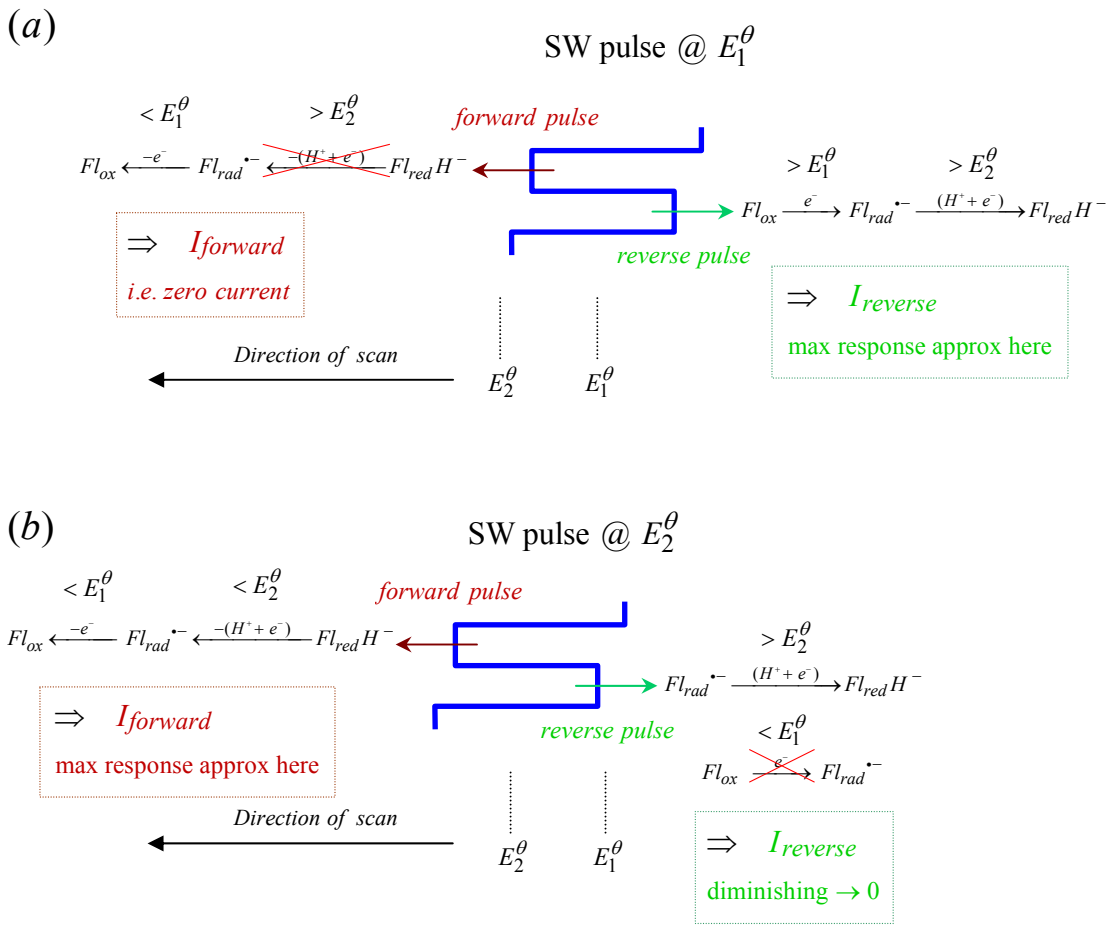

Figure 5.12 A snapshot of the SW pulse as it centres on (a) the formal potential E_1^θ of the first electron transfer and (b) the formal potential E_2^θ of the second electron transfer. The direction of scan is as shown from -1 to 0V. Note: a more negative potential is represented by the symbol ($>$) and a more positive potential by the symbol ($<$).

Re-oxidation of the accumulated flavin anion $Fl_{red}H^-$ is only achievable at potentials less negative than E_2^θ as depicted in the snapshot scheme shown in Figure 5.12(b). During the forward SW pulse the electrode potential becomes less negative than E_2^θ and a current begins to flow as electrons are removed from the system in order to restore equilibrium at that potential. However during the reverse SW pulse the electrode becomes more negative than E_2^θ but less negative than E_1^θ. As a result the SW pulse is only able to reduce any accumulated flavin radical anion $Fl_{rad}^{\bullet -}$ and eventually the reverse current response (I_{rev}) begins to diminish. The forward SW response (I_{for}) reaches a minimum (i.e. a maximum negative response) at approximately this potential as it responds to the abrupt changes in equilibrium. Ultimately as both forward and reverse SW pulses become less negative than E_2^θ the electrode steady state equilibrium slowly becomes restored.

We can therefore summarize what has been observed during the axle SWV response by the following two irreversible reactions. When the direction of scan is from $0 \rightarrow -1\text{V}$ the reverse response becomes reduced due to the irreversible electrochemical reaction shown in Equation 5.1 to the extent that the position of its minimum appears before the accompanied forward response maximum in the direction of scan. When the direction of scan is from $-1 \rightarrow 0\text{V}$ the reverse response becomes reduced due to the irreversible electrochemical reaction shown in Equation 5.2. The position of the reverse response maximum again leads the forward response minimum in the direction of the scan. As a result the peaks of the overall response cannot be accurately relied upon to provide a value for either the E_1^{θ} or E_2^{θ} formal potentials. However we can see from Table 5.1 that these values are on close agreement with the value of the half wave potential $E_{1/2}$ from the CV of the axle obtained earlier in Figure 5.7.

$$Fl_{ox} \underset{-e^-}{\overset{e^-}{\rightleftharpoons}} Fl_{rad}^{\bullet -} \xrightarrow{(H^+ + e^-)} Fl_{red}H^- \qquad \text{(Eqn 5.1)}$$

(irreversible at approx E_1^{θ})

$$Fl_{red}H^- \underset{(H^+ + e^-)}{\overset{-(H^+ + e^-)}{\rightleftharpoons}} Fl_{rad}^{\bullet -} \xrightarrow{-e^-} Fl_{ox} \qquad \text{(Eqn 5.2)}$$

(irreversible at approx E_2^{θ})

Direction of scan	Flavin-fumaramide axle			
	SW Results (Volts)			CV Results (Volts)
	$E_p(I_{Diff})$	$E_p(I_{for})$	$E_p(I_{rev})$	Formal potential E^{θ}
0 to −1V	-0.554	-0.558	-0.546	-0.549
−1 to 0V	-0.550	-0.544	-0.558	

Table 5.1 Comparison of the obtained CV formal potential E^{θ} with the SWV results for flavin-fumaramide axle **C-43**. Peak positions for I_{Diff} response during direction of scan from 0 to −1V (−0.554V) and −1 to 0V (−0.550V) are in close agreement with the CV formal potential $E^{\theta} = -0.549\text{V}$.

5.4.3 Cyclic voltammetry for the pseudorotaxane in DCM / DMF (9:1).

As described earlier in Section 5.4.1 the voltammograms for the pseudorotaxane were obtained by adding the macrocycle in solid form directly to cell containing a solution of the axle and dissolving fully. The comparison of the CV for the axle and the pseudorotaxane shown in Figure 5.13 shows a slight decrease in the cathodic (reductive) peak (*wave I*) followed by an extremely diminished 1st oxidation peak (*wave II*) accompanied by the emergence of a 2nd oxidation peak (*wave III*). The decrease in peak height may be explained using the Randles-Sevcik equation[61, 62] which describes a square-root relationship between peak current and the slower diffusion of a now much larger molecule. Depletion of the oxidized species close to the electrode surface would be achieved much earlier. The larger pseudorotaxane molecules would take longer to diffuse to and replenish the electrode with reducible species. As a result the cathodic peak is observed slightly earlier during the sweep to give the apparent anodic shift.

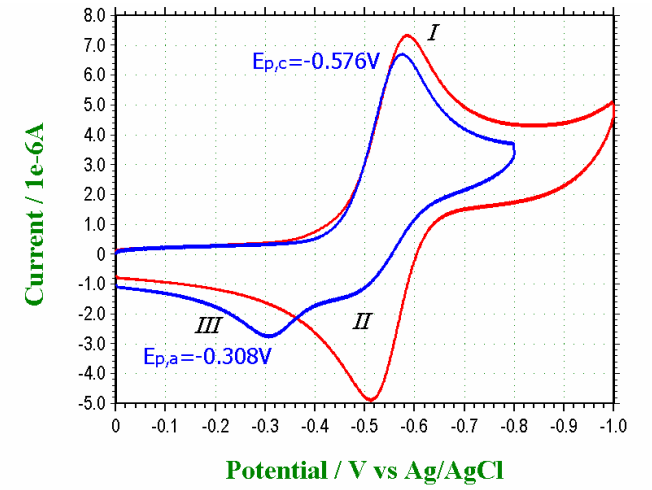

Figure 5.13 Cyclic voltammogram (CV) recorded for the flavin-fumaramide axle **C-43** after dissolving of 1 equivalent of tri-ethylene glycol BA macrocycle **C-40** (*blue line*) at a sweep rate $\upsilon = 0.1$ Vs^{-1}. The CV for axle **C-43** (*red line*) is also shown for comparison.

The formation of the new anodic peak (*wave III*) at $E_{p,a} = -0.308\text{V}$ corresponds to the oxidation of the pseudorotaxane co-conformation $Fl_{ox} - [fum] \xrightarrow{e^-} Fl_{rad} - [fum]$ and a subsequent translocation of the macrocycle to form $[Fl_{rad}] - fum$, where fum =fumaramide. As expected the re-oxidation of this new co-conformer would take place at more positive potential due to the stabilization effect inferred by the H-bonding interaction between the flavin radical anion and the macrocycle. This provided the first confirmation that pseudorotaxane formation was able to occur in a non-polar/polar solvent mixture. However, it should also be understood that the voltammograms produced are undoubtedly produced in the presence of both axle and pseudorotaxane at an equilibrium ratio yet to be determined. Therefore before beginning the analysis of the SW voltammetry, it may be useful to have a picture representation of the possible redox species involved. Figure 5.14 therefore combined the electrochemically quasireversible two electron transfer scheme (*green box*) for the axle previously shown in Figure 5.8 in equilibrium with the electrochemically irreversible one electron transfer (*blue box*) and possible 2nd electron transfer of the pseudorotaxane.

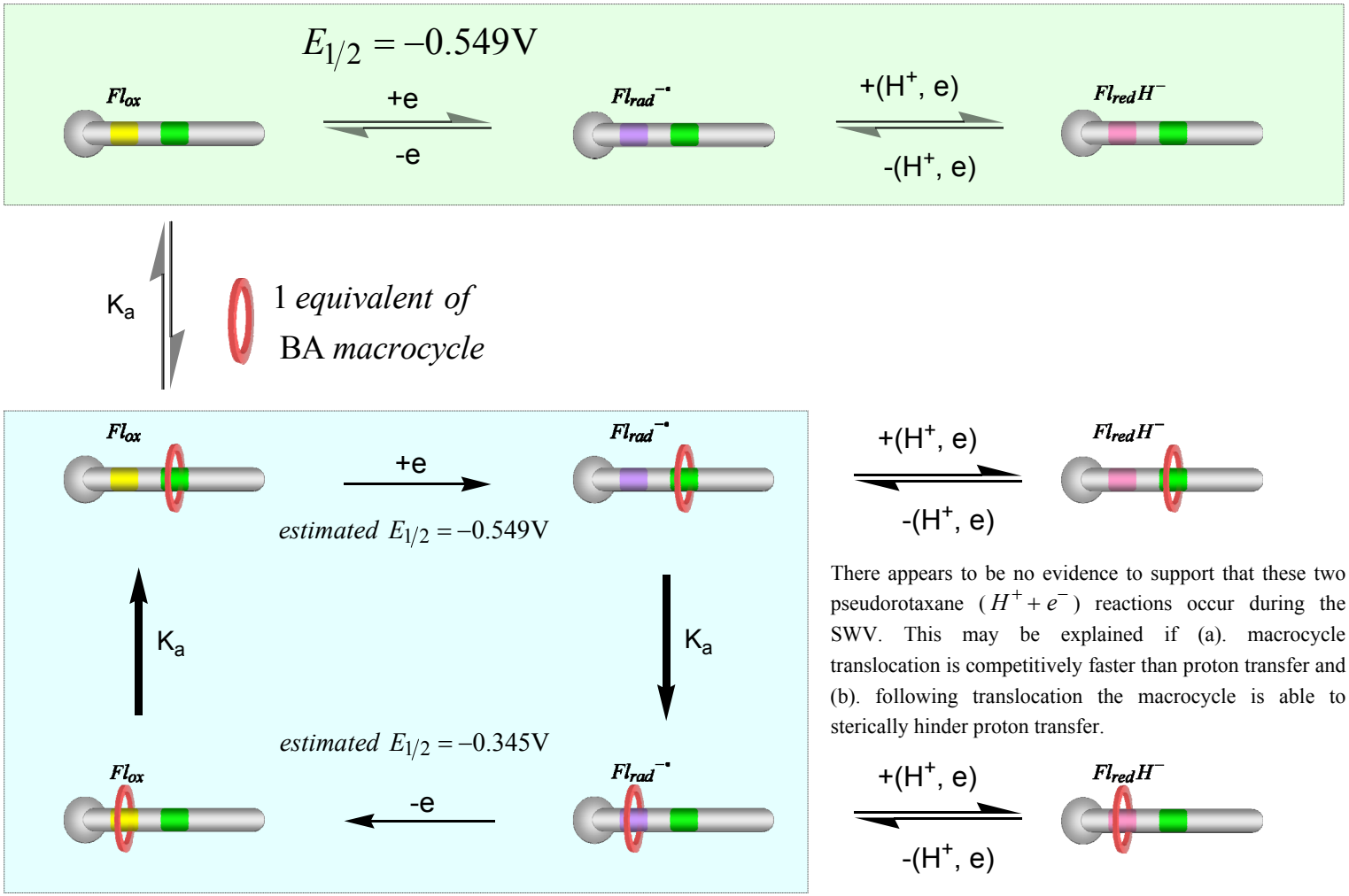

Figure 5.14 Proposed electrochemical scheme for the flavin-fumaramide axle with 1 equivalent of macrocycle. Transfer of a second electron is only possible once the flavin radical has adopted a more positive charge from a chemical reaction such as a proton (H^{+}) transfer from either another flavin or some other source.

5.4.4 Square Wave voltammetry for the pseudorotaxane in DCM.

The SWV overall response (I_{Diff}) for the pseudorotaxane is shown in Figure 5.15(a) and depicts a single peak when the direction of the scan is from $-1 \rightarrow 0$V ($vs\ Ag/AgCl$). The components of the overall response I_{for} and I_{rev} shown separately in Figure 5.15(b) depict a large forward response and a virtually non-existent minimum for the reverse response. To understand why this happens we need to examine the scheme shown in Figure 5.16 which shows a snapshot of the SW pulse as it centres on the formal potential of the flavins 1st electron transfer.

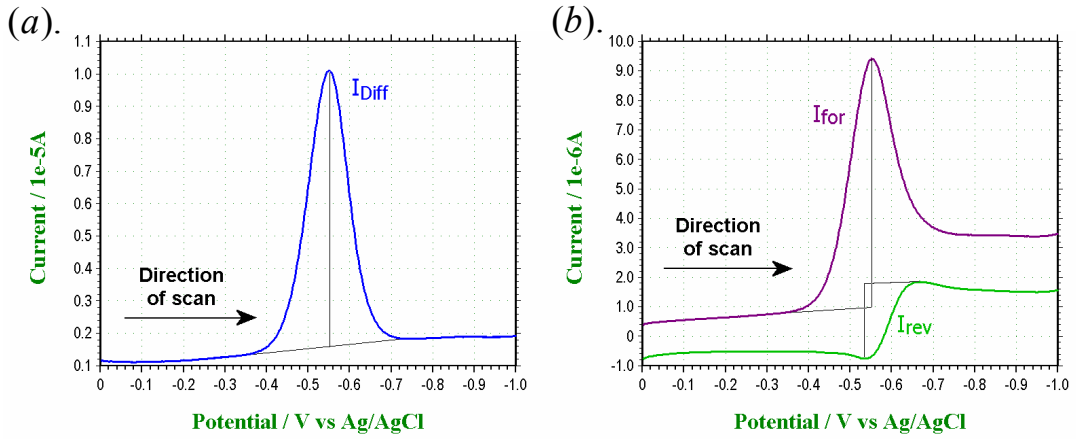

Figure 5.15 Square Wave voltammogram for the flavin-fumaramide axle **C-43** plus 1eq macrocycle **C-40**, with direction of scan from 0 to -1 V (a) the overall response (I_{Diff}) and (b) the forward (I_{for}) and reverse (I_{rev}) responses. Other SW parameters $E_{SW} = 0.025$V, $E_{step} = 0.002$V and $SW_{freq} = 25$Hz.

During the forward SW pulse shown in Figure 5.16 the electrode potential becomes more negative than the formal potential E_1^{θ}. At this potential the flavin oxide Fl_{ox} component of both axle and pseudorotaxane become reduced to the flavin radical anion $Fl_{rad}^{\bullet -}$. The axle as we've just discussed would become reduced further following a proton transfer, presumably from a second flavin molecule. With regards to the pseudorotaxane, two things can happen. The BA macrocycle can translocate from the fumaramide component of the axle to the electron rich $Fl_{rad}^{\bullet -}$ thus forming the more stable $[Fl_{rad}^{\bullet -}]$ co-conformer. Alternatively, as the electrode potential is more negative than E_2^{θ}, the flavin oxide may undergo a proton and 2nd electron transfer. These reaction pathways are most likely competitive and subject to proton availability. Macrocycle translocation rate has been reported by Leigh as being extremely fast ($1 \times 10^4\ \text{sec}^{-1}$)[49, 50], subsequently although proton transfer may still be achievable following translocation, it seems very likely that this process would be sterically hindered by the macrocycle, particularly if the only proton source is a second Fl_{ox} pseudorotaxane molecule. Either translocation or proton transfer would form electrochemically irreversible products and therefore explains the non-existent reverse current I_{rev} response. During the reverse SW pulse depicted in Figure 5.16, the overpotential available for the reoxidation of any $Fl_{red}H^{-}$ or $Fl_{rad}^{\bullet -}$ species (axle only) would be small and consequently reoxidation would be slow. The main reason however for the non-existent I_{rev} response minimum is via the formation of the stable $[Fl_{rad}^{\bullet -}]$ pseudorotaxane which can only be re-oxidized at the much more positive formal potential E_3^{θ}.

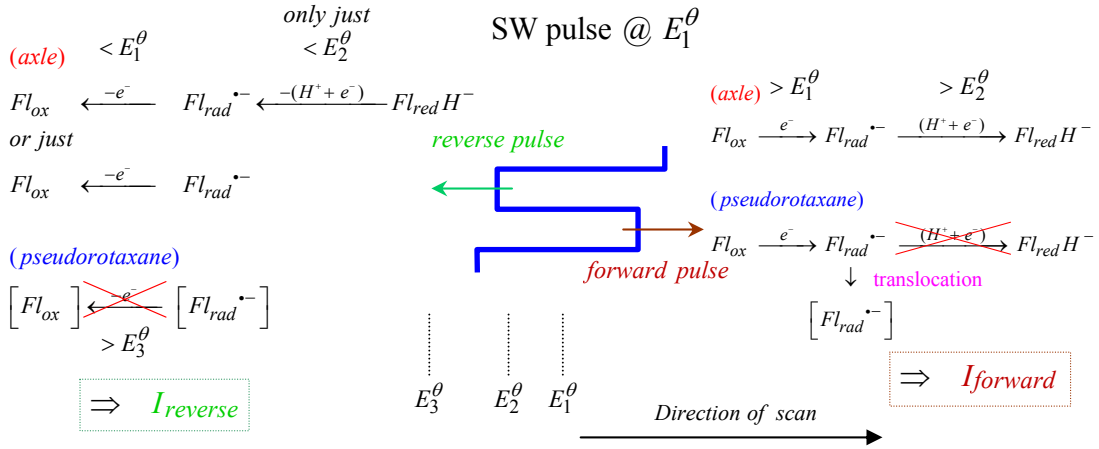

Figure 5.16 A snapshot of the SW pulse as it centres on the formal potential E_1^θ of the first electron transfer. The direction of scan is as shown from 0 to -1V. Note: a more negative potential is represented by the symbol (>) and a more positive potential by the symbol (<).

The SWV starts to get more interesting and a bit more complicated once the direction of scan is reversed from -1 to 0V (*vs* $Ag/AgCl$). Now we observe a second redox peak at approximately -0.32V as shown in the overall SW response (I_{Diff}) shown in Figure 5.17(a). This would correspond to the oxidation reaction $[Flrad^{\bullet -}] \xrightarrow{-e^-} [Flox]$ and appears in the region of the cyclic voltammogram half wave potential $E_{1/2}$ for the 2nd oxidation peak (*wave III*) previously observed in Figure 5.13. To understand the EC sequence of events that produce the SW responses I_{for} and I_{rev} shown in Figure 5.17(b) we will need to examine the three snapshots of the SW pulse shown in Figure 5.18. First (a) as it centres on E_1^θ, (b) as it centres on E_2^θ and finally (c) as it centres on E_3^θ.

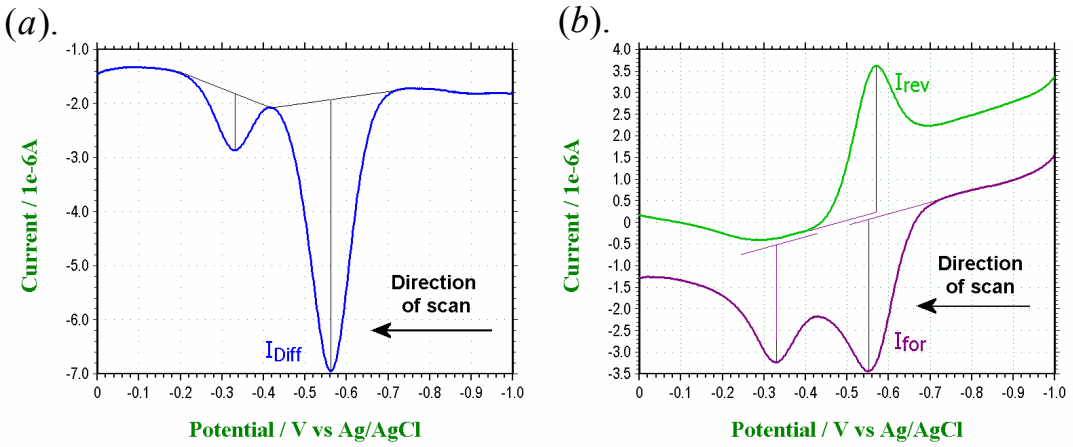

Figure 5.17 Square Wave voltammogram (SWV) for the flavin-fumaramide axle **C-43** plus 1eq macrocycle **C-40**, in direction of scan from -1 to 0 V. (a) the overall response (I_{Diff}) and (b) the forward (I_{for}) and reverse (I_{rev}) responses. Other SW parameters $E_{SW} = 0.025$V, $E_{step} = 0.002$V , $SW_{freq} = 25$Hz and accumulation period $E_{accum} = 10$sec.

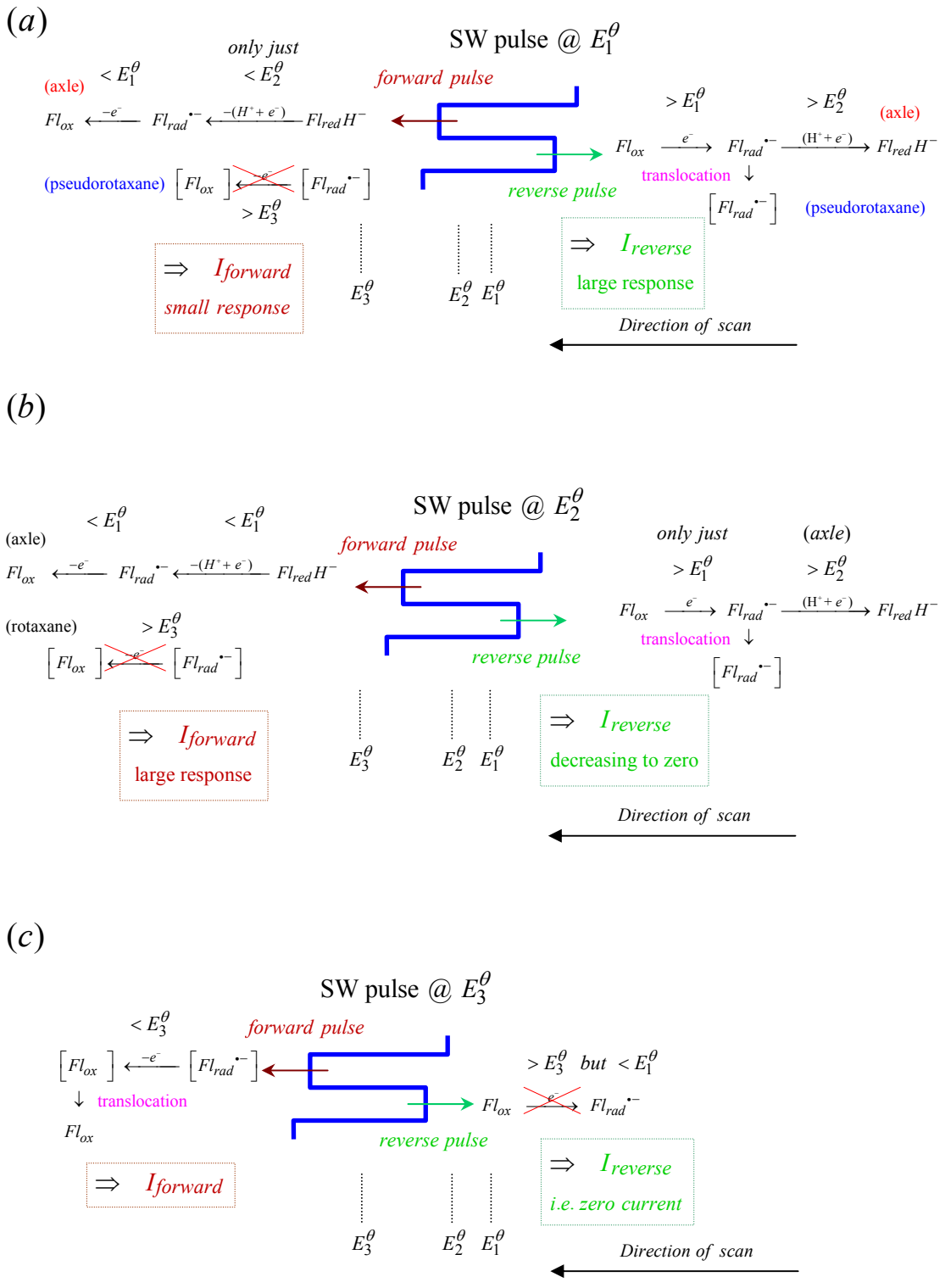

Figure 5.18 A snapshot of the SW pulse as it centres on (a) the formal potential E_1^θ of the axle first electron transfer (b) the formal potential E_2^θ of the axle 2nd electron transfer (c) the formal potential E_3^θ of the pseudorotaxane $[Flrad^{\bullet -}]$ electron transfer. The direction of scan is as shown from -1 to 0V . Note: a more negative potential is represented by the symbol ($>$) and a more positive potential by the symbol ($<$).

Prior to the snapshot shown in Figure 5.18(a), the electrode potential had been held at a potential more negative than E_1^θ for a pre-set period of 10 seconds. This prolonged period at a large negative potential allowed the accumulation of reduced products $Fl_{ox} \xrightarrow{e^-} Fl_{rad}^{\bullet -} \xrightarrow{(H^+ + e^-)} Fl_{red}H^-$ (for the axle and possibly the pseudorotaxane) and $Fl_{ox} \xrightarrow{e^-} Fl_{rad}^{\bullet -} \xrightarrow{translocation} [Fl_{rad}^{\bullet -}]$ (pseudorotaxane). During the forward SW pulse shown in Figure 5.18(a), the potential is just beginning to become more positive than E_2^θ. This now makes the re-oxidation of $Fl_{red}H^-$ now possible and as a consequence a small current response begins to flow disturbing the previous equilibrium. During the reverse SW pulse the potential is $> E_1^\theta$ (and E_2^θ) and the reduction of $Fl_{ox} \xrightarrow{e^-} Fl_{rad}^{\bullet -} \xrightarrow{(H^+ + e^-)} Fl_{red}H^-$ is restarted. It is at approximately this potential that the reverse response I_{rev} reaches a maximum.

In Figure 5.18(b) the SW pulse has now centred on the formal potential E_2^θ. During the forward SW pulse the rate of re-oxidation of $Fl_{red}H^- \xrightarrow{-(H^+ + e^-)} Fl_{rad}^{\bullet -} \xrightarrow{-e^-} Fl_{ox}$ is starting to gain momentum as the accumulated $Fl_{red}H^-$ becomes consumed. The reverse SW pulse is now only just above E_1^θ so there is less of an overpotential drive to reduce the oxidized flavin and restore equilibrium. It will be at approximately this potential that the forward response will begin to reach a maximum. This sequence of events also explains why the I_{rev} achieves a maximum before the forward response minimum (see Figure 5.17(b)) as opposed to lagging in the direction of scan which as previously discussed would be the case for a reversible single electron transfer. It should also be pointed out that since the peak positions of I_{for} and I_{rev} are dependant on a number of unknowns including the difference $E_1^\theta - E_2^\theta$ they should not be used to accurately determine their position but instead be used as a close estimate.

Finally it is only as the SW pulse becomes centred on E_3^θ do we observe a current response from the re-oxidation of $[Fl_{rad}^{\bullet -}] \xrightarrow{-e^-} [Fl_{ox}]$ and subsequent translocation to Fl_{ox}. However during the reverse SW pulse this reoxidized product cannot be reduced back again as the potential is much more positive than both E_1^θ and E_2^θ. Consequently the reverse current response I_{rev} becomes zero and the forward current response I_{for} is generated by the electrode current trying to restore equilibrium by re-oxidizing the accumulated $[Fl_{rad}^{\bullet -}]$ species.

5.4.5 Addition of a second equivalent of BA macrocycle.

5.4.5.1 Cyclic Voltammetry @ 2 equivalents.

The voltammograms for the following experiments were produced by dissolving a 2nd equivalent of the macrocycle in solid form directly in the cell mixture used in the previous set of voltammetry experiments and then restoring the solvent level to allow for evaporation loss. A comparison of the CV's for 1 equivalent (*blue line*) and 2 equivalents (*pink line*) of BA macrocycle are shown in Figure 5.19. Here we see a further decrease in the height of the cathodic (reductive) peak (*wave I*) followed by a decrease in the 1st oxidation peak (*wave II*) and a modest increase in the 2nd oxidation peak (*wave III*). The differences in the two oxidation peak can be attributed to the increase in ratio of pseudorotaxane to axle brought about by the increased availability of macrocycle. The decrease in peak height may be attributed again to the Randles-Sevcik equation and the larger pseudorotaxane molecules taking longer to diffuse to and replenish the electrode with reducible species. The result observed is again an apparent anodic shift of the cathodic peak.

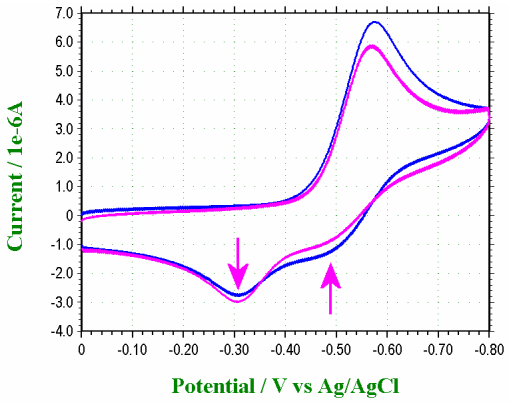

Figure 5.19 Cyclic voltammogram (CV) for flavin-fumaramide axle **C-43** with 2 equivalents of macrocycle **C-40** (*pink line*) at a sweep rate $\upsilon = 0.1 Vs^{-1}$. The CV for the axle with 1 equivalent of macrocycle (*blue line*) is also shown for comparison. The addition of the 2nd equivalent of macrocycle clearly shows an increase in pseudorotaxane formation by the downward arrow and a reduced presence of the free axle by the upwards arrow.

5.4.5.2 Square Wave Voltammetry @ 2 equivalents of C-40.

The SWV's for the pseudorotaxane are shown in Figure 5.20 with the direction of scan from 0 to −1V. A single peak is observed at −0.54V in the overall response current (I_{Diff}). Very little difference is observed in the forward and reverse responses I_{for} and I_{rev}. The I_{for} maximum has decreased approx 18% in magnitude from approx 8.5 → 7.0μA. This could be diffusion related or it could be the result of the reduced contribution from the axle which is capable of undergoing a 2 electron transfer. The I_{rev} minimum which we have attributed to the axle reaction $Fl_{ox} \xleftarrow{-e^-} Fl_{rad}^{\bullet -} \xleftarrow{-(H^+ + e^-)} Fl_{red}H^-$ as the SW pulse centres approximately on E_1^{θ} (see Figure 5.15) has now completely disappeared.

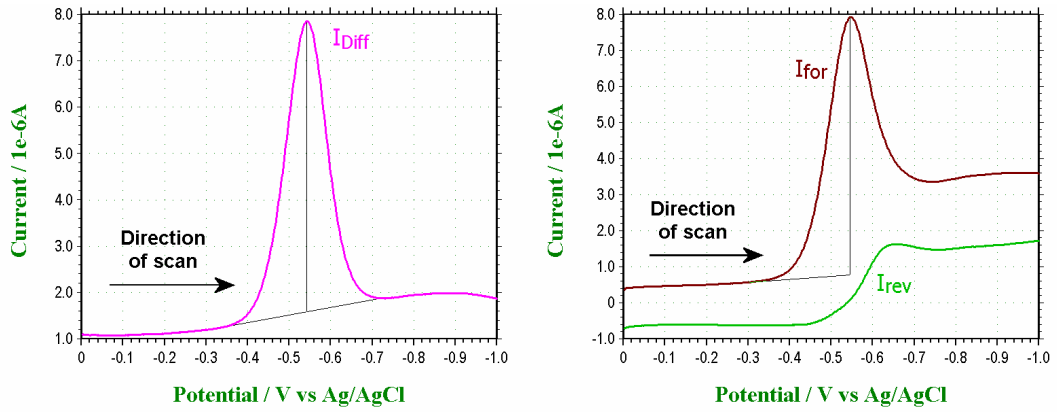

Figure 5.20 Square Wave voltammogram for the flavin-fumaramide axle **C-43** (with 2eq **C-40**) in direction of scan from 0 to −1 V showing: (a) the overall response (I_{Diff}) and (b) both the forward (I_{for}) and reverse (I_{rev}) responses. Other SW parameters $E_{SW} = 0.025$V, $E_{step} = 0.002$V and $SW_{freq} = 25$Hz.

The most relevant differences appear when the direction of scan is from −1 to 0 V as shown in Figure 5.21. From an initial comparison of the I_{Diff} response shown in Figure 5.21(a) with that of Figure 5.21(a) we could immediately conclude that the response at approx −0.55V has diminished while the peak at approx −0.32V and which corresponds to the macrocycle translocation, has increased at its expense. However a closer examination reveals that this 2nd peak has increased only marginally and the comparative difference in magnitudes is mainly due to the reduced contributions from the forward (I_{for}) and reverse (I_{rev}) current responses between −0.5 and −0.6V as shown in Figure 5.21(b).

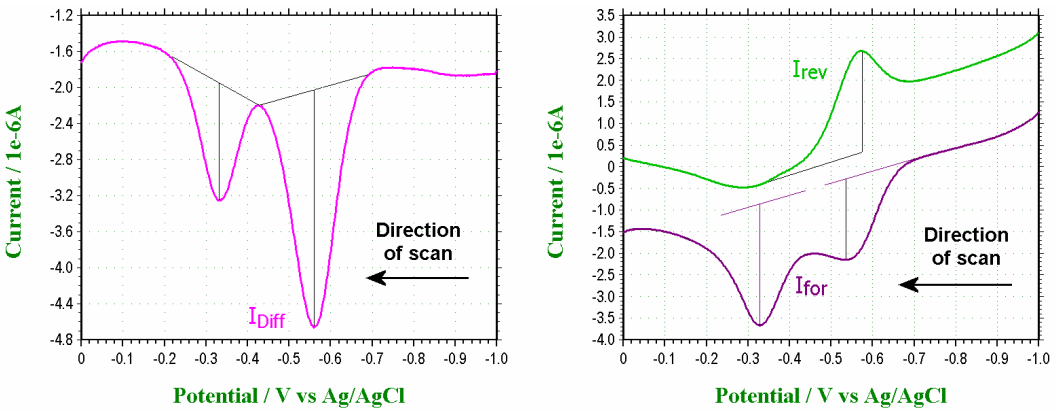

Figure 5.21 Square Wave voltammogram for the flavin-fumaramide axle **C-43** (with 2eq **C-40**) in direction of scan from −1 to 0 V showing: (a) the overall response (I_{Diff}) and (b) both the forward (I_{for}) and reverse (I_{rev}) responses. Other SW parameters $E_{SW} = 0.025$V, $E_{step} = 0.002$V, $SW_{freq} = 25$Hz and accumulation period $E_{accum} = 10$sec.

Here we observe an approximate 30% decrease in both the I_{for} and I_{rev} current response peaks (i.e. from 3.5μA in Figure 5.21(b) to less than 2.5μA in Figure 5.21(b)). However if we account for the 18% decrease in the response observed in Figure 5.20 then we could translate this into an approximate 20% increase for the I_{for} peak response at -0.32V and an approximate 10% decrease for both I_{for} and I_{rev} peak responses between -0.5 and -0.6V.

5.4.6 Effect of increased solvent polarity.

5.4.6.1 Cyclic Voltammetry.

Solvent polarity was increase by adjusting the ratio of DMF in the sample solution from 10% to 20% and then finally 30%, each time maintaining analyte concentration though the evaporation of the more volatile DCM solvent. The CV results are shown in Figure 5.22. At 20% DMF (*green line*) the cathodic peak (*wave I*) increases slightly in magnitude as the ratio of axle to pseudorotaxane is restored in favour of the smaller, faster diffusing axle molecule. The voltammogram also demonstrate a slight anodic shift relative to the original 10% DMF (*pink line*) CV. At 30% DMF (*orange line*) this anodic shift increases and the magnitude decreases slightly. This anodic shift can be attributed to the more positive flavin redox potential commonly observed when CV's are carried out in polar solvents, the decrease in peak magnitude may be explained by an increases solvent shell effect.

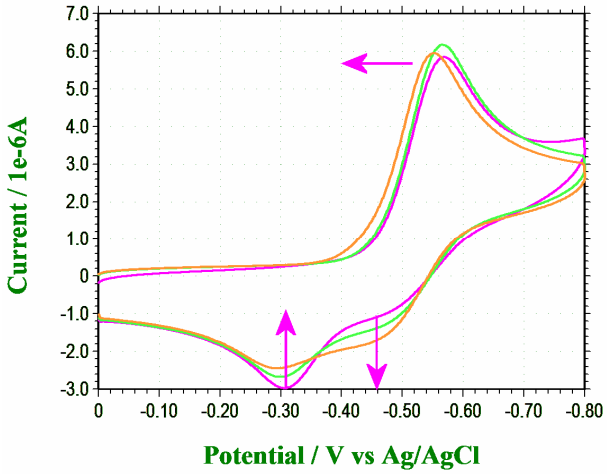

Figure 5.22 Cyclic voltammogram (CV) showing the effect of increasing solvent polarity on flavin-fumaramide axle **C-43** with 2 equivalents of macrocycle (*pink line*) in solvent mixture DCM/DMF(9:1) at a sweep rate $\upsilon = 0.1 Vs^{-1}$. CV's for pseudorotaxane in solvent mixtures DCM/DMF(8:2) (*green line*) and DCM/DMF(7:3) (*orange line*) indicate a gradual decrease in the pseudorotaxane formation by the upward arrow and an increase in free axle concentration by the upward arrow.

During the oxidation sweep of the CV we observe and increase in *wave II* and a corresponding decrease in *wave III* which also appears to demonstrate a slight anodic shift. As expected these features reconfirm the above proposal that the more polar solvent is inhibiting pseudorotaxane formation.

5.4.6.2 Square Wave Voltammetry.

Finally to further demonstrate the effect of increased polarity on pseudorotaxane formation, we need only discuss Figure 5.23 which shows the SW overall response (I_{Diff}) in the direction of scan from -1 to 0V. The voltammogram clearly shows the increase in magnitude of the peak between -0.5 and -0.6V and the corresponding decrease in magnitude of the peak between -0.3 and -0.4V. Both peaks also clearly demonstrate the anodic shift observed during the cyclic voltammetry and also reconfirms the adverse effect that polar solvent has on pseudorotaxane formation.

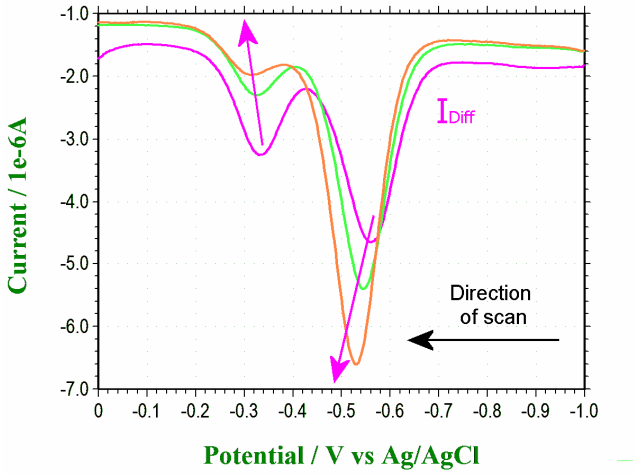

Figure 5.23 Square Wave voltammogram overall response (I_{Diff}) for the flavin-fumaramide axle **C-43** plus equivalents of **C-40** in direction of scan from -1 to 0V showing effect of increasing polar solvent ratio on from 10% DMF (*pink line*) to 20% DMF (*green line*) and finally to 30% DMF (*orange line*). Decrease in pseudorotaxane formation indicated by the upward angled arrow whereas the increase in free axle concentration of indicated by the downward angled arrow. Other SW parameters $E_{SW} = 0.025\text{V}$, $E_{step} = 0.002\text{V}$, $SW_{freq} = 25\text{Hz}$ and accumulation period $E_{accum} = 10\,\text{sec}$.

5.5 Photochemistry.

5.5.1 Absorbance spectra.

The absorbance spectra for the axle **C-43** at 1×10^{-5}M and at macrocycle **C-40** concentration equivalents of 1, 2 and 5 are shown in Figure 5.24. The spectrum for the axle shows the typical two main absorbance bands maxima (*band I* = 432nm and *band II* = 319nm). The spectra for the free BA macrocycle, was recorded at 10 times the concentration of the axle (i.e. 1×10^{-4}M) and is represented by the dashed black line. The spectrum clearly indicates an absorbance minimum at 270nm and a maximum at 295nm which has decreased to zero by approx 320nm. Using this spectrum as a comparison we can clearly observe the effect that addition of the macrocycle has to the absorbance spectra of the axle. Most noticeable is the dramatic increase of the peak at 265nm. The absorbance spectrum in Figure 5.25 shows this peak would correspond to the fumaramide component of the axle and it would seem to support previous evidence that some interaction must be taking place between the macrocycle and the fumaramide part of the axle. A less dramatic increase is observed in the flavins *band II* absorbance region at approx 320nm. Although partially masked by the absorbance band of the macrocycle we can clearly see that it increases in magnitude with the number of macrocycle equivalents added and also appears to be accompanied by a significant red-shift. Since the macrocycle absorbance band has already been shown to terminate by 320nm, we can conclude that this must be an interaction effect rather than a concentration effect. We have observed similar *band II* increases and red-shifts with other flavin [2]rotaxane systems described within this thesis. This characteristic behaviour was reported then to be due to the sensitivity of the flavin heterogeneous atoms to hydrogen bonding interactions in particular O(4) and N(5).

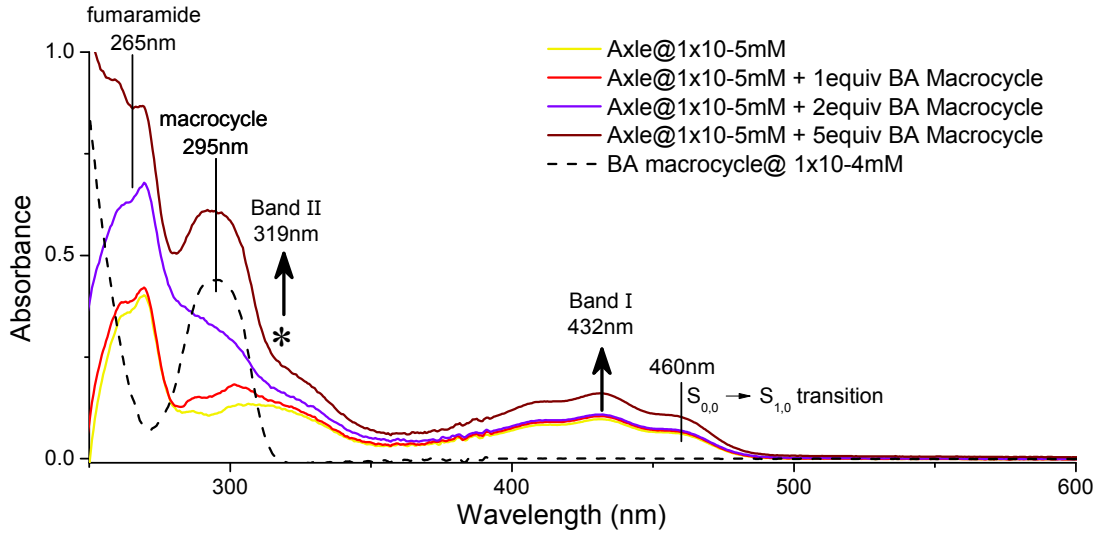

Figure 5.24 Absorbance spectra for axle **C-43** and macrocycle **C-40** in DCM/DMF(<1%).

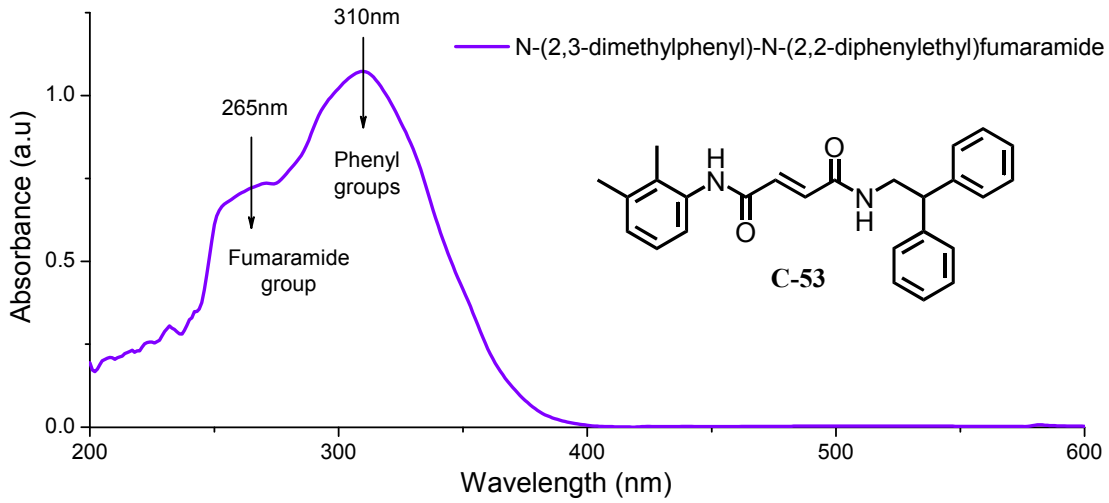

Figure 5.25 Absorbance spectra for N-(2,3-dimethyl)-N-(2,2-diphenylethyl)fumaramide (**C-53**) at 1×10^{-4}M in solvent mixture DCM/DMF(99:1). This spectra was used to determine the absorbance maxima for the fumaramide component of the pseudorotaxane.

5.5.2 Fluorescence spectra.

The fluorescence emission for axle **C-43** and pseudorotaxane (1, 2 and 5 equivalents of macrocycle **C-40**) in DCM are shown in Figure 5.26. The *band I* absorbance $\lambda_{max} = 432\text{nm}$ was used as the excitation wavelength. Despite using samples with an absorbance of approx $A = 0.1$, an order of magnitude more concentrated that normal, it is clearly obvious from the weak emission that at the start the fluorescence is heavily quenched. Overall however there is very little difference between the emission responses at this excitation wavelength. In general there appears to be a small decrease in response as the macrocycle equivalent is increase.

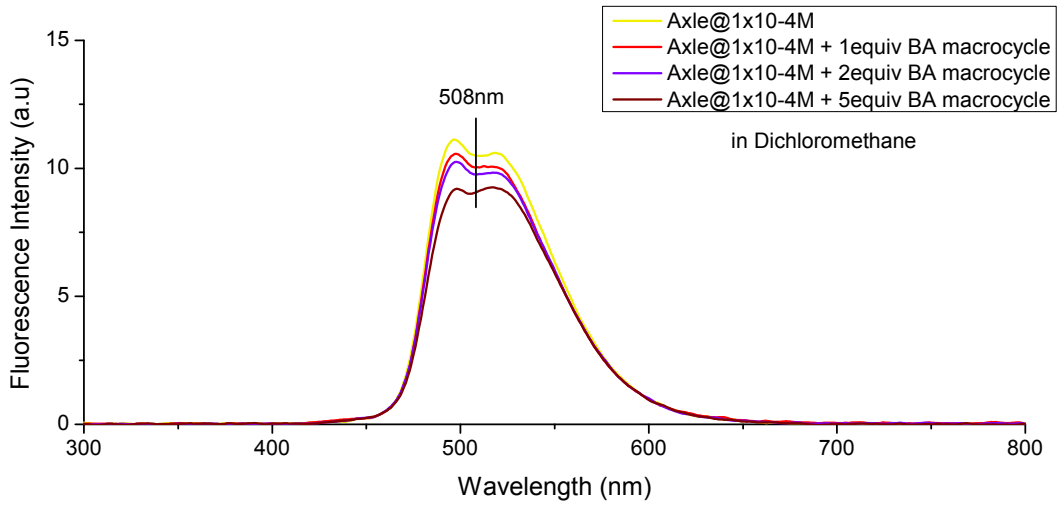

Figure 5.26 Fluorescence emission spectra for axle **C-43** and pseudorotaxane (with 1 ,2 and 5 equivalents of BA macrocycle **C-40** in a DCM/DMF (99:1) solvent mixture.

5.5.3 Excitation spectra.

The excitation spectra was produced by varying the excitation wavelength and monitoring the emission at the fluorescent maximum $\lambda_{max}^{F} = 508\text{nm}$. Normally an excitation versus emission intensity such as this would be expected to trace a spectrum similar to the absorbance spectra in so far as that at wavelengths where the absorbance is greatest we would to observe maximum fluorescence. This phenomenon can be explained by Kasha's and Vavilov's rules[46, 63] which describe respectively the independence of emission maxima and quantum yield on excitation wavelength.

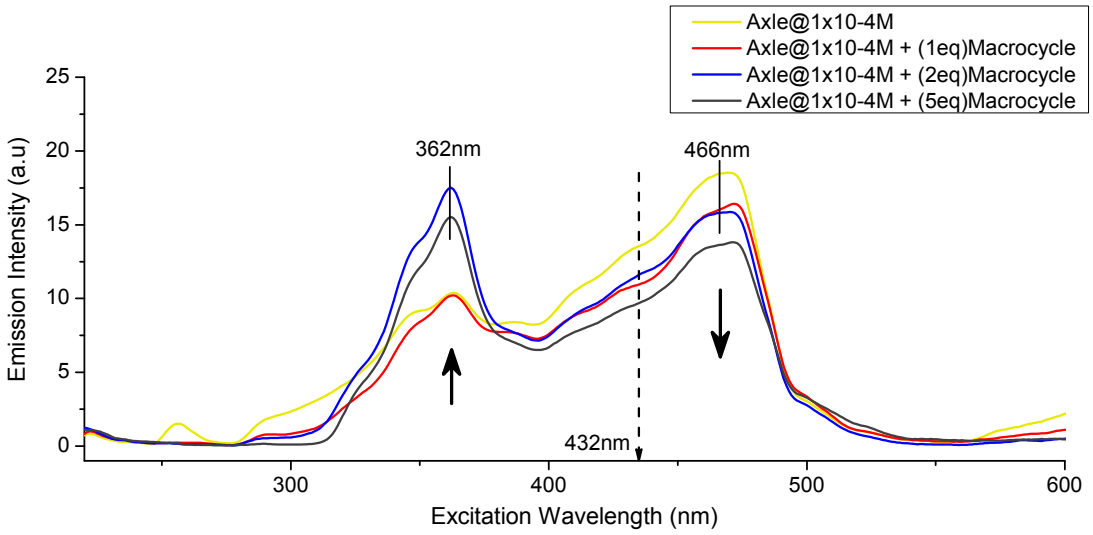

Figure 5.27 Excitation spectra for the axle **C-43** in DCM/DMF(99:1).

Interestingly the first observation from the spectra shown in Figure 5.27 is that it shows no emission at excitation wavelengths less than 300nm. This could be explained by the other non-flavin components of the axle and macrocycle which strongly absorb in these wavelengths. It may also suggest that energy from these wavelengths is able to be transferred away from the flavin to these other pseudorotaxane components.

The second observation was that the excitation maxima have red-shifted relative to the absorbance maxima (i.e. $319 \rightarrow 362\text{nm}$ (*Band II*) and $432 \rightarrow 466\text{nm}$ (*Band I*)). In an attempt to explain this unusual phenomenon, the author initially explored a spectroscopic property called Red-Edge Excitation Shift (REES).[46] This characteristic behaviour usually occurs under conditions were the solvent relaxation is incomplete. The emission spectrum shifts to longer wavelengths when the excitation wavelength is on the longer wavelength edge (red-edge) of the absorption spectrum. REES therefore normally takes place in very viscous solvents and at very low temperatures. We reasoned that the BA macrocycle could be replicating this viscous environment while interacting with the flavin axle. However the spectrum shown above in Figure 5.27 was recorded at a fixed emission wavelength of 508nm, therefore in order to determine whether (or not) this excitation red-shift had any correlation with REES, we began by first recording the fluorescence spectra for both axle and pseudorotaxane over a short range of excitation wavelength as shown in Figure 5.28(a) and (b) respectively.

Figure 5.28(a) shows the fluorescence intensity of the free axle (i.e. no macrocycle present) increasing from approx 15 arbitrary units (a.u) at the absorbance maxima of 435nm to a maximum of approx 22 a.u at the longer wavelength of 465nm but with very little shift in peak position. Both show the prominent double peak which common feature of flavin fluorescence and has been explained to be due to availability of two fluorescent ground state vibrational levels ($S^F_{0,\nu=1}$ and $S^F_{0,\nu=0}$).[52] As the excitation wavelength is increased further there is an apparent red-shift of the maximum as the emission intensity decays. This could just be the result of one of these ground state vibrational levels becoming less accessible. We can observe this as the longer wavelength edge of any of these fluorescence intensity spectra (i.e. between 550-650nm) never exceeds that of the maximum intensity spectra at $\lambda_{excit} = 465\text{nm}$.

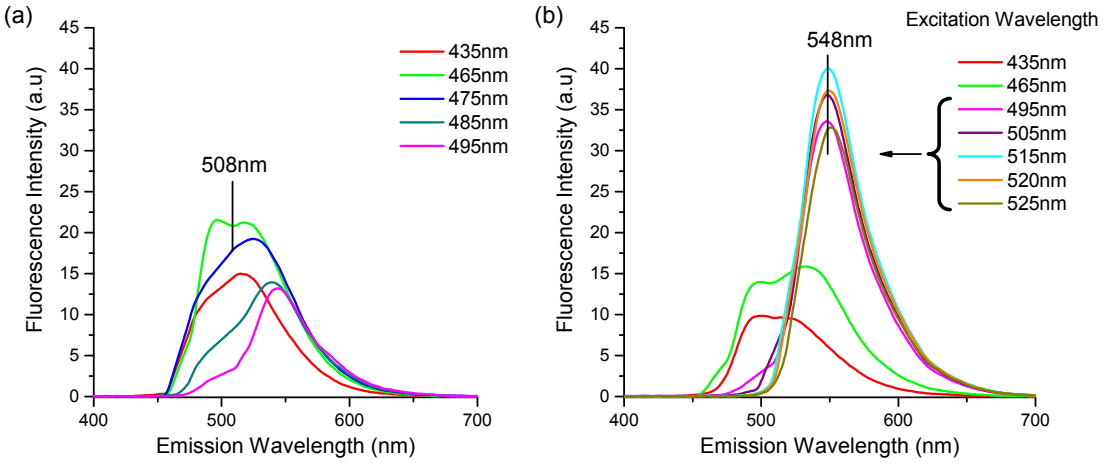

Figure 5.28 Fluorescence emission spectra for (a) the axle and (b) the pseudorotaxane (at 5 equivalents of macrocycle) in dichloromethane recorded over a range of different excitation wavelengths. Note that for clarity, the high intensity spikes produced by Rayleigh scattering have been removed using the "zapped" function provided by LabCognition Panasonic software.

However when we examine the fluorescence intensity profile for the pseudorotaxane (with 5 equivalents of macrocycle) as shown in Figure 5.28(b), we observe an almost tripling of emission intensity and a red shift of peak position from 508 to 548 nm. The immediate conclusion was that we were observing the REES behaviour previously discussed, however looking again at the excitation wavelengths that produce these large emission intensities we see that they are all produced at wavelengths $\geq 495\text{nm}$ as emphasised by the curly bracket in Figure 5.28(b). The absorbance spectra previously depicted in Figure 5.24 has shown us that the zero absorption point starts from approx 490nm so clearly this emission cannot be the result of a direct absorption. This now presents us two main questions to try and answer, how can the pseudorotaxane system absorb such low energy light photons and which part of the pseudorotaxane is responsible for emitting radiation that peaks at 548nm. To help try and understand this we compared the 3D excitation/emission contour maps for the pseudorotaxane (Figure 5.29), the axle (Figure 5.30) and the tri-ethylene glycol BA macrocycle (Figure 5.34). Apart from Rayleigh scattering, no clear distinguishing features were observed in the 3D excitation map for the fumaramide compound, *N-(2,3-dimethylphenyl)-N-(2,2-diphenylethyl)fumaramide*). Consequently this was not included in the following sections.

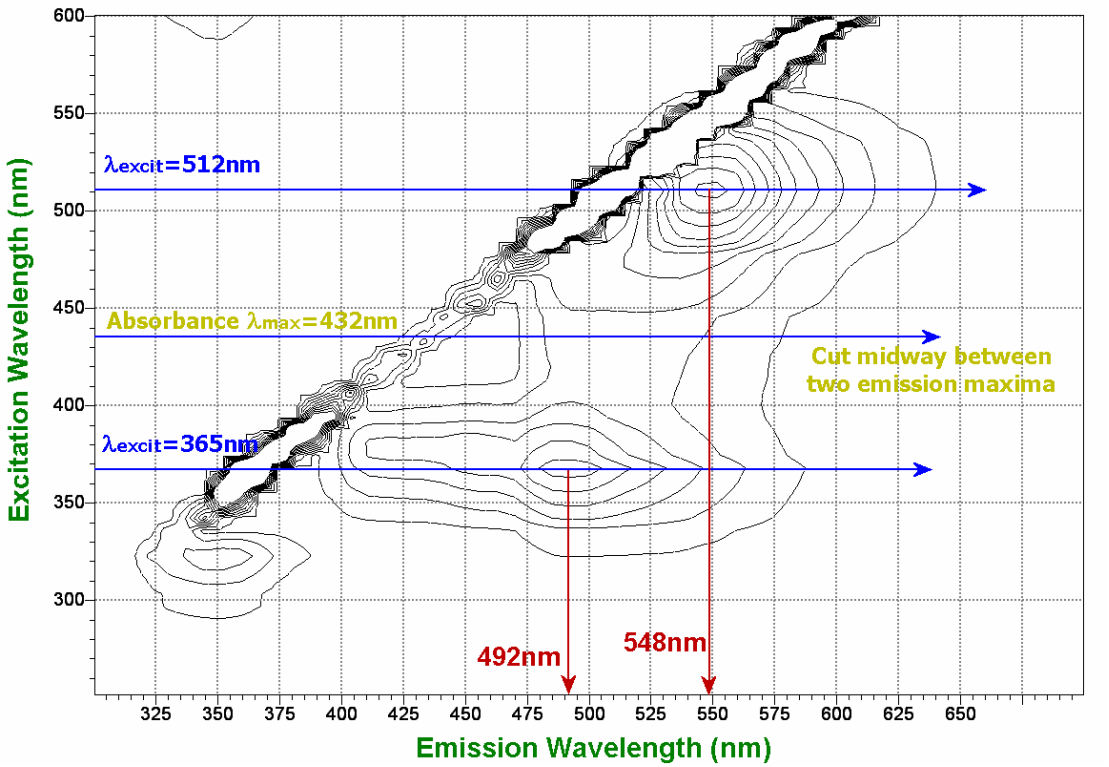

Figure 5.29 Fluorescence emission spectra for the pseudorotaxane in a DCM/DMF (99:1) mixture. The high intensity diagonal contour line ranging from coordinates 350,350 to 600,600 were produced by Rayleigh scattering. Isointensity lines are spaced by approx 4 *a.u* .

From the 3D excitation/emission contour maps for the pseudorotaxane shown in Figure 5.29 we can clearly see two major emission peaks at 492nm and 548nm. There is also a smaller emission peak at approx 350nm which as we will see later is believed to be produced by the macrocycle. The emission maxima at 492nm is produced by excitation wavelength of around 365nm. Both wavelengths correspond to regions of weak absorbance in the spectra shown previously in Figure 5.24. The flavin *band II* is believed to be the merging of $\pi \rightarrow \pi^*$ and $n \rightarrow \pi^*$ excitation transition levels.[52] We would tentatively suggest that this red-edge excitation at 365nm may produce an excitation to the S_2 transition level followed by rapid internal conversion to the S_1 transition level and subsequent emission before Stokes loss has a chance to occur through relaxation pathways. Any emission at approx 492nm is easily transmitted through the sample as the absorbance spectra show no evidence of photon absorption at wavelengths greater than 490nm.

For this very same reason it is therefore difficult to comprehend how the emission maxima at 548nm is produced by excitation photons at around at 512nm. If a photon of light cannot be absorbed how is it able to produce significant emission response? Interestingly we observe a strong absorbance band between 250 and 275nm (Figures 5.24) which we believe corresponds to the fumaramide component of the axle, based on the test compound shown in Figure 5.25. We therefore considered that the excitation maximum observed at 512nm may correspond to a double photon absorption by the fumaramide component of the axle which would ultimately bring about a fumaramide excited state (i.e. two photons of light with wavelength centred on approx 512nm combine to photoexcite the fumaramide component of the axle). The emission could then be the product of fumaramide fluorescence (rather than the flavin) since the emission maximum at 548nm appears intriguingly very close to the 546nm

predicted but "unobserved" fluorescence maximum for the fumaramide group which was described recently by Garavelli and Leigh.[51] This fumaramide fluorescence is typically unobserved because the normal relaxation pathways of the photoexcited fumaramide group has been shown to involve energy loss though rotation or twisting motion around the C=C bond. Is it possible that hydrogen-bonding interaction between the fumaramide station and the BA macrocycle increases the rigidity of the C=C? If so then the relaxation energy would now be able to follow alternative minimum energy pathways (MEP's) which could lead to the predicted emission maximum. This is supported by the evidence that we do not observe this emission maximum in the 3D excitation/emission contour map for the flavin-fumaramide axle shown below in Figure 5.30 (i.e. without the macrocycle). However it still contradicts the observation that absorbance is not evident at this excitation wavelength. Even a two photon absorbance suggests some reduction in transmittance.

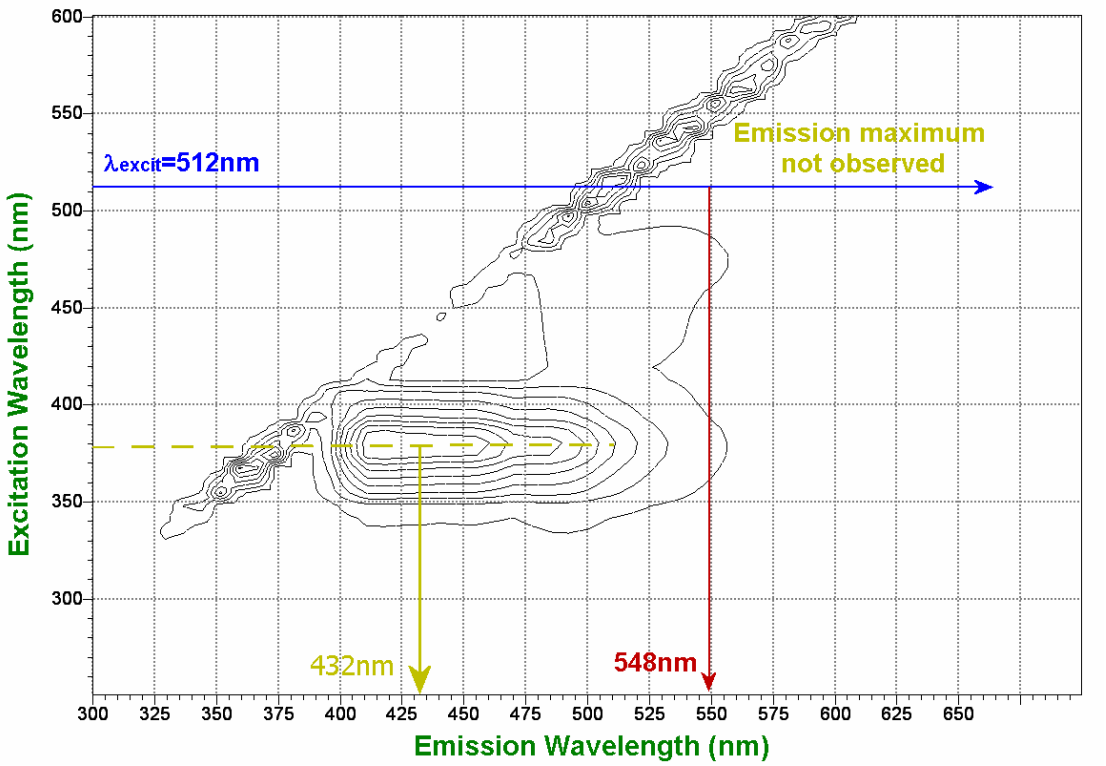

Figure 5.30 Flavin-fumaramide axle (i.e. without the BA macrocycle). This clearly shows that the 548nm emission maximum previously observed for the pseudorotaxane is absent. Surprisingly the strong emission maximum at 432nm coincides with the flavin absorbance maximum. We would therefore have expected this emission wavelength to have been re-absorbed by the sample. Isointensity lines are spaced by approx 15 *a.u* .

5.5.4 The effect of polar solvent on the fumaramide pseudorotaxane.

In an attempt to determine whether or not the interaction between the axle and macrocycle was influencing factor in the emission spectra, the DCM solvent from the original sample was evaporated and then made up to the initial concentration using 100% DMF solution. Strong hydrogen bonding interaction between the axle and macrocycle would no longer take place. The 3D excitation/emission contour map recorded in DMF is shown below in Figure 5.31. Surprisingly we still observed an emission maximum which had slightly blue shifted from 548 to 546nm. Although not clearly obvious from the isointensity lines shown this contour map, *peak A* at coordinates $x = 546nm, y = 513nm$ is approximately 40% larger (i.e. 42 *a.u* in DCM versus 59 *a.u* in DMF). In comparison with *peak B* at coordinates $x = 480nm, y = 370nm$ which is almost identical in height (i.e. 27 *a.u* in DCM versus 28 *a.u* in DMF). This would seem to suggest that this emission maximum may be the product of hydrogen bonding interactions either with the macrocycle or polar solvent molecules.

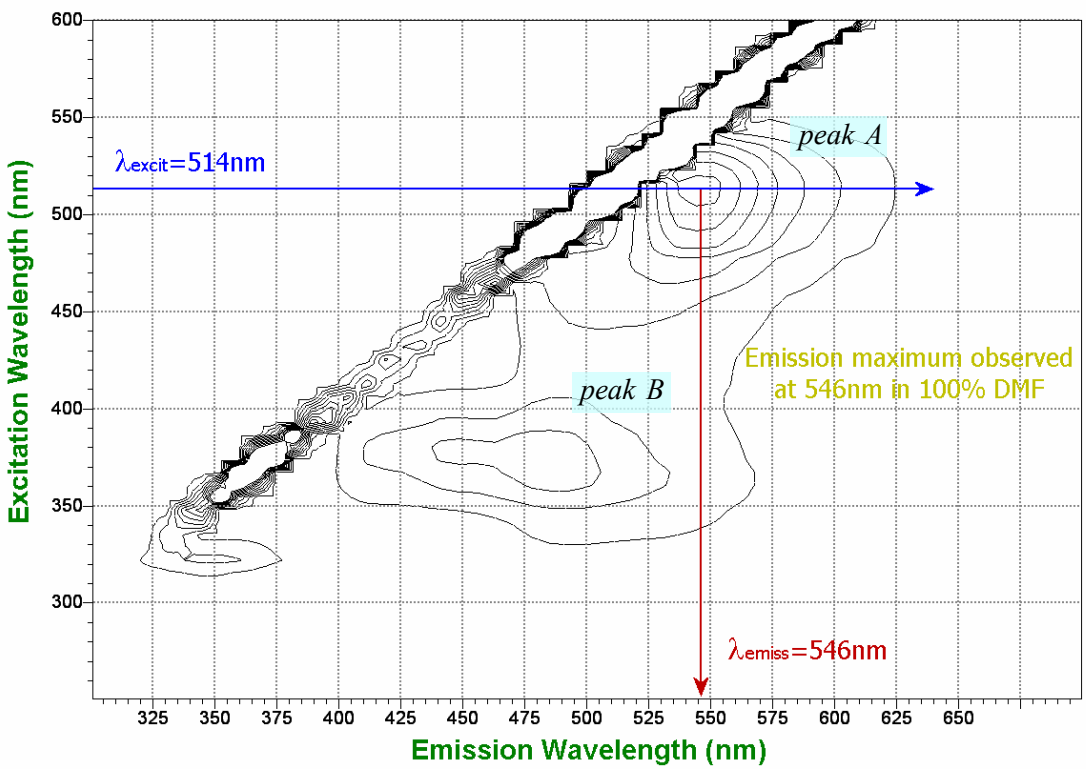

Figure 5.31 3D contour map showing pseudorotaxane (i.e. axle + 5equiv of macrocycle) showing an emission maximum at 546nm exists even in 100% DMF solution. Hydrogen-bonding interactions with the macrocycle is competitively unable to occur in this polar solvent. Isointensity lines are spaced by approx 6 *a.u* .

Furthermore the 546nm emission maximum is clearly present in the 2D spectra of the pseudorotaxane even with only 1 equivalent of macrocycle shown Figure 5.32(a) recorded over a narrow range of excitation wavelengths. These spectra are shown alongside a similar 2D spectra in Figure 5.32(b) of the pseudorotaxane at 5 equivalents of macrocycle. In both cases the emission maximum reaches its peak intensity between $500 - 510$nm .

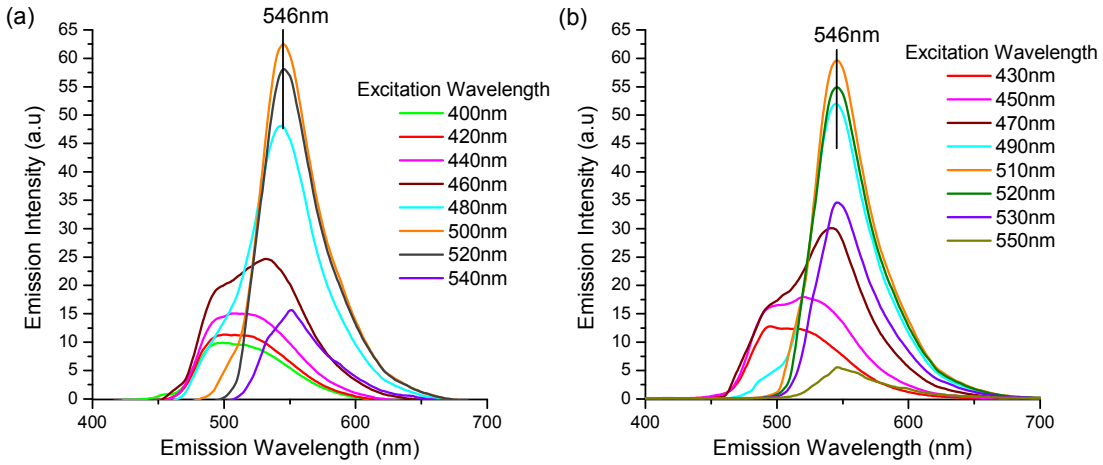

Figure 5.32 Fluorescence emission spectra for the pseudorotaxane at (a) 1 equivalent and (b) 5 equivalents of BA macrocycle both recorded in 100% DMF solution over a range of different excitation wavelengths. Shows that an emission maximum at 546nm exists even in very polar environment where hydrogen-bonding interactions with the BA macrocycle cannot be achieved.

5.5.5 The effect of polar solvent on the fumaramide axle.

If this emission maximum is the result of polar solvent interaction then we would expect to see a similar emission magnitude at approx 546nm for the free axle (i.e. no macrocycle present) in DMF solution. To determine this we evaporated the DCM solvent from the free axle sample used to produce the 3D excitation spectrum previously shown in Figure 5.30 and then dilute to the initial concentration using 100% DMF. The results are shown in Figure 5.33(b) alongside the 2D spectra for the same free axle in DCM/DMF(99:1). There is perhaps a not so obvious difference in these spectra. Although Figure 5.33(b) shows the emission at 545nm was not as intense as that observed for the pseudorotaxane it is still relatively more intense that that for the free axle in DCM. In non-polar solvent the emission intensity at 545nm is approximately half the intensity recorded at 508nm and this is when the excitation wavelength is only 495nm. In polar solvent even at an excitation wavelength of 510nm the emission intensity is just below the overall maximum emission intensity. We can therefore say that this is a very definite red-shift in fluorescence emission with very little emission intensity variation between excitation wavelengths 450 and 510nm. We can therefore conclude that although the polar solvent does have some influence on the emission spectrum of the free axle it is clearly not as dramatic as that for the pseudorotaxane.

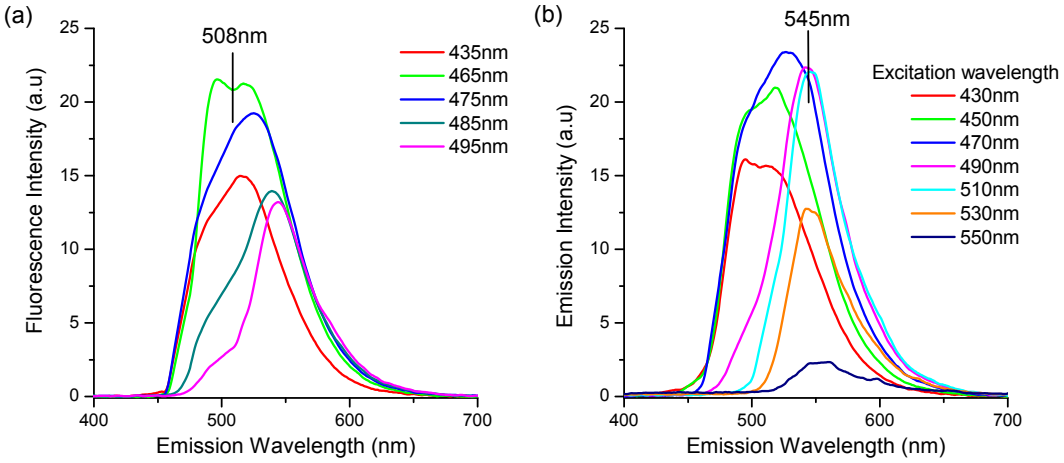

Figure 5.33 Variation in the fluorescence maxima and intensity with excitation wavelength for the flavin-fumaramide axle (i.e no BA macrocycle present) under solvent conditions: (a) DCM/DMF (99:1) and (b) in DMF (100%).

So does the macrocycle presence play a part in this difference? It has not gone unnoticed that the strong absorbance maxima of the BA macrocycle at 295 nm (excitation maxima 310 nm) may even help contribute to the overall excitation process via energy transfer. The emission observed (maxima at 335 nm) from the macrocycle does appear to be severely quenched in the pseudorotaxane excitation/emission contour map compared with that of the macrocycle on it own as shown in Figure 5.34. However the emission peaks intensities at 335 nm is approx 650 a.u for the macrocycle ($@1\times10^{-4}$M) and only 15 a.u for the pseudorotaxane (i.e axle $@1\times10^{-4}$M and macrocycle $@5\times10^{-4}$M). At a 5:1 ratio of macrocycle to axle, this cannot possibly be the full explanation. Therefore, it would seem more likely that this decrease in intensity can be simply explained by being due to the re-absorbed into that region of the absorbance spectra occupied by the flavin's *band II* as shown in Figure 5.24.

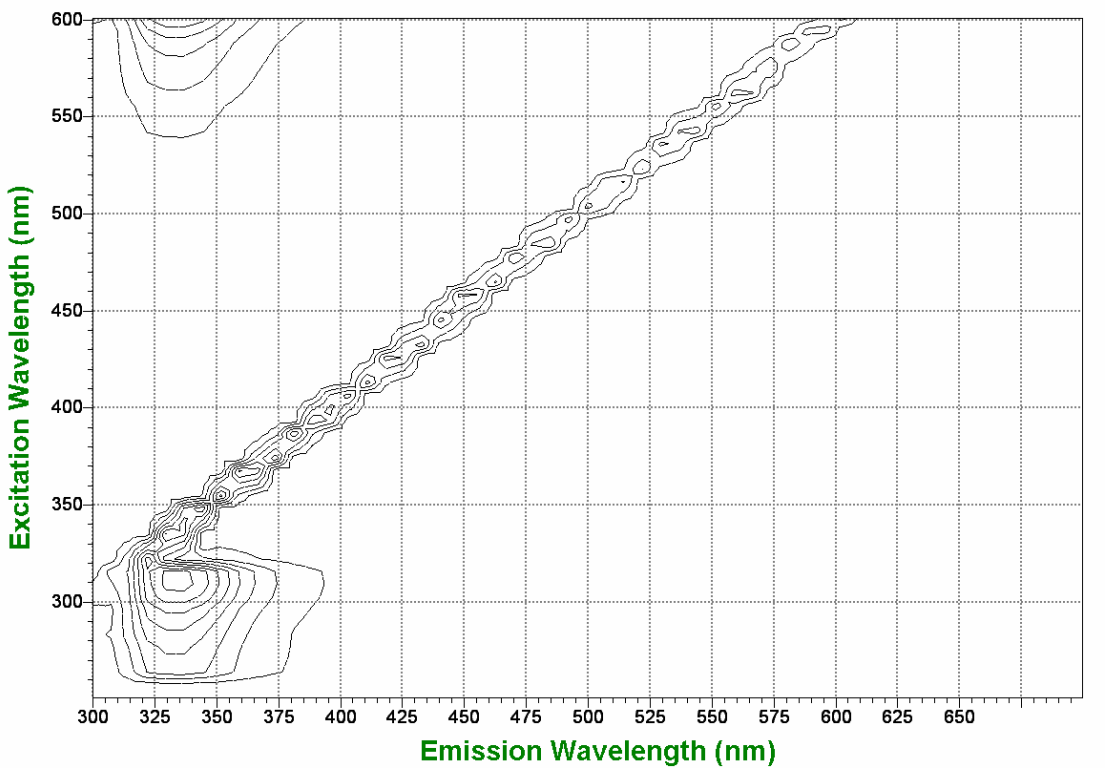

Figure 5.34 3D excitation/emission contour map for the free BA macrocycle showing a very strong emission maximum at approx 335nm in DCM/DMF(99:1) solution. Isointensity lines are spaced by approx 80 *a.u* .

5.5.6 Fluorescence variation in the absence of a fumaramide group.

Finally, since we have observed a red-shift from 508nm to 546nm in the emission spectrum of the flavin fumaramide axle in polar solvent (with or without macrocycle present) can we determine then if this solvent interaction involves the fumaramide or the flavin component of the axle. To achieve this explored the emission spectra of a previously synthesised flavin-succinamide axle, the structure of which is depicted in Figure 5.35 alongside it's 2D emission spectra over a narrow range of excitation wavelengths. We can clearly see by comparison with the flavin-fumaramide axle also in DMF at $\lambda_{excit} = 460$ nm (dashed red line) that the flavin-succinamide emission is highly quenched. Although just as we observed previously in the spectrum shown in Figure 5.33(a) for the flavin-fumaramide axle in non-polar solvent (i.e. DCM/DMF 99:1) there is some red-shift in the emission as the excitation wavelength increases. However by approx 500nm (excitation) the intensity has again decreased to approx half the overall maximum.

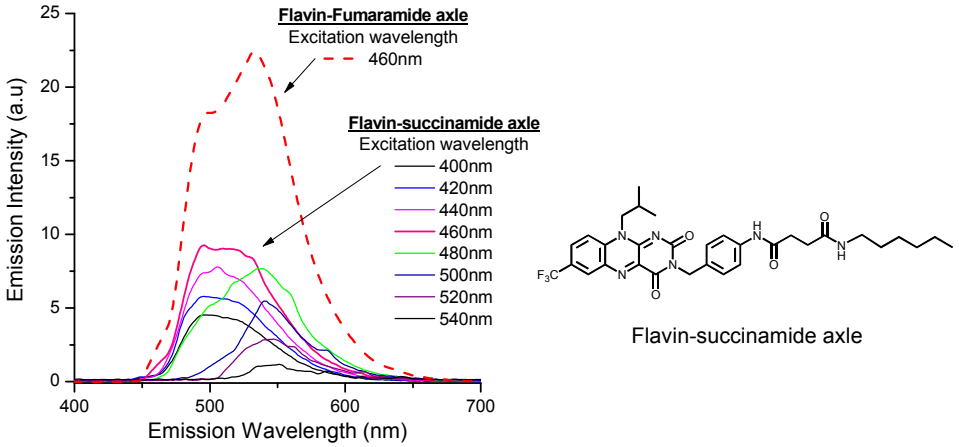

Figure 5.35 Emission intensity at various excitation wavelengths for the flavin-succinamide axle(i.e. no macrocycle) in 100% DMF solution.

These results are far from conclusive evidence that the axle fumaramide component is the source of the 546 nm fluorescence emission. All that we can state with certainty is that at approx three times the magnitude of the flavin's 508 nm fluorescence it appears more intense and when the macrocycle is present regardless of whether the solvent environment is polar of non-polar. Whatever role the macrocycle plays it does not necessarily involve pseudorotaxane formation.

5.6 Conclusions.

5.6.1 Evidence for the 2 electron & 1 proton transfer process.

Square wave voltammetry provides us with a fundamental insight into the flavin electrochemistry over the extremely short time scale of the SW pulse. The evidence shows that two electron and one proton transfer rationally fits the observed axle SW responses. Over the same SW pulse time scale, the pseudorotaxane has been shown to undergo a rapid and electrochemically irreversible translocation of the BA macrocycle to form a co-conformation in which the macrocycle stabilizes the flavin radical anion $Fl_{rad}^{\bullet -}$. The author believes that this stable redox state may still be able to undergo subsequent proton and 2nd electron transfer to produce the flavin anion $[Fl_{red}H^{-}]$ pseudorotaxane but that this process is much slower than that observed during the free axle redox process. Consequently the SW responses from the pseudorotaxane contribution appear smaller in magnitude since over the short times scale of the SW pulse the pseudorotaxane appears to undergo a single electron transfer process. However during the more prolonged timescale of cyclic voltammetry experiments the cathodic peak (i.e. *wave I*) of the pseudorotaxane is only marginally smaller than that of the free axle. If we were to consider effect of number of electrons transferred $n^{3/2}$ versus current peak height as described by the Randles-Sevcik equation, then we would have expected the one electron transfer peak height of the pseudorotaxane to be almost one third the two electron transfer current peak height of the free axle. As this is not observed the we must conclude that over the longer CV sweep the pseudorotaxane does undergo a proton and 2nd electron transfer.

5.6.2 Further investigation of fluorescence properties.

Question still remain over the origin of the fluorescence maximum at approx $546\ \text{nm}$. The most curious conundrum is how, when no absorption bands are evident at or around the excitation wavelength $\lambda_{excit} = 512\ \text{nm}$ (in fact there is no noticeable absorbance at wavelengths $> 490\ \text{nm}$), is the pseudorotaxane still able to demonstrate fluorescence emission. Perhaps because the excitation and emission maximum wavelengths are so close (*approx* $35\ \text{nm}$) the emission displays similar characteristics to Raman scattering but instead of paralleling the diagonal line of Rayleigh scatter peaks on the 3D excitation/emission contour map occurs only appear within a small region of the spectrum. Scattered light would certainly alleviate any requirement for photon absorption. Also, how does the macrocycle play a part in this, as it presence clearly has an impact even in a polar solvent environment. As far as the author is aware these emission or scattering characteristics have not been previously been reported for the benzylic amide rotaxane system but further study may provide some insight in the excited transition level state of either the fumaramide or flavin rotaxane. One of the advantages of utilizing a pseudorotaxane to probe these properties is that the ratio of free axle to rotaxane can be continually controlled by adjusting the number of macrocycle equivalents.

CHAPTER 6

FLAVIN-FUMARAMIDE [2]ROTAXANE.

6.1 Introduction.

6.1.1 Experimental design strategy.

The axle of the flavin [2]rotaxane to be described here incorporates two stations, the dicarbonyl of a flavin unit and a fumaramide group, as shown in Figure 6.1. A non-covalently attached benzylic amide ring becomes the second or [2] component of the rotaxane and was self-assembled around the fumaramide stations of the flavin axle by means of the template mechanism first described by Leigh.[25, 26] The electrochemical and photochemical properties of both axle and rotaxane will be explored and compared. Cyclic voltammetry (CV) will be used as both effector and detector used to probe the redox properties of these multicomponent electroactive species. Square wave voltammetry (SWV) will be used in combination with CV to provide some further insight into the multi-state redox mechanisms. The sensitivity of the flavin's *band II* to hydrogen bonding interactions will be briefly explored using UV/Visible absorbance spectroscopy. Emission and excitation spectra of axle and rotaxane will be also be compared as environmental indicators. Proton NMR will be used to detect the hydrogen bond interactions by comparing proton shift variations. This will be used to verify the location occupied by the macrocycle on the axle while in the electrochemical and photochemical ground state.

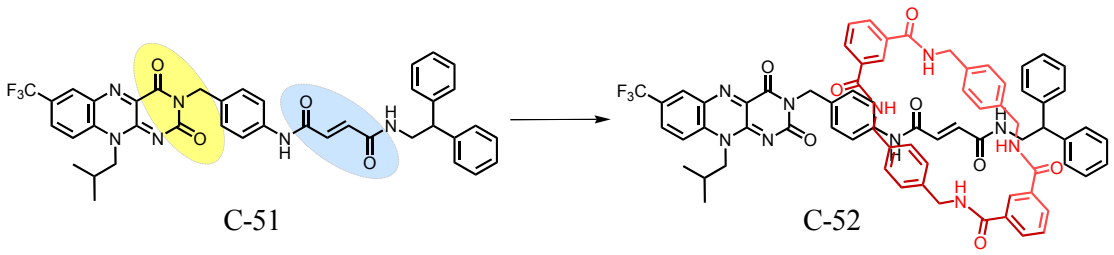

C-51 C-52

flavin – fumaramide axle *flavin – fumaramide* [2]rotaxane

Figure 6.1 The two stations of the flavin [2]rotaxanes. The 1st station is the flavin dicarbonyl (coloured yellow), the 2nd station is a fumaramide group (coloured blue).

6.2 Synthesis

6.2.1 Synthesis of a flavin-fumaramide based [2]rotaxane.

The reaction scheme is shown in Figure 6.2 and starts by synthesising in two steps the N-(diphenylethyl)fumaramic acid **C-50** which would ultimately form the fumaramide component of the axle. Fumaramic acid monoethyl ester **C-49** was first synthesised using commercially available diphenylethyl amine and fumaric acid monoethyl ester. The ester was hydrolysed under alkali conditions to provide the fumaramic acid. The axle was formed through the EDCI coupling with the 3-benzylamine-7-trifluoromethyl-10-isobutyl flavin **C-48**, the synthesis of which was described in Chapter 5. The rotaxane was synthesised using the flavin axle as a template for the benzylic macrocycle formation from 2 equivalents each of isophthaloyl dichloride and p-xylylenediamine dissolved in dry DCM and added simultaneously using a motor driven syringe pump at a dropwise rate over 3h.

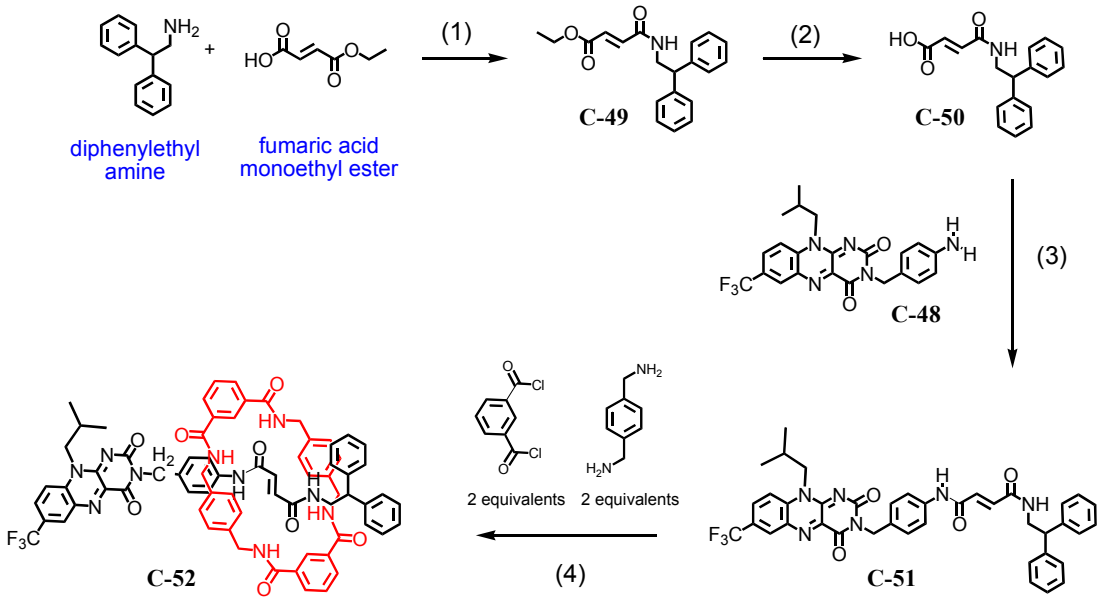

Figure 6.2 (**1**). DMAP in DCM cooled by ice-bath for 10 min before adding EDCI. Temp slowly raised to r.t while stirring for 21h; (**2**). Aq NaOH added dropwise to product from (1) in ethanol, rxn stirred for 25h at r.t. Product precipitated by pH adjustment to 4-5 by addition of aq HCl; (**3**). HOBt, EDCI and cat DMAP in DCM (room temp, 6h); (**4**). Isophthaloyl chloride (in dry DCM 10mL), p-xylylenediamine (in dry DCM 10mL) simultaneously added dropwise over 3h to flavin axle in dry DCM and NEt_3.

6.3 NMR Spectroscopy.

Figure 6.3 shows the ^{1}H NMR for the axle and [2]rotaxane in a deuterated solvent mixture of $CDCl_3$/DMF-d7 at a ratio of 95:5 and at concentrations of 2 mM which is approx $1/10th$ the concentration normally employed when performing ^{1}H NMR analysis. The peaks are labelled in small case letters form a-r for the axle protons and capital case A-F for the macrocycle as shown in Figure 6.4. These conditions were required to prevent the gradual precipitation of both compounds during the experiment. Despite the high

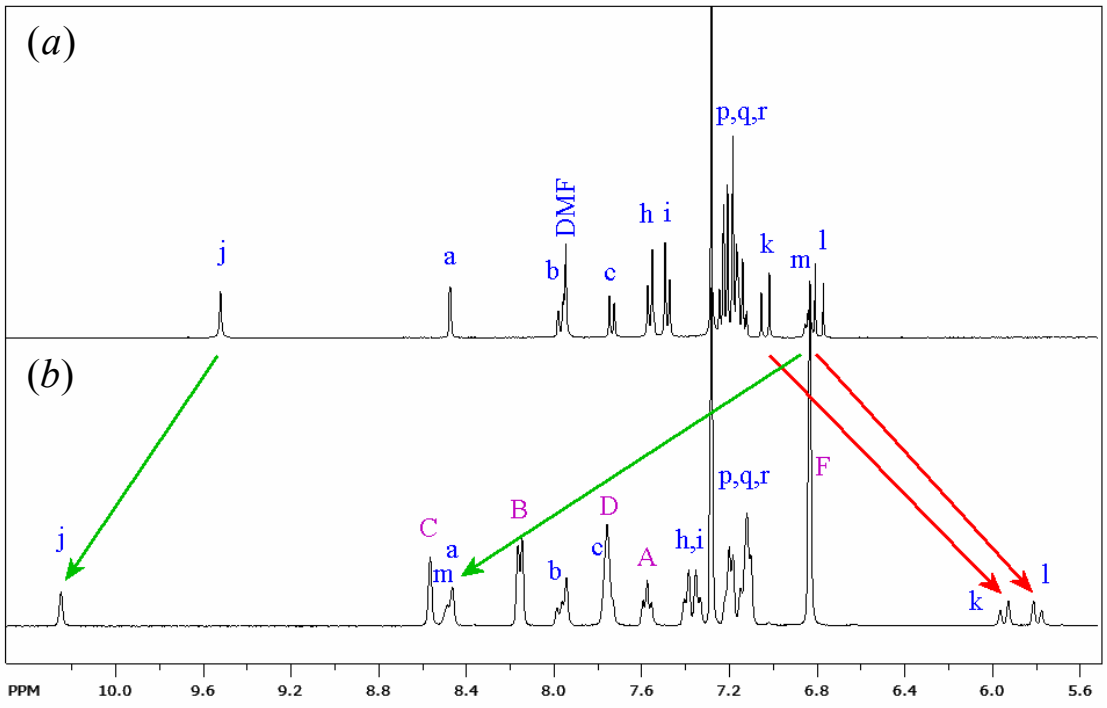

Figure 6.3 Stacked partial ^{1}H *NMR* spectra preformed in $CDCl_3$/DMF-d7 (ratio 95:5) for: (a) axle **C-51** and (b) [2]rotaxane **C-52** indicating the concomitant amide NH downfield shift and alkene CH upfield shift. This difference induced by the hydrogen-bonding interactions between the macrocycle and fumaramide component of the axle.

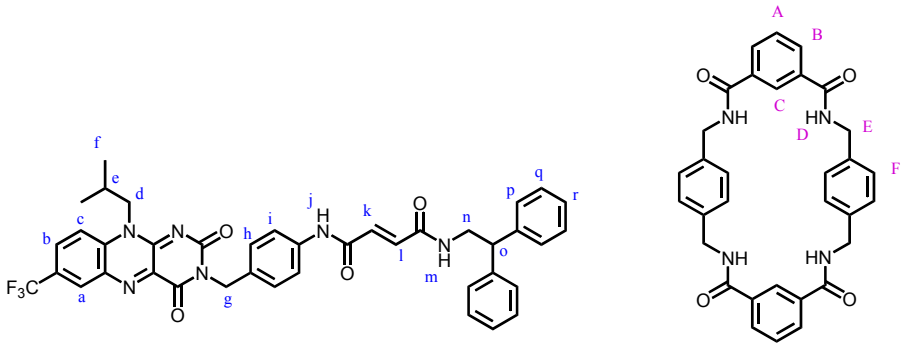

Figure 6.4 Proton peak identification system uses small case letters from $a \rightarrow r$ for the axle and capital case letters from $A \rightarrow F$ for the macrocycle. The [2]rotaxane NMR shown in Figure 6.3 therefore employs a combination of both these letter systems.

percentage of polar solvent the effect of hydrogen bonding were still significantly evident as demonstrated by the concomitant downfield shift of the fumaramide amide ($\delta(j) = 0.73\ ppm$ and $\delta(m) = 1.65\ ppm$) and the fumaramide alkene upfield shift ($\delta(k) = -1.09\ ppm$ and $\delta(l) = -1.00\ ppm$). Interestingly we also observe a small but significant upfield shift in the four aromatic protons *h and i* ($\delta(h,i) = -0.15\ ppm$) which are located between the fumaramide and the flavin. It was initially thought that this might support the proposal that the macrocycle was able to occupy a position midway between the two stations. Unfortunately if this was the case we would also expect to see a significant shift in the $-CH_2-$ group at position *g*. Instead the position of these two protons are identically located at $\delta = 5.15\ ppm$ for both axle and rotaxane (not shown in Figure 6.3).

All attempts at exploring the intermolecular proton interactions though *NOESY NMR* have proved unsuccessful because of the [2]rotaxane's poor solubility in non-polar solvents. Despite using low concentrations and up to 10% deuterated DMF solvent mixtures the [2]rotaxane precipitates after only several hours, too short a period for any reasonable scan. At 20% concentrations this solubility periods was extended but the *NOESY* NMR experiment was unable to detect any sensible interactions.

6.4 Electrochemistry.

The diphenyl component of the flavin-fumaramide axle **C-51** preformed a dual role of forming a bulky stopper group at one end of the axle and enhancing the solubility in non-polar solvents relative to the dodecyl side chain of the pseudorotaxane axle in Chapter 5. Despite this both axle **C-51** and [2]rotaxane **C-52** proved only partially soluble in many organic solvents including THF and MeCN. To overcome this solubility predicament the axle (or [2]rotaxane) was first dissolved in DMF (0.1 mL) and then diluted with the non-polar solvent DCM (6 mL) which is equivalent to >98% by volume. This method allowed both the axle and [2]rotaxane to remain soluble sufficiently long enough for voltammetry experiments to be carried out. Full experimental details can be found in Chapter 8: Experimental section.

6.4.1 Cyclic voltammetry for the axle in DCM / DMF (98:2).

Cyclic voltammograms for the flavin-fumaramide axle in a DCM/DMF (98:2) solvent mixture are shown in Figures 6.5 and 6.6 at sweep rates $\upsilon = 0.1$ and $1\ \mathrm{Vs^{-1}}$ respectively. Both voltammograms appear to show a single reduction and oxidation wave during both cathodic and anodic sweeps. At a sweep rate $\upsilon = 0.1\mathrm{Vs^{-1}}$, the system displayed reasonably good electrochemical reversibility with peak separation $\Delta E_p = 73$ mV (125 mV @ $1\ \mathrm{Vs^{-1}}$) with cathodic and anodic currents $I_c \approx I_a$. The half wave potentials shown are in close agreement averaging out at $E_{1/2} = -0.555$ V. Both voltammograms appear typical of an expect single electron transfer which we might expect to occur in the absence of a proton source a second electron transfer from the flavin N(3). However as we shall discover though analysis of the SWV this is not the case.

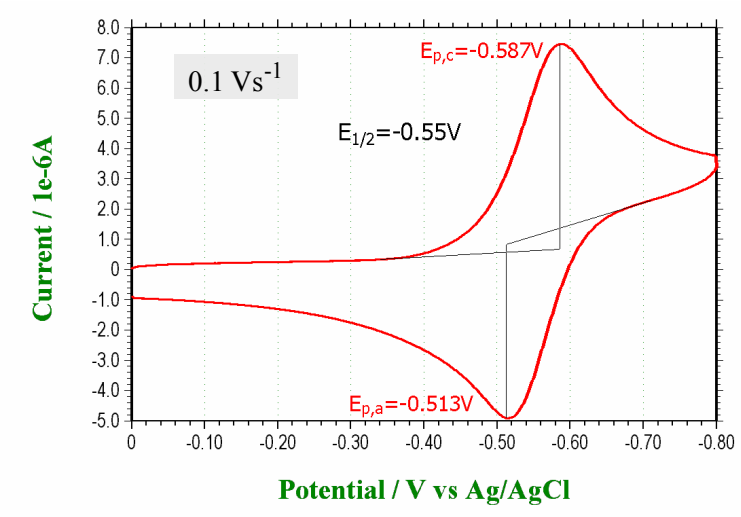

Figure 6.5 Cyclic voltammogram (CV) for the isobutyl flavin-fumaramide axle between 0 and 0.8V at a sweep rate $\upsilon = 0.1\mathrm{Vs^{-1}}$ in a DCM/DMF (98:2) solvent mixture.

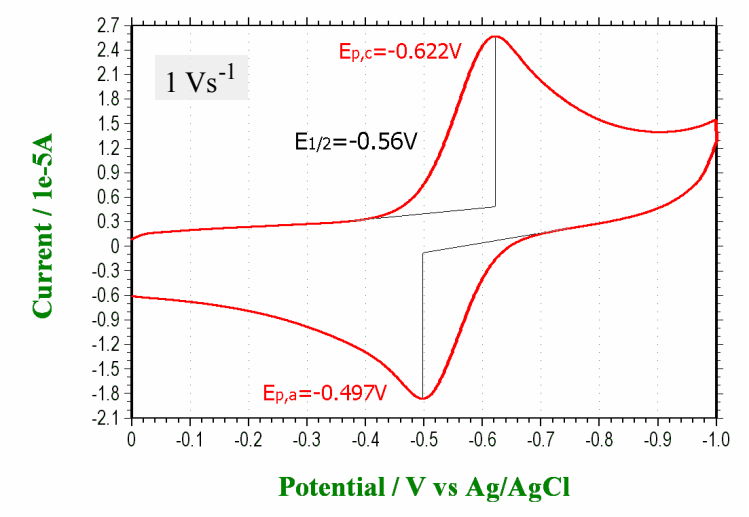

Figure 6.6 Cyclic voltammogram for the isobutyl flavin-fumaramide axle between 0 and 1 V at sweep rate $\upsilon = 1\,\mathrm{Vs}^{-1}$ in a DCM/DMF (98:2) solvent mixture.

6.4.2 Square Wave Voltammetry for the axle in DCM / DMF (98:2).

Figure 6.7 below shows the SW voltammograms for the flavin-fumaramide axle with the direction of scan from 0 to −1 V in a DCM/DMF (9:2) solvent mixture. The overall net response (I_{Diff}) is shown Figure 6.7(a) and is depicted by the single peak. The plot shown in Figure 6.7(b) provides a closer analysis of the components that make up the net response $I_{Diff} = I_{for} - I_{rev}$ and shows a significantly larger maximum (I_{for}) accompanied by a smaller minimum (I_{rev}). For a single reversible electron transfer process the I_{rev} peak height would not only be comparable in height to the I_{for} peak but the position of the I_{rev} peak would be more negative than the I_{for} maximum for reasons previously discussed in Appendix A: SWV. Figure 6.7(b) therefore suggests that within the extremely short SW pulse period, the redox process is displaying electrochemically irreversible characteristics. The flavin can typically undergo a 2nd electron transfer but this is subject to a proton transfer reaction which reduces the overall negativity of the molecule transforming it into a more favourable electron acceptor. In aprotic solvent this proton source has been shown to be the N(3) hydrogen of a second flavin oxide molecule. However the N(3) hydrogen of the flavin has been substituted by the (benzyl)fumaramide component of the axle. As we shall see, despite this, the shape of the reverse response I_{rev} best fits the profile of an electrochemically irreversible re-oxidation process that could be rationally explained by reaction such as a proton transfer followed the first electron transfer. Rotello and coworkers[5] demonstrated that a suitable proton source must have a $pKa < 10$. Both DMF and H_2O are reported to have pKa values of 35 and 15 respectively and therefore do not fit this criterion. The most obvious candidate is the fumaramide component of a second axle molecule with a pKa believed to be in the region of 4.6. [64] The SW characteristics depicted here are similar to those observed in Chapter 5 during an electrochemical examination of the pseudorotaxane the exact mechanism of which has therefore already been described in detail using a series of SW pulse "snapshots". We will therefore limit the following discussion to the possible reduction and oxidation pathways available during the SW pulse as shown in Figures 6.8 and 6.9 respectively, as comparisons made here will be helpful when it comes to discussing equivalent pathways for the [2]rotaxane.

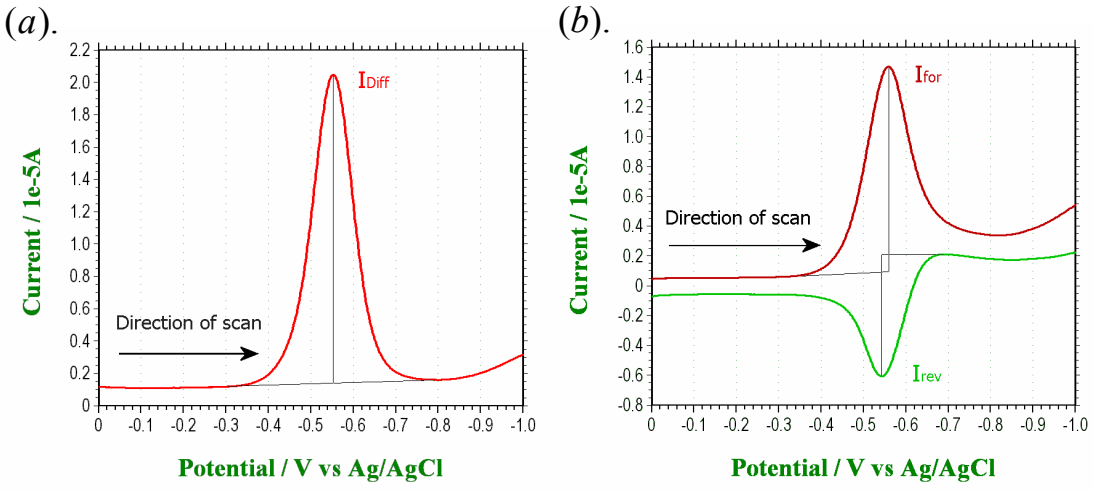

Figure 6.7 Square Wave voltammogram (SWV) for the flavin-fumaramide axle with direction of scan from 0 to −1V (a) the overall response (I_{Diff}) and (b) the forward (I_{for}) and reverse (I_{rev}) responses. Other SW parameters $E_{SW} = 0.025\text{V}$, $E_{step} = 0.002\text{V}$ and $SW_{freq} = 25\text{Hz}$.

The scheme in Figure 6.8 shows the reduction pathway which the flavin can pursue in order to achieve the fully reduced neutral $Fl_{red}H_2$ species. It entails a two electron and two proton transfer that commences at a potential E_1^θ, the formal redox potential for the first electron transfer. As described earlier, a subsequent proton transfer (presumably from the fumaramide component on a second axle) will reduce the overall negative charge on the flavin thus making it easier to accept a second electron. This second electron transfer typically takes place at a formal potential E_2^θ which is less negative than that of the first electron transfer. The overpotential driving the electron transfer would be large and the transfer rate would therefore be fast. The final proton transfer however is believed to be a relatively slower process than the 1st proton transfer. This will be discussed again in more detail later when it will be used to help explain observations made during follow-up voltammograms recorded during fast and slow sweep rates. At least one academic paper can be found that reports a ten fold decrease in the 2nd proton transfer. [65]

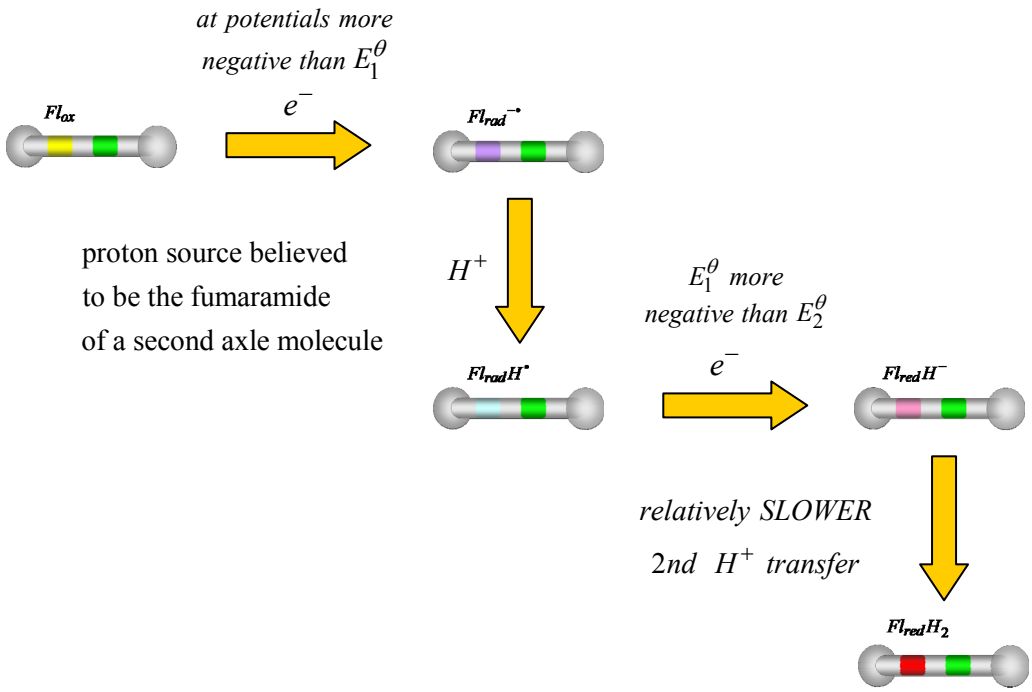

Figure 6.8 **Reduction pathway**. Subject to proton availability the reduction pathway undergoes a two electron transfer process at potentials more negative than E_1^θ.

The overall response of course depends on what occurs during the proceeding SW pulse. For example, when both forward and reverse SW pulses are more positive than E_1^θ, there is no reduction, no concentration equilibrium change to respond to and therefore no response. At the other extreme when both forward and reverse SW pulses are much more negative than E_1^θ then the potential difference between each pulse will have little effect on the concentration equilibrium and both the forward and reverse SW response will be small. We observe an optimal SW response at approximately E_1^θ as during the forward SW pulse the electrode responds to the two electron reduction pathway shown in Figure 6.8. During the subsequent reverse SW pulse the electrode potential is now less negative than E_1^θ but more negative than E_2^θ. The oxidation pathways shown in Figure 6.9 is now limited to re-oxidation of $Fl_{rad}^{\bullet-}$ as shown in the *blue* box, and a concomitant reduction of $Fl_{rad}H^\bullet$. This process will be repeated over a narrow potential window where the reverse SW pulse remains between E_1^θ and E_2^θ.

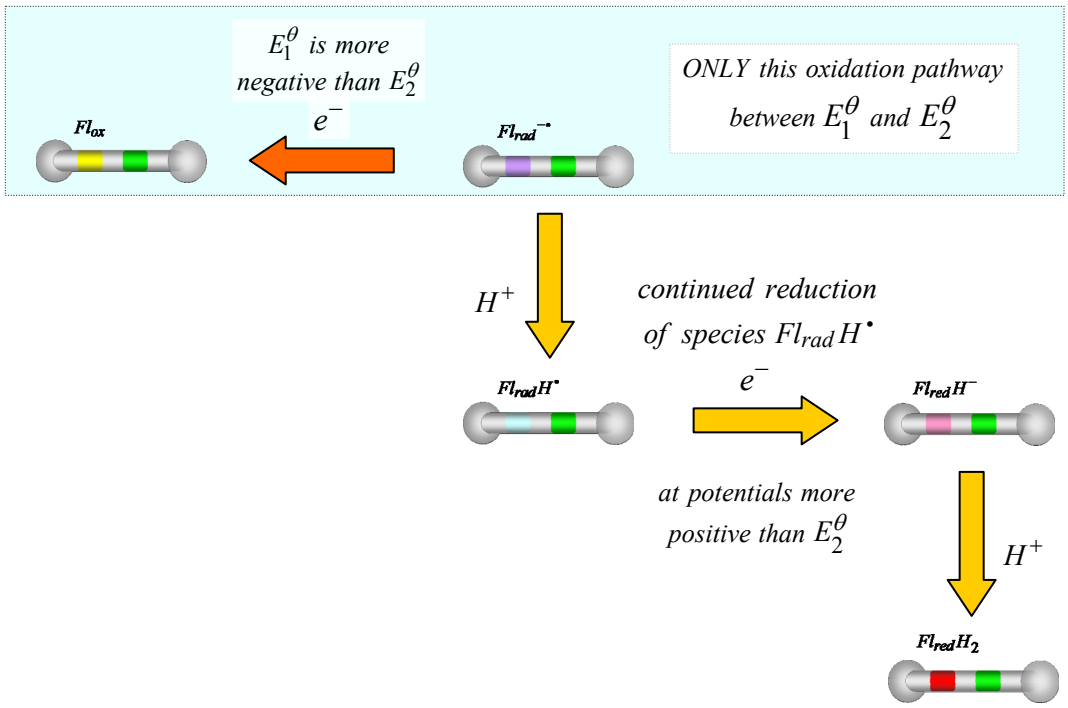

Figure 6.9 **Oxidation pathway**. The separation between formal potentials E_1^θ and E_2^θ is greater than twice the amplitude of the SW pulse (i.e. $E_{SW} = 25\text{mV}$) therefore the reoxidation of $Fl_{red}H^-$ is unable to take place. The reoxidation process here is therefore confined to the pathways within the *blue* box.

6.4.3 Follow-up CV's for the axle in DCM / DMF (98:2).

These CV's were recorded again for follow-up purposes (the reason to be discussed later) several days after the original CV and SWV results using the same EC cell contents which had been left in the open air to evaporate. They therefore possibly contained trace amounts of moisture. The sample was re-dissolved at the original concentration in the same manner as previously described. The results are shown below in Figures 6.10(a) and (b) for sweep rates $0.1\,\mathrm{Vs^{-1}}$ and $1\,\mathrm{Vs^{-1}}$ respectively by the *green lines* alongside the original CV's from Figure 6.5 (*red lines*) shown overlaid for comparison. The voltammograms at the slower sweep rate of $0.1\,\mathrm{Vs^{-1}}$ is an almost perfect fit of the original but the most obvious difference in both these new voltammograms is that the two oxidations peaks now appear better defined. It would seem therefore that the area between these two oxidation peaks on the original CV had previously merged to become one broad peak thus fooling an observer into concluding the presence of a single electron transfer process. We have just verified via the previous electrochemically irreversible SWV results the EC reaction is demonstrating typical two electron transfer characteristics. These more recent CV results would seem to reconfirm this by demonstrating better defined oxidation waves at approx $-0.31\mathrm{V}$ @ $0.1\ \mathrm{Vs^{-1}}$ and $-0.28\mathrm{V}$ @ $1\ \mathrm{Vs^{-1}}$. Using the peak separation of the first redox reaction as a template this would correspond to an estimated half wave potential of $E^2_{1/2} = -0.34\ \mathrm{V}$.

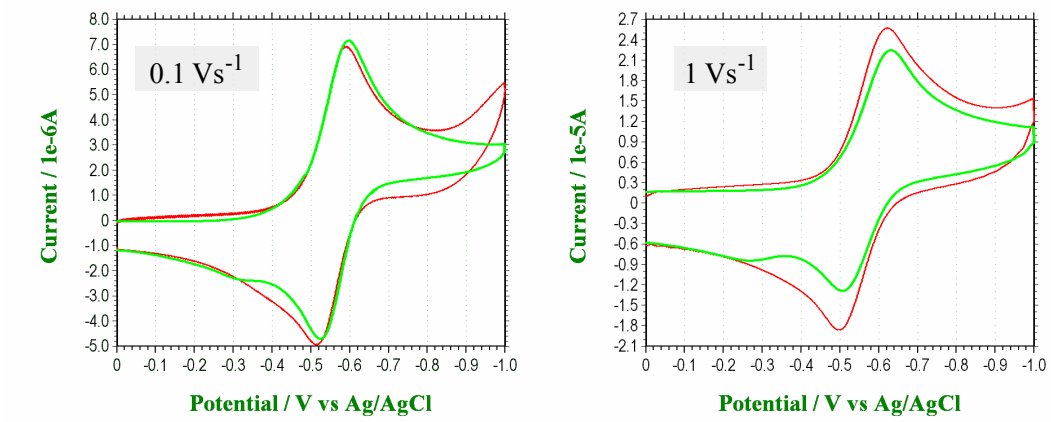

Figure 6.10 Follow-up cyclic voltammograms (*green lines*) for the isobutyl flavin-fumaramide axle between 0 and $1\,\mathrm{V}$ at sweep rates (a) $\upsilon = 0.1\,\mathrm{Vs^{-1}}$ and (b) $\upsilon = 1\,\mathrm{Vs^{-1}}$ in a DCM/DMF (98:2) solvent mixture. The original cyclic voltammograms (*red lines*) from Figure 6.5 are shown for comparison.

How can explain this peak merging effect? We believe the key to this is the 2nd proton transfer of this EC reaction which ultimately provides the fully reduced and stable neutral species $Fl_{red}H_2$. Although less stable than the fully oxidized and aromatic Fl_{ox} species it must nevertheless lose the two protons it has acquired before it can undergo the full re-oxidation process during the CV's reverse sweep. In natural circumstances this it instigated by an oxygen molecule reacting at the $C(4a)$ carbon of the flavin which ultimately removes the $N(5)$ proton as shown in Figure 6.11. The $Fl_{rad}H^{\bullet}$ hydrogen would be liberated following dissociation process. [66] However in the O_2-*free* nitrogen purged environment of the EC cell this re-oxidation process must follow an alternative route. The initial proton donor, presumable a second flavin-fumaramide axle molecules, would have diffused into the bulk solution away from the electrode and subsequently be sparsely available for re-appropriation

of it's proton. It therefore would seem more likely that the reduced flavin will undergo a comproportionation reaction [67] with a second and more readily available oxidized flavin to form two equivalents of the radical $Fl_{rad}H^{\bullet}$. Proton transfers are rate determining steps during both reduction and oxidation electrochemical reaction. Therefore if during reduction the final proton transfer rate is slower than the first, it would be reasonable to assume that during the faster (i.e. $1\,Vs^{-1}$) CV sweep, the EC process will predominately be confined to with the boxed area shown in Figure 6.12. The oxidation sweep would therefore demonstrate a relatively large oxidation peak (*wave III*) at $E^{2}_{p,a}$ which represents the oxidation of $Fl_{red}H^{-} \xrightarrow{-e^{-}} Fl_{rad}H^{\bullet}$ as shown in Figure 6.10(b). During a slower CV sweep (i.e. $0.1\,Vs^{-1}$) the 2nd proton transfer process $Fl_{red}H^{-} \xrightarrow{H^{+}} Fl_{red}H_2$ would have both longer to deplete the concentration of $Fl_{red}H^{-}$ during the reductive sweep but also longer to form the radical $Fl_{rad}H^{\bullet}$ through the comproportionation reaction $Fl_{ox} + Fl_{red}H_2 \leftrightarrow 2\times Fl_{rad}H^{\bullet}$. This would produce larger oxidation peak (*wave II*) at $E^{1}_{p,a}$ and a smaller oxidation peak at (*wave III*) at $E^{2}_{p,a}$. In other words during the slower sweep rate the EC reaction would effectively bypass the redox step at E^{θ}_{2} through a comproportionation reaction between $Fl_{red}H_2$ and $Flox$. The region between these two CV peaks may therefore become blurred according to the availability of proton sources other than the surrogate fumaramide axle as this would allow an increase the concentration of the fully reduced flavin $Fl_{red}H_2$. We would suspect that during the follow-up voltammetry moisture may have contaminated the original sample and somehow contributed as a proton source.

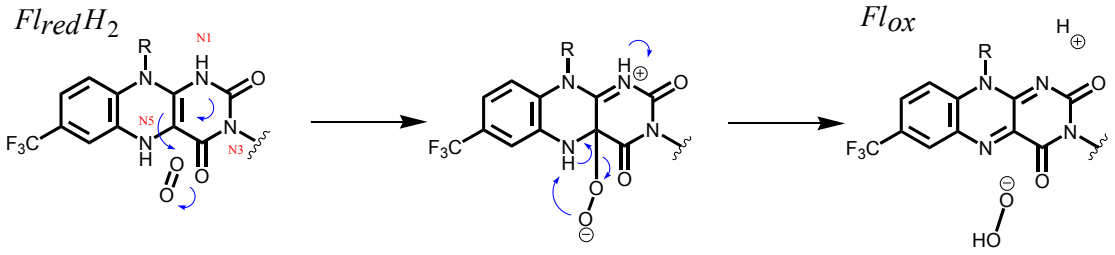

Figure 6.11 Oxidation of the fully reduced flavin $Fl_{red}H_2$ by a molecule of oxygen to form the neutral flavin oxide Fl_{ox} and hydrogen peroxide. Revised from reference [66].

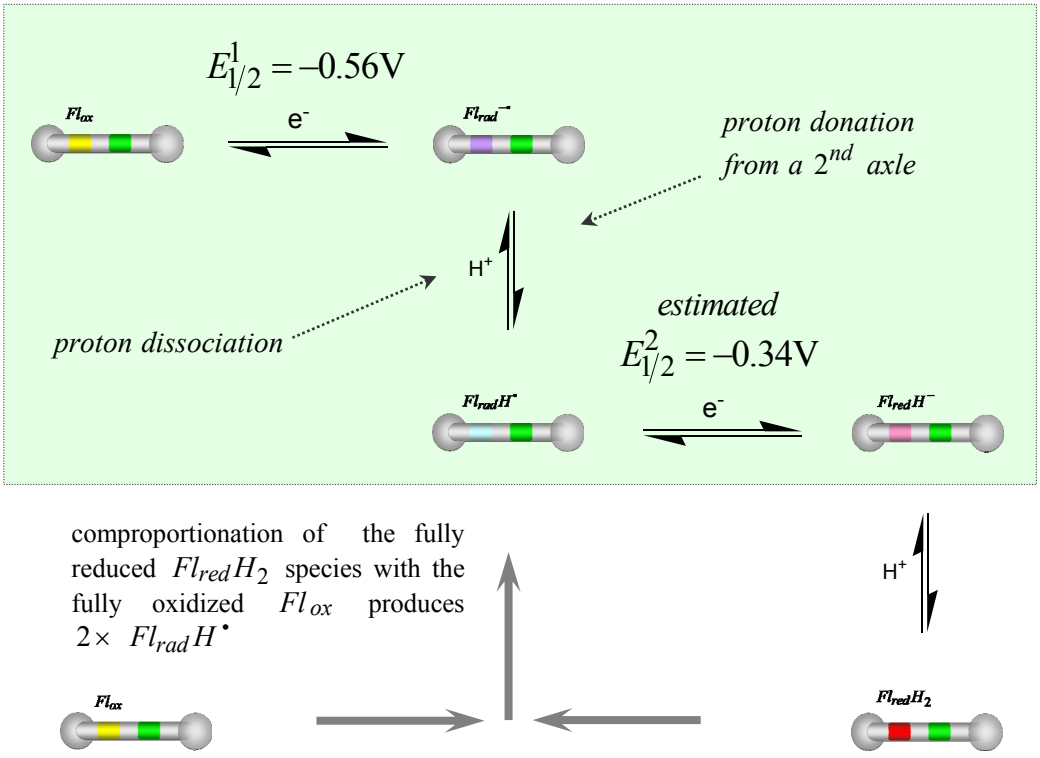

Figure 6.12 Proposed electrochemical scheme for the flavin-fumaramide axle. The ability of the flavin to accept a second electron is only possible once the flavin radical has adopted a more positive charge from a chemical reaction such as a proton (H^+) transfer. In aprotic solvent this has been shown to come from a second neutral Fl_{ox} molecule. The faster CV is confined predominately to the pathways in the *green* box whereas the slower CV would proceed though a comproportionation reaction following a second proton transfer.

6.4.4 *Reverse direction SW voltammograms for the axle.*

The final piece of evidence which support this comes from SWV of the original sample but with the direction of scan reversed. This type of SW scan has previously been used provide further useful information regarding the electrochemical mechanism. The reasoning behind this method is that by maintaining the electrode at a high negative potential allows the accumulation of reduced species at the surface. The oxidation process starts only when the forward SW pulse becomes more positive than E_1^{θ}. Up to this point there would have been a continual reduction of $Fl_{ox} \longrightarrow Fl_{rad}^{\bullet -} \longrightarrow Fl_{red}H^{-}$ etc., and the forward SW pulse would only now begin to reverse this process. The response differences observed during subsequent forward and reverse components of the SWV must therefore be derived from (i) a high concentration of reduced species at the electrode species, (ii) the low concentration of oxidized species and (iii) perhaps most importantly, the sequence order in which the SW pulses perform the oxidation/reduction reactions as the step voltage progressively becomes more positive.

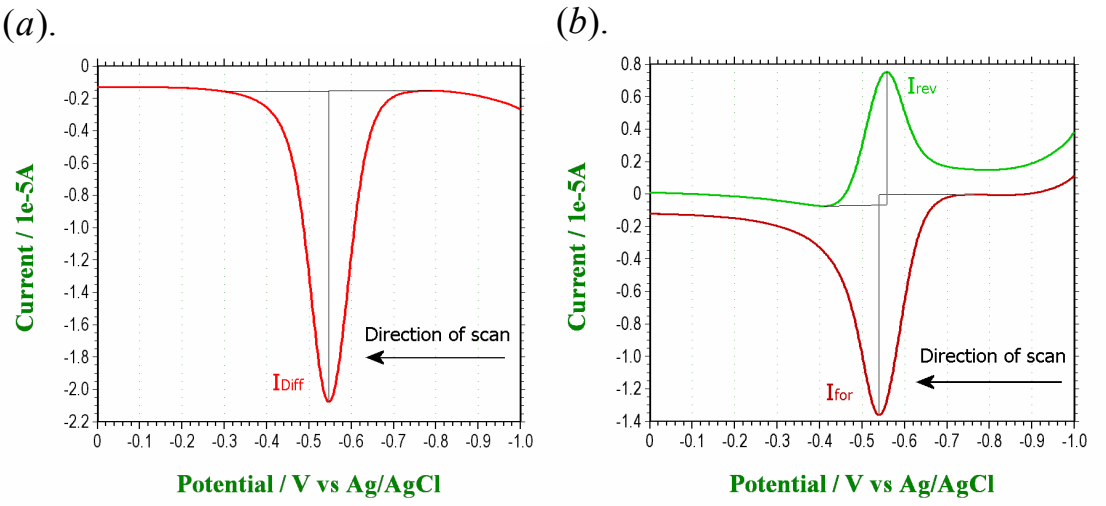

Figure 6.13 Square Wave voltammogram (SWV) for the flavin-fumaramide axle with direction of scan from -1 to 0V (a) the overall response (I_{Diff}) and (b) the forward (I_{for}) and reverse (I_{rev}) responses. Other SW parameters $E_{SW} = 0.025\text{V}$, $E_{step} = 0.002\text{V}$, $SW_{freq} = 25\text{Hz}$ and accumulation period $E_{accum} = 10\,\text{sec}$.

With regards to the flavin-fumaramide axle however, we only observe a single peak overall response (I_{Diff}) during the direction of scan from $-1 \rightarrow 0\text{V}$ as shown in Figure 6.13(a). This corresponds to a single large oxidative forward (I_{for}) SW response at approx -0.54V and a smaller reverse (I_{rev}) response which appears at approx -0.56V (i.e. it occurs first in the direction of scan). The larger I_{for} response we can only attribute to the oxidation of $Fl_{rad}^{\bullet -} \longrightarrow Fl_{ox}$ since this is the only possible oxidation process which can occurs at this potential. If as described earlier the formal potential E_2^{θ} is approximately -0.34V then oxidation of $Fl_{red}H^{-} \longrightarrow Fl_{rad}^{\bullet -}$ will only take place at potentials more positive than E_2^{θ} and we would observe a separate second forward response peak much later during the scan. Yet this is the only oxidation peak that we observe. It is also much larger than expected since we would anticipate that the predominant species at the electrode to now be $Fl_{red}H^{-}$ and/or $Fl_{red}H_2$. The concentration of $Fl_{rad}^{\bullet -}$ at the electrode surface should in fact be low in

comparison to $Fl_{red}H^-$ and the reduction reaction $Fl_{ox} \longrightarrow Fl_{rad}^{\bullet -}$ will by now be diffusion limited. The large response however reveals a high concentration of the radical anion. This could be explained easily by the comproportionation reaction pathway shown below in Figure 6.14 which produces two equivalents of the radical $Fl_{rad}H^{\bullet}$.

The smaller I_{rev} response we attribute to the reduction of the species $Fl_{ox} \longrightarrow Fl_{rad}^{\bullet -} \longrightarrow Fl_{red}H^-$. The reduction pathway followed is essentially identical to that shown previously in Figures 6.8. The response is small because the concentration of Fl_{ox} is low and only being replenished by the diffusion gradient and the previous oxidation SW pulse. As the SW step potential becomes increasingly positive this reverse SW pulse reduction process diminishes while the forward SW pulse oxidation process $Fl_{rad}H^{\bullet} \xrightarrow{-(H^+ + e^-)} Fl_{ox}$ continues to be fed by the comproportionation reaction. Although the SW voltammogram performs oxidation/reduction reactions over the smaller timescale of the SW pulse, it does in reality take longer to perform the SW scan given the parameters used (i.e. with $SW_{freq} = 25\text{Hz}$ and $E_{\text{step}} = 0.002\text{V}$ the scan from $-1 \rightarrow 0\text{V}$ takes $(0.002 \times 25)^{-1} = 20\,\text{s}$. In comparison the CV at the slower sweep rate 0.1Vs^{-1} takes 10 s to go from $-1 \rightarrow 0\text{V}$ during the oxidation sweep. Using this same argument we suggest that by the time the SW step potential has reached the formal potential $E_2^{\theta} = -0.34\text{V}$ the remaining flavin anion $Fl_{red}H^-$ would have been protonated and re-oxidized via this alternative pathway. This therefore explains the absence of an equivalent redox peak at -0.34V during SWV since the comproportionation pathway would have essentially depleted the electrode concentration of $Fl_{red}H_2$.

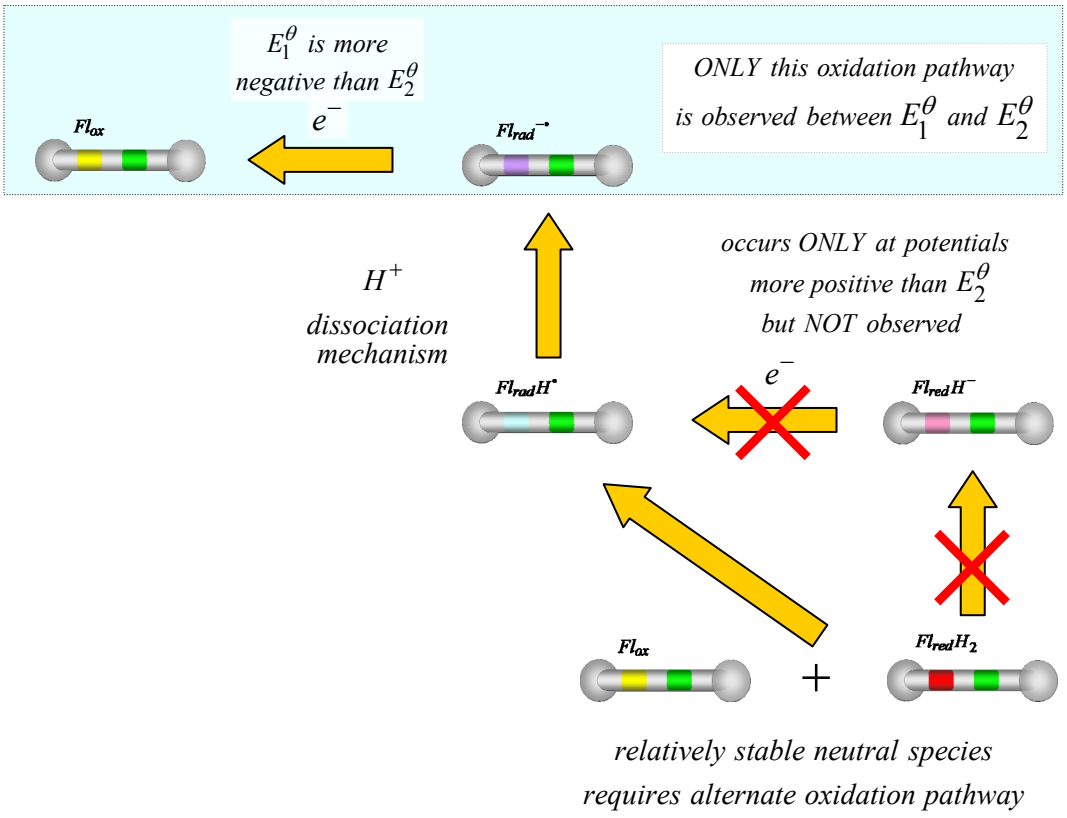

Figure 6.14 **Oxidation pathway**. The separation between formal potentials E_1^{θ} and E_2^{θ} is greater than twice the amplitude of the SW pulse (i.e $E_{SW} = 25\text{mV}$) therefore the reoxidation of $Fl_{red}H^-$ is unable to take place. The reoxidation process here is therefore confined to the pathways within the *blue* box.

The CV and SWV results for the flavin-fumaramide axle are summarized below in Table 6.1.

(*a*).

Sweep Rate (Vs^{-1})	CV Results (Volts)					
	1st electron transfer				2nd electron transfer	
	$E_{p,c}$	$E_{p,a}$	ΔE	$E_{1/2}$	$E_{p,a}$	$E_{1/2}$
0.1	-0.587	-0.513	-0.074	-0.55	-0.31	-0.34*
1	-0.622	-0.497	-0.125	-0.56	-0.27	-0.34*

* estimated using $\Delta E = (E_{p,c} - E_{p,a})$ from 1st electron transfer

(*b*).

Direction of scan	SWV Results (Volts)		
	$E_p(I_{Diff})$	$E_p(I_{for})$	$E_p(I_{rev})$
0 to -1V	-0.552	-0.560	-0.542
-1 to 0V	-0.546	-0.540	-0.558

Table 6.1 Comparison of (a). the CV half wave potential $E_{1/2}$ with (b). the SWV peak position results for the flavin-fumaramide axle. Peak positions for I_{Diff} response during direction of scan from 0 to -1V (-0.552V) and -1 to 0V (-0.546V) are in close agreement with the CV average $E_{1/2} = -0.555$V .

6.4.5 Cyclic voltammetry for the [2]rotaxane in DCM / DMF (98:2).

The cyclic voltammogram for the flavin-fumaramide [2]rotaxane (*blue line*) is shown in Figure 6.15. A comparison with the axle (*red line*) shows a slight decrease in the cathodic (reductive) peak (*wave I*) at $E_{p,c} = -0.529\text{V}$ and a main anodic (oxidation) peak (*wave II(r)*) at $E_{p,a} = -0.312\text{V}$. The cathodic peak (*wave I*) can therefore be attributed to the reduction of the non-macrocycle bound flavin $Fl_{ox} - [fum]$ whereas the main anodic peak (*wave II(r)*) can be attributed to the oxidation stabilized macrocycle bound flavin $[Fl_{rad}^{\bullet -}] - fum$ (see footnote). The label *wave II* is used to indicate where the [2]rotaxane flavin species $Fl_{rad}^{\bullet -}$ would become oxidized were it not bound and stabilized by the BA macrocycle. The absence of this peak would suggest that translocation onto the reduced flavin is fast and effective within the timescale of the voltammogram. The Randles-Sevcik equation[61, 62] was used in Chapter 5 to explain the decrease in cathodic peak height with regards to the pseudorotaxane. The rotaxane molecule would diffuse slower and the resulting peak current would reflect the $\sqrt{D}$ relationship of the larger molecule. Depletion of the oxidized species close to the electrode surface would be achieved much earlier. This resulted in the cathodic peak being observed slightly earlier during the sweep giving the appearance of an anodic shift. However this may be only part of the explanation here as the leading slope of the cathodic peak has unquestionably moved more positive. At the moment the reason for this is undetermined but it is undoubtedly related to some interaction between the BA macrocycle and the flavin. Whether this is due to the macrocycle partial hydrogen bonding with both flavin oxide and fumaramide, which leads to an easier reduced species, still needs to be investigated.

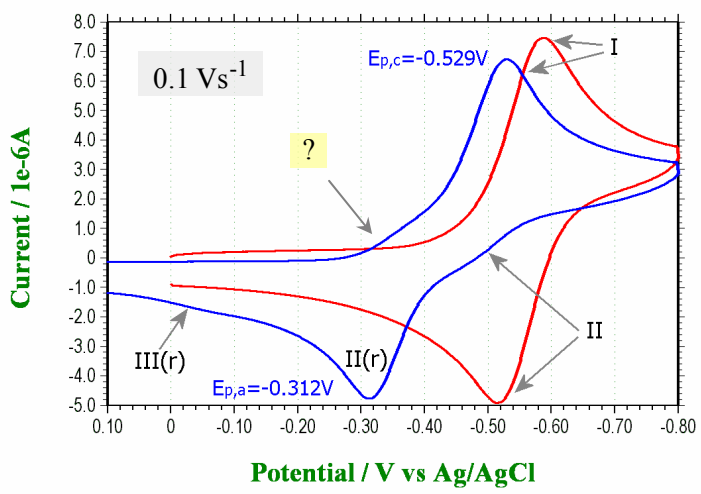

Figure 6.15 Cyclic voltammogram (CV) for the flavin-fumaramide [2]rotaxane (*blue line*) at a sweep rate $\upsilon = 0.1\text{Vs}^{-1}$. CV for the axle (*red line*) at the same sweep rate is shown for comparison.

Note: Continuing the text methodology employed to describe the axle, the fumaramide component will still be depicted as "*fum*" while the location of the macrocycle on the axle will be symbolized here by the square red brackets [ ].

If we re-examination of the CV in Figure 6.15 we see the presence of weak oxidation peak (*wave III*(r)). This peak increases in comparative magnitude to the main oxidation peak (*wave II*(r)) when the CV sweep rate is increased to $\upsilon = 1\ \mathrm{Vs}^{-1}$ as shown in Figure 6.16. The rotaxane therefore demonstrates the same redox behaviour which was observed with the axle in that the $[Fl_{red}H^-]$ species of the rotaxane remains stable enough during the faster sweep rates to undergo re-oxidation process $[Fl_{red}H^-] \xrightarrow{-(H+e)} [Fl_{rad}{}^{\bullet -}] \xrightarrow{-e} [Fl_{ox}]$ and thereby produces a significant redox peak at *wave III*(r). During the slower sweep rate this again becomes bypassed and undergoes the comproportionation reaction $[Fl_{red}H_2] + Fl_{ox}$ to produce $[Fl_{rad}{}^{\bullet -}] \times 2$. The comproportionation reaction may also be hindered slightly by the macrocycle which could also perform the role of a steric shield to proton transfer. This might explain why *wave III*(r) of the rotaxane is more visible than the corresponding *wave III* of the axle under the same preparation conditions. Theoretically although the amide's of BA macrocycle could act as proton source, these hydrogen's would be strongly bound to the carbonyls either of the fumaramide or the flavin radical anion.

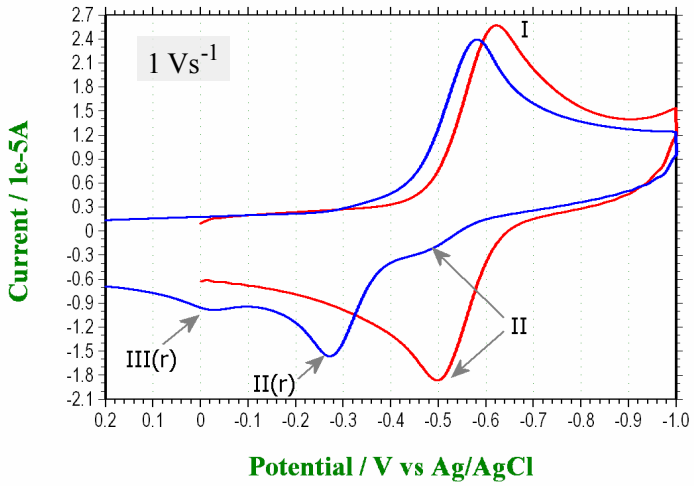

Figure 6.16 Cyclic voltammogram (CV) for the flavin-fumaramide [2]rotaxane (*blue line*) at a sweep rate $\upsilon = 1\ \mathrm{Vs}^{-1}$. CV for the axle (*red line*) at the same sweep rate is shown for comparison.

6.4.6 Square Wave voltammetry for the rotaxane in DCM / DMF (98:2).

SWV scan direction from $0 \rightarrow -1\text{V}$**.**

The overall SWV response (I_{Diff}) for the rotaxane when the direction of the scan is from $-1 \rightarrow 0\text{V}$ (*vs* $Ag/AgCl$) is shown in Figure 6.17(a). The response depicts a large redox peak at approx -0.52V and a smaller peak at approx -0.34V. The most reasonable explanation for this is that the [2]rotaxane exists in one of either two statistically different co-coformational distributions. The larger *peak B* can be attributed to a co-conformation where the macrocycle is predominately located over the stronger hydrogen binding fumaramide station (i.e. $Fl_{ox}-[fum]$). The weaker *peak A* can then be attributed to smaller co-conformational population where the macrocycle demonstrates hydrogen bonding interaction with the flavin station (i.e. $[Fl_{ox}]-fum$). One strikingly obvious difference with the CV's shown in the previous section is that we observed no significant redox wave corresponding to this smaller SWV *peak A*. However closer examination of the CV in Figure 6.15 at the slower sweep rate $v = 0.1\text{Vs}^{-1}$ (as highlighted by the question mark) reveals a subtle gradient increase during reductive sweep in the region between approx -0.29 and -0.43V before increasing abruptly to produce the main cathodic peak. This is less noticeable during the faster sweep voltammogram (i.e. $v = 1\text{Vs}^{-1}$). However, if we now examine the I_{for} and I_{rev} components which make up the SWV overall response and shown separately in Figure 6.17(b) we observe a similar gradient increase during the forward response I_{for} between approx -0.26 and -0.4V (i.e. shifted approx $+25\text{mV}$ by the SW amplitude E_{SW}). In fact the smaller peak in the overall response is only defined by the distinctive reverse response I_{rev} minimum at -0.31V which we attribute to the oxidation of the rotaxane co-conformation $[Fl_{rad}{}^{\bullet -}] \xrightarrow{-e} [Fl_{ox}]$. We must therefore conclude that this small redox peak would have gone unnoticed were it not for the sensitivity of SWV.

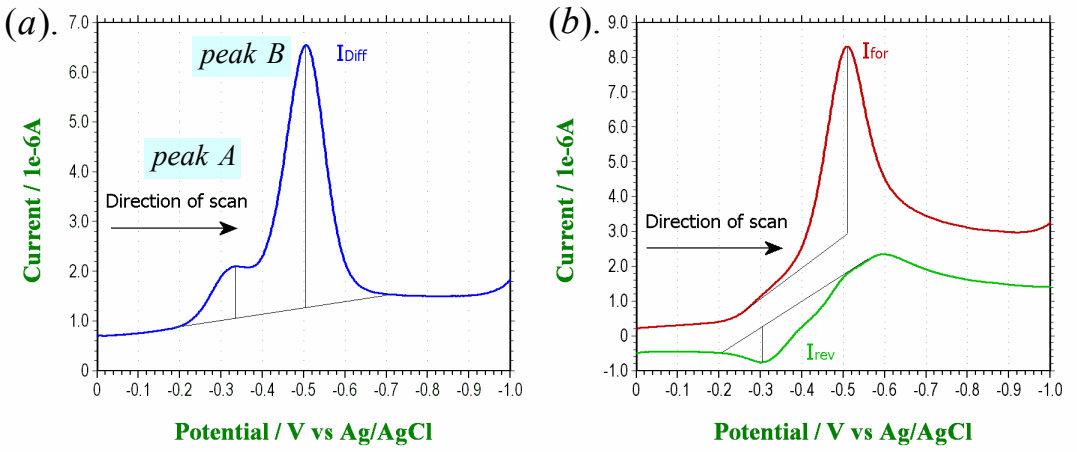

Figure 6.17 Square Wave voltammogram for the flavin-fumaramide pseudorotaxane with direction of scan from 0 to -1V (a) the overall response (I_{Diff}) and (b) the forward (I_{for}) and reverse (I_{rev}) responses. Other SW parameters $E_{SW} = 0.025\text{V}$, $E_{step} = 0.002\text{V}$ and $SW_{freq} = 25\text{Hz}$.

We will start by describing the reduction and oxidation pathways shown in Figures 6.18 and 6.19 respectively which produce the smaller SWV *peak A*. They are based on the BA macrocycles ability to stabilize the radical anion $[Fl_{rad}{}^{\bullet-}]-fum$ which will ultimately be oxidized at a more positive redox potential compared to the non-macrocycle bound flavin radical $Fl_{rad}{}^{\bullet-}-[fum]$. The reduction process shown in Figure 6.18 depicts the forward SW pulse just as it becomes more negative than E_3^θ, the formal potential of the $[Fl_{ox}] \overset{e}{\rightleftharpoons} [Fl_{rad}{}^{\bullet-}]$ electron transfer. Note that alternative pathways for the rotaxane have been shaded out as they are considered irrelevant at this stage, but still provide an overall process. Maximum concentration changes will occur at approximately E_3^θ and therefore it is around this potential that we start to observe the increased forward SW response. We would not expect to observe a redox peak at E_4^θ, the formal potential of the $[Fl_{rad}H^\bullet] \overset{e}{\rightleftharpoons} [Fl_{red}H^-]$ electron transfer, which would typically occur at a more positive electrode potential. As the direction of scan progresses increasingly negative, the potential E_4^θ would have already come and gone.

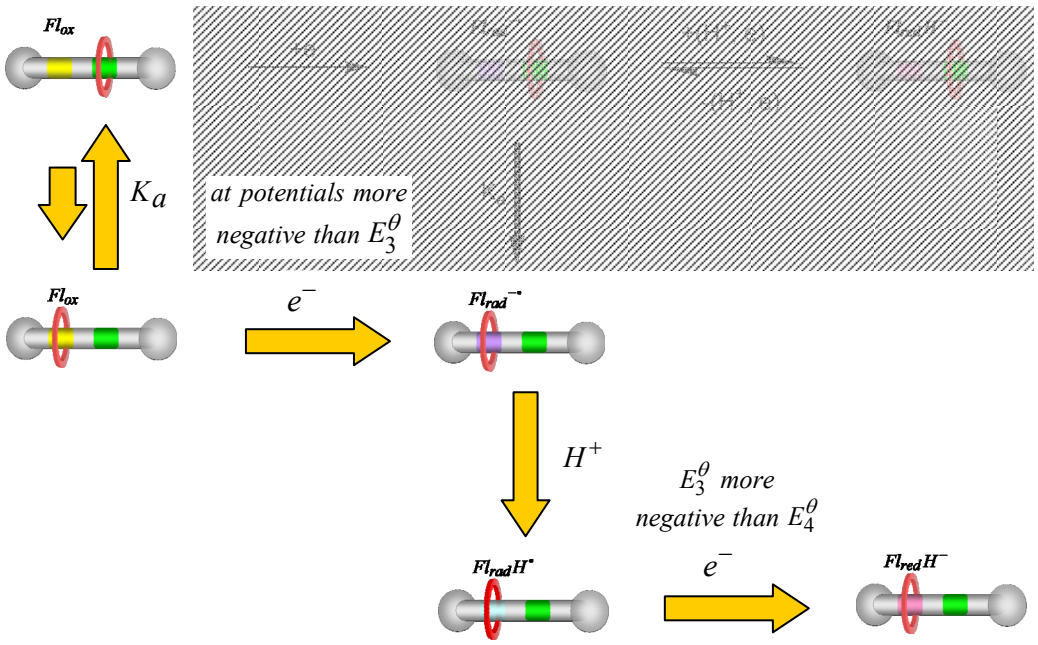

Figure 6.18 **Reduction pathway for "peak A"**: The population of the rotaxane co-conformation $Fl_{ox}-[fum]$ and $[Fl_{ox}]-fum$ is at equilibrium which favours the former. The species $[Fl_{ox}]-fum$ is easily reduced at potentials $\geq E_3^\theta$ to form the radical anion $[Fl_{rad}H^{\bullet-}]-fum$. Since $E_3^\theta \geq E_4^\theta$ this will undergo and further rapid reduction following a proton transfer to produce $[Fl_{red}H^-]-fum$. This will therefore continue to take place even if the reverse SW pulse is $\geq E_4^\theta$ but $< E_3^\theta$.

If the potential separation between E_4^θ and E_3^θ is greater than twice the SW pulse amplitude (i.e. $2\times E_{SW} = 50\text{mV}$), then the oxidation pathway shown in Figure 6.19 will in fact involve simultaneous oxidation $[Fl_{rad}{}^{\bullet-}]-fum$ and reduction of $[Fl_{rad}H^{\bullet}]-fum$. The reverse SW response I_{rev} which for a single electron transfer process would normally reach a minimum (i.e. max negative response) at a potential more negative than E_3^θ will therefore appears early during the scan as the oxidation of $[Fl_{rad}{}^{\bullet-}]$ becomes competitively less relevant to the reduction process $[Fl_{rad}{}^{\bullet-}] \xrightarrow{H} [Fl_{rad}H^{\bullet}] \xrightarrow{e} [Fl_{red}H^{-}]$ which continues during both forward and reverse SW pulses.

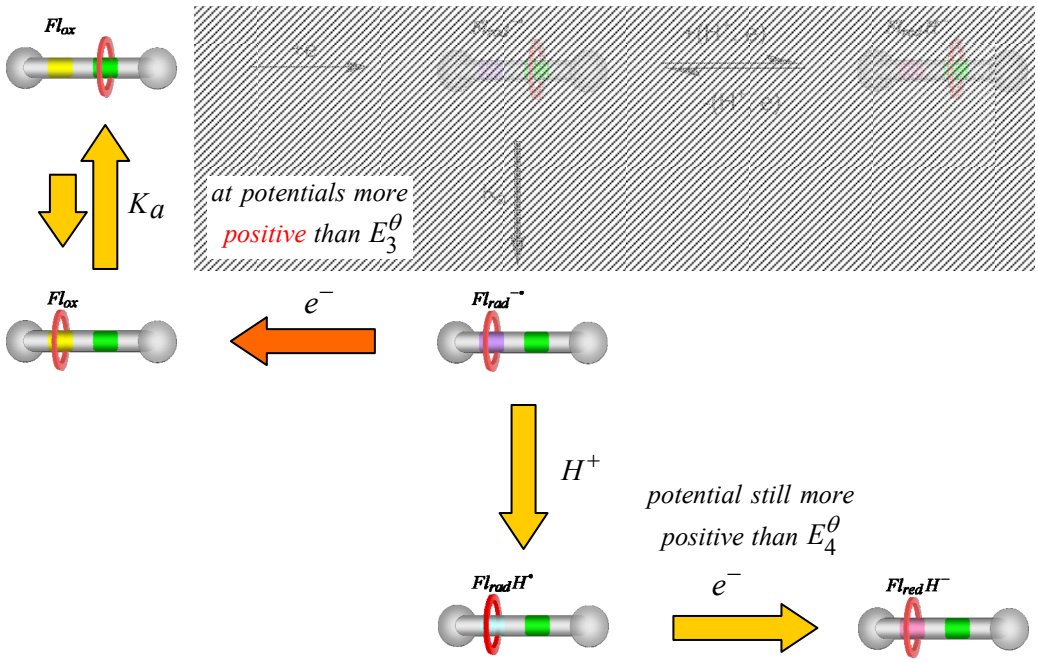

Figure 6.19 **Oxidation pathway for "peak A"**: Although both $[Fl_{rad}{}^{\bullet-}]-fum$ and $[Fl_{red}H^{-}]-fum$ rotaxane co-conformations are present during an oxidation SW pulse the oxidation of $[Fl_{red}H^{-}] \xrightarrow{-(H^{+}+e^{-})} [Fl_{rad}{}^{\bullet-}]$ only occurs at potentials more positive than E_4^θ. This oxidation pathway is unavailable if the SW pulse amplitude is less than half the potential difference between E_3^θ and E_4^θ. The reverse response will achieve a minimum somewhere between the potentials E_3^θ and E_4^θ as at one extreme insufficient $[Fl_{rad}{}^{\bullet-}]$ is produces and at the other extreme the potential is too negative to carry out oxidation.

We now turn our attention to the main peak of the SW response, *peak B*, Figure 6.17. Here we observed a large I_{for} response accompanied by what could be described as a grossly distorted I_{rev} response. With regards to the flavin-fumaramide axle, a weak I_{rev} minimum previously shown in Figure 6.13(b) had been determined as being due to the continued reduction of the flavin radical anion $Fl_{rad}^{\bullet -}$ to form the flavin anion $Fl_{red}H^{-}$ which occurs at a more positive redox potential following the proton transfer. However, the reverse SW response for the rotaxane is significantly more positive compared to the negative reverse SW response of the flavin-fumaramide axle. In order to illustrate how this might occur we need to look at two snapshots during a period of the SW pulse. First during the forward SW pulse as the electrode potential becomes more negative than the formal potential E_1^{θ} which is shown in Figure 6.20 and labelled the "reduction pathway of *peak B*" and then during the reverse SW pulse when the potential becomes more positive than E_1^{θ} as is shown in Figure 6.21 and labelled the "oxidation pathway of *peak B*". Again in both these figures, the area partially hidden by shading has been regarded as irrelevant.

Figure 6.20 shows the reduction pathway during the forward SW pulse as the potential just becomes more negative than the formal potential E_1^{θ}. The flavin oxide Fl_{ox} component of the rotaxane now becomes reduced to the flavin radical anion $Fl_{rad}^{\bullet -}$. Just as with the axle, since E_1^{θ} is more negative than E_2^{θ}, the non-macrocycle bound flavin $Fl_{rad}^{\bullet -}-[fum]$ could become further reduced at this stage following a proton transfer to form $Fl_{red}H^{-}-[fum]$. Alternatively it would seem more likely that the BA macrocycle will rapidly translocate from the fumaramide component of the axle to the now electron rich $Fl_{rad}^{\bullet -}$ thus forming the more stable $[Fl_{rad}^{\bullet -}]-fum$ rotaxane co-conformer. Translocation in other word forms an electrochemically irreversible product. Figure 6.20 also shows a simultaneous trickle background process going on where residual amounts of $[Fl_{ox}]-fum$ become reduced to $[Fl_{rad}^{\bullet -}]-fum$, etc,. The reduction overpotential for these macrocycle stabilized flavin species is already extremely large any change in SW pulse potential would have negligible effect on electron transfer rates.

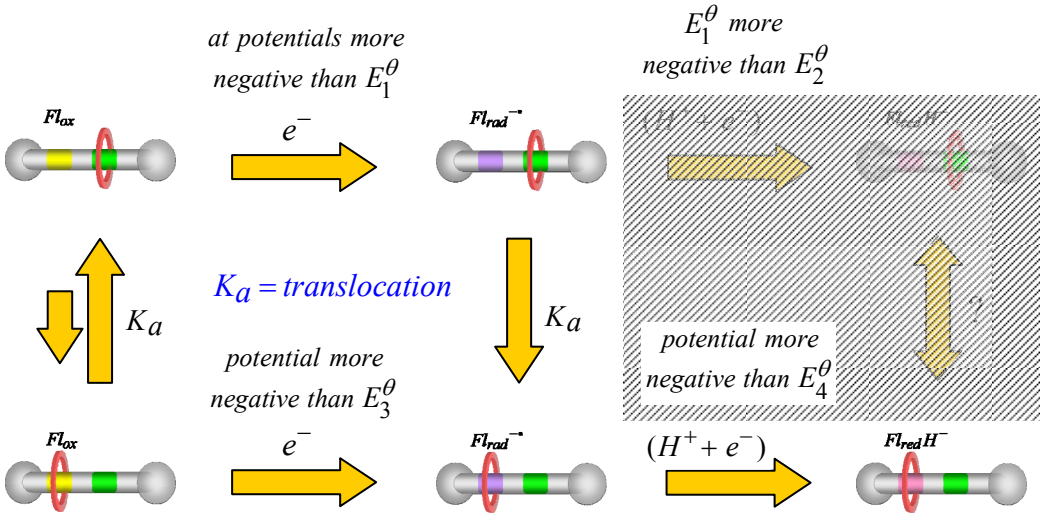

Figure 6.20 **Reduction pathway for "peak B"**: Reduction of both co-conformations $Fl_{ox}-[fum]$ and residual $[Fl_{ox}]-fum$ will take place at potentials more negative than E_1^{θ}. The redox product $Fl_{rad}^{\bullet -}-[fum]$ is most like to be followed by macrocycle translocation which would result in both pathway leading to the same co-coformational product, $[Fl_{rad}^{\bullet -}]-fum$. Subject to proton availability this species will be easily reduced to $[Fl_{red}H^{-}]-fum$ as E_1^{θ} is much more negative than both E_3^{θ} and E_4^{θ}.

This same trickle background process will therefore continue as shown in Figure 6.21 during the oxidation pathway of the reverse SW pulse when it becomes less negative than E_1^θ. The $[Fl_{ox}]-fum$ species continues to become reduced to form $[Fl_{rad}^{\bullet-}]-fum$ and then $[Fl_{red}H^-]-fum$ as the SW pulse potential is much more negative than E_3^θ and E_4^θ. However it will start to deplete any concentration build up near the electrode of $[Fl_{rad}^{\bullet-}]-fum$ which resulted through the translocation pathway. It must be remembered that the SW response is a result of the transient current that occurs in response to the current flowing to restore the concentration equilibrium for redox species that corresponds to that specific potential. During the subsequent forward SW pulse the reduction process must try to restore the previous concentration of $Fl_{rad}^{\bullet-}$ species. During the reverse SW pulse the reduction process continued with $[Fl_{rad}^{\bullet-}]\longrightarrow[Fl_{red}H^-]$ as a trickle "positive" current tries to restore the steady state equilibrium concentration. This hopefully illustrates the differences in how a positive reverse SW response $Irev$ can be achieved at this potential rather than the shallow negative "minimum" response that was observed for the flavin-fumaramide axle. At that time we attributed this shallow $Irev$ minimum to the electrochemically quasireversible oxidation of low concentrations of $Fl_{red}H^-$ (and $Fl_{rad}^{\bullet-}$) within the SW potential region between E_2^θ and E_1^θ. This pathway is unavailable to the rotaxane co-conformation $[Fl_{rad}^{\bullet-}]-fum$

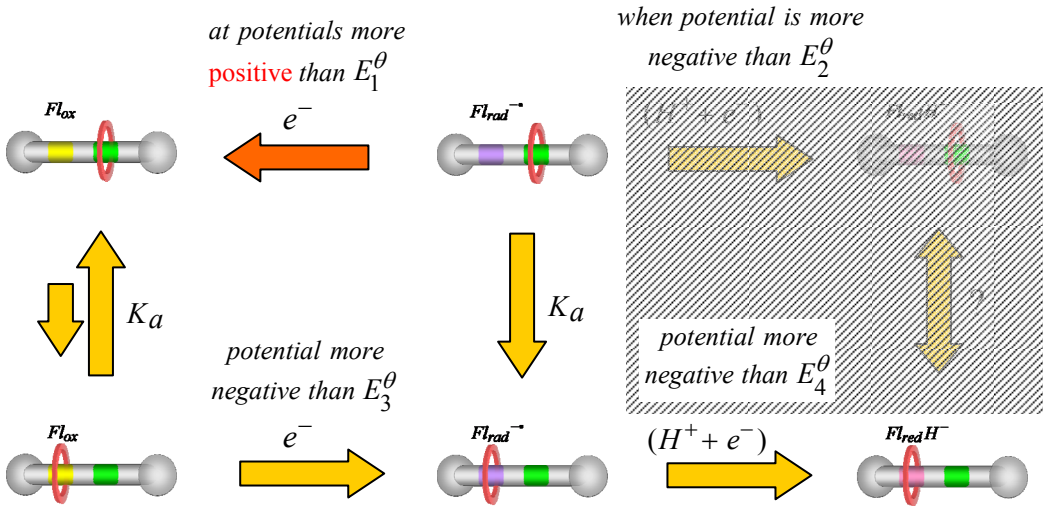

Figure 6.21 **Oxidation pathway for "peak B"**: This shows a continued reduction process taking place during the reverse SWV pulse even though the potential has now become more "positive" than E_1^θ.

6.4.6.1 SWV scan direction from $-1 \rightarrow 0\text{V}$.

The overall SW response (I_{Diff}) with the direction of scan from $-1 \rightarrow 0\text{V}$ ($vs\ Ag/AgCl$) is shown in Figure 6.22(a) and displays two main redox peaks at approximately -0.33V and -0.53V. The redox process for the second peak at -0.53V is most likely related to the oxidation/reduction of the non-macrocycle bound $Fl_{ox} \overset{e^-}{\rightleftharpoons} Fl_{rad}^{\bullet -}$. We did not observe any significant redox wave corresponding to this potential during the preceding rotaxane CV's. However closer examination of the SW responses I_{for} and I_{rev} shown in Figure 6.22(b) tells us that although both responses are weak, the main component of the I_{Diff} peak is the reverse current response I_{rev}. The forward response I_{for} is in fact very weak. Therefore the simplest answer which explains this peak -0.53V is that it is the irreversible reduction of the diffusion limited $Fl_{ox}-[fum]$ rotaxane.

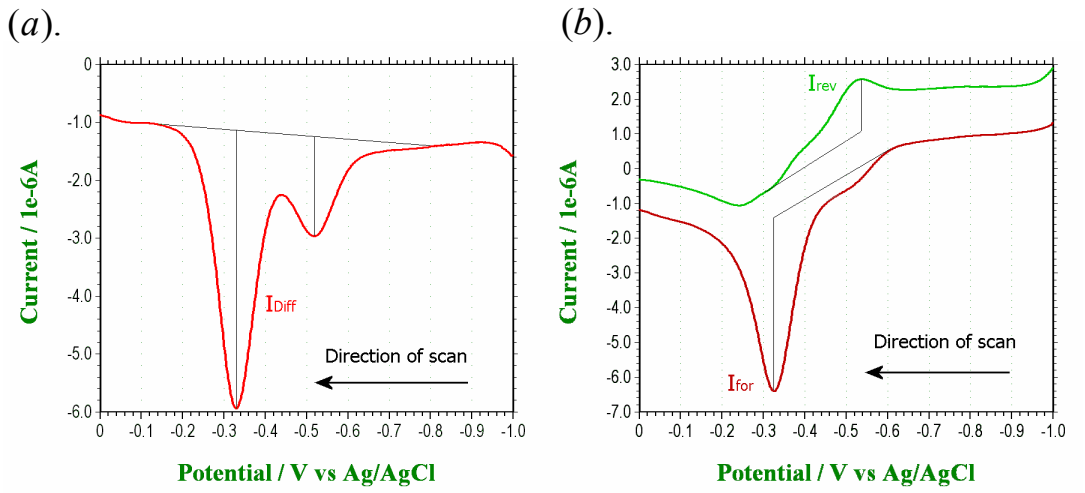

Figure 6.22 Square Wave voltammogram (SWV) for the flavin-fumaramide axle with direction of scan from -1 to 0V. (a) the overall response (I_{Diff}) and (b) the forward (I_{for}) and reverse (I_{rev}) responses. Other SW parameters $E_{SW} = 0.025\text{V}$, $E_{step} = 0.002\text{V}$, $SW_{freq} = 25\text{Hz}$ and accumulation period $E_{accum} = 10\text{sec}$.

The peak at -0.33V appears in the region of the rotaxane CV's 2nd oxidation peak ($wave\ II(r)$) previously observed in Figure 6.16 and most likely corresponds to the oxidation reaction $[Fl_{rad}^{\bullet -}]-fum \xrightarrow{-e^-} [Fl_{ox}]-fum$. By commencing the SW voltammogram at a high negative potential which has been paused at that potential for a short period to allow the accumulation of reduced species at the electrode provides us with useful information regarding the presence of stable quasireversible redox species that were not detected during the standard SW scan. The forward response tells us that the reduced rotaxane co-conformation is irreversibly oxidized at approximately $E_3^\theta = -0.3\text{V}$ (i.e. the forward response will peak at approx $E_3^\theta - E_{SW}$ where $E_{SW} = 25\text{mV}$). The non-existent reverse response confirms that the macrocycle has effectively shuttled back to hydrogen bond with the fumaramide component of the rotaxane within the time scale of the SW pulse. In doing so it has removed the stabilizing influence it had on the flavin.

There is no SWV evidence of an oxidation reaction at the even more positive redox potential E_4^θ which would correspond to the reduced flavin anion rotaxane co-conformation $[Fl_{rad}H^-]-fum \xrightarrow{-(H^++e^-)} [Fl_{rad}{}^{\bullet-}]-fum$. We identified a corresponding small anodic peak (*wave IV*) at approx $E_{p,a} = -0.01\,\text{V}$ during the faster sweep rate $v = 1\,\text{Vs}^{-1}$ as shown in Figure 6.1. The absence of this peak during the SWV can be explained again using the comproportionation reaction. The possible oxidation pathways at a potential just positive of E_3^θ for the accumulated fully reduced flavin rotaxane during a relatively slow voltammogram are shown in Figure 6.23. To discuss the figure we start at the co-conformation $[Fl_{red}H^-]$.

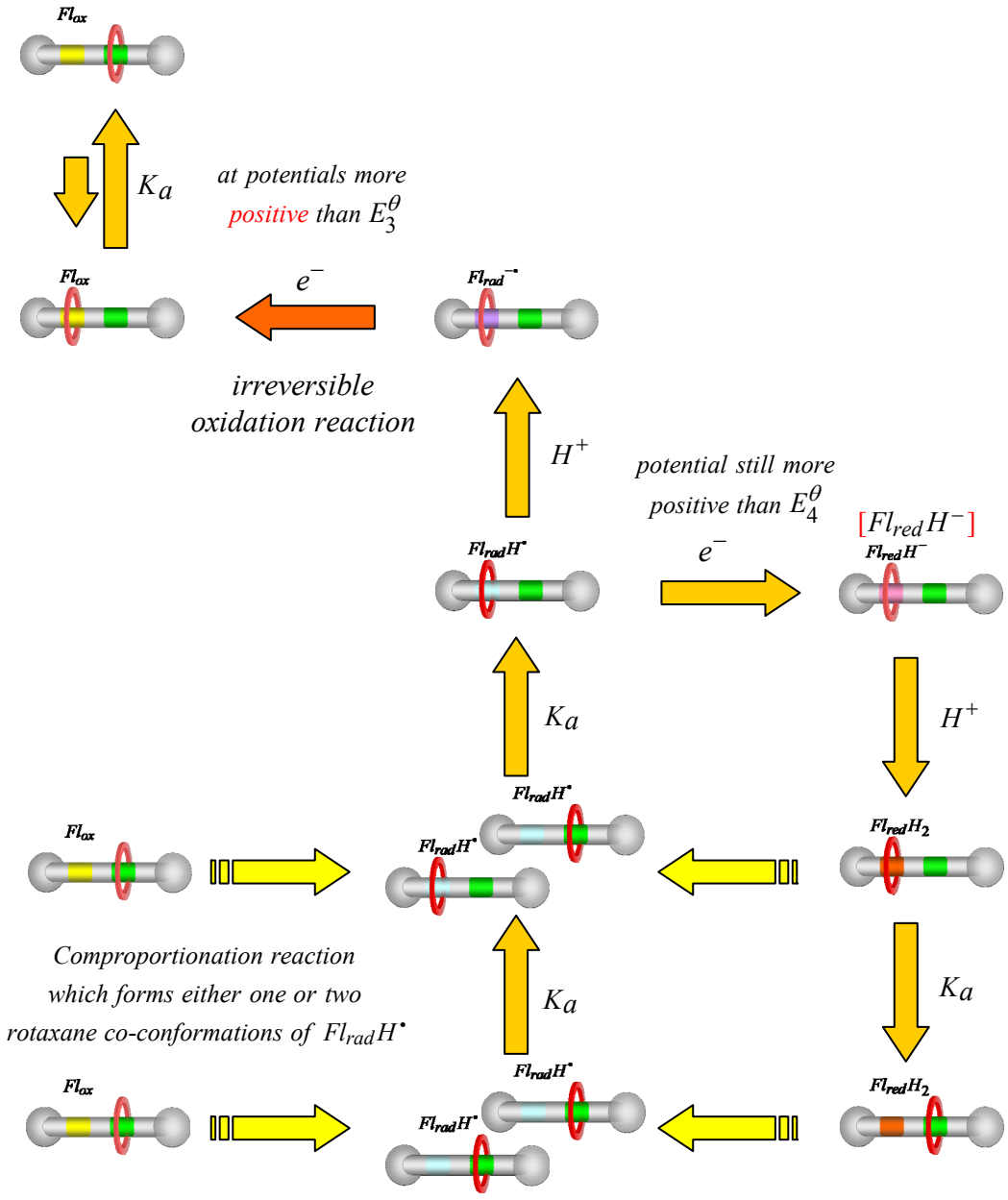

Figure 6.23 **Oxidation pathway for slow voltammograms**: Fully reduced flavin rotaxane that has accumulated at the electrode may exist as two possible co-conformations. Either of these may undergo the comproportionation reaction (yellow arrows) with another neutral flavin oxide. Any combination order of proton dissociation and macrocycle translocation results ultimately in the co-conformation $[Fl_{rad}{}^{\bullet-}]-fum$ which will undergo an electrochemically irreversible reaction at an electrode potential more positive than E_3^θ.

Although there is an accumulation of reduced flavin at the electrode the reduction reaction which produces $[Fl_{red}H^-]$ is still able to continue as the potential is still more negative than E_4^θ. The fully reduced flavin $Fl_{red}H_2$ is a less-aromatic neutral molecule which would most probably act as a poor hydrogen bonding station for the macrocycle. Therefore following the second proton transfer which produces $[Fl_{red}H_2]$ it would seem most likely that the macrocycle would shuttle from the neutral flavin to the stronger hydrogen bonding fumaramide station to form the co-conformation $Fl_{red}H_2-[fum]$. The non-macrocycle bound reduced flavin is probably more likely to interact with another non-macrocycle bound flavin oxide during the comproportionation reaction. As can be seen in Figure 6.23 the comproportionation reaction with the $[Fl_{red}H_2]-fum$ has also been displayed as shown by the yellow arrows. The predicted outcome from these reactions has been cautiously depicted as a pair of either identical or non identical co-conformations of the radical $Fl_{rad}H^\bullet$ and which would be defined by the starting co-conformation combination. Translocation may or may not be possible as this will depend on how effective the radical is as a binding site for the macrocycle. However proton dissociation will provide the flavin radical anion $Fl_{rad}^{\bullet -}$ which we know does effectively carry out this task. The final step therefore is the irreversible oxidation reaction which takes place at E_3^θ. As with the axle, this process provides a bypass mechanism for the reduction of the reduced anion $Fl_{red}H^-$. At a faster scan or sweep rate we would expect to observe a more pronounced redox wave at E_3^θ. This could be achieved during the SWV by using a higher SW frequency and/or a larger step potential E_{step}.

A summary of [2]rotaxane **C-52** CV results is shown below in Table 6.2. Rather than calculate a single half wave potential $E_{1/2}$ for irreversible redox reaction $Fl_{ox}-[fum] \overset{e}{\longleftrightarrow} [Fl_{rad}^{\bullet -}]-fum$ the system has been treated as two separate quasireversible reactions for rotaxane co-conformations $Fl_{ox}-[fum] \overset{e}{\longleftrightarrow} Fl_{rad}^{\bullet -}-[fum]$ and $[Fl_{ox}]-fum \overset{e}{\longleftrightarrow} [Fl_{rad}^{\bullet -}]-fum$. The peak separation obtained for axle **C-51** in Figures 6.5 and 6.6 have been used as a crude measure of determining the reversibility of the two rotaxane co-conformations by assuming that the cathodic and anodic peak separation would be similar at a given sweep rate. The half wave potentials $E_{1/2}(1)$ and (2) respectively correspond to the reduction of $Fl_{ox}-[fum]$ and oxidation of $[Fl_{rad}^{\bullet -}]-fum$. The half wave potentials $E_{1/2}(3)$ corresponds to the oxidation of $[Fl_{rad}H^{-}]-fum$.

Sweep Rate (Vs^{-1})	CV Results for [2]rotaxane **C-52** (Volts)						
	1st electron transfer					2nd electron transfer	
	$E_{p,c}$	$E_{p,a}$	ΔE	$E_{1/2}(1)$	$E_{1/2}(2)$	$E_{p,a}$	$E_{1/2}(3)$
0.1	-0.529	-0.312	-0.217	-0.49	-0.35	---	---
1	-0.581	-0.271	-0.310	-0.52	-0.33	-0.02	-0.08

Note:

$E_{1/2}(1)$ was estimated by subtracting the value $0.5\times\Delta E = 37\text{mV}@0.1\text{Vs}^{-1}$ and $62\text{mV}@1\text{Vs}^{-1}$ from the axle's 1st electron transfer from the cathodic peak potential $E_{p,c} = -0.529\text{V}$ and -0.581V.

$E_{1/2}(2)$ was estimated adding the value $0.5\times\Delta E = 37\text{mV}@0.1\text{Vs}^{-1}$ and $62\text{mV}@1\text{Vs}^{-1}$ from the axle's 1st electron transfer to the anodic peak potentials $E_{p,a} = -0.312\text{V}$ and -0.271V.

$E_{1/2}(3)$ was estimated adding the value $0.5\times\Delta E = 62\text{mV}@1\,\text{Vs}^{-1}$ from the axle's 1st electron transfer to the anodic peak potential $E_{p,a} = -0.02\text{V}$.

Table 6.2 Summary of cyclic voltammetry (CV) results for flavin-fumaramide [2]rotaxane **C-52** at sweep rates $v = 0.1$ *and* $1\,\text{Vs}^{-1}$.

6.4.7 Fumaramide electrochemistry.

The fumaramide analogue **C-53** shown in Figure 6.25 was synthesised using readily available chemical from our laboratory and designed in order to provide a comparative electroanalysis of the fumaramide component of the flavin axle compound. The cyclic voltammograms for **C-53** shown in Figure 6.24 reveal the fumaramide to be electrochemically fully irreversible (i.e. no oxidation peak observed) during sweep rates $\upsilon = 0.1$ and 1 Vs^{-1}. Two proposed electrochemical mechanisms based on the carbonyl radical formation are depicted in Figure 6.26. This shows how the fumaramide may undergo one, two electron, two proton transfer or alternatively two, one electron, one proton transfers. In an aprotic solvent the amines from a second fumaramide molecule may again operate as the main proton source. In the case of a BA [2]rotaxane the macrocycle may become an alternative source.

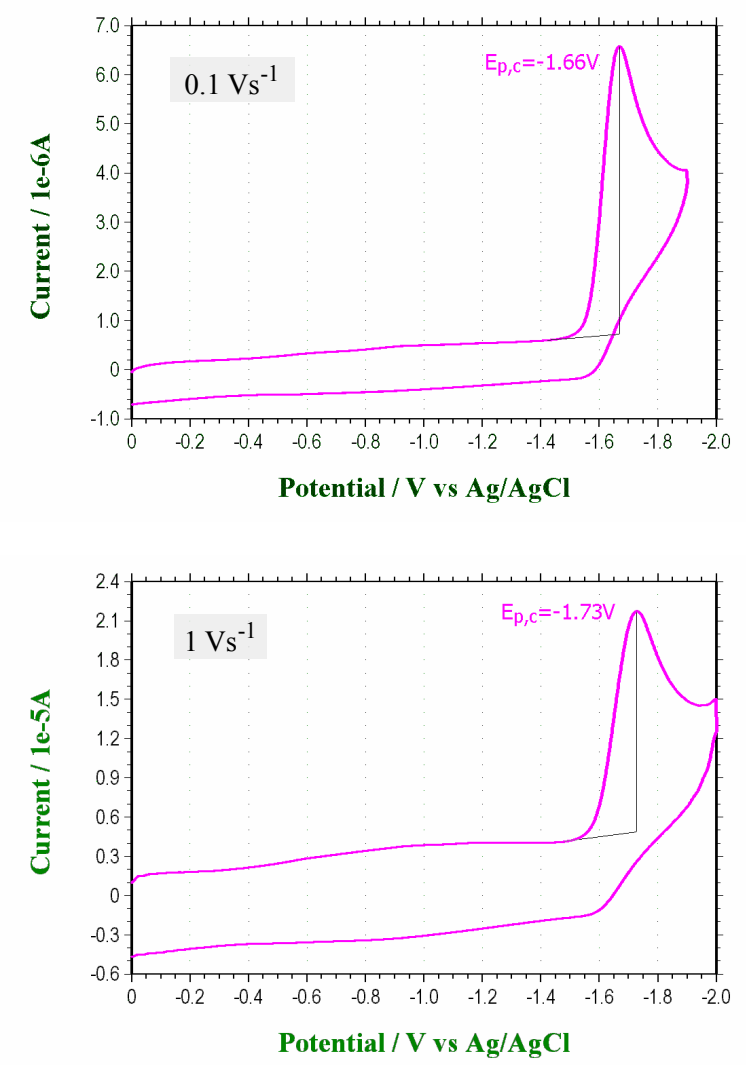

Figure 6.24 Cyclic voltammogram showing the electrochemically fully irreversible reduction of the fumaramide compound shown in Figure 6.1, at concentration 0.5mM in DCM with $0.1\,\text{M}\ \text{TBA}\cdot\text{PF}_6$ as the supporting electrolyte. Voltammogram were recorded at sweep rates: **(a)** $\upsilon = 0.1\ Vs^{-1}$ and **(b)** $\upsilon = 1\ Vs^{-1}$.

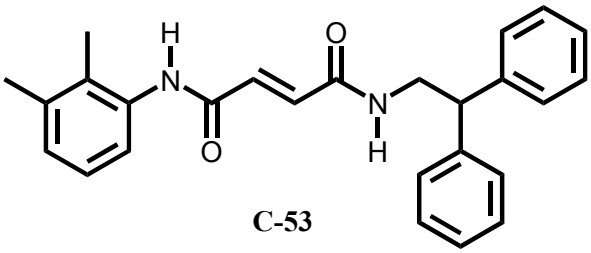

C-53

Figure 6.25 Compound N^1-(2,3-dimethylphenyl)-N^4-(2,2-diphenylethyl)fumaramide **C-53** was synthesised from readily available chemicals in the lab, in order to explore the electrochemical (and photochemical) properties of the fumaramide component of the axle and [2]rotaxane.

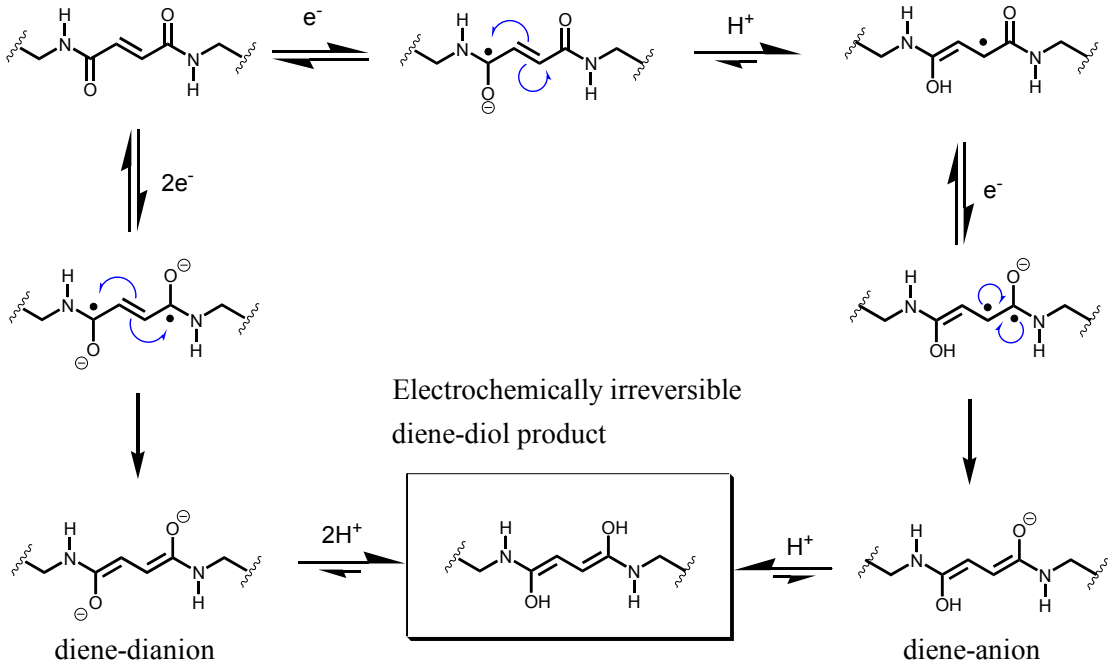

Figure 6.26 Proposed electrochemically induced isomerisation of the fumaramide component of the axle (and [2]rotaxane) following either a 2 electron and 2 proton transfer or two 1 electron, 1 proton transfers. This scheme is based on the principle of carbonyl radical formation.[65, 68]

It should also be pointed out that the reduced "fumaramide" just prior to the formation of the diene-diol product (i.e before proton transfer) may become a more favourable hydrogen bond acceptor and consequently stronger binding station for the benzylic amide macrocycle of the [2]rotaxane. Conformational rigidity between the two *trans* carbonyls may still be imposed through a delocalization process.

6.4.8 Cyclic voltammograms recorded at higher reduction potentials.

If the maximum reduction potential for the rotaxane CV sweep is increased (in the negative direction) from -1V (*blue line*) to -1.5V (*red line*) in steps of 0.1V as shown in Figure 6.27 we observe a significant increase in the magnitude of *wave III*(r). This is accompanied by a concomitant decrease in the oxidation *wave II*(r) and a small increase in the magnitude of oxidation *wave II*. This clearly suggests an increase presence of the rotaxane co-conformation $[Fl_{rad}H^{-}]-fum$, the oxidation of which results in the redox peak at *wave III*(r). We have already explained the increased presence of this redox peak during the faster sweep rate by suggesting that $Fl_{rad}H^{-}$ has capacity to competitively evade the slow 2nd proton transfer step and thus circumvent the comproportionation reaction. This further increase could therefore be explained either by the depletion of proton source (i.e. neutral fumaramide) thereby slowing down the 2nd proton transfer and/or a diminished concentration of flavin oxide Fl_{ox} though extended reduction at the electrode. The presence of Fl_{ox} would of course be required during the comproportionation reaction.

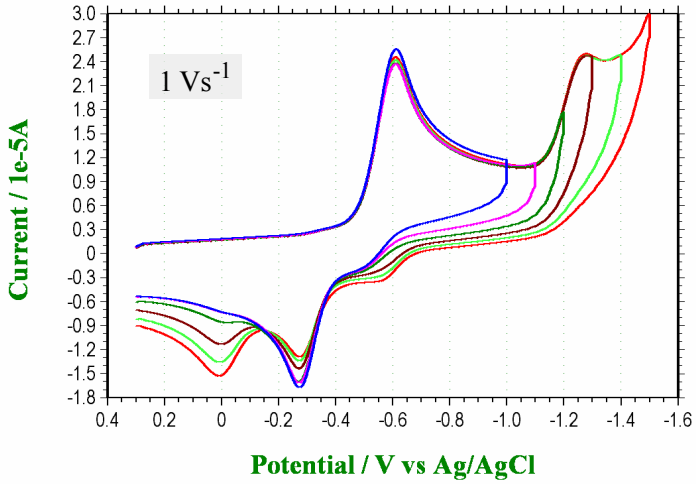

Figure 6.27 Cyclic voltammogram (CV) for flavin-fumaramide [2]rotaxane **C-52** (*blue line*) demonstrating increasing magnitude of oxidation *wave III*(r) with increasing maximum reduction potential from -1.0 *to* -1.5V.

The second cathodic peak at -1.3V is thought to correspond to the irreversible reduction of the fumaramide. This second cathodic peak however inexplicably occurs at approx 400mV less negative than that for the fumaramide analogue shown in Figure 6.24. We can rule out any stabilization effect induced by the BA macrocycle on the neutral fumaramide since, as we shall see later in Figure 6.30, the axle under similar conditions also shows this second cathodic peak at approx -1.3V (see Note). Nevertheless, as the potential therefore becomes increasingly negative the reduced "fumaramide" would be more likely to act as a proton acceptor rather than a proton source. We should also consider the possibility that $Fl_{red}H_2$ may become a less favourable binding station for the BA macrocycle than the neutral or reduced "fumaramide". The "fumaramide" dianion would certainly become a more favourable station due to the increased negative charge on the oxygen atoms. The co-coformation $[Fl_{red}H_2]-fum^{2-}$ would thus become transformed to $Fl_{red}H_2-[fum^{2-}]$. Without the steric shielding from the macrocycle the reduced flavin would more readily

undergo a comproportionation reaction in bulk solution to produce $Fl_{rad}H^{\bullet}-[fum^{2-}]$ and $Fl_{rad}H^{\bullet}-[fum]$. The later species could then undergo rapid translocation and transform to either $[Fl_{rad}^{\bullet-}]-fum$ plus a proton or $[Fl_{red}H^{-}]-fum$ following electron transfer. Oxidation of these species (including $Fl_{rad}H^{\bullet}-[fum^{2-}]$) would contribute individually to redox *waves* $III(r)$, $II(r)$ *and* II. The possibilities of intersystem proton transfer which would trigger axle-macrocycle fusing are obvious. The neutral fumaramide could act as a proton donor to the reduced macrocycle while the diene-dianion (i.e. reduced fumaramide) could act as a proton acceptor to neutral macrocycle. Evidence of ring fusing and the generation of a new species is perhaps displayed during the third segment of the CV (i.e. the immediately ensuing reductive sweep of the same *green line* voltammogram in Figure 6.29) which shows the oxidation peaks for both flavin and fumaramide both demonstrating extremely weak responses and which also appear to have shifted slightly more negative. The initial response can be recovered upon either tapping the electrode to refresh the diffusion layer or just by leaving it for a minute or two. Further work would need to be carried out in order to test these proposals.

As might be expected, for the same reasons discussed previously in subsection 6.4.6, the oxidation peak (*wave* $III(r)$) becomes much weaker when the CV is preformed at the slower sweep rate $v = 0.1\ \mathrm{Vs}^{-1}$ even when the reduction maximum is negatively increased to $-2\mathrm{V}$. The accumulated $[Fl_{red}H_2]-fum$ (or $Fl_{red}H_2-[fum]$) species have now longer to interact with the bulk Fl_{ox} via the comproportionation reaction pathway to form two radical cation of $[Fl_{rad}H^{\bullet}]$ which oxidize at the more negative redox potential corresponding to *wave* $II(r)$.

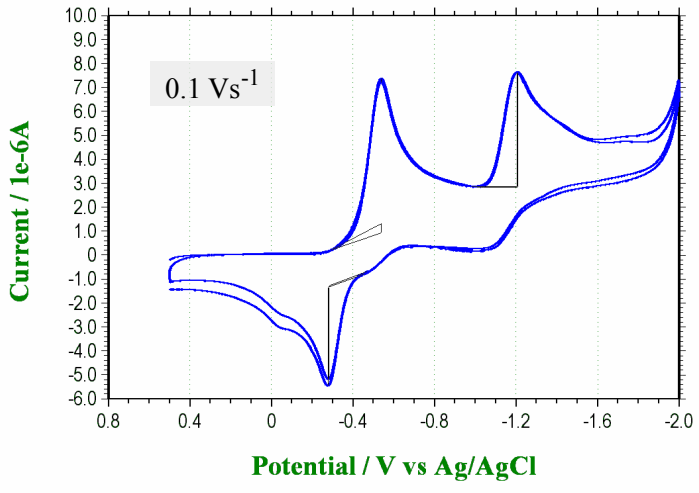

Figure 6.28 Cyclic voltammogram (CV) for flavin-fumaramide [2]rotaxane **C-52** at the slower sweep rate $\upsilon = 0.1\ \mathrm{Vs}^{-1}$ between $+0.5$ *and* $-2.0\,\mathrm{V}$.

Note: The author needs to confirm that this is not a $2e^{-}$ transfer to the flavin which produces the flavin dication Fl_{red}^{2-} and that the fumaramide redox wave is simply absent by consequence of an irreversible reduction process during earlier sweeps.

Conversely, as shown by Figure 6.29 (*green line*), if the reduction potential is elevated to -3V during the faster sweep rate of $1\,\text{Vs}^{-1}$, the oxidation peak (*wave IV*) disappears. Furthermore, during the same oxidation sweep the peak positions of *wave II* and *wave III* appear at a slightly more positive potential. The fully reduced flavin $Fl_{red}H_2$ has been reported as being less soluble than the flavin oxide and therefore liable to produce an impermeable film build up on the electrode surface, however the increased presence of oxidation peaks *wave II* and *wave III* confirms that *wave IV* 's absence cannot be caused by this. The absence therefore must involve a decrease in the concentration of $[Fl_{red}H^-]$. Before proposing an explanation for this, we refer the reader to a publication by Ceroni and Leigh [65] who describe in detail the electrochemistry for the benzylic amide [2]catenane, with comparisons to the macrocycle and its subcomponents. They suggested a fusing mechanism for the ring system which takes place following the $8e^-$ reduction and intersystem proton exchange. Using a similar mechanism we propose that the higher (-3V) reduction maximum produces the electroactive BA macrocycle radical anion which fuses with whatever binding partner it engages with at the time, either flavin or fumaramide. Fusing would require both axle and macrocycle components to simultaneously exist as radicals. Thus with regards to flavin radical formation (either $Fl_{rad}^{\bullet -}$ or $Fl_{rad}H^{\bullet}$) this would undoubtedly entail the comproportionation reaction.

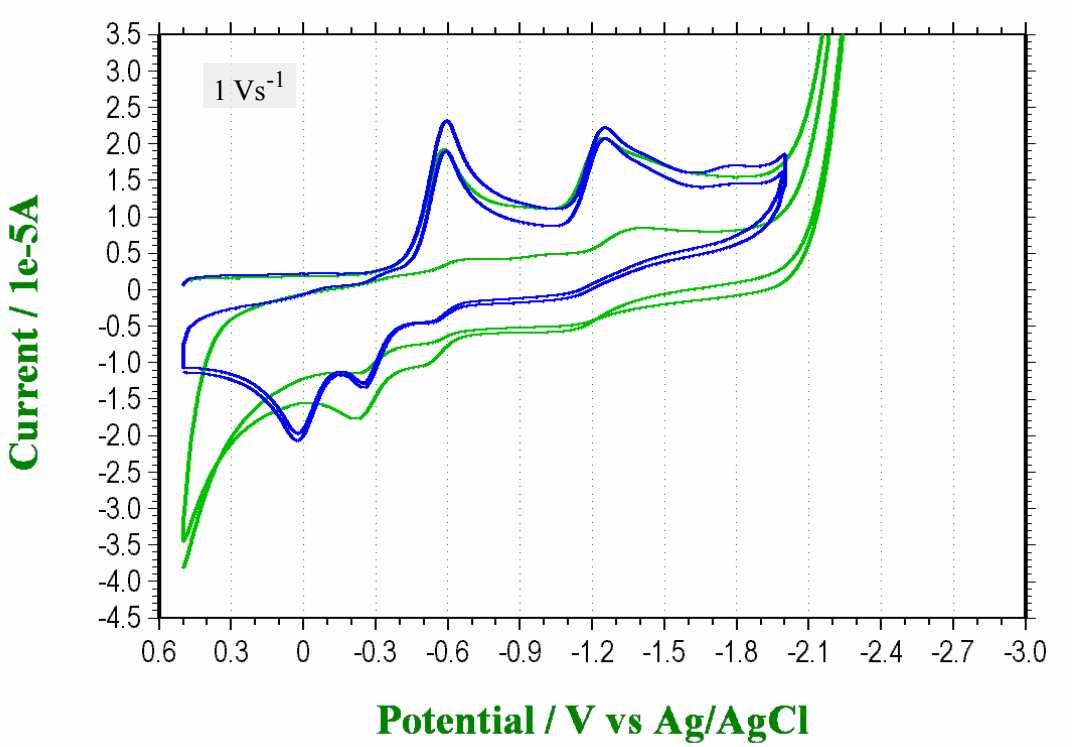

Figure 6.29 A four segment cyclic voltammogram for the flavin-fumaramide [2]rotaxane displaying electrochemical irreversibility (*green line*) during the third segment immediately following an elevated reduction potential of -3V. The four segment CV for the same [2]rotaxane under a maximum reduction potential of -2V (*blue line*) is shown for comparison.

Finally, for comparison, Figure 6.30 shows the four segment CV for axle **C-51** following an elevated reduction potential (*green line*). Note that this was recorded several days later using the original EC cell contents which had been left in the open air to evaporate. The sample was then re-dissolved at the original concentration in the same manner as previously described. The CV for axle **C-51** between $+0.5$ and -1 V is shown by the *red line* and the irreversible CV for the fumaramide analogue from Figure 6.24 by the *pink line*. Segment 3 for the *green line* CV shows significantly diminished cathodic waves for both flavin and "fumaramide" (refer to previous Note). Axle-macrocycle fusing is not an option here, and we are therefore only left with the possibility of flavin-fumaramide dimerization as an explanation. It is clearly obvious from the *red line* CV for the axle this process does not take place if the reduction potential is limited to -1 V. However, conversion of the fumaramide dianions formed at this higher negative potential into the stable dien-diol (shown in Figure 6.26) would deplete the diffusion layer close to the electrode of protons. This would have a knock-on effect during the subsequent reduction sweep (i.e. segment 3)

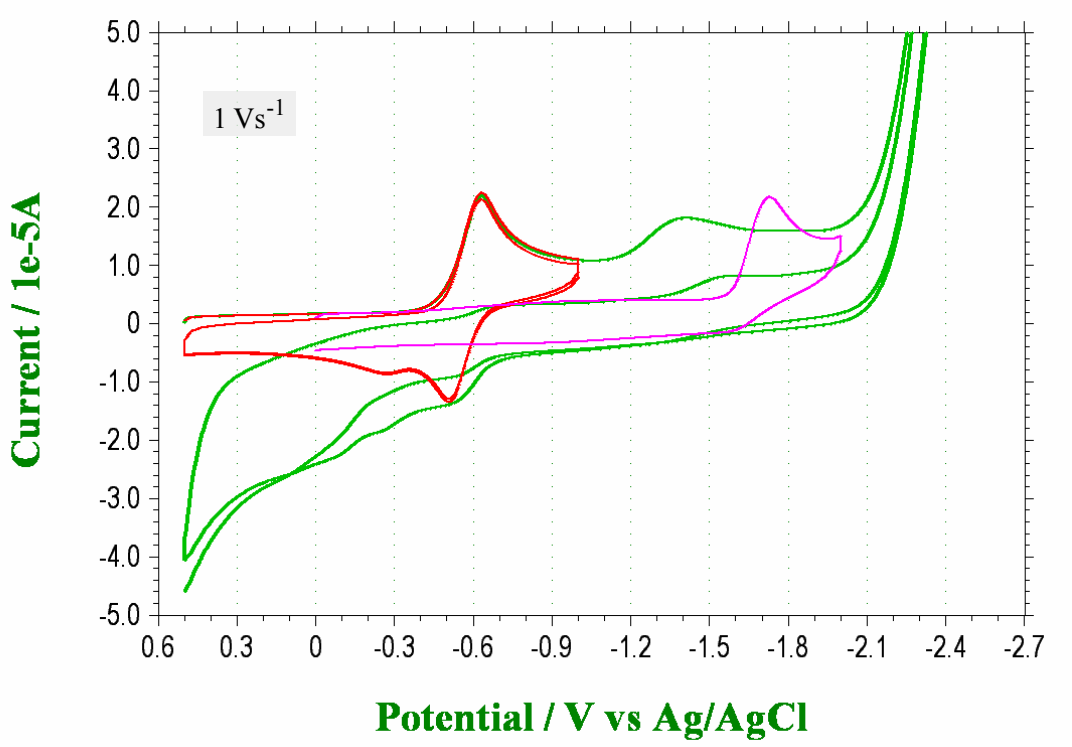

Figure 6.30 A four segment cyclic voltammogram for the flavin-fumaramide axle (*green line*) between $+0.5$ and -3 V showing the electrochemically irreversible reaction which is believed to be taking place via axle dimerization. Superimposed is the 4 segment CV for the axle (*red line*) between $+0.5$ and -1 V and the 2 segment CV for the fumaramide compound A (*pink line*) between 0 and -2 V. Sweep rate $\upsilon = 1$ Vs^{-1}.

6.5 Photochemistry.

6.5.1 Absorbance spectra.

The absorbance spectra for the axle and [2]rotaxane shown in Figure 6.31 display the two typical characteristic flavin band maxima. At *band I* = 439 nm the spectral overlap for both the axle and rotaxane is almost indistinguishable. The most noticeable difference can be found at *band II* = 315 nm for the axle and 322 nm for the rotaxane where there is also a significant increase in absorbance, These latter two peaks appear better defined in Figure 6.32 when the concentration used was 1×10^{-4}M. The absorbance spectra of the benzylic amide macrocycle previously shown in Chapter 5, describes a maximum at approx 295 nm which has decreased to zero absorbance by approx 320 nm. Therefore this red-shift and increased absorbance in the rotaxane's *band II* cannot simply be explained the by the presence of the macrocycle alone. Nishimoto[53-55] highlighted the sensitivity of *band II* to hydrogen bonding interactions. This combination of red-shift and absorbance increase seems to suggest some interaction between the flavin and the macrocycle does exist, despite it having previously been shown that the macrocycle will predominantly hydrogen bond with the fumaramide in non-polar solvent. It was suggested in previous chapters of this thesis that the macrocycle may occupy a stable co-conformation midway between the flavin and fumaramide components of the axle. Ideally this would be verified through NOESY ^{1}H NMR spectroscopy. Unfortunately, due to the gradual precipitation of both the rotaxane even in solvent mixtures containing 10-15% deuterated DMF and at $1/10^{th}$ normal concentrations, all attempts to determine this have been unsuccessful.

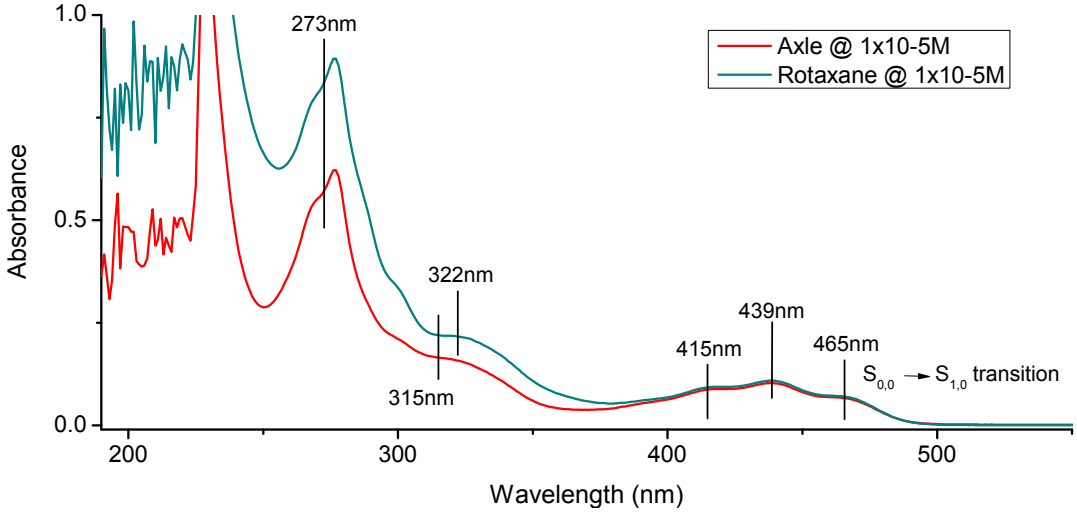

Figure 6.31 Absorbance spectra for axle and [2]rotaxane in DCM/DMF(< 0.1%) at concentration 1×10^{-5}M.

These spectra also demonstrate a large double peaked absorbance maximum at 273nm. Although no shift in peak position is observed here, the difference in absorbance is substantially more that that observed *band II*. Based on the absorbance spectra of the fumaramide analogue **C-53** shown in Figure 6.33, we can confidently assign the major contribution of this absorbance maximum to the fumaramide of the axle. This increased absorbance could therefore be identified as interaction between the macrocycle and the

fumaramide. The less dramatic increase that we observed in the flavins *band II* absorbance region may therefore reflect the statistical share of macrocycle interaction. Other major contributors to this absorbance maximum would include the diphenyl axle stopper and the aromatic groups of the macrocycle which of course may in turn be influenced by either flavin or fumaramide interaction.

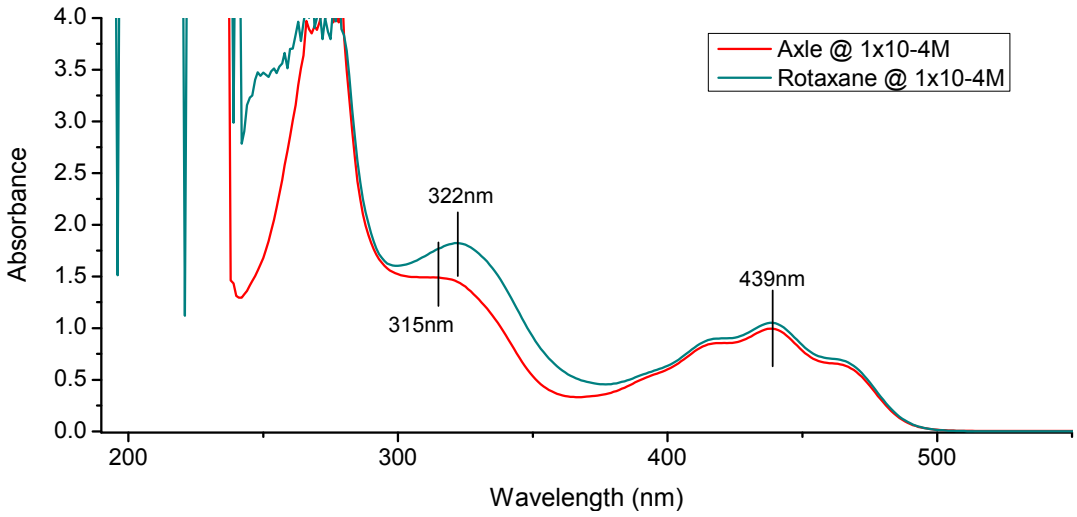

Figure 6.32 Absorbance spectra for axle and [2]rotaxane in DCM/DMF($<1\%$) at concentration $1\times10^{-4}\mathrm{M}$.

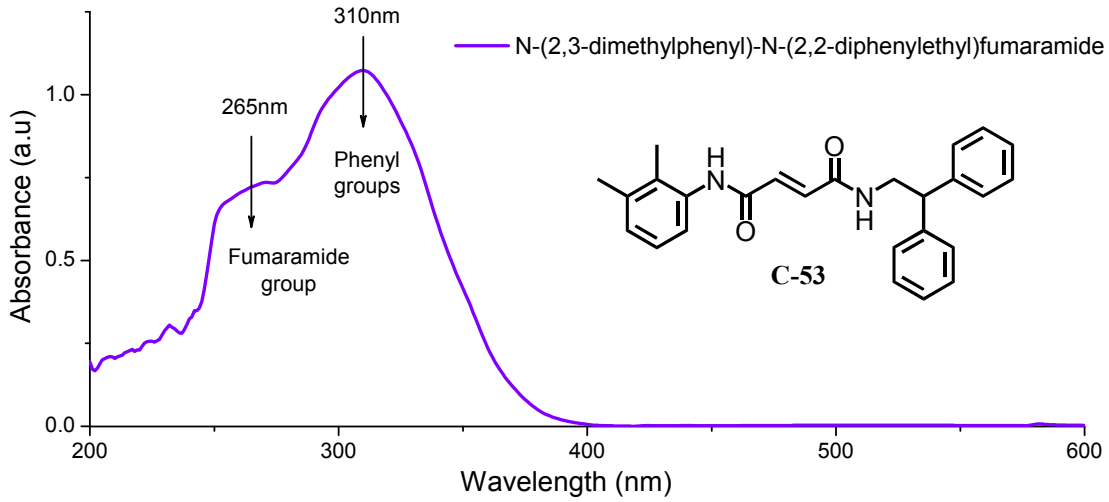

Figure 6.33 Absorbance spectra for N-(2,3-dimethyl)-N-(2,2-diphenylethyl)fumaramide (**C-53**) at $1\times10^{-4}\mathrm{M}$ in solvent mixture DCM/DMF(99:1). This spectra was used to determine the absorbance maxima for the fumaramide component of the rotaxane.

6.5.2 Fluorescence spectra.

Previous analysis in this thesis has been revealed that the fluorescence spectra for the multi-component axle and rotaxane do not demonstrate maximum emission at the flavins $\lambda_{\max}$ for absorbance *band I* . The spectra shown below in Figure 6.34(a) and (b) therefore correspond to the emission of the axle and rotaxane respectively in solvent mixture DCM/DMF($< 1\%$) over a range of different excitation wavelengths. In both compounds the maximum emission is achieved at approximately $\lambda_{excit} = 470\text{nm}$ and with apart form one exception (*axle* —— 490nm), no obvious change in the fluorescence emission maximum is observed. Excitation at this longer wavelength would correspond to the absorbance shoulder at 465nm shown in Figure 6.31. This has been attributed to the vibrational ground state to ground state $S_{0,0} \rightarrow S_{1,0}$ transition. Due to Franck-Condon restrictions that occur within polyatomic molecules, excitation to the $S_{0,0} \rightarrow S_{1,0}$ transition is statistically less likely to occur than the $S_{0,0} \rightarrow S_{1,1}$ transition which commonly corresponds to $\lambda_{\max}$ [52], however it is closer in energy to the first excited fluorescent state $S_{1,0}^{Fluor}$, The Stokes shift transition $S_{1,0} \rightarrow S_{1,0}^{Fluor}$ may consequently become more favourable than other non-radiative pathways.

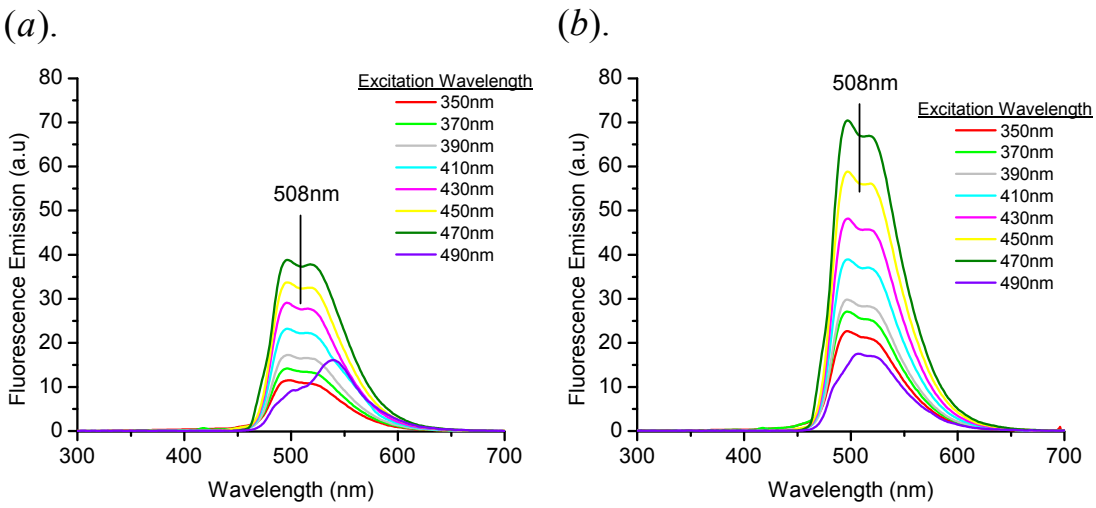

Figure 6.34 Fluorescence emission spectra for the (a) axle and (b) rotaxane in a DCM/DMF (99:1) solvent mixture at concentrations of $1\text{x}10^{-4}$ M.

6.5.3 Excitation spectra.

The excitation spectra in Figure 6.35 was produced by varying the excitation wavelength and monitoring the emission at the fluorescent maximum $\lambda_{\max}^{Fluor} = 508\text{nm}$. Normally an excitation versus emission intensity such as this would be expected to trace a spectrum similar to the absorbance spectra in so far as that at wavelengths where the absorbance is greatest we would to observe maximum fluorescence. This phenomenon can be explained by Kasha's and Vavilov's rules which describe respectively the independence of emission maxima and quantum yield on excitation wavelength. The spectra allows us to more accurately identify the emission maximum at excitation wavelengths $\lambda_{excit} = 465$ *and* 443nm with a shoulder at 415nm. These peaks we can attribute to the flavin absorbance *band I* and despite the absorbance at 465nm being approx 35% less than at $\lambda_{\max}$ this spectra clearly shows that the emission quantum yield is undoubtedly greater at this wavelength. As the excitation wavelength decreases the emission intensity decreases developing a weak shoulder at 415nm which correspond to the absorbance shoulder in Figure 6.31 before increasing again as it infringes the flavins absorbance *band II*. In contrast the two maximums here (343 and 361nm) are significantly different from the *band II* absorbance maxima of 315nm (*axle*) and 322nm (rotaxane). It has been suggested that the absorbance *band II* can been attributed to a $n \rightarrow \pi^*$ mixing of the flavin $N(1)$ non-bonding electrons with the main $\pi \rightarrow \pi^*$ transition.[52] This quasi-bathochromic shift relative to the absorbance spectra may reflect differences between the transition moments of these two electronic transitions and the fluorescent transition moment. In other words the $n \rightarrow \pi^*$ transition moment may be more aligned with the fluorescent transition moment allowing for smoother transition. Interestingly these excitation peak positions here are identical in both axle and rotaxane as opposed to the approximate 7nm difference (322 ↔ 315nm) observed in the absorbance spectrum. They also appear to show vibronic structure similar to that observed in *band I*.

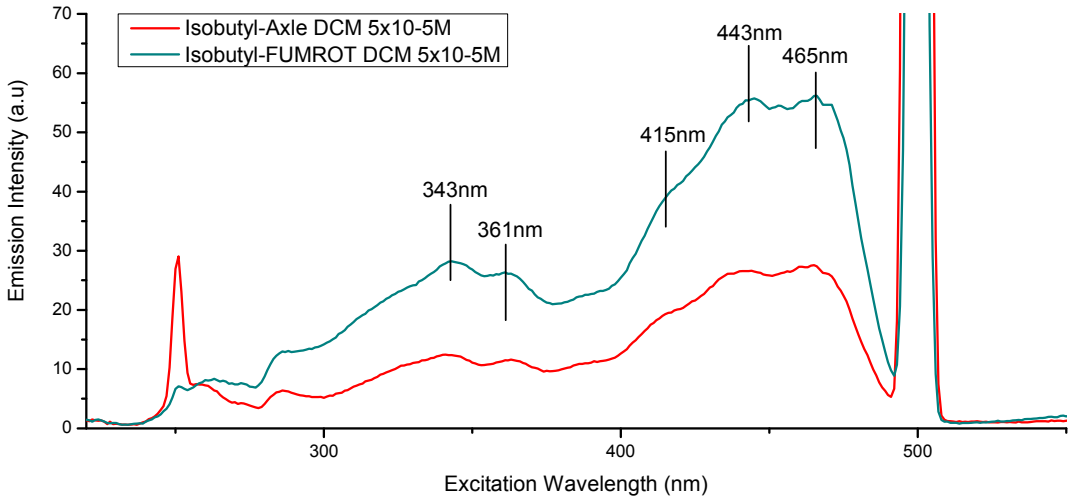

Figure 6.35 Excitation spectra for the axle (*red line*) and rotaxane (*green line*) in a DCM/DMF (99:1) solvent mixture at concentrations of $5 \times 10^{-5}\text{M}$. Rayleigh scatter peaks are visible at approx 500 *and* 250 nm..

6.6 Conclusions.

^{1}H NMR spectroscopy has been used to demonstrate that hydrogen bonding interaction is achievable even at high concentrations of polar solvent mixtures such as 5% DMF (see Section 6.3). This was verified though the comparative concomitant downfield shift in the amide NH protons and an upfield shift in the two alkene CH protons. Similar observations have been observed and will be discussed in the following chapter, "Flavin-succinamide [2]catenane", which due to the macromolecules increased solubility in non-polar solvent has allowed us to clearly identify the combined effect that the hydrogen bonding interactions and aromatic shielding generated by the presence of BA macrocycle is able to project onto the proton NMR shifts where these effects have been demonstrated using both COSY and NOESY NMR spectroscopy (see Figure 7.5).

We have observed the presence of a 2nd peak (*wave III*) during cyclic voltammetry experiments. The relative magnitude of this peak to the 1st oxidation peak (*wave II*) appears to be dependant on the sweep rate of the voltammograms, (see Figure 6.10). We have used the comproportionation reaction to explain this discrepancy by suggesting that the eventual pathway followed during the sweep is determined by the fixed kinetic rate of collision interaction between a neutral flavin $Flox$ from bulk solution and the fully reduced flavin $Flred H_2$. During a faster sweep voltammogram this pathway will becomes less likely to be followed and as a consequence $Flred H_2$ must undergo oxidation at a more positive redox potential and in doing so produces the peak response *wave III* . This is also observed in the cyclic voltammograms of the [2]rotaxane system as shown in Figure 6.15 and 6.16. Increasing the maximum CV reductive potential $E_{\max}$ in steps of $-0.1\,\mathrm{V}$ up to $-1.5\,\mathrm{V}$ produces a simultaneous increase in $wave\ III(r)$ and decrease in $wave\ II(r)$ during the CV oxidation sweep as shown in Figure 6.17. This behaviour was explained by a depletion of neutral flavin $Flox$ at the electrode which was produces in response to the higher negative redox potential. These findings are supported by SWV experiments. Although this procedure is known to perform rapid oxidation/reduction process during the short duration of each successive SW pulse, the full SW scan will be dependant on the inverse product of a two parameters, the SW frequency f_{SW} and the step voltage E_{step}. For example if $f_{SW} = 25\,\mathrm{Hz}$ and $E_{step} = 0.002\ \mathrm{V}$ the scan rate would be $40\ \mathrm{mVs^{-1}}$ and require 20 sec to cover $-1 \rightarrow 0\ \mathrm{V}$. This therefore takes considerable longer than the CV sweep at $1\ \mathrm{Vs^{-1}}$. Consequently the SW reverse scan from $-1 \rightarrow 0\ \mathrm{V}$ shows no trace of a peak corresponding to the CV $wave\ III(r)$ which would suggest the re-oxidation step $Flred H_2 \longrightarrow Flrad^{\bullet -} \longrightarrow etc,.$ Instead the slow SW scan supports a comproportionation reaction pathway $(Flox + Flred H_2) \longrightarrow 2 \times Flrad H^{\bullet} \longrightarrow etc,.$

CHAPTER 7

FLAVIN-SUCCINAMIDE [2]CATENANE.

7.1 Introduction.

7.1.1 Experimental design strategy.

Several examples of intramolecular metathesis have previously been published demonstrating the formation of large ring systems. The hydroxylhexyl sidechain of flavin **C-14** shown overleaf in Figure 7.2, offered the opportunity to form such an intramolecular linkage directly to the pyrimidine N(3) nitrogen. The catenane design strategy was to first synthesise a large macrocycle by attaching flexible alkyl chain arms with terminal alkenes to both the flavin alcohol and N(3) nitrogen. The inclusion of succinamide group spaced several atoms away from the flavin by a benzyl group would serve the dual function of not only providing a strong hydrogen bonding template for the benzylic amide ring formation [25, 26], but also extend the size of the macrocycle. The two terminal alkene arms would then be joined using a 2nd generation Grubbs catalyst ultimately providing the flavin macrocycle as a 43 atom ring system. To reduce the likelihood of unwanted intermolecular metathesis, the reaction was preformed under high dilution conditions (2×10^{-4} M). The design strategy would require some careful compromise over the size of the macrocycle. Too large and the intramolecular ring closure may be compromised yet too small and the challenge of looping the B.A thread through the flavin ring system would become more difficult. Fortunately the flavin macrocycle described here seems to have successfully achieved this balance, providing a satisfactory 50% yield of the macrocycle and an acceptable 26% yield of the [2]catenane.

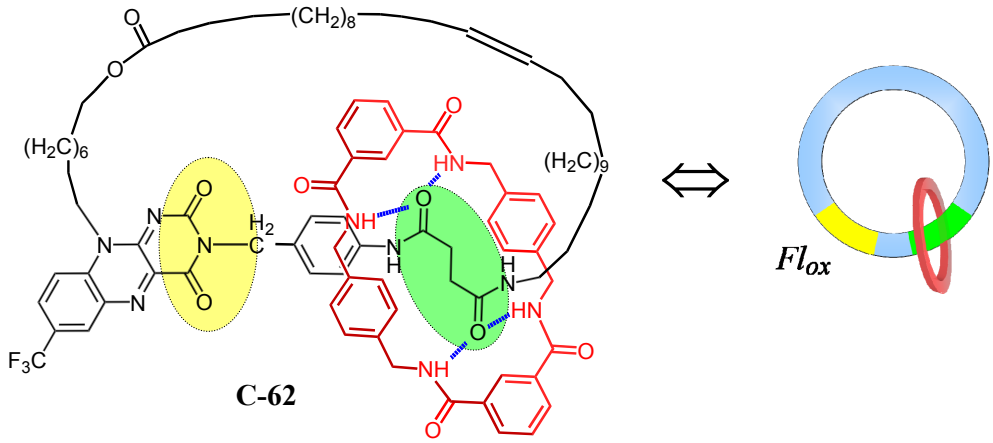

Figure 7.1 The basic structure of the flavin [2]catenane emphasising the construction of the main ring system as composed of two hydrogen acceptor binding stations, the flavin (*yellow*) and the succinamide group (*green*), both linked on one side by a short benzyl spacer and on the other side by a large alkyl chain to ultimately form a 43 atom macrocycle. The benzylic amide macrocycle (*red*) functions as the hydrogen donor shuttle which can influenced to translocate between stations though either electrochemical or photochemical means. The two ring cartoon shown to the left of the figure is a simple pictorial representation of the [2]catenane which will be used later within this chapter.

7.2 Synthesis

7.2.1 Synthesis of the [2]catenane.

The initially proposed synthetic route explored the coupling of one of the terminal alkene alkyl side chains to the flavin alcohol group before attempting Pd(C) reduction of the nitro benzyl at the flavin N(3) nitrogen as shown in Figure 7.2 below. It was hoped that this reduction method might be "soft" enough to avoid reduction of the terminal alkene. Had this been successful we would have avoided the extra two steps (i.e. protection and deprotection of the flavin alcohol). These two steps as it turns out were therefore necessary for the eventual synthesis.

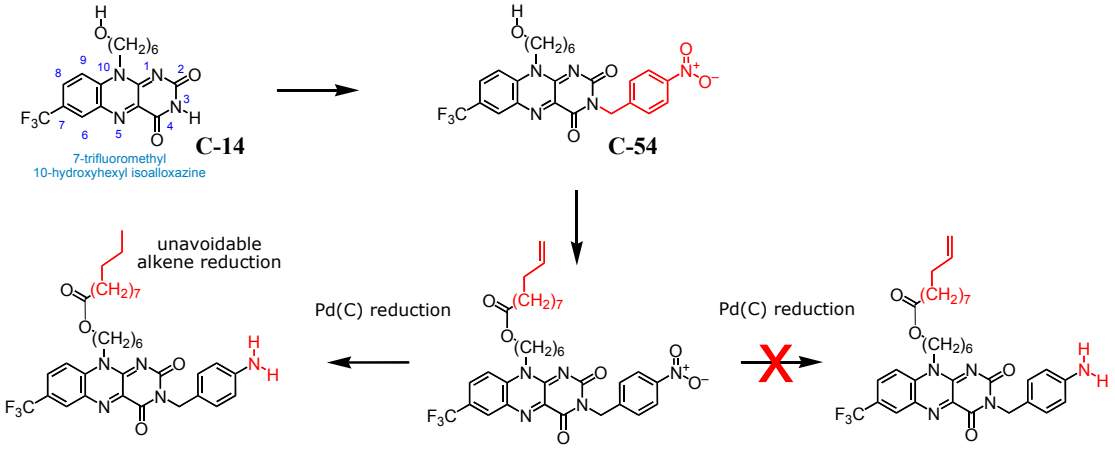

Figure 7.2 The initial synthesis route explored a prospectively quicker strategy that did not require protection groups.

The overall final synthesis as shown in Figure 7.3, starts with the 7-trifluoromethyl 10-hydroxyhexyl isoalloxazine **C-14**, the synthesis of which has previously been reported within the Cooke group.[69] A simple S_N1 reaction with 4-nitrobenzyl chloride in acetonitrile and potassium carbonate as a mild base to neutralize HCl formation provide compound **C-54**. Protection of the flavin alcohol using TBS.Cl was both fast and almost quantitive under the conditions employed. The flavin first was dissolved in the minimum amount of DMF and TBSCl and a catalytic amount of DMAP were added. The mixture stirred for approx 20min at r.t before adding NEt_3 dropwise over several minutes. It was found that if the conditions were altered the reaction would only partially work regardless of the reaction time. Reduction of the nitro group was preformed by activated Pd(C) in methanol using ammonium formate as the hydrogen source. A catalytic amount of DMAP in dry DCM was used to ring open succinic anhydride to form the succinamic acid **C-57**. This was then coupled to 10-undecene amine [70] using EDCI.HCl in dry DCM. The TBS protecting group was easily removed by adding 10% aqueous HCl to a solution of the flavin **C-58** in THF. A second EDCI coupling with commercially available 10-undecenoic acid provided the di-alkene **C-60** which was metathesised under high dilution conditions using a 2nd generation Grubbs catalyst to provide the flavin macrocycle **C-61** in a reasonably respectable 50% yield. This yield may have been even higher had precautions, such as nitrogen gas bubbling, been taken to avoid the by-

product ethylene gas poisoning of the ruthenium catalyst. The flavin [2]catenane **C-54** was finally afforded in a 26% yield by following the template procedure for BA ring formation described by Leigh [25] where isophthaloyl dichloride and p-xylylenediamine were dissolved separately in DCM and then simultaneously added dropwise using a motor driven syringe pump to a stirring solution of the flavin macrocycle in dry DCM and at least 4-5 equivalents of NEt_3.

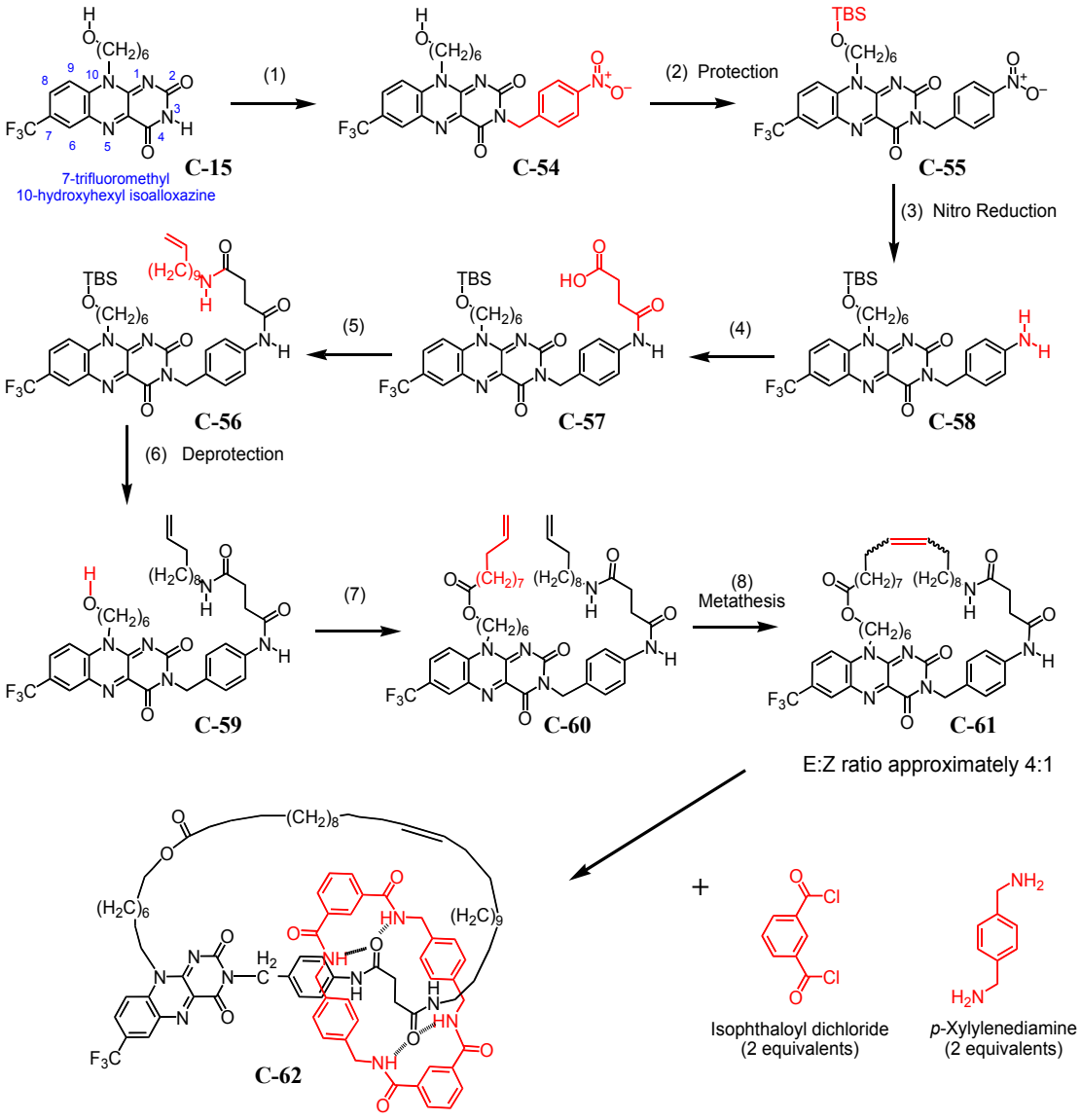

Figure 7.3 (**1**). 4-Nitro benzyl chloride, K_2CO_3 in acetonitrile (30°C, 3d, yield=68%); (**2**). tert-butyl dimethyl silyl chloride, DMAP, NEt_3 in DMF, (r.t, 1h, yield=96%); (**3**). Pd(C) in MeOH, (r.t, 1Hr, yield=75%); (**4**). Succinic anhydride, DMAP in CH_2Cl_2 (50°C, overnight, yield=85%); (**5**). 10-undecen-amine, EDCI, HOBt, cat DMAP, in CH_2Cl_2 (r.t, 18h, Yield=96%); (**6**). 10% aq HCl in THF (r.t, 1h, yield=94%); (**7**). 10-undecenoic acid, HOBt, EDCI, cat DMAP in CH_2Cl_2 (r.t, 24h, yield=77%); (**8**). 2nd generation Grubbs' catalyst, in dry CH_2Cl_2, (40°C, 18h, yield=50%); (**9**). Isophthaloyl chloride (in dry CH_2Cl_2 10mL), p-xylylenediamine (in dry CH_2Cl_2 10mL) simultaneously added dropwise over 3h to the flavin macrocycle in dry CH_2Cl_2 and NEt_3 (yield=26%).

7.3 NMR Spectroscopy.

7.3.1 Confirmation of hydrogen-bonding interactions in $CDCl_3$.

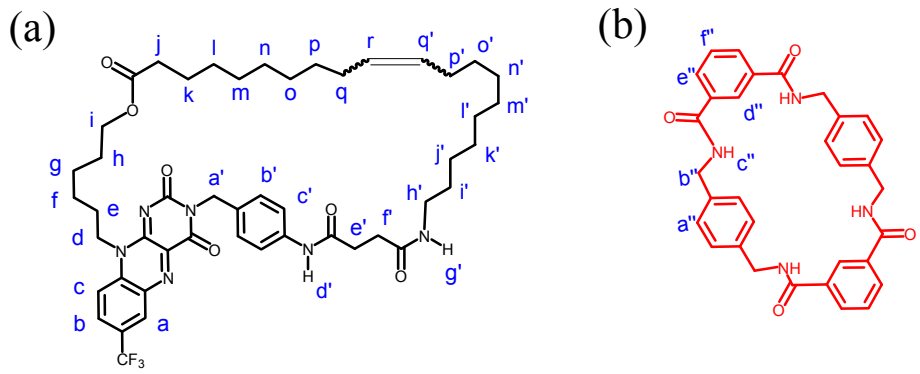

Figure 7.4 Labelling system employed for the ^{1}H NMR spectra shown in Figure 7.1. The flavin macrocycle is represented here by figure **(a)** while the [2]catenane is represented by the combination of figures **(a)** & **(b)** where the rings have been separated for clarity.

The ^{1}H NMR spectra for the flavin macrocycle and [2]catenane in $CDCl_3$ are shown overleaf in Figure 7.5. The peaks have been assigned to the relevant protons using the labelling system shown above in Figure 7.4. The effects of hydrogen bonding interactions between the succinamide station and the B.A macrocycle are clearly displayed by the concomitant shifts in the two amide NH's and methylene CH_2's. The two amide protons both demonstrate a downfield shift of between $+0.6 ppm$ (NH-g') and $+1.3 ppm$ (NH-d') due to the weakening of proton shielding induced by the indirect result of hydrogen bonding between neighbouring carbonyls and the BA macrocycle. On the other hand the four methylene protons shift upfield between $-0.8 ppm$ (CH_2-e') and $-1.2 ppm$ (CH_2-f') presumably as a direct result of increased shielding from the aromatic rings of the B.A macrocycle. The disproportionate shift would seem to suggest that other factors such as induction and resonance play an important role.

The exact location of the methylene protons required a combination of COSY and NOESY NMR of the [2]catanene. The partial COSY spectra shown in Figure 7.6 highlights specifically the correlation between the methylene pair $CH_2 - e'$ and f'. These are the only two methylene peaks in the entire spectrum that demonstrate correlation with only each other. The second piece of evidence that confirms the peak position is from the partial NOESY spectra shown in Figure 7.7, which shows long distance intramolecular correlation between the two succinamide methylene's $CH_2 - e'$ and f' and the succinamide NH-g' and NH-d' as highlighted by the *green* horizontal/vertical line intersection. It is also perhaps worth pointing out that there appears to be some significant intermolecular correlation between the aromatic groups of the B.A macrocycle and these methylene group protons as shown by the vertical *red* lines intersection with the horizontal *green* lines. This would support the previously discussed shielding effect used to explain the methylene upfield peak shift. However this correlation appears stronger between the methylene group $CH_2 - e'$ the peaks for which have shifted much less dramatically than that for $CH_2 - f'$.

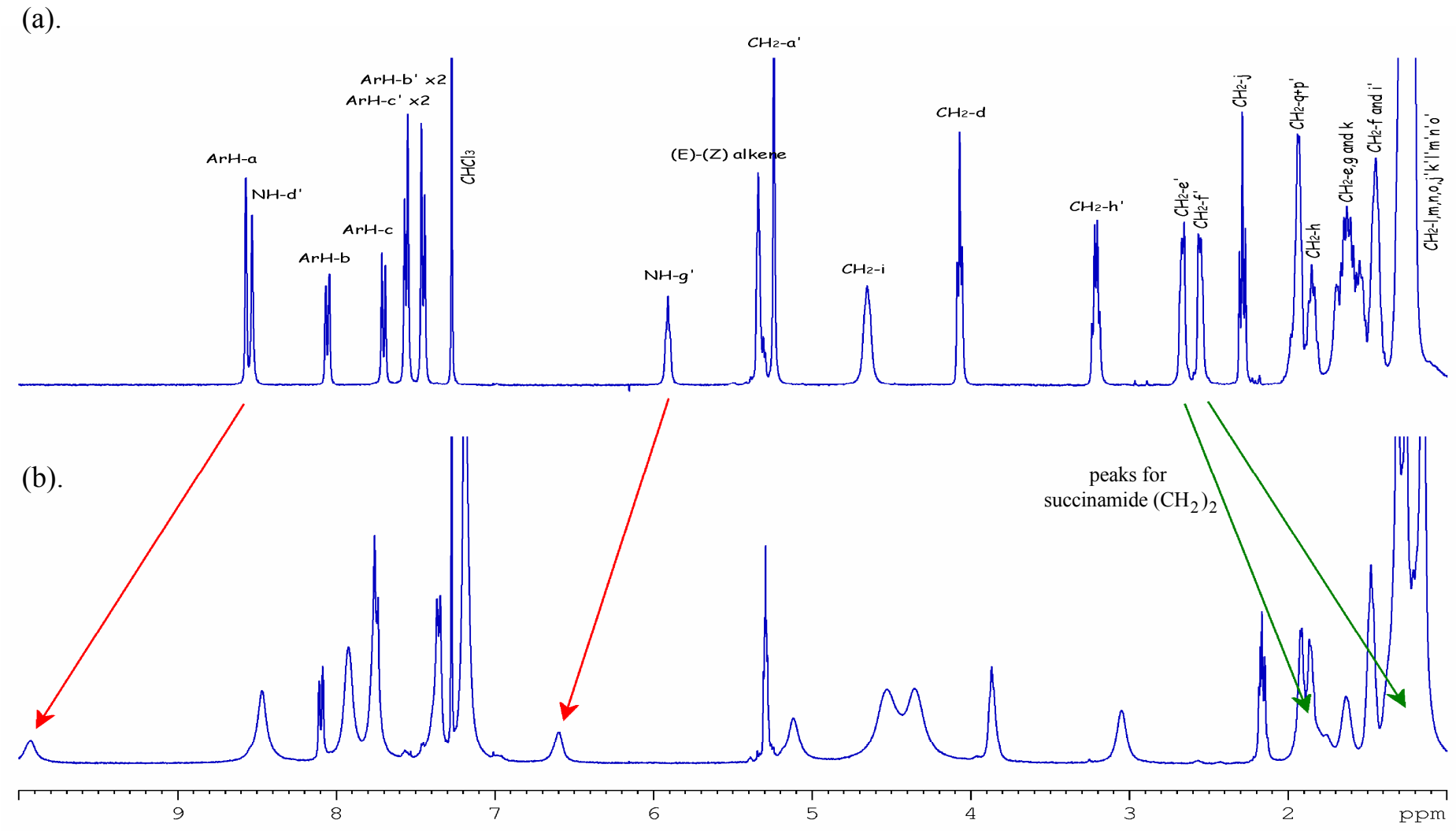

Figure 7.5 ^{1}HNMR spectra comparison for: (a) the flavin macrocycle and (b) the [2]catenane in $CDCl_3$ shows a downfield shift in the 2 amide NH peaks and a concomitant upfield shift in the 4 hydrogen peaks of the succinamide $(CH_2)_2$ groups. Buried peak position verified by COSY NMR of the [2]catenane.

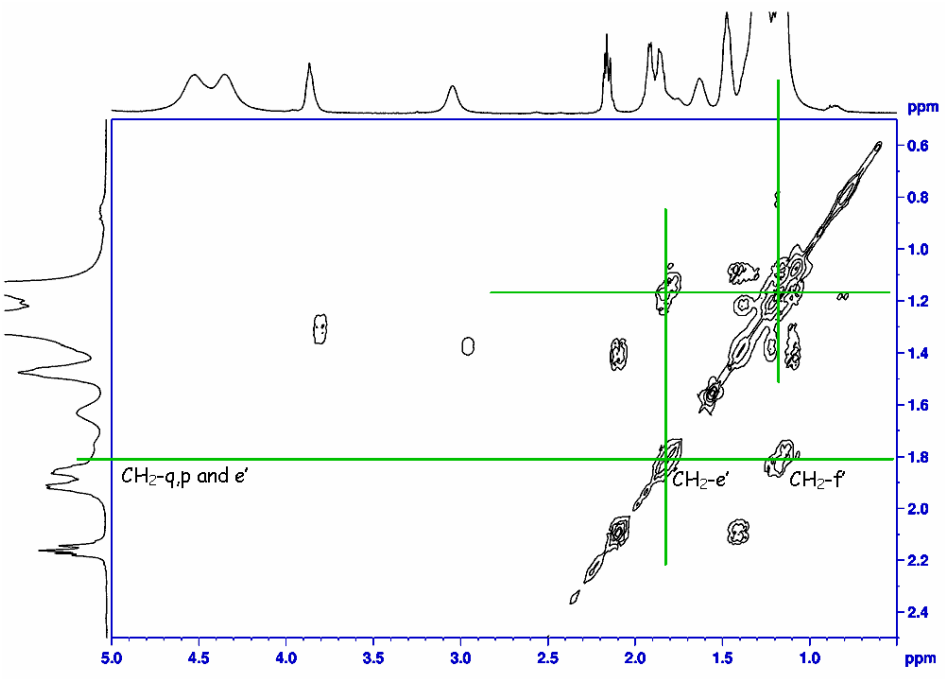

Figure 7.6 COSY of [2]catenane **C-62** in $CDCl_3$ showing the correlation between succinamide methylene groups CH2-e' and f', the peaks for which are hidden under a mass of other methylene peaks.

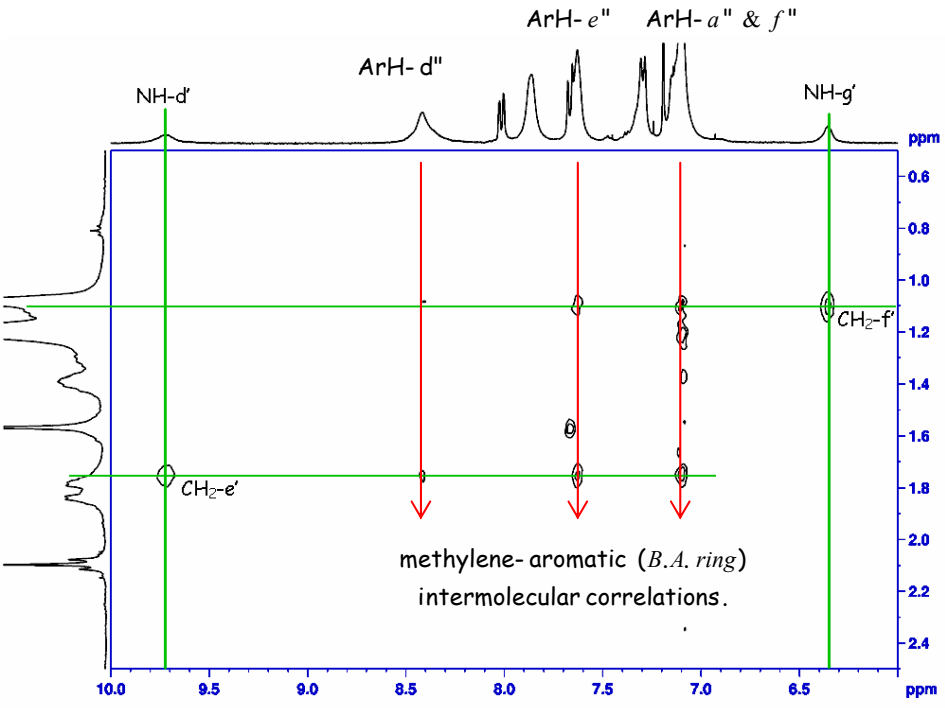

Figure 7.7 NOESY of [2]catenane **C-62** in $CDCl_3$ showing the long distance correlation between the amides NH-d' and NH-g' and their nearest methylene groups, CH_2-e' and CH_2-f' respectively. There also appears to be some intermolecular correlation between the aromatic protons on the BA macrocycle and the methylene groups on the succinamide as indicated by the red arrows.

7.3.2 Determination of the alkene conformation.

The relative ratio of *trans* : *cis* isomer conformation which occurred as a result of the metathesis reaction has been determined by ^{1}H NMR. A close examination of the peak region corresponding to the single alkene is shown below in Figure 7.8. Due to the near symmetry of the surrounding methylene groups the alkene peaks presents themselves as two broad overlapped triplets. The larger of the triplets can logically be identify as due to the trans conformation. [71] This is due of the nature of the ruthenium catalyst reaction and also because the J(H,H) coupling for the *trans* is commonly known to be much smaller than the J(H,H) coupling for the *cis* conformation. In this example $J_{trans} = 3.5$ Hz and $J_{cis} = 5.1$ Hz which are both notably smaller than normal (i.e. for trans isomers the range is generally between 12–18 Hz (typically 15 Hz) whereas for cis isomers the range is generally between 6–12 Hz (typical: 8 Hz).[71] [72] Regrettably however we cannot at present conclude to a satisfactorily explanation for this.

Due to the overlap of these triplets, the relative population for the two isomers can only be determined by integration of half of each peak as being approx 3.824 : 1 as shown below. This therefore corresponds to roughly 80% trans and 20% cis conformer. Similar large ring metathesis reported elsewhere has found similar ratios of alkene isomer. [73]

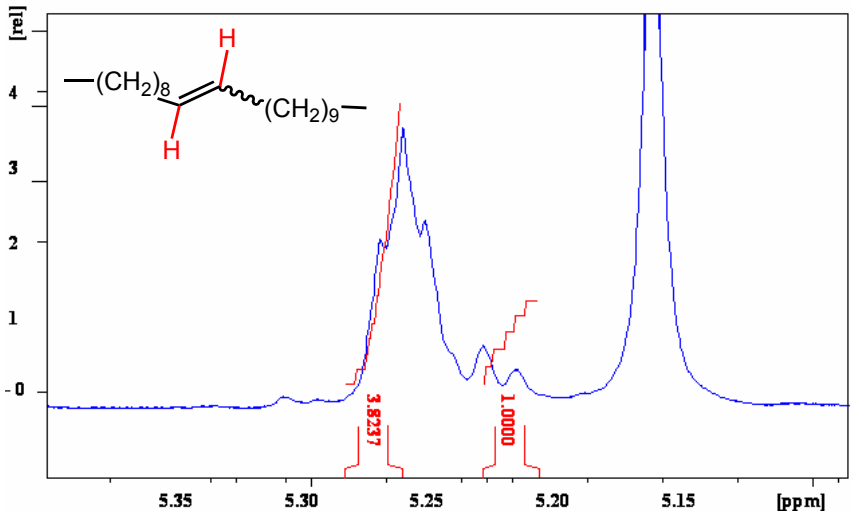

Figure 7.8 Flavin macrocycle's alkene peaks. Integration of the two triplets (based on half peaks due to overlap) shows the relative population of the *trans* : *cis* isomers as approximately 80:20 respectively.

7.4 X-ray structure.

Crystals of the catenane were grown over several days in ethanol/$CHCl_3$ (1:3) and the used to obtain an X-ray image of its structure as shown in Figure 7.9. Interestingly, although the macrocycle was observed to be a 80:20 mixture of trans:cis isomers, the crystallization of the catenane seems to have involved the separation and purification of the trans isomer. Again similar examples of this behaviour have been reported elsewhere. [73]

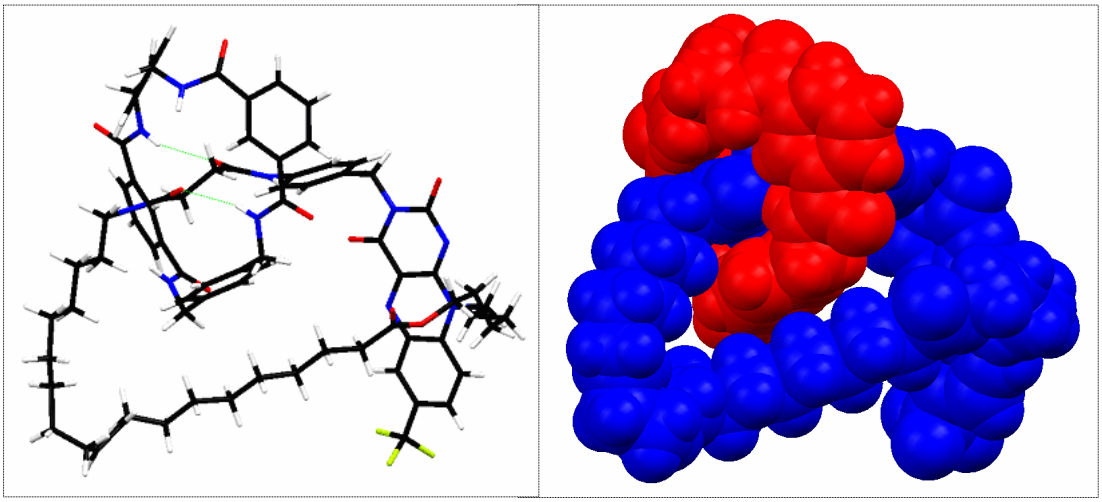

Figure 7.9 X-ray crystal structure of flavin [2]catenane **C-62** showing the flavin macrocycle (*BLUE*) and the benzylic amide ring (*RED*) . Although difficult to make out, the image on the left shows the newly formed alkene in the trans conformation.

7.5 Electrochemistry.

7.5.1 Cyclic voltammetry of the [2]catenene in DCM.

Figure 7.10 shows overlaid CV's for the flavin-succinamide macrocycle and [2]catenane in DCM recorded using a platinum working electrode at a slow sweep rate $\upsilon = 0.05 \mathrm{Vs}^{-1}$. Both voltammogram appear to show a well formed reduction and oxidation wave during the cathodic and anodic sweeps respectively with the ratio of cathodic to anodic peak currents $i_c / i_a \approx 1$. The peak current for the macrocycle voltammogram is approximately 60% greater than the corresponding [2]catenane voltammogram. Furthermore, despite using a extremely slow sweep rate both the system exhibit extremely poor electrochemical reversibility as demonstrated by appreciably large Nerstian peak separation (i.e. $\Delta E_p = 179\,\mathrm{mV}$ and $135\,\mathrm{mV}$ for the macrocycle and catenane respectively). However as we shall see later when we discuss the follow-up voltammetry which were recorded using a glassy carbon electrode, this large peak separation is shown as characteristic of flavin electrochemistry while using a platinum working electrode.

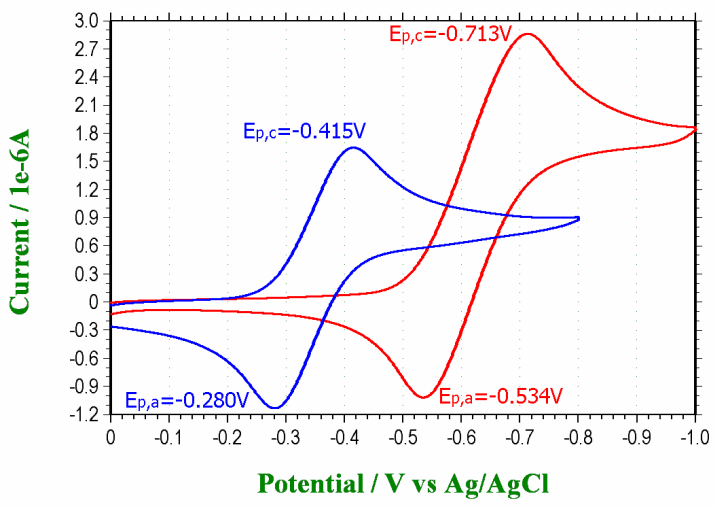

Figure 7.10 Overlaid cyclic voltammograms of flavin-macrocycle (*RED*) and [2]catenane (*BLUE*) at a slow sweep rate $v = 0.05\,\mathrm{Vs}^{-1}$. Concentration: $7 \times 10^{-4}\,\mathrm{M}$ in DCM using $0.1\,\mathrm{M}$ $\mathrm{TBA \cdot PF_6}$ as the supporting electrolyte. Platinum working electrode $1.6\,\mathrm{mm}$ diameter.

A comparison of the half wave potential $E_{1/2} = -0.624\,\mathrm{V}$ (macrocycle) and $-0.347\,\mathrm{V}$ (catenane) would suggest a stabilization influence of approx $+300\,\mathrm{mV}$ induced as a direct result of hydrogen bonding interaction with the benzylic amide ring. [4] However in contrast to electrochemistry preformed during the previous chapters involving the flavin-fumaramide [2]rotaxane and [2]pseudorotaxane, the cyclic voltammograms of the [2]catenane shown here demonstrates no equivalent cathodic peak for the reduction of the non-macrocycle bound flavin. The ^{1}H NMR spectroscopy in the previous section demonstrated that the benzylic amide (BA) macrocycle preferentially occupied a locality with the stronger hydrogen bonding succinamide station of the [2]catenane. This unbound flavin should therefore, in theory, become reduced at approximately the same potential as the flavin-succinamide macrocycle (i.e. $E_{1/2} = -0.624\,\mathrm{V}$) since the stabilization influence of the benzylic amide ring

does not apply to the neutral flavin oxide Fl_{ox}. Interestingly, when the sweep rate is increased to $v = 1\,\mathrm{Vs^{-1}}$ as shown in Figure 7.11 the cathodic segment of the [2]catenane voltammogram (*blue*) starts to demonstrate a second and more negative reduction peak. Labelled here as *wave I* we have attributed this peak to the reduction of the unbound flavin component of the [2]catenane. Nevertheless this peak appears to occur, as may have noticed, almost 200mV more positive than the macrocycle (*red*) cathodic peak. This assignment might perhaps be difficult to justify since in comparison to previous chapters describing cyclic voltammetry of [2]rotaxane and [2]pseudorotaxane systems we observed similar although less pronounced anodic shifts. At the time we attributed those anodic shifts to slower diffusing larger molecule (Randles-Sevcik equation [61, 62]), but this 200 mV shift cannot be explained by diffusion alone. It turns out as we shall encounter in the next subsection that this extreme anodic shift is mainly a characteristic of the platinum electrode, as a follow-up CV with a glassy carbon electrode resulted in a much smaller shift. However it does suggest that other factors may be contributing to the anodic shift of *wave I* thus giving the overall appearance that the unbound flavin reduction is occurring at a more positive potential. We therefore tentatively suggest that this behaviour is due to some fast dynamic equilibrium where the BA ring could reside at localities which partially influence the flavins redox potential. This equilibrium effect would seem more applicable here when we make a comparison between the weaker and more flexible succinamide station with the more rigid and stronger hydrogen bonding fumaramide group designed into our [2]rotaxane systems. Other observations are as expected, and as the sweep rate increases the electrochemical reversibility of the system diverges further from ideal Nerstian behaviour. Thus at a moderate sweep rate of $1\ \mathrm{Vs^{-1}}$ this is demonstrated by large peak separations $\Delta E_p = 450\,\mathrm{mV}$ and $340\,\mathrm{mV}$ for the macrocycle and catenane respectively. Comparison of the half wave potential at this faster sweep rate shows $E_{1/2} = -0.665\mathrm{V}$ (macrocycle) and $-0.347\mathrm{V}$ (catenane) which corresponds to a $-0.04\mathrm{V}$ shift in macrocycle $E_{1/2}$ whereas no change is observed for the [2]catenane.

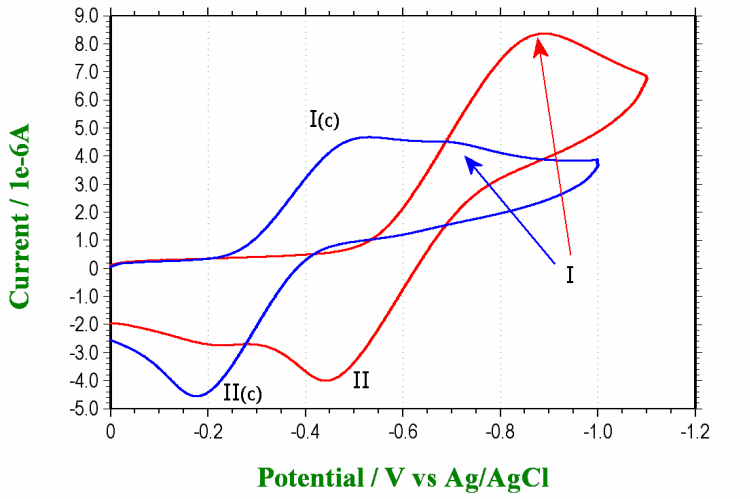

Figure 7.11 Overlaid cyclic voltammograms of flavin-macrocycle (*RED*) and [2]catenane (*BLUE*) at a faster sweep rate of $v = 1\,\mathrm{Vs^{-1}}$. Concentration: $7\times10^{-4}\,\mathrm{M}$ in DCM using $0.1\mathrm{M}\ \mathrm{TBA}\cdot\mathrm{PF_6}$ as the supporting electrolyte. Platinum working electrode 1.6 mm diameter.

The electrochemical scheme proposed in Figure 7.12(b) is therefore used to demonstrate the mechanism by which these two [2]catenane cathodic peaks are formed. We start by describing the EC scheme for the macrocycle (Figure 7.12(a)) as a

simple 2 electron, 1 proton transfer. As previously discussed in Chapter 6: "Flavin-fumaramide [2]rotaxane", the second anodic peak (*wave III*) now becomes more defined at these faster sweep rates due to the comproportionation reaction. The EC scheme describing the [2]catenane (Figure 7.12(b)) is based on a dynamic equilibrium pathway between the two catenane co-conformations $[Flox]-succ \rightleftharpoons Flox-[succ]$. During a very slow and increasingly negative-going sweep, the co-conformation $[Flox]-succ$ becomes reduced at a less negative redox potential than $Flox-[succ]$. Furthermore, it is continually replenished by this equilibrium process. As the sweep rates increases the equilibrium becomes competitively slower and we should start to observe a comparative decrease in the peak for *wave* $I(c)$ and an concomitant increase in *wave* I. In other words as the sweep rate increases more unbound flavin is available at the electrode for reduction at the more negative redox potential, whereas during a slower sweep it would have become practically depleted within the timescale it takes to reach this more negative potential.

(*a*). Flavin-*macrocycle*

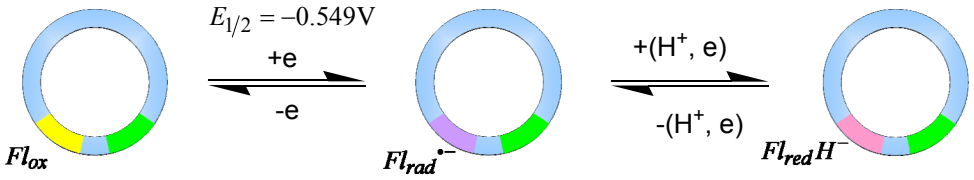

(*b*). Flavin-[2]*Catenane*

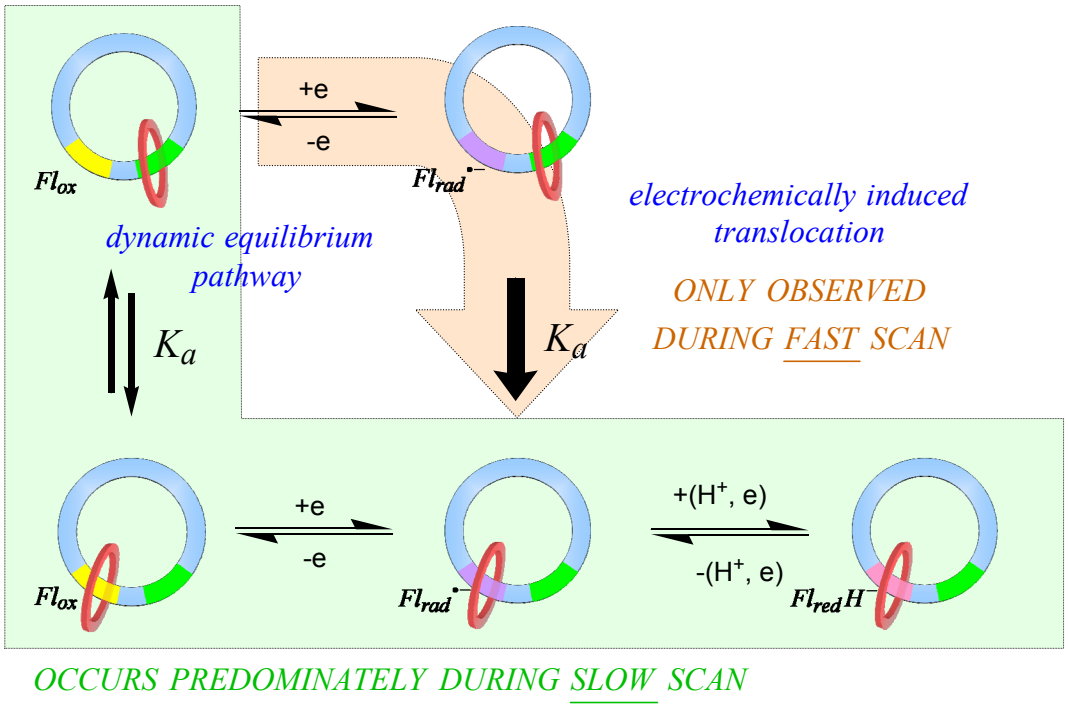

Figure 7.12 Proposed EC scheme for the: (a) flavin-macrocycle and (b). flavin-[2]catenane. The dynamic equilibrium between the $Fl_{ox}-[Succ]$ and $[Fl_{ox}]-Succ$ catenane provides a more favourable pathway for the flavin reduction during slow sweep rate voltammetry.

7.5.2 Follow-up CV using a glassy carbon electrode.

The next logical course of action would therefore be to continue increasing the CV sweep rate furthering in order to determine if this trend continues. Although the follow-up experiments were inadvertently carried out using a glassy carbon electrode, rather than the platinum electrode used the original experiments, the same principles apply. The main goal was to verify the decrease influence dynamic equilibrium described in Figure 7.12. One very dramatic difference we observed during these experiments while using a GC rather than platinum working electrode was that both systems now displayed significantly improved electrochemical reversibility. This is shown in the CV of Figure 7.13 by the cathodic and anodic peak separation between *wave I* and *wave II*, i.e. $\Delta Ep = 110$ mV (macrocycle) and 135 mV (catenane) at sweep rates $\nu = 1\ \mathrm{Vs^{-1}}$ (compared to the CV previously shown in Figure 7.11 where $\Delta Ep = 450$ mV (macrocycle) and 340 mV (catenane)). This is repeated again in the next subsection when significant differences in SW response.

However, returning to the CV's shown below in Figure 7.13 we also observe that the small emerging peak labelled *wave I* of the *blue* catenane CV has anodically shifted only approximately +60 mV relative to the corresponding macrocycle *wave I*. This is now of similar magnitude to the small shift observed in the voltammograms of previous chapters involving the [2]rotaxane and pseudorotaxane. This we believe smaller anodic shift is in some way connected to the kinetics at the electrode surface and is a characteristic that has already been shown to be much larger for the platinum working electrode.

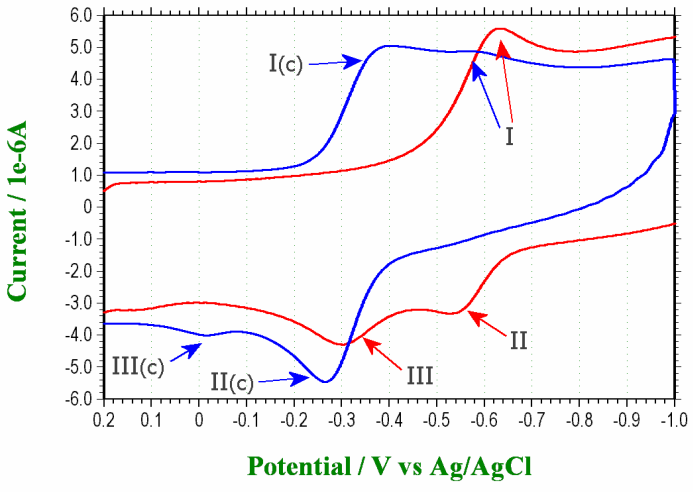

Figure 7.13 Overlaid cyclic voltammograms of flavin-macrocycle (*RED*) and [2]catenane (*BLUE*) at a faster sweep rate of $\nu = 1\ \mathrm{Vs^{-1}}$. Concentration: 1×10^{-4} M in DCM using $\mathrm{TBA\cdot PF_6}$ as the supporting electrolyte. GCE electrode 3.1mm diameter.

Another observation is that the 2nd oxidation peaks *wave III*(c) and *wave III* for the catenane and macrocycle are now both clearly visible within the CV window at approximately 0 V and −0.3 V. The oxidation peak for the macrocycle appears much larger compared to the corresponding peak observed with a platinum electrode at the same sweep rate of $\nu = 1\ \mathrm{Vs^{-1}}$. The peak also occurs at a more negative redox potential, this again we attribute to the electron transfer kinetic characteristics produced by the different electrode surfaces.

As shown in Figures 7.14(a-c), subsequent voltammograms recorded at increasingly faster sweeps rates, revealed, as predicted, the simultaneous decrease in the catenane reduction peak *wave* $I(c)$ and increase in the unbound flavin reduction peak *wave* I. By $50\,Vs^{-1}$ the catenane reduction peak *wave* $I(c)$ which represents the reduction of benzylic amide macrocycle bound flavin has almost entirely disappeared (compared to the CV at $1\,Vs^{-1}$). We have not shown CV at higher sweep rates than this as the redox peaks become flat and featureless as they become overshadowed by the increasingly large capacitive currents produces as a consequence of using large diameter electrodes. Interestingly, this is also the reason why we observe such a "depth" of current or separation between the two segments of the voltammogram in the 3.1mm GC electrode as opposed to the smaller 1.6mm platinum electrode. It would have been interesting to repeat these experiments using micro (or ultra-micro) electrodes.

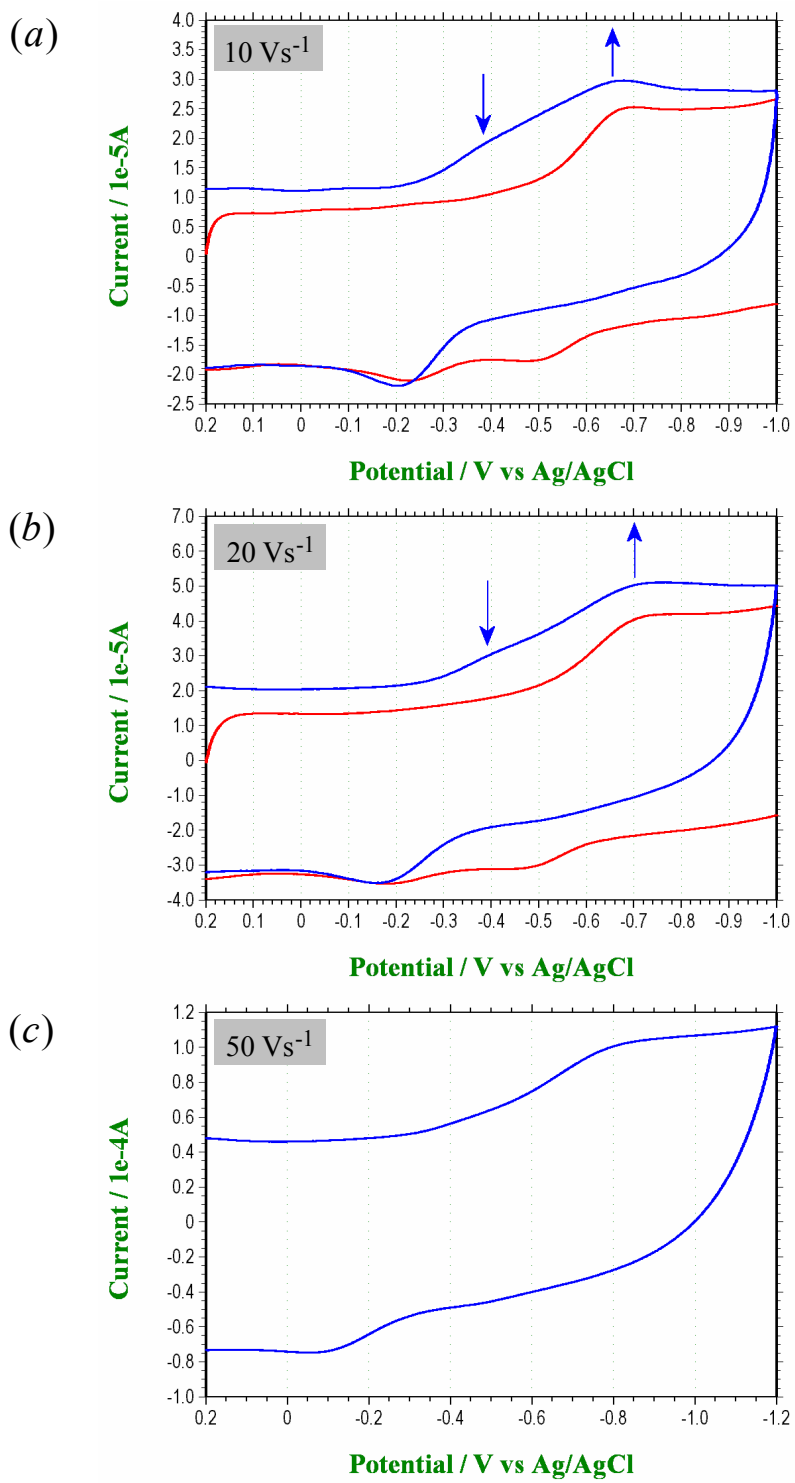

Figure 7.14 Overlaid cyclic voltammograms of flavin-macrocycle (*red*) and [2]catenane (*blue*) at a faster sweep rate (a) $\nu = 10$ Vs^{-1}. (b) $\nu = 20$ Vs^{-1}. (c) $\nu = 50$ Vs^{-1}. Concentration: 1×10^{-4} M in DCM using $TBA\cdot PF_6$ as the supporting electrolyte. Glassy carbon (GC) electrode 3.1mm diameter.

7.5.3 SWV with using a platinum working electrode.

Figure 7.15 below shows the overlaid SW voltammogram overall response (I_{Diff}) for the flavin-succinamide macrocycle (*red*) and [2]catenane (*blue*) in a DCM from the original experiments using a platinum working electrode. Each response produces a main single broad peak net response (-0.34 V (catenane) and -0.65 V (macrocycle)) when the SW direction of scan is as shown from 0 to -1 V. The catenane response also produces a smaller satellite peak at approximately -0.62 V which corresponds to the unbound flavin redox process. Furthermore the catenane peak height is approximately 60% that of the macrocycle at the same concentration.

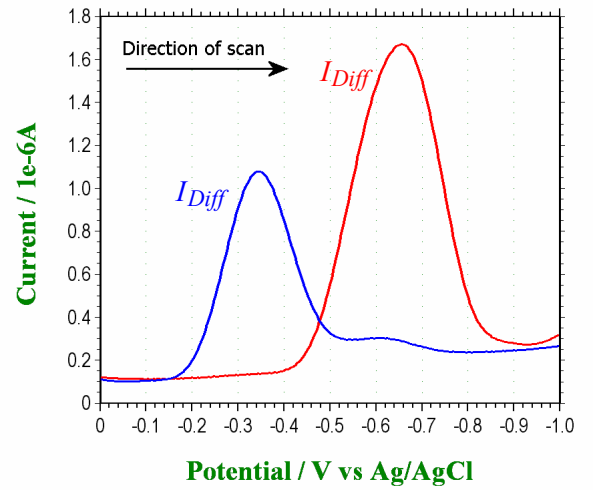

Figure 7.15 Overall SW response for the flavin macrocycle (*red*) and [2]catenane (*blue*). Other SW parameters are: $E_{SW} = 0.025$ V , $E_{step} = 0.004$ V and $SW_{freq} = 15$ Hz .

Figure 7.16(b) provides a closer analysis of the components that make up the net response $I_{Diff} = I_{for} - I_{rev}$ and allows us to understand the construct of these broad and different magnitude peaks. Both systems reveal a significantly larger maximum (I_{for}) accompanied by a small, practically non-existent minimum (I_{rev}) which indicates electrochemical irreversibility. As previously discussed in the Square Wave Voltammetry section, the position of the I_{rev} minimum (when it exists) should also be more negative than the I_{for} maximum. Therefore within the extremely short SW pulse period, the redox process is displaying electrochemically irreversible characteristics which, as we proposed in previous chapters is a consequence of a proton transfer reaction which immediately follows the first electron transfer and is a prerequisite of the 2nd electron transfer. The catenane I_{for} maximum is approx 50% that of the macrocycle I_{for} maximum which implies a reduction in electron transfer. This can be explained either due to a slower electron transfer rate and/or because of the BA macrocycle presence sterically hinders the proton transfer and hence any subsequent 2nd electron transfer (i.e. $H^+ + e^-$ reaction). This can occur when either the BA macrocycle is bound to the reduced flavin (proton acceptor) or the succinamide (proton donor). The catenane overall response I_{Diff} previously shown in Figure 7.15 is boosted slightly to 60% by the presence of a small I_{rev} minimum which is visibly absent from the flavin macrocycle response. Although it is clear that both systems are electrochemically irreversible, this subtle difference in I_{rev} may in a small way substantiate the proposal that the $H^+ + 2^{nd}\, e^-$ transfer is a less effective process for the catenane as more of the reduced flavin from the first electron transfer can be re-oxidized at least during the early stages of the reverse SW response. In

other words a smaller percentage of flavin catenane would undergo the 2nd electron transfer compared to the flavin macrocycle.

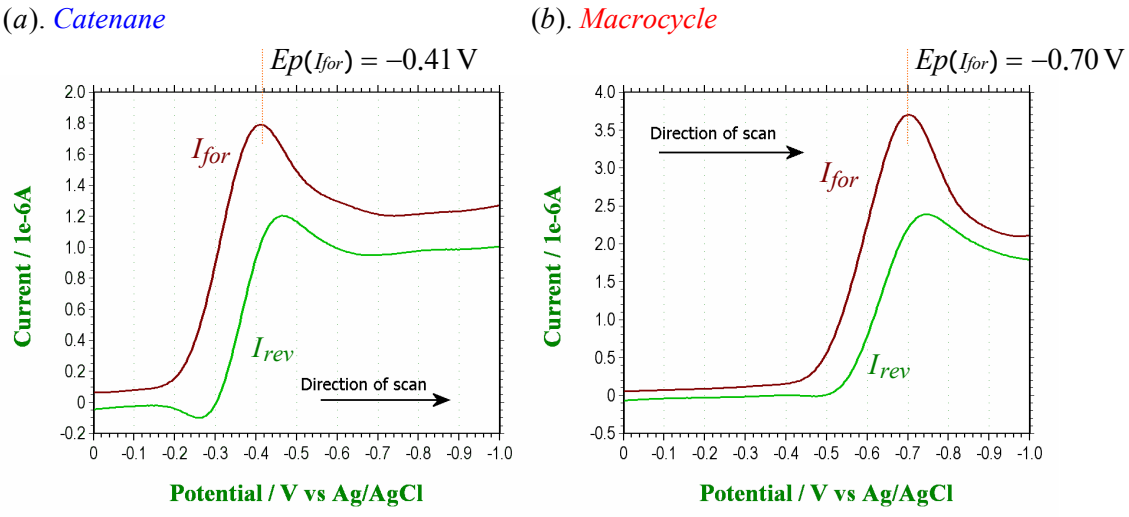

Figure 7.16 The forward (I_{for}) and reverse (I_{rev}) SW response for (a) the flavin [2]catenane and (b) the flavin macrocycle. These are the components that constitute the overall response ($I_{Diff} = I_{for} - I_{rev}$) Other SW parameters are: $E_{SW} = 0.025\text{V}$, $E_{step} = 0.004\text{V}$ and $SW_{freq} = 15\text{Hz}$.

Finally we should reiterate that because both systems are electrochemically irreversible, the exact peak "minimum" for the reverse SW response cannot be determined. For this reason the formal potential $E^{\theta} = 1/2\ (Ep(I_{for}) + Ep(I_{rev}))$ of the first (or second) electron transfer also cannot be determined. However based primarily on the positions of the forward current SW response peak I_{for} we can clearly identify an approx +300 mV positive shift in the redox potential accredited to the stabilization effect of hydrogen bonding with the B.A macrocycle.

7.5.4 Follow-up SWV using a glassy carbon electrode.

7.5.4.1 SWV direction of scan from $0 \rightarrow -1\text{V}$.

These experiments were carried out during the same period as the follow-up cyclic voltammetry experiments discussed in sub-section 7.5.3 and therefore also recorded using a GC working electrode. The results are shown below in Figure 7.17 and Figure 7.18 for the flavin macrocycle and [2]catenane respectively. Both systems again show a single reasonably sharp peaked overall SW response at $-0.58\,\text{V}$ (macrocycle) and $-0.32\,\text{V}$ ([2]catenane), when the direction of scan is from -1 to 0V. The [2]catenane also shows a small but significant peak at approx $-0.55\,\text{V}$ which would correspond to the redox process of the unbound flavin.

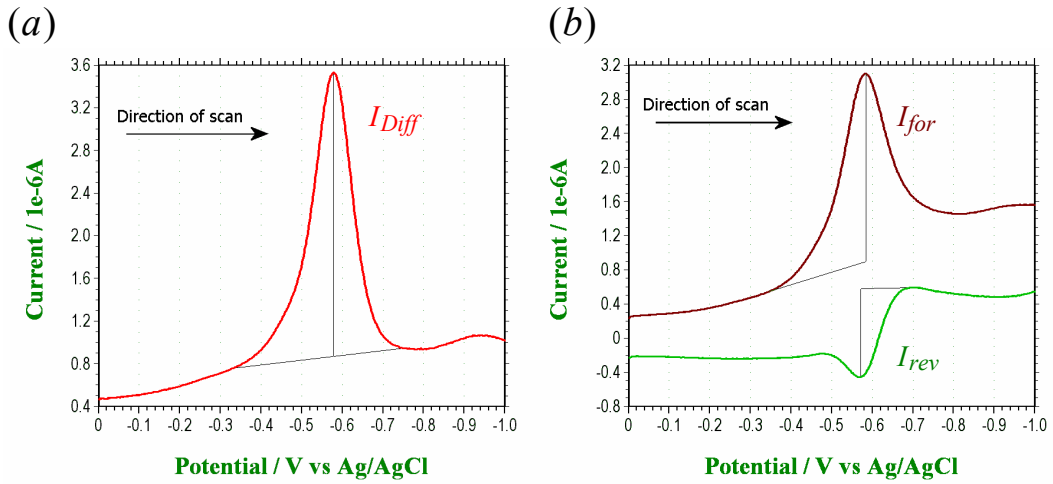

Figure 7.17 Square Wave voltammogram (SWV) for the flavin macrocycle showing separately (a) the net response (I_{Diff}) and (b) the forward (I_{for}) and reverse (I_{rev}) responses with a direction of scan from $0 \rightarrow -1\text{V}$. Other SW parameters are: $E_{SW} = 0.025\text{V}$, $E_{step} = 0.002\text{V}$ and $SW_{freq} = 25\text{Hz}$.

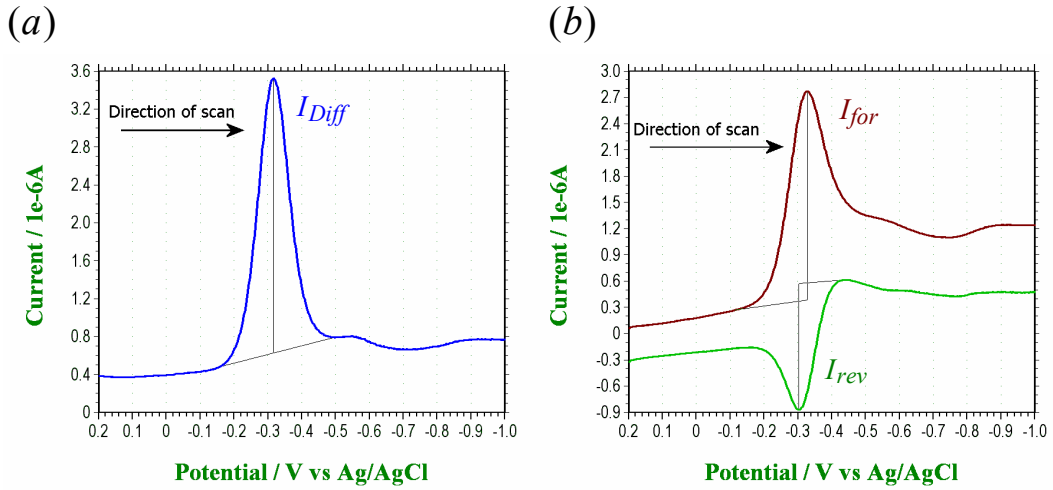

Figure 7.18 Square Wave voltammogram (SWV) for the flavin [2]catenene showing separately (a) the net response (I_{Diff}) and (b) the forward (I_{for}) and reverse (I_{rev})responses with a direction of scan from $0 \rightarrow -1\text{V}$. Other SW parameters are: $E_{SW} = 0.025\text{V}$, $E_{step} = 0.002\text{V}$ and $SW_{freq} = 25\text{Hz}$.

Interestingly the overall response peak heights are fairly similar in both systems. Closer examination of the components that make up the overall response $I_{Diff} = I_{for} - I_{rev}$ reveals that a significant part of the [2]catenane overall response comes from the larger reverse current SW response (I_{rev} minimum). Both systems display a diminished reverse response relative to the forward SW response. Although this diminished reverse SW response represents electrochemically irreversibility which was explained by the existence of the $H^+ + 2^{nd}\, e^-$ transfer, when we compare the reverse SW response from the glassy carbon electrode versus a platinum electrode we immediately see that there is a significant difference in the level of irreversibility. The reverse SW response from the glassy carbon electrode is much better defined and suggests that the electrochemistry at the surface of this electrode is more quasireversible. This supports previous findings recorded during the CV experiments using a GC electrode when we observed a decreased peak separation compared to the CV of the platinum electrode. Both these factors represent a measure of electrochemical reversibility.

7.5.4.2 SWV direction of scan from $-1 \rightarrow 0\,\mathrm{V}$.

Single peaks are also observed when the direction of scan is reversed from -1 to $0\mathrm{V}$ as shown in Figure 7.19 and Figure 7.20 for the flavin macrocycle and [2]catenane respectively. Both systems are demonstrated as quasireversible by a small but reasonably well defined reverse SW response. As expected the overall response shown in Figure 7.20 for the flavin [2]catenane there is a small presence of a redox peak between -0.5 and $-0.6\,\mathrm{V}$ which represents a presence of unbound flavin. Presumably the source is diffusion limited as the higher negative potential would have reduced the flavin [2]catenane in the immediate vicinity of the electrode to produce a B.A stabilized catenane co-conformation.

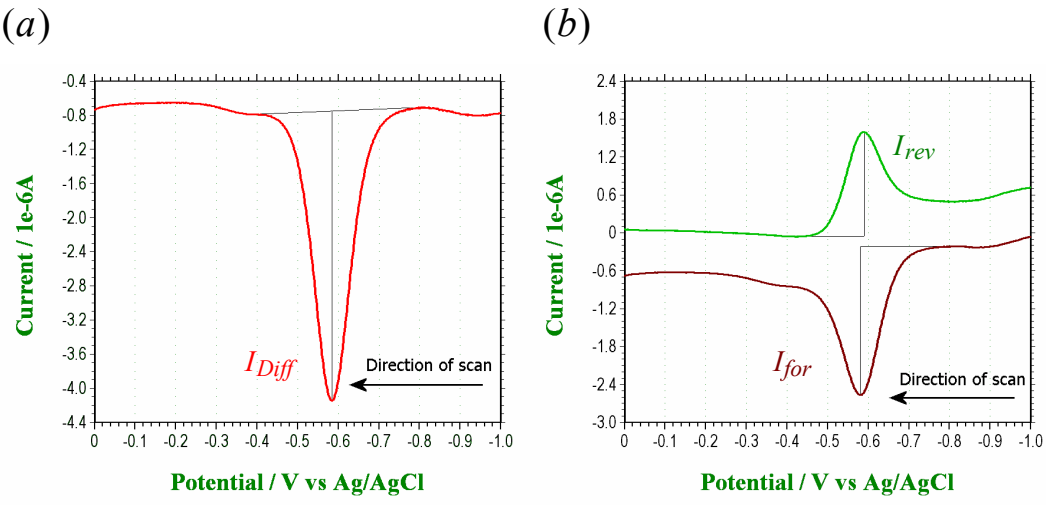

Figure 7.19 Square Wave voltammogram (SWV) for the flavin macrocycle showing separately (a) the net response (I_{Diff}) and (b) the forward (I_{for}) and reverse (I_{rev}) responses with a direction of scan from. Other SW parameters are: $E_{\mathrm{SW}} = 0.025\mathrm{V}$, $E_{\mathrm{step}} = 0.002\mathrm{V}$ and $SW_{freq} = 25\mathrm{Hz}$.

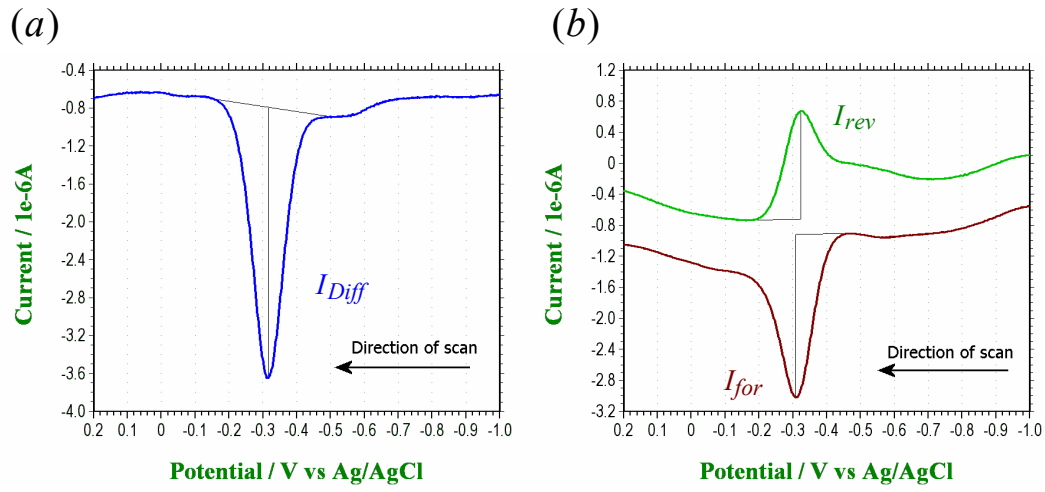

Figure 7.20 Square Wave voltammogram (SWV) for the flavin [2]catenane showing separately (a) the net response (I_{Diff}) and (b) the forward (I_{for}) and reverse (I_{rev}) responses with a direction of scan from $-1 \rightarrow 0\,\mathrm{V}$. Other SW parameters are; $E_{\mathrm{SW}} = 0.025\mathrm{V}$, $E_{\mathrm{step}} = 0.002\mathrm{V}$ and $SW_{freq} = 25\mathrm{Hz}$.

7.5.5 Summary of voltammetry.

The most significant differences observed in these voltammetry experiments when compared to those obtained in previous chapters is the absence of reduction waves for the unbound flavin catenane $Fl_{ox} - [succ]$. The results seem to suggest that the weaker hydrogen bonding and flexible succinamide station readily exhibits a more dynamic equilibrium compared to the flavin-fumaramide [2]rotaxane systems. The major catenane population would exist as the co-conformation $Fl_{ox} - [succ]$ where the B.A macrocycle is bound to the stronger hydrogen bonding succinamide station ($succ$). A minor population of flavin [2]catenane would exist where the B.A macrocycle is bound to the flavin rather than the succinamide group (i.e. $[Fl_{ox}] - succ$) but which would undergo reduction at a more positive redox potential due to the hydrogen bonding stabilization effects. During slow scans or sweep, this dynamic equilibrium is able to feed the depletion of the catenane co-conformation $[Fl_{ox}] - succ$ as the reduction process transforms it into the stable species $[Fl_{rad}{}^{\bullet -}] - succ$. If the sweep is very slow, as demonstrated during the CV sweep rate $v = 50\,\mathrm{mVs^{-1}}$ we observed no remaining evidence of unbound flavin catenane $Fl_{ox} - [succ]$ at more negative redox potentials as conversion would have been fully achieved. The opposite extreme to this hypothesis would be to repeat the voltammetry experiments with the flavin-fumaramide [2]rotaxane systems but using very slow scan rates in order to observe any evidence of a less active dynamic equilibrium.

Another significant feature of these voltammetry experiments was the dramatic difference in electrochemical reversibility demonstrated just by changing the electrode surface. Nevertheless, despite these differences, we are able to obtain half wave potential $E_{1/2}$ values by cyclic voltammetry which are in close agreement with one another. These results are summarized in Table 7.1 below along with the SWV results. As previously mentioned however due to the irreversible characteristics of the reverse SW response we are unable to use these SW values to accurately determine the formal potential. They should only be used as a rough measure of the stabilization effect of the BA macrocycle.

Flavin system	Working electrode	SWV Results (V)			CV Results (V)
		scan direction 0 to −1V			$v = 1\,\mathrm{Vs^{-1}}$
		$E_p(I_{Diff})$	$E_p(I_{for})$	$E_p(I_{rev})$	E^θ
macrocycle	glassy carbon	-0.58	-0.58	-	-0.60
	platinum	-0.66	-0.70	-	-0.66
[2]catenane	glassy carbon	-0.32	-0.33	-	-0.33
	platinum	-0.33	-0.41	-	-0.34

Table 7.1 Summary of cyclic voltammetry and square wave voltammetry results comparing the platinum with glassy carbon working electrode.

7.6 Photochemistry.

7.6.1 Absorbance spectra.

The absorbance spectra for the flavin macrocycle and catenane are shown below in Figure 7.21. With both analyte concentrations identical at 1×10^{-4}M the spectra demonstrates very good overlap in the *band I* region. The absorbance maxima in both spectra is shown to be $\lambda_{max} = 436\text{nm}$. According to Heelis [52] this can be attributed to the transition from electronic ground / vibrational ground state to the 1st electronic / 1st vibrational transition state of our polyaromatic flavin molecule (i.e. $S_{0,0} \rightarrow S_{1,1}$). The two shoulders of *band I* can be attributed to the transition to the other two vibrational states of the 1st electronic state, $S_{1,0}$ and $S_{1,2}$. The is a small but detectable red shift and increase in magnitude of the [2]catenane *band II* peak relative to the macrocycle. This has been observed in the flavin-fumaramide [2]rotaxane systems previously described within this thesis and is due to the sensitivity of the heterogeneous atoms of the flavin to hydrogen bonding interactions. If this explanation is valid then the red shift observed in these examples may suggest photoexcitation induced translocation of the B.A macrocycle. Otherwise it would be difficult to comprehend how the macrocycle can effect this shift.

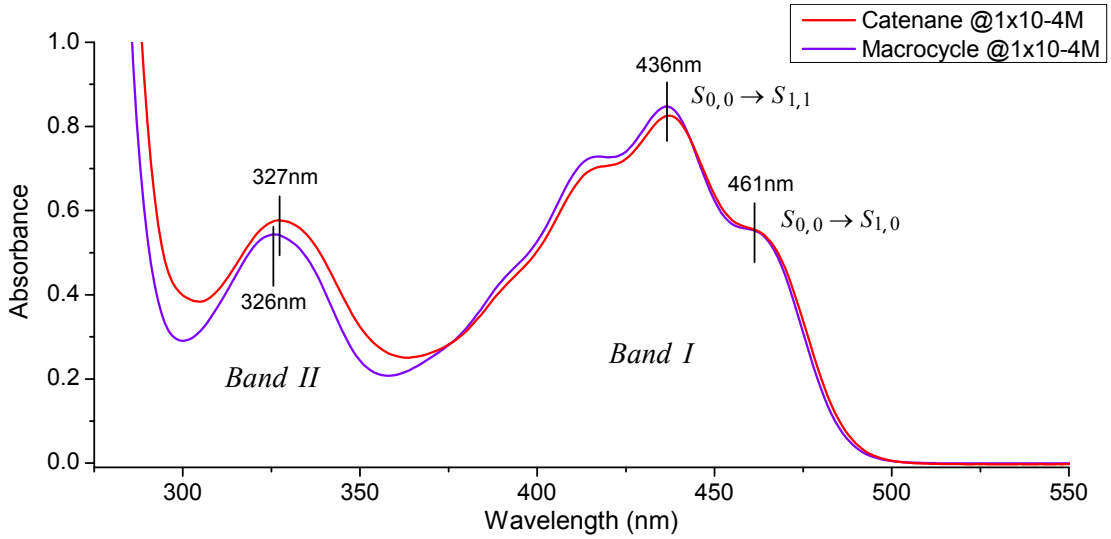

Figure 7.21 Absorbance spectra for flavin macrocycle (*blue*) and [2]catenane (*red*) in DCM at a concentration of 1×10^{-4}M.

7.6.2 Fluorescence Spectra.

Fluorescence emission spectra for the flavin macrocycle and [2]catenane in DCM are shown in Figures 7.22 (a) and (b) respectively. The spectra were produced from the same cuvette sample taken immediately after the recording of the absorbance spectra shown above. The excitation wavelength for fluorescence analysis is typically taken as λ_{max} (in this case $=436\text{nm}$) as this is generally considered to be wavelength which will effect the maximum absorbance and transfer of energy to the fluorescence excited state S_1' (i.e. produce the highest fluorescence quantum yield Φ_F). However recent fluorescent analysis of some of the flavin systems described with this thesis has revealed deviations from basic textbook photochemistry. Therefore out of curiosity the author expanded the excitation wavelength to include the range between 330 and 490nm. The results first of all show that the [2]catenane fluorescence is generally 4 times more intense that the macrocycle and also that the emission maximums are identically located at 505nm. However one intriguing observation, perhaps not immediately obvious from the spectra shown here is that the emission intensity is greater at excitation wavelengths much longer than $\lambda_{max} = 436\,\text{nm}$. In fact as we demonstrate more precisely in the next section, we observed maximum emission intensity at an excitation wavelength of 461nm (macrocycle) and $457\,\text{nm}$ (catenane). This small, approx 25nm difference might not seem important but we can relate the wavelength 461nm to the excited state transition $S_{0,0} \rightarrow S_{1,0}$ in the vibrational ground state. (Note that according to Heelis [52] λ_{max} for a polyaromatic molecule such as our flavin corresponds to the transition to the 1st vibrational state on the 1st electronic transition state i.e. $S_{0,0} \rightarrow S_{1,1}$). This transition is represented in the Absorbance spectra of Figure 7.21 by the the lower energy (lower wavelength) shoulder at 461nm of the *band I* absorbance peak. It would seem, and perhaps make more sense that transition from the 1st electronically excited vibrational ground state $S_{1,0}$ to the fluorescence excited state S_1' is closer energy wise and results therefore in a more efficient transition. We will examine this again in the next section.

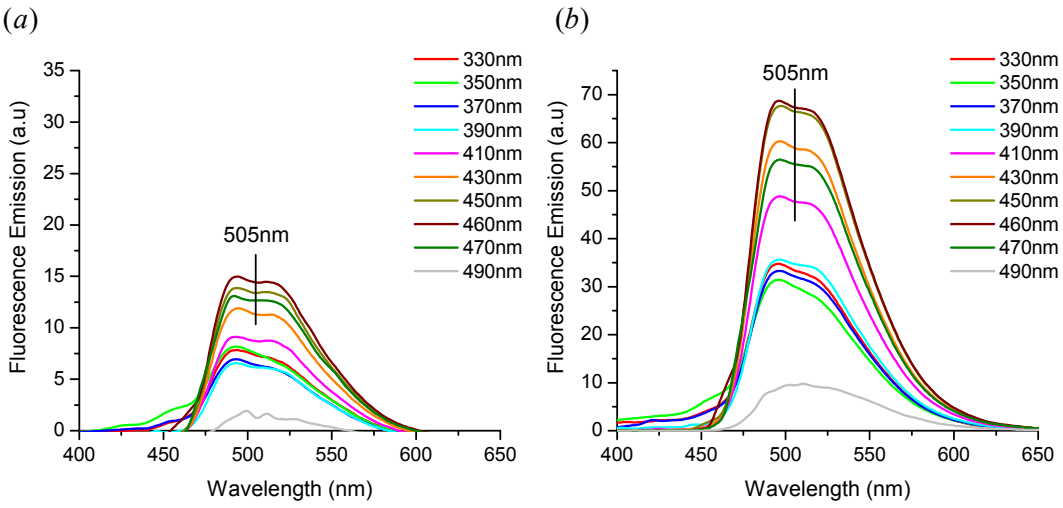

Figure 7.22 Comparison fluorescence emission spectra for: (a) the flavin macrocycle and (b) the flavin [2]catenane. Note the difference in emission intensity scale. The catenane fluorescence intensity is more than 4 times that of the macrocycle.

7.6.3 Excitation Spectra.

The excitation spectra for the flavin macrocycle and [2]catenane are shown below in Figure 7.23 and were produced by recording the fluorescence emission at $\lambda f\,\mathrm{max} = 505\,\mathrm{nm}$ over the range of excitation wavelengths from 220 to 550 nm. The spectra readily show the excitation wavelengths which produces the maximum fluorescence emission as 457 nm (catenane) and 461 nm (macrocycle). By referring back to the absorbance spectra shown in Figure 7.21 we can clearly see for the [2]catenane for example that despite the absorbance at 461 nm being approx 75% of the maximum absorbance at $\lambda_{\max} = 436\,\mathrm{nm}$ it is still able to produce an emission intensity over 10% greater. This corresponds to a relative fluorescence quantum yield of approx 50% greater that that achievable at $\lambda_{\max}$ (i.e. $110/0.75 = 147\%$). Whether this photochemical property is unique to this flavin system and in particular these bimolecular systems so far reported is currently unanswered, but we can clearly see in the excitation spectra below that there is a significant increase in the [2]catenane fluorescent emission intensity in particular for *band I* absorbance. A mechanism was proposed in Chapter 4: "Flavin-fumaramide [2]rotaxane poly(PEG) systems", which suggested how the trans to cis isomerisation of the fumaramide alkene might influence the electron donation ability of the flavin N(3) benzyl amide. This decrease in macrocycle fluorescence activity may be related to the succinamide flexibility. However only through further investigation into this intriguing property as well as the role that hydrogen bonding interactions with the BA macrocycle might play, will we be able to answer these questions.

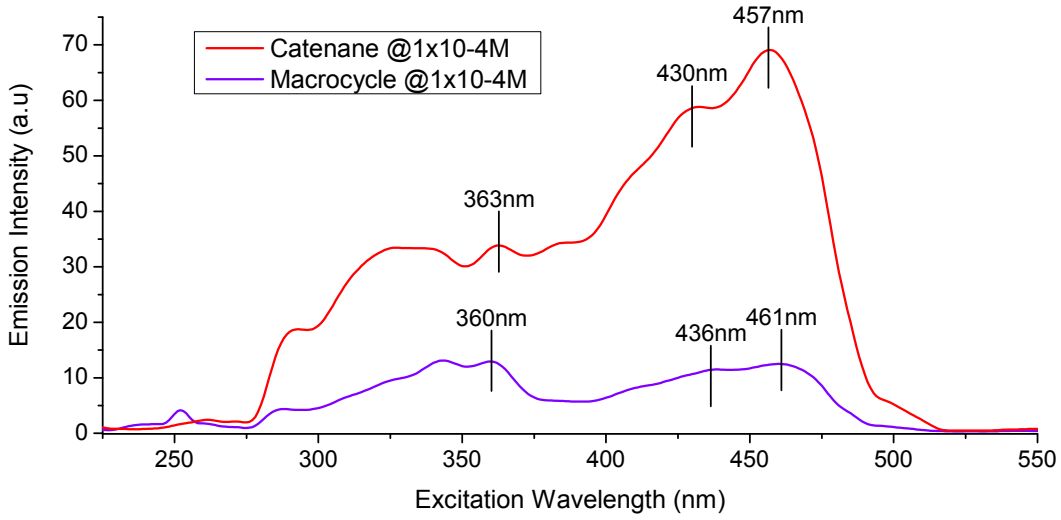

Figure 7.23 Comparison excitation spectra for the flavin macrocycle (*blue line*) and the flavin [2]catenane (*red line*). Note the relative increase in emission intensity for the [2]catenane in the *band I* absorbance region.

7.7 Conclusions.

Flavin electrochemistry is not straight forward. The availability of a proton source such as the succinamide group of a second flavin [2]catenane (or macrocycle) in bulk solution enables the reduced flavin radical to undergo a second electron transfer. The flavin [2]catenane can statistically exist in two co-conformational states, one where the BA macrocycle is predominately localized through hydrogen bonding to the succinamide station, and the other less favourable, minor co-conformation where the BA macrocycle is localised in the vicinity of the flavin and where, though hydrogen bonding interactions, it can influence its redox properties. A dynamic equilibrium will therefore exist where this small percentage of the flavin [2]catenane can becomes reduced to a new stable species at this more positive redox potential. However because the equilibrium $[Fl_{ox}]-succ \rightleftharpoons Fl_{ox}-[succ]$ must be maintained the reduction process now becomes a type of "kinetic leak" which ultimately leads, depending on the timescale, to the depletion of the predominant neutral [2]catenane species near the electrode surface. A slow sweep voltammetry experiment will therefore only detect the presence of the reduction/oxidation of $[Fl_{ox}]-succ \rightleftharpoons [Fl_{rad}{}^{\bullet -}]-succ$. During fast sweep voltammetry experiments this kinetic leak does not have sufficient time to depletion of the predominant [2]catenane species $Fl_{ox}-[succ]$ therefore the reduction process will involve the process $Fl_{ox}-[succ] \xrightarrow{e} Fl_{rad}{}^{\bullet -}-[succ]$ followed by $\xrightarrow{translocation} [Fl_{rad}{}^{\bullet -}]-succ$ of the BA macrocycle. The oxidation sweep of the same fast voltammetry experiment will involve the reaction $[Fl_{rad}{}^{\bullet -}]-succ \longrightarrow [Fl_{ox}]-succ$ and the reverse $\xrightarrow{translocation} Fl_{ox}-[succ]$. However as we have discovered in previous chapters this oxidation is the simplified version of the overall process as we have only considered the re-oxidation of a one electron transfer to the flavin. The flavin will undergo a second electron transfer following a proton transfer. It can even undergo a second proton transfer to form the stable neutral species $Fl_{red}H_2$. The oxidation reactions predominant observed will again depend on the timescale involved during the voltammetry experiment. As a result of the comproportionation reaction and a slow sweep voltammetry experiment the fully reduced flavin $Fl_{red}H_2$ will dimerize with a neutral flavin Fl_{ox} in bulk solution to form 2 molecules of $Fl_{rad}H^{\bullet}$ where dissociation of the hydrogen produces the easily oxidized radical anion species $Fl_{rad}{}^{\bullet -}$ and a single oxidation is observed. However during fast sweep voltammetry experiments the comproportionation reaction becomes competitive and kinetically less achievable within the available timescale and subsequently both the fully reduced species $Fl_{red}H_2$ (and its precursor anion $Fl_{red}H^-$) must become oxidized via the direct, two electron pathway which can only at a more positive redox potential. Consequently during the faster voltammogram sweep we observe this process as the second oxidation peak (*wave III* or *wave III*(c) for the catenane).

CHAPTER 8

EXPERIMENTAL.

General analytical procedures:

Dynamic Light Scattering (DLS) analysis.

Particle sizing was carried out using a Zetasizer Nano (Malvern Instruments Ltd) with the Zetasizer software was used to collect and analyse the data. The polymer solutions were made at concentrations of 10 mg/mL (monoblock polymers) and 2 mg/mL (copolymers) both in $CHCl_3$. These were pass through a $0.2\mu m$ PTFE syringe filter into a glass cuvette (round aperture) then allowed to equilibrate for 5 minutes at 25°C in the Zetasizer's "Peltier" temperature controlled unit before running the particle sizing experiment. Data was recorded under the "General purpose (normal resolution)" analysis model. The particle size results shown are based on size distribution by volume. The Z-average diameters when depicted provide are based in size by intensity. This variation is believed to be attributed to a number of estimated parameters utilized during the automated calculations performed by the Zetasizer software.

Gel Permeation Chromatography (GPC) analysis.

The polymer molecular weights were characterised by Gel Permeation Chromatography (GPC) using a PolymerLab GPC50 instrument from Varian Inc. The GPC consisted of two 600 x 7.5mm "PLgel $5\mu m$ MIXED-D ResiPore" columns. The recording sample time was set to 25 minutes to allow for full elution of the column volume under a flow rate of 1mL/min and the column oven temperature was set to 30°C. The polymers were detected using a refractive index (RI) detector and calibration was performed using MMA standards supplied from PolymerLab. All analysis was performed in the Cirrus software also supplied by Varian Inc.

UV/Visible, fluorescence and excitation spectroscopy.

Absorbance spectra were recorded with a Perkin Elmer Lambda 25 (Cambridge, U.K) at 20°C first in either DCM, chloroform or distilled water at concentrations of 1×10^{-4}M calculated using the molecular weights (M_n values) obtained by GPC. Fluorescence emission spectra were recorded with a Shimadzu *RF 3501PC* spectrofluorimeter (Milton Keynes, U.K.) at 20°C in either DCM, chloroform or distilled water at concentrations of 1×10^{-4} and/or 1×10^{-5}M. Spectral band widths were 1.5nm (excitation) and 3nm (emission), excitation wavelength in both solvents was recorded at λ_{max} obtained from the UV/Vis absorbance spectra. When possible and for increased clarity, Rayleigh scatter peaks were removed form the emission spectra using the "zapped" function of the manufacturer supplied LabCognition Panorama software. Occasionally to provide a direct comparison of the fluorescence quantum yield $\Phi_F = (photons \text{ radiated})/(photons \text{ absorbed})$ the absorbance of the samples were adjusted to $A = 0.1 \pm 0.005$ at λ_{max}.

Due to poor solubility of the flavin-fumaramide [2]pseudorotaxane (Chapters 5) and [2]rotaxane (Chapters 6) the absorbance spectra were recorded in first DCM/DMF (99:1) and then DMF(100%) at concentrations of 1×10^{-5}M. Fluorescence emission and excitation spectra were recorded using higher concentrations of 1×10^{-4}M due to weak emission characteristics.

Analysis of these spectra has been base on the photophysical and photochemical properties of flavins reported by Heelis[52] and the effects of hydrogen-bonding on the first two absorption band (*Band I* and *II*) by Nishimoto [53-55]. *Band I* corresponds to the $S_0 \rightarrow S_1$ transition (see Figure 4.29) and *Band II* corresponds to the $S_0 \rightarrow S_2$ transition. Some useful information regarding the fluorescence emission spectra has been provided by both Yagi[57] and Heelis[52] and transition moments for the different electronic transitions was provided by Johansson and Davidsson[74].

Photoisomerization of the fumaramide to the malemide [2]rotaxane isomer in Chapter 4: "Flavin-fumaramide [2]rotaxane poly(PEG) system" was performed by placing the sealed quartz cuvette into a glove box (lined with aluminium foil) in close proximity to a UVGL-55, 6 Watt UV lamp (UVP, Cambridge, U.K).

Electrochemical experimental procedures.

All non-aqueous voltammetry experiments were performed using dry dichloromethane with $0.1M\ TBA \cdot PF_6$ as the supporting electrolyte. All aqueous voltammetry experiments were performed using deionised water (Millipore, 18 M Ω cm) with $0.5M\ NaCl$ as the supporting electrolyte stabilized at pH7.0 ±0.02 with phosphate buffer. Cyclic voltammograms (CV) and Square Wave Voltammograms (SWV) were recorded using a CH Instrument Inc (Austin, TX, USA.), 440a EC Analyser, employing a glassy carbon (GC) electrode (diameter 3.1mm) for both solution phase voltammetry in DCM and surface immobilized against water. Voltammograms were referenced against a $Ag/AgCl$ (4M KCl) electrode, saved in their "raw" data form then afterwards smoothed before analysing any peak data using the internal software's Fourier Transform function. The background subtraction function of the same software was also used to modify the CV's of the surface confined polymers.

Prior to voltammetry, the GC electrode surface was polished with $0.05\ \mu m$ alumina, washed thoroughly with distilled water (or DCM if non-aquoeus voltammogram was to be recorded) then buffed on a clean polishing pad to remove any remaining alumina then washed again. A series of background scans were recorded before each new experiment to ensure that all previous electrode history had been removed. After background scans were complete, the electrode was removed and the electrode washed as previously described then dried with clean tissue. The cell mixture was degassed by bubbling nitrogen gas through this solution for 4 minutes and then purged under a nitrogen blanket for the duration of the experiment.

Variations in procedure:

Chapter 2:

Separate solutions of polymers in acetone were made ready 30min before any voltammetry using concentrations based on weight/volume of $2.5mg/0.1mL$. Approx $5\ \mu L$ of the polymer solution was carefully applied to the electrode surface, resulting in a domed shaped droplet coverage. After a few seconds the droplet was retracted back into the micro-syringe leaving the remaining residue to quickly dry onto the electrode surface as a thin film. Unfortunately, voltammograms recorded at this stage showed either little or no response, seemingly as if the thin film was behaving as an insulator. However if the thin film was allowed to dry for about 1 minute and then removed by gently polishing the electrode with some clean filter paper, a much stronger signal was achieved and this method was consistently applied for these experiments.

Chapter 4:

Solution concentrations were based on molecular weights (M_n values) obtained from gel permeation chromatography (GPC) analysis. The concentrations were 0.2mM for the **axle** (54.2mg/mL) and 0.4mM for the **rotaxane** (109mg/mL) for reason discussed later.

Surface immobilized voltammograms were obtained after simply pressing the clean electrode face onto a drop of the polymer spotted onto a sheet of clean filter paper and rotating firmly but gently in a small circular motion. The excess was removed from the electrode which was then placed immediately into the electrochemical cell. All solutions were purged by nitrogen gas for 4 min prior to voltammetry.

Chapter 5:

Voltammetry experiments were performed using pseudorotaxane axle **C-43** concentrations 0.5mM with 0.1M $TBA \cdot PF_6$ as the supporting electrolyte. Due to the poor solubility, axle **C-43** was first dissolved in DMF (0.6mL) and then diluted with dry DCM (6mL). Axle **C-43** remained soluble up to between 20-30min before slowly becoming cloudy. This allowed sufficient time for the initial voltammetry experiments to be carried out.

Chapter 6:

Voltammetry experiments were performed using 0.5mM analyte concentrations with 0.1 M $TBA \cdot PF_6$ as the supporting electrolyte. Due to the poor solubility, the axle was first dissolved in DMF (0.1 mL) and then diluted with dry DCM (6 mL). The cell mixture was degassed by bubbling nitrogen gas through this solution for 4 minutes and then purged under a nitrogen blanket for the duration of the experiment. Both the axle and rotaxane remained soluble up to between $30-60$ minutes before slowly becoming cloudy. This allowed sufficient time for the initial voltammetry experiments to be carried out.

Since both flavin macrocycle **C-61** and [2]catenane **C-62** dissolved in non-polar solvents, all voltammetry experiments could easily be carried out in DCM. Initial experiments concentrations of 0.7mM with 0.1M $TBA \cdot PF_6$ as the supporting electrolyte and a platinum working electrode (1.6 mm diameter). Due to a limited amount of remaining analyte material, crucial follow-up voltammetry experiments were preformed at analyte concentrations of 0.1mM with 0.1M $TBA \cdot PF_6$ as the supporting electrolyte. These voltammetry experiments were also preformed using a glassy carbon working electrode (3.1 mm diameter).

Chapter 2: Copolymers flavoenzyme model systems.

(a). Flavin ATRP initiator synthesis:

C-1:

N-(hydroxyhexyl)-3,4-dimethylaniline: [75]

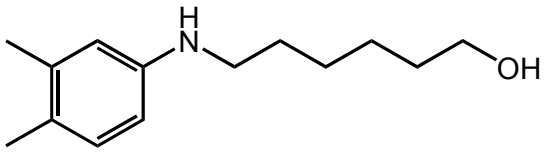

3,4-Dimethylaniline (25.4g, 0.21mol, 2eq), 6-chlorohexanol(14.3g, 0.1mol, 1eq) and NEt_3 (20mL, 0.144mol, 1.4eq) were heated under reflux at 120°C with stirring for 3H. After cooling to r.t, the NEt_3.HCl salt was removed by filtration and the solids washed with THF (30mL x3). The filtrate was condensed under vacuum and then subjected to column chromatography (silica) using eluent DCM/petroleum ether (50:50), followed by DCM (100%). The product was provided as a white solid after crystallization from hexane. Yield= 13.0g (58%). $C_{14}H_{23}NO$ (221.34). Mpt.= 39-40°C. (lit = 42-43°C [75]). ^{1}HNMR (400MHz, d_6-DMSO) δ_H 6.911 (1H, d, J = 8.5 Hz, ArH), 6.389 (1H, d, J = 2 Hz, ArH), 6.331 (1H, dd, J=8.5Hz and 2Hz, ArH), 3.612 (2H, t J=5Hz, NH), 3.341 (2H, t J=6Hz, OCH2), 3.055 (2H, t J=5Hz, NCH2), 2.048 (3H, s, CH3), 2.156 (3H, s, CH3), 1.59-1.51 (4H, m, CH2 x2), 1.41-1.35 (4H, m, CH2 x2).

C-2:

5-Chlorouracil: [76]

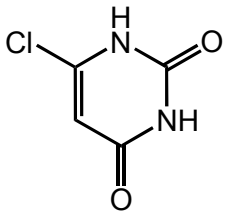

2,4,6-Trichloropyrimidine (24.2g, 132mmol) was added to a solution of 10% aqueous NaOH (22.0g in 220mL) then heated under reflux at 110°C for 2H. The mixture was collected to r.t then the pH was adjusted to 3 using conc HCl (approx 40mL). The precipitate formed was collected by filtration and recrystallized from distilled water. After filtering the remaining white solid was dried overnight under high vacuum at r.t. Yield = 8.24g (43%). $C_4H_3N_2O_2Cl$ (146.4). Mpt.= 294-295°C (dec), (lit = 292-293°C [76]). ^{1}HNMR (400MHz, $d_6 - DMSO$) δ_H 11.985 (1H, s, NH), 11.211 (1H, s, NH), 5.635 (1H, s, CH).

C-3:

6-[N-(6'-hydroxyhexyl)-3,4-xylidino] uracil: [75]

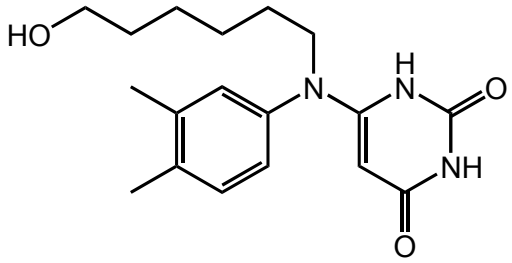

C-1 (5.6g, 25.3mmol, 2eq) and **C-2** (1.85g, 12.65mmol, 1eq) were stirred under nitrogen gas and heated under reflux at 105°C in dioxane/water (25mL:25mL) for 48H. After cooling to r.t the pH was adjusted to 11 by addition of 10% aqueous NaOH (approx 25mL). Unreacted N-(hydroxyhexyl)-3,4-dimethylaniline was extracted by washing with DCM (100mL x3). The pH of the aqueous layer was adjusted to 3 by addition of 6M aqueous HCl (approx 30mL). The resulting precipitate was collected by filtration and then crystallized from water to provide the product as a white solid. Yield = 2.65g (61%). $C_{18}H_{25}N_3O_3.½H_2O$ (335.9). Mpt.= 190-191°C, (lit = 188-190°C [75]). ^{1}HNMR (400MHz, $d_6 - DMSO$) δ_H 10.291 (1H, s, NH), 10.033 (1H, s, NH), 7.130 (1H, d, J = 6Hz, ArH), 6.992 (1H, s, ArH), 6.875 (1H, d, J = 6Hz, ArH), 4.334 (1H, t J=5Hz, OH), 4.110 (1H, s, CH), 3.725 (2H, t J=5Hz, OCH2), 3.315 (2H, t J=6Hz NCH2), 2.198 (6H, s, CH3 x2), 1.38-1.33 (4H, m, CH2 x2), 1.30-1.21 (4H, m, CH2 x2);

C-4:

Isoalloxazine 5-oxide: [75]

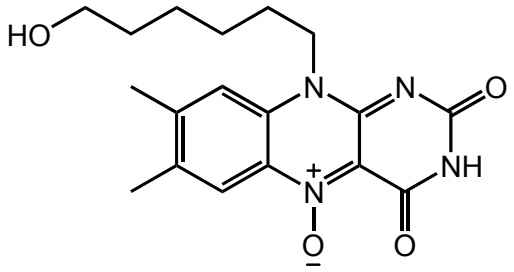

Sodium nitrite (2.62g, 38mmol, 4.8eq) was added to **C-3** (2.62g, 7.8mmol, 1eq) dissolved in acetic acid (18mL) and the mixture stirred at r.t for 3H in the dark. Distilled water (10mL) was then added and the mixture was left stirring for a further 3H. The solvents were evaporated under vacuum and the remaining orange solids were collected by filtration and washed with water (50mL x3). The product was provided by crystallization from 50% aqueous acetic acid (approx 300mL). Yield =2.58g (92%). $C_{18}H_{22}N_4O_4$ (358.16). Mpt.= 225°C (dec); (lit = 225°C (dec) [75]). ^{1}HNMR (400MHz, d_6-DMSO) δ_H 11.052(1H, s, NH), 8.095 (1H, s, ArH), 7.779 (1H, s, ArH), 4.522 (2H, m, OCH2), 4.399 (1H, br s, OH), 3.416 (2H, m, NCH2), 2.485 (3H, s, CH3), 2.395 (3H, s, CH3), 1.706 (2H, m, CH2) 1.450 (4H, m, CH2 x2), 1.392 (2H, m, CH2).

C-5:

N-(6'-hydroxyhexyl) flavin: [75]

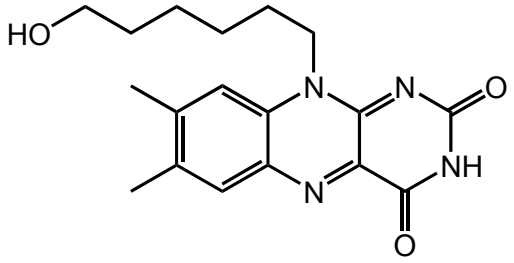

C-4 (2.58g, 7.2mmol, 1eq) and dithioreitol (4.2g, 27.2mmol, 3.7eq) were heated under reflux in a nitrogen atmosphere at 100°C in ethanol/acetic acid (500mL:200mL) for 16H. After cooling to r.t, the solvent was evaporated and the remaining yellow solids subjected to a dry silica column for separation of the product. Yield = 2.4g (95%). $C_{18}H_{22}N_4O_3.½H_2O$ (351.4). Mpt.= 272°C (dec); (lit = 270°C (dec) [75]). ^{1}HNMR (400MHz, $d_6 - DMSO$) δ_H 10.982 (1H, br s, NH), 7.880 (1H, s, ArH), 7.471 (1H, s, ArH), 4.423 (2H, br t J=4.5Hz, OCH2), 4.351 (1H, m, OH), 3.455 (2H, t J=6Hz, NCH2), 2.481 (3H, s, CH3), 2.362 (3H, s, CH3), 1.74-1.69 (2H, m), 1.48-1.39 (6H, m).

C-6:

N(3)-methyl-N(10)-(6'-hydroxyhexyl) flavin: [33]

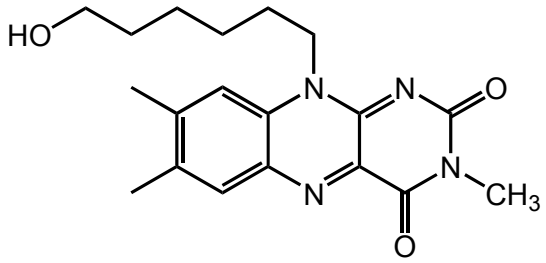

Methyl iodide (1.0mL, 2.28g, 16.0mmol, 2eq) was added to a stirring solution of **C-5** (2.5g, 7.3mmol, 1eq) and potassium carbonate (4.4g, 32mmol, 4eq) in acetone (1000mL) in a reaction flask pre-flushed with nitrogen gas. The flask was then heated under reflux in a nitrogen atmosphere at 60°C for 20H. The reaction was cooled to r.t, filtered to remove the K_2CO_3 and the acetone evaporated under vacuum. The product was provided by column chromatography using eluent $CHCl_3$ followed by a mixture of $CHCl_3$/acetone (60:40). Yield =2.4g (92%). $C_{19}H_{24}N_4O_3$ (356.4). Mpt.= 239°C, (lit = 235-238°C [33]). ^{1}HNMR (400MHz, $d_6 - DMSO$) δ_H 7.913 (1H, s, ArH), 7.818 (1H, s, ArH), 4.686 (2H, t, J=7.5 Hz, OCH2), 4.262 (1H, t, J=6Hz, OH), 3.411 (2H, m, NCH2), 3.243 (3H, s, NCH3), 2.505 (3H, s, CH3), 2.367 (3H, s, CH3), 1.61-1.56 (2H, m, CH2), 1.41-1.35 (6H, m, CH2 x3).

C-7: [33]

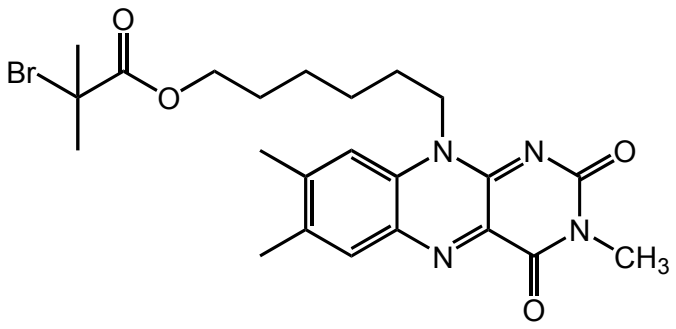

2-Bromoisobutryl bromide (3mL, 5.58g, 24mmol, 8eq) was added slowly to a stirring solution of **C-6** (1.03g, 2.9mmol, 1eq) and NEt_3 (5mL, 36mmol, 10eq) in a r.t solution of $CHCl_3$/THF (40mL:120mL) for 2 days. The NEt_3.HCl salts were removed by filtration and the solvents evaporated under vacuum. The product was then subjected column chromatography using eluent DCM followed by a mixture of DCM/ethyl acetate (75:25). Fractions containing the product were combined and the solvent evaporated to give an orange residue. The product was provided after adding acetone (10mL) and swirling for several seconds to give an orange-yellow solid precipitate. This was collected by filtration and washed with diethyl ether (20mL x3). Yield = 1.27g (87%). $C_{23}H_{29}N_4O_4Br$ (504.14). Mpt.= 148°C, (lit = 148-149°C [33]).

^{1}HNMR (400MHz, *CDCl*$_3$) δ_H 8.017 (1H, s, ArH), 7.372 (1H, s, ArH), 4.699 (2H, br t J=5.5Hz, OCH2), 4.194 (2H, t J=6.5Hz, NCH2), 3.528 (3H, s, NCH3), 2.563 (3H, s, ArCH3), 2.450 (3H, s, ArCH3), 1.930 (6H, s, CBr(CH3)2), 1.89-1.82 (2H, m, CH2), 1.80-1.68 (2H, m, CH2), 1.62-1.48 (4H, m, CH2 x2).

C-8:

1-naphthalene methanol: [77]

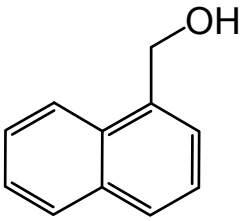

$NaBH_4$ (6.5g, 0.17mol, 0.67eq) was added to a stirring solution of 1-naphthaldehyde (35mL, 40g, 0.256mol, 1eq) in MeOH (50mL) at r.t. After stirring for 1H, the pH was adjusted to 4 by dropwise addition of a solution of 20% HCl in methanol was added dropwise until white precipitate appeared. The precipitate was removed by filtration and the filtrate condensed under vacuum to provide an oily brown residue. This was dissolved in ethyl acetate (100mL) and washed (x3) with a 10% aqueous solution of $NaHCO_3$. The organic layer was dried ($MgSO_4$) and condensed under vacuum. The remaining residue was dissolved in diethyl ether to precipitate a small amount of brown solid. This was removed by filtration and the remaining clear filtrate was condensed under vacuum and crystallized after dissolving in warmed petroleum ether. Yield=36g (89%). $C_{11}H_{10}O$ (158.2). Mpt.= 60-61°C (lit = 59-63°C [77]).

^{1}HNMR (400MHz, $CDCl_3$) δ_H 8.067 (1H, d J=8Hz, ArH), 7.95-7.85 (2H, m, ArH x2), 7.60-7.45 (4H, m, ArH x4), 5.654 (2H, d J=6Hz, CH2), 2.880 (1H, br t J=6Hz, OH).

C-9:

(1-naphthalenyl)methyl methacrylate:

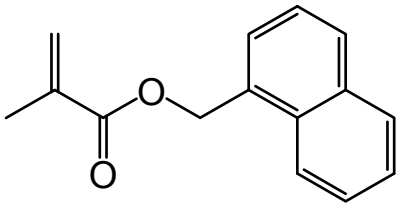

Methacryloyl chloride (3.8mL, 4.0g, 38mmol, 1eq) was added dropwise to a solution of **C-8** (6.0g, 38mmol, 1eq) and NEt_3 (7mL, 5.0g, 50mmol, 1.3eq) in diethyl ether (50mL). The reaction was left stirring at r.t for 1H after which hexane (50mL) was added and the mixture filtered to remove NEt_3.HCl salts. The solvent was evaporated under vacuum and the product was purified by column chromatography (silica) using an eluent of petroleum ether followed by petroleum ether/$CHCl_3$ (8:2) to provide the product as a colourless oil.

Yield =6.2g (72%). $C_{15}H_{14}O_2$ (226.2).

m/z (EI+) = 226.2 ([M]+, 45%), 208.1 (10), 156.1 (15), 141.1 (100), 115.1 (30), 83.9 (15). Accurate mass expected: 226.0994, found: 226.0994.

^{1}HNMR (400MHz, $CDCl_3$) δ_H 8.064 (1H, d J=8.2Hz, ArH), 7.93-7.84 (2H, m, ArH x2), 7.61-7.44 (4H, m, ArH x4), 6.154 (1H, s, CH alkene), 5.670 (2H, s, CH2), 5.582 (1H, s, CH alkene), 1.980 (3H, s, CH3).

^{13}CNMR (100MHz, $CDCl_3$) δ_C 167.33(C=O), 136.23(C=CH2), 133.75(ArC), 131.66(ArC), 129.25(ArCH), 128.75(ArCH), 127.32(ArCH), 126.57(ArCH), 125.99(ArCH), 125.32(ArCH), 123.63(ArCH), 64.89(CH2), 18.41(CH3).

(b). Hydrophobic monoblock ATRP synthesis:

ARTP general procedure.

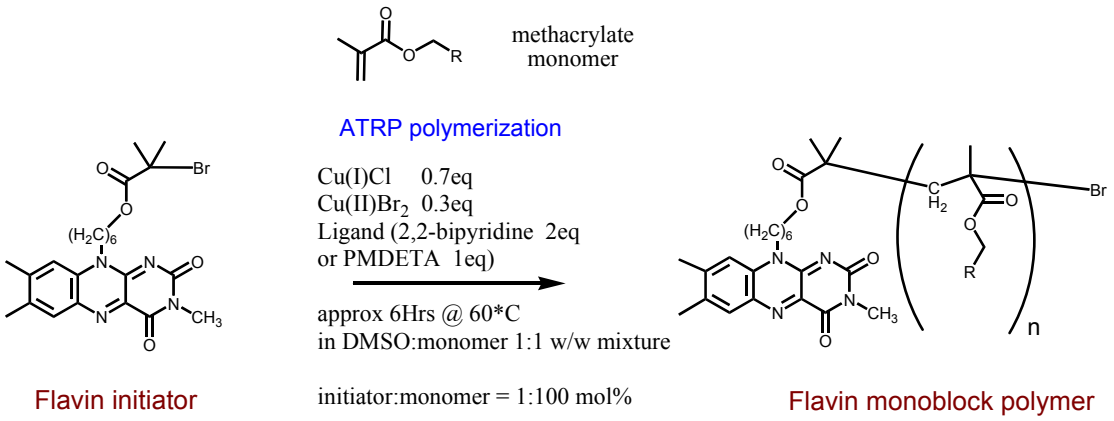

Initiator **C-7** (100mg, 0.198mmol, 1eq) was dissolved in a solvent mixture of DMSO:monomer (generally 1:1 w/w, see Table 7.1) which had been carefully measured into a two neck r.b flask. This would become the reaction flask. The catalytic system (Cu(I), Cu(II) and ligand, see Table 7.1) was added to a second r.b flask and dissolved in DMSO (5mL). Both flasks underwent three cycles of "freeze-pump-thaw" to evacuate all trace of the free radical oxygen gas using nitrogen gas (O_2 free) as the protective atmosphere. After the final thaws, a gas tight syringe was used to inject 0.5mL of the Cu(I)/Cu(II)/ligand mixture directly into the centre of the reaction flask while stirred under a fast flowing nitrogen purge. The reaction flask was sealed under a nitrogen atmosphere, then lowered into the thermostatically controlled oil bath and stirred at the reaction temperature (generally 60°C, see Table 7.1). Monomer conversion was determined via the GPC response of samples withdrawn periodically during the reaction. The reaction was terminated at approximately 85% conversion by slowly pouring the reaction mixture into 300ml of either polar or non-polar solvent (depending on the polymer, see Table 7.1) which was being vigorously stirred at r.t. After allowing the precipitate approximately 1H to settle the polymer was collected by filtering (solid) or decanting (residue). The polymer was then dissolved in $CHCl_3$ (40mL) and passed through a short column of Al_2O_3 to remove trace copper catalyst. The filtrate was reduced in volume under vacuum to approx 20mL and after passing through a $0.2\mu m$ syringe filter, the polymer was re-precipitated and collected in the same manner as before to provide the polymer as either a bright yellow solid or clear brown residue. The polymer was then finally dried under high vacuum for 24H.

Monomer		reaction mixture	catalyst system	reaction		solvent system used	polymer
chemical name	abbreviation	DMSO/monomer ratio	ligand	temp (°C)	time (Hrs)	to precipitate polymer	appearance
benzyl methacrylate	**benzyl**	1:1	bpy	60	6	methanol (300mL)	yellow solid
2,2,2 trifluoroethyl methacrylate	**CF3**	1:1	bpy	60	5	methanol/H_2O (225:75mL)	yellow solid
2-(dimethylamino) ethyl methacrylate	**DMAEM**	1:1	bpy (1eq)*	40	1.5	diethyl ether/hexane (150mL:150mL)	brown residue
methyl methacrylate	**methyl**	1:1	bpy	60	6	methanol/H_2O (200:100mL)	yellow solid
1-naphthalenylmethyl methacrylate	**naphth**	1:1	bpy	60	8	methanol (300mL)	yellow solid
2-methyl-2-nitropropyl methacrylate	**nitro**	3:1	bpy	40	4	methanol (300mL)	yellow solid
2-(methylthio)ethyl methacrylate	**thio**	1:1	bpy	60	6	methanol (300mL)	yellow solid
2-(methylthio)ethyl methacrylate	**thio2**	1:1	PMDETA (1eq)	60	2.5	methanol (300mL)	yellow solid

Table 7.1: Table layout demonstrating the exact reaction conditions utilized during the ATRP synthesis of the monoblock polymers. Main variations are: (1). Low reaction temp and time required for poly(**DMAEM**) and poly(**nitro**). (2). Dilution factor of 3:1 w/w DMSO:monomer for reasons previously discussed. Catalyst system generally used was Cu(I)Cl, Cu(II)Br_2 and 2,2-bipyridine (bpy) in molar equivalents 0.7, 0.3 and 2 respectively (*0.35, 0.15 and 1 eq for ATRP with DMAEM). This system was modified for poly(**thio2**) when the 2 equivalents of the 2,2-bipyridine ligand was replaced with 1 equivalent of N,N',N''-pentamethyldiethyltetraamine (PMDETA) due to poor yields previously obtained synthesising poly(**thio**). A solvent system of diethyl ether/hexane was used to precipitate amphiphatic poly(**DMAEM**) while addition water to methanol was required to precipitate poly(**methyl**) and poly(**CF3**).

(**C-7**)-poly(**benzyl**):

^{1}HNMR (400MHz, $CDCl_3$) δ_H 7.205 (5H, br s, ArH), 4.810 (2H, br s, CH2), 2.0-1.5 (2H, m, CH2), 1.0-0.5 (3H, m, CH3).

GPC: (THF, 30°C@1 mL/min), $Mn =$ 13944 g/mol, $M_W =$ 16059 g/mol, $PDI = 1.15$.

(**C-7**)-poly(**CF3**):

^{1}HNMR (400MHz, $CDCl_3$) δ_H 4.266 (2H, br s, CH2), 2.2-1.6 (2H, m, CH2), 1.1-0.6 (3H, m, CH3).

GPC: (THF, 30°C@1 mL/min), $Mn =$ 14984 g/mol, $M_W =$ 18385 g/mol, $PDI = 1.23$.

(**C-7**)-poly(**DMAEM**):

^{1}HNMR (400MHz, $CDCl_3$) δ_H 3.995 (2H, br s, CH2), 2.501 (2H, br s, CH2), 2.216 (6H, br s, CH3 x2), 2.0-1.6 (2H, m, CH2), 1.1-0.6 (3H, m, CH3).

GPC: (THF, 30°C@1 mL/min), $Mn = 10863$ g/mol, $M_W = 14687$ g/mol, $PDI = 1.35$.

(THF(+1% NEt_3), @1 mL/min), $Mn = 30309$ g/mol, $M_W = 37633$ g/mol, $PDI = 1.24$.

(**C-7**)-poly(**methyl**):

^{1}HNMR (400MHz, $CDCl_3$) δ_H 3.532 (3H, br s, CH2), 2.0-1.6 (2H, m, CH2), 1.1-0.6 (3H, m, CH3).

GPC: (THF, 30°C@1 mL/min), $Mn =$ 9023 g/mol, $M_W =$ 9831 g/mol, $PDI = 1.09$.

(**C-7**)-poly(**naphth**):

^{1}HNMR (400MHz, $CDCl_3$) δ_H 8.0-7.5 (3H, m, ArH), 7.5-7.1 (4H, m, ArH), 5.45-5.05 (2H, m, CH2), 2.0-1.4 (2H, m, CH2), 0.8-0.3 (3H, m, CH3).

GPC: (THF, 30°C@1 mL/min), $Mn =$ 6068 g/mol, $M_W =$ 6997 g/mol, $PDI = 1.153$.

(**C-7**)-poly(**nitro**):

^{1}HNMR (400MHz, $CDCl_3$) δ_H 4.3-4.0 (2H, m, CH2), 2.0-1.4 (8H, m, CH2 and CH3 x2), 1.0-0.5 (3H, m, CH3).

GPC: (THF, 30°C@1 mL/min), $Mn =$ 16906 g/mol, $M_W =$ 20663 g/mol, $PDI = 1.22$.

(**C-7**)-poly(**thio(2)**):

^{1}HNMR (400MHz, $CDCl_3$) δ_H 4.2-3.9 (2H, m, CH2), 2.75-2.55 (2H, m, CH2), 2.110 (3H, m, CH3), 2.0-1.6 (2H, m, CH2), 1.1-0.7 (3H, m, CH3).

GPC: (THF, 30°C@1 mL/min), $Mn =$ 14324 g/mol, $M_W =$ 16213 g/mol, $PDI = 1.13$.

(c). PEG co-polymer ATRP synthesis:

ATRP general procedure.

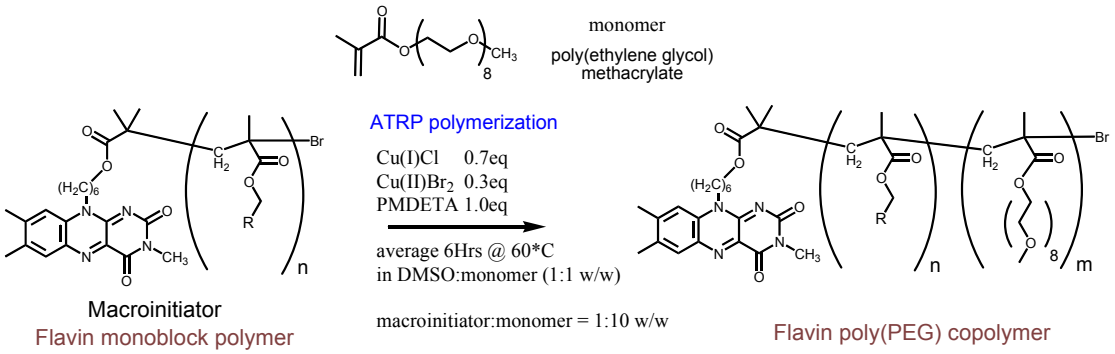

The flavin monoblock polymer (0.5g) was first dissolved in DMSO (4.5mL) in a two neck r.b flask by stirring at r.t for approx 30min before adding PEG methacrylate (5.0g, 0.01mol, 1:100 w/w). This would become the reaction flask. The catalytic system (Cu(I)Cl (26mg, 0.26mmol), Cu(II)Br_2 (25mg, 0.11mmol) and ligand PMDETA (70mg, 0.40mmol) at molar equivalents 7:3:10 respectively) was added to a second r.b flask and dissolved in DMSO (5mL). (This 10 fold scale-up was necessary in order to maintain reasonable accuracy with the small quantities of catalyst involved). Both flasks underwent three cycles of "freeze-pump-thaw" to evacuate all trace of the free radical oxygen gas using nitrogen gas (O_2 free) as the protective atmosphere. After the final thaws, a gas tight syringe was used to inject 0.5mL of the Cu(I)/Cu(II)/PMDETA mixture directly into the centre of the reaction flask while stirred under a fast flowing nitrogen purge. The reaction flask was sealed under a nitrogen atmosphere, then lowered into the thermostatically controlled oil bath and stirred at the reaction temperature of 60°C for 6H. The reaction was monitored by periodically withdrawing small sample to process by GPC. The reaction was terminated after 6H by slowly pouring the reaction mixture into 400ml of diethyl ether which was vigorously stirred at r.t. The copolymer precipitated as a green-yellow residue which was allowed to settle for approximately 1H before collecting by decanting. The copolymer residue was then dissolved in $CHCl_3$ (60mL) and passed through a short column of Al_2O_3 to remove trace copper catalyst. The subsequent cloudy yellow filtrate was reduced in volume under vacuum to approx 30mL and then centrifuged for 1H in order to sediment aluminium oxide particulates. The copolymer was re-precipitated and decanted in the same manner as before to provide a clear yellow residue. The copolymer was then finally dried under high vacuum for 48H.

*The "*reference integral*" has been identified in each example below as the best defined and well separated ^{1}HNMR peak from the macroinitiator and was used as an integration comparison to determine the relative number ratio of first block monomers to second block monomers, (i.e. ratio $m:n$).

Note: some of the GPC results for two of these PEG copolymers have been run at a higher temperature (i.e. 50°C@1 mL/min) and have subsequently provided results indicating both higher molecular weights with lower polydispersity index values (*PDI*). This procedure was preformed as it was believed that the components of the diblock copolymer were interacting in a way to increase the retention time through the GPC column. Increasing the temperature was considered as a simple way of disrupting this interaction and resolving this problem. It clearly has had a significant influence, unfortunately however, high temperature GPC results for the remaining polymers are at this time pending a repair of the GPC apparatus.

(**C-7**)-poly(**benzyl**)-b(**PEG**):

^{1}HNMR (400MHz, $CDCl_3$) δ_H 7.240 (5.47H, br s, ArH x5 **benzyl**+$CHCl_3$), 4.844 (2.0H (*reference integral*), br s, CH2 **benzyl**), 4.048 (9.0H, br s, CH2 **PEG**), 3.75-3.45 (145.2H, CH2 x15 **PEG**), 3.347 (14.67H, s, CH3 **PEG**), 2.0-1.5 (8.2H, m, CH2 **benzyl**+**PEG**), 1.0-0.5 (15.4H, m, CH3 **benzyl**+**PEG**). ratio $m:n \simeq 4.6$

GPC: (THF, 50°C@1 mL/min), $Mn =$ 64372 g/mol, $M_W =$ 99785 g/mol, $PDI = 1.55$.

(**C-7**)-poly(**CF3**)-b(**PEG**):

^{1}HNMR (400MHz, $CDCl_3$) δ_H 4.276 (2H (*reference integral)*, br s, CH2 **CF3**), 4.012 (5.9H, br s, CH2 **PEG**), 3.70-3.45 (103.5H, m, CH2 x15 **PEG**), 3.313 (10.2H, s, CH3 **PEG**), 2.1-1.5 (6.0H, m, CH2 **PEG**+**CF3**), 1.1-0.6 (11.7H, m, CH3 **PEG**+**CF3**). ratio $m:n \simeq 3.0$

GPC: (THF, 30°C@1 mL/min), $Mn =$ 33264 g/mol, $M_W =$ 50029 g/mol, $PDI = 1.50$.

GPC: (THF, 50°C@1 mL/min), $Mn =$ 102904 g/mol, $M_W =$ 115905 g/mol, $PDI = 1.26$.

(**C-7**)-poly(**DMAEM**)-b(**PEG**):

^{1}HNMR (400MHz, $CDCl_3$) δ_H 4.011 (8.3H, br s, CH2 **DMAEM**+**PEG**), 3.70-3.45 (97.7H, m, CH2 x15 **PEG**), 3.325 (9.7H, s, CH3 **PEG**), 2.498 (3.9H, br s, CH2 **DMAEM**), 2.223 (6H (*reference integral)*, br s, CH3 x2 **DMAEM**), 2.0-1.6 (6.22H, m, CH2 **DMAEM**+**PEG**), 1.1-0.6 (12.1H, m, CH3 **DMAEM**+**PEG**). ratio $m:n \simeq 1.0$

GPC: (THF, 30°C@1 mL/min), $Mn =$ 44593 g/mol, $M_W =$ 65099 g/mol, $PDI = 1.46$.

(**C-7**)-poly(**methyl**)-b(**PEG**):

^{1}HNMR (400MHz, $CDCl_3$) δ_H 4.021 (2H (*reference integral*), br s, CH2 **PEG**), 3.85-3.35 (33.5H, m, CH2 x15 **PEG** + CH3 **methyl**), 3.320 (3.2H, s, CH3 **PEG**), 2.0-1.6 (1.96H, m, CH2 **PEG**+**methyl**), 1.1-0.6 (3.5H, m, CH3 **PEG**+**methyl**). ratio $m:n \simeq 1.15$ (i.e. CH3 methyl estimates as 3.5H between 3.85-3.35 ppm).

GPC: (THF, 30°C@1 mL/min), $Mn =$ 34370 g/mol, $M_W =$ 45719 g/mol, $PDI = 1.33$.

(**C-7**)-poly(**naphth**)-b(**PEG**):

^{1}HNMR (400MHz, $CDCl_3$) δ_H 7.9-7.5 (3.0H, m, ArH **naphth**), 7.5-7.1 (4.6H, m, ArH **naphth**+$CHCl_3$), 5.45-5.05 (2H (*reference integral*), m, CH2 **naphth**), 4.030 (10.7H, br s, CH2 **PEG**), 3.70-3.45 (174.7H, m, CH2 x15 **PEG**), 3.329 (17.1H, s, CH3 **PEG**), 2.1-1.5 (10.7H, m, CH2 **PEG**+**naphth**), 1.2-0.5 (19.8H, m, CH3 **PEG**+**naphth**). ratio $m:n \simeq 5.3$

GPC: (THF, 30°C@1 mL/min), $Mn =$ 27940 g/mol, $M_W = 38555$ g/mol, $PDI = 1.38$.

(**C-7**)-poly(**nitro**)-b(**PEG**):

^{1}HNMR (400MHz, $CDCl_3$) δ_H 4.159 (2H (*reference integral*), br s, CH2 **nitro**), 4.012 (6.2, br s, CH2 **PEG**), 3.65-3.45 (105.1H, m, CH2 x15 **PEG**), 3.313 (10.8H, s, CH3 **PEG**), 2.0-1.5 (13.8H, m, CH2 **PEG**+**nitro** and CH3 x2 **nitro**(1.597ppm)), 1.1-0.6 (12.2H, m, CH3 **PEG**+**nitro**). ratio $m:n \simeq 5.4$

GPC: (THF, 30°C@1 mL/min), $Mn =$ 52299 g/mol, $M_W =$ 77585 g/mol, $PDI = 1.48$.

GPC: (THF, 50°C@1 mL/min), $Mn =$ 128853 g/mol, $M_W =$ 158472 g/mol, $PDI = 1.23$.

(**C-7**)-poly(**thio**)-b(**PEG**):

^{1}HNMR (400MHz, $CDCl_3$) δ_H 4.2-3.8 (8.3H, m, CH2 **thio** (4.059ppm) + CH2 **DMAEM** (4.015ppm)), 3.70-3.45 (112.3H, m, CH2 x15 **PEG**), 3.313 (12.3H, s, CH3 **PEG**), 2.73-2.65 (2H (*reference integral*), m, CH2 **thio**), 2.111 (3H, s, CH3 **thio**), 2.0-1.6 (7.2H, m, CH2 **PEG**+**thio**), 1.1-0.7 (13.0H, m, CH3 **PEG**+**thio**). ratio $m:n \simeq 3.75$

GPC: (THF, 30°C@1 mL/min), $Mn =$ 28727 g/mol, $M_W =$ 38359 g/mol, $PDI = 1.34$.

(d). TMAEM co-polymer synthesis:

ATRP of DMAEM copolymer: general procedure.

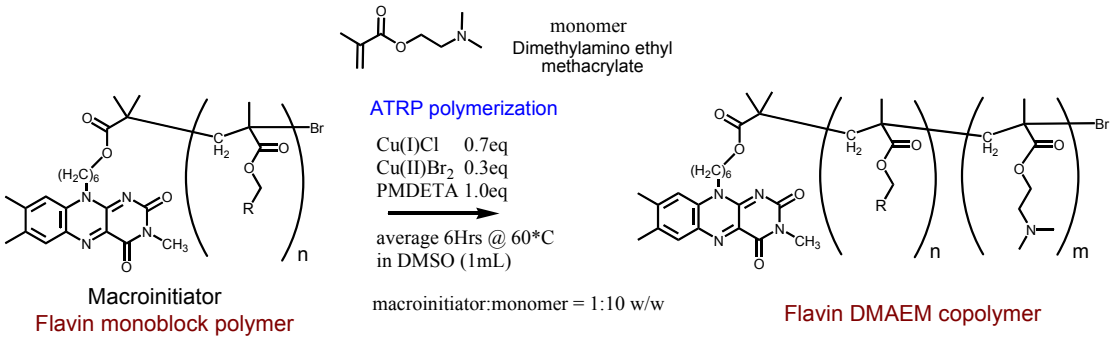

The flavin monoblock polymer (0.35g) was first dissolved in monomer DMAE methacrylate (3.5g, 22.3mmol, 1:100 w/w) in a two neck r.b flask by stirring at r.t for approx 1H. This would become the reaction flask. The catalytic system (Cu(I)Cl (26mg, 0.26mmol), $Cu(II)Br_2$ (25mg, 0.11mmol) and ligand PMDETA (70mg, 0.40mmol) at relative molar equivalents 7:3:10 respectively) was added to a second r.b flask and dissolved in DMSO (10mL). Both flasks underwent three cycles of "freeze-pump-thaw" to evacuate all trace of the free radical oxygen gas using nitrogen gas (O_2 free) as the protective atmosphere. After the final thaws, a gas tight syringe was used to inject 1mL of the Cu(I)/Cu(II)/PMDETA mixture directly into the centre of the reaction flask while stirred under a fast flowing nitrogen purge. The reaction flask was sealed under a nitrogen atmosphere, then lowered into the thermostatically controlled oil bath and stirred at the reaction temperature of 60°C for 6H. The reaction was monitored by periodically withdrawing small sample to process by GPC. The reaction was terminated after 6H by slowly pouring the reaction mixture into a conical flask containing diethyl ether (200mL) and hexane (200mL) which was vigorously stirred at r.t. The copolymer precipitated as a green-yellow residue which was allowed to settle for approximately 1H before collecting by decanting. The copolymer residue was then dissolved in $CHCl_3$ (40mL) and passed through a short column of Al_2O_3 to remove trace copper catalyst. The subsequent cloudy yellow filtrate was reduced in volume under vacuum to approx 20mL and then centrifuged for 1H in order to sediment aluminium oxide particulates. The copolymer was re-precipitated and decanted in the same manner as before to provide a clear yellow residue. The copolymer was then finally dried under high vacuum for 48H.

(**C-7**)-poly(**methyl**)-poly(**DMAEM**):

^{1}HNMR (400MHz, $CDCl_3$) δ_H 4.06 (2.0H (*reference integral*), br s, CH2 **DMAEM**), 4.06 (0.802H, br s, CH3 **methyl**), 2.57 (2.03H, br s, CH2 **DMAEM**), 2.28 (6.12H, br s, CH3 x2 **DMAEM**), 2.0-1.7 (2.26H, m, CH2 **DMAEM**+**methyl**), 1.1-0.8 (3.63H, m, CH3 **DMAEM**+**methyl**).

GPC: (THF, 30°C@1 mL/min), $M_n =$ 42990 g/mol , $M_W =$ 102181 g/mol , $PDI = 2.38$.

(**C-7**)-poly(**benzyl**)-poly(**DMAEM**):

^{1}HNMR (400MHz, $CDCl_3$) δ_H 7.26 (1.27H, br s, ArH x5 **benzyl**+$CHCl_3$), 4.886 (0.39H, br s, CH2 **benzyl**), 4.053 (2.0H (*reference integral*), br s, CH2 **DMAEM**), 2.56 (2.035H, br s, CH2 **DMAEM**), 2.286 (6.22H, br s, CH3 x2 **DMAEM**), 2.1-1.7 (2.17H, m, CH2 **DMAEM**+**benzyl**), 1.15-0.65 (3.54H, m, CH3 **DMAEM**+**benzyl**).

GPC: (THF, 30°C@1 mL/min), $M_n =$ 34134 g/mol , $M_W =$ 83440 g/mol , $PDI = 2.44$.

(**C-7**)-poly(**naphth**)-poly(**DMAEM**):

^{1}HNMR (400MHz, $CDCl_3$) δ_H 8.0-7.5 (0.41H, m, ArH x3 **naphth**), 7.5-7.1 (0.74H, m, CH2 **naphth**+$CHCl_3$), 5.5-5.1 (0.27H, m, CH2 **naphth**) 4.060 (2.0H (*reference integral*), br s, CH2 **DMAEM**), 2.563 (2.07H, br s, CH2 **DMAEM**), 2.281 (6.05H, br s, CH3 x2 **DMAEM**), 2.1-1.55 (2.16H, m, CH2 **DMAEM**+**naphth**), 1.2-0.5 (3.40H, m, CH3 **DMAEM**+**naphth**).

GPC: (THF, 30°C@1 mL/min), $M_n =$ 40287 g/mol , $M_W =$ 45312 g/mol , $PDI = 1.13$.

Cationic copolymer synthesis: general procedure.

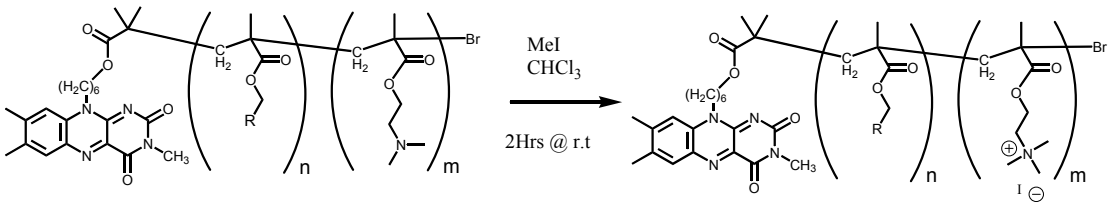

DMAEM copolymer TMAEM copolymer

The flavin DMAEM copolymer (1.0g, 1eq) was dissolved in $CHCl_3$ (10mL) and stirred at r.t for 30min before directly injecting methyl iodide (1mL, 2.28g, 16mmol, approx 2-3eq) into the centre of the reaction. Within approximately 1-2 minutes the mixture had set into an opaque orange gel. This was left for 1H before diluting with acetone (20mL) and broken into smaller pieces using a glass rod. The resulting slurry was stirred for another 1H after which the orange solids were collected by filtration and washed thoroughly with acetone (50mL x5). The remaining copolymer was carefully transferred onto a watch-glass and left to dry overnight at room temperature.

(**C-7**)-poly(**methyl**)-poly(**TMAEM**):
^{1}HNMR (400MHz, $DMSO-d6$) δ_H 4.7-4.2 (m, CH2 **TMAEM**), 4.2-3.7 (m, CH2 **TMAEM**), 3.598(br s, CH3 **methyl**), 3.343 (br s, CH3 x3 **TMAEM**), 2.1-1.4 (m, CH2 **TMAEM+methyl**), 1.3-0.2 (m, CH3 **TMAEM+methyl**).

(**C-7**)-poly(**benzyl**)-poly(**TMAEM**):
^{1}HNMR (400MHz, $DMSO-d6$) δ_H 7.302 (br s, ArH **benzyl**), 4.908 (br s, CH2 **benzyl**), 4.7-4.2 (m, CH2 **TMAEM**), 4.2-3.7 (m, CH2 **TMAEM**), 3.364 (br s, CH3 x3 **TMAEM**), 2.1-1.4 (m, CH2 **TMAEM+benzyl**), 1.3-0.2 (m, CH3 **TMAEM+benzyl**).

(**C-7**)-poly(**naphth**)-poly(**TMAEM**):
^{1}HNMR (400MHz, $DMSO-d6$) δ_H 8.1-7.6 (m, ArH **naphth**), 7.6-7.1 (m, ArH **naphth**), 5.5-5.1 (m, CH2 **naphth**), 4.7-4.2 (m, CH2 **TMAEM**), 4.2-3.7 (m, CH2 **TMAEM**), 3.7-3.0 (m, CH3 x3 **TMAEM**), 2.1-1.4 (m, CH2 **TMAEM+naphth**), 1.3-0.2 (m, CH3 **TMAEM+naphth**).

Note: Since these cationic TMAEM copolymers formed solid gels in water and viscous solution in DMSO, all subsequent ^{1}HNMR spectra were at best a compilation of very broad peaks with poorly defined baseline. Consequently accurate integration of the relevant assigned proton NMR peaks was not possible. However, spectra recorded in DMSO-d6 provided the clearest results and thus allowed us at least to assign the appropriate peak data as shown above. Absence of the two DMEAM methyl peaks from theses spectra also confirmed that full conversion of DMAEM to TMAEM had been achieved.

Chapter 3. Flavin-DAP poly(PEG) systems

(a). Flavin ATRP initiator synthesis.

C-10:

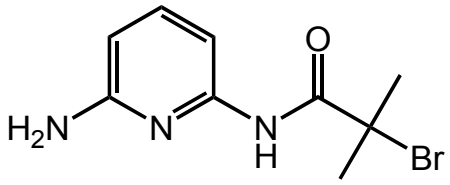

2-Bromoisobutryl bromide (7.9g, 4.25mL, 34.3mmol) was added dropwise to a stirred solution of 2,6-diaminopyridine (4.5g, 41.2mmol, 1.2 eq) and NEt_3 (8.3g, 11.5mL, 82.3mmol, 2.4 eq) in THF (150mL). After stirring at r.t for 2H, the mixture was filtered to remove precipitated NEt_3.HCl salts after which the filtrate was then condensed under vacuum to give a light brown solid. This was subjected to column chromatography (silica) using eluent DCM followed by a DCM/ethyl acetate (90:10) mixture to provide the product. Yield = 4.19g (47.5%). $C_9H_{12}BrN_3O$ (258.12). Mpt.= 63°C.

^{1}HNMR (400MHz, $CDCl_3$) δ_H 8.159(1H, s, NHC=O), 7.727(1H, dd J=9Hz and 1.5hz, ArH), 7.538(H, d J=9Hz, ArH), 6.489(1H, d J=9Hz, ArH), 4.530(2H, br s, NH2), 2.068 (6H, s, CH2 x2).

^{13}CNMR (100MHz, $CDCl_3$) δ_C 175.88(C=O), 157.90(ArC(NH2)), 150.34(ArC(NH)), 142.08(ArC), 105.77(ArC), 105.25(ArC), 51.88(CBr), 33.92(CH3 x2).

C-11:

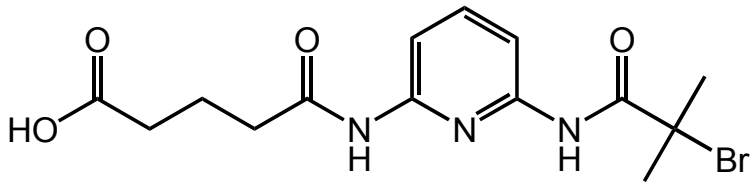

C-10 (4.19g, 16.3mmol), glutaric anhydride (2.8g, 24.5mmol, 1.5 equiv) and DMAP (210mg, 1.7mmol, 0.1eq) were heated under reflux in DCM (50mL) for 17H. After cooling to r.t the mixture was filtered to provide the pure product as a white solid. A further portion of the product was obtained by condensing the filtrate under vacuum and crystallizing overnight from warm $CHCl_3$. Yield = 5.05g (83%). $C_{14}H_{18}BrN_3O_4$ (371.05). Mpt.= 130-131°C.

m/z (EI+) = 373.02 ([M]+, 20%), 371.02 (20%), 312.02 (10%), 314.02 (10%), 256.97 (65%), 258.97 (64%) 530.16 (15), 452.09 (30), 450.11 (10), 282.1 (100), 211.0 (75), 167.1 (50). Accurate mass found: 371.0485 (^{79}Br) and 373.0460 (^{81}Br), expected: 371.0481 and 373.0446.

λ_{max} (thin film)/cm^{-1} 3399, 3258, 2955, 2867, 1696, 1664, 1585, 1537, 1501, 1445, 1333, 1296, 1284, 1149, 1134, 1110, 1082, 1019.

^{1}HNMR (400MHz, $DMSO-d_6$) δ_H 13.541 (1H, br s, OH), 10.328 (1H, s, NH), 8.651 (1H, s, NH), 8.111 (1H, d J=9.5Hz, ArH), 7.906 (1H, d J=9.5Hz, ArH), 7.813 (1H, t J=9.5Hz, ArH), 2.724 (1H, t J=5hz, CH2), 2.579 (2H, t J=5Hz, CH2), 2.045 (2H, pent J=4Hz, CH2), 2.083 (6H, s, CH3 x2).

^{13}CNMR (100MHz, $DMSO-d_6$) δ_C 178.04 (COOH), 172.20(BrC**C**=ONH), 170.38(C=ONH), 150.32(ArC), 148.57(ArC), 142.26(ArCH), 110.90(ArCH), 109.58(ArCH), 60.66(CBr), 35.86(CH2), 32.35(CH2), 32.00(CH3 x2), 20.16(CH2).

C-12:

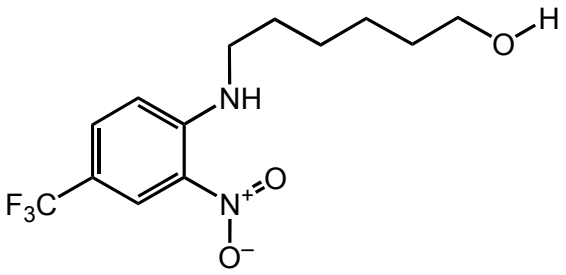

1-Chloro-2-nitro-4-trifluoromethyl benzene (21.65g, 14.0mL, 96.0mmol), 6-amino-1-hexanol (22.5g, 192.0mmol, 2eq) and NEt_3 (19.3g, 14.0mL, 191.0mmol, 2eq) were heated under reflux at 70°C in THF (200mL) for 24H. The mixture was allowed to cool and then filtered to remove NEt_3.HCl salt. The filtrate was condensed to a viscous brown residue under vacuum. This was then dissolved in DCM (100mL) and washed with distilled water (100mL x3), dried over $MgSO_4$ and then the DCM was evaporated under vacuum. The product was provided by column chromatography (silica) using eluent DCM followed by a DCM/acetone mixture (90:10) to give a yellow orange residue. Yield = 26.0g (88%). $C_{13}H_{17}N_2O_3F_3$ (306.28).

λ_{max} (thin film)/cm^{-1} 3378, 3095, 2937, 2862, 1710, 1638, 1577, 1538, 1438, 1329, 1273, 1236, 1119. MS (EI+) m/z = 306 (M+); HRMS (ES+) calculated for $C_{13}H_{17}N_2O_3F_3$ [M+H]+ 306.1191; found 306.1190.

^{1}HNMR (400MHz, d_6-DMSO) δ_H 11.338(1H, s, ArH), 7.942(1H, d J=8Hz, ArH), 7.831(H, d J=8Hz, ArH), 4.603(2H, t J=7.7Hz, NCH2CH2), 4.416(1H, t J=5Hz, NH), 3.434(2H, m, NCH2CH2), 1.80-1.70(2H, m, CH2), 1.54-1.36(6H, m, CH2 x3).

^{13}CNMR (100MHz, $CDCl_3$) δ_C 147.2 (ArCNH), 132.0(ArCNO2), 130.3(ArCH), 124.8(ArCCF3), 117.7(CF3), 116.8(ArCH), 114.3(ArCH), 62.3(CH2OH), 43.1(CH2NH), 32.3(CH2), 28.9(CH2), 27.0(CH2), 25.4(CH2).

C-13:

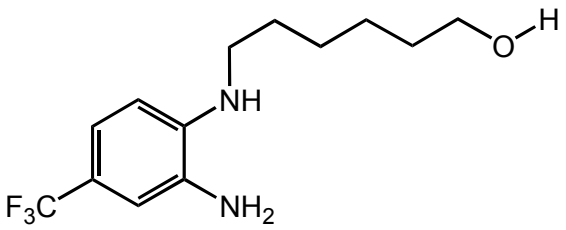

C-12 (28.7g, 94.0mmol, 1eq), ammonium formate (21.0g, 0.33moles, 3.5eq), 10% Pd(C) (1.4g) and 4 drops of glacial acetic acid were stirred in MeOH (300mL) for 1H at r.t in a sealed r.b flask, pre-flushed with nitrogen gas and fitted with an expansion balloon. The mixture was then filtered through cellite to remove the Pd(C) and the filtrate was reduced in volume under vacuum. The remaining residue was dissolved in DCM (150mL), washed with distilled water (100mL x3), dried under $MgSO_4$ and the organic layer reduced again in volume under vacuum to give a dark oily residue. This was carried on to the next stage without further preparation. Yield = 25.2g (97%). $C_{13}H_{19}F_3N_2O$ (276.1).

λ_{max} (thin film)/cm^{-1} 3372, 3321, 2931, 2860, 1604, 1516, 1476, 1363, 1306, 1235, 1153, 1101, 1050. MS (EI+) m/z = 276 (M+); HRMS (ES+) calculated for $C_{13}H_{19}N_2OF_3$ [M+H]+ 277.1528; found 277.1524

^{1}HNMR (400MHz, *CDCl*$_3$) δ_H 7.007(1H, d J=8.5Hz, ArH), 6.841(1H, s, ArH), 6.538(1H, d J=8.5Hz, ArH), 3.571(2H, t J=5.5Hz, ArNHCH2), 3.314(2H, br s, ArNH2), 3.059(2H, t J=6Hz, OCH2), 2.990(1H, t J=5.5Hz, NH), 1.70-1.45(4H, m, CH2 x2), 1.45-1.30(4H, m, CH2 x2).

^{13}CNMR (100MHz, *CDCl*$_3$) δ_C 143.8(ArCNH), 138.4(ArCNO2), 123.1(ArCCF3), 118.2(CF3), 116.3(ArCH), 104.0(ArCH), 102.2(ArCH), 66.0(CH2), 43.1(CH2), 32.9(CH2), 29.3(CH2), 27.4(CH2), 25.8(CH2).

C-14:

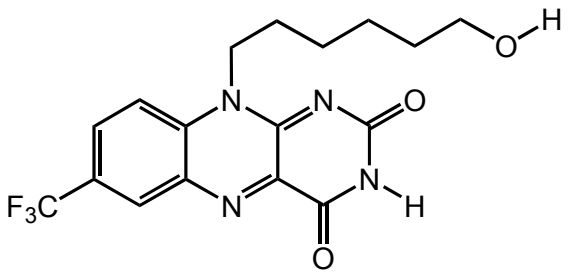

C-13 (24.8g, 90mmol, 1eq), alloxan monohydrate (14.3g, 100mmol, 1.1eq) and boron anhydride (12.6g, 180mmol, 2eq) were dissolved in glacial acetic acid (400mL) and stirred at r.t for 2H. The mixture was reduced in volume under vacuum then diluted with distilled water (300mL) and filtered. The dark yellow solids were then washed with distilled water (100mL x 3) then after dying under high vacuum at 40°C overnight, subjected to column chromatography (silica) using eluent DCM followed by a mixture of DCM/acetone (80:20). All fractions containing the product were combined and reduced in volume under vacuum. The final pure product was precipitated using a mixture of DCM/petroleum ether (40:60) to yield the pure product. Yield = 12.6g (36.7%). $C_{17}H_{17}N_4O_3F_3$ (382). Mpt.= 105-106°C (dec).
λ_{max} (KBr)/cm^{-1} 3436 br, 2938, 2861, 1718, 1632, 1596, 1561, 1455, 1412, 1363, 1327, 1253, 1181, 1130. MS (EI+) m/z = 382 (M+); HRMS (ES+) calculated for $C_{17}H_{17}N_4O_3F_3$ [M+H]+ 383.1331; found 383.1324.
^{1}HNMR (400MHz, d_6-DMSO) δ_H 11.564 (1H, s, NH), 8.528 (1H, s, ArH), 8.233 (1H, dd J=9Hz and 2Hz), 8.171 (1H, d J=9Hz, ArH), 4.609 (2H, t J=7Hz, OCH2), 4.397 (1H, t J=5Hz, OH), 3.433 (2H, sextet J=5.5Hz, NCH2), 1.82-1.70 (2H, pent J=7Hz, CH2), 1.56-1.36 (6H, m, CH2 x6).

C-15:

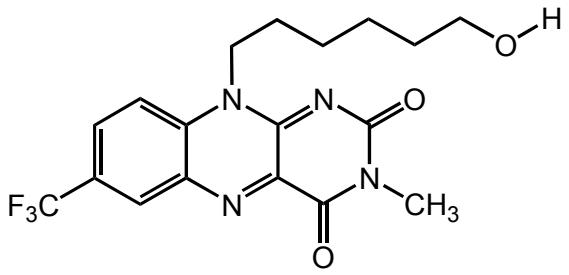

Methyl iodide (0.25mL, 590mg, 4.16mmol, 2eq) was added dropwise to a stirring solution of **C-14** (873mg, 2.3mmol, 1eq) and potassium carbonate (1.2g, 8.4mmol, 4eq) in acetone (25mL). The reaction was stirred at r.t for 16H. The K_2CO_3 was then removed by filtration and the filtrate condensed under vacuum to give a dark orange solid. The product was provided by column chromatography (silica) using eluent $CHCl_3$ followed by a mixture of $CHCl_3$/MeOH (98:2). Yield = 860mg (95%). $C_{18}H_{19}F_3N_4O_3$ (396.2). Mpt.= 235°C, (lit = 235-238°C).

m/z (EI+) for $C_{18}H_{19}N_4O_3F_3$. [M+H]calc. = 396.1409, found. 396.1411.

^{1}HNMR (400MHz, *CDCl*3) δ_H 7.89 (1H, s, ArH), 7.776 (1H, d), 7.679 (1H, d J=9Hz, ArH), 4.556 (2H, br t J=7Hz, NCH2), 4.367 (1H, t J=5.5Hz, OH), 3.379 (2H, m, OCH2), 3.249 (3H, s, CH3), 1.75-1.65 (2H, m, CH2), 1.45-1.31 (6H, m, CH2 x3).

C-16:

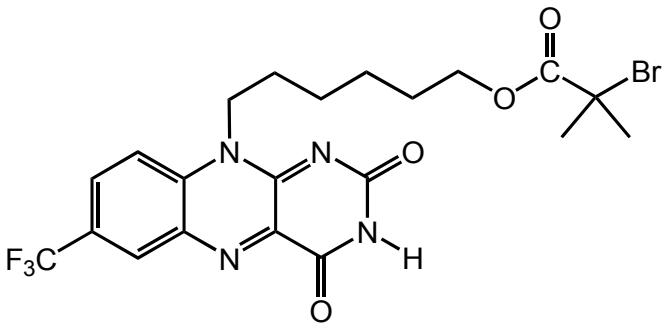

2-Bromoisobutyryl bromide (0.07mL, 130mg, 0.56 mmol) was added dropwise to a stirring solution of **C-15** in THF (25mL) and NEt_3 (0.15mL, 100mg, 1.0mmol) at r.t. The reaction was left stirring for 2H then filtered to remove NEt_3.HCl salt, washed with water and extracted with DCM (50mL x2) dried over $MgSO_4$ and concentrated under vacuum. The remaining residue was subjected to column chromatography (silica) using eluent $CHCl_3$/ethyl acetate (80:20). Fractions containing the product were combined and then concentrated under vacuum to provide an oily residue. The product was precipitated into a yellow solid by adding diethyl ether (10mL) and swirling for several seconds. Hexane was then added (30mL) and the product collect by filtration, washed with more hexane (10mL x3) and dried under vacuum. Yield = 180mg (60%). $C_{21}H_{22}N_4O_4F_3Br$ (530.08). Mpt.= 162-163°C.

m/z (EI+) = 532.14 ([M]+, 15%), 530.16 (15), 452.09 (30), 450.11 (10), 282.1 (100), 211.0 (75), 167.1 (50). Accurate mass found: 530.0767 (^{79}Br) and 532.0762 (^{81}Br), expected: 530.0777 and 532.0756.

λ_{max} (thin film)/cm^{-1} 3175, 3117, 3047, 2949, 2842, 1721, 1661, 1593, 1554, 1515, 1426, 1328, 1247, 1179, 1158, 1134.

^{1}HNMR (400MHz, *CDCl*3) δ_H 8.793 (1H, s, NH), 8.612 (1H, d J=2Hz, ArH), 8.103 (1H, dd J=9Hz and 2Hz, ArH), 7.750 (1H, d J=9Hz), 4.712 (2H, t J=7Hz, OCH2), 4.203 (2H, t J=6.5Hz, NCH2), 1.932 (6H, s, CH3 x2), 1.97-1.84 (2H, m, OCH2-CH2-), 1.748 (2H, quin J=7Hz, NCH2-CH2-), 1.66-1.46 (4H, m, CH2 x2).

^{13}CNMR (100MHz, *CDCl*3) δ_C 170.67 (OC=O), 157.30 (ArC=O), 153.61 (ArC=O), 149.60 (ArC pyrimidine), 138.00 (ArC pyrimidine), 133.82 (ArC benzene), 133.53 (ArC benzene), 130.76 (ArCH, q J=3Hz), 129.89 (ArCH, q, J=4Hz), 127.9 (q, J=35Hz, ArC-CF3), 121.85(q, J=272Hz, CF3), 115.30 (ArCH benzene), 64.52 (CH2-O), 55.10 (CBr), 44.54 (NCH2), 29.73 (CH3 x2), 27.12 (CH2), 25.95 (CH2), 25.28 (CH2), 24.48 (CH2).

C-17:

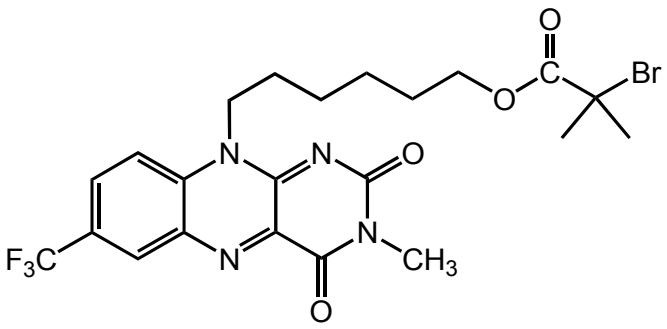

2-Bromoisobutyryl bromide (0.15mL, 280mg, 1.21mmol) was added dropwise to a stirring solution of **C-16** in THF (25mL) and tri-ethylamine (0.5mL, 350mg, 3.4mmol) at r.t. The reaction was left stirring for 2H then filtered to remove NEt_3.HCl salt, washed with water and extracted with DCM (50mL x2) dried over $MgSO_4$ and concentrated under vacuum. The remaining residue was subjected to column chromatography (silica) using eluent $CHCl_3$/ethyl acetate (80:20). Fractions containing the product were combined and then concentrated under vacuum to provide an oily residue. The product was precipitated into a yellow solid by adding diethyl ether (10mL) and swirling for several seconds. Hexane was then added (30mL) and the product collect by filtration, washed with more hexane (10mL x3) and dried under vacuum. Yield = 385mg (56%). $C_{22}H_{24}N_4O_4F_3Br$ (545.35). Mpt.= 95°C.

m/z (EI+) = 544.10 ([M]+, 5%), 546.13 (5), 464.09 (10), 466.06 (13), 310.1 (20), 296.0 (22), 239.0 (10). Accurate mass found: 544.0935 (^{79}Br) and 546.0920 (^{81}Br), expected: 544.0933 and 546.0913.

λ_{max} (thin film)/cm^{-1} 3064, 2943, 2859, 1716, 1668, 1655, 1596, 1557, 1530, 1322, 1266, 1201, 1160, 1121.

^{1}HNMR (400MHz, *CDCl*3) δ_H 8.621 (1H, d J=2Hz,), 8.076 (1H, dd J=9Hz and 2Hz, ArH), 7.727 (1H, d J=9Hz, ArH), 4.702 (2H, t J=7.5Hz, OCH2), 4.196 (2H, t J=6Hz, NCH2), 3.540 (3H, s, NCH3), 1.930 (6H, s, CH3 x2), 1.96-1.84 (2H, m, OCH2CH2-), 1.78-1.69 (2H, quin J=7Hz, NCH2CH2-), 1.64-1.46 (4H, m, CH2 x2).

^{13}CNMR (100MHz, *CDCl*3) δ_C 170.67 (OC=O), 158.04 (ArC=O), 154.48 (ArC=O), 148.06 (ArC pyrimidine), 137.44 (ArC pyrimidine), 133.86 (ArC benzene), 133.47 (ArC benzene), 130.35 (ArCH, q J=3Hz), 129.82 (ArCH, q, J=4Hz), 127.52 (q, J=35Hz, ArC-CF3), 121.94(q, J=272Hz, CF3), 115.08 (ArCH benzene), 64.54 (CH2-O), 55.07 (CBr), 44.94 (NCH2), 29.73 (CH3 x2), 27.91 (NCH3), 27.13 (CH2), 25.98 (CH2), 25.29 (CH2), 24.51 (CH2).

C-18:

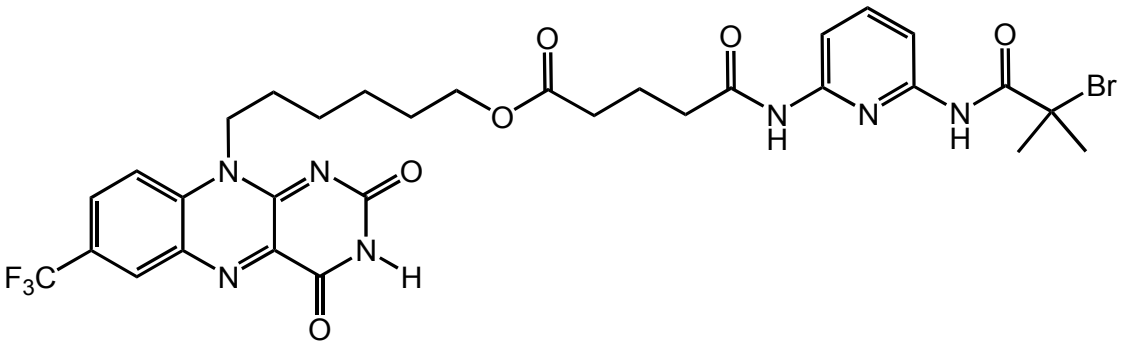

DMAP (20mg, 0.16mmol, 0.1eq) was added to a stirring suspension of **C-11** (490mg, 1.28mmol, 1eq) and HOBt (210mg, 1.54mmol, 1.2eq) in DCM (30mL) at r.t. Flavin **C-14** (490mg, 1.28mmol, 1eq) and EDCI (300mg, 1.54mmol, 1.2eq) were added after the activated ester of **C-11** had fully dissolved (approx 30 min). The reaction mixture left stirring overnight at r.t, then washed using distilled water (50mL x 3), dried ($MgSO_4$) and the solvent evaporated under vacuum. The crude mixture was then subjected to column chromatography (silica), using DCM followed by DCM/MeOH (96:4) mixture to provide an impure product. This was purified further by a second silica chromatogram column using ethyl acetate (100%) as the eluent. Yield = 440mg (47%). $C_{31}H_{33}BrF_3N_7O_6$ Exact Mass: 735.163g/mol. $C_{31}H_{33}N_7O_6F_3Br$ (735.55). Mpt.= 125°C.

m/z (FAB+) = 738.08 ([M+H]+, 5%), 736.22 (5), 226.9 (5), 147.0 (15), 74.6 (100), 73.6 (75). Accurate mass found: 736.1631 (^{79}Br) and 738.1609 (^{81}Br), expected: 736.1628 and 738.1607

λ_{max} (thin film)/cm^{-1} 3260 br, 2900 br, 1673, 1594, 1584, 1447, 1518, 1411, 1325, 1288, 1245, 1179, 1152, 1130, 1112, 1073.

^{1}HNMR (400MHz, *CDCl*$_3$) δ_H 10.619 (1H, s, NH pyrimidine), 9.035 (1H, s, NH pyridine), 8.920 (1H, s, NH pyridine), 8.639 (1H, d J=2Hz, ArH benzene), 8.104 (1H, dd J=9Hz and 2Hz, ArH benzene), 7.981 (1H, d J=8Hz, ArH benzene), 7.84-7.70 (3H, m, ArH pyridine), 4.736 (2H, t J=7Hz, NCH2-), 4.112 (2H, t J=7Hz, OCH2-), 2.537 (2H, t J=7.5Hz, OC=OCH2-), 2.440 (2H, t J=7Hz, NC=OCH2-), 2.074 (6H, s, CH3 x2), 2.1-2.0 (2H, m, CH2 succin), 1.920 (2H, quin, CH2), 1.78-1.67 (2H, m, CH2), 1.63-1.47 (4H, m, CH2 x2).

^{13}CNMR (100MHz, *CDCl*$_3$) δ_C 172.13(NC=OCBr), 170.40(OC=O succ), 169.52(NC=O succ), 158.01(ArC=O pyrim), 154.69(ArC=O pyrim), 149.70(ArC pyrim), 149.06(ArC pyrid), 148.28(ArC pyrid), 139.88(ArCH pyrid), 138.02(ArC pyrim), 133.93(ArC benzene), 133.48(ArC benzene), 130.75(ArCH, q J=3Hz), 129.97(ArCH, q, J=4Hz), 127.90(q, J=35Hz, ArC-CF3), 121.85(q, J=272Hz, CF3), 115.33(ArCH benzene), 109.52 (ArCH pyrid), 109.31(ArCH pyrid), 63.31(OCH2), 60.06(CBr), 44.26(NCH2), 35.30(CH2 succ), 32.46(CH2 succ), 30.87(CH3 x2), 26.80(CH2), 25.37(CH2), 24.76(CH2), 24.04(CH2), 19.63 (CH2 succ).

C-19:

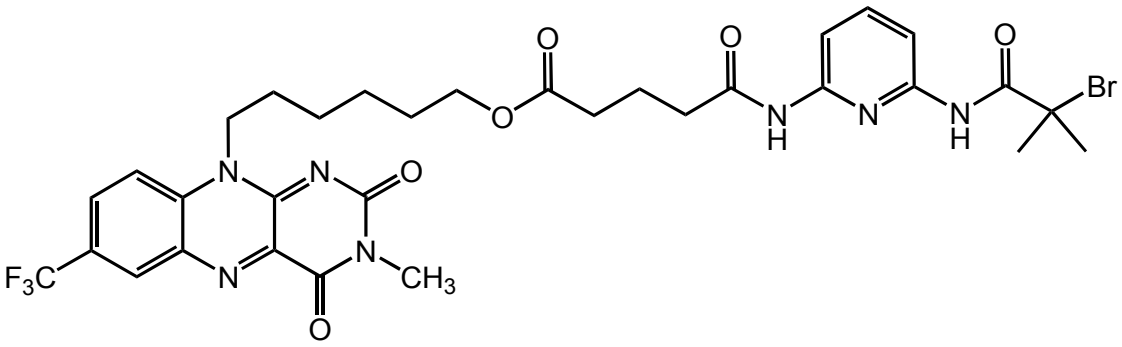

DMAP (13mg, 0.1mmol, 0.1eq) was added to a stirring suspension of **C-11** (410mg, 1.03mmol, 1eq) and HOBt (170mg, 1.24mmol, 1.2eq) in DCM (30mL) at r.t. Flavin **C-15** (410mg, 1.03mmol, 1eq) and EDCI (240mg, 1.24mmol, 1.2eq) were added after the activated ester of **C-11** had fully dissolved (approx 30 min). The reaction mixture was left stirring overnight at r.t, then washed using distilled water (50mL x 3), dried ($MgSO_4$) and the solvent evaporated under vacuum. The product was provided after column chromatography (silica), using mixture $CHCl_3$/ethyl acetate (80:20) as the eluent. Yield = 425mg (55%). $C_{32}H_{35}N_7O_6F_3Br$ (750.5). Mpt.= 105°C.

m/z (FAB+) = 752.07 ([M+H]+, 35%), 750.11 (33), 670.16 (5), 628.19 (12), 379.0 (20), 296.9 (20), 74.6 (100). Accurate mass found: 750.1786 (^{79}Br) and 752.1765 (^{81}Br), expected: 750.1784 and 752.1764. λ_{max} (thin film)/cm^{-1} 3300 br, 2961, 2929, 2868, 1662, 1596, 1558, 1447, 1325, 1296, 1244, 1197, 1154, 1129, 1074.

^{1}HNMR (400MHz, *CDCl*$_3$) δ_H 8.668 (1H, s, NH pyridine), 8.617 (1H, d J=2Hz, ArH), 8.074 (1H, dd J=9Hz and 2Hz, ArH), 7.905 (1H, d J=7.8Hz, ArH), 7.757 (1H, dd J=8Hz and 1Hz), 7.739 (1H, s, NH pyridine), 7.75-7.65 (2H, m, ArH pyridine), 4.684 (2H, t J=7.5Hz, OCH2), 4.103 (2H, t J=6.5Hz), 3.542 (3H, s, NCH3), 2.487 (2H, t J=Hz, CH2 succin), 2.450 (2H, t J=Hz CH2 succin), 2.1-2.0 (2H, m, CH2 succin), 2.034 (6H, s, CH3 x2), 1.870 (2H, quin J=8Hz, OCH2C**H2**-), 1.73-1.61 (2H, m, NCH2C**H2**-), 1.61-1.51 (2H, m, OCH2CH2C**H2**-). 1.51-1.41 (2H, m, NCH2CH2C**H2**-).

^{13}CNMR (100MHz, *CDCl*$_3$) δ_C 172.05(N**C**=OCBr), 169.67(OC=O succ), 169.18(NC=O succ), 158.04(ArC=O pyrim), 154.52(ArC=O pyrim), 148.52(ArC pyrim), 148.05(ArC pyrid), 148.02(ArC pyrid), 139.80(ArCH pyrid), 137.42(ArC pyrim), 133.86(ArC benzene), 133.48(ArC benzene), 130.34(ArCH, q J=3Hz), 129.80(ArCH, q, J=4Hz), 127.51(q, J=35Hz, ArC-CF3), 121.93(q, J=272Hz, CF3), 115.10(ArCH benzene), 108.89(ArCH pyrid), 108.07(ArCH pyrid), 63.18(OCH2), 60.70(CBr), 43.95(NCH2), 35.39(CH2 succ), 32.17(CH2 succ), 31.19(CH3 x2), 27.35(CH2), 25.95(CH2), 25.34(CH2), 24.64(CH2), 19.42 (CH2 succ).

(b). Flavin-DAP poly(PEG) synthesis.

ATRP general procedure.

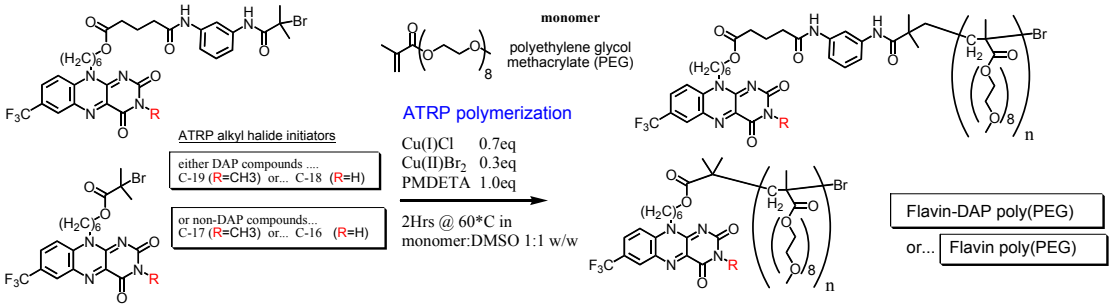

The flavin initiator (either C-16 = 79.7mg, C-17 = 81.8mg, C-18 = 110.5mg or C-19 = 112.6mg 0.15mmol, 1eq) was dissolved in DMSO (9.7mL) in a two neck r.b flask by stirring at r.t before adding PEG methacrylate (10.7g, 22.5mmol, 150eq). This would become the reaction flask. The catalytic system (Cu(I)Cl (104mg, 1.05mmol, 7eq), $Cu(II)Br_2$ (100mg, 0.45mmol, 3eq) and ligand PMDETA (260mg, 0.75mmol, 10eq) was added to a second r.b flask and dissolved in DMSO (10mL). (This 10 fold scale-up was necessary in order to maintain reasonable accuracy with the small quantities of catalyst involved). Both flasks underwent three cycles of "freeze-pump-thaw" to evacuate all trace of the free radical oxygen gas using nitrogen gas (O_2 free) as the protective atmosphere. After the final thaws, a gas tight syringe was used to inject 1mL of the Cu(I)/Cu(II)/PMDETA mixture directly into the centre of the reaction flask while stirred under a fast flowing nitrogen purge. The reaction flask was sealed under a nitrogen atmosphere, then lowered into the thermostatically controlled oil bath and stirred at the reaction temperature of 60°C for 2H. The reaction was monitored by periodically withdrawing small sample to process by GPC. The reaction was terminated after 2H by slowly pouring the reaction mixture into 400ml of diethyl ether which was vigorously stirred at r.t. The polymer precipitated as a green-yellow residue which was allowed to settle for approximately 1H before collecting by decanting. The polymer was then dissolved in $CHCl_3$ (50mL) and passed through a short column of Al_2O_3 to remove trace copper catalyst. The filtrate was reduced in volume under vacuum to approx 25mL and after passing through a $0.45\mu m$ syringe filter, the polymer was re-precipitated and collected in the same manner as before to provide the polymer as either a clear yellow residue. The polymer was then finally dried under high vacuum for 48H.

(**C-19**)-poly(**PEG**):

^{1}HNMR (400MHz, $CDCl_3$) δ_H 4.042 (2H, br s, CH2 **PEG**), 3.601 (28H, m, CH2 x14 **PEG**), 3.502 (2H, br s, CH2 **PEG**), 3.324 (3H, CH3 **PEG**), 2.2-1.5 (2H, m, CH2 **PEG**), 1.2-0.6 (3H, m, CH3 **PEG**).

GPC results: (THF, @1 mL/min), $M_n = 24722\, g/mol$, $M_W = 28365\, g/mol$, $PDI = 1.15$.

(**C-18**)-poly(**PEG**):

^{1}HNMR (400MHz, $CDCl_3$) δ_H 4.032 (2H, br s, CH2 **PEG**), 3.598 (28H, m, CH2 x14 **PEG**), 3.500 (2H, br s, CH2 **PEG**), 3.324 (3H, CH3 **PEG**), 2.2-1.4 (2H, m, CH2 **PEG**), 1.2-0.6 (3H, m, CH3 **PEG**).

GPC results: (THF, @1 mL/min), $M_n = 17325\, g/mol$, $M_W = 21017\, g/mol$, $PDI = 1.21$.

(**C-17**)-poly(**PEG**):

^{1}HNMR (400MHz, $CDCl_3$) δ_H 4.022 (2H, br s, CH2 **PEG**), 3.599 (28H, m, CH2 x14 **PEG**), 3.495 (2H, br s, CH2 **PEG**), 3.319 (3H, CH3 **PEG**), 2.2-1.4 (2H, m, CH2 **PEG**), 1.2-0.6 (3H, m, CH3 **PEG**).

GPC results: (THF, @1 mL/min), $M_n = 11540\, g/mol$, $M_W = 14406\, g/mol$, $PDI = 1.25$.

(**C-16**)-poly(**PEG**):

^{1}HNMR (400MHz, $CDCl_3$) δ_H 4.022 (2H, br s, CH2 **PEG**), 3.591 (28H, m, CH2 x14 **PEG**), 3.495 (2H, br s, CH2 **PEG**), 3.319 (3H, CH3 **PEG**), 2.2-1.4 (2H, m, CH2 **PEG**), 1.2-0.6 (3H, m, CH3 **PEG**).

GPC results: (THF, @1 mL/min), $M_n = 13136\, g/mol$, $M_W = 15556\, g/mol$, $PDI = 1.18$.

Chapter 4: Flavin-fumaramide [2]Rotaxane poly(PEG).

(a). Synthesis of the ATRP initiator.

C-20:

N-(2,2-diphenylethyl) fumaramic acid monoethyl ester: [32]

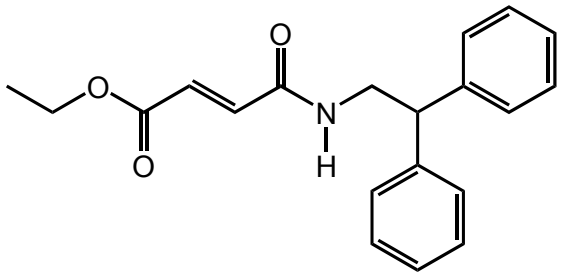

2,2-Diphenylethyl amine (2.03g, 10.3mmol, 1eq), fumaric acid monoethyl ester (1.49g, 10.3mmol, 1eq), HOBt (1.68g, 12.4mmol, 1.2eq) and DMAP (160mg, 1.3mmol, 0.1eq) were stirred for several minutes at r.t in DCM (50mL) before adding EDCI.HCl (2.37g, 12.4mmol, 1.2eq). The reaction was stirred for 2H at r.t before the solvent was evaporated under vacuum. The product was provide after column chromatography (silica) using eluent DCM followed by a mixture of DCM/ethyl acetate (90:10). Yield = 2.8g (84%). Mpt.= 114°C (lit = 112-113°C [32]).

^{1}HNMR (400MHz, *CDCl*$_3$) δ_H 7.30-7.10 (10H, m, ArH x10), 6.882 (1H, d J= 15Hz, CH alkene), 6.761 (1H, d J= 15Hz, CH alkene), 6.143 (1H, br t J=6Hz, NH), 4.155 (1H, t J=8Hz, CH-Ph2), 4.021 (2H, q J=7Hz, OCH2CH3), 3.933 (2H, d, J=8Hz, CH2CH), 1.279 (3H, t J=7Hz, CH3).

C-21:

N-(2,2-diphenylethyl) fumaramic acid: [32]

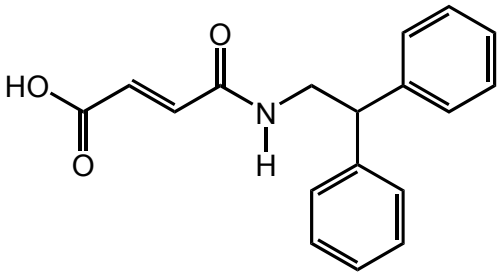

Aqueous NaOH (0.53g, 11.5mmol, 13mL) was added to a stirred solution of **C-20** (3.71g, 11.5mmol) in ethanol (150mL) at r.t. After 20H the solvent was evaporated under vacuum to provide a white solid. Distilled water (100mL) was added and the pH of the stirring suspension adjusted to 4 by dropwise addition of conc HCl. The product was extracted by washing with ethyl acetate (100mL x3), dried over $MgSO_4$ and the solvent evaporated under vacuum to provide the product as a white solid. Yield = 3.1g (91%). $C_{18}H_{17}NO_3$ (295). Mpt.= as published dec >270 °C [32].

^{1}HNMR (400MHz, $DMSO-d6$) δ_H 12.782 (1H, s, br), 8.577 (1H, br t J=6Hz, NH), 7.35-7.20 (10H, m, Ph2 ArH x10), 6.931 (1H, d J=15Hz, CH alkene), 6.548 (1H, d J=15Hz, CH alkene), 4.171 (1H, t J=7Hz, CHCH2) and 3.779 (2H, d J=7Hz, CH2).

C-22:

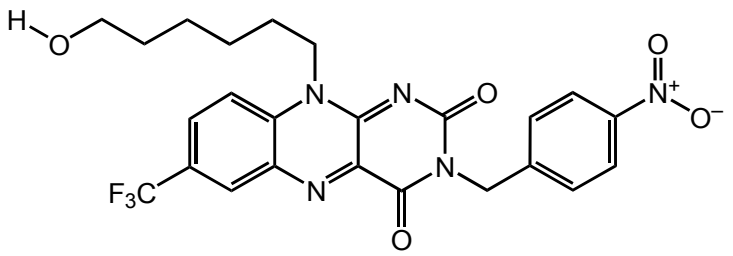

Flavin **C-14** (2.5g, 6.5mmol, 1eq) was stirred with nitro benzyl chloride (1.66g, 9.7mmol. 1.5eq) under reflux in acetone (150mL) for 4 days. The mixture was filtered and the filtrate evaporated under vacuum. The remaining solids were dissolved in $CHCl_3$ and subjected to column chromatography using eluent DCM followed by DCM/acetone (9:1). All fractions containing the product were combined, dissolved in the minimum amount of acetone and precipitated by adding petroleum ether to give the pure product.

Yield = 2.43g (72%). Mpt.= 163-165°C.

m/z (FAB) = 518.3 ([M+H]+,100%), 502.3 (9), 418 (8), 137 (19). Found 518.1649. $C_{24}H_{23}F_3N_5O_5$ requires [M+H]+, 518.1651.

λ_{max} (thin film)/cm^{-1} 3400 br, 2916, 2858, 1703, 1660, 1596, 1566, 1344, 1285, 1224, 1197, 1128.

^{1}HNMR (400MHz, $CDCl_3$) δ_H 8.59(1H, br s, ArH-a), 8.16(2H, d, J=8.8Hz, ArH-b' x2), 8.09(1H, dd, J=9.0 and 1.7Hz, ArH-b), 7.76(1H, d, J=7.7Hz, ArH-c and 2H, d, J=8.8Hz, ArH-c' x2), 5.36(2H, s, CH2-a'), 4.69(2H, br t, CH2-d), 3.67(2H, t, J=6.0Hz, CH2-i), 1.89(2H, quint, J=7.5Hz, CH2-e), 1.65-1.50(6H, m, CH2-f,g,h).

^{13}CNMR (100MHz, $CDCl_3$) δ_C 158.9(ArC=O), 154.9(ArC=O), 149.1(ArC=N), 147.4(ArC=N), 143.5(ArC), 138.3(ArC), 135.0(ArC), 134.5(ArC), 131.7(ArCH, q, J=3Hz), 130.8(ArCH, q, J=3.9Hz), 130.3(2xArCH, AB), 128.8(q, J=35Hz, ArC-CF3), 122.8(q, J=272Hz, CF3), 123.7(2xArCH, AB), 116.3(ArCH), 62.4(CH2), 45.1(CH2), 44.6(CH2), 32.2(CH2), 26.7(CH2), 26.3(CH2), 25.0(CH2).

C-23:

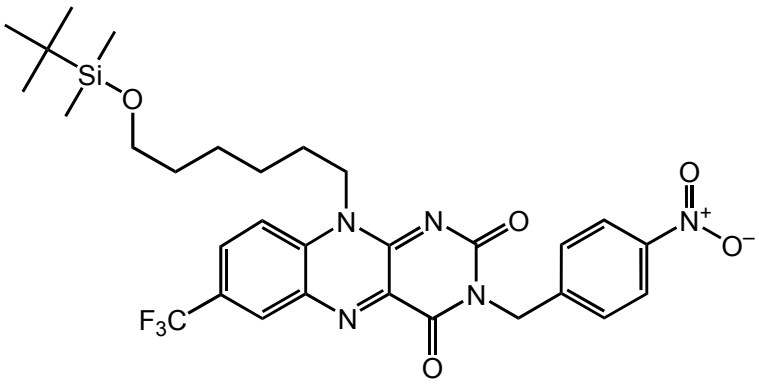

C-22 (3.3g, 6.38mmol, 1eq) was dissolved in DMF (5mL) before adding TBSCl (2.13, 14.13mmol, 1.5eq) and DMAP (106mg, 0.87mmol, 0.1eq). The mixture was stirred at r.t for 20min before adding NEt_3 (2mL) dropwise by pipette. The mixture was stirred for a further 1H then diluted with distilled water (100mL) and the product extracted with DCM (100mL x2), dried over $MgSO_4$ and the solvent removed under vacuum to give an orange crystalline solid. This was dried under high vacuum at r.t for 3H before dissolving in diethyl ether (50mL). The pure product precipitated as a yellow solid within 1 to 2 minutes and was easily collected by filtration. Yield = 3.77g (93.5%). $C_{30}H_{36}N_5O_5F_3Si$ (631.7). Mpt.= 163-165°C.

m/z (FAB) = 632.4 ([M+H]+,100%), 616.4(20), 574.3(40). Accurate mass: Found 632.2513. $C_{30}H_{37}O_5N_5F_3Si$ requires [M+H]+, 632.2516.

λ_{max} (thin film)/cm^{-1} 2939, 2860, 1717, 1669, 1596, 1559, 1457, 1337, 1239, 1192, 1127, 1014.

^{1}HNMR (400MHz, $CDCl_3$) δ_H 8.59 (1H, d, J=1.2Hz, ArH-a), 8.16 (2H, d, J=8.9Hz, Ar-b' x2), 8.09 (1H, dd, J=9.2 and 1.9Hz, ArH-b), 7.75 (2H, d, J=8.9Hz, ArH-c' x2), 7.74 (1H, d, J= 9.2Hz, ArH-c), 5.36 (2H, s, CH2-a'), 4.68 (2H, t, broad, J=7.5, CH2-d), 3.61 (2H, t, J=6.2Hz, CH2-i), 1.87 (2H, quint, J=7.6Hz, CH2-e), 1.60-1.40 (6H, m, CH2-f,g,h), 0.88 (9H, s, CH3-k x3), 0.04 (6H, s, CH3-j x2).

^{13}CNMR (100MHz, $CDCl_3$) δ_C 158.9(ArC=O), 154.8(ArC=O), 149.1(ArC=N), 147.4(ArC=N), 143.5(ArC flavin), 138.3(ArC benzyl), 134.9(ArC flavin), 134.5(ArC benzyl), 131.6(ArCH, q, J=3Hz), 130.7(ArCH, q, J=3.9Hz), 130.3(2xArCH, AB), 128.7(q, J=35Hz, ArC-CF3), 124.2(ArCH), 123.6(q, J=272Hz, CF3), 116.3(2xArCH, AB), 62.8(CH2), 45.3(CH2), 44.6(CH2), 32.5(CH2), 27.1(CH2), 26.6(CH2), 25.9(3x CH3), 25.5(CH2), 18.3(CSi), -5.3(2x CH3).

C-24:

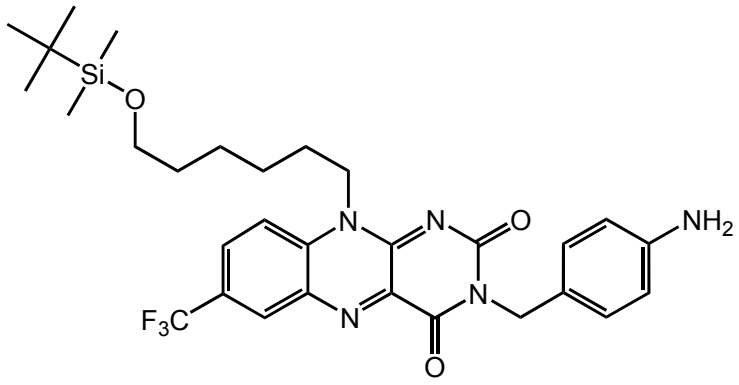

C-23 (3.65g, 5.77mmol, 1eq) and ammonium formate were dissolved in MeOH (100mL) before adding 5% Pd(C) (153mg) in a sealed r.b flask, pre-flushed with nitrogen gas and fitted with an expansion balloon. The reaction was stirred at r.t for 1H. The mixture was then filtered through cellite to remove the Pd(C) and the filtrate was concentrated under vacuum to give a dark brown solid. The solid was then dissolved in DCM (100mL) and washed with water (100mL x3), dried over $MgSO_4$ and the DCM evaporated under vacuum. The product was provided after column chromatography (silica) using eluent DCM followed by a mixture of DCM/acetone (90:10). Yield = 2.95g (85%). $C_{30}H_{38}N_5O_3F_3Si$ (601.27). Mpt.= 94-95°C.

λ_{max} (thin film)/cm^{-1} 3452, 3357, 2939, 2859, 1712, 1664, 1600, 1559, 1459, 1331, 1284, 1242, 1192, 1128, 1005.

m/z (FAB) = 624.4 ([M+ Na]+, 92%), 601.4 (23), 519.4 (23), 439.3 (48), 107.7 (95), 75.2 (100). Found 624.2596. $C_{30}H_{38}O_3N_5F_3SiNa$ requires [M+Na]+, 624.2594.

^{1}HNMR (400MHz, *CDCl*$_3$) δ_H 8.55 (1H, d, J=1.5Hz, ArH-a), 8.03 (1H, dd, J=9Hz and 2Hz, ArH), 7.69 (1H, d, J=9Hz, ArH), 7.42 (2H, d, J=8.5Hz, ArH-b' x2), 6.58 (2H, d, J=8.5Hz, ArH), 5.15 (2H, s, CH2), 4.63 (2H, br t, J=6.5Hz, NCH2CH2), 3.63 (2H, s, NH2), 3.61 (2H, t, J=6.5Hz, OCH2CH2), 1.83 (2H, quint, J=7.7Hz, CH2), 1.58-1.38 (6H, m, CH2 x3), 0.88 (9H, s, CH3 x3), 0.04 (6H, s, CH3 x2).

^{13}CNMR (100MHz, *CDCl*$_3$) δ_C 158.8(ArC=O), 155.2(ArC=O), 148.9(ArC=N), 146.1(ArC=N), 138.7(ArC), 134.7(ArC), 134.5(ArC), 131.2(2xArCH AB), 131.1(ArCH, br s), 130.6(ArCH, q, J=4Hz), 128.3(q, J=35Hz, ArC-CF3), 126.5(ArC), 122.9(q, J=272Hz, CF3), 116.1(ArCH), 114.7(2xArCH AB), 62.8(CH2), 45.0(CH2), 44.7(CH2), 32.5(CH2), 27.0(CH2), 26.6(CH2), 25.9(3x CH3), 25.5(CH2), 18.3(CSi), -5.3(2x CH3).

C-25:

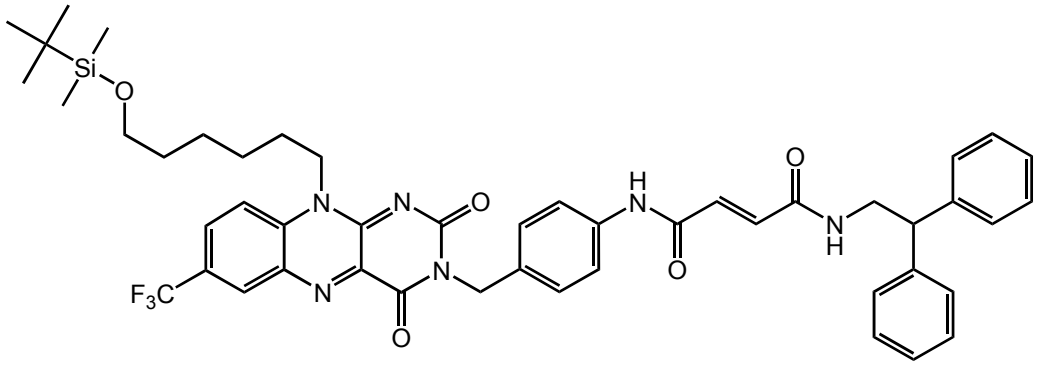

C-21 (2.97g, 4.94mmol, 1eq), HOBt (810mg, 6.0mmol, 1.2eq) and DMAP (122mg, 1.0mmol, 0.2eq) were stirred in DCM (40mL) for several minutes at r.t before adding EDCI.HCl (1.15g, 6.0mmol, 1.2eq). After a further 5-10 min and the solution had cleared, flavin **C-24** pre-dissolved in DCM (40mL) was added to the mixture and the reaction stirred at r.t for 18H. The mixture was provide by column chromatography using eluent DCM followed by DCM/acetone (90:10). Yield = 2.63g (61%). $C_{48}H_{53}N_6O_5F_3Si$ (879.05). Mpt.= 184-186°C.

m/z (FAB) = 879.54 ([M+H]+, 32%), 880.54 (29), 821.3 (12), 497.0 (16), 438.9 (24), 73.6 (100). Elemental analysis cald. (%) for $C_{48}H_{53}N_6O_5F_3Si$ (878.54): C, 65.58; H, 6.08; F, 6.48; N, 9.56; O, 9.10; Si, 3.19. Found C, 65.72; H, 5.99; N, 9.63.

^{1}HNMR (400MHz, *CDCl*$_3$) δ_H 9.11 (1H, s, ArNH), 8.48 (1H, s, ArH), 8.00 (1H, d, J=9Hz, ArH), 7.65 (1H, d, J=9Hz, ArH), 7.51 (2H, d, J=8.5Hz, AA'BB' ArH x2), 7.40 (2H, d, J=8.5Hz, AA'BB' ArH x2), 7.29-7.09 (11H, m, Ph2 ArH x10 and CH alkene), 6.87 (1H, d, J=14.8Hz, CH alkene), 6.30 (1H, br t, J=5Hz, NHCH2), 5.17 (2H, s, ArCH2), 4.58 (2H, br t J=6Hz, NCH2CH2), 4.16 (1H, br t, J=7.7Hz, CH), 3.93 (2H, br t, J=7Hz, NHCH2CH), 3.56 (2H, br t, J=6Hz, OCH2CH2), 1.78 (2H, pent, J=6.5Hz, CH2), 1.55-1.30 (6H, m, CH2 x3), 0.84 (9H, s, CH3 x3), 0.00 (6H, s, CH3 x2).

^{13}CNMR (100MHz, *CDCl*$_3$) δ_C 164.33(NC=O), 162.45(NC=O), 159.44(N(N)C=O flavin), 158.89(NC=O flavin), 155.17(N=CC=N flavin), 149.01(N=CC=N flavin), 141.51(Ph2 ArC x2), 138.62(N-CC-N flavin), 137.61(ArCCH2), 134.88(ArCNH), 134.53(N-CC-N flavin), 134.30(CH alkene), 133.31(CH alkene), 131.35(ArCH, q, J=3Hz), 130.69(ArCH, q, J=4Hz), 130.41(ArCH benzyl x2), 128.86(Ph2 ArCH x4), 127.92(Ph2 ArCH x4), 127.01(Ph ArCH x2), 126.45(q, J=35Hz, ArC-CF3), 122.96 (q, J=272Hz, CF3), 120.27(ArCH x2 benzyl), 116.19(ArCH flavin), 62.93(OCH2), 50.27(CH), 45.20(Ar-CH2), 44.85(CH2CH), 44.25(NCH2CH2), 32.60(OCH2CH2), 27.07(CH2), 26.68(CH2), 26.00(Si(CH3)3), 25.60(CH2), 18.38 (SiC), -5.24(SiCH3 x2).

C-26:

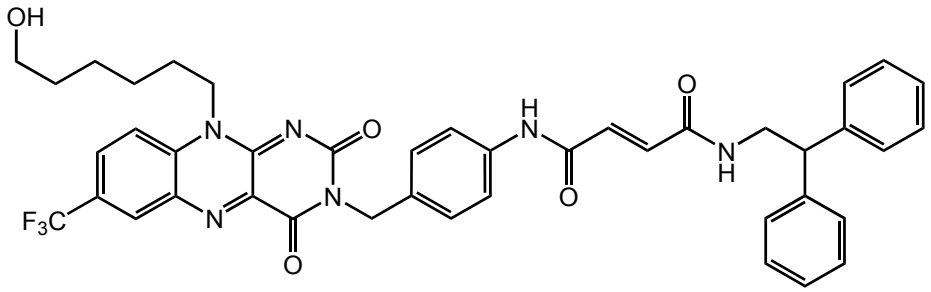

C-25: (800mg, 0.91mmol) was dissolved in THF (30mL) and aqueous HCl (5mL, 7.5M) was added to the stirring solution at r.t. The mixture was stirred for 1H then precipitated by adding distilled water (150mL). This was filtered, washed with water (20mL x3), acetone (20mL x3) and diethyl ether (20mL x3) and dried under vacuum. Yield = 670mg (96%).

$C_{42}H_{39}N_6O_5F_3$ (764.79). Mpt.= 186-187°C.

m/z (FAB) = 765.0 ([M+H]+, 100%), 764.1 (50), 383.1 (75), 180.9 (20), 106.3 (53), 74.6 (32).

Elemental analysis cald. (%) for $C_{42}H_{39}F_3N_6O_5$ (764.): C, 65.96; H, 5.14; F, 7.45; N, 10.99; O, 10.46. Found C, 65.84; H, 5.22; N, 10.80.

^{1}HNMR (400MHz, $DMSO-d_6$) δ_H 10.453 (1H, NH-Ar), 8.581 (2H, m, NH-CH2 and ArH), 8.260 (1H, d J=9Hz, ArH), 8.210 (1H, d J=9Hz, ArH), 7.616 (2H, d J=9Hz, AA'BB' ArH x2), 7.377 (2H, d J=9Hz, AA'BB' ArH x2), 7.340 (8H, m, Ph2 ArH x8), 7.228 (2H, m, Ph2 ArH x2), 7.028 (1H, d J=15Hz, CH alkene), 6.912 (1H, d J=15Hz, CH alkene), 5.095 (2H, s, CH2-Ar), 4.638 (2H, br t J=7Hz, NCH2CH2), 4.413 (1H, t J=5Hz, CH), 4.266 (1H, t J=8Hz, OH), 3.869 (2H, t J=6.5Hz, NCH2CH), 3.421 (2H, pent J=6Hz, OCH2CH2), 1.760 (2H, pent J=6.5Hz, NCH2CH2), 1.55-1.36 (6H, m, CH2 x3),

^{13}CNMR (100MHz, $DMSO-d_6$) δ_C 163.54(NC=O), 162.13(NC=O), 159.04(N(N)C=O flavin), 154.77(NC=O flavin), 149.70(N=CC=N flavin), 142.70(Ph2 ArC x2), 139.80(N=CC=N flavin), 137.74(ArC-CH2), 134.81(N-CC-N flavin), 134.26(N-CC-N flavin), 133.71(CH alkene), 132.81(CH alkene), 132.56(ArC-NH), 130.23(ArCH, q, J=3Hz), 129.01(ArCH, q, J=4Hz), 128.43(Ph2 ArCH x4), 128.38(ArCH benzyl x2), 127.83(Ph2 ArCH x4), 126.39(Ph ArCH x2), 125.90(q, J=35Hz, ArC-CF3), 123.46 (q, J=272Hz, CF3), 119.19(ArCH benzyl x2), 118.03(ArCH flavin), 60.53(OCH2), 49.97(CH), 44.34(Ar-CH2), 43.79(CH2CH), 43.37(NCH2CH2), 32.37(OCH2CH2), 26.47(CH2), 25.99(CH2), 25.26(CH2).

C-27:

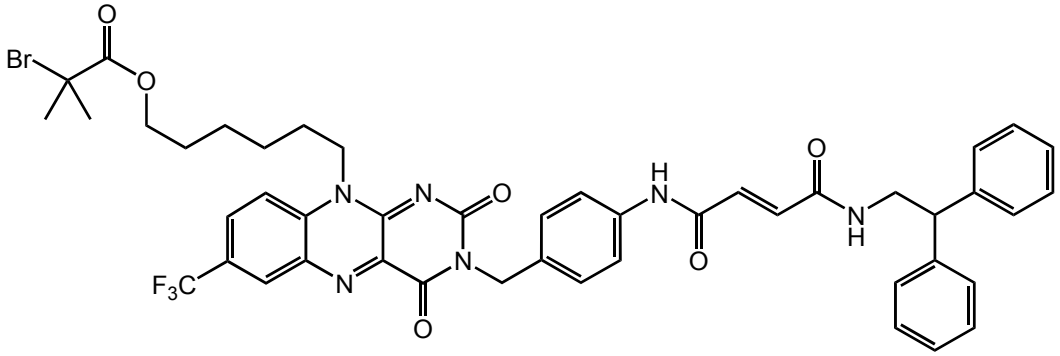

C-26 (600mg, 0.78mmol, 1eq) was first dissolved in DMF (2mL) and then diluted with THF (50mL) and tri-ethylamine (1mL, 0.7g, 7.2mmol, 9eq). 2-Bromoisobutryl bromide (0.3mL, 0.56g, 2.4mmol, 3eq) was added dropwise to the stirring mixture at r.t. The reaction was left stirring overnight, filtered to remove NEt_3.HCl salt and the filtrate evaporated under vacuum to provide an orange residue. This was precipitated by adding diethyl ether (50mL) and filtered. The product was provide by column chromatography (silica) using eluent DCM followed by DCM/THF (95:5) and finally DCM/THF/EtOH (93:5:2). Yield = 625mg (87%). $C_{46}H_{44}N_6O_6F_3Br$ (913.4). Mpt.= 194-195°C.

m/z (FAB) = 915.42 ([M+H]+, 75%), 914.44 (65), 913.46 (68), 532.8 (23), 530.8 (22), 383.1 (78), 180.9 (33), 106.3 (100). Elemental analysis cald. (%) for $C_{46}H_{44}N_6O_6F_3Br$ (913.4): C, 60.46; H, 4.85; Br, 8.74; F, 6.24; N, 9.20; O, 10.51 Found C, 59.98; H, 4.72; N, 9.30.

^{1}HNMR (400MHz, $CDCl_3$) δ_H 9.344(1H, s, ArNH), 8.586(1H, d J=1.5Hz, ArH), 8.119(1H, dd J=9Hz and 1.5Hz, ArH), 7.762(1H, d J=9Hz, ArH), 7.601(2H, d J=8.4Hz, AA'BB' ArH), 7.496(2H, d J=8.4Hz, AA'BB' ArH), 7.436(1H, d J=15Hz, alkene), 7.38-7.30(4H, m, Ph2 ArH x4), 7.28-7.20(4H, m, Ph2 ArH x4), 7.031(1H, d J=15Hz, alkene), 6.529(1H, br t J=5Hz, N<u>H</u>CH2), 5.274(2H, s, CH2), 4.680(2H, br t J=7Hz, CH2), 4.3-4.2(3H, m, CH and CH2), 4.043(2H, t J=6.5Hz, CH2), 1.995(6H, s, CH3 x2), 1.901(2H, pent J=7Hz, CH2), 1.775(H, pent J=7Hz, CH2), 1.66-1.50(4H, m, CH2 x2).

^{13}CNMR (100MHz, $DMSO-d_6$) δ_C 170.77(OC=O), 163.54(NC=O), 162.13(NC=O), 159.03(N(N)C=O flavin), 154.73(NC=O flavin), 149.72(N=<u>C</u>C=N), 142.70(Ph2 Ar<u>C</u>-CH x2), 139.78(N=C<u>C</u>=N flavin), 137.75(Ar<u>C</u>-CH2), 134.82(N-C<u>C</u>-N flavin), 134.27(N-<u>C</u>C-N flavin), 133.71(alkene), 132.81(alkene), 132.56(Ar<u>C</u>-NH), 130.20(ArCH, q, J=3Hz), 128.96(ArCH, q, J=4Hz), 128.43(Ph2 ArCH x4), 128.38(ArCH benzyl x2), 127.83(Ph2 ArCH x4), 126.39(Ph ArH x2), 125.73(q, J=35Hz, ArC-CF3), 123.48(q, J=272Hz, CF3), 119.18(ArCH x2 benzyl), 118.03(ArCH flavin), 65.48(OCH2), 57.40(CBr), 49.97(CH), 44.23(Ar-CH2), 43.78(<u>C</u>H2CH), 43.37(N<u>C</u>H2CH2), 30.20(CH3 x2), 27.66(CH2), 26.31(CH2), 25.59(CH2), 25.04(CH2).

C-28:

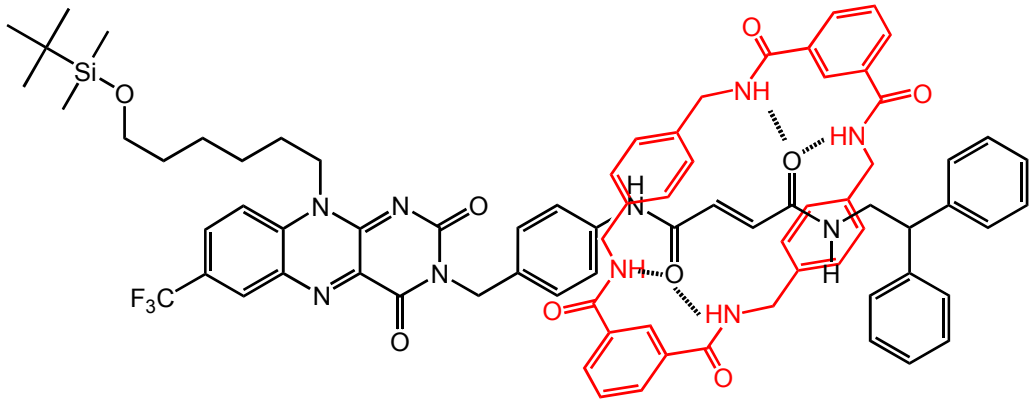

C-25 (1.6g, 1.82mmol, 1eq) was dissolved in dry DCM (300mL) and NEt_3 (5mL, 3.67g, 36.4mmol, 20eq). Isophthaloyl dichloride (1.85g, 9.1mmol, 5eq) and p-xylylenediamine (1.25g, 9.1mmol, 5eq) were dissolved in two separate units of DCM (10mL x2) and feed simultaneously into the reaction mixture at r.t using a motor driven syringe pump over 4H. The reaction was left stirring overnight then the DCM was evaporated under vacuum. The remaining solids were dissolved in DMF (25mL) and then precipitated by adding water (100mL). The solids were collected by filtration and dried under high vacuum. The solids were dissolved again in DMF (10mL) and precipitated by adding DCM (150mL). The product was collected by filtration, washed with DCM then dried under vacuum. Yield = 1.5g (61%). $C_{80}H_{81}F_3N_{10}O_9Si$(1411.2). Mpt.= 263°C

m/z (FAB) = 1412.2 ([M+H]+, 100%), 1383.5 (27), 497.9 (92), 383.0 (100), 282.9 (85).

Elemental analysis cald. (%) for $C_{80}H_{81}F_3N_{10}O_9Si$(1411.2). C, 68.07; H, 5.78; F, 4.04; N, 9.92; O, 10.20; Si, 1.99. Found. C, 68.12; H, 5.24; N, 9.77.

^{1}HNMR (400MHz, $DMSO-d_6$) δ_H 10.223(1H, s, NH-Ar), 8.631(2H, s, ArH(2-isophth)), 8.597(1H, t J=6Hz, NH-CH2), 8.553(1H, s, ArH flavin), 8.226(6H, m, NH x4 and ArH x2 flavin), 8.101(4H, dd J=7.6Hz and 1.1Hz, ArH(4- and 6-isophth) x2), 7.724(2H, t J=7.6Hz, ArH(5-isophth) x2), 7.408(2H, d J=8.7Hz, AA'BB' ArH x2), 7.324(2H, d J=8.7Hz, AA'BB' ArH x2), 7.285(4H, d J=7.2Hz, Ph2 ArH x4), 7.26-7.18(6H, m, Ph2 ArH x6), 6.844(8H, s, ArH(xylylene) x8), 5.965(1H, d J=15Hz, CH alkene), 5.854(1H, d J=15Hz, CH alkene), 5.073(2H, s, CH2-Ar), 4.632(2H, br t J=7.5, NCH2CH2), 4.288(8H, qd, J=16.5Hz and 5Hz, CH2 x4), 4.144(1H, t J=7.7Hz, CH), 3.727(2H, br t J=6Hz, CH2-NH), 3.593(2H, t J=6Hz, OCH2CH2), 1.748(2H, pent J=7Hz, CH2), 1.54-1.43(4H, m, CH2 x2), 1.43-1.32(2H, m, CH2), 0.866(9H, s, Si-C(CH3)x3), 0.034(6H, s, Si(CH3)2).

^{13}CNMR (100MHz, $DMSO-d_6$) δ_C 165.77(ring C=O x4), 164.82(NC=O), 163.40(NC=O), 159.07(NC=O flavin x2), 154.73(N=CC=N flavin), 149.68(N=CC=N flavin), 142.54(Ph2 ArC x2), 139.78(N-CC-N flavin), 136.59(ring ArC(xylylene) x4), 136.44(ArC-

CH2), 134.78(ArCNH), 134.27(ring ArC(1,3-isophth) x4), 133.45(N-CC-N flavin), 130.76(ring ArCH(4,6-isophth) x4 + CH alkene x2), 129.66(ArCH, q, J=3Hz), 129.08(ring ArCH(5-isophth) x2), 128.98(ArCH, q, J=4Hz), 128.57(ring ArCH(xylxylene) x8), 128.51(Ph2 ArCH x4), 128.35(ArCH x2 benzyl), 127.71(Ph2 ArCH x4), 126.54(Ph2 ArCH x2), 125.92(q, J=35Hz, ArC-CF3), 125.29(ring ArCH(2) x2), 122.46 (q, J=272Hz, CF3), 120.13(ArCH x2 benzyl), 118.06(ArCH flavin), 62.36(OCH2), 49.94(CH), 44.31(Ar-CH2), 43.7(CH2CH), 43.21(NCH2CH2 + ring Ar-CH2 x4), 32.15(OCH2CH2), 27.2(CH2), 26.49(CH2), 25.80(Si-C(CH3)3), 25.13(CH2), 17.92(SiC), -5.33(Si(CH3)2).

C-29:

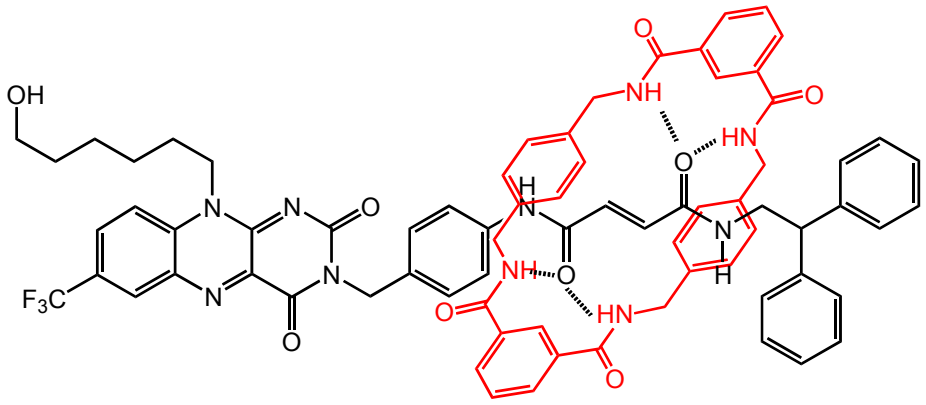

C-28 (0.5g) was dissolved in DMF (2mL) then diluted with THF (20mL) and NEt_3 (1mL, 0.7g, 7.2mmol, 9eq). The solution was stirred at r.t while aqueous HCl (5mL, 7.5M) was added portion wise. The mixture was stirred for 1H then precipitated by adding distilled water (100mL) to provide a yellow solid. This was filtered then washed with water (10mL x3), methanol (10mL x3) and diethyl ether (10mL x3) and dried under vacuum. Yield = 450mg (98%). $C_{74}H_{67}N_{10}O_9F_3$ (1296.5). Mpt.= 215-216°C.

m/z (FAB) = 1297.81 ([M+H]+, 70%), 1269.8 (10), 555.6 (20), 383.1 (40), 329.4 (85), 232.5 (95). Elemental analysis cald. (%) for $C_{74}H_{67}F_3N_{10}O_9$(1297.4). C, 68.51; H, 5.21; F, 4.39; N, 10.80; O, 11.10. Found. C, 68.77; H, 5.36; N, 10.57.

^{1}HNMR (400MHz, $DMSO-d_6$) δ_H 10.228(1H, s, NH-Ar), 8.640(2H, s, ArH(2-isophth)), 8.599(1H, t J=6Hz, NH-CH2), 8.556(1H, s, ArH flavin), 8.3-8.2(6H, m, NH x4 and ArH x2 flavin), 8.107(4H, dd J=7.6Hz and 1.1Hz, ArH(4- and 6-isophth) x2), 7.729(2H, t J=7.6Hz, ArH(5-isophth) x2), 7.415(2H, d J=8.7Hz, AA'BB' ArH x2), 7.329(2H, d J=8.7Hz, AA'BB' ArH x2), 7.289(4H, d J=7.2Hz, Ph2 ArH x4), 7.27-7.18(6H, m, Ph2 ArH x6), 6.850(8H, s, ArH(xylylene) x8), 5.973(1H, d J=15Hz, CH alkene), 5.860(1H, d J=15Hz, CH alkene), 5.079(2H, s, CH2-Ar), 4.634(2H, br t J=7.5, NCH2CH2), 4.294(8H, qd, J=16.5Hz and 5Hz, CH2 x4), 4.150(1H, t J=7.7Hz, CH), 3.730(2H, br t J=6Hz, CH2-NH), 3.381(2H, pent J=6Hz, OCH2CH2), 1.754(2H, pent J=7Hz, CH2), 1.54-1.30(6H, m, CH2 x3).

^{13}CNMR (100MHz, $DMSO-d_6$) δ_C 165.80(ring C=O x4), 164.81(NC=O), 163.40(NC=O), 159.06(NC=O flavin x2), 154.77(N=CC=N flavin), 149.67(N=CC=N flavin), 142.54(Ph2 ArC x2), 139.78(N-CC-N flavin), 136.59(ring ArC(xylylene) x4), 136.47(ArC-CH2), 134.77(ArCNH), 134.26(ring ArC(1- and 3-isophth) x4), 133.42(N-CC-N flavin), 130.74(ring ArCH(4- and 6-isophth) x4 + CH alkene x2), 129.69(ArCH, q, J=3Hz), 129.04(ring ArCH(5-isophth) x2), 128.97(ArCH, q, J=4Hz), 128.57(ring ArCH(xylxylene) x8), 128.49(Ph2 ArCH x4), 128.33(ArCH x2 benzyl), 127.70(Ph2 ArCH x4), 126.52(Ph2 ArCH x2), 125.90(q, J=35Hz, ArC-CF3), 125.36(ring ArCH(2) x2), 122.45(q, J=272Hz, CF3), 120.12(ArCH x2 benzyl), 118.06(ArCH flavin), 60.53(HOCH2), 49.91(CH), 45.70(ring

Ar-CH2 x4), 44.36(Ar-CH2), 43.63(CH2CH), 43.21(NCH2CH2), 32.36(HOCH2CH2), 26.47(CH2), 25.98(CH2), 25.26(CH2).

C-30:

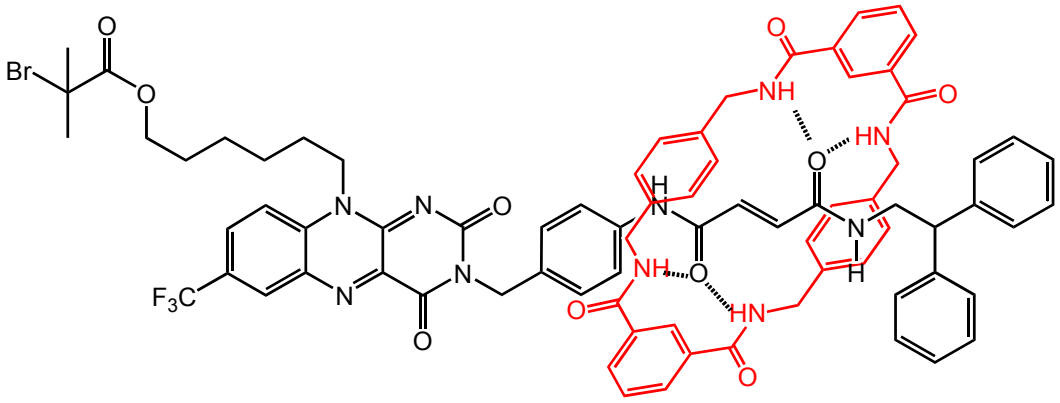

C-29 (0.4g, 0.31mmol, 1eq) was first dissolved in DMF (2mL) and then diluted with THF (30mL) and NEt_3 (1mL, 0.7g, 7.2mmol, 9eq). 2-Bromoisobutryl bromide (0.2mL, 0.56g, 2.4mmol, 7eq) was added dropwise to the stirring mixture at r.t. The reaction was allowed to precede over 1H, before filtering to remove NEt_3.HCl salt. The filtrate was evaporated under vacuum to provide an orange residue. This was precipitated by adding diethyl ether (50mL) and filtered. The product was provide by column chromatography (silica) using eluent DCM followed by DCM/EtOH (98:2). Yield = 400mg (90%). $C_{78}H_{72}N_{10}O_{10}F_3Br$ (1446.1). Mpt.= 183-184°C (dec). m/z (FAB+) = 1445.7 ([M+H]+, 90%), 1447.7 (70), 1446.7 (55), 1325.8 (10), 532.8 (24), 383.1 (100), 282.9 (18). Accurate mass: expected 1445.4568, found 1445.4572. Elemental analysis cald. (%) for $C_{78}H_{72}N_{10}O_{10}F_3Br$ (1446.1). C, 64.77; H, 5.02; Br, 5.52; F, 3.94; N, 9.68; O, 11.06. Found. C, 65.21; H, 5.16; N, 9.49.

^{1}HNMR (400MHz, $DMSO-d_6$) δ_H 10.224(1H, s, NH-Ar), 8.640(2H, s, ArH(2-isophth)), 8.598(1H, t J=6Hz, NH-CH2), 8.544(1H, s, ArH flavin), 8.27-8.15(6H, m, NH x4 and ArH x2 flavin), 8.105(4H, dd J=7.5Hz and 1.1Hz, ArH(4- and 6-isophth) x2), 7.724(2H, t J=7.5Hz, ArH(5-isophth) x2), 7.416(2H, d J=9Hz, AA'BB' ArH x2), 7.331(2H, d J=9Hz, AA'BB' ArH x2), 7.285(4H, d J=7Hz, Ph2 ArH x4), 7.27-7.18(6H, m, Ph2 ArH x6), 6.849(8H, s, ArH(xylylene) x8), 5.973(1H, d J=15Hz, CH alkene), 5.860(1H, d J=15Hz, CH alkene), 5.079(2H, s, CH2-Ar), 4.641(2H, br t J=7.5Hz, NCH2CH2), 4.293(8H, qd, J=16.5Hz and 5Hz, CH2 x4), 4.151(3H, m, CH and OCH2), 3.730(2H, br t J=6Hz, CH2-NH), 1.904(6H, s, CH3 x2), 1.754(2H, pent J=7Hz, CH2), 1.54-1.30(6H, m, CH2 x3).

^{13}CNMR (100MHz, $DMSO-d_6$) δ_C 170.76(OC=O), 165.78(ring C=O x4), 164.83(NC=O), 163.41(NC=O), 159.05(NC=O flavin x2), 154.74(N=CC=N flavin), 149.66(N=CC=N flavin), 142.52(Ph2 ArC x2), 139.75(N-CC-N flavin), 136.59(ring ArC(xylylene) x4), 136.46(ArC-CH2), 134.76(ArCNH), 134.27(ring ArC(1,3-isophth) x4), 133.44(N-CC-N flavin), 130.75(ring ArCH(4,6-isophth) x4 + CH alkene x2), 129.69(ArCH, q, J=3Hz), 129.05(ring ArCH(5-isophth) x2), 128.95(ArCH, q, J=4Hz), 128.57(ring

ArCH(xylxylene) x8), 128.49(Ph2 ArCH x4), 128.38(ArCH x2 benzyl), 127.70(Ph2 ArCH x4), 126.53(Ph2 ArCH x2), 125.90(q, J=35Hz, ArC-CF3), 125.30(ring ArCH(2) x2), 123.41(q, J=272Hz, CF3), 120.13(ArCH x2 benzyl), 118.04(ArCH flavin), 65.46(OCH2), 57.27(CBr), 49.94(CH), 48.59(OCH2CH2), 44.36(Ar-CH2), 43.64(CH2CH), 43.64(NCH2CH2), 43.22(ring Ar-CH2 x4), 30.19(CH3 x2), 26.33(CH2), 25.59(CH2), 25.03(CH2).

(b). Flavin poly(PEG) synthesis.

ATRP general procedure.

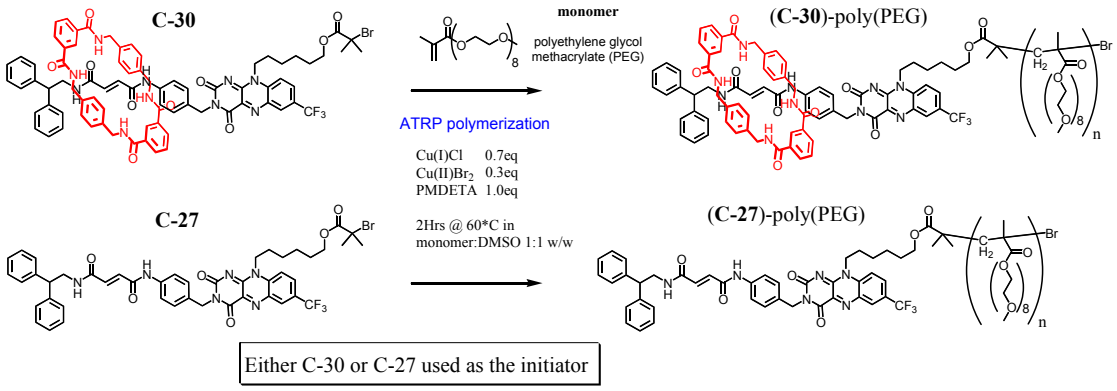

The flavin initiator (either rotaxane C-30 (145 mg) or axle C-27 (91.5 mg) , 0.10mmol, 1eq) was dissolved in DMSO (8.5mL) in a two neck r.b flask by stirring at r.t before adding PEG methacrylate (9.5g, 20mol, 200eq). This would become the reaction flask. The catalytic system (Cu(I)Cl (69.3mg, 0.7mmol, 7eq), $Cu(II)Br_2$ (67.0mg, 0.3mmol, 3eq) and ligand PMDETA (174mg, 1.0mmol, 10eq) was added to a second r.b flask and dissolved in DMSO (10mL). (This 10 fold scale-up was necessary in order to maintain reasonable accuracy with the small quantities of catalyst involved). Both flasks underwent three cycles of "freeze-pump-thaw" to evacuate all trace of the free radical oxygen gas using nitrogen gas (O_2 free) as the protective atmosphere. After the final thaws, a gas tight syringe was used to inject 1mL of the Cu(I)/Cu(II)/PMDETA mixture directly into the centre of the reaction flask while stirred under a fast flowing nitrogen purge. The reaction flask was sealed under a nitrogen atmosphere, then lowered into the thermostatically controlled oil bath and stirred at the reaction temperature of 60°C for 2H. The reaction was monitored by periodically withdrawing small sample to process by GPC. The reaction was terminated after 2H by slowly pouring the reaction mixture into 400ml of diethyl ether which was vigorously stirred at r.t. The polymer precipitated as a green-yellow residue which was allowed to settle for approximately 1H before collecting by decanting. The polymer was then dissolved in $CHCl_3$ (50mL) and passed through a short column of Al_2O_3 to remove trace copper catalyst. The filtrate was reduced in volume under vacuum to approx 25mL and after passing through a $0.45\mu m$ syringe filter, the polymer was re-precipitated and collected in the same manner as before to provide the polymer as either a clear yellow residue. The polymer was then finally dried under high vacuum for 48H.

(**C-30**)-poly(**PEG**):

^{1}HNMR (400MHz, $CDCl_3$) δ_H 4.042 (2H, br s, CH2 **PEG**), 3.601 (28H, m, CH2 x14 **PEG**), 3.502 (2H, br s, CH2 **PEG**), 3.324 (3H, CH3 **PEG**), 2.2-1.5 (2H, m, CH2 **PEG**), 1.2-0.6 (3H, m, CH3 **PEG**).

GPC results: (THF, @1 mL/min), $M_n = 26649\, g/mol$, $M_W = 29309\, g/mol$, $PDI = 1.10$.

(**C-27**)-poly(**PEG**):

^{1}HNMR (400MHz, $CDCl_3$) δ_H 4.042 (2H, br s, CH2 **PEG**), 3.601 (28H, m, CH2 x14 **PEG**), 3.502 (2H, br s, CH2 **PEG**), 3.324 (3H, CH3 **PEG**), 2.2-1.5 (2H, m, CH2 **PEG**), 1.2-0.6 (3H, m, CH3 **PEG**).

GPC results: (THF, @1 mL/min), $M_n = 25350\, g/mol$, $M_W = 28173\, g/mol$, $PDI = 1.11$.

Chapter 5: Flavin-fumaramide [2]pseudorotaxane.

(a). Tri-ethylene glycol benzylic amide macrocycle synthesis

C-31:

4-hydroxybenzyl ammonium bromide: [78, 79]

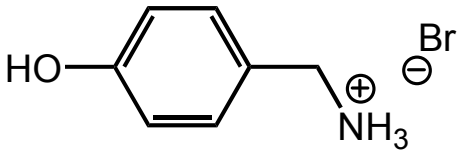

4-Methoxybenzylamine (14mL, 14.7g, 107mmol, 1eq) was slowly added to a stirring solution of 48% HBr (40mL, 59.6g, 353mmol, 3eq) then stirred under reflux at 130°C for 18Hrs. The mixture was allowed to cool to r.t then dried under vacuum to give a pink-brown solid. MeCN (10mL) was added and the solid collected by filtration, washed with a small quantity of acetone (5mL), dried under vacuum and used in the next step without further purification. Yield = 17.5g (80.5%). $C_7H_{10}NOBr$ (203.02). Mpt.= 210°C, (lit = 210-211°C [78, 79]).
^{1}HNMR (400MHz, D_2O) δ_H 7.217 (2H, ArH x2), 6.810 (2H, d J=8.6Hz, ArH x2), 3.975 (2H, s, CH2).

C-32:

N,N'-di(4-hydroxybenzyl) isophthalamide: [80]

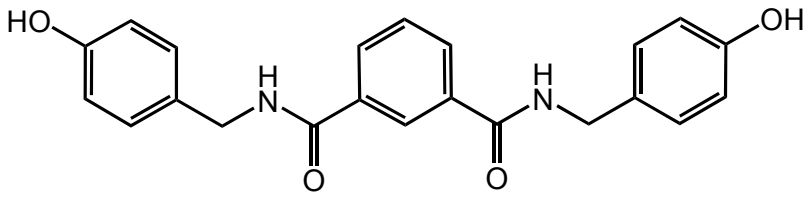

C-31 (17.4g, 85.7mmol) was heated under reflux in dry THF (200mL) and NEt_3 (60mL, 43.6g, 0.43mol) for 30min then allowed to cool to r.t. Isophthaloyl dichloride was dissolved in dry THF (40mL) and added dropwise to the stirring reaction before leaving to stir at r.t over the weekend. The mixture was then filtered and the filtrate washed with 0.5M HCl (100mL x2). The organic layer was dried over $MgSO_4$ and evaporated under vacuum. The crystallized product was obtained after dissolving the remaining pale yellow residue in acetone (50mL) and leaving to stand for 48H. Yield = 11.4g (71%). $C_{22}H_{20}N_2O_4$ (376). Mpt.= 243°C, (lit = 241-243°C [80]).

^{1}HNMR (400MHz, $CDCl_3$) δ_H 9.068 (2H, t J=6Hz, NH), 8.391 (1H, s, isophth 2-H), 8.031 (2H, dd J=7.7Hz and 1.6Hz isophth 4- and 6-H), 7.590 (1H, t J=7.7Hz, isophth 5-H), 7.170 (4H, d J=8.5Hz, p-xylylene ArH-CH2), 6.747 (4H, d J=8.5Hz, p-xylylene ArH-OH), 4.407 (4H, d J=6Hz, CH2 x2).

C-33:

N,N'-di(4-diphenylacetoxybenzyl) isophthalamide: [80]

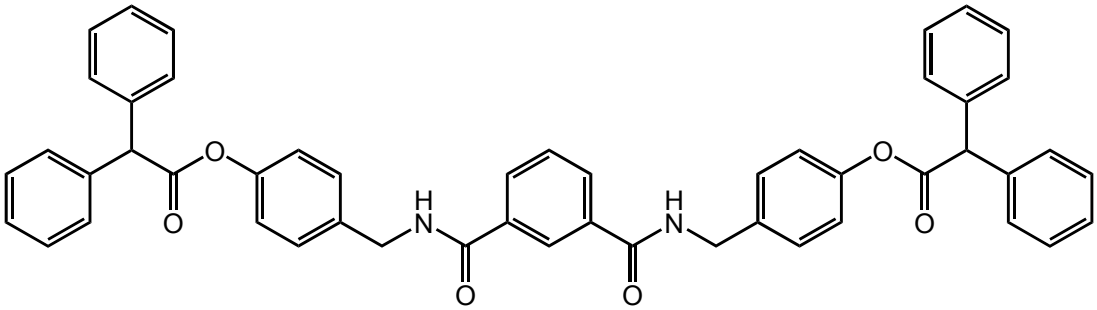

A solution of diphenylacetyl chloride (2.7g, 11.7mmol, 2eq) in DCM (20mL) was added dropwise over 1.5H to a stirring suspension of **C-32** (2.0g, 5.3mmol, 1eq) in DCM (50mL) and tri-ethylamine (2mL, 1.45g, 14.4mmol). After a further 4H, the now clear yellow solution was washed with distilled water (100mL x2), and the organic layer dried over $MgSO_4$ and evaporated under vacuum. The product was purified by column chromatography using eluent DCM followed by DCM/acetone (90:10). Yield = 3.2g (79%). $C_{50}H_{40}N_2O_6$ (764.1). Mpt.= 74°C (lit = 72-73°C [80]).

^{1}HNMR (400MHz, *CDCl*$_3$) δ_H 8.201 (1H, s, isophth 2-H), 7.839 (2H, dd J=7Hz and 1Hz, isophth 4- and 6-H), 7.44-7.28(21H, m, Ph_2C x20 and isophth 5-H), 7.149 (6H, m, p-xylylene ArH x4 and NH x2), 6.839 (4H, d J=8.7Hz, p-xylylene ArH x4), 5.248 (2H, s, CH), 4.418 (4H, d J=5.7Hz, CH2 x2).

C-34:

2-(2-(2-methoxyethoxy)ethoxy)ethyl p-toluenesulfonate: [81]

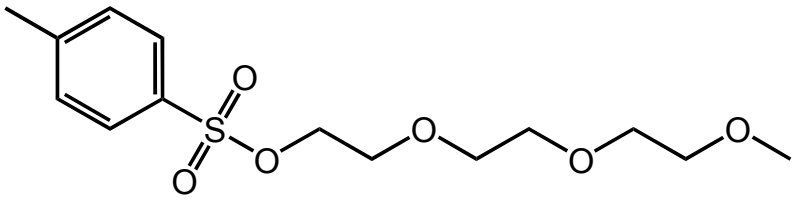

p-Toluenesulfonyl chloride (12.6g, 66mmol) was added to as stirring solution of triethylene glycol mono-methyl ether (9.6mL, 9.85g, 60mmol) in pyridine (9.7mL, 120mmol) at 0°C. After stirring at 0°C for 4H, toluene (100mL) was added and the mixture washed with aqueous HCl (100mL). The layers were separated and the organic phase dried over $MgSO_4$ and concentrated under vacuum to give a colourless oil. Yield = 17.7g (93%). $C_{14}H_{22}O_6S$ (318.11).

^{1}HNMR (400MHz, *CDCl*3) δ_H 7.801(2H, d J=8Hz, ArH x2), 7.344(2H, d J=8Hz, ArH x2), 4.162(2H, t J=4.5Hz, CH2), 3.689(2H, t J=4.5Hz, CH2), 3.614(2H, t J=4.5Hz, CH2), 3.595(4H, s, CH2 x2), 3.531(2H, t J=4.5Hz, CH2), 3.374(3H, s, OCH3), 2.450(3H, s, ArCH3).

C-35:

Dimethyl 5-hydroxyisophthalate: [81]

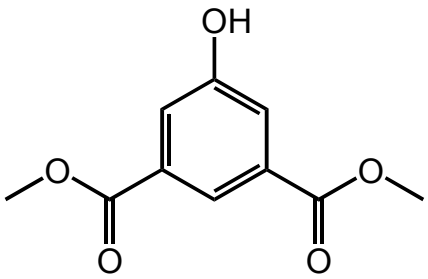

5-Hydroxyisophtahlic acid (10.0g, 54.9mmol) was dissolved in MeOH (100mL). 5 drops of conc H_2SO_4 were added and the mixture heated under reflux at 80°C for 17Hrs. The methanol was evaporated under vacuum and the remaining white solid dissolved in DCM. Any residual acid was neutralized by careful addition of $NaHCO_3$ until effervescence ceased. The organic layer was then filtered $MgSO_4$, the solvent evaporated and the remaining white solid dried under high vacuum. Yield = 11.76g (100%). $C_{10}H_{10}O_5$ (210.18). Mpt.= 164-165°C (lit =163-166°C [81]). ^{1}HNMR (400MHz, *CDCl*3) δ_H 8.258(1H, s, ArH), 7.802(2H, s, ArH), 6.231(1H, br s, OH), 3.958(6H, s, OCH3 x2).

C-36:

Dimethyl 5-(2-(2-(2-methoxyethoxy)ethoxy)ethoxy) isophthalate: [82]

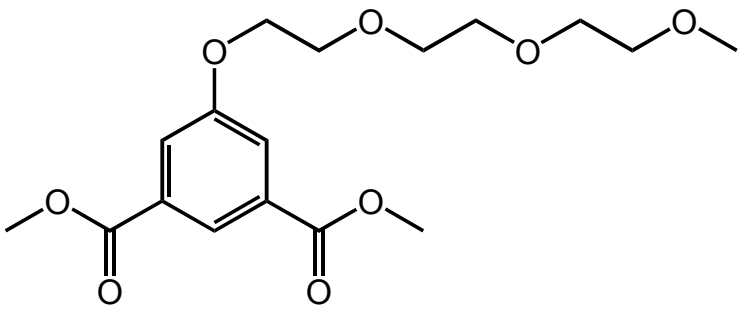

C-35 (17.7g, 55.6mmol, 1.02eq), **C-34** (11.5g, 54.7mmol, 1eq) and potassium carbonate (9.0g, 65.1mmol, 1.2eq) were heated under reflux in MeCN (350mL) for 15H. The mixture was cooled to room temp, filtered through a short plug of silica and the filtrate evaporated under vacuum to provide a clear oil. The product was afforded as a colourless oil by column chromatography (silica) using eluent DCM/petroleum ether (50:50). Yield = 18.6g (95.5%). $C_{17}H_{24}O_8$ (356.15).

^{1}HNMR (400MHz, *CDCl*$_3$) δ_H 8.279 (1H, s, ArH), 7.773 (2H, s, ArH), 4.218(2H, t,), 3.936(6H, s, COOCH2 x2), 3.891(2H, t J=4.5Hz, CH2), 3.754(2H, t J=4.5Hz, CH2), 3.689(2H, t J=4.5Hz, CH2), 3.661(2H, t J=4.5Hz, CH2), 3.552(2H, t J=4.5Hz, CH2), 3.380(3H, s, OCH3),

C-37:

5-(2-(2-(2-methoxyethoxy)ethoxy)ethoxy) isophthalic acid: [83]

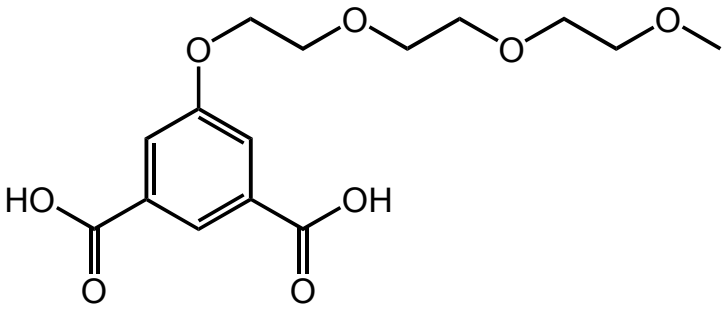

Aqueous NaOH (4.7g into 75mL, 0.12moles) was added to a solution of **C-36** (10.45g, 29.3mmol, 1eq) in ethanol (200mL) and heated under reflux at 80°C for 14H. After cooling to room temp, the ethanol was evaporated and the remaining aqueous solution (approx 50mL) was cooled to 4°C and then acidified to pH 3 by addition of 3M HCl. The resulting white precipitate was collected by filtration and dried under high vacuum at 60°C. It was then dissolved in EtOAc (150mL), filtered and concentrated under vacuum to provide a white solid. Yield = 7.81g (81%). $C_{15}H_{20}O_8$ (328.12). Mpt.= 132°C, (lit = 132°C [83]).

^{1}HNMR (400MHz, *CDCl*3) δ_H 7.994(1H, s, ArH), 7.582(2H, s, ArH x2), 4.169(2H, br t J=3.5Hz, CH2), 3.926(2H, br t J=3.5Hz, CH2), 3.834(4H, s, CH2 x2), 3.750(2H, t J=4.5Hz, CH2), 3.623(2H, t J=4.5Hz, CH2), 3.407(3H, s, OCH3).

C-38:

5-(2-(2-(2-methoxyethoxy)ethoxy)ethoxy) isophthaloyl dichloride:

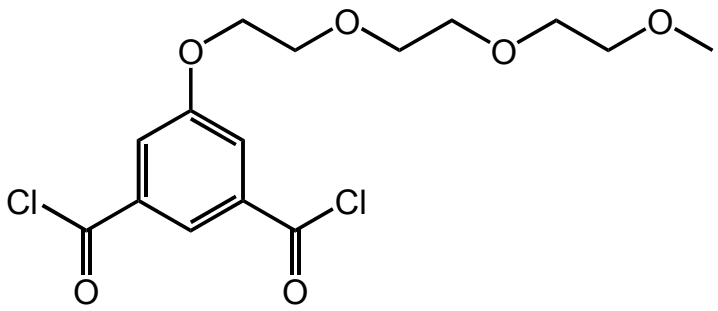

C-37 (5.65g, 17.2mmol, 1eq) was dissolved in dry THF (120mL) and 4 drops of DMF were added. Oxalyl chloride (3.25mL, 38.7mmol, 2.2eq) was dissolved in dry THF (20mL) and added dropwise to the solution while stirring at room temp. After stirring under nitrogen for 3H the reaction mixture was then concentrated under vacuum. Toluene (15mL) was added and the solution concentrated again under vacuum before further drying under high vacuum to provide the acid chloride as a colourless oil in quantitative yield. $C_{15}H_{18}O_6Cl_2$ (365.2). Used without further purification.

^{1}HNMR (400MHz, $CDCl_3$) δ_H 8.471 (1H, s, ArH), 7.955 (2H, s, ArH x2), 4.291 (2H, t J=4.5Hz, CH2), 3.942 (2H, t J=4.5Hz, CH2), 3.779 (2H, t J=4.5Hz, CH2), 3.716 (2H, t J=4.5Hz, CH2), 3.682 (2H, t J=4.5Hz, CH2), 3.579 (2H, t J=4.5Hz, CH2), 3.406 (3H, s, OCH3).

^{13}CNMR (100MHz, $CDCl_3$) δ_C 167.3 (C=O x2), 159.1 (ArC-O x2), 134.7 (ArC-C=O x2), 124.8 (ArCH), 122.5(ArCH x2), 71.8(CH2), 70.7(CH2), 70.4(CH2 x2), 69.1(CH2), 68.7(CH2), 58.4(CH3).

C-39:

Rotaxane template:

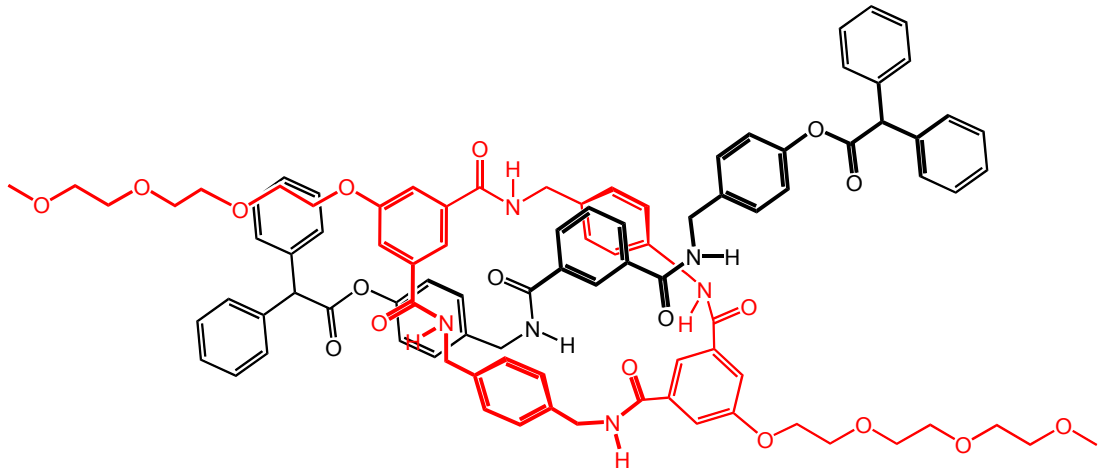

C-33 (7.0g, 9.15mmol) was dissolved in a solution of dry $CHCl_3$ (200mL) and NEt_3 (14.7mL, 106mmol, 10eq). **C-38** (6.3g, 17.2mmol, 2eq) and p-xylylenediamine (2.34g, 17.2mmol, 2eq) were separately dissolved in dry $CHCl_3$ (20mL) and added dropwise to the above solution over a 6H period using a motor-driven syringe pump. This was repeated another two times over the following two days. The mixture was concentrated under vacuum then redissolved in $CHCl_3$ and purified by column chromatography (silica) eluting with $CHCl_3$ followed by $CHCl_3$/EtOH (96:4). The column was repeated to provide the product as a white solid. Yield = 1.05g (7%). $C_{96}H_{96}O_{18}N_6$ (1620.7). Mpt.= 85-86°C.

m/z (FAB+) = 1620.7 ([M+H]+, 35%), 765.3 (25), 764.2 (20), 447.8(14), 380.1(12), 166.8(100). Accurate mass found: 1620.6785, expected: 1620.6781. Elemental analysis expected: C, 71.09; H, 5.97; N, 5.18; O, 17.76. Found : C, 71.13 ; H, 5.87; N, 5.20;

^{1}HNMR (400MHz, $CDCl_3$) δ_H 8.099(1H, br s, thread isophth 2-H x2), 7.948(2H, d J=7Hz, thread isophth 4- and 6-H x2), 7.730(2H, br s, macro isophth 2-H x2), 7.515(5H, m, macro NH x4 + thread isophth 5-H), 7.395(18H, d J=3Hz, thread phenyl-H x16 + thread NH x2), 7.328(4H, m, phenyl-H x4), 7.162(4H, m, macro isophth 4- and 6-H x4), 6.927(8H, br s, macro p-xylylene ArH x4), 6.604(8H, thread p-xylylene ArH x8), 5.245(2H, br s, thread CH x2), 4.326(8H, br s, macro xylylene CH2 x4), 4.130(4H, thread xylylene CH2 x2), 3.799(4H, m, macro CH2 x2), 3.696(4H, m, macro CH2 x2), 3.67-3.60(12H, m, macro CH2 x6), 3.537(4H, br s, macro CH2 x2), 3.357(6H, br s, macro CH3 x2).

^{13}CNMR (100MHz, $CDCl_3$) δ_C 171.31, 166.74, 166.57, 158.57, 149.35, 138.31, 140.73, 137.85, 135.89, 135.91, 134.22, 130.35, 129.15, 128.78, 128.62, 128.45, 128.45, 127.62, 125.46, 125.14, 121.31, 116.73, 116.28, 71.82, 70.54, 70.45, 70.39, 69.15, 67.40, 58.82, 57.31, 44.10, 43.46.

C-40:

Tri-ethylene glycol benzylic amide macrocycle:

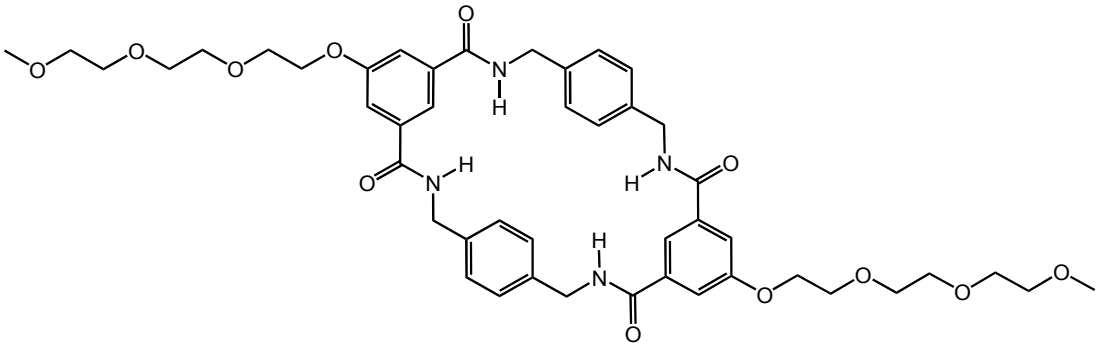

Sodium methoxide (50mg, 0.94mmol, 1.5eq) dissolved in methanol (20mL) was added to a stirring solution of the **C-39** (1.05g, 0.64mmol, 1eq) dissolved in THF (100mL). After stirring for 4H the mixture was concentrated under vacuum. The resulting white solid was dissolved in MeOH (50mL) and precipitated by adding diethyl ether (50mL). The precipitate was collected by filtration to provide the macrocycle as a white solid. Yield = 430mg (78%). $C_{46}H_{56}O_{12}N_4$ (856.9). Mpt.= 243-244°C.

m/z (FAB+) = 857.5 ([M+H]+, 40%), 226.9 (15), 147.0 (15), 74.6 (100). Accurate mass found: 857.3889, expected: 857.3895. Elemental analysis expected: C, 64.47; H, 6.59; N, 6.54; O, 22.40. Found : C, 64.53 ; H, 6.55; N, 6.61;

^{1}HNMR (400MHz, $CDCl_3$) δ_H 7.657(4H, br t J=4.1Hz, NH), 7.353(8H, br s, p-xylylene ArH x8), 7.327(2H, br s, isophth 2-H x2), 7.192(4H, br s, isophth 4- and 6H x4), 4.573(8H, d J=4.1Hz, xylylene CH2 x4), 3.636 (4H, br s, CH2 x2), 3.520(4H, br s, CH2 x2), 3.424(12H, br s, CH2 x6), 3.341(4H, br s, CH2 x2), 3.209(6H, br s, CH3 x2).

^{13}CNMR (100MHz, $CDCl_3$) δ_C 166.71(C=O x4), 158.60(ArC-O x2), 138.29(ArC-C x2 xylylidine), 135.93(ArC-C x2 isophthaloyl), 129.11(ArC-H x4 xylylidine), 116.66(ArC-H x2 isophthaloyl), 116.37(ArC-H x4 isophthaloyl), 71.78(CH2), 70.59(CH2), 70.52(CH2), 70.44(CH2), 69.35(CH2), 67.44(CH2-O x2), 58.88(CH3 x2), 44.05(CH2 x4 p-xylylidine),

(b). Synthesis of the pseudorotaxane axle:

C-41:

N-(dodecyl) fumaramic acid monomethyl ester:

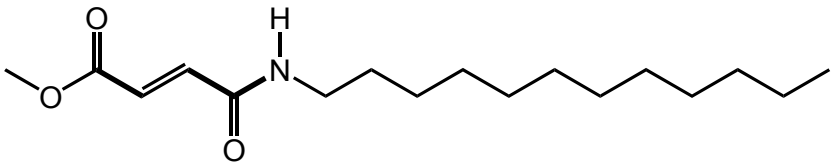

Mono-methyl fumarate (845mg, 6.5mmol, 1eq), HOBt (968mg, 7.2mmol, 1.1eq) and DMAP (100mg, 0.81mmol, 0.12eq) were stirred in $CHCl_3$ (50mL) before adding EDCI.HCl (1.4g, 7.3mmol, 1.1eq). The reaction was stirred at r.t for 30min before adding dodecylamine (1.2g, 6.5mmol, 1eq). The reaction was allowed to stir for a further 2H then passed through a short flash chromatography column (silica) using DCM as the eluent. After concentrating under vacuum, the remaining solid was washed with warm petroleum ether to remove un-reacted dodecylamine. Yield =1.5g (80%). $C_{17}H_{31}NO_3$ (297.4). Mpt.= 97-98°C.

m/z (EI+) = 297.3 ([M]+, 60%), 184.2(45), 169.2 (15), 113.1 (28), 79.8 (35), 59.1 (30). Accurate mass found: 297.2307, expected: 297.2304. Elemental analysis expected; C, 68.65; H, 10.51; N, 4.71; O, 16.14; found; C, 68.59; H, 10.58; N, 4.79.

^{1}HNMR (400MHz, $CDCl_3$) δ_H 6.935 (1H, d J=15Hz, CH), 6.853 (1H, d J=15Hz, CH), 5.944 (1h, t J=5Hz, NH), 3.822 (3H, s, OCH3), 3.380 (2H, q J=6.5Hz, NCH2), 1.575 (2H, m, NCH2CH2), 1.4-1.2 (18H, m, CH2 x9), 0.906 (3H, t J=7.5Hz, CH3).

^{13}CNMR (100MHz, $CDCl_3$) δ_C 166.24(OC=O), 163.54(NC=O), 136.84(CH), 129.73(CH), 52.18(OCH3), 40.02(NCH2), 31.92(CH2), 29.65(CH2), 29.59(CH2), 29.54(CH2 x2), 29.40(CH2), 29.36(CH2), 29.28(CH2), 26.94(CH2), 22.70(CH2), 14.14(CH3).

C-42:

N-(dodecyl) fumaramic acid:

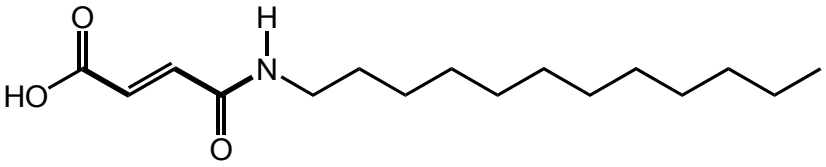

10% Aqueous HCl (5mL) was added to a stirring solution of **C-41** (1.3g, 4.37mmol) in THF (100mL) at r.t. The reaction was left stirring overnight then dried over $MgSO_4$, filtered and the filtrate concentrated under vacuum. The remaining solid was washed with DCM (50mL), filtered again and the solvent evaporated under vacuum to provide the product as white solid. Yield = 1.14g (92%). $C_{16}H_{29}NO_3$ (283.2). Mpt.= 188-189°C.

m/z (EI+) = 283.3 ([M]+, 45%), 184.2(25), 169.2 (10), 113.1 (15), 79.8 (35), 59.1 (20). Accurate mass found: 283.2149, expected: 283.2147. Elemental analysis expected; C, 67.81; H, 10.31; N, 4.94; O, 16.94; found; C, 67.75; H, 10.28; N, 4.90.

^{1}HNMR (400MHz, $DMSO-d_6$) δ_H 12.095 (1H, br s, COOH), 8.508 (1H, t J=5.5, NH), 6.955 (1H, d J=15.2Hz, alkene), 6.530 (1H, d J=15.2Hz, alkene), 3.168 (2H, q J=6Hz, NCH2), 1.52-1.40 (2H, m, CH2), 1.32-1.20 (18H, m, CH2 x9), 0.882 (3H, t J=6Hz, CH3).

^{13}CNMR (100MHz, $DMSO-d_6$) δ_C 168.53(OC=O), 166.57(NC=O), 137.16(CH), 130.44(CH), 39.81(NCH2), 31.22(CH2), 29.66(CH2), 29.60(CH2), 29.56(CH2x2), 29.51(CH2), 29.45(CH2), 29.40(CH2), 26.98(CH2), 22.86(CH2), 14.21(CH3).

C-43:

Flavin pseudorotaxane axle:

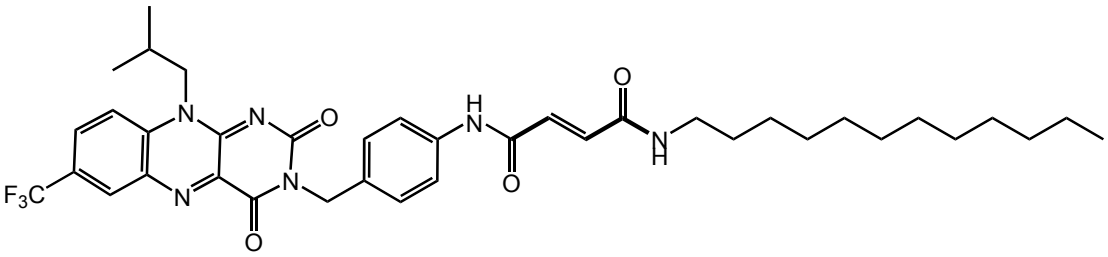

EDCI.HCl (200mg, 1.04mmol, 1.2eq) was added to a stirring suspension of **C-42** (240mg, 0.85mmol) and flavin **C-48** (370mg, 0.83mmol) in $CHCl_3$ (30mL) at 0°C. The reaction was allowed to warm to r.t and then left stirring overnight. The product was provided by chromatography column (silica) using eluent DCM followed by DCM/EtOH (98:2). Yield = 450mg (77%). $C_{38}H_{47}N_6O_4F_3$ (708.8). Mpt.= >300°C.

m/z (FAB+) = 709.4 ([M+H]+, 55%), 708.3 (40), 371.1 (50), 338.9 (35), 282.9 (20), 237.8 (18). Accurate mass found: 709.3613, expected: 709.3611. Elemental Analysis expected: C, 64.39; H, 6.68; F, 8.04; N, 11.86; O, 9.03. Found: C, 64.33; H, 6.71 : N, 11.76.

^{1}HNMR (400MHz, $DMSO-d_6$) δ_H 10.465(1H, s, NH), 8.579(1H, d J=1.5Hz, ArH), 8.479(1H, t J=5.6Hz. NH), 8.284(1H, d J=9.1Hz, ArH), 8.221(1H, dd J=9.1Hz and 2Hz, ArH), 7.634(2H, d J=8.5Hz, AA'BB' ArH x2), 7.386(2H, d J=8.5Hz, AA'BB' ArH), 7.045(1H, d J=15.1Hz, alkene), 6.968(1H, d J=15.1Hz, alkene), 5.094(2H, s, NCH2Ar), 4.559(2H, br s, CH2-CH), 3.177(2H, q J=6.3Hz, C=ONCH2), 2.379(1H, sept J=6.7Hz, CHCH2), 1.462(2H, pent J=6.5Hz, CH2-CH3), 1.33-1.24(18H, m, CH2 x9), 1.011(6H, d J=6.6Hz, CH3 x2), 0.878(3H, t J=6.7Hz, CH3).

^{1}HNMR (400MHz, $CDCl3+(5\%\ DMF-d_7)$) δ_H 9.672(1H, s, NH), 8.418(1H, s, ArH), 7.927(1H, d J=9Hz, ArH), 7.891(1H, s, $DMF(CH)$), 7.723(1H, d J=9Hz, ArH), 7.546(2H, d J=15Hz, AA'BB' ArH), 7.436(2H, d J=15Hz, AA'BB' ArH), 7.100(1H, t J=5Hz, NH), 6.996(1H, d, alkene), 6.871(1H, d, alkene), 5.111(2H, s, NCH2-Ar), 4.490(2H, br s, CH2-CH), 3.194(2H, q J=6.5Hz, C=ONCH2), 2.816(1H, s $DMF(CH_3)$), 2.720(1H, s, $DMF(CH_3)$), 2.318(1H, sept J=6.7Hz, CHCH2), 1.425(1H, pent J=6.5Hz, CH2-CH3), 1.25-1.00(18H, m, CH2 x9), 0.925(1H, 6H, d J=6.6Hz, CH3 x2), 0.752(3H, t J=6.5Hz, CH3),

^{13}CNMR (100MHz, $DMSO-d_6$) δ_C 163.3(NC=O), 162.2(NC=O), 159.1(NC=ON flavin), 154.7(NC=O flavin), 150.3(N=C-C=N x2), 139.9(C=CN-isobutyl), 137.8(CH2-ArC benzyl), 135.4(**C**=CN-isobutyl), 134.2(ArC-NH benzyl), 133.9(ArCH flavin, q, J=3.9Hz), 132.6(alkene), 132.5(alkene), 128.3(q, J=35Hz, ArC-CF3), 128.4(ArCH x2 benzyl), 125.7(ArCH flavin), 124.2(q, J=272Hz, CF3), 119.2(ArCH x2 benzyl), 118.5(ArCH flavin), 50.5(CHCH2-), 43.8(NCH2-Ar), 38.8(NCH2CH2-), 31.3(CH2), 29.03(CH2), 29.00(CH2), 28.96(CH2), 28.84(CH2), 28.69(CH2), 28.68(CH2), 28.65(CH2), 26.8(CH), 26.4(NCH2CH2), 22.1(CH2CH3), 19.7(CH3 x2), 14.0(CH3).

Chapter 6: Flavin-fumaramide [2]Rotaxane.

(a). [2]Rotaxane synthesis:

C-44:

4-(trifluoromethyl)-N-isobutyl-2-nitroaniline: [84]

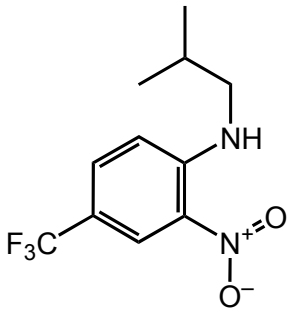

1-Chloro-2-nitro-4(trifluoromethyl) benzene (18.5g, 81.85mmol, 1eq) isobutyl amine (18.4g, 251mmol) and tri-ethylamine (18mL) were dissolved in THF (180mL) and heated under reflux at 70°C with stirring for 20H. After cooling to r.t, the NEt_3.HCl salt was removed by filtration and the THF evaporated under vacuum. The remaining residue was dissolved in DCM (100mL) and washed with distilled water (100mL x3), dried over $MgSO_4$ and then filtered. The filtrate was evaporated under vacuum to provide the product as a yellow solid. Yield = 18.2 (85%). $C_{11}H_{13}N_2O_2F_3$ (262.1). Mpt.= 52-53°C (lit = 52-54°C [84]).

^{1}HNMR (400MHz, $CDCl_3$) δ_H 8.53 (1H, d, J=2Hz); 8.46 (1H, br s,); 7.64 (1H, dd, J=9Hz and 2Hz); 6.98 (1H, d, J=9Hz); 3.25 (2H, m); 2.10 (1H, sept, J=6Hz); 1.12 (6H, d, J=6Hz).

C-45:

4-(trifluoromethyl)-N-isobutyl-2-aminoaniline: [84]

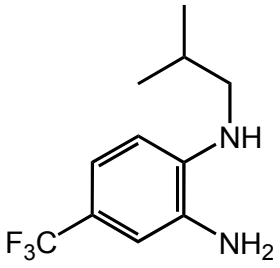

C-44 (18.1g, 69.3mmol) ammonium formate (22.0g, 0.34moles, 5eq) and 10% palladium(carbon) (1.4g) were stirred in methanol (300mL) for 1H at room temp in a sealed r.b flask, pre-flushed with nitrogen gas and fitted with an expansion balloon. The mixture was then filtered through cellite to remove the Pd(C) and the filtrate was reduced in volume under vacuum. The remaining residue was dissolved in DCM (150mL), washed with distilled water (100mL x3), dried under $MgSO_4$ and the organic layer reduced again in volume under vacuum to give a dark oily residue. This was taken on to the next stage without much delay to prevent unnecessary air oxidation. Yield = 15.7g (98%). $C_{11}H_{15}N_2F_3$ (232.1).

^{1}HNMR (400MHz, *CDCl*3) δ_H 7.077 (1H, dd J=9Hz and 1.5Hz, ArH), 6.743 (1H, d J=1.5Hz, ArH), 6.525 (1H, d, J=9Hz, ArH), 3.901 (2H, br s, NH2), 2.892 (2H, d, J=8Hz, CH2CH), 2.177 (1H, br s, NH), 1.867 (1H, sept J=7Hz, CH), 0.956 (6H, d, J=8Hz, CH3 x2).

C-46:

7-(trifluoromethyl)-10-isobutyl isoalloxazine: [84]

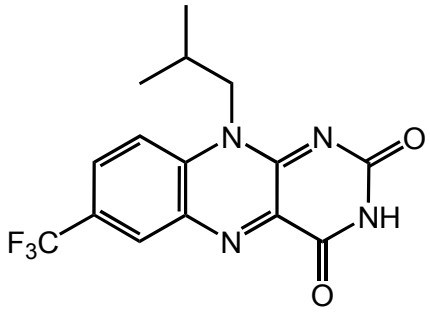

C-46 (15.5g, 67.1mmol), alloxan monohydrate (11.5g, 80.5mmol, 1.2eq) and boron oxide (9.4g, 135.0mmol, 2eq) were dissolved in glacial acetic acid (350mL) and stirred at r.t for 2H. The mixture was reduced in volume under vacuum then diluted with distilled water (300mL) and extracted with DCM (300mL x3). These organic layers along with solid material were separated from the aqueous layer and the dull yellow solid was isolated by filtration. The product was provided by crystallization from ethanol (250mL) producing a yield of 12.4g (54%). A second fraction of the product was provided after combining both the organic filtrates from the previous wash and the crystallization and then condensing under vacuum to produce a black solid. This was then crystallized from ethyl acetate (200mL). Total yield = 17.4g (76%). $C_{15}H_{13}N_4O_2F_3$ (338.3). Mpt.= as published decomposes >220°C [84].

^{1}HNMR (400MHz, *CDCl*3) δ_H 8.978 (1H, s, NH), 8.611 (1H, d, J=2Hz, ArH), 8.067 (1H, dd, J=9Hz and 2Hz, ArH), 7.783 (1H, d, J=9Hz, ArH), 4.461 (2H, br s, NCH2), 2.274 (1H, sept, J=7Hz, CH-isobutyl), 1.082 (6H, d, J=7Hz, CH3 x2).

C-47:

3-(4-nitrobenzyl)-7-(trifluoromethyl)-10-isobutyl isoalloxazine: [84]

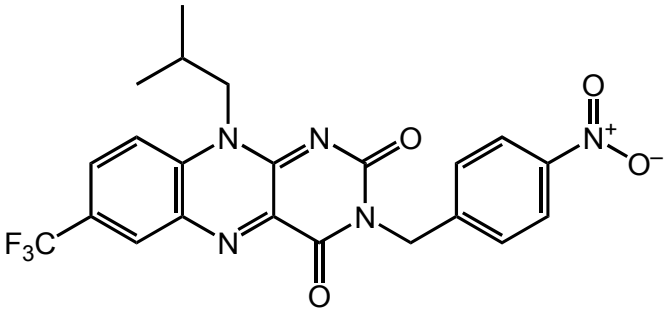

C-46 (2.8g, 8.3mmol, 1eq) was dissolved in DMF (45ml) by heating gently. Acetone (200mL) was then added followed by p-nitrobenzyl chloride (2.1g, 12.4mmol, 1.5eq) and potassium carbonate (4.0g, 28.9mmol, 3.5eq). The reaction was stirred at r.t for 2 days. The K_2CO_3 was removed by passing the reaction through a short flash column (silica) and washing with acetone. The filtrate was condensed under vacuum and rinsed with a 1:1 mixture of diethyl ether/hexane (50mL) to remove DMF residue and unreacted nitro-benzyl chloride. The product was provided after column chromatography (silica) using eluent DCM followed by DCM/acetone (90:10). Yield = 3.79g (96%). $C_{22}H_{18}N_5O_4F_3$ (473.13). Mpt.= 184°C (lit = 184-186°C [84]).

^{1}HNMR (400MHz, *CDCl*3) δ_H 8.587 (1H, d, J=2Hz, ArH), 8.164 (2H, d, J=8.5, AA'BB' x2), 8.058 (1H, dd, J=8Hz and 2Hz, ArH), 7.760 (3H, m, AA'BB' x2 + ArH), 5.311 (2H, s, ArCH2), 4.551 (2H, br s, NCH2), 2.441 (1H, sept, J=7Hz, CH), 1.062 (6H, d, J=6.5Hz, CH3 x2).

C-48:

3-(4-aminobenzyl)-7-(trifluoromethyl)-10-isobutyl isoalloxazine: [84]

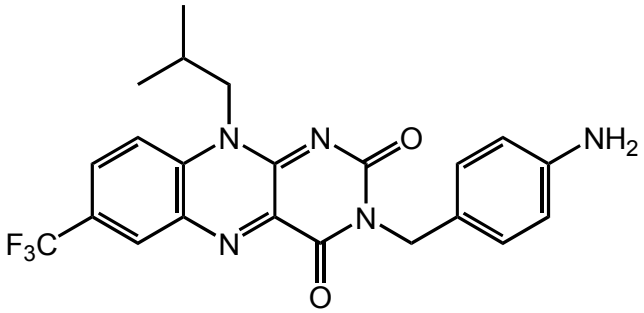

C-47 (2.65g, 5.6mmol, 1eq) was stirred as a semi suspension in a solvent mixture of MeOH (150mL) and THF (50mL). The flask was flushed with nitrogen gas before adding ammonium formate (1.07g, 17mmol, 3eq), 5% palladium(carbon) (400mg) and 5 drops of glacial acetic acid. The flask was then fitted with an expansion balloon and stirred at r.t for 30min. The mixture was filtered though a short plug of cellite to remove Pd(C). The filtrate was concentrated under vacuum and the remaining brown residue dissolved in THF (150mL), stirred to precipitate ammonium formate and filtered. After concentrating the filtrate under vacuum, the product was provided by column chromatography (silica) using eluent DCM followed by DCM/acetone (80:20). Yield = 2.42g (97%). $C_{22}H_{20}N_5O_2F_3$ (443.16). Mpt.= as published dec >230°C [84].

^{1}HNMR (400MHz, *CDCl*3) δ_H 8.520 (1H, d J=2Hz, ArH), 7.987 (1H, dd, J=9Hz and 2Hz, ArH), 7.713 (1H, d, J=9Hz, ArH), 7.396 (2H, d, J=8.3, AA'BB' x2), 6.557 (2H, d, J=8.3, AA'BB' x2), 5.120 (2H, s, ArCH2), 4.567 (2H, br s, NCH2), 3.634 (2H, s, NH2), 2.396 (1H, sept, J=7Hz, CH), 1.012 (6H, d, J=6.6Hz, CH3 x2).

C-49:

N-(2,2-diphenylethyl) fumaramic acid monoethyl ester: [32]

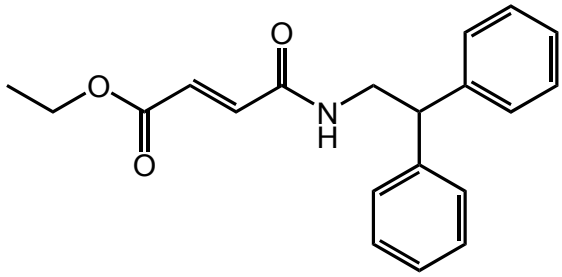

EDCI.HCl (2.1g, 10.9mmol) was added to a stirred solution of 2,2-diphenyl amine (2.0g, 10.1mmol), fumaric acid monoethyl ester (1.48g, 10.2mmol) and DMAP (1.32g, 10.8mmol) in DCM (300mL) at 0°C. The solution was left stirring for 24H as the mixture gradually warmed to r.t. The reaction mixture was then washed with a saturated solution of citric acid (100mL x3) and distilled water (100mL x3) then dried over $MgSO_4$ and reduced in volume to give a colourless solid. The product was provided after crystallization from ethyl acetate. Yield = 2.9g (89%). $C_{20}H_{21}NO_3$ (323.0). Mpt.= 114°C (lit = 112-113°C [32]).

^{1}HNMR (400MHz, *CDCl*3) δ_H 7.30-7.10 (10H, m, ArH x10), 6.882 (1H, d J= 15Hz, CH alkene), 6.761 (1H, d J= 15Hz, CH alkene), 6.143 (1H, br t J=6Hz, NH), 4.155 (1H, t J=8Hz, CH-Ph2), 4.021 (2H, q J=7Hz, OCH2CH3), 3.933 (2H, d, J=8Hz, CH2CH), 1.279 (3H, t J=7Hz, CH3).

C-50:

N-(2,2-diphenylethyl) fumaramic acid: [32]

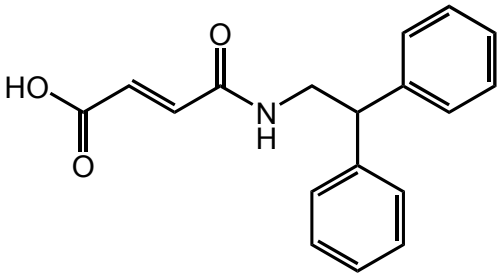

Aqueous NaOH (390mg into 10mL, 1.2eq) was added dropwise to a stirring solution of **C-49** (2.6g, 8.05mmol, 1eq) in EtOH (150mL). The reaction was left stirring at room temp overnight after which the solvent was evaporated under vacuum, and the remaining solids were washed with diethyl ether (100mL x2). The whiter solids were dissolved in distilled water (100mL) and filtered to provide a clear solution. The product was precipitated after adjusting the pH by addition of 20% aqueous HCl. This was collected by filtration, washed with distilled water (20mL x2) and dried under high vacuum at 40°C for 24Hrs. Yield = 2.1g (88%). Mpt.= as published decomposes >270°C [32]. ^{1}HNMR (400MHz, $DMSO-d6$) δ_H 12.782 (1H, s, br), 8.577 (1H, br t J=6Hz, NH), 7.35-7.20 (10H, m, Ph2 ArH x10), 6.931 (1H, d J=15Hz, CH alkene), 6.548 (1H, d J=15Hz, CH alkene), 4.171 (1H, t J=7Hz, CHCH2) and 3.779 (2H, d J=7Hz, CH2).

C-51:

Flavin-fumaramide axle:

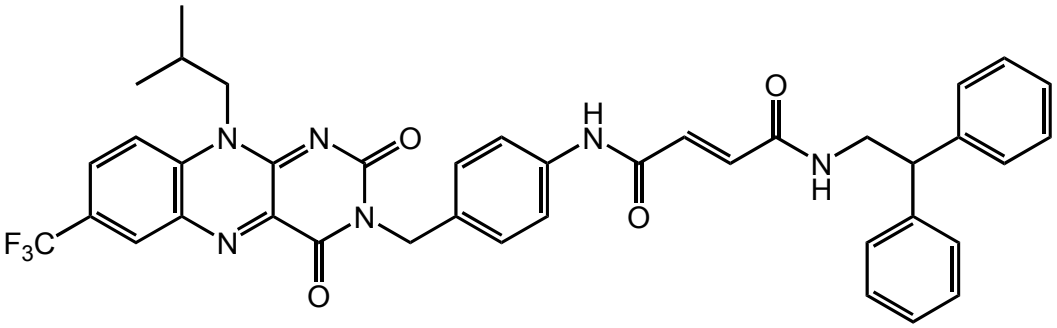

EDCI.HCl (780mg, 4.07mmol, 1.2eq) and DMAP (83mg, 0.68mmol, 0.2eq) were added to a stirring suspension of **C-50** (1.0g, 3.38mmol, 1eq) in DCM (100mL). The mixture was stirred at r.t until complete dissolution (approx 5-10min) before adding **C-48** (1.5g, 3.38mmol, 1eq). The reaction was left stirring for 17H and the resulting orange precipitate collected by filtration, washed with DCM (10mL x2), diethyl ether (10mL x2) and then dried under vacuum. Yield = 730mg (30%). $C_{40}H_{35}N_6O_4F_3$ (720.7). Mpt.= 253°C.

m/z (FAB) = 721.2 ([M+H]+, 100%), 720.2 (40), 383.1 (47), 338.9 (35), 282.9 (20), 106.3 (38).

Elemental analysis calcd. (%) for $C_{40}H_{35}N_6O_4F_3$: C, 66.66; H, 4.89; F, 7.91; N, 11.66; O, 8.88; found: C, 66.73 H, 4.86 N. 11.54.

^{1}HNMR (400MHz, $DMSO-d6$) δ_H 10.433 (1H, s, NH-Ar), 8.573 (2H, m, ArH and NH-CH2), 8.279 (1H, d, J=9Hz, ArH), 8.219 (1H, dd J=9Hz and 2Hz, ArH), 7.616 (2H, d J=, AA'BB' ArH x2), 7.340 (2H, d J=, AA'BB' ArH x2), 7.36-7.29 (8H, m, Ph2 ArH x8), 7.233 (2H, m, Ph2 ArH x2), 7.027 (1H, d J=15Hz, alkene), 6.613 (1H, d J=15Hz, alkene), 5.093 (2H, s, CH2-Ar), 4.560 (2H, br s, NCH2CH), 4.269 (1H, t J=8Hz, CH-Ph2), 3..870 (2H, t J=7Hz, NCH2CHPh2), 2.382 (1H, sept J=6Hz, CH(CH3)2), 1.014 (6H, d J=7Hz, CH3 x2).

^{1}HNMR (400MHz, $CDCl_3 + (5\%\ DMF-d_7)$) δ_H 9.517(1H, s, NH-Ar), 8.465(1H, d J=2Hz, ArH), 7.959(1H, dd J=9Hz and 2Hz, ArH), 7.936(DMF), 7.724(1H, d J=9Hz, ArH), 7.550(2H, d J=8.5Hz, AA'BB' ArH x2), 7.470(2H d J=8.5Hz, AA'BB' ArH x2), 7.25-7.10(10H, m, Ph x2), 7.022(1H, d J=15Hz, alkene), 6.826(1H, t J=5.8Hz, NH-CH2), 6.774(1H, d J=15Hz, alkene), 5.150(2H, s, NCH2Ar), 4.521(2H, br s, NCH2CH), 4.191(1H, t J=8Hz, CH-Ph2), 3.898(2H, t J=6.9Hz, NCH2CHPh2), 2.892(DMF), 2.808(DMF), 2.353(1H, sept J=6Hz, CH(CH3)2), 0.965(6H, d J=6.8Hz, CH3 x2).

^{13}CNMR(100*MHz*, *DMSO* − *d*6) δ_C 163.53(NC=O), 162.13(NC=O), 159.08(N(N)C=O flavin), 154.72(NC=O flavin), 150.33(N=CC=N flavin), 142.69(Ph2 ArC x2), 139.91(N=CC=N flavin), 137.71(ArC-CH2), 135.36(N-CC-N flavin), 134.19(N-CC-N flavin), 133.69(CH alkene), 132.80(CH alkene), 132.56(ArC-NH), 129.83(ArCH, q, J=3Hz), 128.97(ArCH, q, J=4Hz), 128.44(Ph2 ArCH x4), 128.37(ArCH benzyl x2), 127.82(Ph2 ArCH x4), 126.40(Ph ArCH x2), 125.90(q, J=35Hz, ArC-CF3), 123.46 (q, J=272Hz, CF3), 119.19(ArCH benzyl x2), 118.52(ArCH flavin), 50.50(N-CH2-CH), 49.95(Ph2-CH), 43.79(CH2-Ar), 43.35(CH2-CH-Ph2), 26.76(CH-isobutyl), 19.74(CH3 x2),

C-52:

Flavin-fumaramide [2]Rotaxane:

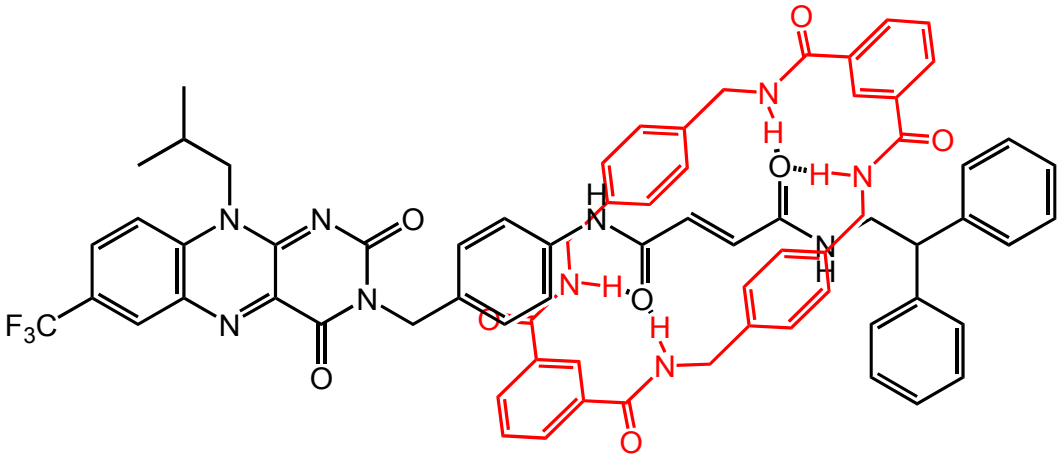

C-51 (300mg, 0.41mmol, 1eq) was dissolved in DMF (10mL) using gentle heating then diluted with dry $CHCl_3$ (100mL) (stabilized with amylenes not ethanol) and NEt_3 (2mL, 1.45g, 14.4mmol, 35eq). Isophthaloyl dichloride (416mg, 2.05mmol, 5eq) and p-xylylene diamine (280mg, 2.05mmol, 5eq) were separately dissolved in $CHCl_3$ (10mL each) and added dropwise by motor-driven syringe pump to a vigorously stirring solution of the above at room temp over a 3H period. The mixture was allowed to stir for a further 1H before passing through a short flash column of silica using acetone as an eluent. The yellow filtrate was concentrated under vacuum. The product was provided after dry-loaded column chromatography using eluent $CHCl_3$ followed by a solvent mixture of $CHCl_3$/EtOAc/EtOH (86:10:4). Yield = 250mg (50%). $C_{72}H_{63}N_{10}O_8F_3$ (1253.3). Mpt.= 222-223°C.

m/z (FAB) = 1254.2 ([M+H]+, 100%), 383.0 (91), 338.9 (88), 282.9 (73), 151.4 (67).

Elemental analysis calcd. (%) for $C_{72}H_{63}N_{10}O_8F_3$: C, 69.00; H, 5.07; F, 4.55; N, 11.18; O, 10.21; found: C, 69.10 H, 4.93 N. 11.32.

^{1}HNMR (400MHz, $DMSO-d_6$) δ_H 10.227(1H, s, NH-Ar), 8.630(2H, s, ArH(2-isophth)), 8.601(1H, t J=6Hz, NH-CH2), 8.561(1H, s, ArH flavin), 8.31-8.19(6H, m, NH x4 and ArH x2 flavin), 8.104(4H, dd J=7.6Hz and 1.1Hz, ArH(4- and 6-isophth) x2), 7.727(2H, t J=7.5Hz, ArH(5-isophth) x2), 7.414(2H, d J=8.5Hz, AA'BB' ArH x2), 7.332(2H, d J=8.5Hz, AA'BB' ArH x2), 7.286(4H, d J=7Hz, Ph2 ArH x4), 7.235(6H, m, Ph2 ArH x6), 6.849(8H, s, ArH(xylylene) x8), 5.961(1H, d J= 15Hz, CH alkene), 5.846(1H, d J= 15Hz, CH alkene), 5.074(2H, s, CH2-Ar), 4.551(2H, br s, NCH2-isobutyl), 4.293(8H, qd, J=16Hz and 4.5Hz, CH2 x4), 4.147(1H, t J=7.5Hz, CH-Ph2), 3.731(2H, br t J=5.5Hz, NCH2CHPh2), 2.369(1H, sept J=6.5Hz, CH(CH3)2), 0.997(6H, d J=6.5Hz, CH3 x2).

^{1}HNMR (400MHz, $CDCl_3$ + (5% $DMF-d_7$)) δ_H 10.250(1H, s, NH-Ar), 8.560(2H, s, ArH(2-isophth)), 8.480(1H, t J=6Hz, NH-CH2), 8.458(1H, s, ArH flavin), 8.147(4H, m, NH

x4), 7.967(1H, d J=9Hz, ArH), 7.934(1H, s, ArH flavin), 7.748(5H, m, ArH(4- and 6-isophth) x2 and ArH x1), 7.564(2H t J=7.6Hz, ArH(5-isophth) x2), 7.388(2H, d J=8.5Hz, AA'BB' ArH x2), 7.329(2H, d J=8.5Hz, AA'BB' ArH x2), 7.181(4H, m, Ph2 ArH x4), 7.108(6H, m, Ph2 ArH x6), 6.820(8H, s, ArH(xylylene) x8), 5.928(1H, d J= 15Hz, CH alkene), 5.776(1H, d J= 15Hz, CH alkene), 5.125(2H, s, CH2-Ar), 4.515(2H, br s, NCH2-isobutyl), 4.285 (8H, br s, CH2 x4), 4.117(1H, t J=7.5Hz, CH-Ph2), 3.738(2H, br t J=5.5Hz, NCH2CHPh2), 2.327(1H, sept J=7Hz, CH(CH3)2), 0.961(6H, d J=6.2Hz, CH3 x2),

^{13}CNMR (100MHz, $DMSO-d_6$) δ_C 165.81(ring C=O x4), 164.84(NC=O), 163.41(NC=O), 159.11(N(N)C=O flavin), 154.73(NC=O flavin), 150.32(N=CC=N flavin), 142.54(Ph2 ArC x2), 139.93(N=CC=N flavin), 136.60(ring ArC(xylylene) x4), 136.41(ArC-CH2), 135.32(N-CC-N flavin), 134.27(ring ArC(1,3-isophth) x4), 134.16(N-CC-N flavin), 133.47(ArC-NH), 130.77(ring ArCH(5-isophth) x2), 130.67(CH alkene), 129.94(ArCH, q, J=3Hz), 129.10(CH alkene), 128.97(ArCH, q, J=4Hz), 128.57(ring ArCH(xylxylene) x8), 128.52(Ph2 ArCH x4), 128.33(ArCH x2 benzyl), 127.70(Ph2 ArCH x4), 126.55(Ph2 ArCH x2), 125.86(q, J=35Hz, ArC-CF3), 125.30(ring ArCH(2) x2), 122.80(q, J=272Hz, CF3), 120.16(ArCH benzyl x2), 118.54(ArCH flavin), 50.52(N-CH2-CH), 49.94(Ph2-CH), 43.76(CH2-Ar), 43.62(CH2-CH-Ph2), 43.20(ring Ar-CH2 x4), 26.75(CH-isobutyl), 19.72(CH3 x2).

C-53:

N^1-(3,4-dimethylphenyl)-N^4-(2,2-diphenylethyl)fumaramide:

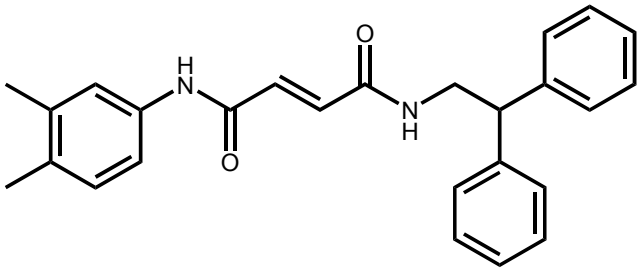

EDCI.HCl (236mg, 1.23mmol, 1.2eq) was added to a stirring suspension of **C-50** (304mg, 1.03mmol, 1eq) and 3,4-dimethylaniline (125mg, 1.03mmol, 1eq) in DCM (50mL) at r.t. The semi-solution quickly became clear after 1-2 minutes before forming a white solid precipitate. The solid was broken up using a glass rod and diluted with chloroform (200mL) and stirred for a further 1H. The solution was then filtered, washed with distilled water (150mL x3), dried over $MgSO_4$ and the solvent evaporated under vacuum to provide a white solid. The pure product was finally afforded after crystallization from DCM. Yield=340mg (83%). $C_{26}H_{26}N_2O_2$ (398.5) . Mpt.= 240°C.

m/z (EI+) = 398.2 ([M+H]+, 20%), 218.1 (40), 202.1 (60), 167.1 (100), 121.1 (30), 91.1 (15). Accurate mass expected: 398.1994; found: 398.1944.

^{1}HNMR (400MHz, $DMSO-d_6$) δ_H 10.291(1H, s, NH-Ar), 8.591(1H, t J=5.5Hz, NH-CH2), 7.457(1H d J=2Hz, ArH), 7.421 (1H, dd J=8.1Hz and 2Hz, ArH), 7.37-7.29(8H, m, Ph2 ArH x8), 7.26-7.20(2H, m, Ph2 ArH x2), 7.101(1H, d J=8.1Hz, ArH), 7.045(1H, d J=15Hz, CH alkene), 6.912(1H, d J=15Hz, CH alkene), 4.279(1H, t J=8Hz, CH-Ph2), 3.878(2H, dd J=5.5Hz and 2Hz, NHCH2CH), 2.211(6H, d J=Hz, CH3 x2).

^{13}CNMR (100MHz, $DMSO-d_6$) δ_C 163.64(C=O), 161.96(C=O), 142.71(ArC-CH x2), 136.52(ArC-CH3), 136.39(ArC-NH), 133.41(CH alkene), 133.05(CH alkene), 131.63(ArC-CH3), 129.63(ArCH), 128.43(ArCH x4), 127.83(ArCH x4), 126.38(ArCH x2), 120.46(ArCH), 116.87(ArCH), 49.98(CH), 43.39(CH2), 19.58 (CH3), 18.80(CH3).

Chapter 7: Flavin-succinamide [2]Catenane. [85]

C-54.

N-(4-nitrobenzyl) 7-trifluoromethyl 10-hydroxyhexyl isoalloxazine.

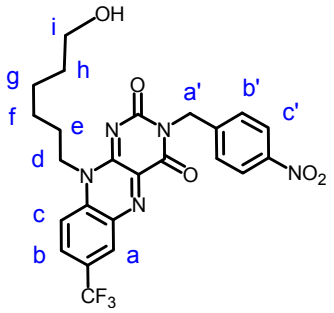

Flavin **C-46** (5.0g, 13.1mmol), nitrobenzyl chloride (8.07g, 47.0mmol) and K_2CO_3 (5.4g, 39.1mmol) were stirred in acetonitrile at r.t and protected from light for 8 days. The solvent was evaporated under vacuum and the crude mixture dissolved in DCM then filtered to remove the K_2CO_3. The DCM was reduced in volume and the product isolated by column chromatography, eluent initially DCM, increasing polarity to DCM/acetone (8:2). All fractions containing the product were combined and the solvent evaporated to reveal a yellow solid that was then dissolved in minimum amount acetone and precipitated by adding petroleum ether to give pure product. Yield = 4.58g (68%). Mpt.= 163-165°C.

^{1}HNMR(400*MHz*, *CDCl*$_3$) δ_H 8.59(1H, br s, ArH-a), 8.16(2H, d, J=8.8Hz, ArH-b' x2), 8.09(1H, dd, J=9.0 and 1.7Hz, ArH-b), 7.76(1H, d, J=7.7Hz, ArH-c and 2H, d, J=8.8Hz, ArH-c' x2), 5.36(2H, s, CH2-a'), 4.69(2H, br t, CH2-d), 3.67(2H, t, J=6.0Hz, CH2-i), 1.89(2H, quint, J=7.5Hz, CH2-e), 1.65-1.50(6H, m, CH2-f,g,h). ^{13}CNMR(100*MHz*, *CDCl*$_3$) δ_C 158.9(ArC=O), 154.9(ArC=O), 149.1(ArC=N), 147.4(ArC=N), 143.5(ArC), 138.3(ArC), 135.0(ArC), 134.5(ArC), 131.7(ArCH, q, J=3Hz), 130.8(ArCH, q, J=3.9Hz), 130.3(2xArCH, AB), 128.8(q, J=35Hz, ArC-CF3), 122.8(q, J=272Hz, CF3), 123.7(2xArCH, AB), 116.3(ArCH), 62.4(CH2), 45.1(CH2), 44.6(CH2), 32.2(CH2), 26.7(CH2), 26.3(CH2), 25.0(CH2).

λ_{max} (thin film)/cm^{-1} 3400 br, 2916, 2858, 1703, 1660, 1596, 1566, 1344, 1285, 1224, 1197, 1128.

m/z (FAB) = 518.3 ([M+H]+,100%), 502.3 (9), 418 (8), 137 (19). Found 518.1649. $C_{24}H_{23}F_3N_5O_5$ requires [M+H]+, 518.1651.

C-55.

N-(4-nitrobenzyl) 7-trifluoromethyl 10-(TBDMS)oxyhexyl isoalloxazine.

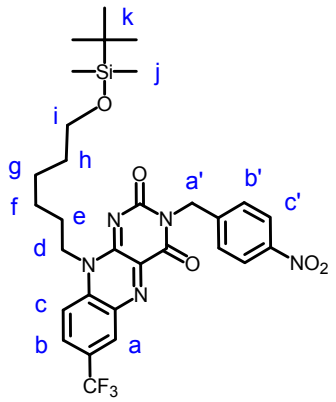

C-54 (3.30g, 6.38mmol) was dissolved in DMF (5mL) with some gentle heating and once the flask had cooled to touch, tert-butyl dimethyl silyl chloride (2.13mg, 1.5eq) and DMAP (110mg, 0.1eq) were added. The mixture was then stirred at room temp for 30min before adding the NEt_3 (2.0mL, 1.5eq) dropwise by pipette. TLC analysis shortly after this showed no visible trace of **C-54** but the reaction was allowed to continue stirring for 1h, then diluted with distilled water (100mL) and extracted with CH_2Cl_2 (100mL x2), dried ($MgSO_4$) and the CH_2Cl_2 evaporated under vacuum. The product was isolated using column chromatography with eluent CH_2Cl_2/Petroleum Ether (80:20) to give an orange crystalline solid. A trace amount of TBDMS chloride was visible on the initial HNMR but was easily removed by adding diethyl ether (in which the product is semi-soluble, precipitating with petroleum ether and collecting the yellow solid by filtration. Yield =3.85g (96%). Mpt.= 163-165°C.

^{1}HNMR(400*MHz*, *CDCl*$_3$) δ_H 8.59 (1H, d, J=1.2Hz, ArH-a), 8.16 (2H, d, J=8.9Hz, Ar-b' x2), 8.09 (1H, dd, J=9.2 and 1.9Hz, ArH-b), 7.75 (2H, d, J=8.9Hz, ArH-c' x2), 7.74 (1H, d, J= 9.2Hz, ArH-c), 5.36 (2H, s, CH2-a'), 4.68 (2H, t, broad, J=7.5, CH2-d), 3.61 (2H, t, J=6.2Hz, CH2-i), 1.87 (2H, quint, J=7.6Hz, CH2-e), 1.60-1.40 (6H, m, CH2-f,g,h), 0.88 (9H, s, CH3-k x3), 0.04 (6H, s, CH3-j x2).

^{13}CNMR(100*MHz*, *CDCl*$_3$) δ_C 158.9(ArC=O), 154.8(ArC=O), 149.1(ArC=N), 147.4(ArC=N), 143.5(ArC), 138.3(ArC), 134.9(ArC), 134.5(ArC), 131.6(ArCH, q, J=3Hz), 130.7(ArCH, q, J=3.9Hz), 130.3(2xArCH, AB), 128.7(q, J=35Hz, ArC-CF3), 124.2(ArCH), 123.6(q, J=272Hz, CF3), 116.3(2xArCH, AB), 62.8(CH2), 45.3(CH2), 44.6(CH2), 32.5(CH2), 27.1(CH2), 26.6(CH2), 25.9(3x CH3), 25.5(CH2), 18.3(CSi), -5.3(2x CH3).

λ_{max} (thin film)/cm^{-1} 2939, 2860, 1717, 1669, 1596, 1559, 1457, 1337, 1239, 1192, 1127, 1014.

m/z (FAB) = 632.4 ([M+H]+,100%), 616.4(20), 574.3(40). Found 632.2513. $C_{30}H_{37}O_5N_5F_3Si$ requires [M+H]+, 632.2516.

C-56.

N-(4-aminobenzyl) 7-trifluoromethyl 10-(TBDMS)oxyhexyl isoalloxazine.

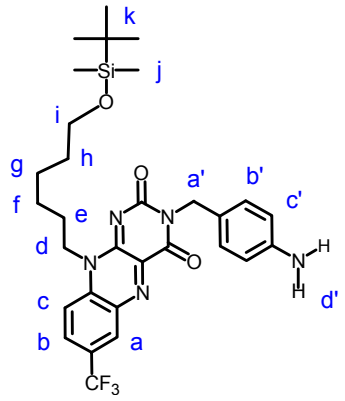

C-55 (1.30g, 2.05mmol), ammonium formate (2.50g, 39.6mmol) and 10% Pd(C) (350mg) were stirred in MeOH (50mL) at r.t for 1H. The Pd(C) was removed by filtration under an N_2 blanket. The filtrate was evaporated under vacuum, dissolved in CH_2Cl_2, washed with water (x3), dried ($MgSO_4$), condensed and then purified by column chromatography, eluent initially CH_2Cl_2, increasing polarity to CH_2Cl_2/ethyl acetate (9:1).

Yield = 924mg (75%). Mpt.= 94-95°C.

^{1}HNMR(400*MHz*, *CDCl*$_3$) δ_H 8.55 (1H, d, J=1.38Hz, ArH-a), 8.03 (1H, dd, J=8.96 and 1.95Hz, ArH-b), 7.69 (1H, d, J=8.96Hz, ArH-c), 7.42 (2H, d, J=8.57Hz, ArH-b' x2), 6.58 (2H, d, J=8.57Hz, ArH-c'), 5.15 (2H, s, CH2-a'), 4.63 (2H, br t, J=6.5Hz, CH2-d), 3.63 (2H, s, NH2-d'), 3.61 (2H, t, J=6.5Hz, CH2-i), 1.83 (2H, quint, J=7.7Hz, CH2-e), 1.58-1.38 (6H, m, CH2-f,g,h), 0.88 (9H, s, CH3-k x3), 0.04 (6H, s, CH3-j x2).

^{13}CNMR(100*MHz*, *CDCl*$_3$) δ_C 158.8(ArC=O), 155.2(ArC=O), 148.9(ArC=N), 146.1(ArC=N), 138.7(ArC), 134.7(ArC), 134.5(ArC), 131.2(2xArCH AB), 131.1(ArCH, br s), 130.6(ArCH, q, J=3.9Hz), 128.3(q, J=35Hz, ArC-CF3), 126.5(ArC), 122.9(q, J=272Hz, CF3), 116.1(ArCH), 114.7(2xArCH AB), 62.8(CH2), 45.0(CH2), 44.7(CH2), 32.5(CH2), 27.0(CH2), 26.6(CH2), 25.9(3x CH3), 25.5(CH2), 18.3(CSi), -5.3(2x CH3).

λ_{max} (thin film)/cm^{-1} 3452, 3357, 2939, 2859, 1712, 1664, 1600, 1559, 1459, 1331, 1284, 1242, 1192, 1128, 1005.

m/z (FAB) = 624.4 ([M+ Na]+, 92%), 601.4 (23), 519.4 (23), 439.3 (48), 107.7 (95), 75.2 (100). Found 624.2596. $C_{30}H_{38}O_3N_5F_3SiNa$ requires [M+Na]+, 624.2594.

C-57.

N-(4-(butanoic acid) amidobenzyl) 7-trifluoromethyl 10-(TBDMS)oxyhexyl isoalloxazine.

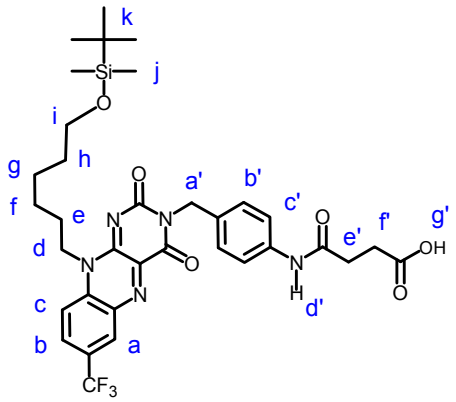

C-56 (800mg, 1.33mmol), succinic anhydride (266mg, 2eq) and DMAP (17mg. 0.1eq) were heated under reflux in CH_2Cl_2 (50mL) for 22H. The mixture was allowed to cool and continue stirring at room temp for 2 days. The mixture was concentrated under vacuum then purified by column chromatography, eluent initially CH_2Cl_2/Petroleum Ether (90:10), increasing polarity to CH_2Cl_2/acetone (80:20). Yield =775mg (85%). Mpt.= 104-105°C.

^{1}HNMR(400*MHz*, *CDCl*$_3$) δ_H 9.78 (1H, s, broad, OH-g'), 8.86 (1H, s, NH-d'), 8.52 (1H, d, J=1.39Hz, ArH-a), 8.03 (1H, dd, J=8.97 and 2.0Hz, ArH-b), 7.71 (1H, d, J=9.1Hz, ArH-c), 7.68 (2H, d, J=8.5Hz, ArH-b' x2), 7.16 (2H, d, J=8.5Hz, ArH-c' x2), 5.26 (2H, s, CH2-a'), 4.62 (2H, t, broad, J=6Hz, CH2-d), 3.58 (2H, t, J=6.2Hz, CH2-i), 2.851 (4H, br s, CH2-e' and f') 1.82 (2H, quint, J=7.4Hz, CH2-e), 1.55-1.35 (6H, m, CH2-f,g,h), 0.85 (9H, s, CH3-k x3), 0.01 (6H, s, CH3-j x2).

^{13}CNMR(100*MHz*, *CDCl*$_3$) δ_C 176.2(C=O), 170.6(C=O), 158.9(ArC=O), 155.4(ArC=O), 148.8(ArC=N), 138.3(ArC=N), 137.5(ArC), 134.7(ArC), 134.3(ArC), 131.8(ArC), 131.2(ArCH, br s), 130.3(ArCH, br s), 129.7(2x ArCH AB), 128.2(q, J=35Hz, ArC-CF3), 122.8(q, J=272Hz, CF3), 119.7(2x ArCH AB), 116.4(ArCH), 62.8(CH2), 45.1(CH2), 44.6(CH2), 32.3(CH2), 31.3(CH2), 29.1(CH2), 26.9(CH2), 26.4(CH2), 25.8(3x CH3), 25.4(CH2), 18.2(CSi), -5.5(2x CH3).

λ_{max} (thin film)/cm^{-1} 3740, 3508, 3323, 2938, 2860, 1715, 1659, 1600, 1557, 1459, 1419, 1329, 1244, 1194, 1132, 1010.

m/z (FAB) = 702.4 ([M+H]+,52%), 644.3(20), 497.3 (25), 439.3 (40), 206.5 (70). Found 702.2938. $C_{34}H_{43}O_6N_5F_3Si$ requires [M+H]+, 702.2935.

C-58.

N-(4-(butanoic 10-undecenylamide) amidobenzyl) 7-trifluoromethyl 10-(TBDMS)oxyhexyl isoalloxazine.

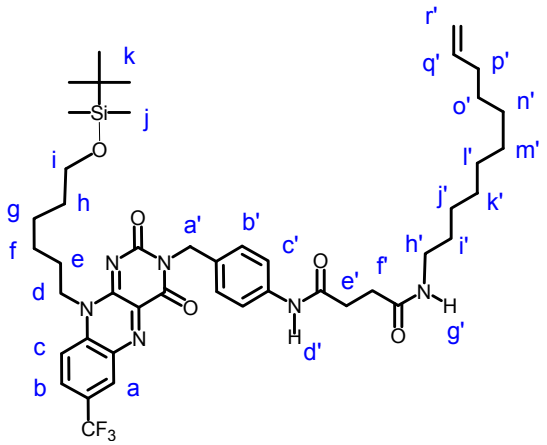

C-57 (2.3g, 3.28mmol) was first dissolved in CH_2Cl_2 (30mL) before adding EDCI (817mg, 4.26mmol 1.3eq), HOBt (575mg, 4.26mmol, 1.3eq), 10-undecen-amine [70] (1.3g, 7.68mmol, 2eq) and DMAP (40mg, 0.33mmol, 0.1eq). The reaction was left stirring at room temp for 18H then the product was condensed and purified by subjecting the mixture to column chromatography, eluent initially CH_2Cl_2, increasing polarity to CH_2Cl_2/acetone (8:2). Yield = 2.68g (96%). Mpt.= 148-149°C.

^{1}HNMR(400*MHz*, *CDCl*$_3$) δ_H 8.56 (1H, d, J=1.3Hz, ArH-a), 8.54 (1H, s, NH-d'), 8.04 (1H, dd, J=9.1 and 2.0Hz, ArH-b), 7.70 (1H, d, J=9.1Hz, ArH-c), 7.55 (2H, d, J=8.6Hz, ArH-b'), 7.44 (2H, d, J=8.6Hz, ArH-c'), 5.86 (1H, br t, J=4.9Hz, NH-g'), 5.86-5.74 (1H, m, CH-q'), 5.23 (2H, s, CH2-a'), 5.02-4.90(2H, m, CH2-r'), 4.64 (2H, br t, J=6.6Hz, CH2-d), 3.61 (2H, t, J=6.1Hz, CH2-i), 3.25-3.16 (2H, m, CH2-h'), 2.68-2.64 and 2.57-2.53 (4H, mx2, CH2-e' and f'), 2.07-1.98 (2H, m, CH2-p'), 1.84 (2H, quint, J=7.3Hz, CH2-e), 1.58-1.40 (6H, m, CH2-f,g,h), 1.40-1.30 (2H, m, CH2-o'), 1.32-1.20 (12H, m, CH2-I',j',k',l',m',n'), 0.88 (9H, s, CH3-k x3), 0.04 (6H, s, CH3-j x2).

^{13}CNMR(100*MHz*, *CDCl*$_3$) δ_C 172.2(C=O), 170.6(C=O), 158.8(ArC=O), 155.0(ArC=O), 149.0(ArC=N), 139.2(CH alkene), 138.7(ArC=N), 137.7(ArC), 134.8(ArC), 134.5(ArC), 132.1(ArC), 131.3(ArCH, q, J=3Hz), 130.7(ArCH, q, J=3.9Hz), 130.4(2xArCH AB), 128.5(q, J=35Hz, ArC-CF3), 122.9(q, J=272Hz, CF3), 119.7(2xArCH AB), 116.1(ArCH), 114.1(CH2 alkene), 62.9(CH2), 45.1(CH2), 44.8(CH2), 39.8(CH2), 33.8(CH2), 33.0(CH2), 32.5(CH2), 31.7(CH2), 29.5(CH2), 29.41(CH2), 29.36(CH2), 29.2(CH2), 29.1(CH2), 28.9(CH2), 27.0(CH2), 26.8(CH2), 26.6(CH2), 25.9(3x CH3), 25.6(CH2), 18.3(CSi), -5.3(2x CH3).

λ_{max} (thin film)/cm^{-1} 3302, 2927, 2856, 1709, 1656, 1600, 1556, 1459, 1421, 1330, 1243, 1193, 1130, 1006. m/z (FAB) = 853.5 ([M+H]+,20%), 795.4(10), 439.3 (30), 252.4 (90), 107.7 (100). Found 853.4654. $C_{45}H_{64}N_6O_5F_3Si$ requires [M+H]+, 853.4660.

C-59.

N-(4-(butanoic 10-undecenylamide) amidobenzyl) 7-trifluoromethyl 10-hydroxyhexyl isoalloxazine.

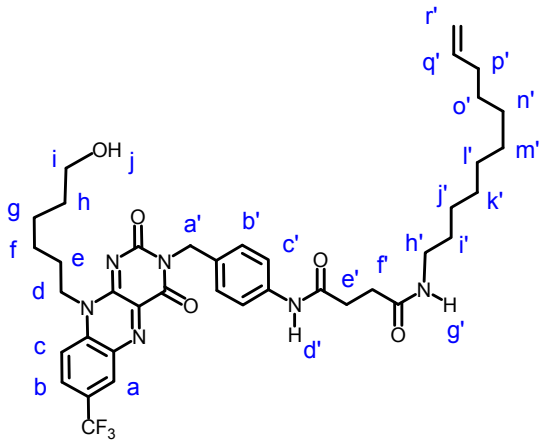

After dissolution of **C-58** (560mg, 0.657mmol) in THF (17ml), distilled water (14ml) was added, followed by conc HCl (1.5mL) syringed in one go to the continually stirring mixture. Although no trace of the starting material was visible by TLC within just 5 minutes after the reaction start, the mixture was allowed to continue stirring at room temp for 1H. The mixture was then diluted by addition of distilled water (100mL) and extracted with CH_2Cl_2 (100mL x2). The organic layers were combined, washed with saturated brine, dried ($MgSO_4$) and evaporated under vacuum to give a yellow/orange solid. Trace TBDMS chloride could be removed by rinsing the flask in warm petroleum ether. Yield = 453mg (94%). Mpt.= 135-136°C.

^{1}HNMR(400*MHz*, *CDCl*$_3$) δ_H 8.86 (1H, s, NH-d'), 8.54 (1H, d, J=1.18Hz, ArH-a), 8.04 (1H, dd, J=9.02 and 1.92Hz, ArH-b), 7.72 (1H, d, J=9.02Hz, ArH-c), 7.47 (2H, d, J=8.57Hz, ArH-b'), 7.41 (2H, d, J=8.57Hz, ArH-c'), 6.12 (1H, t, J=5.5Hz, NH-g'), 5.86-5.73 (1H, m, CH-q'), 5.20 (2H, s, CH2-a'), 5.02-4.89 (2H, m, CH2-r'), 4.64 (2H, br t, J=6.5Hz, CH2-d), 3.64 (2H, t, J=6.1Hz, CH2-i), 3.22-3.15 (2H, m, CH2-h'), 2.67-2.61 and 2.54-2.49 (4H, mx2, CH2-e' and f'), 2.05-1.98 (2H, m, CH2-p'), 1.84 (2H, quint, J=7.7Hz, CH2-e), 1.62-1.40 (6H, m, CH2-f,g,h), 1..39-1.30 (2H, m, CH2-o'), 1.30-1.19 (12H, m, CH2-i',j',k',l',n',m').

^{13}CNMR(100*MHz*, *CDCl*$_3$) δ_C 172.2(C=O), 170.7(C=O), 158.8(ArC=O), 155.3(ArC=O), 149.0(ArC=N), 139.2(CH alkene), 138.6(ArC=N), 137.8(ArC), 134.9(ArC), 134.5(ArC), 132.0(ArC), 131.3(ArCH, q, J=3Hz), 130.6(ArCH, q, J=3.9Hz), 130.2(2xArCH AB), 128.4(q, J=35Hz, ArC-CF3), 122.9(q, J=272Hz, CF3), 119.7(2xArCH AB), 116.2(ArCH), 114.1(CH2 alkene), 62.4(CH2), 44.7(CH2), 39.7(CH2), 33.8(CH2), 32.8(CH2), 32.2(CH2), 31.6(CH2), 29.5(CH2), 29.43(CH2), 29.42(CH2), 29.38(CH2), 29.2(CH2), 29.0(CH2), 28.9(CH2), 26.9(CH2), 26.7(CH2), 26.3(CH2), 25.0(CH2).

λ_{max} (thin film)/cm^{-1} 3440 br, 3303, 2925, 2855, 1653, 1601, 1555, 1426, 1329, 1236, 1188, 1133. m/z (FAB) = 739.6 ([M+H]+,100%), 421.6 (60), 252.4 (100), 107.7 (85). Found 739.3788. $C_{39}H_{50}O_5N_6F_3$ requires [M+H]+, 739.3795.

C-60.

N-(4-(butanoic 10-undecenylamide) amidobenzyl) 7-trifluoromethyl 10-(10-undecen-1-onoxyhexyl) isoalloxazine.

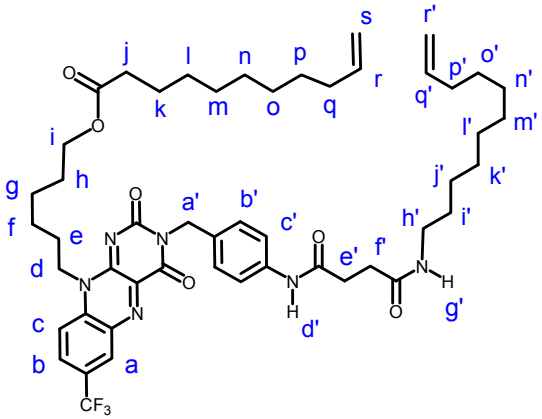

EDCI (774mg, 4.04mmol, 1.4eq) was added to a stirring solution of **C-59** (2.05g, 2.78mmol), HOBt (550mg, 4.07mmol, 1.4 eq), DMAP (495mg, 4.05mmol, 1.4 eq) and 10-undecenoic acid (765mg, 0.8mmol, 1.4 eq) in CH_2Cl_2 (40mL). The reaction was stopped after 2 days, washed with distilled water (x3), dried ($MgSO_4$) and the solvent removed under vacuum. The product was purified by column chromatography, eluent initially CH_2Cl_2, increasing polarity to CH_2Cl_2/methanol (96:4). Yield = 1.93g (77%). Mpt.= 170°C.

^{1}HNMR(400*MHz*, *CDCl*$_3$) δ_H 8.56 (2H, s, NH-d' and ArH-a), 8.03 (1H, dd, J=8.9 and 1.8Hz, ArH-b), 7.70 (1H, d, J=8.9Hz, ArH-c), 7.54 (2H, d, J=8.57Hz, ArH-b' x2), 7.44 (2H, d, J= 8.57Hz, ArH-c' x2), 5.86 (1H, t, J=5.2Hz, NH-g'), 5.86-5.74 (2H, m, CH-r and q'), 5.23 (2H, s, CH2-a'), 5.01-4.89 (4H, m, CH2-s and r'), 4.64 (2H, br t, J=6.2Hz, CH2-d), 4.06 (2H, t, J=6.65Hz, CH2-i), 3.22 (2H, q, J=6.7Hz, CH2-h'), 2.68-2.64 and 2.57-2.53 (4H, mx2, CH2-e' and f'), 2.29 (2H, t, J=7.6Hz, CH2-j), 2.02 (4H, q, J=7.1Hz, CH2-q and p'), 1.85 (2H, quint, J=7.5Hz, CH2-e), 1.69-1.50 (6H, m, CH2-f,g,h), 1.50-1.40 (4H, m, CH2-p and o'), 1.40-1.32 (4H, m, CH2-k and I'), 1.32-1.20 (18H, m, CH2-l,m,n,o,j',k',l',m',n).

^{13}CNMR(100*MHz*, *CDCl*$_3$) δ_C 174.0(C=O), 172.2(C=O), 170.6(C=O), 158.7(ArC=O), 155.0(ArC=O), 148.9(ArC=N), 139.2(CH alkene), 139.1(CH alkene), 138.6(ArC=N), 137.7(ArC), 134.8(ArC), 134.4(ArC), 132.1(ArC), 131.3(q, J=3Hz ArCH), 130.7(q, J=3.9Hz, ArCH), 130.4(2xArCH AB), 128.5(q, J=35Hz, ArC-CF3), 122.9(q, J=272Hz, CF3), 119.7(2xArCH AB), 116.1(ArCH), 114.13(CH2 alkene), 114.10(CH2 alkene), 63.8(CH2), 45.0(CH2), 44.8(CH2), 39.8(CH2), 34.3(CH2), 33.8(CH2), 33.8(CH2), 33.0(CH2), 31.7(CH2), 29.6(CH2), 29.5(CH2), 29.42(CH2), 29.36(CH2), 29.30(CH2), 29.26(CH2),

29.2(CH2), 29.11(CH2), 29.06(CH2), 29.0(CH2), 28.8(CH2), 28.4(CH2), 26.9(CH2), 26.8(CH2), 26.4(CH2), 25.6(CH2), 24.9(CH2).

λ_{max} (thin film)/cm^{-1} 3302, 2925, 2855, 1721, 1655, 1599, 1557, 1532, 1458, 1420, 1328, 1238, 1183, 1130, 1074, 1005.

m/z (FAB) = 905.5 ([M+H]+, 80%), 653 (25), 383 (40), 252(100), 106 (80). Found 905.5167. $C_{50}H_{68}O_6N_6F_3$ requires [M+H]+, 905.5152.

C-61.

Flavin Macrocycle Ring.

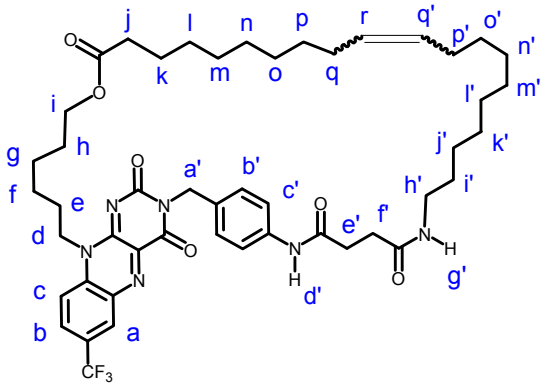

C-60 (181mg, 0.2mmol) was dissolved in dry CH_2Cl_2 (150mL) (0.0013M concentration) and degassed by N_2 bubbling for 10 minutes before adding the 2nd generation Grubbs' catalyst (4.25mg, 2.5mol%) to the stirring mixture protected under a N_2 blanket. The mixture was then heated under reflux at 40°C for 18H. The solvent was evaporated under vacuum and the remaining solid subjected to two column chromatography procedures in order to completely eliminate a green residue, Following the 1st column, eluent CH_2Cl_2/methanol (90:10), all fractions containing two yellow TLC spots were combined and condensed. The subsequent 2nd column, eluent CH_2Cl_2/methanol (98:2), thus afforded the product (second fraction eluted) as a yellow solid. Yield = 90mg(50%). Mpt.= 226°C.

^{1}HNMR(400*MHz*, *CDCl*$_3$) δ_H 8.57 (1H, d, J=1.33Hz, ArH-a), 8.54 (1H, s, NH-d'), 8.05 (1H, dd, J=9.0 and 1.9Hz, ArH-b), 7.70 (1H, d, J=9.0Hz, ArH-c), 7.56 (2H, d, J=8.6Hz, ArH-b' x2), 7.45 (2H, d, J=8.6Hz, ArH-c' x2), 5.90 (1H, t, J=5.65), 5.34 (2H, t, J=3.5Hz, (E)alkene, [4:1 ratio minor triplet at 5.30, J=5.0Hz, (Z)alkene]), 5.24 (2H, s, CH2-a'), 4.65 (2H, br t, J=6.2Hz, CH2-d), 4.07 (2H, t, J=6.3Hz, CH2-i), 3.21 (2H, q, J=6.6Hz, CH2-h'), 2.68-2.64 and 2.57-2.53 (4H, mx2, CH2-e' and f'), 2.29 (2H, t, J=7.4Hz, CH2-j), 2.00-1.50 (6H, m, CH2-q,p' and e), 1.50-1.40 (6H, m, CH2-f,g,h), 1.33-1.17 (4H, m, CH2-p and o'), 1.19 (22H, m, CH2-k,l,m,n,o,i',j',k',l',m',n).

^{13}CNMR(100*MHz*, *CDCl*$_3$) δ_C 174.0(C=O), 172.2(C=O), 170.6(C=O), 158.7(ArC=O), 154.9(ArC=O), 148.9(ArC=N), 138.6(ArC), 137.7(ArC), 134.8(ArC=N), 134.5(ArC), 132.2(ArC), 131.3(q, J=3Hz, ArCH), 130.7(q, J=3.9Hz, ArCH), 130.5(2xArCH AB), 130.4(CH alkene), 130.3(CH alkene), 128.5(q, J=35Hz, ArC-CF3), 122.9(q, J=272Hz, CF3), 119.7(2xArCH AB), 116.0(ArCH), 63.8(CH2), 45.0(CH2), 44.7(CH2), 39.7(CH2), 34.3(CH2), 33.1(CH2), 32.4(CH2), 31.9(CH2), 29.6(CH2), 29.40(CH2), 29.35(CH2), 29.3(CH2), 29.2(CH2), 29.1(CH2), 29.1(CH2), 28.98(CH2), 28.96(CH2), 28.8(CH2),

28.7(CH2), 28.4(CH2), 27.0(CH2), 26.9(CH2), 26.7(CH2), 26.4(CH2), 25.7(CH2), 24.9(CH2).

λ_{max} (thin film)/cm^{-1} 3300, 2924, 2854, 1721, 1652, 1598, 1560, 1531, 1458, 1417, 1329, 1241, 1176, 1134, 1075, 1015.

m/z (FAB) = 877.5 ([M+H]+, 100%), 722 (15), 383 (20), 106 (23). Found 877.4836. $C_{48}H_{64}N_6O_6F_3$ requires [M+H]+, 877.4839.

C-62.

Flavin-succinamide [2]Catenane.

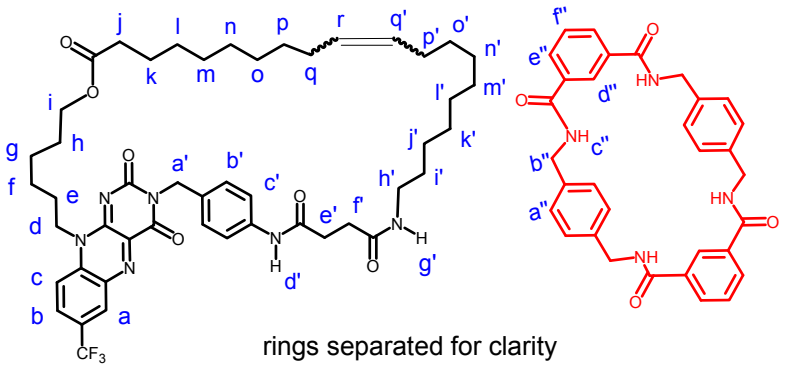

Flavin macrocycle **C-61** (190mg, 0.21mmol) was dissolved by stirring with some gentle heating in 100mL of dry CH_2Cl_2 (stabilized with amylenes not ethanol) prior to adding NEt_3 (1.0mL, 7.2mmol, 34 eq). After cooling to room temp, two pre-prepared 10mL solutions of dry CH_2Cl_2, one with isophthaloyl dichloride (213mg, 1.05mmol, 5eq), the other p-xylylenediamine (145mg 1.06mmol, 5eq), were simultaneously fed into the reaction mixture, dropwise over a 3H period using a motor-driven syringe pump. The NEt_3.HCl salt was removed by filtration and the filtrate condensed under vacuum. The product was then purified by careful column chromatography (eluent: CH_2Cl_2/methanol: 98:2).

Yield =76mg (26%). Mpt.= 188-189°C.

^{1}HNMR(400*MHz*, *CDCl*$_3$) at 25°C δ_H 9.86 (1H, br s, NH-d'), 8.47 (3H, m, ArH-a and ArH-d'' x2), 8.09 (1H, dd, J=9.1 and 1.69Hz, ArH-b), 7.93 (4H, br s, ArH-e''), 7.78-7.70 (5H, m, ArH-c and NH-c'' x4), 7.40-7.32 (4H, m, ArH-b' x2 and ArH-c' x2), 7.22-7.10 (10H, m, ArH-f'' and ArH-a''), 6.55 (1H, br s, NH-g'), 5.31-5.26 (2H, m, CH-r and q'), 5.11 (2H, br s, CH2-a'), 4.60-4.28 (10H, m, CH2-b'' x4 and CH2-i), 3.88 (2H, t, J=5.4Hz, CH2-d), 3.03 (2H, br s, CH2-h'), 2.17 (2H, t, J=7.5Hz, CH2-j), 1.90-1.55 (8H, m, CH2-e,f,g,h), 1.55-1.05 (34H, m, CH2-k,l,m,n,o,p,q,i',j'k'l'm'n'o'p' and e',f').

^{1}HNMR(400*MHz*, *CDCl*$_3$) at 55°C δ_H 9.31 (1H, br s, NH-d'), 8.45 (2H, br s, ArH-d''), 8.29 (1H, br s, ArH-a), 7.99 (1H, d, J=8.2Hz, ArH-b), 7.90 (4H, br s, ArH-e''), 7.63 (1H, d, J=8.2Hz, ArH-c), 7.38 (4H, br s, NH-c''), 7.38-7.24 (4H, m, ArH-b' and c'), 7.18 (2H, s, ArH-f''), 7.04 (8H, s, ArH-a''), 6.04 (1H, br s, NH-g'), 5.24-2.18 (2H, m, CH-r and q'), 5.02 (2H, s, CH2-a'), 4.50-4.30 (10H, m, CH2-b'' x4 and CH2-i), 3.81 (2H, t, J=6.0Hz, CH2-d), 2.99-2.91 (2H, m, CH2-h'), 2.12-2.04 (2H, m, CH2-j), 1.90-1.50 (8H, m, CH2-e,f,g,h), 1.40-1.05 (34H, m, CH2-k,l,m,n,o,p,q,i',j'k'l'm'n'o'p' and e',f').

^{13}CNMR(100*MHz*, *DMSO* − *d*6) δ_C 172.8(C=O), 171.1(C=O), 170.3(C=O), 165.5(4x C=O), 159.1(ArC=O), 156.2(ArC=O), 149.9(ArC=N), 140.1(ArC=N), 138.0(4x ArC),

137.9(ArC), 134.6(4x ArC), 134.4(ArC), 131.13(ArC), 130.7(ArCH, br s), 130.1(CH alkene), 130.0(CH alkene), 129.7(ArC), 129.4(4x ArCH), 128.9(ArCH, br s), 128.2(2x ArCH), 127.8(8x ArCH), 127.5(2x ArCH), 126.5(2x ArCH), 126.0(q, J=33.5Hz, ArC¬-CF3), 123.7(q, J=272.0Hz, CF3), 118.5(2x ArCH), 118.3(ArCH), 63.2(CH2), 43.8(CH2), 42.4(4x CH2), 38.4(CH2), 33.2(CH2), 31.9(CH2), 31.8(CH2), 31.6(CH2), 30.3(CH2), 29.0(CH2), 28.9(CH2), 28.8(CH2), 28.69(CH2), 28.66(2x CH2), 28.61(2x CH2), 28.57(CH2), 28.4(CH2), 28.3(CH2), 28.1(CH2), 27.3(CH2), 26.5(CH2), 26.2(CH2), 25.2(CH2), 24.9(CH2), 24.3(CH2).

λ_{max} (thin film)/cm^{-1} 3309 br, 2926, 2855, 1719, 1652, 1599, 1531, 1422, 1326, 1236, 1192, 1131, 1081.

m/z (FAB) = 1409.7 ([M+H]+, 24%), 877.4 (10), 460.1 (12), 307.0 (100), 289.0 (50).

Elemental analysis calcd. (%) for $C_{80}H_{91}F_3N_{10}O_10$: C, 68.16; H, 6.51; F, 4.04; N, 9.94; O, 11.35; found: C, 68.35; H, 6.63, N9.90.

APPENDICES.

Appendix A: *Square Wave Voltammetry.*

Appendix B: *The transfer coefficient.*

Appendix C: *Marcus theory.*

Appendix A:

Square Wave Voltammetry.

A.1 The Square Wave method.

There are several variations of square wave voltammetry (SWV) that differ by the technique used to superimpose a low-amplitude square wave voltage onto either a ramp or staircase potential and the sampling procedure. [61] The SWV method to be described here is the most commonly used method and was first proposed by Ramaley and Krause [86, 87]. It is however generally referred to as the Osteryoung SWV method due to the extensive development undertaken by the Osteryoungs and co-workers.[88-91] Detection limits as low as 10^{-8} M are achievable by adapting methodologies from various other forms of pulse voltammetric techniques, such as the background suppression and sensitivity of differential pulse voltammetry with the diagnostic value of normal pulse voltammetry and the ability to interrogate products directly in much the same manner as reverse pulse voltammetry. [62]

The Osteryoung SWV waveform is produced by superimposing a square wave signal onto a staircase signal as shown in Figure A.1.

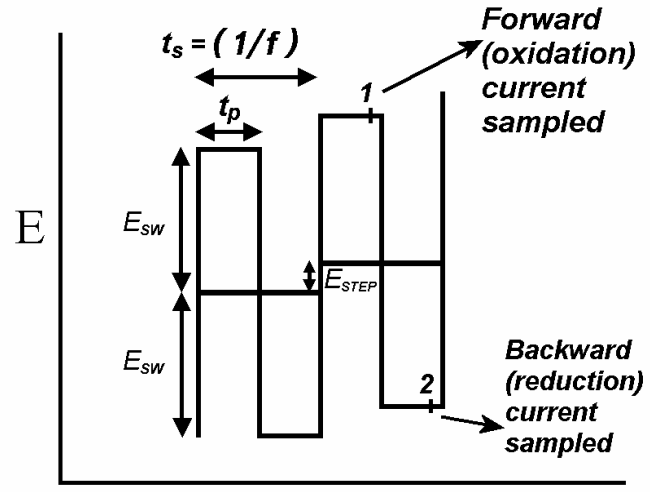

Figure A.1 SWV waveform shown schematically as the sum of a staircase and a square wave where $t_S = 2t_P$.

The square wave is characterised by four main parameters, the pulse height (or SW amplitude) E_{SW} , the staircase step height E_{step} , the pulse time t_p and the cycle period t_s . The pulse time can also be expressed in terms of the SW frequency $f = (2t_p)^{-1}$ whereas the magnitude of potential E_{step} defines the density of information in the response. Hence the apparent scan rate ν can be calculated as the product of the staircase potential E_{step} times the SW frequency f , as shown in Equation A.1.

$$\nu = f \times E_{step} \qquad (\mathrm{Vs}^{-1}) \qquad \text{Eqn (A.1)}$$

The current is measured at two points at the end of each pulse (points 1 and 2 in Figure A.1.). These correspond to positions just before the end of the forward and reverse peaks of the SW signal. The current recorded at these points are referred to as the SW forward and reverse response currents, I_{for} and I_{rev} respectively. The objective of this is to minimise the influence of the double layer capacitive current I_C (induced by potential change at the electrode) relative to the measurement of Faradaic current I_F (obeying the Nernst Equation). During each half cycle, I_C will decay exponentially with time while the I_F will decay inversely proportional to the square root of time as shown in Figure A.2.

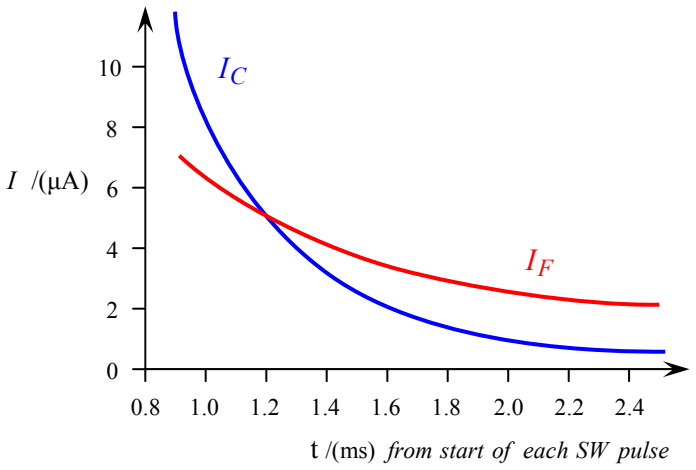

Figure A.2 Current decay versus time of a double layer capacitive current (I_C) and the Faradaic current (I_F) during one half-cycle of a SW potential signal. [92]

Toward the end of the pulse the capacitive current I_C will be smaller than the Faradaic current I_F. Also any residual charging current can be further minimized by the subtraction of those currents measured at the end of two successive half-cycles. The magnitude of I_C also depends on the difference between the electrode potential and its potential of zero charge. Therefore if the SW amplitude is small, the difference between the capacitive currents of the forward and reverse SW pulse half-cycles will also be small. The difference ΔI is usually plotted against the staircase potential as the principle result of the experiment. However since as we shall there is significant diagnostic value in the peak positions and heights of the forward and reverse currents, the SWV will generate and preserve three separate voltammograms showing I_{for}, I_{rev} and ΔI as a function of the staircase potential as shown in Figure A.3.

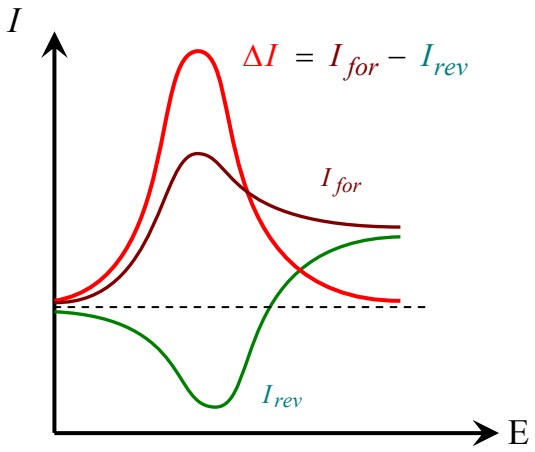

Figure A.3 Schematic voltammetric profiles of the current measured during the forward (I_{for}) and reverse (I_{rev}) pulses and the resultant difference (ΔI) plotted against the staircase potential E_{step}.

Interpretation of the SWV is not always immediately obvious especially if irreversible kinetic's are being observed. For reasons which will be discussed and explained shortly, two peaks can often appear in the difference response ΔI. This can sometimes lead to the erroneous conclusion that two redox species are actually present. However, this behaviour is generally caused as a result of the sampling method used during the SWV procedure and in particular the extreme sensitivity of the reverse current response I_{rev}. This response is dependant on both the electrochemical reversibility of the redox couple and the chemical stability of any subsequent products generated during the forward SW pulse. [61] Therefore recognition and interpreting of this process requires a deeper understanding of both the current sampling procedure and the electrode kinetics. As mentioned earlier, much diagnostic value can be obtained from the voltammograms of the forward and reverse currents. Although digital simulation techniques have not been utilized during this thesis, it is perhaps worth mentioning the combined elucidation potential of SWV and mathematical modelling. It is ultimately not only possible to obtain values for the formal potential of simultaneous redox processes but also obtain both heterogeneous and homogeneous standard rate constants, k_s and k, the transfer coefficients α_{ox}, α_{red} and diffusion coefficients D_{ox} and D_{red} for both oxidized and reduce species.[92]

A.2 Current sampling procedure.

The characteristic bell shaped SWV response as shown in Figure A.3, is best be understood by considering what impact the SW pulse potential has at the electrode during various periods of the scan while bearing in mind that the overall concentrations of oxidant and reductant at the electrode surface will differ according to the redox reaction shown in Equation A.2.

$$O^{m+} + ne^- \underset{k_b}{\overset{k_f}{\rightleftharpoons}} R^{(m-n)+} \qquad \text{Eqn. (A.2)}$$

During the early stages of the SW scan, when the potential is more positive than the formal potential E^θ, any change in potential manifested by the pulse will too small to alter the redox balance and therefore unable generate a Faradaic current, (i.e. $I_{for} - I_{rev}$ is virtually zero). At the opposite extreme, much later in the scan when the potential is far more negative than E^θ and the diffusion-limited-current region has been reached, O^{m+} is already being reduced at the maximum possible rate and therefore any potential change during the forward peak will not increase the rate further. Furthermore, although the surface concentration of $R^{(m-n)+}$ may have attained its maximum concentration, any potential change during the reverse peak will be insufficient to re-oxidize the product. Maximum response is therefore achieved at a potential only when the concentration change from $R \rightarrow O$ and back is greatest. For a reversible system this will occur when the ratio of the two species involved in the redox couple are equal and when the potential is at or near the formal potential E^θ. [92]

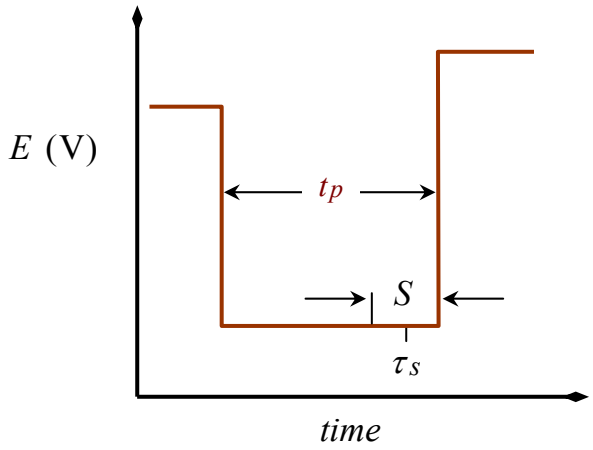

Figure A.4 A scheme of the current sampling technique used in pulse techniques where τ_s is the sampling point within the sampling window S at the end of the SW pulse.

Understanding this sampling procedure will be important later when it comes describing the SWV of surface electrode reactions and an unusual feature called the *quasirevesible maximum*. This phenomenon describes a balance between the current sampling point τ_s at the end of the SW pulse which has a short but fixed duration (e.g. $t_p = 10\,\text{ms}$) as shown in Figure A.4. If the reaction is very slow then a low current will be collected, however if the reaction is very fast, a larger current will be produced but within the same time period the current will have severely decay and the reading will be also low. It is therefore only by adjusting the frequency of the SW pulse to accommodate the rate of the reaction can optimum response be obtained.

A.3 Electrode mechanism of dissolved redox species.

This section is a basic summary of the kinetics (reversible, quasi-reversible and irreversible) of electrode reactions for a redox species (either in solution or surface immobilized) on a stationary planar electrode. The aim is to describe the methods applied in optimizing experimental conditions; primarily with regards to the research topic of polymeric flavo-enzyme model systems (initial results from both SWV and cyclic voltammetry experiments were confusing and difficult to interpret).

The rate of an electron transfer reaction is measured by the heterogeneous standard rate constant k_S, whilst the rate of mass transport is measured by the mass transport coefficient $m^T = D/\delta$ where δ is the diffusion layer thickness. For a dissolved redox species, the definition of electrochemical reversibility at an electrode is generally regarded as when $k_S \gg m^T$, and similarly electrochemical irreversibility is defined as when $k_S \ll m^T$. When electron transfer is extremely rapid and the process is only dependant on the supply of new material. Electrode reactions where k_S is either comparable in magnitude or $k_S < m^T$ are generally referred to as *kinetically controlled* since the electrode reaction has now started to become the rate determining step. These reactions are broadly described as being either quasireversible or irreversible. However the diffusion layer thickness δ is a function of time according to the Cottrell equation, $\delta \propto (Dt)^{1/2}$. Therefore in theory at least, if an experiment is carried out at a sufficiently fast scan rate any reaction could be made to appear electrochemically irreversible and it is only when electrochemical reactions stray from the reversible into the quasireversible and irreversible region do things start to become interesting to the electrochemist. As previously mentioned through a combination of mathematical modelling and digital simulations it is possible to gain insight into reaction mechanisms and allow the calculation of many experimental parameters.

Note: Unless otherwise stated most of the information in the following sections has been sourced from reference [92], which focuses exclusively on Square Wave Voltammetry. Many of the images utilized have been revised from this source and have been and tailored specifically to emphasize certain features.

A.3.1 Definitions of electrochemical reversibility in SWV.

The reversibility of similar electrode reaction in SW voltammetry is primarily dependant on the value of something known as the dimensionless kinetic parameter $\kappa = k_s(Df)^{-1/2}$. This parameter is a ratio of k_s $(cm\ s^{-1})$ to the square root of the diffusion coefficient D $(cm^2 s^{-1})$ times the frequency f (s^{-1}) of the SW pulse. For a given system the diffusion coefficient will usually be fixed, therefore the kinetic parameter will vary according to the $(f)^{-1/2}$ of the SW experiment. The SW frequency can only be varied within a narrow bandwidth which is typically fixed for the electrode (e.g. $10-2000\text{Hz}$ for planar electrodes). The value of κ will therefore be only variable by a factor of $(2000/10)^{1/2}$ or 14 times. However this narrow window is enough to allow the behaviour of the electrode reaction to be adjusted for one of two extreme cases: either the reaction can behave as (1). *reversible* at low frequencies and *quasireversible* at high frequencies or (2). *quasireversible* at low frequencies and *irreversible* at higher frequencies.

Note: For surface electrode reactions the electroactive species has been immobilized at the electrode surface. Mass transport is either zero or close to zero and only variations in the surface concentrations of the redox couple with time is considered. The definitions of electrochemical reversibility and irreversibility with regards to these reactions will be discussed in Section A.7.

A.4 Reversible electrode reactions.

The SW voltammogram shown in Figure A.5 is characterised by a maximum net response $\Delta\Psi p$ where Ψ is known as the dimensionless current ($\Psi = -I/nFAc_o^*(Df)^{1/2}$), and occurs at a corresponding net peak potential Ep and with a half-peak width $\Delta Ep/2$. The response is also characterised by a minimum forward (reductive)(Ψfor) peak and backward (oxidative)(Ψrev) maximum which occurs at potentials Ep,for and Ep,rev respectively (not shown). Dimensionless current is generally used in mathematical modelling as all three peak potentials are independent of the SW frequency f and therefore greatly simplifies the digital simulation calculations. This feature also provides one of the various indications the electrode reaction is reversible within a given range of applied frequencies. However we should emphasise here that the voltammograms demonstrated during the analytical work of this thesis are current response based. Therefore since $\Psi \propto -I$ (as shown above) the reader will find that the forward current response I_{for} is characterised by a maximum and the reverse current response I_{rev} "ideally" by a minimum. Consequently the overall current response ΔI (or I_{Diff}) becomes equal to $I_{for} - I_{rev}$.

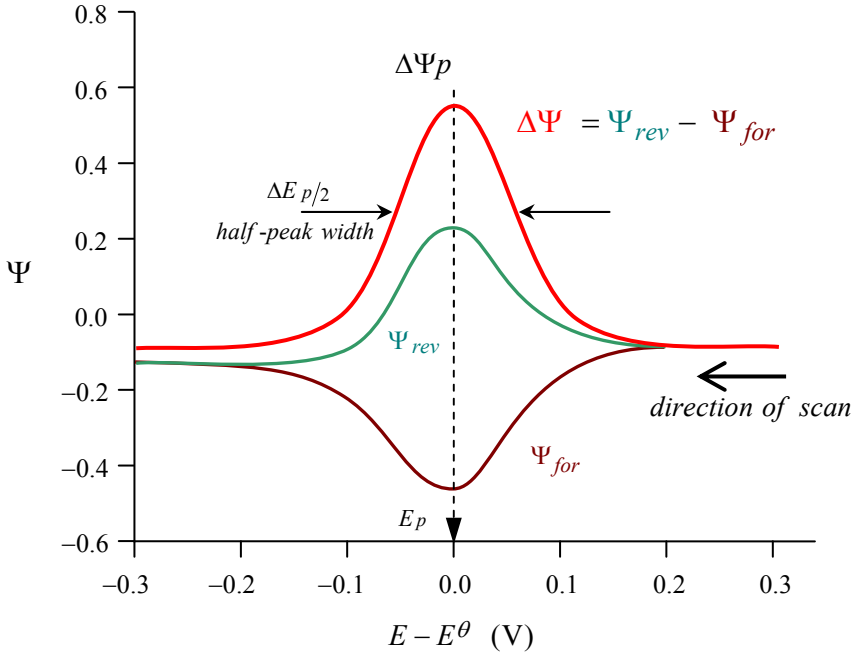

Figure A.5 Theoretical SW voltammograms of a fast and reversible electrode reaction shown in Equation (A.1).

A.5 Kinetically controlled electrode reactions.

When the electrode reaction is not electrochemically reversible (i.e. quasi-irreversible or irreversible) and the electrode reactions become *kinetically controlled*. The response becomes dependant on the dimensionless kinetic parameter $\kappa = k_S(Df)^{-1/2}$ and to some extent, the transfer coefficient α. We can see this clearly in Figure A.7 which shows a plot of $\Delta\Psi p$ versus $\log(\kappa)$ for three different values of α = 0.2, 0.5 and 0.75. The reaction is defined as reversible if $\kappa > 10$, quasireversible if $0.01 < \kappa < 10$ and irreversible if $\kappa < 0.01$. The graph demonstrates how peak response $\Delta\Psi$p rapidly diminishes as the electrochemical reaction goes from reversible to quasireversible. Within the irreversible region the response is appreciably affected by the transfer coefficient α of the system (for a brief explanation of the transfer coefficient see *Appendix B.*). Although no attempt has been made in this thesis to calculate the kinetic parameter κ the aim of this discussion is primarily to demonstrate the conditions that influence electrochemical reversibility. In the equation at the beginning of this paragraph we see that κ is not only proportional to the electrode heterogeneous rate constant k_S but also inversely proportional to the square root of the diffusion coefficient D and the SW frequency f. In other words, for a small molecule system where $D = 1\times10^{-5}$cms^{-1} as oppose to an bulky polymer system where $D = 1\times10^{-8}$cms^{-1} or less, the value of κ would be a >30 fold difference (i.e. $\Delta\log(\kappa) \simeq 1.5$). The range SW frequency (e.g. typically $10 < f <$ 2000 Hz) will also have a significant effect on the electrochemical reversibility of the system, with the reaction becoming more electrochemically irreversible when the SW frequency f is increased.

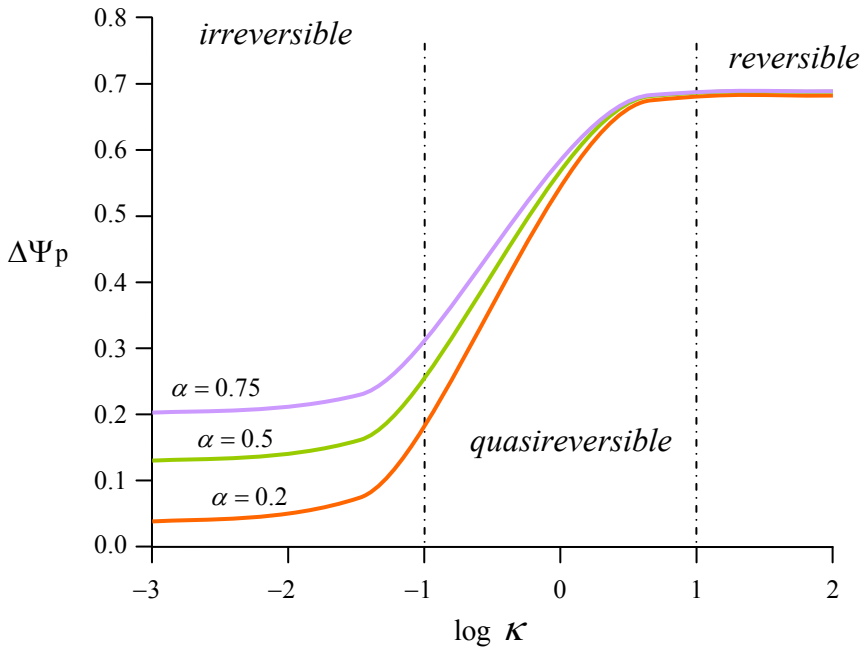

Figure A.6 The dependence of the dimensionless net peak current ($\Delta\Psi p$) with the logarithm of the dimensionless kinetic parameter (κ), for three different values of the transfer coefficient (α).

A.5.1 Quasireversible kinetics.

Two theoretically simulated voltammograms are shown below in Figures A.7(a) with $\kappa = 0.3$ and A.7(b) with $\kappa = 0.05$. Both values of κ place the kinetics of these reactions along the slope of the quasireversible region in Figure A.6. This explains why the magnitude of their $\Delta\Psi p$ values have shrunk to just a fraction of that shown for the reversible example previously shown in Figure A.5. A significant part of the explanation for this sizable decrease is in due to the deteriorating backward response Ψ_b. This becomes more apparent in Figure A.7(b) which shows the peak reverse response Ψ_{rev} just barely protruding into the positive region. It should also be notice that the absolute value of Ψ_{for} also decreases though not as dramatically. The ratio $\Psi_{p,for}/\Psi_{p,rev}$ also increases from -1.47 for this example reversible reaction.

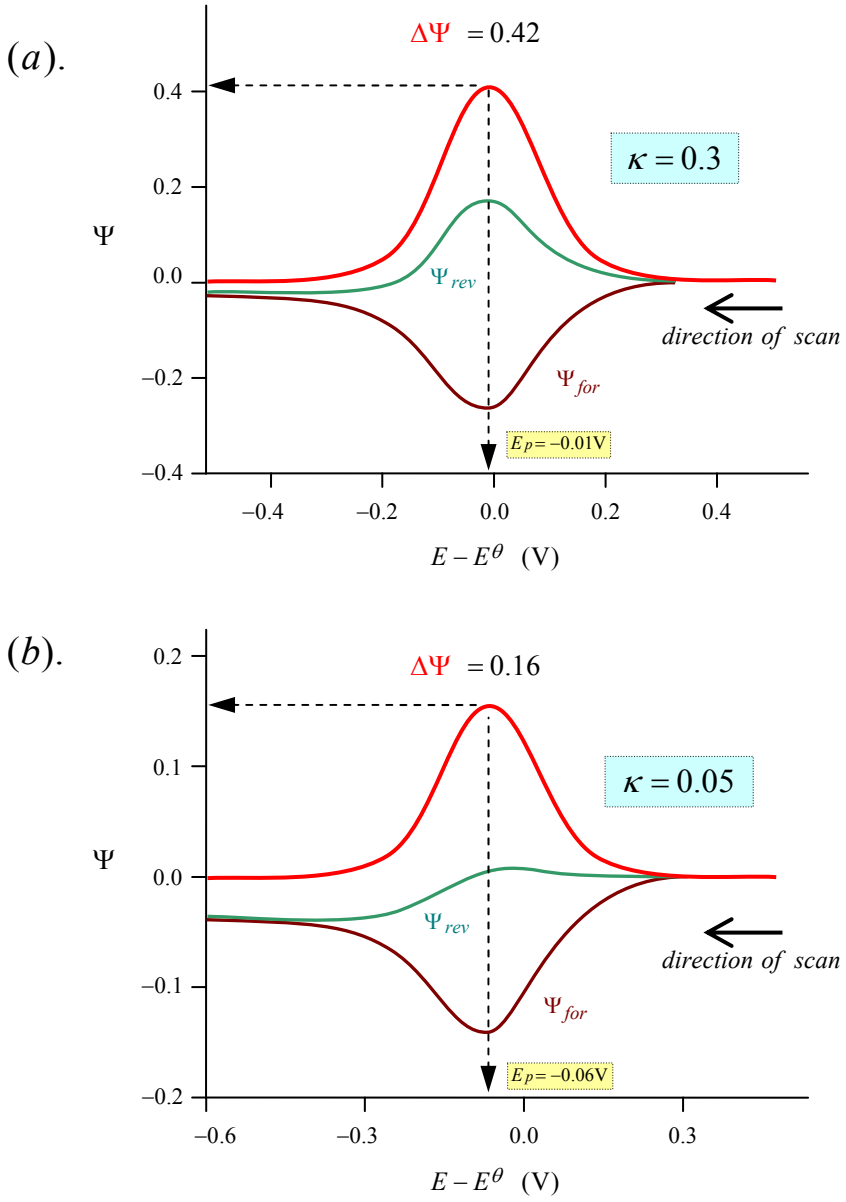

Figure A.7 SW voltammograms of an irreversible electrode reaction (Equation A.2); where dimensionless kinetic parameter κ is equal to: **(a).** 0.3 and **(b).** 0.05. Other parameters are, $\alpha = 0.5$, $nE_{SW} = 50\,\text{mV}$ and $nE_{step} = -2\,\text{mV}$.

Two other significant features are demonstrated during the quasireversible reactions shown in Figure A.7 which shows all three peaks shift position relative to the formal potential E^{θ} with as much as $-60\,\text{mV}\,(\Delta\Psi_p)$ and $-80\,\text{mV}$ $(\Psi_{p,\,for})$ when $\kappa = 0.05$. It is unclear from the source textbook [92] whether this anodic shift is a characteristic of the reduction reaction of bulk analyte when the direction of scan is as shown and which will consequently converts to a cathodic shift when the direction of scan is reversed during oxidation of bulk analyte. The second feature may not be immediately obvious from the two voltammograms in Figure A.7 because the x-axis scales are different on each plot, but the peak net response become broader as the parameter κ decreases. This characteristic of the quasireversible electrode reaction is usually described in terms of the half-peak width $\Delta E_{p/2}$ and clearly contributes to the ability to detect an electrochemically irreversible $\Delta\Psi_p$ response.

A.5.2 Irreversible kinetics.

The irreversible range shown in Figure A.6, where $\kappa < 0.01$. There are several of things to notice about the irreversible voltammograms shown in Figure A.8, the first of which is that the reverse response Ψ_{rev} is negative at all potentials. This therefore means that the overall response $\Delta\Psi = \Psi_{rev} - \Psi_{for}$ will ultimately be smaller than the absolute value of its forward component Ψ_{for}.

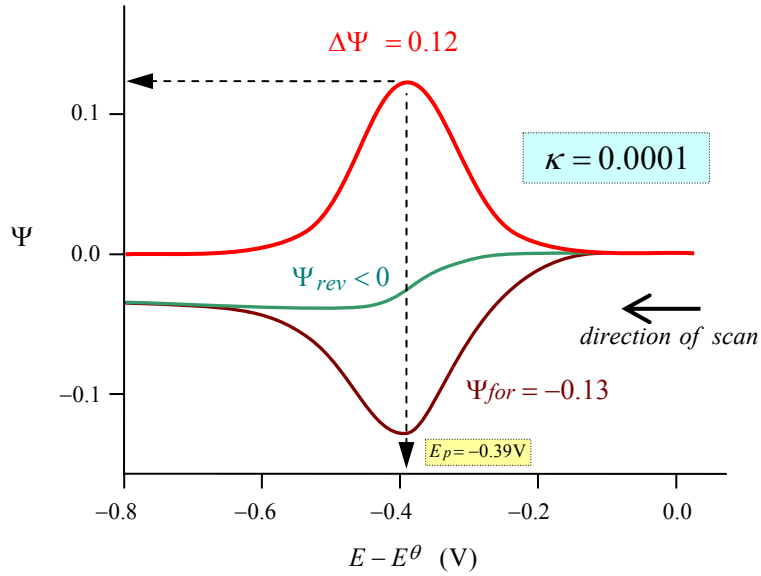

Figure A.8 SW voltammograms of an irreversible electrode reaction (Eqn A.1) showing how the overall net response $\Delta\Psi$ can be less than Ψ_{for}. Other parameters were $\kappa = 10^{-4}$, $\alpha = 0.5$, $nE_{SW} = 50mV$ and $nE_{step} = -2mV$.

The overall net response $\Delta\Psi$ is also now independent of the kinetic parameter κ, as is the half-peak height $\Delta E_{p/2}$. Figure A.9 show that any change in $\Delta\Psi_p$ is now linear dependant on the transfer coefficient α according to the function $\Delta\Psi_p = 0.235\alpha$. This relationship provides a simple and easy method of approximating α for an unknown irreversible reaction.

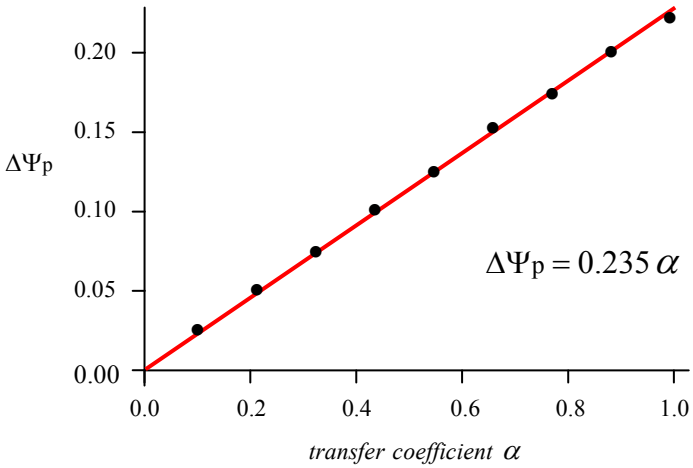

Figure A.9 The dependence of the dimensionless net peak current $\Delta\Psi$ of an irreversible electrode reaction versus the transfer coefficient α. Other parameters are, $\kappa = 10^{-3}$, $nE_{SW} = 50\,\text{mV}$ and $nE_{step} = -2\,\text{mV}$.

A.5.3 Split net response in irreversible electrode reactions.

Sometimes a reversal of scan direction can be used to provide additional information about the mechanism of an electrode reaction. In the simulated examples shown below in Figure A.10 of an irreversible electrode reaction, we observe a split in peaks of the net response. The presence of this second peak depends on the starting potential and the direction of the scan. If the starting potential of the scan $E_{start} = +0.3\text{V}$ *vs* E^{θ} as shown in Figure A.10a, the relatively flat response of the reverse component indicates that re-oxidation of the product does not occur during the short period of the SW pulse. The net response is therefore a single peak which corresponding primarily to the increased rate of reduction during the forward scan.

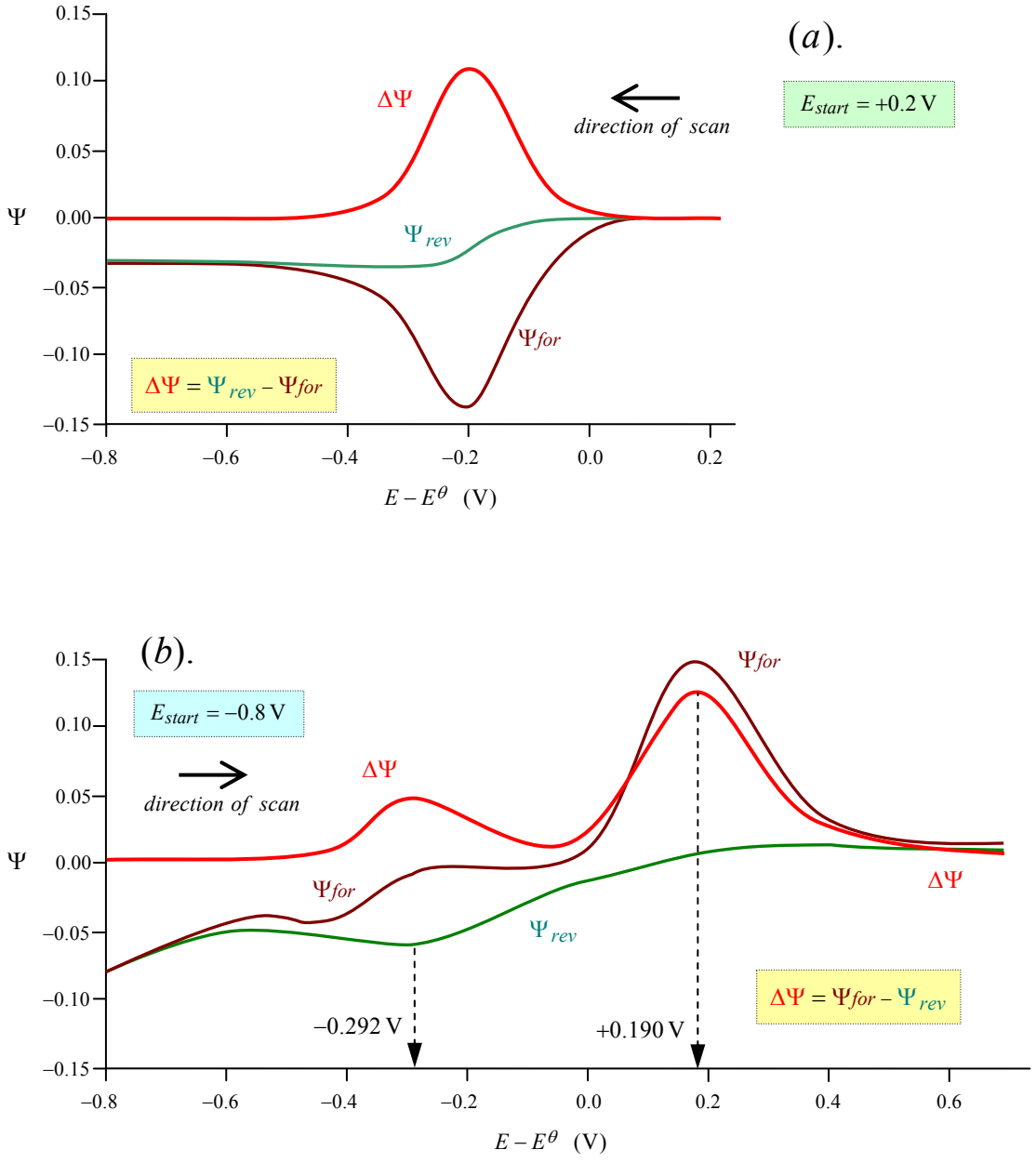

Figure A.10 Simulation of SWV for an irreversible electrode reaction (Eqn A.1).
Case (a). $E_{start} = 0.3\text{V}$ and $nE_{step} = -2mV$. **Case (b).** $E_{start} = -0.8\text{V}$ and $nE_{step} = +2mV$.
Other parameters are $\alpha = 0.5$, $\kappa = 0.015$ and $nE_{SW} = 50mV$.

However, if the starting potential $E_{start} = -0.8\text{V}$ *vs* E^{θ} as shown in Figure A.10b, two peaks are observed in the net response. The split appears because a certain amount of product will have accumulated during the period when the reaction is held at a potential more negative than the redox potential. As the scan approaches E^{θ} from a more negative potential, the rate of reduction will be greater during the reverse (reductive) SW pulses compared to the rate of reduction during the forward (oxidative) SW pulses. This is demonstrated by an increased minimum for the reverse component (at $-0.292\,\text{V}$) and a small maximum of the forward component. It is only when the potential becomes more positive than E^{θ} does the entire accumulated product become re-oxidized. This is observed as a maximum of the forward component at around $+0.190\,\text{V}$. The size of this peak will depend on the accumulation period and therefore how long the reaction is held at the starting potential.

This technique was used on several occasions during the voltammetry experiments to detect and confirm the presence of a second redox species. For example, the reduction of the flavin component of flavin-fumaramide [2]rotaxane during the forward SW pulse would induce a rapid translocation of the benzylic amide macrocycle from the fumaramide station to the flavin to produce an electrochemically more stable flavin [2]rotaxane co-conformation. Consequently the re-oxidation peak would be absent during the reverse SW pulse. It is only through the accumulation of this reduced flavin [2]rotaxane co-conformation at the electrode prior to the SW scan are we able the re-oxidation peak.

A.6 Surface electrode reactions.

Surface electrode reactions encompass any reaction where the electroactive species are confined to a narrow region of limited diffusion close to the electrode surface. Immobilization of the electroactive species within this region can take the form of absorption, self-assembly, covalent bonding, etc. However in keeping to the context of this thesis, several electrochemistry experiments were carried out during this research involving electro-inactive polymers attached to a single electroactive flavin unit. The polymers were either applied directly to the electrode surface as a paste or the working electrode was inserted into a viscous polymer-electrolyte solution. In this latter case, the diffusion coefficients of the polymers could be measure by Dynamic Light Scattering (DLS) and shown to be in the order of $10^{-8} cm^2 s^{-1}$. The diffusion coefficients of typical small molecules are generally in the order of $10^{-5} cm^2 s^{-1}$, a factor of 1000 times faster. Although diffusion of the electroactive species close to the electrode is influence by a concentration gradient generated during the experiment, for calculation purposed it is generally assumed constant. [93] However, any weak concentration gradient generated by compositionally similar oxidized and reduced flavin-polymer units along with their large, bulky hydrodynamic diameter would seems to suggest that mass transport of material in and out of the layer next to the electrode surface is likely to remain frozen for the duration of the scan. Putting guesses and assumptions aside, it would be prudent to make comparisons with theoretical models describing surface and dissolved electroactive species with actual responses.

Mathematical modelling processes used to describe the immobilized electroactive material at the electrode, start by assuming the total surface concentration of the redox material at the electrode surface remains fixed throughout the reaction and as a consequence mass transport is no longer considered. This surface concentration is given a new symbol $\Gamma\ (mol\ cm^{-2})$ to distinguish it from the diffusion dependant surface concentration $c\ (mol\ cm^{-3})$. The surface reaction is typically of the form given in Equation 1.6, where the term *(ads)* defines both R and O as absorbed or immobilized species.

$$O^{m+}_{(ads)} + ne^- \rightleftharpoons R^{(m-n)+}_{(ads)} \qquad \text{Eqn (A.6)}$$

The total concentration Γ^* at any point during the experiment will remain fixed and equal to the sum of the surface concentration of reductant R and oxidant O.

$$\Gamma_R + \Gamma_O = \Gamma^* \qquad \text{Eqn (A.7)}$$

The dimensionless current Ψ (note: a function of concentration) now becomes …

$$\Psi = \frac{I}{nFA\Gamma^* f} \qquad \text{Eqn (A.8)}$$

and the dimensionless electrode kinetic parameter is given a new symbol ω, where…

$$\omega = \frac{k_{sur}}{f} \qquad \text{Eqn (A.9)}$$

and k_{sur} is known as the *surface standard rate constant*. Its units are s^{-1}. In comparison, the units of the heterogeneous standard rate constant k_S are $cm\ s^{-1}$.

In the complex equations involved in solving the mathematical model of the surface electrode reaction (refer to *reference 97*) the *dimensionless current* Ψ is shown to be dependant on the kinetic parameters ω, the transfer coefficient α_a and the SW amplitude E_{SW}. The "*reversibility"* of the electrode reaction is predominately defined by the *dimensionless kinetic parameter* ω. The value of ω can dramatically alter the shape, size and position of the voltammetric response and this effect is illustrated in Figure A.11. The overall response increases from practically base level for very slow electrode reactions, i.e. $\log(\omega) < -1.5$ then increases to displays an overall maximum at about $\log(\omega) = 0$. The net response then diminishes for faster electrode reactions and eventually begins to show a characteristic splitting of the peak for values of $\log(\omega) > 0.5$. These two peaks continue to diminish in size as the separate before eventually disappearing for very fast electrode reactions, i.e. $\log(\omega) > 1.5$. True reversible reactions thus display no response.

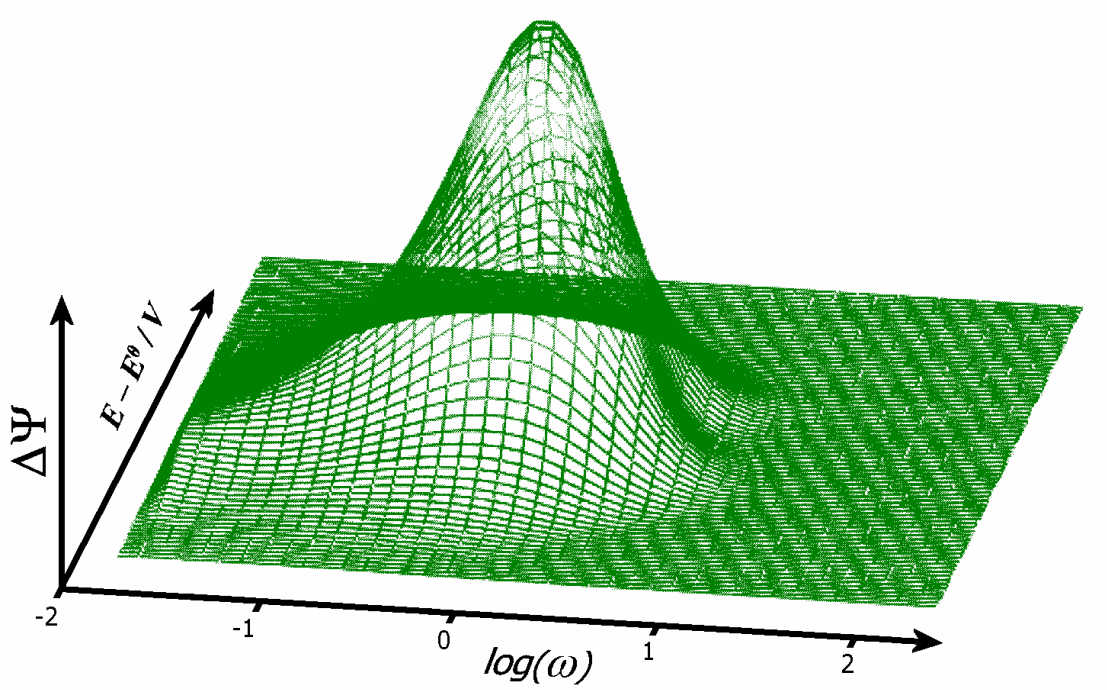

Figure A.11 Theoretical net voltammograms simulated for different values of ω. The electrode kinetic parameter increases from left to right in increments of 0.1 from $\log(\omega) = -1.7$ to 2.2. Other parameters are $\alpha_a = 0.5$, $nE_{step} = 2\,\text{mV}$ and $nE_{SW} = 50\,\text{mV}$.
Partly revised from reference [92].

The reversible electrode reaction shown in Figure A.12a ($\omega = 5$), indicates how the splitting of the overall response $\Delta\Psi$ is shaped by the peak positions of the forward and reverse components (Ψfor and Ψrev) of the SW response being situated either side of the formal potential E^θ. As the electrode reaction becomes slower, Figure A.12b ($\omega = 0.9$), shows the peak positions of Ψfor and Ψrev begin to merge towards E^θ. The value of $\Delta\Psi$ for this midrange value of $\omega = 0.9$ is the highest of all four diagrams shown in Figure A.17. As the electrode reactions continue to slow for $\omega = 0.1$ and $\omega = 0.01$ in Figures A.17c&d, the peak positions of Ψfor and Ψrev are roughly in sync but have started to shift to more positive values relative to E^θ. The magnitude of Ψrev has also started to decrease relative to Ψfor and for $\omega = 0.01$ has even started to reverse sign ($-ve$ to $+ve$). This results in the net response $\Delta\Psi$ having a lower value than Ψfor.

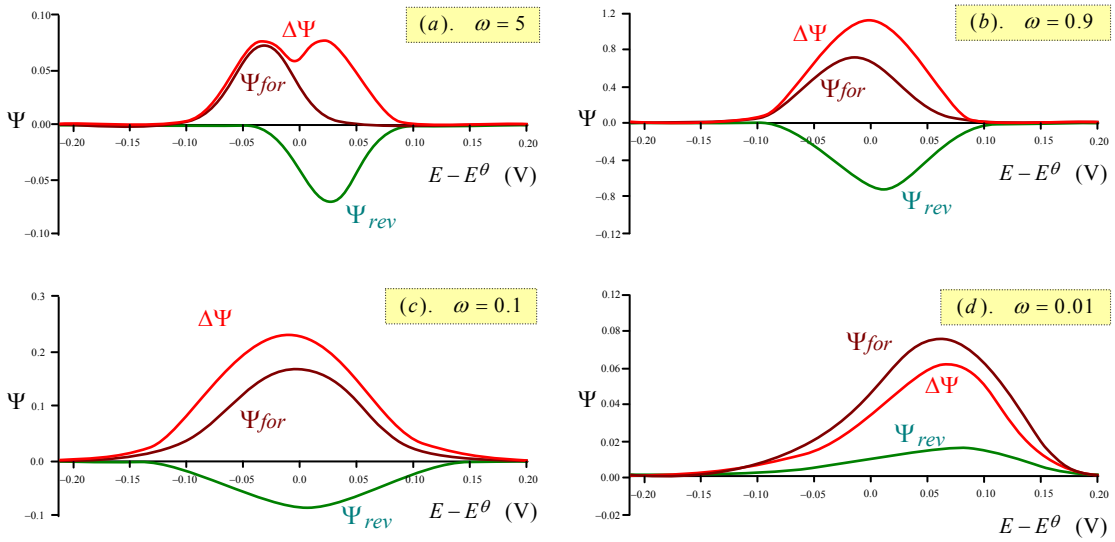

Figure A.12(a-d) Theoretical voltammograms simulated for (a). fast $\omega = 5$ to (d). slow $\omega = 0.01$ electrode reactions. Symbols Ψ_{for}, Ψ_{rev} and $\Delta\Psi$ are the forward, reverse and overall response currents of the SW voltammogram.
Other parameters are $\alpha_a = 0.5$, $nE_{SW} = 50\,\text{mV}$ and $nE_{step} = 5\,\text{mV}$.

Figure A.13 shows a cross sectional view of the parabolic response displayed in Figure A.11. It identifies three distinct regions with respect to electrochemical reversibility. For values of $\log(\omega) < -2$ the reaction is identified as totally irreversible and for values of $\log(\omega) > 1$ the reaction is reversible. In between these intervals the reaction is quasireversible and the maximum in this region is called the "*quasireversible maximum*".

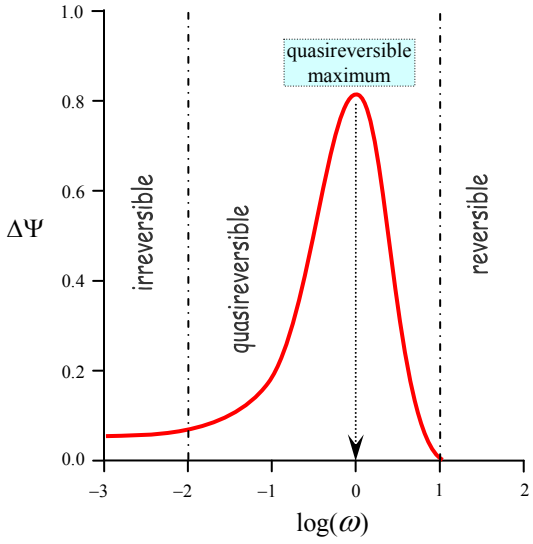

Figure A.13 Cross sectional view of the parabolic response displayed in Figure A.11, where Ψ_{net} is a function of $\log(\omega)$. Maximum response is found within the quasireversible region between $-2 < \log(\omega) < 1$. The "quasireversible maximum" is located around $\log(\omega) = 0$.

The *quasireversible maximum* was briefly mentioned in Section A.2 as a consequence of the sampling procedure. The combination of a small SW amplitude and narrow pulse width within which equilibrium is quickly established between the immobilized redox species. We can see the effects of this by examining the chronoamperogram in Figure A.14, recorded for a simulation of a surface reaction at different standard rate constants when the SW pulse is centred at the formal potential E^{θ}.

Figure A.14 show the variation in response for five different surface reaction rates, each response is recorded at the end of the SW pulse of a fixed duration equal to 10 ms (corresponding to SW pulse frequency of 50 Hz). If the reaction is very slow, a low current will be collected (e.g. $k_{sur} = 1$ and 10 s^{-1}) however if the reaction is very fast, a larger current will be produced but within the same time period the current will have severely decay and the reading will be also low (e.g. $k_{sur} = 100$ and 500 s^{-1}). Maximum response is seen to occurs at $k_{sur} = 50$ s^{-1} which coincidently is equal to the frequency of the SW pulse (50 Hz or s^{-1}). It turns out that the maximum response (i.e. the quasireversible maximum) occurs when the ratio of k_{sur} to the frequency f is approximately equal to 1. By adjusting the frequency of the SW pulse to accommodate the rate of the reaction an optimum response can be obtained. This maximum occurs at the "critical kinetic parameter" $\omega_{max} \simeq 1$. The frequency which satisfies this condition is called the "critical frequency", f_{max}. At this frequency the rate of reaction becomes synchronised with the duration of the pulses enabling repetitive reuse of the immobilized electroactive material. The forward and backward components of the response become strongly enhanced with minimal separation of peak position which reinforces the net response to produce that largest and narrowest peak.

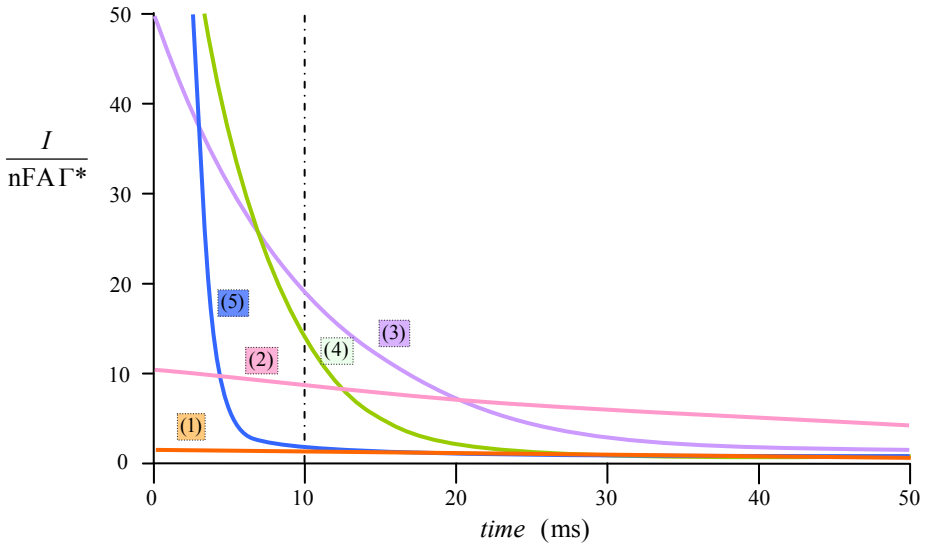

Figure A.14 Theoretical chronoamperogram simulated for SW pulse centred at $E = E^{\theta}$ for five different values of k_{sur} = 1 (1); 10 (2); 50 (3); 100 (4); 500 s^{-1} (5).
Current sampled at the end of a SW pulse of fixed duration = 10 ms (dashed vertical line).

A.6.1 Experimental data obtained from peak separation.

The characteristic splitting of the net response peak observed in reversible surface electrode reactions develops as a function of increasing ω and normalised SW amplitude nE_{SW}. The splitting tends to occur around $\log(\omega) > 0.5$ as shown in Figure 15a. The forward and backward components move in opposite directions in proportion to increases in ω and the net peak response becomes smaller and broader as shown in Figure A.15b. The direction of peak shift provides a useful method of distinguishing between surface electrode reactions and diffusion controlled processes. The forward (oxidative or anodic) and reverse (reductive or cathodic) components shift towards more negative and more positive potentials respectively. This is opposite to the quasireversible reaction model of a dissolved redox couple observed during either SWV or Cyclic Voltammetry experiments.

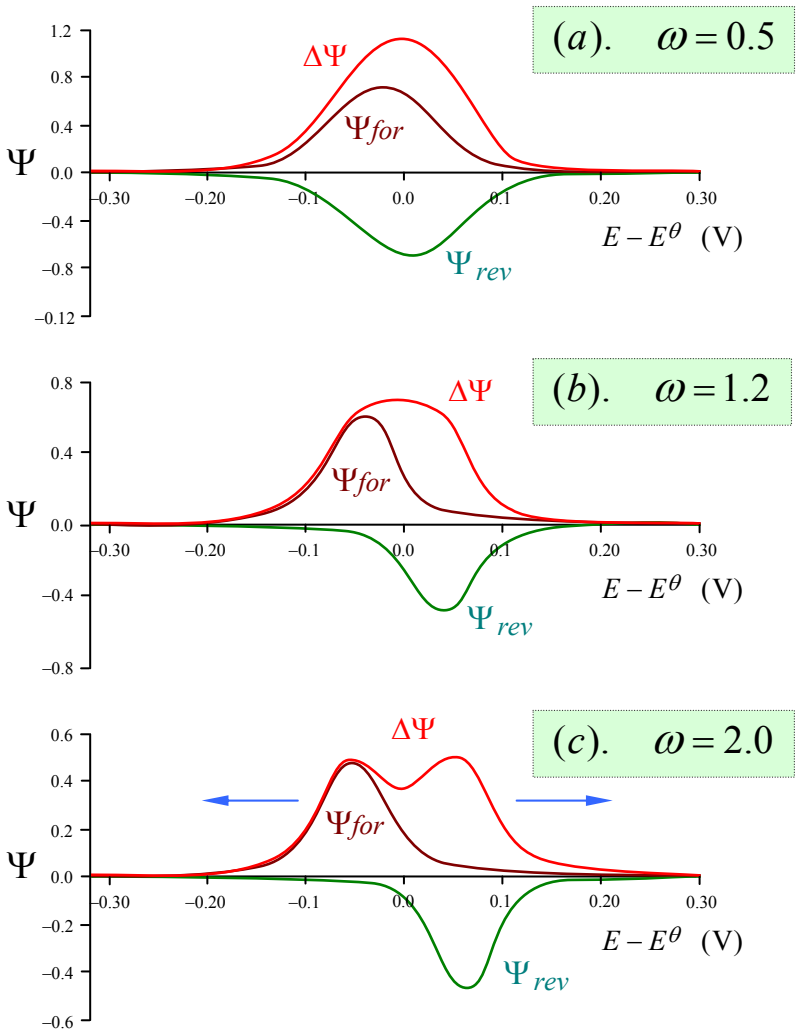

Figure A.15 Theoretical voltammograms simulated for $\omega = 0.5$ (**a**); 1.2 (**b**); 2 (**c**). Other parameters are: $\alpha_a = 0.5$, $nE_{step} = 5\,\text{mV}$ and $nE_{SW} = 80\,\text{mV}$.

One particularly useful feature of splitting is that precise determination of the formal potential E^θ of the surface electrode reaction can easily be obtained because the split peaks will be symmetrically located either side of it, as shown in Figure A.15c.

A.7 Summary.

This section on SWV has focused on model systems solely for dissolved and immobilized redox reactions at a stationary planar electrode. The scope of coverage found in reference [92] extends further to include EC reactions (as described by the Testa and Reinmuth notation where the **E**lectrode reaction is followed by a **C**hemical reaction), CE reactions, ECE reactions, EC' (electrode catalytic reactions) for dissolved, immobilised or a combination of dissolved and immobilized redox couples at both stationary planar electrodes and non-planar microelectrodes, etc,. This brief discussion on SWV was primarily intended to introduce the reader to the SWV technique which is a very useful but elusively described in literature. The used of SWV to help unravel the mechanisms involved during the ECE reactions of the electroactive flavin will be continued during the "Conclusion" sections found at the end of each relevant chapter.

Appendix B:

The transfer coefficient α.

B.1. The definition of the transfer coefficient.

Figure B.1 shows at a quick glance that at the transfer coefficient α is related to the symmetry of the free energy profiles of the redox reaction shown in Equation (B.1). The horizontal axis labelled here as the "reaction coordinate" is an arbitrary axis representing the motion of all the atomic nuclei. When $\alpha = 0.5$ the profiles are symmetrical for other value of α the free energy profiles are asymmetrical.

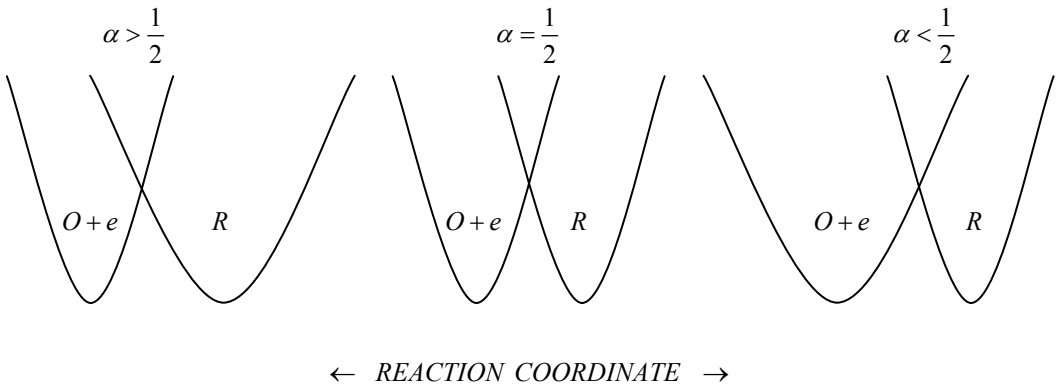

Figure B.1 Free energy profiles for a redox reaction (Eqn B.1) showing the transfer coefficient α, is an indicator of the symmetry of the energy barrier to an electron transfer reaction.

$$O + e^- \underset{k_h}{\overset{k_f}{\rightleftharpoons}} R \qquad \text{(B.1)}$$

Figure B.2 gives a pictorial comparison of the two extremes shown above for $\alpha > 0.5$ and $\alpha < 0.5$ and emphasises the effect a relative shift in the free energy $\Delta(\Delta G^o)$ has on decreasing the energy barrier ΔG_f.

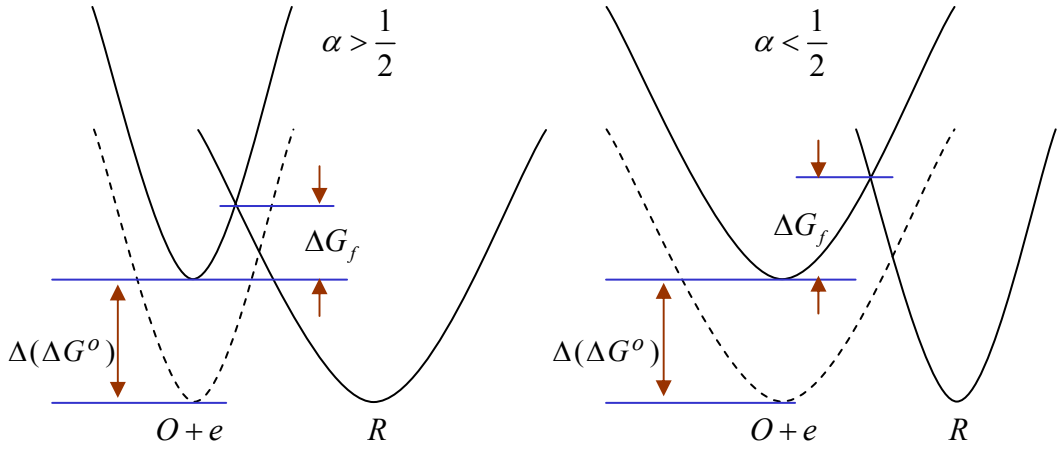

Figure B.2 A pictorial comparison of the two extremes where $\alpha > 0.5$ and $\alpha < 0.5$ showing how if the free energy of the system is change by $\Delta(\Delta G^o)$ (same reaction coordinate spacing) a smaller energy barrier ΔG_f need to be surmounted and hence a faster (forward) electron transfer is achieved when the transfer coefficient is $\alpha > 0.5$.

It can be seen that when $\alpha > 0.5$ the energy barrier ΔG_f is smaller and consequently the rate of electron transfer in the forward direction will be faster. This energy barrier is much larger when the same free energy input is applied to a system where α is less than unity. The transfer coefficient α could therefore be considered as a measure of the systems electron transfer efficiency. Although values of the transfer coefficient can be found to be between $0.1 < \alpha < 0.9$, the typical value found is $\alpha = 0.5$ as most energy profiles are generally symmetrical.

There are many good references [61, 62] explaining the theory and calculations behind the transfer coefficient, but a few key features will be emphasized. At zero overpotential (or standard potential) for the redox reaction shown in Equation B.1 the heterogeneous rates of forward electron transfer and the backward electron transfer are equal to the standard heterogeneous rate constant, i.e, $k_f = k_b = k_o$. The standard heterogeneous rate constant k_o is also known for this reason as the standard ET "exchange" rate constant at zero driving force and is defined according to the Arrhenius equation as…

$$k_o = Ae^{-\Delta G^o/RT} \tag{B.2}$$

…where A is the pre-exponential factor.

When a potential difference $E - E^\theta$ is applied to the electrode the free energy of the system will change, $k_f \neq k_b$ and current will start to flow. The forward and backward electron transfer rate constants consequently become…

$$k_f = Ae^{-\Delta G_f/RT} = Ae^{-\Delta G^o/RT}\ e^{-\alpha nF(E-E^\theta)/RT} \tag{B.3}$$

$$\therefore \qquad k_f = k_o\ e^{-\alpha nF(E-E^\theta)/RT}$$

and

$$k_b = Ae^{-\Delta G_b/RT} = Ae^{-\Delta G^o/RT}\ e^{(1-\alpha)nF(E-E^\theta)/RT} \tag{B.4}$$

$$\therefore \qquad k_b = k_o\ e^{(1-\alpha)nF(E-E^\theta)/RT}$$

… where n, F, R, T *and* E^θ have their usual meanings .

The exponential effect of voltage change on the rate constants can clearly be seen. Just by altering the overpotential by 1 Volt and making $E = E^\theta - 1$ with a typical value of $\alpha = 0.5$ will increase the forward rate constant k_f by a factor of over 5×10^8 at room temp. This factor becomes 4.4×10^{15} when the transfer coefficient increases to $\alpha = 0.9$. This difference dramatically highlights the influence the transfer coefficient bears on the electron transfer rate over small potential difference beyond the formal potential of a redox system and subsequently the rate at which that species would be depleted at the electrode surface and how that might impact the profile of a voltammogram. It can however be shown (Appendix C: Marcus theory) that this exponential increase in forward electron transfer rate does not continue indefinitely.

Appendix C:

Marcus Theory.

C.1. A brief introduction to Marcus theory.

Marcus theory has been used to describe deviations observed in the transfer of electron rates predicted by the Butler-Volmer model, and explains a number of important processes in chemistry and biology, including photosynthesis, corrosion, chemiluminescence, and charge separation in solar cell. It is basically a modified form of the Eyring-Polanyi equation shown in Equation C.1, where k_{et} is the electron transfer rate, k_B is the Boltzmans constant, $\hbar$ is Planks constant, T is absolute temperature and ΔG^* is the energy of activation.

$$k_{et} = \frac{k_B T}{\hbar} \cdot \exp^{-\frac{\Delta G^*}{k_B T}} \qquad \text{(C.1)}$$

Figure C.1 show the free energy profiles of a redox reaction. Marcus simplified the calculations for determining the activation energy ΔG^* by representing the energy profiles of reactant and product as quadratic parabolas and the motion of the electron within those profiles as simple harmonic oscillations. [94] This lead to the simple formulae for ΔG^* shown in Equation C.2.

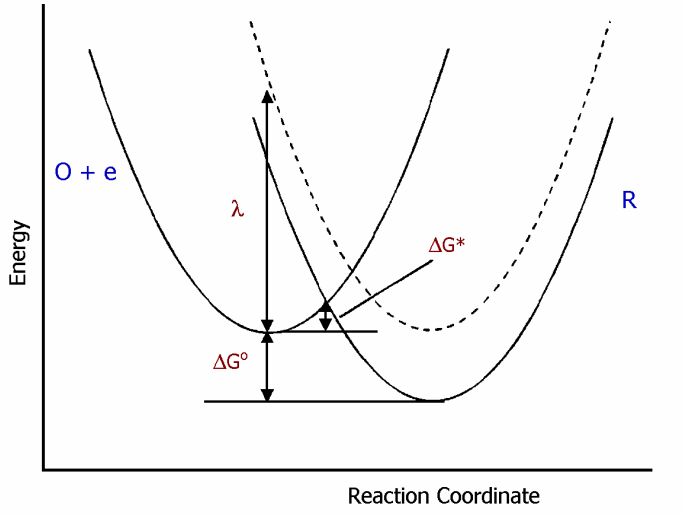

Figure C.1 Free energy profiles showing relevant kinetic parameters for the electron transfer process.

$$\Delta G^* = \frac{(\lambda + \Delta G^o)}{4\lambda} \qquad \text{(C.2)}$$

where ΔG^o is the free energy difference product and reactant and λ is the total reorganizational energy and represents the vertical energy necessary to transfer the nuclear configuration of the reactant and the solvent to those of a product state (as represented in Figure C.1 by the dashed parabola) in a virtual isergonic process.

The reorganizational energy λ is made up from two components called the inner λ_i and the outer λ_o reorganizational energies. The first term λ_i is due to the vibrational rearrangement (bending & stretching of bond) following electron transfer. The second term λ_i arises from the reorganization of surrounding solvent molecules (repolarisation) that must take place after electron transfer. (In reference to experiments carried out in this Thesis the solvent molecules would be replaced by the polymer encapsulating the electroactive flavin).

Using a number of quantum mechanical approximations, Marcus eventually ended up with the expression for non-adiabatic electron transfer rate shown in Equation C.3.

$$k_{et} = \frac{2\pi}{\hbar} H_{AB}^2 \frac{1}{\sqrt{4\pi\lambda k_B T}} \cdot \exp^{-\frac{(\lambda+\Delta G^o)}{4\lambda k_B T}} \qquad \text{(C.3)}$$

where H_{AB}^2 is the resonance energy describing the electronic coupling of the reactants electronic state with the products and is equal to one-half the separation (dashed curves) at the intersection of the reactant and product surfaces as shown in Figure C.2

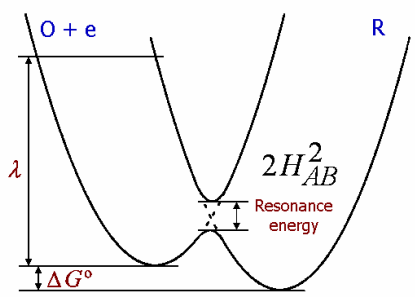

Figure C.2 Free energy plot showing the resonance energy of the electronic coupling between reactant and product electronic states. H_{AB}^2 is equal to half the separation at the intersection.

Armstrong [95] adopted a method to calculate the electrochemical rate constants as a function of potential using the Marcus equation for non-adiabatic electron transfer in combination with the Fermi-Dirac distribution, since electron transfer can occur to or from any Fermi level in the electrode.

The resulting equation was the following complicated looking equation …

$$k_{red/ox} = k_{\max} \sqrt{\frac{RT}{4\pi\lambda}} \int_{-\infty}^{\infty} \frac{\exp\{-\{(\lambda \pm F(E-E^{\theta})/RT - x\}^2 RT/4\lambda\}}{\exp(x)+1}\, dx \qquad \text{(C.4)}$$

where…

$$k_{\max} = \frac{4\pi^2}{N_A \hbar} V_o^2 e^{-\beta r} \frac{1}{RT} \qquad \text{(C.5)}$$

and depending on whether the equations is used to derive k_{red} or k_{ox} …

$$x = (E - E_i)F / RT \qquad \text{for } k_{red}$$

and $$x = (E_i - E)F / RT \qquad \text{for } k_{ox}.$$

Equation C.4 show that as the overpotential $E - E^{\theta}$ increases toward infinity the limit of the electron transfer rate $k_{\max}$ is ultimately reached and Equation C.5 show that this maximum is independent of λ. Chidsey [96] described a technique that measure the electron transfer rates k_{red} and k_{ox} by best fitting the current transient decay of potential-step experiments. As predicted by the Butler-Volmer equation the sum of $k_{red} + k_{ox}$ increased exponentially at low overpotential. As predicted by Marcus this then begins to plateau as the electron transfer rate approaches $k_{\max}$ passing through $0.5k_{\max}$ at an overpotential equal to λ. [36] Therefore as can be seen in Figure C.3, higher values of the reorganizational energy λ do tend to lead to a higher value of $k_{red} + k_{ox}$ and hence $k_{\max}$. Figure C.4 demonstrates how the value $k_{\max}$ can be estimated using digital simulation. The figure effectively shows a plot of I_{for} and I_{rev} peak separation versus SW frequency for three different values of $k_{\max}$. It can clearly be seen that the peaks converge earlier for the lower values of $k_{\max}$.

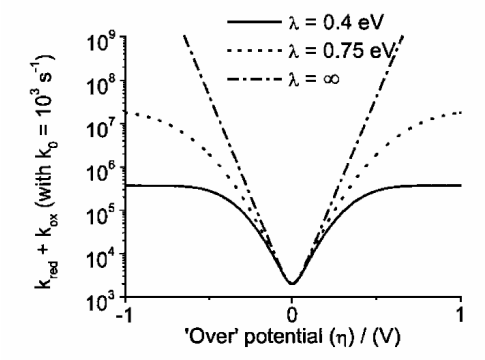

Figure C.3 Theoretical Tafel plot ($[k_{red} + k_{ox}]$ *versus* $\eta = \mathrm{E} - \mathrm{E}^{\theta}$) based on Marcus theory with $k_o = 10^3 s^{-1}$ and λ as shown in the figure. Reference [36].

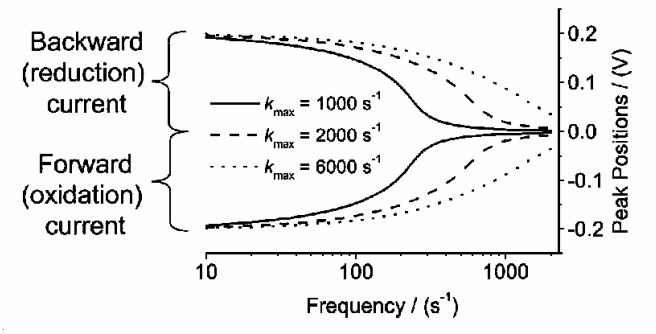

Figure C.4 Square wave voltammetry simulation showing the variation of forward and backward peak positions as a function of frequency on the value of $k_{\max}$. Reference [42].

Marcus [94] also shows the transfer coefficient α to be dependant on the Gibbs energy ΔG^o and the reorganizational energy λ according to Equation (C.6).

$$\alpha = \frac{1}{2}\left(1 + \frac{\Delta G^o}{\lambda}\right) \qquad \text{(C.6)}$$

Since the Gibbs energy term is not fixed and is dependant on electrode potential changes, α will therefore also vary with overpotential. At potentials close to the formal potential E^θ, $\Delta G^o \simeq 0$ and hence $\alpha \to 1/2$. However if $\Delta G^o \gg 0$ (i.e. $\Delta G_P - \Delta G_R$ is positive) and the reaction is thermodynamically uphill and as a consequence $\Delta G^o/\lambda \to 1$ and $\alpha \to 1$. However when the reaction is driven hard by the electrode potential and $\Delta G^o \ll 0$ (i.e. $\Delta G_P - \Delta G_R$ is negative) $\Delta G^o \to -\lambda$ and $\alpha \to 0$. Here electron transfer becomes favourable and the kinetics moves into the "Normal" regime as shown in Figure C.5. This is one of three kinetic regimes identified by the Marcus theory and which are classified according to the dependence of the electron transfer rate on the driving force. Within the "Normal" regime a small increase in the driving force will cause a similar change in the electron transfer rate and vice versa. Alternatively within the "Activationless" regime $-\lambda = \Delta G^o$ (Figure C.5), altering the driving force makes no difference to the electron transfer rate.

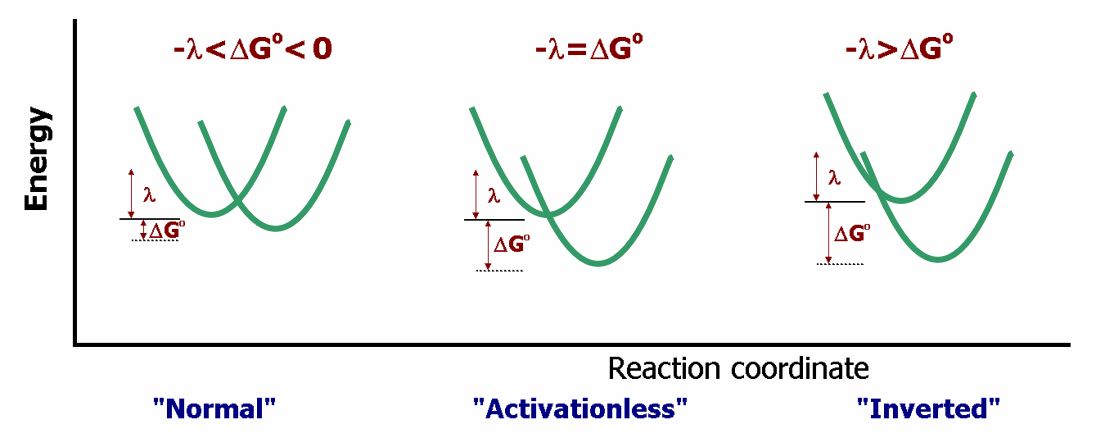

Figure C.5 Free energy curves for reactant and product states of an electron transfer process in the three kinetic regimes of the Marcus model. Remember that ΔG^o is negative therefore if we substitute some imaginary values for ΔG^o using a fixed value of $\lambda = 1.0\ eV$ the conditions become clearer. For example, $\Delta G^o = -0.5eV$ (Normal), $\Delta G^o = -1.0eV$ (Activationless) and $\Delta G^o = -1.5eV$ (Inverted). Revised from reference [97].

However, one significant prediction of the Marcus theory was that of the "Inverted" regime, also shown in Figure C.5, where $-\lambda > \Delta G^o$. Here the electron transfer rate will actually decrease with increasing driving force for strongly exergonic reactions. However, where as in the "normal" regime increasing λ will slow down electron transfer, it will accelerate it in the inverted regime. This remarkable result has important implications in both natural and artificial photosynthesis and energy conversion. It predicts that following electron transfer quenching of the excited state A^*-B to the charge separated species $A^+ - B^-$, any subsequent back transfer of the electron while in the inverted regime will become slower as the energy stored increases. [97] This ultimately prolongs the lifetime of the sought-after charge separated species and it should be clear from Figure C.5 that his condition would be easier to achieve if the reorganizational energy λ was small.

REFERENCES.

References:

[1] S. Ghisla, V. Massey, *European Journal of Biochemistry* **1989**, *181*, 1-17.

[2] F. Mueller, *Topics in Current Chemistry* **1983**, *108*, 71-107.

[3] F. Mueller, *Chemistry and Biochemistry of Flavoenzymes, Vol. 1, 2 & 3*, **1991-1992**.

[4] A. Niemz, V. M. Rotello, *Accounts of Chemical Research* **1999**, *32*, 44-52.

[5] A. Niemz, J. Imbriglio, V. M. Rotello, *Journal of the American Chemical Society* **1997**, *119*, 887-892.

[6] A. Niemz, V. M. Rotello, *Journal of the American Chemical Society* **1997**, *119*, 6833-6836.

[7] A. Mattevi, G. Obmolova, K. H. Kalk, W. J. H. van Berkel, W. G. J. Hol, *Journal of Molecular Biology* **1993**, *230*, 1200-1215.

[8] E. Breinlinger, A. Niemz, V. M. Rotello, *Journal of the American Chemical Society* **1995**, *117*, 5379-5380.

[9] A. Niemz, V. M. Rotello, *Journal of Molecular Recognition* **1996**, *9*, 158-162.

[10] M. L. Ludwig, C. L. Luschinsky, *Chem. Biochem. Flavoenzymes* **1992**, *3*, 427-466, 422 plates.

[11] W. Watt, A. Tulinsky, R. P. Swenson, K. D. Watenpaugh, *Journal of Molecular Biology* **1991**, *218*, 195-208.

[12] R. P. Swenson, G. D. Krey, *Biochemistry* **1994**, *33*, 8505-8514.

[13] E. C. Breinlinger, V. M. Rotello, *Journal of the American Chemical Society* **1997**, *119*, 1165-1166.

[14] *Handbook of Radical Polymerization* Vol, K. M. a. T. P. Davis (Ed.), John Wiley & Sons, **2002**.

[15] T. E. Patten, K. Matyjaszewski, *Advanced Materials (Weinheim, Germany)* **1998**, *10*, 901-915.

[16] J. Lad, S. Harrisson, G. Mantovani, D. M. Haddleton, *Dalton Transactions* **2003**, 4175-4180.

[17] K. Matyjaszewski, *Macromolecules* **1998**, *31*, 4710-4717.

[18] K. Matyjaszewski, *Development of Controlled Living Radical Polymerization*, http://www.chem.cmu.edu/groups/maty/about/research/02.html, *Feb 2009*.

[19] H. G. Kim, C.-W. Lee, S. Yun, B. H. Hong, Y.-O. Kim, D. Kim, H. Ihm, J. W. Lee, E. C. Lee, P. Tarakeshwar, S.-M. Park, K. S. Kim, *Organic Letters* **2002**, *4*, 3971-3974.

[20] E. M. Pérez, D. T. F. Dryden, D. A. Leigh, G. Teobaldi, F. Zerbetto, *Journal of the American Chemical Society* **2004**, *126*, 12210-12211.

[21] W. R. Browne, B. L. Feringa, *Nat Nano* **2006**, *1*, 25-35.

[22] Y. Shirai, A. J. Osgood, Y. Zhao, K. F. Kelly, J. M. Tour, *Nano Letters* **2005**, *5*, 2330-2334.

[23] P. D. Beer, P. A. Gale, D. K. Smith, *Supramolecular Chemistry*, Oxford University Press, Oxford Chemistry Primer, **1999**.

[24] P. J. Cragg, *A Practical Guide to Supramolecular Chemistry*, Wiley, **2005**.

[25] A. G. Johnston, D. A. Leigh, R. J. Pritchard, M. D. Deegan, *Angewandte Chemie, International Edition in English* **1995**, *34*, 1209-1212.

[26] A. G. Johnston, D. A. Leigh, L. Nezhat, J. P. Smart, M. D. Deegan, *Angewandte Chemie, International Edition in English* **1995**, *34*, 1212-1216.

[27] F. G. Gatti, D. A. Leigh, S. A. Nepogodiev, A. M. Z. Slawin, S. J. Teat, J. K. Y. Wong, *Journal of the American Chemical Society* **2001**, *123*, 5983-5989.

[28] M. H. Abraham, *Chemical Society Reviews* **1993**, *22*, 73-83.

[29] Y. Marcus, *Chemical Society Reviews* **1993**, *22*, 409-416.

[30] F. G. Gatti, D. A. Leigh, S. A. Nepogodiev, A. M. Z. Slawin, S. J. Teat, J. K. Y. Wong, *Journal of the American Chemical Society* **2001**, *123*, 5983-5989.

[31] D. A. Leigh, E. M. Perez, *Chemical Communications (Cambridge, United Kingdom)* **2004**, 2262-2263.

[32] A. Altieri, G. Bottari, F. Dehez, D. A. Leigh, J. K. Y. Wong, F. Zerbetto, *Angewandte Chemie, International Edition* **2003**, *42*, 2296-2300.

[33] G. Cooke, F. M. A. Duclairoir, P. John, N. Polwart, V. M. Rotello, *Chemical Communications (Cambridge, United Kingdom)* **2003**, 2468-2469.

[34] *Electroanalytical Methods*, 1st ed., Springer, **2005**.

[35] F. A. Armstrong, H. A. Heering, J. Hirst, *Chemical Society Reviews* **1997**, *26*, 169-179.

[36] L. J. C. Jeuken, J. P. McEvoy, F. A. Armstrong, *Journal of Physical Chemistry B* **2002**, *106*, 2304-2313.

[37] R. S. Nicholson, I. Shain, *Anal. Chem.* **1964**, *36*, 706-723.

[38] R. S. Nicholson, *Anal. Chem.* **1965**, *37*, 1351-1355.

[39] R. J. Klingler, J. K. Kochi, *Journal of Physical Chemistry* **1981**, *85*, 1731-1741.

[40] U. Eisner, E. Gileadi, *Journal of Electroanalytical Chemistry and Interfacial Electrochemistry* **1970**, *28*, 81-92.

[41] E. Laviron, *Journal of Electroanalytical Chemistry and Interfacial Electrochemistry* **1979**, *101*, 19-28.

[42] L. J. C. Jeuken, A. K. Jones, S. K. Chapman, G. Cecchini, F. A. Armstrong, *Journal of the American Chemical Society* **2002**, *124*, 5702-5713.

[43] J. Clayden, N. Greeves, S. Warren, p. Wothers, *Organic Chemistry*, Oxford University Press, **2001**.

[44] *Flavoprotein Protocols*, Humana Press. Totowa, New Jersey.

[45] R. D. Spencer, G. Weber, *Thermodynamics and kinetics of the intarmolecular complex in flavin-adenine dinucleotide*, Pergamon Press (N.Y), **1972**.

[46] J. R. Lakowicz, *Principles of Fluorescence Spectroscopy*, 3rd ed., Springer, **2006**.

[47] C. B. Aakeroy, K. R. Seddon, *Chemical Society Reviews* **1993**, *22*, 397-407.

[48] Atkins, in *Physical Chemistry*, 7th ed. (Ed.^(Eds.), Oxford University Press, p. 704.

[49] A. Altieri, G. Gatti Francesco, R. Kay Euan, A. Leigh David, D. Martel, F. Paolucci, M. Z. Slawin Alexandra, K. Y. Wong Jenny, *J Am Chem Soc* **2003**, *125*, 8644-8654.

[50] A. M. Brouwer, C. Frochot, F. G. Gatti, D. A. Leigh, L. Mottier, F. Paolucci, S. Roffia, G. W. Wurpel, *Science (New York, N.Y.)* **2001**, *291*, 2124-2128.

[51] P. Altoe, N. Haraszkiewicz, F. G. Gatti, P. G. Wiering, C. Frochot, A. M. Brouwer, G. Balkowski, D. Shaw, S. Woutersen, W. J. Buma, F. Zerbetto, G. Orlandi, D. A. Leigh, M. Garavelli, *Journal of the American Chemical Society* **2009**, *131*, 104-117.

[52] P. F. Heelis, *Chemical Society Reviews* **1982**, *11*, 15-39.

[53] K. Nishimoto, Y. Watanabe, K. Yagi, *Biochimica et Biophysica Acta, Enzymology* **1978**, *526*, 34-41.

[54] K. Nishimoto, E. Kai, K. Yagi, *Biochimica et Biophysica Acta, General Subjects* **1984**, *802*, 321-325.

[55] K. Yagi, N. Ohishi, K. Nishimoto, J. D. Choi, P.-S. Song, *Biochemistry* **1980**, *19*, 1553-1557.

[56] K. Nishimoto, H. Fukunaga, K. Yagi, *Journal of Biochemistry* **1986**, *100*, 1647-1653.

[57] K. Yagi, M. Osamura, N. Ohishi, *Journal of Biochemistry* **1972**, *71*, 551-553.

[58] H. Yang, G. Luo, P. Karnchanaphanurach, T.-M. Louie, I. Rech, S. Cova, L. Xun, X. S. Xie, *Science (New York, N.Y.)* **2003**, *302*, 262-266.

[59] P. A. W. Van den Berg, A. Van Hoek, C. D. Walentas, R. N. Perham, A. J. W. G. Visser, *Biophysical Journal* **1998**, *74*, 2046-2058.

[60] M. K. Singh, H. Pal, A. V. Sapre, *Photochemistry and Photobiology* **2000**, *71*, 300-306.

[61] *Laboratory Techniques in Electroanalytical Chemistry*, 2nd ed., Marcel Dekker, Inc. (N.Y), **1996**.

[62] A. J. Bard, L. R. Faulkner, *Electrochemical Methods*, 2nd ed., Wiley, **2001**.

[63] *Fluorescence Spectroscopy in Biology (*Springer Series on Fluorescence: Methods and Applications. Vol: 3), O. S. Wolfbeis (Ed.), Springer, **2005**.

[64] C. Azuma, N. Ogata, *Journal of Polymer Science, Polymer Chemistry Edition* **1974**, *12*, 751-760.

[65] P. Ceroni, D. A. Leigh, L. Mottier, F. Paolucci, S. Roffia, D. Tetard, F. Zerbetto, *Journal of Physical Chemistry B* **1999**, *103*, 10171-10179.

[66] A. Eberhard, J. W. Hastings, *Biochemical and Biophysical Research Communications* **1972**, *47*, 348-353.

[67] S. P. Vaish, G. Tollin, *Journal of Bioenergetics* **1971**, *2*, 61-72.

[68] A. Dobbs, *Radical reactions in organic chemistry*, Royal Society of Chemistry.

[69] G. Cooke, J. Garety, S. Mabruk, V. Rotello, G. Surpateanu, P. Woisel, *Chemical Communications (Cambridge, United Kingdom)* **2004**, 2722-2723.

[70] K. Cheng, C. C. Landry, *Journal of the American Chemical Society* **2007**, *129*, 9674-9685.

[71] D. H. Williams, I. Fleming, *Spectroscopic Methods in Organic Chemistry.*, 4th ed. revised ed., McGraw-Hill Book Company (UK) Limited, **1989**, Table 3.27.

[72] D. J. Frost, F. D. Gunstone, *Chem. Phys. Lipids.* **1975**, *15*, 53-85.

[73] T. Umemiya, D. Takeuchi, K. Osakada, *Journal of Organometallic Chemistry* **2006**, *691*, 5260-5266.

[74] L. B. A. Johansson, A. Davidsson, G. Lindblom, K. R. Naqvi, *Biochemistry* **1979**, *18*, 4249-4253.

[75] C. Frier, J.-L. Decout, M. Fontecave, *Journal of Organic Chemistry* **1997**, *62*, 3520-3528.

[76] I. Ishikawa, T. Itoh, R. G. Melik-Ohanjanian, H. Takayanagi, Y. Mizuno, H. Ogura, N. Kawahara, *Heterocycles* **1990**, *31*, 1641-1646.

[77] B. Zeynizadeh, T. Behyar, *Bulletin of the Chemical Society of Japan* **2005**, *78*, 307-315.

[78] K. S. Chichak, A. J. Peters, S. J. Cantrill, J. F. Stoddart, *Journal of Organic Chemistry* **2005**, *70*, 7956-7962.

[79] V. Rossetti, A. Dondoni, G. Fantin, (Francis S.p.A., Italy). Application: FR, **1984**, p. 11 pages.

[80] A. G. Johnston, D. A. Leigh, A. Murphy, J. P. Smart, M. D. Deegan, *Journal of the American Chemical Society* **1996**, *118*, 10662-10663.

[81] H. Brunner, N. Gruber, *Inorganica Chimica Acta* **2004**, *357*, 4423-4451.

[82] D. Felder, M. D. P. Carreon, J.-L. Gallani, D. Guillon, J.-F. Nierengarten, T. Chuard, R. Deschenaux, *Helvetica Chimica Acta* **2001**, *84*, 1119-1132.

[83] J. J. Ferreiro, J. G. de la Campa, A. E. Lozano, J. de Abajo, J. Preston, *Journal of Polymer Science, Part A: Polymer Chemistry* **2007**, *45*, 4671-4683.

[84] G. Cooke, J. F. Garety, B. Jordan, N. Kryvokhyzha, A. Parkin, G. Rabani, V. M. Rotello, *Organic Letters* **2006**, *8*, 2297-2300.

[85] S. T. Caldwell, G. Cooke, B. Fitzpatrick, D.-L. Long, G. Rabani, V. M. Rotello, *Chemical Communications (Cambridge, United Kingdom)* **2008**, 5912-5914.

[86] M. S. Krause, Jr., L. Ramaley, *Anal. Chem.* **1969**, *41*, 1365-1369.

[87] L. Ramaley, M. S. Krause, Jr., *Anal. Chem.* **1969**, *41*, 1362-1365.

[88] J. Osteryoung, *Accounts of Chemical Research* **1993**, *26*, 77-83.

[89] R. A. Osteryoung, J. Osteryoung, *Philosophical Transactions of the Royal Society of London, Series A: Mathematical, Physical and Engineering Sciences* **1981**, *302*, 315-326.

[90] D. P. Whelan, J. J. O'Dea, J. Osteryoung, K. Aoki, *Journal of Electroanalytical Chemistry and Interfacial Electrochemistry* **1986**, *202*, 23-36.

[91] J. H. Christie, J. A. Turner, R. A. Osteryoung, *Anal. Chem.* **1977**, *49*, 1899-1903.

[92] V. Mirčeski, Š. Komorsky-Lovrie, M. Lovrić, *Square Wave Voltammetry*, Springer, **2007**.

[93] R. G. Compton, C. E. Banks, *Understanding Voltammetry*, World Scientific.

[94] R. A. Marcus, N. Sutin, *Biochimica et Biophysica Acta, Reviews on Bioenergetics* **1985**, *811*, 265-322.

[95] J. Hirst, F. A. Armstrong, *Anal. Chem.* **1998**, *70*, 5062-5071.

[96] C. E. D. Chidsey, *Science (New York, N.Y.)* **1991**, *251*, 919-922.

[97] *Electrochemistry of Functional Supramolecular Systems (*Wiley Series on Electrocatalysis and Electrochemistry Vol: 2), P. Ceroni, A. Credi, M. Venturi (Eds.), Wiley, **2010**.